TESIS DE LA UNIVERSIDAD DE ZARAGOZA
2024 365

Miguel Pardo Sainz

Non-collinear magnetism in chiral, spinel and organic magnets
TESIS CORREGIDA

Director/es
Hosokoshi, Yuko
Campo Ruiz, Jesús Javier

ISSN 2254-7606

Prensas de la Universidad
Universidad Zaragoza

Universidad de Zaragoza
Servicio de Publicaciones

ISSN 2254-7606

Universidad Zaragoza
1542

Tesis Doctoral

NON-COLLINEAR MAGNETISM IN CHIRAL, SPINEL AND ORGANIC MAGNETS
TESIS CORREGIDA

Autor

Miguel Pardo Sainz

Director/es

Hosokoshi, Yuko
Campo Ruiz, Jesús Javier

UNIVERSIDAD DE ZARAGOZA
Escuela de Doctorado

Programa de Doctorado en Física

2024

Universidad Zaragoza
1542

Tesis Doctoral

Non-collinear magnetism in chiral, spinel and organic magnets

Autor

Miguel Pardo Sainz

Director/es

Jesús Javier Campo Ruiz
Yuko Hosokoshi

Facultad de Ciencias

2024

"It's the questions we can't answer that teach us the most. They teach us how to think. If you give a man an answer, all he gains is a little fact. But give him a question and he'll look for his own answers."

- Patrick Rothfuss, The Wise Man's Fear

Acknowledgements

This journey has been one of personal and academic growth, a path illuminated by the support and guidance of many who have contributed to the completion of this thesis.

First and foremost, I extend my deepest gratitude to my supervisor, Javier, whose mentorship has been invaluable since our paths crossed six years ago. His unwavering support, insightful feedback, and encouragement have been pivotal to my development as a researcher and individual. I am equally indebted to my co-supervisor, Yuko Hosokoshi, for the opportunity to study in Japan and broaden my perspectives. Yuko's expertise, patience, and guidance have enriched my experience and contributed significantly to the success of this project.

The collaborative efforts of numerous individuals have been essential to the experiments conducted for this thesis. I wish to express my sincere appreciation to all the collaborators for their dedication, insights, and the sharing of their expertise. Their contributions have not only enriched the research but also my personal development within the academic field. In particular, I would like to thank Prof. Yusuke Kousaka for the samples provided; Dr. Kenji Kojima, Dr. Kazuki Ohishi, and Prof. Masaki Mito for their invaluable help with the measurement and analysis of μSR, SANS, and a.c. magnetization experiments, respectively. I am also grateful to Dr. Alberto Rodríguez-Velamazán, Dr. Oscar Fabelo, and Dr. Gabriel Cuello for their assistance with the neutron diffraction experiments at ILL, as well as to Dr. James Hester for his help with similar experiments at ANSTO. My sincere thanks go to the Servicio General de Apoyo a la Investigación and in particular to Prof. Ana Arauzo for her help with the magnetization and heat capacity measurements at the University of Zaragoza. I am indebted to Prof. Antonio Galdámez, Dr. Silvana Moris and Dr. Cristina Piquer for providing samples and for our fruitful discussions about magnetic spinels, as well as to Prof. Toshio Ono, Prof. Hironori Yamaguchi and Prof. Yoshi Kamiya for the discussions about the magnetism of organic compounds, and to Prof. Victor Laliena for sharing some of his immense knowledge on chiral magnetism. Additionally, I appreciate Dr. Takumi Kihara and Prof. Hiroyuki Nojiri for their assistance with very low temperature experiments at IMR. If I have inadvertently forgotten to mention anyone, I sincerely apologize.

My gratitude extends to the predoctoral research fellowship DGA and all other funding sources that supported the numerous research stays, experiments, and conference attendances essential for the development of this thesis.

To all my friends in Calahorra, Zaragoza and Osaka, and in particular to Ana, who have provided a constant source of encouragement, laughter, and support throughout

this journey, I am immensely grateful. Your presence has been a constant reminder of life beyond the research, helping me maintain balance and perspective.

Finalmente, y más importante, le doy las gracias de todo corazón a mi familia, especialmente a mis padres. Vuestro amor, apoyo y creencia indondicional en mis capacidades han sido la base sobre la cual he podido construir mis éxitos. Este logro no es solo mío sino también vuestro, ya que sin vuestro ánimo y sacrificios, nada de esto hubiera sido posible.

To everyone who has been a part of this journey, I extend my deepest gratitude. Thank you for making this achievement possible.

Abstract

Magnetism has intrigued humans for centuries, transitioning from early discoveries of lodestones to a core element in modern technology and physics, impacting daily life and global issues such as climate change and energy sustainability. Recently, the field of non-collinear magnetism, featuring unique, tilted magnetic alignments within materials, has emerged, offering new potential for developing intricate and efficient magnetic structures. In this doctoral thesis, conducted in joint supervision between the University of Zaragoza and the Osaka Prefecture University, we consider three factors that can contribute to non-collinear magnetism: the antisymmetric Dzyaloshinskii-Moriya (DM) interaction, magnetic frustration in Heisenberg exchange interactions, and magnetic anisotropy due to the crystal field effect. These factors, influenced by crystal symmetry and geometry, can lead to topologically non-trivial magnetic textures with a variety of length scales and physical properties. Specifically, this thesis focuses on the sources of non-collinear magnetism in three key types of materials: chiral, spinel, and organic magnets, each presenting unique challenges and opportunities. The study of these materials opens the door not only to theoretical advances but also to revolutionary technological applications, from high-density and energy-efficient information storage solutions to the forefront of quantum computing and the development of next-generation sensors.

The thesis is organized into three parts, each exploring a different source of non-collinear magnetism in multifunctional materials. After a general introduction to the experimental techniques, the first part focuses on the role of DM interactions in generating non-collinear magnetic phases in the cubic chiral magnets MnSi and $Fe_{0.75}Co_{0.25}Si$.

- To confirm previous theories about the existence of new magnetic phases in MnSi, specific heat and magnetization curves (d.c. and a.c.) were measured as a function of field and temperature. An anomaly is clearly observed in the a.c. magnetization, suggesting **the existence of a new phase** that could correspond to the predicted unknown state. To understand the possible differences between this new phase (*B-phase*) and the skyrmion phase (*A-phase*), small angle neutron scattering (SANS) and muon spin rotation (μSR) experiments were carried out. The results indicate that the *B-phase* could be **compatible with a reorientation of the magnetic helices in MnSi**. Additionally, the μSR experiments in the *A-phase* highlight the need for a detailed theoretical study of the skyrmion lattice profile in MnSi.

- The effect of disorder and different anisotropy on the presence of new magnetic phases in the compound $Fe_{0.75}Co_{0.25}Si$ was also investigated using d.c.

and a.c. magnetization, SANS, and μSR. The results reveal anomalies in the a.c. magnetization similar to those observed in MnSi, as well as a dependence of the stability of the *B-phase* on the history and direction of the magnetic field, suggesting **the influence of disorder in the development of the *B-phase***. The SANS experiments show that **such disorder also alters both the structure of the skyrmion lattice (*A-phase*) and its stability**. Additionally, they allow discarding the same origin for the *B-phase* as proposed in other materials. The analysis of the μSR data shows a wide distribution of local fields, suggesting a combination of the range of possible muon implantation sites and an increase in magnetic fluctuations induced by substitutional disorder.

The next part explores the combined effect of frustration and disorder on the magnetic properties of the spinel families $Mn_{1-x}Mg_xCr_2O_4$ and $CuCr_{2-x}Sn_xSe_2S_2$.

- The nuclear and magnetic structure of the spinel $MnCr_2O_4$ has been reinvestigated as a function of the temperature in samples synthesized under different conditions, using magnetization, specific heat, and neutron powder diffraction (NPD) experiments. These experiments confirm the existence of three long-range order (LRO) magnetic phases; a ferrimagnetic (FIM) phase, an incommensurate spiral phase, and **a new phase, never reported before**. The symmetry of each magnetic phase has been determined using the formalism of magnetic superspace groups (MSSG). The transition temperatures of the three magnetic phases depend on the atmosphere in which the samples were synthesized. A possible explanation for these transitions has been discussed based on experimental and theoretical results. Finally, **the presence of transverse conical magnetic structures allows for the existence of multiferroicity**, and the direction of electric polarization has been derived using the spin current mechanism.

- Next, the effect of magnetic dilution on the frustration of the $Mn_{1-x}Mg_xCr_2O_4$ family has been studied. NPD experiments similar to those performed for $MnCr_2O_4$ ($x = 0$) show that the nuclear symmetry is analogous to that of said compound over a wide range of temperatures. For low Mg contents, the same FIM and incommensurate spiral phases, both long-range order, are observed. **As the Mg content increases, the FIM phase is no longer observed, while the long-range order of the spiral phase is destroyed, forming small clusters of short-range order**. The evolution of magnetic order with x agrees with previous studies, explained by the weakening of exchange interactions and the compression of Cr-O octahedra as the Mg content increases.

- A structural and magnetic characterization has been carried out in solid solutions of the $CuCr_{2-x}Sn_xSe_2S_2$ family using d.c. and a.c. magnetization, high-resolution transmission electron microscopy (HRTEM), and NPD experiments. The crystal structure of these spinel series has been refined, revealing **a new and unexpected monoclinic secondary phase**. The magnetism of these compounds is understood as the result of a random competition between

ferromagnetic Cr^{3+} -Cr^{4+} interactions (double exchange process) and antiferromagnetic Cr^{3+}- Cr^{3+} interactions (superexchange process). Our results allow proposing a long-range FM order for samples with $x \leq 0.4$. In samples with a relatively high Sn concentration ($x > 0.4$), **frustration and random diamagnetic dilution by Sn suppress the long-range FM order**, replacing it with spin glass-like behavior.

In the last part, we examine the evolution of the magnetic properties with dimensionality in the purely organic magnets 4-F-2-NNBIP and TNN·CH_3CN, which exhibit a combination of low anisotropy and frustration.

- The organic compound 4-F-2-NNBIP has been characterized using X-ray diffraction, electron paramagnetic resonance (EPR), specific heat, magnetization, and susceptibility measurements at high magnetic fields and very low temperatures. Numerical calculations have also been performed to obtain the relevant magnetic parameters of the system. The joint analysis of diffraction data and EPR measurements implies that **this system can be described by a two-leg antiferromagnetic Heisenberg ladder with** $S = 1/2$. The magnetic exchange interactions have been estimated from the fit of the susceptibility data using quantum Monte Carlo (QMC) and exact diagonalization (ED) calculations. With the help of specific heat data, we propose **a phase diagram with 3 distinct magnetic phases**: a quantum disordered (QD) or spin liquid phase, a phase with gapless excitations (Tomonaga-Luttinger liquid (TLL) or quantum critical paramagnet (QC)), and a fully polarized (SP) phase. In addition, a region is observed where magnetization data deviate from theory, and several models to account for this deviation are proposed.

- Finally, the organic compound TNN·CH_3CN has been studied, focusing on the determination of its magnetic structure at low magnetic fields using single crystal neutron diffraction (SCND), polarized neutron diffraction (PND), and μSR experiments. At zero field, the magnetic signal is too weak to be observed in SCND experiments. Nevertheless, by making use of a computational model and DFT calculations, **the absence of oscillations in the μSR spectra is shown to be compatible with a high-symmetry magnetic structure** at the muon site. The proposed magnetic configuration is consistent with previous studies, as well as with theoretical predictions of its multiferroic nature. The trimer formation is also explored at the 1/3 plateau ($1.25 \leq B \leq 8.49$ T). After a low-temperature magnetic and structural characterization, the spin density distribution has been obtained from PND experiments by using the wavefunction and multipole approach. The computational model used to interpret the μSR spectra agrees with the PND results and the theoretical ground state, where **the magnetic moment in the TNN molecule is equally distributed among the three NN radicals.**

In conclusion, these findings collectively underscore the multifaceted origins of non-collinear magnetism, propelled by intrinsic and extrinsic factors, and underscore

the potential for topologically non-trivial magnetic textures across different material systems.

Resumen

El magnetismo ha intrigado a los humanos durante siglos, pasando de los primeros descubrimientos de piedras imán hasta convertirse en un elemento fundamental en la física y la tecnología moderna, con un impacto significativo en la vida diaria y problemas globales como el cambio climático y la sostenibilidad energética. En los últimos años, el campo del magnetismo no colineal, que presenta alineaciones magnéticas únicas dentro de los materiales, ha emergido ofreciendo nuevas posibilidades para el desarrollo de estructuras magnéticas complejas y eficientes. En esta tesis doctoral, realizada bajo la supervisión conjunta de la Universidad de Zaragoza y la Universidad Prefectural de Osaka, consideramos tres factores que pueden contribuir al magnetismo no colineal: la interacción anti-simétrica de Dzyaloshinskii-Moriya (DM), la frustración magnética en las interacciones de intercambio de Heisenberg, y la anisotropía magnética debido al efecto del campo cristalino. Estos factores, condicionados por la simetría cristalina y la geometría, pueden dar lugar a texturas magnéticas topológicamente no triviales con una variedad de escalas de longitud y propiedades físicas. En concreto, esta tesis se centra en las fuentes de magnetismo no colineal en tres tipos clave de materiales magnéticos: quirales, espinelas y orgánicos, cada uno presentando desafíos únicos y oportunidades. El estudio de estos materiales abre la puerta no sólo a avances teóricos, sino también a revolucionarias aplicaciones tecnológicas, desde soluciones de almacenamiento de información de alta densidad y eficiencia energética hasta la vanguardia de la computación cuántica y el desarrollo de sensores de nueva generación.

La tesis está organizada en tres partes, cada una explorando una fuente diferente de magnetismo no colineal en materiales multifuncionales. Tras una introducción general sobre las técnicas experimentales, la primera parte está centrada en el papel de las interacciones DM en la generación de fases magnéticas no-colineales en los imanes cúbicos quirales MnSi y $Fe_{0.75}Co_{0.25}Si$.

- Para confirmar teorías previas sobre la existencia de nuevas fases magnéticas en MnSi, se han medido curvas de calor específico e imanación (d.c. y a.c.) en función del campo y la temperatura. Se observa claramente que la imanación a.c. presenta una anomalía, sugiriendo **la existencia de una nueva fase** que podría corresponder al estado desconocido predicho. Para comprender las posibles diferencias entre esta nueva fase (*fase-B*) y la fase de skyrmiones (*fase-A*), se han realizado experimentos de dispersión de neutrones a bajo ángulo (SANS) y de rotación de espín de muones (μSR). Los resultados indican que la *fase-B* podría ser **compatible con una reorientación de las hélices magnéticas en MnSi**. Además, los experimentos de μSR en la *fase-A* ponen

de manifiesto la necesidad de un estudio teórico detallado del perfil de la red de skyrmiones en MnSi.

- El efecto del desorden y distinta anisotropía en la existencia de nuevas fases magnéticas en el compuesto $Fe_{0.75}Co_{0.25}Si$ también ha sido investigado mediante imanación d.c. y a.c., SANS y μSR. Los resultados revelan anomalías en la imanación a.c. similares a la observada en MnSi, así como una dependencia de la estabilidad de la *fase-B* con la historia y dirección del campo magnético, sugiriendo la influencia del desorden en el desarrollo de la *fase-B*. Los experimentos de SANS muestran que **dicho desorden también altera tanto la estructura de la red de skyrmiones *fase-A* como su estabilidad**. Además, permiten descartar el mismo origen para la *fase-B* que el propuesto en otros materiales. El análisis de los datos de μSR muestra una amplia distribución de campos locales, sugiriendo una combinación del rango de posibles sitios de implantación de muones y un aumento de las fluctuaciones magnéticas inducidas por el desorden sustitucional.

La siguiente parte explora el efecto combinado de la frustración y el desorden en las propiedades magnéticas de las familias de espinelas $Mn_{1-x}Mg_xCr_2O_4$ y $CuCr_{2-x}Sn_xSe_2S_2$.

- La estructura nuclear y magnética de la espinela $MnCr_2O_4$ ha sido reinvestigada en función de la temperatura en muestras sintetizadas bajo diferentes condiciones, utilizando experimentos de magnetización, calor específico y difracción de neutrones. Estos experimentos confirman la existencia de tres fases magnéticas de orden de largo alcance (LRO); una fase ferrimagnética (FIM), una fase espiral incommensurada, y **una nueva fase, nunca antes reportada**. La simetría de cada fase magnética se ha determinado utilizando el formalismo de los grupos del superespacio magnéticos (MSSG). Las temperaturas de transición de las tres fases magnéticas dependen de la atmósfera en la que se sintetizaron las muestras. Una posible explicación de estas transiciones ha sido discutida basándose en resultados experimentales y teóricos. Finalmente, **la presencia de estructuras magnéticas cónicas transversales permite la existencia de multiferroicidad**, y se ha derivado la dirección de la polarización eléctrica utilizando el mecanismo de corriente de spin.

- En el siguiente paso se ha estudiado el efecto de la dilución magnética en la familia $Mn_{1-x}Mg_xCr_2O_4$. Experimentos de difracción de neutrones de polvo (NPD) similares a los realizados para $MnCr_2O_4$ ($x = 0$) muestran que la simetría nuclear es análoga a la de dicho compuesto en un amplio rango de temperaturas. Para bajos contenidos de Mg se observan las mismas fases FIM y espiral incommensurada, ambas de largo alcance. **Al aumentar el contenido de Mg, la fase FIM se deja de observar, mientras que el orden de largo alcance de la fase espiral es destruido, formando pequeños clusters de orden de corto alcance**. La evolución del orden magnético con x concuerda con lo reportado en estudios previos, explicándose

por el debilitamiento de las interacciones de intercambio y la compresión de los octaedros Cr-O a medida que aumenta el contenido de Mg.

- Se ha llevado a cabo una caracterización estructural y magnética en soluciones sólidas de la familia $CuCr_{2-x}Sn_xSe_2S_2$ mediante imanación d.c. y a.c., microscopía electrónica de transmisión de alta resolución (HRTEM) y experimentos de NPD. La estructura cristalina de estas series de espinelas ha sido refinada, revelando **una nueva e inesperada fase secundaria monoclínica**. El magnetismo de estos compuestos se entiende como resultado de una competencia aleatoria entre las interacciones ferromagnéticas Cr^{3+} - Cr^{4+} (proceso de doble canje) y las interacciones antiferromagnéticas Cr^{3+} - Cr^{3+} (proceso de supercanje). Nuestros resultados permiten proponer un orden de largo alcance FM para muestras con $x \leq 0.4$. En muestras con una concentración relativamente alta de Sn ($x > 0.4$), **la frustración y la dilución diamagnética aleatoria de Sn suprimen el orden FM de largo alcance** y reemplazándolo por un comportamiento tipo vidrio de spin.

En la última parte examinamos la evolución de las propiedades magnéticas con la dimensionalidad en los imanes orgánicos puros 4-F-2-NNBIP y TNN·CH_3CN, los cuales exhiben una combinación de baja anisotropía y frustración.

- Se ha caracterizado el compuesto orgánico 4-F-2-NNBIP mediante difracción de rayos X, resonancia paramagnética electrónica (EPR), calor específico, imanación y mediciones de susceptibilidad en campos magnéticos altos y a muy baja temperatura. También se han realizado cálculos numéricos para obtener los parámetros magnéticos relevantes del sistema. El análisis conjunto de los datos de difracción y las mediciones de EPR implican que **este sistema puede describirse por una escalera antiferromagnética de Heisenberg de dos patas con** $S = 1/2$. Las interacciones de intercambio magnético se han estimado a partir del ajuste de los datos de susceptibilidad usando cálculos de Monte Carlo Cuántico (QMC) y diagonalización exacta (ED). Con ayuda de los datos de calor específico, proponemos un **diagrama de fases con 3 fases magnéticas distintas**: una fase cuánticamente desordenada (QD) o líquido de espín, una fase con excitaciones sin gap (líquido de Tomonaga-Luttinger (TLL) o paramagnético crítico cuántico (QC)) y una fase completamente polarizada (SP). Además, se observa una región en la que los datos de magnetización se desvían de la teoría, y diversos modelos para explicar esta desviación han sido propuestos.

- Finalmente, se ha estudiado el compuesto orgánico TNN·CH_3CN, enfocándose en la determinación de su estructura magnética a bajos campos magnéticos mediante difracción de neutrones en monocristal (SCND), difracción de neutrones polarizados (PND) y experimentos de μSR. A campo cero, la señal magnética es demasiado débil para observarse en los experimentos SCND. Sin embargo, haciendo uso de un modelo computacional y cálculos DFT, se muestra que **la ausencia de oscilaciones en los espectros μSR es compatible con una estructura magnética de alta simetría** en el sitio del muón. La

configuración magnética propuesta es coherente con estudios previos, así como con las predicciones teóricas de su naturaleza multiferroica. La formación del trímero también se ha explorado en el plateau 1/3 ($1.25 \leq B \leq 8.49$ T). Después de una caracterización magnética y estructural a baja temperatura, se ha obtenido la distribución de densidad de spin a partir de experimentos de PND utilizando los métodos de función de onda y multipolos. El modelo computacional utilizado para interpretar los espectros μSR concuerda con los resultados de PND y el estado fundamental teórico, donde **el momento magnético en la molécula de TNN se distribuye equitativamente entre los tres radicales NN**.

En conclusión, estos hallazgos en conjunto subrayan los orígenes multifacéticos del magnetismo no colineal, impulsados por factores intrínsecos y extrínsecos, y destacan el potencial de texturas magnéticas topológicamente no triviales en diversos sistemas de materiales.

Contents

Chapter 1

Scope and Objectives

Magnetism has captivated human curiosity for centuries, evolving from the discovery of naturally magnetized stones (lodestones) to a fundamental pillar in modern physics and technology. Understanding magnetism has not only led to important developments in both theoretical and applied physics, but has had a profound impact in our daily life. Magnets are integral to numerous devices and systems, including power plants, quantum computing, MRI machines, electronic devices, hard drives, and refrigerators, often functioning in ways that go unnoticed.

Additionally, the technological applications of magnetic phenomena have a far-reaching impact, extending to global issues like climate change and energy consumption. The efficient use of magnetic materials in motors and generators is critical in renewable energy technologies, aiding the transition from fossil fuels to cleaner energy sources. This shift is not only a technological challenge but also a geopolitical and environmental one. As the global demand for sustainable technologies grows, so does the competition for control over the necessary raw materials.

It is in this context that a recent field of magnetism, based on non-collinear magnetic arrangements, offers a promising pathway. Unlike the conventional parallel or antiparallel alignments characteristic of ferromagnetic and antiferromagnetic materials, non-collinear magnetism involves a tilted alignment of magnetic moments within a material, which results in fascinating and intricate magnetic structures.

The foundational theoretical model proposed by Yaffet and Kittel in 1952 [1] laid the groundwork for understanding non-collinear magnetic structures. Few years later, the advent of neutron scattering techniques provided the first experimental glimpses into these complex arrangements in the materials MnO_2 [2] and $MnAu_2$ [3], marking a pivotal moment in the field. A recent landmark in the field's ongoing innovation was the discovery of magnetic skyrmions [4, 5], revealing stable, whirl-like structures that hold promise for revolutionizing data storage and processing in spintronics.

Non-collinearity generally arises from the interplay between various magnetic interactions (exchange interactions with multiple neighbor shells, symmetric and anti-symmetric exchange, or a combination of exchange and single-ion anisotropy) and has profound implications for the magnetic properties of materials. Furthermore, the presence of non-collinear magnetic structures facilitates the integration of multiple functions (electronic, optical, thermal) within a single material system.

These multifunctional materials have gained significant attention in recent years due to their broad range of potential applications in fields such as digitalization, energy, and biomedical engineering [6–8]. Therefore, the exploration of non-collinear magnetism is not merely a theoretical curiosity; it holds significant promise for potential technological revolutions, thereby contributing to a sustainable and technologically advanced future.

1.1 Sources of non-collinear magnetism

Relative to this work, we consider three factors that can contribute to non-collinear magnetism: the anti-symmetric Dzyaloshinskii-Moriya (DM) interaction, the magnetic frustration in Heisenberg exchange interactions, and the magnetic anisotropy due to the effect of the crystal field. These interactions, influenced by crystal symmetry and geometry, can give rise to topologically non-trivial magnetic textures with a variety of length scales and physical properties. In some materials, multiple mechanisms may coexist or compete, adding to their complexity.

1.1.1 Dzyaloshinskii-Moriya interaction

The DM interaction, proposed independently by Igor Dzyaloshinskii [9, 10] and Toru Moriya [11], is an anti-symmetric exchange interaction that arises in magnetic systems with strong spin-orbit coupling and lacking inversion symmetry. On a microscopic level, the DM interaction can be understood as arising from an indirect exchange interaction mediated by the spin-orbit coupling. The Hamiltonian for the DM interaction can be expressed as:

$$\mathcal{H}_{\mathrm{DM}} = \sum_{ij} \vec{D}_{ij} \cdot (\vec{S}_i \times \vec{S}_j) \tag{1.1}$$

where $\vec{S}_i$ and $\vec{S}_j$ are spins at sites i and j, and $\vec{D}_{ij}$ is the DM vector, which is specific to each pair of spins and depends on the microscopic details of the system, such as the crystal structure and the nature of the spin-orbit coupling. The cross product $\vec{S}_i \times \vec{S}_j$ indicates that the DM interaction favors a perpendicular alignment of neighboring spins, leading to a tendency towards helical or spiral arrangements, rather than parallel or antiparallel alignments as seen in purely Heisenberg-exchange-dominated systems. The direction and magnitude of the DM vector determine the sense of rotation (clockwise or counterclockwise) and the pitch of the helical structures, thereby defining the chirality of the system.

The presence of the DM interaction is a crucial factor in stabilizing non-collinear magnetic structures. In systems where the DM interaction is comparable to or stronger than the Heisenberg exchange interaction, complex non-collinear configurations such as cycloidal spirals, canted antiferromagnets, and skyrmions can form. These structures are characterized by a spatially varying direction of magnetic moments, and their stability is a result of the competition between DM interaction, Heisenberg exchange, and magnetic anisotropy.

1.1.2 Magnetic frustration

Electrostatic interactions between the electrons from neighboring magnetic ions can lead to interatomic magnetic exchange interactions. These electrostatic interactions can be effectively described by the Heisenberg Hamiltonian:

$$\mathcal{H}_{\text{Heis}} = -\sum_{ij} J_{ij} \vec{S}_i \cdot \vec{S}_j \tag{1.2}$$

The Heisenberg exchange interaction, J_{ij}, typically favors parallel (in ferromagnetic materials) or antiparallel (in antiferromagnetic materials) alignment of neighboring spins. However, in the presence of geometric constraints or competing interactions, this tendency can lead to frustration.

The term 'frustration' was formally introduced in the context of spin glasses [12, 13], and can be defined as the impossibility to minimize all individual interaction terms. Magnetic frustration can arise due to the geometry of the lattice (geometric frustration) or from competing interactions (interaction frustration). The concept of magnetic frustration can be understood by considering a simple triangular arrangement of magnetic moments. In a system with antiferromagnetic interactions, each spin prefers to align antiparallel to its neighbors. However, in a triangular configuration, it's impossible for all the spins to satisfy this condition simultaneously.

In frustrated magnetic systems, the inability to simultaneously satisfy all magnetic interactions leads to a large number of nearly degenerate ground states, which results in complex magnetic orderings. For instance, in some frustrated magnets, the ground state can be a spin liquid, a state where the spins are constantly fluctuating and do not order even at absolute zero temperature. The competition between different magnetic interactions in these materials often stabilizes non-collinear configurations as a compromise to minimize the overall energy. The exact nature of these non-collinear structures can depend on various factors, including the type of magnetic ions, the geometry of the lattice, and the strength of the interactions.

1.1.3 Magnetocrystalline anisotropy

The magnetocrystalline anisotropy has two possible sources: single-ion and two-ion contributions. The single-ion anisotropy (SIA) arises from the electrostatic interaction of atomic spin orbitals with the local crystal environment. The two-ion contribution often reflects the anisotropy of the dipole–dipole interaction. However, this contribution is usually overshadowed by stronger exchange interactions, so the discussion is focused on SIA.

If a free magnetic ion is embedded in a crystal lattice, the $\pm L^z$ states of the outermost shell are mixed, which results in the removing of the degeneracy of the electronic states. The crystal-field, combined with the spin-orbit interaction, tends to stabilize a particular orbital and forces the magnetic moment to align itself along well-defined crystallographic axes (known as easy magnetization axes). The SIA contribution to the magnetic Hamiltonian can be written as:

$$\mathcal{H}_{\text{SIA}} = \sum_{i} \vec{S}_i \cdot \mathcal{A}_i \cdot \vec{S}_i \tag{1.3}$$

with the SIA matrix given by:

$$\mathcal{A}_i = \begin{bmatrix} A_i^{xx} & A_i^{xy} & A_i^{xz} \\ A_i^{yx} & A_i^{yy} & A_i^{yz} \\ A_i^{zx} & A_i^{zy} & A_i^{zz} \end{bmatrix} \tag{1.4}$$

The magnitude of the anisotropy and its directional dependence, therefore, depend on the intrinsic structure of the lattice, such as the crystal symmetry and the chemical composition of the material.

In certain scenarios (e.g. p or d electron in octahedral crystal field), the expectation value of the L^z orbital angular momentum operator becomes zero for all eigenstates of the SIA Hamiltonian. This phenomenon is recognized as the quenching of orbital angular momentum, a process facilitated by the crystal field. As a result of this orbital quenching, the orbital contribution to the magnetic moment is fluctuating and undefined. Therefore the ground state electron configuration is defined exclusively by the spin quantum numbers S and S^z, leading to a total angular momentum $J = S$. Since the effective magnetic moment is only derived from the spin angular moment, it implies an isotropic magnetic moment and the absence of single-ion anisotropy.

1.2 Global objectives

The main objective of this thesis is to identify and understand the relevant factors that control and generate non-collinear magnetism in advanced technological materials. To achieve this goal, we investigate non-collinear magnetism across three distinct material classes – chiral, spinel, and organic magnets – each influenced by DM interactions, magnetic frustration from symmetric exchange interactions, or magnetic anisotropy.

- In cubic chiral magnets, the presence of DM interactions within the chiral crystal structure leads to a rich variety of magnetic textures, including skyrmion lattices and chiral magnetic soliton lattices. These magnetic textures are robust and well-suited for compact information storage due to the protection provided by chirality and topology [14]. In particular, the use of spin waves and skyrmions in chiral magnets have drawn significant scientific interest in the field of magnonics, potentially leading to advanced information processing and storage solutions with low energy dissipation and high-frequency capabilities [15–18]. Therefore, we explore novel magnetic structures in chiral magnets aiming to understand how DM interactions generate non-collinear magnetism.

- Spinel materials exhibit remarkable magnetic properties due to the geometric frustration arising from competing magnetic interactions [19]. These frustrated systems are of fundamental interest and hold promise for potential applications, particularly in multiferroics, where the interplay between magnetic and electrical order is vigorously investigated [20–23]. Thus, we investigate the combined effect of frustration and disorder on the magnetic properties

of magnetic spinels. By understanding these effects, we aim to uncover the mechanisms that control non-collinear magnetism in these materials.

- The study of purely organic magnets, where magnetism originates from unpaired p electrons, offers a unique opportunity to investigate magnetic frustration in highly isotropic systems. Frustrated spin systems in organic magnets have been found to exhibit exotic ground states, including spin liquid and spin glass phases, as well as novel types of excitations [24, 25]. Furthermore, promising predictions of multiferroic ordering in compounds based on organic radicals [26], along with potential applications in quantum computing and magnetic memory [27–29], highlight the potential of this research area. By studying the magnetic properties of organic magnets ranging between 1D and 3D, we aim to understand how low anisotropy and frustration contribute to non-collinear magnetism in low-dimensional systems.

Table 1.1: Properties of the different magnetic materials studied in this thesis. The symbols ✓ and ✗ indicate if a property is predominant or negligible, respectively.

Material	DM interaction	Magnetic frustration	Magnetic anisotropy	Dimension
Cubic chiral magnets	✓	✗	✓	3D
Magnetic spinels	✗	✓	✓	3D
Organic magnets	✗	✓	✗	1D – 3D

1.3 Structure of the thesis

This thesis is organized into three parts, each exploring a different source of non-collinear magnetism in multifunctional materials. After a general introduction about the experimental techniques, we first focus on the role of DM interactions in generating non-collinear magnetic phases in cubic chiral magnets. Next, we explore the combined effect of frustration and disorder on the magnetic properties of magnetic spinels. Finally, we examine the evolution of the magnetic properties with the dimensionality in purely organic magnets. The chapters are organized as follows:

- Chapter 2 focuses on the experimental techniques used in this thesis to characterize the magnetic properties of materials at both macroscopic and atomic-level. A more detailed explanation of the neutron scattering and muon spin rotation experiments is given, as most of the results presented were obtained by these techniques.

- In Chapter 3, we report the existence of a new magnetic phase in the cubic magnet MnSi. Such phase, obtained through macroscopic magnetic characterization, is consistent with previous theoretical predictions. The magnetic structure of this new phase is described based on the results of Small Angle Neutron Scattering (SANS) and muon spin rotation (μSR) experiments. A

magnetic model, related with a relative reorientation of the magnetic helices, is proposed to explain the new magnetic state. Part of the results presented in this chapter are published in Ref. [30, 31].

- In Chapter 4, a similar magnetic phase as reported in MnSi is observed in $Fe_{0.75}Co_{0.25}Si$. Both the macroscopic characterization and the SANS experiments indicate a dependence of its stability with the magnetic field history and the direction of the applied field. Additionally, a metastable SkL phase is observed at a lower temperatures than in previous characterizations. These results are explained on the base that the effect of disorder plays a key role in the appearance of the new magnetic state.

- In Chapter 5, we reinvestigate the nuclear and magnetic structures of $MnCr_2O_4$ as function of the temperature in samples synthesized under different conditions by using magnetization, specific heat and neutron diffraction experiments. Our results confirm the existence of three LRO magnetic phases; one of them never reported before. The symmetry of these magnetic structures, described by the magnetic superspace group (MSSG) formalism, allows the existence of multiferroicity. An explanation of the transitions between the three magnetic phases is discussed based on experimental and theoretical results. Part of the results presented in this chapter are published in Ref. [32].

- In Chapter 6, we study the effect of magnetic dilution in $Mn_{1-x}Mg_xCr_2O_4$ by neutron powder diffraction (NPD) experiments. A transition from long-range to short-range order is observed as the quantity of diamagnetic cations Mg^{2+} is increased, until only small clusters of spins in spiral arrangements are formed. An explanation based on the role of the exchange interactions and the geometrical frustration is given.

- In Chapter 7, the effect of magnetic disorder and exchange interaction competition is investigated in the spinel family $CuCr_{2-x}Sn_xSe_2S_2$. The magnetic behavior, studied by a.c. and d.c. magnetization, suggests that the magnetic ground state evolves from a FM system at low x, to a spin glass-like system for $x = 1$. Both the crystal and magnetic structures are determined from high resolution electron microscopy (HRTEM) and variable temperature NPD experiments. The magnetism of these compounds can be understood within a model of random competition of exchange interactions and magnetic dilution effect.

- In Chapter 8, we present the compound 4-F-2-NN-BIP, which is one of the few purely organic compounds described with a spin ladder model. We study its magnetic behavior by means of X-ray diffraction, electron paramagnetic resonance (EPR), specific heat, magnetization and susceptibility measurements at high magnetic fields and very low temperatures. Numerical calculations are also performed in order to obtain the relevant magnetic parameters of the system. From the results we determine its topology and magnetic phase diagram, where exotic magnetic states resulting from frustration are discussed.

- In Chapter 9, we examine the purely organic compound TNN·CH_3CN, a system which transitions from an effectively 2D triangular lattice to a 3D structure with temperature. We perform neutron diffraction and μSR experiments in order to elucidate the magnetic order which takes place at low magnetic fields. At zero field, a magnetic structure compatible with the experimental results is obtained, which confirms theoretical predictions of the multiferroicity in this compound. At low magnetic field, the trimer formation is observed and the spin distribution is determined from polarized neutron diffraction (PND) and μSR experiments, supporting a theoretical model for the ground state in this region.

Bibliography

[1] Y. Yafet and C. Kittel, "Antiferromagnetic Arrangements in Ferrites," Physical Review, vol. 87, pp. 290–294, July 1952.

[2] A. Yoshimori, "A New Type of Antiferromagnetic Structure in the Rutile Type Crystal," Journal of the Physical Society of Japan, vol. 14, pp. 807–821, June 1959.

[3] A. Herpin, P. Meriel, and J. Villain, "MAGNETIC STRUCTURE OF THE ALLOY $MnAu_2$," Compt. rend., vol. 249, 10 1959.

[4] A. N. Bogdanov and D. A. Yablonskii, "Thermodynamically stable "vortices" in magnetically ordered crystals.The mixed state of magnets," Sov. Phys. JETP, vol. 68, no. 1, p. 101, 1989.

[5] S. Mühlbauer, B. Binz, F. Jonietz, C. Pfleiderer, A. Rosch, A. Neubauer, R. Georgii, and P. Böni, "Skyrmion Lattice in a Chiral Magnet," Science, vol. 323, pp. 915–919, feb 2009.

[6] A. D. B. Ferreira, P. R. Nóvoa, and A. T. Marques, "Multifunctional Material Systems: A state-of-the-art review," Composite Structures, vol. 151, pp. 3–35, 2016.

[7] A. Lendlein and R. S. Trask, "Multifunctional materials: concepts, function-structure relationships, knowledge-based design, translational materials research," Multifunctional Materials, vol. 1, no. 1, p. 010201, 2018.

[8] T. Grancha, J. Ferrando-Soria, M. Castellano, M. Julve, J. Pasán, D. Armentano, and E. Pardo, "Oxamato-based coordination polymers: recent advances in multifunctional magnetic materials," Chem. Commun., vol. 50, pp. 7569–7585, 2014.

[9] I. Dzyaloshinsky, "A thermodynamic theory of "weak" ferromagnetism of antiferromagnetics," Journal of Physics and Chemistry of Solids, vol. 4, pp. 241–255, jan 1958.

[10] I. Dzyaloshinskii, "A GENERAL RELATION IN THE THEORY OF FERROMAGNETIC FERMI FLUIDS," Zh. Eksperim. i Teor. Fiz., vol. 46, 1964.

[11] T. Moriya, "Anisotropic Superexchange Interaction and Weak Ferromagnetism," Physical Review, vol. 120, pp. 91–98, oct 1960.

[12] J. Villain, "Spin glass with non-random interactions," Journal of Physics C: Solid State Physics, vol. 10, pp. 1717–1734, May 1977.

[13] G. Toulouse, Theory of the frustration effect in spin glasses: I, pp. 99–103. WORLD SCIENTIFIC, Nov. 1986.

[14] T. Schulz, R. Ritz, A. Bauer, M. Halder, M. Wagner, C. Franz, C. Pfleiderer, K. Everschor, M. Garst, and A. Rosch, "Emergent electrodynamics of skyrmions in a chiral magnet," Nature Physics, vol. 8, pp. 301–304, feb 2012.

[15] H. Yu, J. Xiao, and H. Schultheiss, "Magnetic texture based magnonics," Physics Reports, vol. 905, pp. 1–59, apr 2021.

[16] X. Zhang, M. Ezawa, and Y. Zhou, "Magnetic skyrmion logic gates: conversion, duplication and merging of skyrmions," Scientific Reports, vol. 5, mar 2015.

[17] A. Fert, V. Cros, and J. Sampaio, "Skyrmions on the track," Nature Nanotechnology, vol. 8, pp. 152–156, mar 2013.

[18] J. Sampaio, V. Cros, S. Rohart, A. Thiaville, and A. Fert, "Nucleation, stability and current-induced motion of isolated magnetic skyrmions in nanostructures," Nature Nanotechnology, vol. 8, pp. 839–844, oct 2013.

[19] V. Tsurkan, H.-A. K. von Nidda, J. Deisenhofer, P. Lunkenheimer, and A. Loidl, "On the complexity of spinels: Magnetic, electronic, and polar ground states," Physics Reports, vol. 926, pp. 1–86, sep 2021.

[20] S.-W. Cheong and M. Mostovoy, "Multiferroics: a magnetic twist for ferroelectricity," Nature Materials, vol. 6, pp. 13–20, jan 2007.

[21] A. Sundaresan and N. V. Ter-Oganessian, "Magnetoelectric and multiferroic properties of spinels," Journal of Applied Physics, vol. 129, feb 2021.

[22] W. Eerenstein, N. D. Mathur, and J. F. Scott, "Multiferroic and magnetoelectric materials," Nature, vol. 442, pp. 759–765, aug 2006.

[23] N. A. Spaldin and R. Ramesh, "Advances in magnetoelectric multiferroics," Nature Materials, vol. 18, pp. 203–212, feb 2019.

[24] S. Kumar, Y. Kumar, S. Keshri, and P. Mukhopadhyay, "Recent Advances in Organic Radicals and Their Magnetism," Magnetochemistry, vol. 2, p. 42, nov 2016.

[25] A. Mizuno, Y. Shuku, M. M. Matsushita, M. Tsuchiizu, Y. Hara, N. Wada, Y. Shimizu, and K. Awaga, "3D Spin-Liquid State in an Organic Hyperkagome Lattice of Mott Dimers," Physical Review Letters, vol. 119, jul 2017.

[26] Y. Kamiya and C. D. Batista, "Multiferroic Behavior in Trimerized Mott Insulators," Physical Review Letters, vol. 108, feb 2012.

[27] W. Fujita, , and K. Awaga, "Room-temperature magnetic bistability in organic radical crystals," Science, vol. 286, pp. 261–262, oct 1999.

[28] S. J. Blundell and F. L. Pratt, "Organic and molecular magnets," Journal of Physics: Condensed Matter, vol. 16, pp. R771–R828, jun 2004.

[29] Z. Chen, Y. Li, and F. Huang, "Persistent and stable organic radicals: Design, synthesis, and applications," Chem, vol. 7, pp. 288–332, feb 2021.

[30] K. Ohishi, Y. Kousaka, S. Iwasaki, J. Akimitsu, M. Pardo-Sainz, V. Laliena, J. Campo, M. Ohkuma, and M. Mito, "Small Angle Neutron Scattering Study near the Critical Field at Low Temperature in MnSi," in Proceedings of the 3rd J-PARC Symposium (J-PARC2019), Journal of the Physical Society of Japan, mar 2021.

[31] M. Ohkuma, M. Mito, M. Pardo, Y. Kousaka, S. Iwasaki, K. Ohishi, J. Akimitsu, K. Inoue, V. Laliena, and J. Campo, "New magnetic intermediate state, "*B-phase*," in the cubic chiral magnet MnSi," APL Materials, vol. 10, p. 041104, apr 2022.

[32] M. Pardo-Sainz, A. Toshima, G. André, J. Basbus, G. J. Cuello, V. Laliena, T. Honda, T. Otomo, K. Inoue, Y. Hosokoshi, Y. Kousaka, and J. Campo, "New (α β γ)-incommensurate magnetic phase discovered in the $MnCr_2O_4$ spinel at low temperatures," Physical Review B, vol. 107, apr 2023.

Chapter 2

Experimental techniques

This chapter describes the experimental techniques employed during the course of this thesis to investigate the magnetic properties of diverse materials.

A diverse range of experiments have been conducted for a complete description and characterization. The initial step involved measuring bulk properties such as magnetization and heat capacity, as they provide important information about the macroscopic magnetic behavior of a material. Subsequently, the crystal and magnetic structures were determined by means of X-ray and neutron scattering techniques. Microscopic local level magnetism was studied using muon spin rotation (μSR), a highly sensitive method. For organic magnets, electron paramagnetic resonance (EPR) was also employed to detect and quantify the anisotropy of unpaired electrons in radicals.

Among the different experimental techniques, neutron scattering and μSR have provided the most powerful results presented in this work. These techniques complement each other well, as most of the neutron scattering techniques provide information about reciprocal space, while μSR provides insight into the local magnetic environment in real space. Therefore, a more detailed description of these techniques is provided in this chapter.

Hereinafter, when we talk about an external applied magnetic field, we will refer to the magnetic induction $\vec{B}$ unless otherwise specified. In air it can be approximated to $\vec{B} \cong \mu_0 \vec{H}$, where $\vec{H}$ is the magnetic-field strength and $\mu_0 = 4\pi \times 10^{-7}$ H/m is the vacuum permeability.

2.1 Magnetization

The isothermal magnetization $M(B)$ and temperature dependent magnetization $M(T)$ curves were measured with a vibrating sample magnetometer (VSM). Additional alternating current (a.c.) susceptibility measurements were performed in a Superconducting Quantum Interference Device (SQUID) to obtain relevant information about the magnetization dynamics. In the case of organic magnets, which require a very high magnetic field ($B > 10$ T) to study their magnetic properties, a pulsed magnetic field was used until 30 T.

2.1.1 Vibrating sample magnetometer

The principle behind the VSM is to make a sample vibrate in the presence of an uniform external magnetic field and measure the magnetic response, based on Faraday's Law of Induction. This measurement is performed by a special pick-up coil that filters out the external field while being able to measure the sample's magnetic moment [1].

The VSM system consists of an electromagnet or superconducting coil that generates the uniform magnetic field and a pair of pick-up coils wound in opposite directions. The spatially homogeneous external magnetic field induces opposite voltages in the two coils, which cancel each other out. However, when the magnetic sample is introduced, it induces different magnetic flux in the two coils, which can be measured. The sample is mounted on a sample-holder which is subjected to a sinusoidal vibration in the vertical axis. The voltage induced in the pick-up coils is proportional to the sample's magnetic moment and does not depend directly on the strength of the applied magnetic field. This voltage is measured using a lock-in amplifier. A scheme in shown in Fig. 2.1(a).

VSM provides quick measurements with a sensitivity of $\sim 10^{-6}$ emu and a large number of experimental points, as it collects data continuously. However, this can also result in measurement conditions that are not stabilized before the measurement is done, which may affect the accuracy of the data.

2.1.2 a.c. susceptibility

Alternating current (a.c.) susceptibility measurements employing a SQUID magnetometer represent an exceptionally sensitive method for characterizing the magnetic properties of materials.

During an a.c. magnetization experiment, the sample is exposed to an alternating

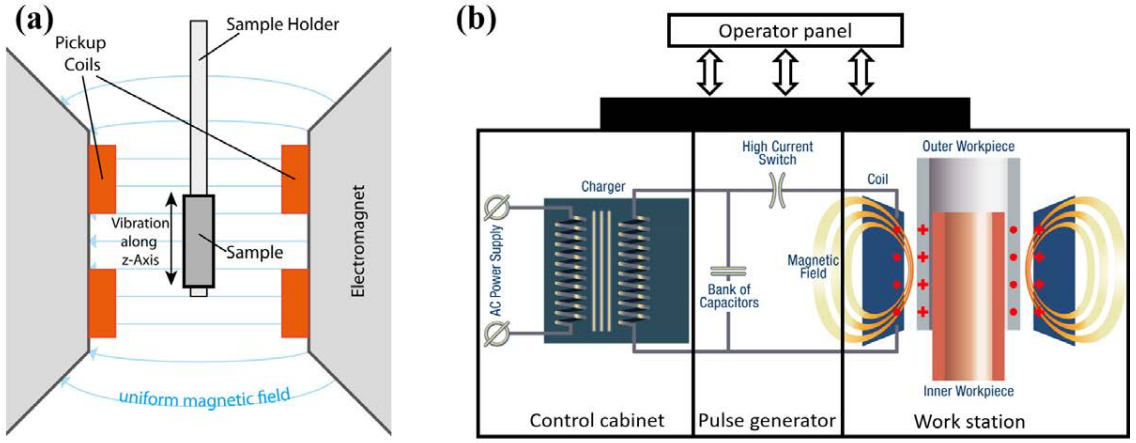

Figure 2.1: (a) Setup of a vibrating sample magnetometer. The sample is vibrated sinusoidally in between the pick-up coils. (b) Schematic magnetic pulse system layout.

magnetic field $H_{\text{a.c.}} \cos(\omega t)$, which is superimposed on a constant direct current (d.c.) field, using a coil within which the sample is placed. The frequency ω and amplitude $H_{\text{a.c.}}$ of the field can be varied depending on the measurement requirements. This setup induces a time-dependent magnetic moment in the sample, which is detected by the SQUID sensor, a superconducting ring containing two Josephson junctions. A biasing current flows through this loop, and any change in the magnetic flux penetrating the loop induces a screening current. Due to the unique property of Josephson junctions, allowing Cooper pairs to tunnel through, the voltage across the superconducting ring oscillates periodically with changes in magnetic flux. This oscillation makes the SQUID an unparalleled detector of magnetic flux changes, with commercial models achieving resolutions better than 10^{-8} emu.

At very low frequencies, the magnetic moment of the sample follows the isotherm magnetization curve that would be observed in a d.c. experiment. However, for high frequencies, the magnetic response does not follow the d.c. magnetization due to dynamic effects in the sample. Consequently, a.c. susceptibility measurements focus on two key parameters: the amplitude of the material's magnetic response $\chi = \frac{dM}{dH}$ and the phase shift φ, indicative of the lag between the applied field and the material's response. The induced a.c. moment can be expressed as:

$$M_{\text{a.c.}} = \chi H_{\text{a.c.}} \cos(\omega t - \varphi) = H_{\text{a.c.}} \left[\chi \cos(\varphi) \cos(\omega t) + \chi \sin(\varphi) \sin(\omega t)\right] \tag{2.1}$$

In the experiment, the in-phase component $\chi' = \chi \cos\varphi$ and out-of-phase component $\chi'' = \chi \sin\varphi$ of the susceptibility are measured through the use of lock-in amplifiers, which are highly sensitive to both the amplitude and phase of the signal. In the limit of low frequencies ($\omega \to 0$) χ' corresponds to the material's real susceptibility. Conversely, at higher frequencies, the out of phase component χ'' indicates energy losses within the material due to phenomena such as magnetic hysteresis.

2.1.3 Pulsed-field magnetization

Pulsed-field magnetization is a technique used to generate a brief and intense magnetic field which induces a magnetic moment in a sample. The duration of the magnetic field pulse is typically in the microsecond to millisecond range, and the magnitude of the magnetic field can be as high as several tens of tesla (T) [2]. This is typically achieved by discharging a high-energy capacitor bank through a coil that surrounds the sample (see Fig. 2.1(b)), which generates a rapidly increasing magnetic field. The short pulse is generated from a magnetizer, which is essentially a set of powerful capacitors connected together with a controller and an ignitor switch, called an Ignitron or SCR. The discharge circuit must be carefully designed and optimized to generate a well-controlled and reproducible pulsed magnetization. This includes selecting the appropriate capacitor bank, coil, and switching devices, as well as properly designing the discharge circuit to ensure a fast and efficient energy transfer to the coil. The discharge circuit must also be designed to minimize inductive and resistive losses, which can reduce the energy available for magnetization.

The magnetic moment generated in the sample is measured by an inductive method using a coil placed around the sample, similar to the VSM technique, and

detected by a lock-in amplifier.

2.2 Heat capacity

Heat capacity measurements are a valuable tool for understanding the physical properties of materials, providing valuable insights into their structural, electronic, and magnetic characteristics. These measurements aid in identifying phase transitions and models through anomalies in the heat capacity and enable the determination of entropy evolution with temperature or magnetic field.

Heat capacity measurements are commonly performed using adiabatic calorimetry, which involves monitoring the sample's temperature change in response to a changing environment. In particular, the data presented in this thesis were obtained through the relaxation and dual-slope methods. Both methods involve a similar setup, as depicted in Fig. 2.2(a). The sample was glued to a calorimeter platform, which consisted of a heater and a thermometer with a well-known thermal link to the heat bath. The platform was thermally isolated by a high vacuum. The starting point for the measurement was a sample thermalized at bath temperature. In both techniques, the sample's heat capacity is obtained by measuring the heat capacity of the empty calorimeter (addenda) and subtracting this contribution from the total heat capacity.

2.2.1 Relaxation method

In the relaxation method, the heater is switched on and a known amount of heat is applied to the sample at constant power for a short time. After the heater is switched off the sample together with the calorimeter platform relaxes back to thermal equilibrium. This procedure allows to measure the relaxation time constant τ by fitting the relaxation curve to an exponential curve:

$$T_{\mathrm{p}}(t) = T_{\mathrm{b}} + \Delta T \cdot \mathrm{e}^{-t/\tau} \tag{2.2}$$

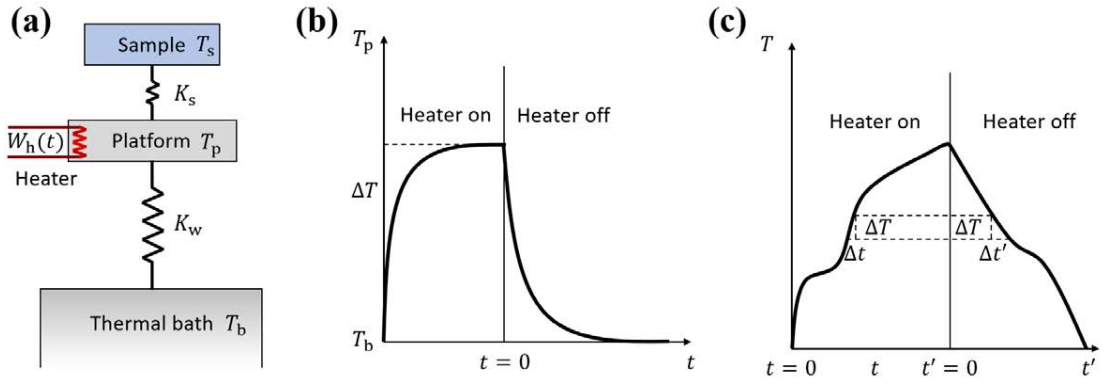

Figure 2.2: (a) General setup of heat capacity measurements. Diagram of a typical measurement cycle in (b) relaxation method and (c) dual slope method.

where T_p is the temperature of the platform, T_b is the temperature of the heat bath, and ΔT is the change in temperature due to the heat pulse. From this relaxation time constant and from the thermal conductance K_w of the thermal link to the heat bath, the heat capacity of the system sample plus calorimeter can be calculated:

$$C_P = \tau \cdot K_w \tag{2.3}$$

However, Eq.(2.2) is obtained by assuming that the sample and platform heat together uniformly. To account for a difference in heating between the sample and the platform, the following equation is sometimes used:

$$T_p(t) = T_b + A \cdot e^{-t/\tau_1} + B \cdot e^{-t/\tau_2} \tag{2.4}$$

where A and B are both constants, τ_1 is the time constant for relaxation between the platform and the heat sink, and τ_2 is the time constant for relaxation between the sample and the platform. Figure 2.2(b) shows the measurement process in which both Eq.(2.2) or Eq.(2.4) could be applied. A good review about heat capacity measurements made on a Quantum Design physical property measurement system (PPMS) is presented in [3].

2.2.2 Dual slope method

In the dual-slope method [4], C_P is evaluated by directly comparing the heating and cooling rates of the sample temperature without explicit use of the thermal conductance between sample and bath. A typical measurement cycle is shown in Fig. 2.2(c). First the specimen is continuously heated by application of heater power W_h to some desired temperature and is then allowed to cool down again to the initial temperature. During both the heating and the cooling parts of the cycle, the temperature of the specimen is recorded. The heat capacity at temperature T is derived from the slopes of the heating and cooling curves taken at temperature T, where the change in temperature ΔT takes a time Δt in the heating process and $\Delta t'$ in the cooling process:

$$C_P(T) = \frac{W_h}{\Delta T/\Delta t + \Delta T/\Delta t'} \tag{2.5}$$

Some advantages of this method are that measurements can be performed in a continuous way over a wide temperature range, and that the knowledge of the thermal conductance to the bath is not needed.

2.3 Neutron scattering

Neutron scattering techniques are a powerful tool in the study of condensed matter, offering insights into both its structure and dynamics at atomic level. For neutrons with relatively low kinetic energy (<500 meV), the corresponding de Broglie wavelength is comparable to interatomic distances in solids. Therefore, neutrons scattered on a crystal lattice can reveal interference patterns and provide information on

crystal structures. Furthermore, their kinetic energy matches typical excitations in condensed matter and their neutral charge allows for direct interaction with atomic nuclei. Neutron scattering is particularly important for studying magnetism and magnetic materials, as neutrons carry a magnetic moment due to their spin that interacts with the different sources of magnetism in the matter (unpaired electrons, magnetic nuclei, etc.).

In this section we cover the basic concepts regarding neutron properties, neutron scattering and the techniques employed in this thesis. A more complete and up-to-date description of the theoretical concepts and experimental results in the field of the neutron scattering techniques can be found in Ref. [5].

2.3.1 Basic concepts

Neutrons are stable within the nuclei, but free neutrons are unstable (lifetime of $\tau_{\mathrm{n}} \sim 881$ s), decaying via the weak interaction into a proton, an electron, and an antineutrino. With a spin of 1/2, the electromagnetic interactions of neutrons are primarily influenced by their dipolar magnetic moment, as described by:

$$\vec{\mu}_{\mathrm{n}} = -\gamma \mu_{\mathrm{N}} \frac{1}{2} \vec{\sigma} \tag{2.6}$$

Here, $\mu_{\mathrm{N}} \approx 5.05 \times 10^{-27}$J/T represents the nuclear magneton, $\gamma = 3.826$ denotes the neutron g-factor, and $\vec{\sigma}$ are the Pauli matrices that act on the neutron spin space.

Neutrons, unlike electromagnetic radiation (such as visible light or X-rays) or electrons, are not easily produced in laboratory settings. Instead, they are generated from two sources: nuclear reactors, where a steady neutron flux is a byproduct of controlled fission, or spallation sources, where neutrons are created when a beam of high-energy protons from linear accelerators (LINACs) strikes a heavy metal target. Regardless of the source, the total neutron flux is still lower compared to synchrotron X-ray sources. Neutrons are classified into cold (0.1–10 meV), thermal (10–100 meV), hot (100–500 meV), and epithermal (>500 meV) based on their energy.

The rest energy of the neutron is much higher than the kinetic energy of these neutrons, which are therefore non-relativistic particles with energy given by $E = \hbar^2 k^2 / 2m$, where $k = 2\pi/\lambda$ is the wave-number, λ is the wavelength, and $\hbar = h/2\pi$ is the reduced Planck's constant. This has important implications for the study of condensed matter systems, as the wavelength of neutrons with energy in the range of meV, which corresponds to the excitation energies of many systems, is in the Å range, which matches the inter-particle distances in these systems.

In a neutron scattering experiment (see Fig. 2.3), the initial neutron beam is prepared according to a specified criteria and scattered neutrons are detected by detectors positioned around the target. Thus, the measurable quantity is the differential scattering cross section, defined as the number of neutrons scattered per unit time, solid angle, and energy, normalized by the incident neutron flux. The neutron-target interaction can be described by the Hamiltonian operator $\mathcal{H}_{\mathrm{int}}$, that contains all information about the scattering process. Since this interaction is weak,

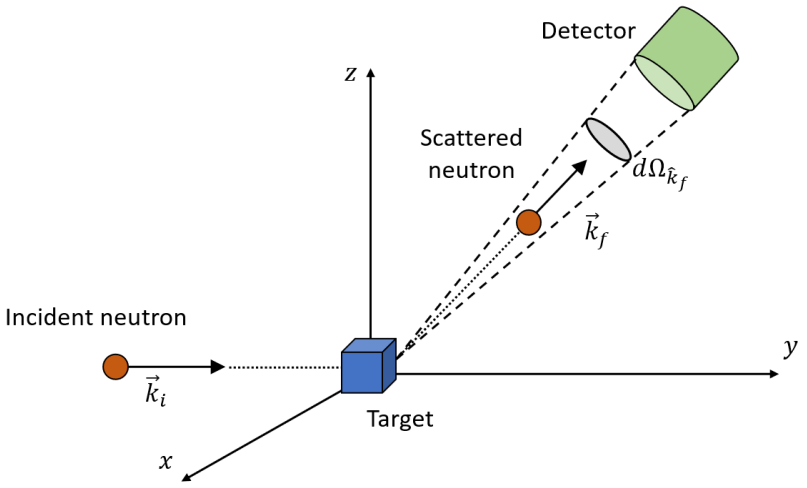

Figure 2.3: Generic process in a neutron scattering experiment.

$\mathcal{H}_{\text{int}}$ can be treated as a perturbation, resulting in the differential scattering cross section given by:

$$\left(\frac{d^2\sigma}{d\Omega_{\hat{k}_f} dE_f}\right)_{\sigma_f} = \frac{k_f}{k_i}\left(\frac{m_{\text{n}}}{2\pi\hbar^2}\right)^2 |\langle \vec{k}_f\sigma_f;\varphi_f|\mathcal{H}_{\text{int}}|\vec{k}_i\sigma_i;\varphi_i\rangle|^2\,\delta(E_{\varphi_i} - E_{\varphi_f} + \hbar\omega) \quad (2.7)$$

Here, m_{n} is the neutron mass, σ_i and φ_i the initial states of the neutron spin and the target, respectively, and E_{φ_i} the energy of the state φ_i. The same quantities denoted by f are the final states of the neutron and the target after the scattering process. The difference between the energies of the incident and scattered neutron is represented by $\hbar\omega = E_i - E_f$.

Elastic scattering occurs when no energy is transferred between the neutron and the target, indicated by $E_i = E_f$, resulting in $k_i = k_f$. On the other hand, if there is some energy transfer, the process is referred to as inelastic scattering. The Dirac delta function, δ, ensures that energy is conserved in the system long after the interaction takes place.

The next sections will be focused on the study of $\mathcal{H}_{\text{int}}$. Low-energy neutrons interact with matter through two mechanisms: the nuclear interaction with the nucleus and the electromagnetic interaction of the neutron magnetic moment $\vec{\mu}_{\text{n}}$ with the unpaired electrons. This means that neutrons can provide insight into both the nuclear and magnetic structures of a material.

2.3.2 Nuclear scattering

The strong nuclear interaction is highly complex and extremely strong, making it difficult to treat it using perturbation techniques. Despite its complexity, the range of the nuclear force is much shorter compared to the wavelength of neutrons with energies smaller than a few eV. As a result, neutrons can be considered as scattered

by a point-like nucleus, leading to isotropic scattering. This makes it possible to use an effective potential, known as the Fermi pseudopotential [6]:

$$V_{\mathrm{F}}(\vec{r}) = \frac{2\pi\hbar^2}{m_{\mathrm{n}}}\, b\, \delta(\vec{r}) \tag{2.8}$$

where $\delta(\vec{r})$ is the Dirac delta function, $\vec{r}$ the vector position of the neutron relative to the nucleus, and b is the so called scattering length, which in general is a complex number. The physical meaning of the imaginary part of b is the absorption of neutrons by nuclei.

The strength of the neutron-nucleus interaction depends on the spins of both the neutron and nucleus. As a result, there are two possible values for the total spin of the neutron-nucleus system, $J^{\pm} = I \pm 1/2$, where I is the total spin of the nucleus. Thus, there are two scattering lengths, b^+ and b^-, corresponding to the two composite states. This dependence on total spin can be taken into account using a scattering amplitude operator $\mathbb{B}$, which can be written as [7]:

$$\mathbb{B} = A + B\frac{1}{2}\vec{\sigma}\cdot\vec{\mathcal{I}} \tag{2.9}$$

where $\vec{\sigma}$ are the Pauli matrices, $\vec{\mathcal{I}}$ is the nucleus vector spin operator, and:

$$A = \frac{1}{2I+1}[(I+1)b^+ + Ib^-], \qquad B = \frac{2}{2I+1}(b^+ - b^-) \tag{2.10}$$

If the target contains N nuclei, where the n-th nucleus is located at $\vec{R}_n$, the nuclear interaction Hamiltonian is:

$$\mathcal{H}^{(\mathrm{n})}_{\mathrm{int}} = \frac{2\pi\hbar^2}{m_{\mathrm{n}}}\sum_{n=1}^{N} \mathbb{B}_n\, \delta(\vec{r} - \vec{R}_n) \tag{2.11}$$

We will restrain the discussion of solving Eq.(2.7) with $\mathcal{H}^{(\mathrm{n})}_{\mathrm{int}}$ to only the elastic scattering ($k_i = k_f$) process, since elastic scattering is often dominant in solids and all the techniques used in this thesis are based on this process. Considering Eq.(2.11) and summing over the neutron final spin states, one can obtain the nuclear elastic scattering cross section, which consists of a coherent and an incoherent part:

$$\frac{d^2\sigma^{(\mathrm{n,e})}}{d\Omega_{\hat{k}_f}} = \frac{d\sigma^{(\mathrm{n,e})}_{\mathrm{coh}}}{d\Omega_{\hat{k}_f}} + \frac{d\sigma^{(\mathrm{n,e})}_{\mathrm{inc}}}{d\Omega_{\hat{k}_f}} \tag{2.12}$$

The coherent nuclear elastic cross section is:

$$\frac{d\sigma^{(\mathrm{n,e})}_{\mathrm{coh}}}{d\Omega_{\hat{k}_f}} = \Big|\sum_n b_n \langle \mathrm{e}^{\mathrm{i}\vec{q}\cdot\vec{R}_n}\rangle\Big|^2 \tag{2.13}$$

and the incoherent nuclear elastic cross section is:

$$\frac{d\sigma^{(\mathrm{n,e})}_{\mathrm{inc}}}{d\Omega_{\hat{k}_f}} = \sum_n b^2_{\mathrm{inc},n}\Big|\langle \mathrm{e}^{\mathrm{i}\vec{q}\cdot\vec{R}_n}\rangle\Big|^2 \tag{2.14}$$

where $\vec{q} = \vec{k}_f - \vec{k}_i$ is the scattering vector, $b_n = \overline{A}_n$ and:

$$b_{\mathrm{inc},n} = \left[(\overline{A_n^2} - \overline{A}_n^2) + (1/4)\overline{B_n^2 I_n (I_n + 1)} \right]^{1/2} \tag{2.15}$$

The bars in Eq.(2.15) indicate the average over the isotopic distribution of the nuclei.

Elastic coherent scattering is characterized by the interference between the scattered waves, leading to peaks in the scattered intensity in specific directions determined by the atomic structure of the sample. In contrast, elastic incoherent scattering can be caused by the random positions of atoms or the presence of isotopes with different scattering lengths within the material, which eliminates the interference terms, resulting in only a smooth background contribution.

In the specific case of a crystal with unit cell $(\vec{a}, \vec{b}, \vec{c})$ and unit cell volume V_c, the equilibrium position of an atom can be written as $\vec{R}^{\,\mathrm{e}}_{ld} = \vec{R}_l + \vec{r}_d$, where $\vec{R}_l = l_a\vec{a} + l_b\vec{b} + l_c\vec{c}$, with l_a, l_b, and l_c integers, represents the position of the origin of the l-th cell, and $\vec{r}_d$ is the position of d-th atom relative to the origin of coordinates of the unit cell. We denote by $\vec{H}$ a node of the reciprocal lattice with $\vec{H} = h\,\vec{a}^{\,*} + k\,\vec{b}^{\,*} + l\,\vec{c}^{\,*}$, where h, k, l are integer numbers called Miller indices.

In such case, the coherent nuclear elastic cross section is computed as:

$$\left| \sum_n b_n \langle \mathrm{e}^{\mathrm{i}\vec{q}\cdot\vec{R}_n} \rangle \right|^2 = \sum_{l,l'} \mathrm{e}^{\mathrm{i}\vec{q}(\vec{R}_{l'} - \vec{R}_l)} |N_{\vec{q}}|^2 \tag{2.16}$$

where

$$N_{\vec{q}} = \sum_d^{N_\mathrm{uc}} b_d\, T_d(\vec{q})\, \mathrm{e}^{\mathrm{i}\vec{q}\cdot\vec{r}_d} \tag{2.17}$$

is the nuclear structure factor of the unit cell and N_uc is the number of atoms inside it. $T_d(\vec{q})$ is the so called Debye-Waller factor:

$$T_d(\vec{q}) = \left\langle \mathrm{e}^{\mathrm{i}\vec{q}\cdot\vec{u}_d} \right\rangle = \mathrm{e}^{-\vec{q}\cdot\tilde{\beta}_d\vec{q}} \tag{2.18}$$

It describes the damping of coherent neutron scattering with increasing temperature due to thermal fluctuations of the atoms $\vec{u}_n$ about their equilibrium positions $\vec{R}^{\,\mathrm{e}}_{ld}$. In the last step of Eq.(2.18) the harmonic approximation has been used. The tensor $\tilde{\beta}_n$ is sometimes referred to as the anisotropic displacement parameter.

Using the Poisson summation formula:

$$\sum_{l,l'} \mathrm{e}^{\mathrm{i}\vec{q}\cdot(\vec{R}_{l'} - \vec{R}_l)} = \frac{N_\mathrm{c}(2\pi)^3}{V_\mathrm{c}} \sum_{\vec{H}} \delta(\vec{q} - \vec{H}) \tag{2.19}$$

where N_c is the number of crystal unit cells in the system, we obtain:

$$\frac{d\sigma^{(\mathrm{n,e})}_\mathrm{coh}}{d\Omega_{\hat{k}_f}} = \frac{N_\mathrm{c}(2\pi)^3}{V_\mathrm{c}} \sum_{\vec{H}} \delta(\vec{q} - \vec{H}) |N_{\vec{q}}|^2 \tag{2.20}$$

Eq.(2.20) states that Bragg reflection will occur only when the direction of the scattered neutrons is equal to the scattering vector, $\vec{q} = \vec{H}$. This means that the

reflection will happen only at specific angles, determined by the nodes of the reciprocal lattice, which are associated with the characteristic distances between crystal planes (d_{hkl}) in the direct space. The intensity of the scattered neutrons for each of these directions is proportional to the square of the modulus of the nuclear structure factor, $N_{\vec{q}}$, evaluated at $\vec{q} = \vec{H}$.

2.3.3 Magnetic scattering

The electromagnetic interactions between neutrons and atoms have a longer range but are much weaker compared to other interactions. Thus, they can be treated using the Born approximation, a perturbative method. From the perspective of this interaction, the neutron can be considered as a neutral point particle with a magnetic moment. The interaction between the neutron magnetic moment and the nucleus is weaker compared to the interaction with the magnetic moment of electrons, since the nuclear magneton is two orders of magnitude smaller than the Bohr magneton. Hence, the interaction between the neutron magnetic moment and the electrons dominates the neutron-atom electromagnetic interaction.

The vector potential at a point $\vec{r}_j$ by the magnetic moment of the neutron $\vec{\mu}_\mathrm{n}$, located at point $\vec{r}$, is:

$$\vec{A}_\mathrm{n}(\vec{r}_j - \vec{r}) = \frac{\mu_0}{4\pi} \nabla_j \times \frac{\vec{\mu}_\mathrm{n}}{|\vec{r}_j - \vec{r}|} \tag{2.21}$$

It originates a magnetic field:

$$\vec{B}_\mathrm{n}(\vec{r}_j - \vec{r}) = \frac{\mu_0}{4\pi} \nabla_j \times \left(\nabla_j \times \frac{\vec{\mu}_\mathrm{n}}{|\vec{r}_j - \vec{r}|} \right) = \frac{\mu_0}{4\pi} \nabla \times \left(\nabla \times \frac{\vec{\mu}_\mathrm{n}}{|\vec{r}_j - \vec{r}|} \right) \tag{2.22}$$

where ∇ and ∇_j stand for the gradient with respect to $\vec{r}$ and $\vec{r}_j$, respectively.

Now we can consider the magnetic interaction Hamiltonian, $\mathcal{H}_\mathrm{int}^\mathrm{(m)}$, of the system composed of a free neutron and a system of N_e electrons. Let us denote by $\vec{p}_j$, $\vec{r}_j$ and $\vec{\mu}_j$ the j-th electron momentum, position and magnetic moment, respectively. Then we have two contributions to $\mathcal{H}_\mathrm{int}^\mathrm{(m)}$. The first one is due to the total vector potential at the position of j-th electron: $\vec{A}(\vec{r}_j) = \vec{A}_\mathrm{S}(\vec{r}_j) + \vec{A}_\mathrm{ext}(\vec{r}_j) + \vec{A}_\mathrm{n}(\vec{r}_j - \vec{r})$, which is a superposition of the internal vector potential of the electron-nuclei system, $\vec{A}_\mathrm{S}(\vec{r}_j)$, any applied external field, $\vec{A}_\mathrm{ext}(\vec{r}_j)$, and the vector potential due to the neutron, $\vec{A}_\mathrm{n}(\vec{r}_j - \vec{r})$. The second contribution is due to the dipole-dipole interaction between the electrons and the neutron, so that we have:

$$\begin{aligned} \mathcal{H}_\mathrm{int}^\mathrm{(m)} &= \sum_{j=1}^{N_\mathrm{e}} \frac{1}{2m_\mathrm{e}} \left[\vec{p}_j - e\vec{A}(\vec{r}_j) \right] - \sum_{j=1}^{N_\mathrm{e}} \vec{\mu}_j \cdot \vec{B}_\mathrm{n}(\vec{r}_j - \vec{r}) = \\ &= \frac{\mu_0 \mu_\mathrm{B}}{2\pi} \vec{\mu}_\mathrm{n} \cdot \sum_{j=1}^{N_\mathrm{e}} \left[-\frac{1}{\hbar} \frac{\vec{r}_j - \vec{r}}{|\vec{r}_j - \vec{r}|^3} \times \vec{p}_j + \nabla \times \left(\nabla \times \frac{\vec{s}_j}{|\vec{r}_j - \vec{r}|} \right) \right] \end{aligned} \tag{2.23}$$

We have neglected the quadratic terms in $\vec{A}$ and used $\vec{p}_j = -i\hbar\nabla_j$ and $\nabla_j \cdot \vec{A}_{\mathrm{n}} = 0$. We have also set $\vec{\mu}_j = -2\mu_{\mathrm{B}}\vec{s}_j$, where $\vec{s}_j$ is the spin operator of the j-th electron. Here μ_{B} is the Bohr magneton defined as $\mu_{\mathrm{B}} = e\hbar/2m_e \approx 9.27 \times 10^{-24}\mathrm{J/T}$, e and m_e are the electron elementary charge and rest mass, respectively.

The calculation of the magnetic scattering cross-section can be obtained by applying the same ideas as in nuclear scattering. However, it involves a much more complex Hamiltonian compared to its nuclear counterpart. To simplify the expressions, we make some assumptions about the system. We consider a scenario where the magnetic moments are produced by unpaired electrons localized at ions. This is the case for molecular orbitals in organic radicals, and in transition metals and rare earths where the unpaired electrons responsible for the magnetic moment belong to the p, d, and f sub-shells, respectively. Let N represent the number of ions, with each n-th ion nucleus located at $\vec{R}_n$. Considering the dipole approximation [8] and a weak coupling between the magnetic moment and nuclear dynamics, a simplified expression for the magnetic scattering cross-section can be obtained:

$$\left(\frac{d^2\sigma^{(\mathrm{m})}}{d\Omega_{\vec{k}_f} dE_f}\right)_{\sigma_f} = p^2 \frac{k_f}{k_i} \sum_{\alpha\beta} \rho^i_{\alpha\beta}(\sigma_f) \sum_{nn'} F^*_n(q) F_{n'}(q) \times \int \frac{dt}{h} \mathrm{e}^{-\mathrm{i}2\pi\nu t} \left\langle \mathrm{e}^{-\mathrm{i}\vec{q}\cdot\vec{R}_n(0)} \mathrm{e}^{\mathrm{i}\vec{q}\cdot\vec{R}_{n'}(t)} \right\rangle \left\langle \mathbb{M}^{\beta\,\dagger}_{n\perp\vec{q}}(0) \mathbb{M}^{\alpha}_{n'\perp\vec{q}}(t) \right\rangle \tag{2.24}$$

where:

$$\rho^i_{\alpha\beta}(\sigma_f) = \langle \sigma_f | \sigma_\alpha \varrho_i \sigma_\beta | \sigma_f \rangle \tag{2.25}$$

and ϱ_i is the density matrix of the incident beam. $p = 0.2695$ is a conversion constant from magnetic moments, given in Bohr magnetons μ_{B}, to scattering lengths in units of 10^{-14} m. $\vec{\mathbb{M}}_n$ denotes the n-th ion magnetic moment density operator, which is given by $-\mu_{\mathrm{B}} g_n$ times either the total angular momentum operator or the total spin operator, depending on the case. $\vec{\mathbb{M}}_{n\perp\vec{q}}$ is the component of the magnetic moment density operator perpendicular to $\vec{q}$. $F_n(q)$ and g_n are the corresponding magnetic form factor and Landé factor, respectively of the n-th ion. The magnetic form factor is related with the Fourier transform of the spatial density of unpaired electrons and arises because such density cannot be approximated by a point scatterer as in the case for nuclear scattering. Since it decreases rapidly with q, the magnetic scattering is limited to low momentum transfer.

For a magnetic crystal in which some of the ions in the unit cell have localized unpaired electrons, the neutrons will suffer magnetic scattering. Let d_{m} label the magnetic ions within a cell. The position of the ld_{m} ion is given by $\vec{R}_l + \vec{r}_{d_{\mathrm{m}}} + \vec{u}_{ld_{\mathrm{m}}}$, where $\vec{u}_{ld_{\mathrm{m}}}$ describes the displacements from the equilibrium position. The magnetic form factors depend only on d_{m}, and not on the cell to which the ion belongs. The elastic scattering component is extracted from the factorization of the time correlations in the $t \to \infty$ limit. Defining the vector $\vec{M}_{ld_{\mathrm{m}}} = \langle \vec{\mathbb{M}}_{ld_{\mathrm{m}}} \rangle$, we have:

$$\left(\frac{d\sigma^{(\mathrm{m,e})}}{d\Omega_{\hat{k}_f}}\right)_{\sigma_f} = p^2 \sum_{\alpha\beta} \rho^i_{\alpha\beta}(\sigma_f) \sum_{l d_\mathrm{m} l' d'_\mathrm{m}} \mathrm{e}^{\mathrm{i}\vec{q}\cdot(\vec{R}_{l'}-\vec{R}_l)} \times \\ \mathrm{e}^{-\mathrm{i}\vec{q}\cdot\vec{r}_{d_\mathrm{m}}} T^*_{d_\mathrm{m}}(\vec{q}) F^*_{d_\mathrm{m}}(\vec{q}) \mathrm{e}^{\mathrm{i}\vec{q}\cdot\vec{r}_{d'_\mathrm{m}}} T_{d'_\mathrm{m}}(\vec{q}) F_{d'_\mathrm{m}}(\vec{q}) M^{\beta\,*}_{l d_\mathrm{m} \perp \vec{q}} M^{\alpha}_{l d_\mathrm{m} \perp \vec{q}} \tag{2.26}$$

In the most general case, $\vec{M}_{l d_\mathrm{m}}$ need not be commensurate with the nuclear lattice, but it can always be expanded in Fourier series as:

$$\vec{M}_{l d_\mathrm{m}} = \sum_{\{\vec{K}\}} \vec{S}_{\vec{K} d_\mathrm{m}} \mathrm{e}^{-\mathrm{i}\vec{K}\cdot\vec{R}_l} \tag{2.27}$$

where the complex vectors $\vec{S}_{\vec{K} d_\mathrm{m}}$ are the Fourier coefficients and $\{\vec{K}\}$ are the set of propagation vectors. The propagation vectors relate the magnetic moment at the l-th unit cell with respect to the zero-th unit cell. In the case of $\vec{K} = 0$, which means that the nuclear and magnetic periodicity are the same, then the Fourier coefficients, $\vec{S}_{\vec{K} d_\mathrm{m}}$ are equal to the magnetic moment, $\vec{M}_{d_\mathrm{m}}$, at site d_m, and do not depend on the lattice index l. Moreover, because the magnetic moment $\vec{M}_{l d_\mathrm{m}}$ must be a real vector, it imposes the condition that summation extends to pairs of propagation vectors $\vec{K}$ and $-\vec{K}$ and the relation $\vec{S}_{-\vec{K} d_\mathrm{m}} = \vec{S}^*_{\vec{K} d_\mathrm{m}}$ between the Fourier coefficients.

Inserting Eq.(2.27) into Eq.(2.26) and using Eq.(2.19) for the sum in $l\,l'$, we get:

$$\frac{d\sigma^{(\mathrm{m,e})}_{\mathrm{coh}}}{d\Omega_{\hat{k}_f}} = \frac{N_\mathrm{c}(2\pi)^3}{V_\mathrm{c}} \sum_{\vec{H}\vec{K}} \delta(\vec{q} - \vec{H} \pm \vec{K}) \, |\vec{M}_{\perp\vec{q}}|^2 \tag{2.28}$$

where we have defined the magnetic interaction vector, $\vec{M}_{\perp\vec{q}}$, and the magnetic structure factor, $\vec{M}_{\vec{q}\vec{K}}$, for the crystal unit cell as;

$$\vec{M}_{\perp\vec{q}} = \hat{q} \times (\vec{M}_{\vec{q}\vec{K}} \times \hat{q}) \tag{2.29}$$

$$\vec{M}_{\vec{q}\vec{K}} = p \sum_{d_\mathrm{m}}^{N_\mathrm{uc}} F_{d_\mathrm{m}}(\vec{q}) T_{d_\mathrm{m}}(\vec{q}) \; \mathrm{e}^{\mathrm{i}\vec{q}\cdot\vec{r}_{d_\mathrm{m}}} \vec{S}_{\vec{K} d_\mathrm{m}} \tag{2.30}$$

Similar to the nuclear scattering, Eq.(2.28) impose that magnetic Bragg peaks will occur only when the scattering vector fulfills the condition $\vec{q} = \vec{H} \pm \vec{K}$. However, one important difference to bear in mind is that in the magnetic scattering, only the component of $\vec{M}_{\vec{q}\vec{K}}$ perpendicular to $\vec{q}$ contributes to the intensity of the magnetic Bragg peaks. Furthermore, the intensity of magnetic peaks is highly sensitive to temperature, as the expectation value of $\vec{M}_{l d_\mathrm{m}}$ decreases with increasing temperature until it vanishes above the magnetic ordering temperature, where only the nuclear peaks persist. The temperature dependence is therefore a useful way to distinguish magnetic and nuclear scattering.

2.3.4 Polarization analysis

So far, we have only considered the scattering of an unpolarized neutron beam. However, the utilization of a polarized neutron beam, along with the analysis of the polarization of the scattered beam, provides us with enhanced information about the target compared to the simpler scattering of an unpolarized beam. This is due to the introduction of correlations between the nuclear and magnetic scattering amplitudes, which are absent in the case of an unpolarized beam. To better understand the scattering of a polarized beam, we consider the following assumptions: (i) the nuclear spins are randomly oriented in space, (ii) the spin orientations of different nuclei are uncorrelated, and (iii) the disorder in magnetic properties is independent of the disorder in nuclear properties.

By introducing the generic nuclear structure factor $W_{\vec{q}}$ and magnetic interaction vector $\vec{V}_{\vec{q}}$ for the whole system:

$$W_{\vec{q}} \;=\; \sum_n b_n \big\langle \mathrm{e}^{\mathrm{i}\vec{q}\cdot\vec{R}_n} \big\rangle \tag{2.31}$$

$$\vec{V}_{\vec{q}} \;=\; p \big\langle \vec{\mathcal{M}}_{\perp\vec{q}} \big\rangle \tag{2.32}$$

and considering only the coherent elastic scattering, one can arrive to the so called Blume-Maleev Equations [9, 10], which provide the intensity and polarization vector of the elastically scattered beam:

$$I_{\vec{q}} = W_{\vec{q}} W^*_{\vec{q}} + \vec{V}_{\vec{q}} \cdot \vec{V}^*_{\vec{q}} + \big(W_{\vec{q}} \vec{V}^*_{\vec{q}} + \vec{V}_{\vec{q}} W^*_{\vec{q}}\big) \cdot \vec{P}_i - \mathrm{i}\big(\vec{V}_{\vec{q}} \times \vec{V}^*_{\vec{q}}\big) \cdot \vec{P}_i \tag{2.33}$$

and

$$\begin{aligned} I_{\vec{q}} \vec{P}_f = {} & \big(W_{\vec{q}} W^*_{\vec{q}} - \vec{V}_{\vec{q}} \cdot \vec{V}^*_{\vec{q}}\big) \vec{P}_i \;+\; \vec{V}_{\vec{q}} \big(\vec{P}_i \cdot \vec{V}^*_{\vec{q}}\big) \;+\; \big(\vec{P}_i \cdot \vec{V}_{\vec{q}}\big) \vec{V}^*_{\vec{q}} \\ & + \mathrm{i}\big(\vec{V}_{\vec{q}} W^*_{\vec{q}} \;-\; W_{\vec{q}} \vec{V}^*_{\vec{q}}\big) \times \vec{P}_i \;+\; W_{\vec{q}} \vec{V}^*_{\vec{q}} \;+\; W^*_{\vec{q}} \vec{V}_{\vec{q}} \;+\; \mathrm{i}\big(\vec{V}_{\vec{q}} \times \vec{V}^*_{\vec{q}}\big) \end{aligned} \tag{2.34}$$

where $\vec{P}_f$ and $\vec{P}_i$ are, respectively, the final and initial beam polarizations. Now, let's consider the elastic scattering by a crystal. As before, we express the ion position as $\vec{R}_l + \vec{r}_d + \vec{u}_{ld}$, resulting in the following forms for Eq. (2.31) and Eq. (2.32):

$$W_{\vec{q}} = N_{\vec{q}} \sum_l \mathrm{e}^{\mathrm{i}\vec{q}\cdot\vec{R}_l} \qquad \vec{V}_{\vec{q}} = \sum_{\vec{K}} \vec{M}_{\perp\vec{q}} \sum_l \mathrm{e}^{\mathrm{i}(\vec{q}+\vec{K})\cdot\vec{R}_l} \tag{2.35}$$

Here, $N_{\vec{q}}$ and $\vec{M}_{\perp\vec{q}}$ are defined by Eq. (2.17) and Eq. (2.29), so that each term in Eq. (2.33) and Eq. (2.34) contains sums over l and l' similar to the forms in Eq. (2.19). Therefore, in these equations every term contains a Dirac delta function $\delta(\vec{q} - \vec{H} \pm \vec{K})$. We obtain the first Blume-Maleev equation for scattered intensity in a crystal:

$$I_{\vec{q}} = |N_{\vec{q}}|^2 + |\vec{M}_{\perp\vec{q}}|^2 + \Big(N_{\vec{q}} \vec{M}^*_{\perp\vec{q}} + N^*_{\vec{q}} \vec{M}_{\perp\vec{q}}\Big) \cdot \vec{P}_i + \mathrm{i}\,\Big(\vec{M}^*_{\perp\vec{q}} \times \vec{M}_{\perp\vec{q}}\Big) \cdot \vec{P}_i \tag{2.36}$$

where the vectors $N_{\vec{q}}\vec{M}^*_{\perp\vec{q}}+N^*_{\vec{q}}\vec{M}_{\perp\vec{q}}$ and $\mathrm{i}\vec{M}^*_{\perp\vec{q}}\times\vec{M}_{\perp\vec{q}}$ are referred to as the nuclear-magnetic interference vector and chiral vector. It should be noted that, by definition, $N_{\vec{q}}$ vanishes unless $\vec{K}$ is a vector of the nuclear reciprocal lattice, and hence, nuclear scattering does not contribute to the magnetic satellites. The second Blume-Maleev equation for the scattered polarization in a crystal is:

$$\begin{aligned} I_{\vec{q}}\vec{P}_f &= \left(|N_{\vec{q}}|^2-|\vec{M}_{\perp\vec{q}}|^2\right)\vec{P}_i+\left(\vec{P}_i\cdot\vec{M}^*_{\perp\vec{q}}\right)\vec{M}_{\perp\vec{q}}+\left(\vec{P}_i\cdot\vec{M}_{\perp\vec{q}}\right)\vec{M}^*_{\perp\vec{q}} \\ &- \mathrm{i}\left(N_{\vec{q}}\vec{M}^*_{\perp\vec{q}}-N^*_{\vec{q}}\vec{M}_{\perp\vec{q}}\right)\times\vec{P}_i+N_{\vec{q}}\vec{M}^*_{\perp\vec{q}}+N^*_{\vec{q}}\vec{M}_{\perp\vec{q}} \\ &- \mathrm{i}\left(\vec{M}^*_{\perp\vec{q}}\times\vec{M}_{\perp\vec{q}}\right) \end{aligned} \tag{2.37}$$

2.3.5 Scattering experiments

This thesis presents the results of a comprehensive study of elastic scattering experiments conducted at various facilities. Here, we survey the different scattering techniques used. Three key advantages can be highlighted that justify the use of such techniques:

As discussed in Section 2.3.2, the scattering length of neutrons depends on several factors such as the type and isotope of the nucleus, and the orientation of the neutron relative to the nuclear spin. Figure 2.4 shows the comparison between the neutron and X-ray interactions with matter, which highlights neutron scattering as a particularly well-suited method for determining the nuclear structure of a sample, especially if the sample contains light elements or a combination of light and heavy elements. Furthermore, if multiple neighboring elements are present in the sample, neutron scattering can effectively distinguish between them.

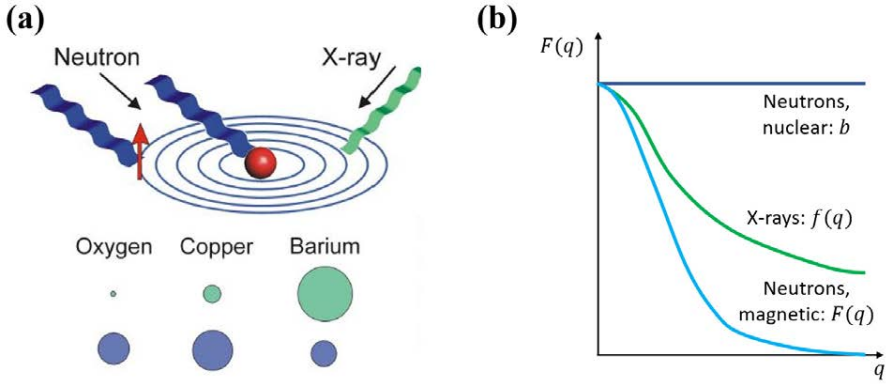

Figure 2.4: (a) Top: Neutrons interact with matter through the nuclear interaction with the nucleus and the electromagnetic interaction with the unpaired electrons, while X-rays interact with the electron cloud via electromagnetic interaction. Bottom: comparison of the neutron and X-ray scattering cross section for different atoms. (b) Form factor dependence with the modulus of the scattering vector for the different interactions considered in (a).

The small size of atoms (~ 1 Å $= 10^{-10}$ m) and nuclei (about 10^{-14} m), combined with the short-range nature of the neutron-nuclei interaction, gives neutrons high penetration power in matter. With the exception of absorbing isotopes, neutrons effectively see matter as empty, as they only interact with the small nuclei. As a result, experiments in complex sample environments, including low and high temperatures (from mK to 3000 K), high pressures (up to 30 GPa), and high magnetic fields (up to 20 T), can be easily performed using neutron diffraction.

Additionally, as described in Section 2.3.3, neutrons also interact with matter via the magnetic dipolar interaction with unpaired electrons, with a scattering cross-section that is comparable to the nuclear one. This makes neutron scattering the primary technique for determining magnetic structures. While powder neutron diffraction is the most common method, single crystal techniques with polarized or unpolarized neutrons may be necessary in certain cases, as will be discussed later.

Neutron Powder Diffraction

Diffraction is a powerful method where the nuclear or magnetic cross section is measured while the scattering vector $\vec{q}$ is varied. In the case of nuclear scattering, given by Eq.(2.20), scattered intensity will be detected only when the Bragg condition is satisfied:

$$\vec{q} = \vec{k}_f - \vec{k}_i = \vec{H} \tag{2.38}$$

$$q = 2k_i \sin\theta = H \Longrightarrow 2d \sin\theta = n\lambda \tag{2.39}$$

where d is the inter-planar spacing between adjacent planes with Miller indices h/n, k/n, l/n.

In neutron powder diffraction (NPD), a monochromatic beam is scattered from a sample formed by a huge number of randomly oriented microscopic single crystals (see Fig. 2.5(a)). These crystallites form a 3-dimensional reciprocal space represented by a set of concentric spherical shells, where the radius of each shell is equal to the magnitude of the reciprocal lattice vector $\vec{H}$. The intersection of these shells with the surface which satisfies the diffraction conditions (Ewald Sphere), gives rise to the characteristic Debye-Scherrer cones of powder diffraction. The intersection of these cones with a 2D detector results in the familiar Debye-Scherrer rings. Integrating the intensity around these rings results in a 1D diffraction pattern, where the x-axis corresponds to the 2θ angle ($n\lambda = 2d\sin\theta$) and the y-axis represents the diffracted intensity. In this way, the 3D reciprocal lattice is condensed into a 1D pattern in powder diffraction. This leads to both accidental and exact overlap of peaks, which can sometimes make it difficult to determine individual peak intensities.

In reactor-based neutron sources, diffractometers typically employ the 2θ angle as the scattering variable due to their constant wavelength operation. However, in spallation neutron sources, which operate in a pulsed manner, diffractometers utilize Time-of-Flight (ToF) techniques, where the scattering variable is the incident neutron wavelength λ_i of a polychromatic beam. The variable λ_i can be determined by measuring the time t_i it takes for a neutron to travel a fixed distance L, since

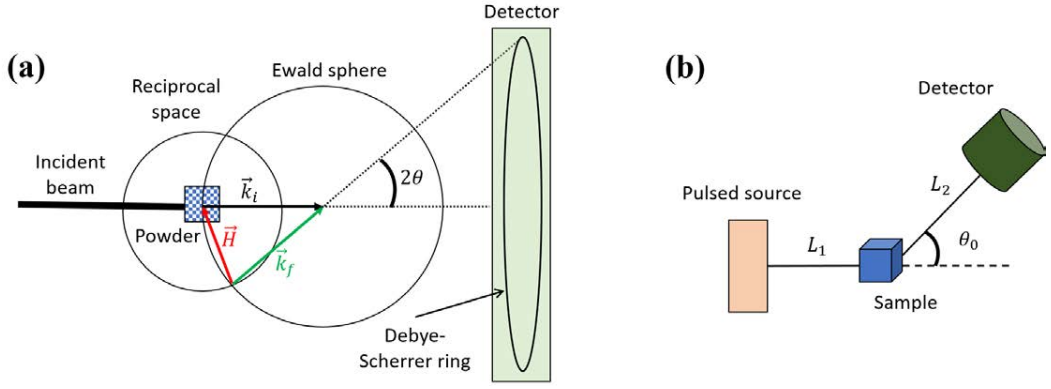

Figure 2.5: (a) Neutron powder diffraction setup. (b) Time-of-Flight setup, where the total length covered by a detected neutron is $L = L_1 + L_2$.

from the de Broglie equation we can relate the wavelength of the neutron to its velocity, v_i, as $\lambda_i = h/m_{\mathrm{n}}v_i$. Combining these concepts with Eq.(2.39) results in:

$$\lambda_i = \frac{ht_i}{m_{\mathrm{n}}L} = 2d_i \sin\theta_0, \qquad t_i = 505.55685(40)\ L\ d_i \sin\theta_0 \tag{2.40}$$

Here, t_i is measured in microseconds (μs), L in meters (m), and d_i in angstroms (Å). The d-spacing is then directly proportional to the time of flight (t_i), and the diffraction patterns are collected at a fixed θ_0 (see Fig. 2.5(b)). To measure t_i, only the arrival time of the neutron at the detector is required, as the starting time of the neutron is fixed using a chopper in reactor sources or a pulse structure in spallation sources.

Single Crystal Neutron Diffraction

One drawback of the NPD techniques is that we have access to only the modulus of the reciprocal lattice $\vec{H}$ node vector, and therefore different reflections $I_{\vec{H}}$ associated to $\vec{H}$ vectors with the same modulus can overlap at the same point in the powder diffractogram. In those cases, the diffraction in single crystals is more suitable, since it permits the full exploration of the 3D reciprocal space and the individual measurement of the Bragg peak intensity is more accurate than in a NPD experiment.

For single-crystal neutron diffraction (SCND), a single incident wavelength is used. The detector is placed at the 2θ position for a specific Bragg peak and the sample is rotated about an axis perpendicular to the scattering plane in order to scan through the Bragg peak (usually referred as ω-scan). Such scans are needed since the Bragg peaks have a finite width due to different factors (finite size of crystal, instrument resolution, crystal imperfections). This process is repeated for a large number of Bragg peaks to obtain their integrated intensities. A dedicated instrument for this purpose is the 4-circle diffractometer, where the crystal is mounted on an Eulerian cradle which allows any orientation of the crystal with respect to the incident neutron beam.

Once the integrated intensities are obtained, several corrections have to be applied to extract the structure factors (nuclear or magnetic) from the experimental data:

$$I_{\vec{q}} = \alpha |F_{\vec{q}}|^2 \tag{2.41}$$

where α includes corrections such as: 1) Lorentz factor, accounting for the geometry of the experimental method, 2) absorption of the sample, which attenuates the intensity of the incident neutron beam, 3) incoherent scattering, which has a similar effect as the absorption, so generally both effects are corrected together, 4) extinction, which accounts for the lost of incident neutron beam intensity due to the intensity already diffracted, and 5) multiple scattering, as the conditions for diffraction can be fulfilled by several Bragg peaks at the same time.

Polarized Neutron Diffraction

Since the magnetic structure factors $\vec{M}_{\vec{q}}$ are the Fourier transform of the magnetization density in the unit cell, the key idea behind a polarized neutron diffraction (PND) experiment is to use the precise measurement of $\vec{M}_{\vec{q}}$ to determine the magnetization density distribution.

For that purpose, the initial polarization $\vec{P}_i$ of the neutron beam is changed between two states, up ($\uparrow$) and down ($\downarrow$) by using ^{3}He spin filters or Heusler-Alloy monochromators. The detector counts for all the scattered neutrons for each initial polarization state up, $I^{\uparrow}_{\vec{q}}$, or down, $I^{\downarrow}_{\vec{q}}$, so that the experimental flipping ratio, $R_{\vec{q}} = I^{\uparrow}_{\vec{q}}/I^{\downarrow}_{\vec{q}}$, is determined. Starting from Eq.(2.36), and assuming that both the magnetization and the polarization of the beam $\vec{P}_i$ are parallel to a magnetic field applied along the $\vec{z}$ axis, $R_{\vec{q}}$ can also be calculated as:

$$R_{\vec{q}} = \frac{I^{\uparrow}_{\vec{q}}}{I^{\downarrow}_{\vec{q}}} = \frac{|N_{\vec{q}}|^2 + p^+ q^2 (N_{\vec{q}} M^{z*}_{\perp\vec{q}} + N^*_{\vec{q}} M^z_{\perp\vec{q}}) + q^2 |\vec{M}_{\perp\vec{q}}|^2}{|N_{\vec{q}}|^2 - p^- q^2 (N_{\vec{q}} M^{z*}_{\perp\vec{q}} + N^*_{\vec{q}} M^z_{\perp\vec{q}}) + q^2 |\vec{M}_{\perp\vec{q}}|^2} \tag{2.42}$$

where p^+ and p^- are the effective polarization for spin-up and spin-down of the incident beam, and $q = \sin\alpha$ with α being the angle between the magnetic field and the scattering vector of the Bragg reflection $\vec{q}$. In order to maximize the signal $\alpha \sim 90°$, so the reflections are measured near the horizontal plane.

Eq.(2.42) is only valid when the nuclear and magnetic Bragg peaks are superposed ($\vec{K} = \vec{0}$). Since Eq.(2.42) also assumes the magnetization to be parallel to the applied field, in most cases the measurements are performed at very high magnetic fields and low temperatures. Only in cases of high magnetic anisotropy the condition of collinearity is not fulfilled.

The flipping-ratio method presents two main advantages. First, the sensitivity to the magnetic signal is highly improved. In addition, the corrections applied to the intensity are multiplicative factors which are canceled in Eq.(2.42), so they are not taken into account in PND experiments.

In these experiments the nuclear structure factors $N_{\vec{q}}$ are known variables, since the crystalline structure is usually obtained from a previous non-polarized neutron experiment. Therefore, the only unknown quantities are $M^z_{\perp\vec{q}}$. When the crystal

structure is non-centrosymmetric, both $N_{\vec{q}}$ and $\vec{M}_{\perp\vec{q}}$ can be complex numbers, complicating the derivation of the magnetic structure factors $\vec{M}_{\vec{q}}$ from Eq.(2.42) through direct methods (Fourier Transform, Maximum Entropy). Instead, the spin density distribution can be easily modeled by using indirect methods. Two approaches have been used in this thesis to model the spin-density distribution of organic radicals:

- Wavefunction approach [11]: in this method the magnetization density $m(\vec{r}) = \left|\left\langle\vec{\mathbb{M}}(\vec{r})\right\rangle\right|$ is described in terms of a magnetic wavefunction ψ, which is a linear combination of atomic magnetic orbitals $|\phi_i^l\rangle$ centered at each ion:

$$m(\vec{r}) = |\psi(\vec{r})|^2 = \sum_i^{atoms} S_i \ |\phi_i^l(\vec{r} - \vec{r}_i)\rangle|^2 \tag{2.43}$$

  The atomic orbitals can be chosen to be a p ($l = 1$), d ($l = 2$) or f ($l = 3$) orbital expressed in terms of spherical harmonics:

$$\phi_i^l = R_i^l(|\vec{r} - \vec{r}_i|) \sum_m a_{ilm} Y_l^m(\theta_i, \varphi_i) \tag{2.44}$$

  where Y_l^m are spherical harmonics as functions of the polar angles (θ_i, φ_i) of the vector $\vec{r} - \vec{r}_i$. The R_i^l radial functions are Slater functions:

$$R_i^l(r) = \frac{\zeta^{n_{il}+3}}{(n_{il}+2)!} r^{n_{il}} \mathrm{e}^{-\zeta_{il} r} \tag{2.45}$$

  where $n_{il} = n-1$, being n the principal quantum number of the atomic orbital. The magnetic structure factors are fitted in a least-squares procedure where the variables are the atomic spin populations S_i, the coefficients a_{ilm}, and the exponents ζ_{il} of the Slater radial functions.

- Multipolar-expansion approach [12]: in this approach the magnetization density is divided into separate atomic contributions, expanded in the basis of real spherical harmonics d_l^m, also referred as multipoles:

$$m(\vec{r}) = \sum_i^{atoms} \sum_l R_i^{l,dens}(|\vec{r} - \vec{r}_i|) \sum_{m=-l}^{m=+l} P_{ilm} d_l^m(\theta_i, \varphi_i) \tag{2.46}$$

  where P_{ilm} are the population coefficients of the real spherical harmonics $d_l^m(\theta_i, \varphi_i)$ and $R_i^{l,dens}$ are Slater radial functions as in the wavefunction approach. In this case $n_{il} = 2(n-1)$, while ζ_{il} is twice the standard Slater exponent tabulated for the atoms. The variables to be fitted in this method are the populations of the multipoles P_{ilm} and the ζ_{il} parameters of the Slater radial functions.

Small-Angle Neutron Scattering

Small Angle Neutron Scattering (SANS) is a widely-used technique for investigating microstructural as well as magnetic inhomogeneities in diverse fields such as materials science, physics, chemistry and biology. SANS stands out among experimental methods as it allows for the examination of mesoscopic length scales (ranging from 1-300 nm) in real space and in bulk materials. Moreover, due to the neutron's spin, SANS possesses remarkable sensitivity in exploring magnetic phenomena and materials at the nano- and mesoscopic levels.

Considering the length scales accessible in SANS, the discrete nature of matter becomes irrelevant, leading to the replacement of the magnetization on each atom $\vec{M}_{d_\mathrm{m}}$ with a continuous vector field $\vec{M}(\vec{r})$. The magnetic SANS signal effectively captures the variation in magnetization modulus and orientation at the nano-scale. Hence, the magnetic structure factor vector $\vec{M}(\vec{q})$ used in SANS is the Fourier Transform of the field $\vec{M}(\vec{r})$. Similarly, the scalar nuclear structure factor $N(\vec{q})$ is defined using a scattering length density $b(\vec{r})$ instead of the atomic scattering length b_n, yielding:

$$\vec{M}(\vec{q}) = \frac{1}{(2\pi)^{3/2}} \int d^3r \; \vec{M}(\vec{r}) \; \mathrm{e}^{-\mathrm{i}\vec{q}\cdot\vec{r}} \tag{2.47}$$

$$N(\vec{q}) = \frac{1}{(2\pi)^{3/2}} \int d^3r \; b(\vec{r}) \; \mathrm{e}^{-\mathrm{i}\vec{q}\cdot\vec{r}} \tag{2.48}$$

Two scattering geometries are commonly used in a typical SANS setup, where the external magnetic field is applied either perpendicular ($\vec{B} \perp \vec{k}_i$) or parallel ($\vec{B} \parallel \vec{k}_i$) to the incoming neutron beam [13]. If $\vec{B} \perp \vec{k}_i$, the neutron beam is assumed to travel along the X axis, the vertical direction corresponds with the Y axis, and the Z axis is determined by applying the right-hand rule. $0 \leq \theta \leq 360°$ corresponds with the angle in the YZ plane (detector azimuthal angle), while ψ is an angle which lies in the XY plane when $\theta = 90°$. In the case that $\vec{B} \parallel \vec{k}_i$, the X and Z axis are interchanged, so that the magnetic field always lies along Z. An example of both geometries is shown in Fig. 2.6.

If we suppose an elastic scattering ($k_i = k_f = 2\pi/\lambda$), the value of the scattering vector is:

$$\vec{q} = \vec{k}_f - \vec{k}_i = k_i \begin{pmatrix} \cos\psi - 1 \\ \sin\psi \sin\theta \\ \sin\psi \cos\theta \end{pmatrix} = q \begin{pmatrix} -\sin(\psi/2) \\ \cos(\psi/2) \sin\theta \\ \cos(\psi/2) \cos\theta \end{pmatrix} \tag{2.49}$$

where $\vec{q}$ has modulus $q = 2k_i \sin(\psi/2)$. The name SANS comes from the consideration of a small value for the ψ angle , which often leads to the approximation:

$$\vec{q} \approx q \begin{pmatrix} 0 \\ \sin\theta \\ \cos\theta \end{pmatrix} \tag{2.50}$$

In order for this approximation to be valid, the radial distance on the detector (measured from the beam center) is usually between 0.04–0.7 m, while the sample-to-detector distance is in the range of 1–40 m.

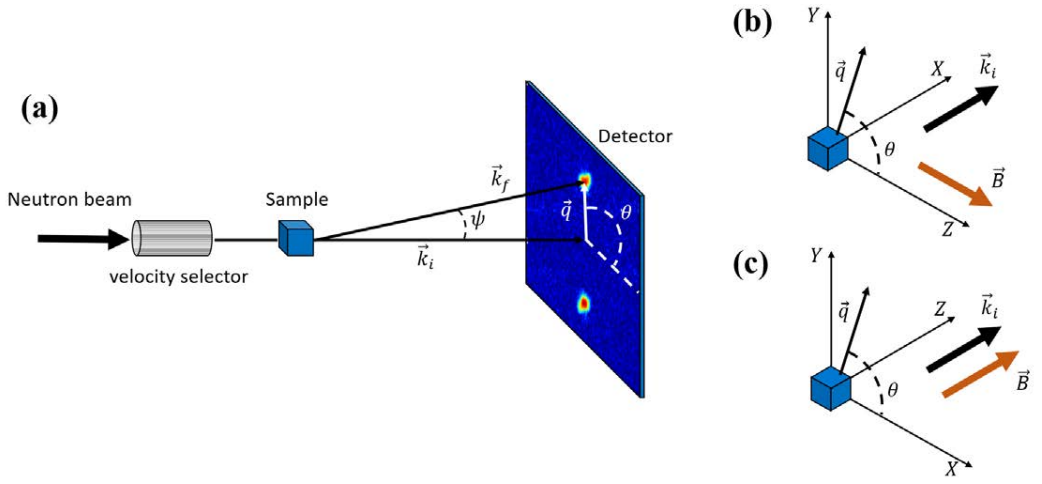

Figure 2.6: Schematic view of the SANS setup (a) and the two commonly employed scattering geometries in magnetic SANS experiments: $\vec{B} \perp \vec{k_i}$ (b) and $\vec{B} \parallel \vec{k_i}$ (c).

The governing equations for SANS cross sections for unpolarized or polarized neutrons are the Blume-Malayev equations (Eq.(2.33) and Eq.(2.34)), which have to be adapted to the SANS configurations $\vec{B} \parallel \vec{k_i}$ or $\vec{B} \perp \vec{k_i}$.

2.4 X-ray diffraction

In this thesis, crystal structure analysis was also performed via X-ray diffraction, which is complementary to neutron diffraction and particularly helpful for the investigation of elements for which neutron diffraction is less sensitive.

X-rays are electromagnetic waves with an energy range of 0.1–100 keV which corresponds to wavelengths of 0.13–130 Å, covering the typical atomic distances in solids. X-rays can be either produced in laboratory X-ray tubes or at synchrotrons, where the latter produces higher intensity and lower divergence X-rays than the former one. X-rays scatter from the electron cloud via electromagnetic interactions, which can be described in analogy to magnetic neutron scattering by an atomic form factor:

$$f_d(\vec{q}) = \frac{1}{(2\pi)^{3/2}} \int d^3r \; \rho_d(\vec{r}) \; \mathrm{e}^{-\mathrm{i}\vec{q}\cdot\vec{r}} \tag{2.51}$$

where $\rho_d(\vec{r})$ is the spatial density of electrons around the d-th nucleus. The X-ray structure factor $N_{\vec{q}}^{\mathrm{X}}$ has similar form as the nuclear structure factor described in Eq.(2.17). Since the electron cloud cannot be considered as a point scatterer the scattering length b_d has to be replaced by the atomic form factor $f_d(\vec{q})$ in Eq.(2.51). For the simplified case of a spherical electron distribution around a given nucleus, the atomic form factor only depends on the modulus of the scattering vector:

$$f(q) = 4\pi \int \rho(r) \, \frac{\sin(qr) r^2}{qr} \, dr \tag{2.52}$$

From Eq.(2.52) it follows that the scattering is maximal for low q, similar to the magnetic form factor dependence. Additionally, since X-rays scatter from electrons, the X-ray scattering amplitude is proportional to the atomic number. Consequently, X-ray scattering is relatively weak for light elements such as hydrogen and oxygen when compared to nuclear neutron scattering.

For a more complete description of the theoretical and practical aspects of X-ray diffraction, refer to Ref. [14].

2.5 Muon Spin Rotation

The muon spin techniques, also known as μSR (muon spin rotation, relaxation, or resonance), are a powerful tool for investigating the electronic and magnetic properties of condensed-matter systems on the atomic scale. These techniques involve implanting spin-polarized muons in the material under study and measuring the time evolution of their spin, which is sensitive to the local environment. From now on we will only consider the positively charged muon, which will simply be referred to as the muon in this thesis. The μSR techniques provide a local probe of hyperfine fields, as do nuclear magnetic resonance (NMR), perturbed angular correlations (PAC) and Mössbauer spectroscopy. Therefore the basic physical concepts developed for the latter techniques can be adapted to μSR. Compared to other microscopic techniques, μSR has several advantages, such as high sensitivity to weak magnetic moments, a unique time window for tracking dynamic processes, the ability to study samples without specific nuclei and the use of relatively complicated sample environments. However, a major drawback is the requirement of large sample mass, typically 150 mg per square centimeter of beam cross section for conventional setups. This results in limited sample thickness of around 1 mm for organic materials (density ≈ 1 g/cm^3) and 100–300 μm for denser materials such as transition metals. Despite this constraint, μSR has been successfully applied to a range of materials, including semiconductors and high-T_C superconductors. A comprehensive overview of its applications and underlying theoretical concepts can be found in Ref. [15]. This section focuses on the aspects relevant for the discussion of the experimental observations and simulation routines included in the thesis.

2.5.1 Basic principles

Intense muon beams are usually produced at intermediate energy particle accelerators in a two-step process. First, a thin target of graphite or beryllium is bombarded with a proton beam. For a usual target (thickness of $\sim$1 cm) only a small fraction of the protons interact with it, typically a few percent. These protons engage in reactions with the protons and neutrons in the target, leading to the generation of pion π particles. Second, since the pion itself is an unstable particle (lifetime of $\tau_\pi = 26$ ns), it decays into a muon and a muonic neutrino (see Fig. 2.7(a)) according to (2.53):

$$\pi^+ \longrightarrow \mu^+ + \nu_\mu \tag{2.53}$$

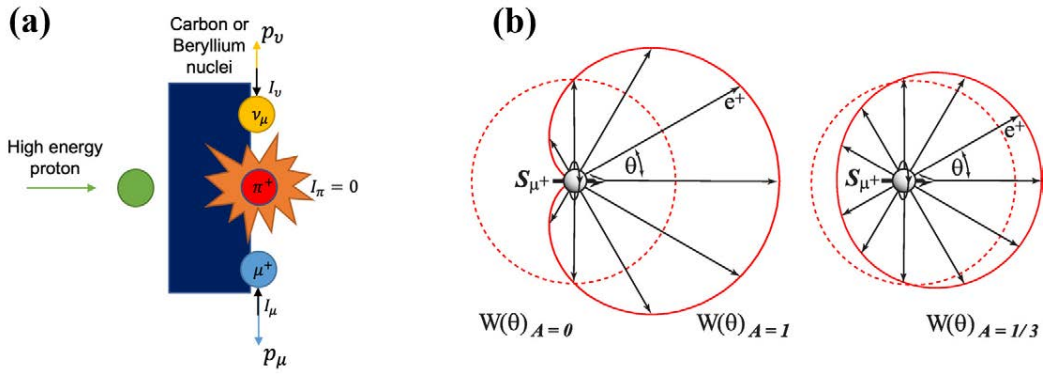

Figure 2.7: (a) Schematic illustration of muon production. Figure from [16]. (b) Polar diagram of the angular distribution $W(\theta)$ of positrons from muon decay. Figure from [17] (License: CC-BY-SA-4.0).

One of the underlying principles of μSR techniques is rooted in reaction (2.53). Linear momentum conservation requires the emission of a muon and muonic neutrino in opposite directions. The neutrino has negative helicity, which means that its spin is antiparallel to its momentum, while the pion has no spin. Due to angular momentum conservation, the muon also has negative helicity, which results in a muon beam that is polarized antiparallel to its linear momentum.

Upon arriving at the sample, the positive-charged muon localizes at an interstitial electronegative site and its spin couples to the local magnetic field, $\vec{B}_{\text{loc}}$, at the site, causing precession. Since its magnetic moment is around 9 times bigger than the neutron, $\mu_\mu = 8.8906\,\mu_{\text{N}}$, the muon acts as a very sensitive magnetometer and can detect the presence of very small magnetic fields.

The muon is also an unstable particle (lifetime of $\tau_\mu = 2.1970\,\mu$s), and decays through a weak nuclear process according to (2.54):

$$\mu^+ \longrightarrow e^+ + \nu_e + \bar{\nu}_\mu \tag{2.54}$$

where ν_e and $\bar{\nu}_\mu$ are the neutrino and antineutrino associated with the positron and muon, respectively. Nevertheless, only the positron is detected, with an energy ranging between 0 and $E_{\text{max}} = 52.3$ MeV.

The second property that allows for the use of muon spin to probe matter is the correlation between the direction of emission of the positron and the direction of the muon spin at decay time. The probability of a positron being emitted at an angle θ with respect to the muon spin direction is denoted as $W(\theta)$. As described by the theory of weak interaction:

$$W(\theta) \propto (1 + A(E)\cos\theta) \tag{2.55}$$

where E is the positron kinetic energy normalized to E_{max}, and $A(E) = (2E - 1)/(3 - 2E)$ is the "asymmetry parameter". The most desirable positrons are those that acquire the maximum allowed kinetic energy and therefore have $A \to 1$, but are scarce in number. When all the positrons are counted, the average value of the

asymmetry parameter is $\bar{A} = 1/3$. A polar diagram of $W(\theta)$ for different values of A is shown in Fig. 2.7(b). The large kinetic energy (approximately 30 MeV) of the positrons enables them to easily escape from the sample and traverse cryostat, furnace, or pressure cell walls, allowing for the use of complex sample-environment equipment.

In a μSR experiment, the spin polarization's time evolution is recorded, which is highly dependent on the magnetic environment's spatial distribution and fluctuations around the muon. A clock is started upon muon implantation, and stops when the positron is detected, generating an histogram of the counts of positrons versus the time elapsed in the sample. The anisotropy of the muon decay is reflected by an excess or a shortage in the actual counts.

Let us consider a simple experimental set-up with two detectors in the forward and backward position relative to the sample. The time-dependent number of positrons counted in either of the detectors is given by:

$$N_{\pm}(t) = N_0\, e^{-t/\tau_\mu}\, (1 \pm a_0 P_{\mathrm{exp}}(t)) \tag{2.56}$$

Here, N_0 sets the count scale, a_0 represents the initial asymmetry (typically $a_0 \sim 0.25$), and $P_{\mathrm{exp}}(t)$ denotes the normalized polarization function. The polarization function encapsulates the physics of the compound under investigation (see next section). The exponential term accounts for the finite muon lifetime. We have replaced $A(E)$ with a_0, since the effective initial asymmetry can be dependent on the experimental conditions.

To extract $a_0 P_{\mathrm{exp}}(t)$, commonly referred to as the asymmetry, the normalized weighted difference between the counts is considered:

$$a_0 P_{\mathrm{exp}}(t) = \frac{N_+(t) - \alpha_{\mathrm{bal}} N_-(t)}{N_+(t) + \alpha_{\mathrm{bal}} N_-(t)} \tag{2.57}$$

Here, α_{bal} corresponds to the balance parameter between the two detectors. Once α_{bal} has been determined, $a_0 P_{\mathrm{exp}}(t)$ can be obtained directly from the counts of the two detectors.

2.5.2 Polarization functions

The direction of the muon polarization measurement $P_\alpha(t)$ is denoted by the Cartesian label α, which can be X, Y, or Z. Here, an orthonormal laboratory reference frame is used, with the external magnetic field $\vec{B}_{\mathrm{ext}}$ determining the direction of the Z axis and the muon spin vector $\vec{S}_\mu$ being parallel to either the X or Z axis, depending on the experimental geometry. For a given direction of the positron momentum $\vec{d}_p$, the polarization function will be:

$$P_\alpha(t) = \frac{\left\langle \vec{S}_\mu(t) \right\rangle}{S_\mu(0)} \cdot \vec{d}_p \tag{2.58}$$

The muon spin polarization vector $\left\langle \vec{S}_\mu(t) \right\rangle$ is the average of $\vec{S}_\mu(t)$ across numerous muon decay events, a few million in a typical experiment. It takes into account the

distribution of muon sites within the sample by including a thermal and ensemble average. The time evolution of the muon spin is solely determined by the local magnetic field, $\vec{B}_{\rm loc}$, encountered by the muon during its lifespan. As the muon is a point-like particle, lacking an electric dipole moment or higher-order multipole terms, its spin is not affected by electric fields.

From now on, we consider a classical treatment of $\vec{S}_\mu(t)$ and assume that $\vec{B}_{\rm loc}$ is time independent. In such case, the time derivative of $\vec{S}_\mu(t)$ is equal to the only torque the muon spin senses: $\vec{m}_\mu \times \vec{B}_{\rm loc}$, and therefore:

$$\frac{d\vec{S}_\mu(t)}{dt} = \gamma_\mu \vec{S}_\mu(t) \times \vec{B}_{\rm loc} \tag{2.59}$$

where $\gamma_\mu = 851.616 \cdot 10^6$ rad·s^{-1}·T^{-1} is the muon gyromagnetic ratio. The solution of Eq.(2.59), known as Larmor equation, can be expressed in a single compact formula by using projection operators [18]. In such case:

$$\vec{S}_\mu(t) = \hat{M}(t)\vec{S}_\mu(0) \tag{2.60}$$

The Cartesian components of the tensor $\hat{M}(t)$ are:

$$M^{\alpha\beta}(t) = \frac{B^\alpha_{\rm loc}B^\beta_{\rm loc}}{B^2_{\rm loc}} + \left(\delta^{\alpha\beta} - \frac{B^\alpha_{\rm loc}B^\beta_{\rm loc}}{B^2_{\rm loc}}\right)\cos(\omega_\mu t) - \sum_\nu \epsilon^{\alpha\nu\beta}\frac{B^\nu_{\rm loc}}{B_{\rm loc}}\sin(\omega_\mu t) \tag{2.61}$$

where we have defined the angular frequency $\omega_\mu = \gamma_\mu B_{\rm loc}$ and $\epsilon^{\alpha\nu\beta}$ is an element of the anti-symmetric Levi–Civita unit pseudotensor. From Eq.(2.58), Eq.(2.60), and Eq.(2.61), we can derive:

$$P_\alpha(t) = \left\langle \hat{M}(t) \right\rangle \frac{\vec{S}_\mu(0)}{S_\mu(0)} \cdot \vec{d}_p = \sum_{\alpha,\beta} \left\langle M^{\alpha\beta}(t) \right\rangle i^\beta_\mu d^\alpha_p \tag{2.62}$$

where i^β_μ specifies the β component in the laboratory reference frame of the direction of the initial muon beam polarization. In general, two types of experimental geometries are employed regarding $\vec{i}_\mu$, which are shown in Fig. 2.8.

Longitudinal/Zero-field configuration

In the longitudinal geometry the applied magnetic field $\vec{B}_{\rm ext}$ is parallel to the direction of the initial muon beam polarization $\vec{i}_\mu$, and the positron detectors are placed forward and backward along the muon beam direction (see Fig. 2.8(a)). Thus, the three vectors $\vec{B}_{\rm ext}$, $\vec{i}_\mu$, $\vec{d}_p$ lie along the Z axis, which implies:

$$P_Z(t) = \left\langle M^{ZZ}(t) \right\rangle = \left\langle \left(\frac{B^Z_{\rm loc}}{B_{\rm loc}}\right)^2 + \left(1 - \left(\frac{B^Z_{\rm loc}}{B_{\rm loc}}\right)^2\right)\cos(\omega_\mu t) \right\rangle \tag{2.63}$$

In the case of a powder sample, in which the local field is randomly oriented, averaging over all directions in Eq.(2.63) yields:

$$P_Z(t) = \frac{1}{3} + \frac{2}{3}\cos(\omega_\mu t) \tag{2.64}$$

If the local magnetic moments are randomly oriented, as it is the case for nuclear moments, the muons sitting at magnetically nonequivalent sites see a Gaussian field distribution. Assuming the variance of the field distribution to be Δ/γ_μ, the time evolution of the polarization is described by the so-called Gaussian-Kubo-Toyabe function [19]:

$$P_Z(t) = \frac{1}{3} + \frac{2}{3}\left(1 - \Delta^2 t^2\right) e^{-\frac{\Delta^2 t^2}{2}} \tag{2.65}$$

Some materials are also analyzed with a Lorentzian envelope, appropriate for diluted magnetic moments; instead of a Gaussian envelope, which is better for describing concentrated magnetic moments [20]. In such case, the time evolution of the polarization is described by [21]:

$$P_Z(t) = \frac{1}{3} + \frac{2}{3}\left(1 - \lambda t\right) e^{-\lambda t} \tag{2.66}$$

where λ/γ_μ is the half-width at half-maximum of the Lorentzian distribution.

Combining the field distributions described by Eq.(2.64) and Eq.(2.65) one obtains a Gaussian distribution with non-zero average field:

$$P_Z(t) = \frac{1}{3} + \frac{2}{3} e^{-\frac{\Delta^2 t^2}{2}} \cos(\omega_\mu t) \tag{2.67}$$

This distribution is often found in long-range magnetically ordered materials where the local field is smeared out due to small temporal or spatial variations. Morevoer, in the presence of magnetic fluctuations, the absence of a spin precession signal allows us to express the muon polarization as [22]:

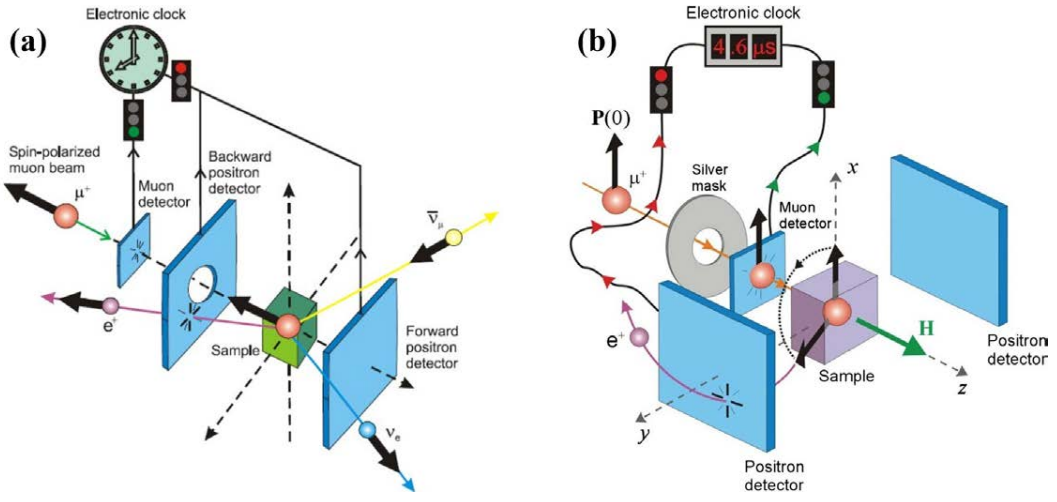

Figure 2.8: (a) Longitudinal or zero-field and (b) transverse-field geometries in a μSR experiment.

$$P_Z(t) = P_Z(0)e^{-\Gamma t} \tag{2.68}$$

The relaxation rate Γ is related to the field-field correlation function. If we assume $\langle B_\perp(t)\, B_\perp(0)\rangle = \langle B_\perp^2(t)\rangle\, e^{-\nu t}$, where ν denotes the field-field correlation rate and $\langle B_\perp^2(t)\rangle = 2\,(\Delta/\gamma_\mu)^2$ is the mean-square field at a specific muon site, we can derive the following expression for Γ:

$$\Gamma = \frac{2\Delta^2\nu}{\nu^2 + \omega_L^2} \tag{2.69}$$

where $\omega_L = \gamma_\mu B_L$ and B_L represents the longitudinal field. It can be seen that the effect of B_L is to decouple the dynamical relaxation, thereby $\Gamma \to 0$ when $\omega_L/\nu \to \infty$. In the presence of static magnetism, a magnetic field applied longitudinal to the initial muon spin direction shifts the polarization function to higher values in a parallel way because of the vector sum of external and internal fields. For sufficiently high longitudinal fields, the muon spin is fully polarized and constant as a function of time with complete loss of oscillations. Therefore longitudinal field μSR measurements are used to distinguish between static and dynamic field distributions.

Zero-field experiments are considered as a special case of longitudinal-geometry measurements in which no external magnetic field is applied. In such case, $\Gamma(B_L = 0) = 2\Delta^2/\nu$. An exotic case is possible in this configuration: the magnetic transition of a compound is crossed as it is cooled down, but there is apparently no μSR signature of the crossing. This can be understood if the local field at the muon site vanishes or does not keep a constant value for a sufficiently long time for the muon spin precession to be observed.

Transverse-field configuration

In the transverse geometry the external magnetic field is applied along the Z axis, while the initial muon spin direction lies parallel to X (see Fig. 2.8(b)). The positron detectors are usually placed in a way that $\vec{d_p}$ lie along the X or Y axis, so that the polarization function can be:

$$P_X(t) = \left\langle M^{XX}(t)\right\rangle = \left\langle \left(\frac{B_{\rm loc}^X}{B_{\rm loc}}\right)^2 + \left(1 - \left(\frac{B_{\rm loc}^X}{B_{\rm loc}}\right)^2\right)\cos(\omega_\mu t)\right\rangle \tag{2.70}$$

or

$$P_Y(t) = \left\langle M^{YX}(t)\right\rangle = \left\langle \frac{B_{\rm loc}^Y B_{\rm loc}^X}{B_{\rm loc}^2}\,(1 - \cos(\omega_\mu t)) - \frac{B_{\rm loc}^Z}{B_{\rm loc}}\sin(\omega_\mu t)\right\rangle \tag{2.71}$$

The muon spin senses a superposition of the internal and external fields and precesses with a frequency that is proportional to the size of the field at the muon site. For a non-magnetic sample the polarization would be a simple cosine function with an oscillation frequency proportional to the external field. However, in a magnetic

sample the frequency is shifted due to the internal field. This can be best seen in the Fourier transform of the polarization function. In the case of static magnetism the time evolution of the polarization is given by the Fourier transform of the external field plus internal magnetic field distribution. Thus an inverse Fourier transform of the polarization function is performed to re-obtain the field distribution.

Similar to what has been discussed for the longitudinal-field configuration, three different relaxation mechanisms can be included in the transverse-field polarization function: 1) dynamical relaxation λ_Z due to the muon spin-lattice interaction, 2) Gaussian field distribution of nuclear spins with variance $\Delta_{\mathrm{TF}}/\gamma_\mu$, 3) damping λ_X induced by magnetic fluctuations. Including these physical phenomena into Eq.(2.70) and Eq.(2.71), we obtain, e.g. for $\vec{d_p}$ along X:

$$P_X(t) = \left\langle \left(\frac{B_{\mathrm{loc}}^X}{B_{\mathrm{loc}}}\right)^2 e^{-\lambda_Z t} + \left(1 - \left(\frac{B_{\mathrm{loc}}^X}{B_{\mathrm{loc}}}\right)^2\right) e^{-\left(\frac{\Delta_{\mathrm{TF}}^2 t^2}{2} + \lambda_X t\right)} \cos(\omega_\mu t) \right\rangle \tag{2.72}$$

2.5.3 Local magnetic field

By considering the magnetic coupling between the muon magnetic moment and its environment, the local magnetic field at the muon site can be generally decomposed into several contributions:

$$\vec{B}_{\mathrm{loc}} = \vec{B}_{\mathrm{ext}} + \vec{B}_{\mathrm{Fermi}} + \vec{B}_{\mathrm{dip}} + \vec{B}_{\mathrm{hyp}} \tag{2.73}$$

Fermi contact field

If we assume a spherical electronic cloud around the muon, the Fermi contact field can be expressed as:

$$\vec{B}_{\mathrm{Fermi}} = \frac{2\mu_0}{3} |\psi_s(\vec{r}_0)|^2 \eta(\vec{r}_0) \vec{m}_e^s \tag{2.74}$$

$\vec{B}_{\mathrm{Fermi}}$ represents the contribution of the electronic density $\psi_s(\vec{r}_0)$ at the muon site $\vec{r}_0$. It is due to conduction electrons whose wavefunction can be overlapped with the muon one. $\eta(\vec{r}_0)$ is a multiplicative enhancement factor to account for the perturbation of the magnetic density at the muon site arising from the muon electric charge, while $\vec{m}_e^s$ is the spin magnetic moment of the electron. This term can be neglected when dealing with transition metals (local $3d$ moments contribute much more than conduction electrons to susceptibility) [15, 23].

Dipolar field

The electronic magnetic moments are characterized by a magnetic moment $\vec{m}_i = -g_i \mu_{\mathrm{B}} \vec{J}_i$, where $\vec{J}_i$ is the total angular momentum and g_i is the spectroscopic splitting factor of atom at site i. In the case of considering rare-earth and actinide ions with f electrons, $\vec{J}_i = \vec{L}_i + \vec{S}_i$, where $\vec{L}_i$ and $\vec{S}_i$ are the orbital and spin angular momenta of the unpaired electrons. However, for a transition element with d unpaired electrons,

the expectation value of $\vec{L}_i$ is small enough that we can consider the approximation $\vec{J}_i = \vec{S}_i$.

In compounds containing d or f unpaired electrons, the magnetic density at each of these ions is consistently large, even for itinerant magnets. The localized magnetic density contributes to $\vec{B}_{\text{loc}}$ in two ways: through the classical dipole interaction, and through the Ruderman–Kittel–Kasuya–Yosida (RKKY) interaction in metals or the transferred hyperfine field in insulators.

The usual dipolar long-range interaction between the muon magnetic moment and the localized electrons magnetic moment can be written as:

$$\vec{B}_{\text{dip}} = \frac{\mu_0}{4\pi} \sum_{i=1}^{N} \left[-\frac{\vec{m}_i}{r_i^3} + \frac{3(\vec{m}_i \cdot \vec{r}_i)\vec{r}_i}{r_i^5} \right] \tag{2.75}$$

The vector $\vec{r}_i$ links the muon to atom i. The sum runs over the N magnetic ions in the sample under investigation.

Hyperfine field

The RKKY field arises from the indirect interaction between the muon and the magnetic moments of the localized unpaired electrons mediated by the conduction electrons [24]. This interaction is the result of a second order process: the conduction electron spins are coupled to the localized electron spins through the exchange interaction, and to the muon spin via the Fermi contact interaction. An additional source for $\vec{B}_{\text{loc}}$ in covalent compounds stems from the possible overlap between the muon wavefunction and electronic wavefunctions. A general functional form which takes into account these two short-range magnetic interactions can be expressed as:

$$\vec{B}_{\text{hyp}} = \frac{\mu_0}{4\pi} \sum_{i=1}^{N'} \frac{H_{\vec{r}_i}}{V_c} \vec{m}_i \tag{2.76}$$

where the sum is restricted to the N' nearest (and, possibly, next nearest) neighbor atoms to the muon, V_c is the volume of the unit cell, while $H_{\vec{r}_i}$ is the hyperfine constant, expected to be temperature independent. Sometimes this field is called contact field, where it may include Eq.(2.74), absorbed into the hyperfine constant $H_{\vec{r}_i}$.

Summation in real space

In practice, the calculation of the external, Fermi or hyperfine field is not a hard task. However, the dipolar field is expressed as a sum of contributions from magnetic moments over the whole crystal. Because the intensity of the field decreases as $\sim r^{-3}$ but the number of moments at that distance increases with $\sim r^2$, the sum is conditionally convergent. Therefore, for the calculation of the dipolar field a specific strategy has to be taken into account.

In general two methods are used to compute this long-range dipolar field, one based on the real space and another based on the reciprocal space and the related Brillouin zone. Here we will focus only on the method applied during this thesis,

which is the real space one. The solution in this method relies in the approximation that the sum can be made continuous rather than discrete if the distance between the muon and the magnetic moments r_i is sufficiently large. Therefore, the dipolar field can be separated into [25]:

$$\vec{B}_{\mathrm{dip}} = \vec{B}'_{\mathrm{dip}} + \vec{B}_{\mathrm{Lor}} + \vec{B}_{\mathrm{dem}} \tag{2.77}$$

The term $\vec{B}'_{\mathrm{dip}}$ is the dipolar field obtained by restricting the sum in Eq.(2.75) to the moments inside a volume V_{Lor}, called the Lorentz sphere, centered at the muon site and with a radius sufficiently large that the lattice sum convergence is reached. Typically a very good accuracy is obtained when a few thousand moments are considered.

The contribution to $\vec{B}_{\mathrm{dip}}$ from dipoles located outside the Lorentz sphere can be computed by introducing magnetic charges and evaluating the field in the continuum approximation. This results in two terms: the Lorentz field $\vec{B}_{\mathrm{Lor}}$ and the demagnetization field $\vec{B}_{\mathrm{dem}}$. The Lorentz field is generated by magnetic charges located at the surface of the Lorentz sphere, while the demagnetization field is produced by magnetic charges located at the surface of the sample. The vector sum of the magnetic moments inside the Lorentz sphere gives the Lorentz field:

$$\vec{B}_{\mathrm{Lor}} = \frac{\mu_0}{3}\vec{M}_{\mathrm{Lor}} = \frac{\mu_0}{3}\sum_{V_{\mathrm{Lor}}}\frac{\vec{m}_i}{V_{\mathrm{Lor}}} \tag{2.78}$$

A simple analytical expression for $\vec{B}_{\mathrm{dem}}$ is usually difficult to obtain. However, in the case of an ellipsoidal sample the demagnetization field becomes uniform [26] and can be defined as:

$$\vec{B}_{\mathrm{dem}} = -\mu_0 \hat{N}\vec{M}_{\mathrm{meas}} \tag{2.79}$$

The magnetization $\vec{M}_{\mathrm{meas}}$ is the bulk magnetisation of the sample, and for a magnetically saturated sample is equal to $\vec{M}_{\mathrm{Lor}}$. The demagnetization tensor $\hat{N}$ is diagonal in the principal axes, denoted by a, b, and c, of the ellipsoid. Its trace is equal to one, i.e. $N^a + N^b + N^c = 1$, implying that the components of $\vec{B}_{\mathrm{dem}}$ and $\vec{M}_{\mathrm{meas}}$ are of opposite sign along the principal axes, thereby justifying the name of this field. Following Ref. [27], the value of the demagnetization coefficients for

Table 2.1: The demagnetization coefficient for simple sample shapes. The given coefficient concerns the direction of the magnetization.

Shape	Magnetization direction	N^a, N^c
Sphere	Any	$\frac{1}{3}$
Thin slab	Normal	1
Thin slab	In plane	0
Long circular cylinder	Longitudinal	0
Long circular cylinder	Transverse	$\frac{1}{2}$

simple sample shapes are listed in Table 2.1. It is an usual approximation to consider cylinders with a length much larger than their radius and very flat disks as prolate and oblate ellipsoids, respectively.

It is worthwhile to notice that if the sample is a sphere, and if $\vec{M}_{\mathrm{Lor}} = \vec{M}_{\mathrm{meas}}$, which is the case for instance for a paramagnet or a saturated magnet, $\vec{B}_{\mathrm{dem}} = -\vec{B}_{\mathrm{Lor}}$ and therefore $\vec{B}_{\mathrm{dip}} = \vec{B}'_{\mathrm{dip}}$.

2.6 Electron Paramagnetic Resonance

The basis for electron paramagnetic resonance (EPR) spectroscopy relies on the perturbation of the electron spin state by the application of applied magnetic field, similar to nuclear magnetic resonance (NMR) spectroscopy. In this thesis, the magnetic properties of organic magnets with one unpaired electron were studied by using continuous wave (CW) EPR spectrometers.

A typical CW EPR spectrometer consists of a microwave source, a magnetic field source, and a detection system that measures the absorbed radiation. The spectrometer operates at a constant frequency, usually in the X-band frequency range ($\nu \sim$ 9–10 GHz), and a variable magnetic field [28].

The magnetic field is typically generated by a superconducting magnet and is carefully controlled and stabilized to ensure accurate measurements. In the absence of a magnetic field, the spin states of a radical with one unpaired electron are degenerate. However, when a magnetic field is applied, the Zeeman effect lifts the degeneracy of the two spin states and the spin state with magnetic moment opposite to the applied field rises in energy, while the spin state having magnetic moment aligned with the applied field decreases in energy (see Fig. 2.9(a)). The energy difference between the two spin states is directly proportional to the magnetic field. When this energy difference matches the energy of the microwave radiation:

$$h\nu = g_e \mu_{\mathrm{B}} B \tag{2.80}$$

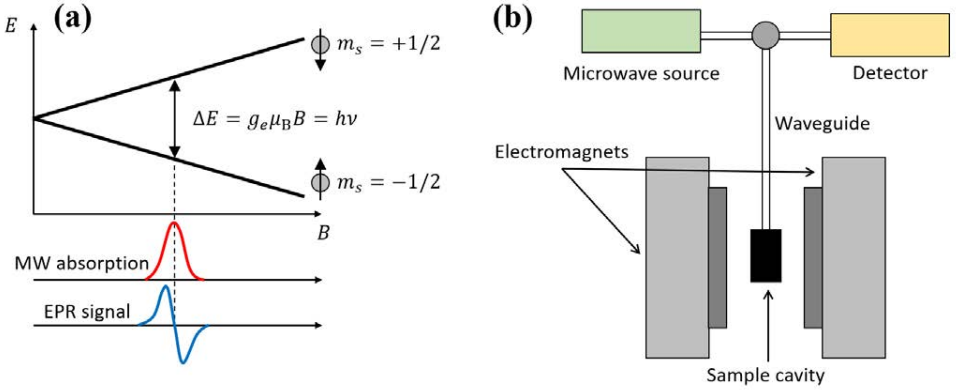

Figure 2.9: (a) Zeeman effect on a radical with one unpaired electron and signal measured in an EPR experiment. (b) General experiment setup.

the sample electrons absorb the microwave radiation, transitioning to an excited state. The electron g-factor, denoted as g_e and having a value of 2.0023 for a free electron, can be determined from Eq.(2.80), providing insights into the atom species on which the unpaired electron lies, the molecular orbitals in which the unpaired electron resides, the nature of the chemical bonds involving the unpaired electron, and the surrounding molecular environments from which the unpaired electron experiences the interactions.

The microwaves reflected back from the cavity are routed to the diode detector to measure the absorption of the microwave radiation, as depicted in Fig. 2.9(b). EPR spectra are usually represented as their first derivative.

Bibliography

[1] S. Foner, "Versatile and Sensitive Vibrating-Sample Magnetometer," Review of Scientific Instruments, vol. 30, pp. 548–557, jul 1959.

[2] N. Miura, "Chapter 7 Experimental techniques for high magnetic fields," in Physics of Semiconductors in High Magnetic Fields, p. 299–325, Oxford University Press, 2007.

[3] J. Lashley, M. Hundley, A. Migliori, J. Sarrao, P. Pagliuso, T. Darling, M. Jaime, J. Cooley, W. Hults, L. Morales, D. Thoma, J. Smith, J. Boerio-Goates, B. Woodfield, G. Stewart, R. Fisher, and N. Phillips, "Critical examination of heat capacity measurements made on a Quantum Design physical property measurement system," Cryogenics, vol. 43, pp. 369–378, jun 2003.

[4] S. Riegel and G. Weber, "A dual-slope method for specific heat measurements," Journal of Physics E: Scientific Instruments, vol. 19, pp. 790–791, oct 1986.

[5] J. Campo and V. Laliena, Neutron Scattering in Magnetism: Fundamentals and Examples, pp. 321–403. Cham: Springer International Publishing, 2021.

[6] E. Fermi, "Sul moto dei neutroni nelle sostanze idrogenate," Ricerca scientifica, vol. 7, no. 2, pp. 13–52, 1936.

[7] J. Schwinger and E. Teller, "The scattering of neutrons by ortho-and parahydrogen," Physical Review, vol. 52, no. 4, p. 286, 1937.

[8] D. Johnston, "On the theory of the electron orbital contribution to the scattering of neutrons by magnetic ions in crystals," Proceedings of the Physical Society, vol. 88, no. 1, p. 37, 1966.

[9] M. Blume, "Polarization effects in the magnetic elastic scattering of slow neutrons," Physical Review, vol. 130, no. 5, p. 1670, 1963.

[10] S. Maleev, V. Bar'yakhtar, and R. Suris, "The scattering of slow neutrons by complex magnetic structures," Soviet Phys.-Solid State (English Transl.), vol. 4, 1963.

[11] E. Ressouche, J. X. Boucherle, B. Gillon, P. Rey, and J. Schweizer, "Spin density maps in nitroxide-copper(II) complexes. A polarized neutron diffraction determination," Journal of the American Chemical Society, vol. 115, pp. 3610–3617, may 1993.

[12] P. Brown, A. Capiomont, B. Gillon, and J. Schweizer, "Spin densities in free radicals," Journal of Magnetism and Magnetic Materials, vol. 14, pp. 289–294, dec 1979.

[13] S. Mühlbauer, D. Honecker, É. A. Périgo, F. Bergner, S. Disch, A. Heinemann, S. Erokhin, D. Berkov, C. Leighton, M. R. Eskildsen, and A. Michels, "Magnetic small-angle neutron scattering," Reviews of Modern Physics, vol. 91, mar 2019.

[14] M. M. Woolfson, An Introduction to X-ray Crystallography. Cambridge University Press, jan 1997.

[15] A. Yaouanc and P. D. de Réotier, Muon Spin Rotation, Relaxation, and Resonance. Oxford University Press, 2011.

[16] Audrey Kwan, "Muon spin spectroscopy." `https://wiki.aalto.fi/display/SSC/Muon+spin+spectroscopy`.

[17] Ernst aus Freiburg, "File:Msr mudecay angle.png." `https://commons.wikimedia.org/wiki/File:Msr_mudecay_angle.png`.

[18] Y. M. Belousov, V. N. Gorelkin, A. L. Mikaélyan, V. Y. Miloserdin, and V. P. Smilga, "Study of metals by means of positive muons," Soviet Physics Uspekhi, vol. 22, pp. 679–702, sep 1979.

[19] R. Kubo and T. Toyabe, "Magnetic resonance and relaxation," in Proceedings of the XIVth Colloque Ampère, pp. 810–823, North-Holland, 1967.

[20] Y. J. Uemura, T. Yamazaki, D. R. Harshman, M. Senba, and E. J. Ansaldo, "Muon-spin relaxation in AuFe and CuMn spin glasses," Physical Review B, vol. 31, pp. 546–563, jan 1985.

[21] R. Kubo, "A stochastic theory of spin relaxation," Hyperfine Interactions, vol. 8, no. 4-6, pp. 731–738, 1981.

[22] S. J. Blundell, F. L. Pratt, T. Lancaster, I. M. Marshall, C. A. Steer, S. L. Heath, J.-F. Létard, T. Sugano, D. Mihailovic, and A. Omerzu, "μSR studies of organic and molecular magnets," Polyhedron, vol. 22, pp. 1973–1980, jul 2003.

[23] A. Amato, P. D. de Réotier, D. Andreica, A. Yaouanc, A. Suter, G. Lapertot, I. M. Pop, E. Morenzoni, P. Bonfà, F. Bernardini, and R. D. Renzi, "Understanding the μSR spectra of MnSi without magnetic polarons," Physical Review B, vol. 89, may 2014.

[24] C. Kittel, Quantum theory of solids. Wiley, New York, 1963.

[25] M. Z. Uritskii and V. Y. Irkhin, "Calculation of dipole fields at interstices of rare-earth metals," Physics of the Solid State, vol. 42, pp. 399–405, mar 2000.

[26] A. H. Morrish, The Physical Principles of Magnetism. Wiley, New York, 2001.

[27] C. Kittel, Introduction to Solid State Physics. Wiley, New York, 7 ed., 1996.

[28] M. Che and E. Giamello, "Chapter 5 Electron Paramagnetic Resonance," in Spectroscopic Characterization of Heterogeneous Catalysts - Part B: Chemisorption of Probe Molecules, pp. B265–B332, Elsevier, 1990.

Part I

Chiral magnetism induced by DM interactions

Chirality is a pivotal and unifying concept in modern science, linking the universe's fundamental properties and its elementary particles. From the simple, yet profound, left-right asymmetry of human hands to the helical twist of DNA that defines genetic codes, and even to everyday objects like screws and snail shells, chirality manifests across various scales and contexts, offering tangible examples that underscore its ubiquity and importance. This concept was first defined in 1893 by Lord Kelvin, who stated that an object is chiral if "*its image in a plane mirror cannot be brought into coincidence with itself*", highlighting the absence of improper symmetry operations. This foundational work was later expanded by Barron, who incorporated the concept of time-reversal symmetry [1]. In the presence of a magnetic field, chiral materials break time-reversal symmetry, leading to the emergence of new properties [2]. This effect is particularly significant in chiral compounds that exhibit magnetic order, such as ferrimagnetism, ferromagnetism, weak ferromagnetism, conical, or helical structures. Thus, the presence of non-collinear magnetic structures in chiral materials offers the possibility of finding chirality not only in the crystal structure but also in the magnetic structure.

In the last two decades, chiral magnets have emerged as a promising research area in modern condensed matter physics [3]. These materials, with interrelated structural, magnetic, electronic, and optical properties, have the potential to reveal new and interesting physical phenomena [4]. Furthermore, chiral materials with simultaneous nuclear and magnetic chirality may pave the way for new applications, particularly in the field of spintronics, where spin and electron charge are utilized for data transmission [5–7]. Additionally, the field of magnonics explores the use of magnons, quanta of spin waves, in these chiral magnetic structures. Since magnons allow for data transmission without the movement of electric charge and can operate at terahertz frequencies, this field holds promise for developing faster, energy-efficient data storage and logic devices, as well as sensitive magnetic sensors. [8].

In non-centrosymmetric cubic magnets, the existence of a Dzyaloshinskii-Moriya interaction with the chiral crystal structure results in a rich variety of magnetic textures, including skyrmion lattices and chiral magnetic soliton lattices. These magnetic textures are not only fascinating from a fundamental physics perspective but also have tremendous potential for technological applications. Their unique topological nature and the ability to be controlled by magnetic fields or electric current offer new avenues for designing and controlling spintronic and magnonic devices, with the potential to revolutionize information storage and processing [9–12].

In the next sections, we introduce concepts relevant to the chapters developed in Part I. We begin with the $B20$ crystal structure, distinguished by its non-centrosymmetric cubic arrangement, which is crucial for the emergence of complex magnetic textures due to the Dzyaloshinskii-Moriya interaction. Understanding this structure is essential to deciphering the magnetic properties of chiral magnets. Following this, we delve into the Bak-Jensen model, which provides a theoretical framework to describe the energy contributions from various interactions, thereby explaining the magnetic ordering within these materials. Finally, we explore one of the most intriguing manifestations of these magnetic interactions: skyrmions – topologically protected magnetic vortices that hold great promise for spintronic

applications.

Crystal structure of $B20$ magnets

The $B20$ crystal structure of cubic magnets lacking inversion centers (space group $P2_13$, No.198) is quite common in nature, one example of a family with this structure type being the monosilicides of transition metals (MeSi, Me = Mn, Fe, Co, etc.). In MeSi compounds, atoms occupy the $4a$ Wyckoff position (x, x, x), with $x_{\mathrm{Me}} = 0.137$ and $x_{\mathrm{Si}} = 0.845$, yielding a left-handed chiral structure, while $x_{\mathrm{Me}} = 0.863$ and $x_{\mathrm{Si}} = 0.155$ result in a right-handed structure, as depicted in Fig. I.1. Consequently, a unit cell of MeSi contains four atoms of each component.

The distinction between right and left-handed chiral structures can be determined for single crystals using X-ray diffraction analysis. In non-centrosymmetric structures an additional anomalous scattering occurs due to the violation of Friedel's law $I(hkl) \neq I(\bar{h}\bar{k}\bar{l})$. Thus, it is possible to identify the different enantiomorphs of a non-centrosymmetric structure by determining the ratio of domains with different crystallographic chirality, known as the Flack parameter [14].

In the ideal binary structure $B20$, the atomic coordinates are given by u_{ideal} and $(1 - u_{\mathrm{ideal}})$, where $u_{\mathrm{ideal}} \approx 0.1545085$ [15]. In this case, the nearest neighbors of an atom are seven atoms of the other type, situated at equal distances from the central atom. However, in the case of monosilicides, instead of seven equal distances, there is one short distance, three long distances, and three intermediate distances [16]. This deviation from equal distances, caused by the absence of an inversion center, induces a DM interaction and a long-period chiral magnetic structure [17].

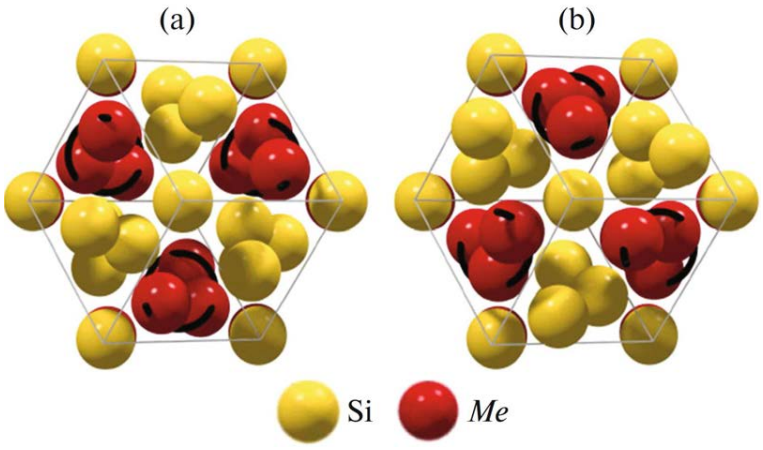

Figure I.1: (a) Right and (b) left-handed crystal structures of MeSi along the $\langle 111 \rangle$ direction. Figure taken from [13].

The Bak-Jensen model

Having established the significance of the $B20$ crystal structure in chiral magnets, we now turn our attention to the theoretical mechanisms that underlie the formation of complex magnetic patterns in such systems.

In 1964, Dzyaloshinski proposed a mechanism to describe long-period spin spirals resulting from the perturbation of the ferromagnetic structure using a relatively small relativistic interaction [18]. This instability, now known as the Dzyaloshinskii-Moriya (DM) interaction, is shown to arise only in non-centrosymmetric crystals. Subsequently, in 1980, Bak and Jensen [19] and an independent group led by Kataoka [20] developed a theory based on this mechanism, which is commonly referred to as the Bak-Jensen model, to explain the magnetic structure of MnSi.

According to the Bak-Jensen model, the stability of the spin spiral arises from the interplay of three main interactions. The strongest interaction is the conventional symmetric isotropic exchange interaction of the Heisenberg type ($\vec{s_i} \cdot \vec{s_j}$), which favors parallel spin alignment. Alongside the ferromagnetic (FM) exchange, an additional isotropic DM interaction [18, 21, 22] emerges due to the lack of center of symmetry in the crystal structure. The DM interaction prefers a perpendicular spin alignment ($\vec{s_i} \times \vec{s}j$) on a weaker scale, leading to a competition between the two interactions that allows only small-angle rotations of spins. The third and weakest interaction is the anisotropic exchange, or cubic anisotropy, which determines the spatial direction of the helical wave vector $\vec{K}_{\mathrm{h}}$.

By performing free-energy minimization [19, 20], which takes into account these three interactions, the modulus of the helical propagation vector is found to be related to the exchange (J) and DM (D) interactions, given by $K_{\mathrm{h}} = \frac{D}{Ja} = \frac{SDa}{A}$, where S represents the mean spin of the system, a is the cubic cell parameter, and $A = SJa^2$ is the stiffness of the spin wave. Since $A \gg SDa$, the value of K_{h} is small, leading to a large spiral period $\lambda_{\mathrm{h}} = 2\pi/K_{\mathrm{h}}$.

Basics of magnetic skyrmions

Among the diverse magnetic textures arising from the complex interplay within $B20$ magnets, one stands out as particularly noteworthy – skyrmions.

Skyrmions are topologically stable configurations first theorized by Tony Skyrme in 1962 [23]. Originally proposed in the context of particle physics, skyrmions have since been found in various condensed matter systems, including liquid crystals [24], quantum Hall systems [25], and Bose-Einstein condensates [26].

In particular, magnetic skyrmions manifest as vortex-like spin configurations, characterized by an integer topological charge:

$$N = \frac{1}{4\pi} \iint_S \hat{n} \cdot \left(\frac{\partial \hat{n}}{\partial x} \times \frac{\partial \hat{n}}{\partial y} \right) d^2\vec{r} \tag{I.1}$$

where $\hat{n}(\vec{r}) = \vec{M}/M$ is the unit vector in the direction of the magnetization $\vec{M}$. This charge, which quantifies how the magnetization vector field $\hat{n}(\vec{r})$ covers the surface of a 3D unit sphere, introduces an energy barrier against topological transitions,

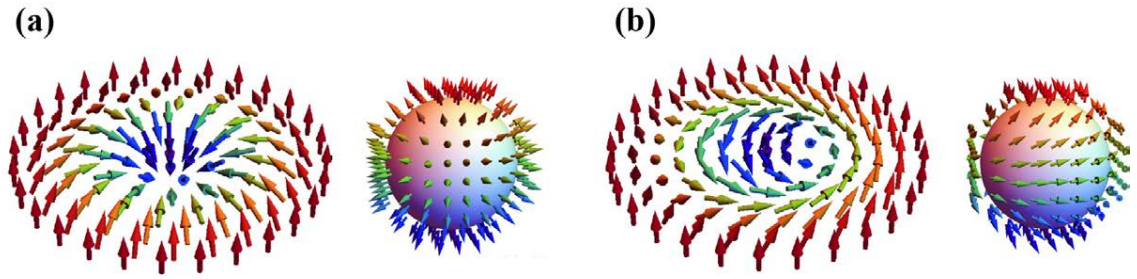

Figure I.2: (a) Néel and (b) Bloch skyrmions, together with their corresponding inverse stereographic projections on the unit sphere. Figure adapted from [28].

thereby enhancing skyrmion stability [27]. Considering the rotational symmetry of an isolated skyrmion, its spin texture in polar coordinates $\vec{r} = (r\cos\varphi, r\sin\varphi, 0)$ can be expressed as:

$$\hat{n}(\vec{r}) = (\sin\Theta(r)\cos\Phi(\varphi), \sin\Theta(r)\sin\Phi(\varphi), \cos\Theta(r)) \tag{I.2}$$

Putting this expression into Eq.(I.1), the skyrmion topological charge can be obtained as:

$$N_{\mathrm{Sk}} = \frac{1}{4\pi}\int_0^{\infty} dr \frac{d\Theta(r)}{dr}\sin\Theta(r)\int_0^{2\pi} d\varphi \frac{d\Phi(\varphi)}{d\varphi} = \frac{1}{4\pi}\left[\cos\Theta(r)\right]_{r=0}^{r=\infty}\left[\Phi(\varphi)\right]_{\varphi=0}^{\varphi=2\pi} \tag{I.3}$$

Consider a model where, at the radial distance $r \to \infty$, the spins are oriented upwards, while at $r = 0$, they point downwards. Then, $\left[\cos\Theta(r)\right]_{r=0}^{r=\infty} = 2$. Now, several possibilities for $\Phi(\varphi)$ exist which describe different skyrmion textures. In order to distinguish between them, the vorticity is defined as $m = \left[\Phi(\varphi)\right]_{\varphi=0}^{\varphi=2\pi}/2\pi$, so the skyrmion number is determined by the vorticity: $N_{\mathrm{Sk}} = m$. Additionally, the helicity is defined by the phase γ given in:

$$\Phi(\varphi) = m\,\varphi + \gamma \tag{I.4}$$

Based on the helicity, skyrmions can be classified in a similar way to domain walls. For Néel-type skyrmions ($m = 1$; $\gamma = 0, \pi$), the magnetic spins rotate along the radial direction as they move away from the core (see Fig. I.2(a)). Meanwhile, in Bloch type skyrmions ($m = 1$; $\gamma = \pm\pi/2$), the magnetic spins rotate perpendicular to the radial direction (see Fig. I.2(b)). It should be noted that some freedom remains in the election of a proper function to describe $\Theta(r)$, as long as it satisfies the boundary conditions previously mentioned.

The topological protection of skyrmions ($N_{\mathrm{Sk}} = 1$), preventing their continuous transformation into trivial states ($N = 0$), implies that they maintain their shape when moved through a sample. This, coupled with their small size relative to magnetic domains (often under 100 nm), high packing density, and maneuverability using low electrical currents, makes them promising for advanced data storage and spintronic applications [29].

Skyrmion lattices (SkL) were predicted to develop in cubic magnets under magnetic field several decades ago [30–32]. In these materials, the observed SkL phase is often interpreted as a hybridized triple-$\vec{Q}$ state [27, 33–35]. If the external magnetic field is applied along the z-axis, this state can be mathematically represented as $\hat{n}(\vec{r}) = \vec{M}_{3Q}/\left|\vec{M}_{3Q}\right|$, where:

$$\vec{M}_{3Q}(\vec{r}) = m_0\hat{e}_z + \sum_{i=1}^{3}\left[\hat{e}_i \sin(\vec{Q}_i \cdot \vec{r} + \Delta_i) + \hat{e}_z \cos(\vec{Q}_i \cdot \vec{r} + \Delta_i)\right] \tag{I.5}$$

Eq.(I.5) results from the combination of a background uniform magnetization m_0, due to the finite magnetic field that stabilizes the SkL, and three helices, each one with propagation vector $\vec{Q}_i$ and phase Δ_i. The three helices satisfy the relations $\sum_i \hat{e}_i = \vec{0}$ and $\cos(\sum_i \Delta_i) = -1$. Additionally, the triad of $\vec{Q}$-vectors are mutually orthogonal to the applied magnetic field, forming an angle of 120° with each other, thereby satisfying the summation $\sum_i \vec{Q}_i = \vec{0}$.

When a single skyrmion is isolated from this hexagonal SkL state, it corresponds to a Bloch type skyrmion, whereas a Néel type skyrmion results if, instead of helices, cycloids are used in Eq.(I.5).

Objectives of Part I

Part I delves into the exploration of chiral magnetism, focusing on the role of DM interactions in generating non-collinear magnetism. In particular, we aim to determine the existence and underlying mechanisms of novel magnetic phases in the $B20$ cubic chiral magnets MnSi and $Fe_{0.75}Co_{0.25}Si$, motivated by theoretical predictions of a new *unknown-state* in such cubic helimagnets [36].

In Chapter 3, we report the existence of a new magnetic phase in the cubic magnet MnSi. Macroscopic characterization experiments are performed to explore the low temperature region of the magnetic phase diagram and detect the conjectured *unknown-state*. Additionally, by employing Small Angle Neutron Scattering (SANS) and muon spin rotation (μSR) techniques, we aim to distinguish the properties and origin of this *unknown-state* from those of the well-documented SkL (*A-phase*). In this research we seek to understand the role of symmetry and the interplay between DM interactions and exchange interactions in generating non-collinear magnetic phases, including the *unknown state*.

In Chapter 4, a similar magnetic phase as reported in MnSi is observed in $Fe_{0.75}Co_{0.25}Si$. Similar macroscopic characterization, SANS and μSR experiments are used to study the influence of disorder and different anisotropy on the stability and appearance of both the new *unknown-state* and the well-known *A-phase*. This objective sheds light on the mechanisms that drive the emergence of new magnetic states, enriched by the combination of DM interactions, exchange interactions, anisotropy, and the pivotal role of disorder.

Chapter 3

New magnetic state, *B-phase*, in the cubic chiral magnet MnSi

In this chapter, we aim to shed light on how DM interactions contribute to the formation of non-collinear magnetism. In particular, we report the existence and underlying mechanisms of a new magnetic phase in the cubic magnet MnSi,

We begin by exploring the magnetic phase diagram of MnSi. Next, we detail the specific heat, d.c and a.c. magnetization, Small Angle Neutron Scattering (SANS) and muon spin rotation experiments we conducted. The results of a.c. magnetization reveal the presence of a new phase, labeled *B-phase*, consistent with previous theoretical predictions. Following this discovery, we delve into the magnetic structure of this phase using SANS and muon spin rotation techniques, and compare these results with those of the well-documented *A-phase*. A magnetic model, related with a relative reorientation of the magnetic helices, is proposed to explain the new magnetic state. Furthermore, we employ a computational model, described in Appendix C, to validate the proposed model for the *B-phase* and to explore the SkL field distribution within the *A-phase*. We conclude the chapter by encapsulating the key discoveries from our research.

3.1 The archetypical cubic chiral magnet: MnSi

The manganese monosilicide MnSi has a $B20$ structure with cell parameter: $a = 4.558$ Å [37] and forms only the left-handed crystal structure, based on measurements of the Flack parameter. At the temperature $T_c = 29.5$ K at zero field, the MnSi magnetic system undergoes a phase transition to a helicoidal spin state with the incommensurate propagation vector $\vec{K}_h = (2\pi/a)(\epsilon, \epsilon, \epsilon)$, where $\epsilon = 0.017$ [38, 39]. The magnetic helix is oriented in a cubic crystal along four equivalent directions $\langle 111 \rangle$, which is determined by the anisotropic-exchange and cubic-anisotropy energies [19]. The modulus of the propagation vector is quasi-independent of both the external field and temperature: $|\vec{K}_h| = K_h = 0.036$ Å^{-1} , which implies a spiral period of about $\lambda_h \sim 180$ Å. The left-handed crystal structures of MnSi always give rise to left-handed magnetic spirals [40, 41].

The MnSi behavior in a magnetic field is shown in Fig. 3.1 and can be described as follows: a helical structure, which is multi-domain in a zero field, becomes a single-

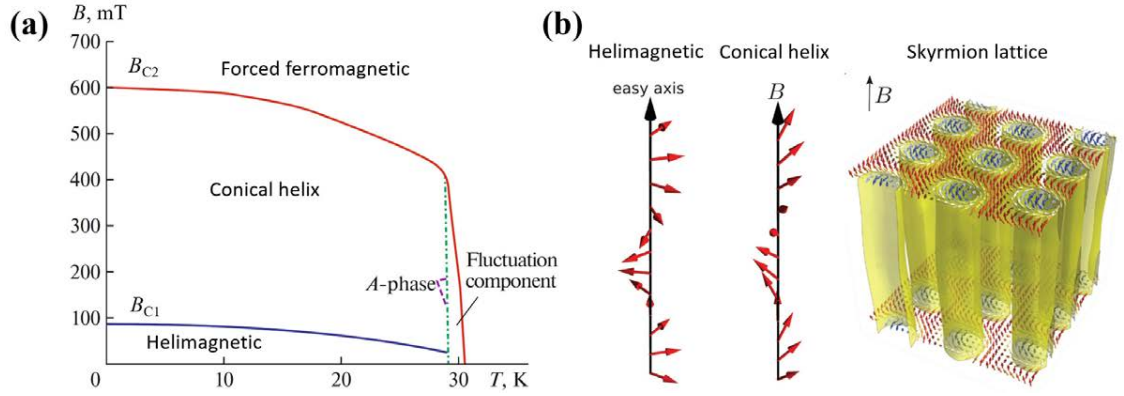

Figure 3.1: (a) Magnetic field–temperature ($B-T$) phase diagram of the magnetic structure of MnSi. Figure adapted from [13]. (b) Schematic of the magnetization in the helimagnetic, conical and skyrmion lattice (SkL) phases. Figure taken from [44].

domain conical structure in a magnetic field $B > B_{c1} \sim 0.08$ T at low temperatures. The value of the first critical field can be related with the parameters of the Bak-Jensen model as: $g\mu_B B_{c1} = FK_h^2/2$, where F is the anisotropy constant and g is the gyromagnetic ratio. In the range of fields $0 < B < B_{c1}$, the propagation vector $\vec{K}_h$ rotates from the preferred orientation towards the magnetic-field direction. Note that the helicoid is distorted, which manifests itself in the occurrence of the second harmonic at $\vec{q} = 2\vec{K}_h$ [42, 43].

In the fields $B > B_{c1}$, the single-domain spin structure is in the conical phase, where it develops a component oriented parallel to the field. The cone becomes narrower with an increase in the field and, at $B_{c2} \approx 0.6$ T, the magnetic structure becomes a ferromagnetic one. The energy difference between the forced ferromagnetic (FFM) state and the helimagnetic (HM) state is given by: $g\mu_B B_{c2} = AK_h^2$. The value of the average moment in the saturated phase (0.4 μ_B per Mn atom) is much smaller than the effective moment in the paramagnetic phase (1.4 μ_B per Mn atom) [38]. A measurement of the magnetization dependence on an external magnetic field yielded that the magnetization of MnSi did not reach saturation in the fields $B < 12$ T regardless of the applied pressure [45].

Regarding the evolution of the magnetic structure with temperature, two important features were observed. First, it was shown that critical fluctuations of a flat helix in MnSi determine the character of the *paramagnet–flat spin helix* phase transition [46–50]. The system undergoes a phase transition through two clearly distinguishable crossovers: from paramagnetic state to partially chiral fluctuating state at $\kappa = K_h$ and from partially chiral state to completely chiral fluctuating state at $\kappa = K_h/2$, where κ is the inverse correlation length. Then, the transition occurs at T_c.

Second, at temperatures slightly smaller than T_c and in some range of fields $B_{fl1} < B < B_{fl2}$, the propagation vector $\vec{K}_h$ jumps from the position parallel to the external magnetic field to the position perpendicular to the field [42, 51–53]. This region is the so-called *A-phase*.

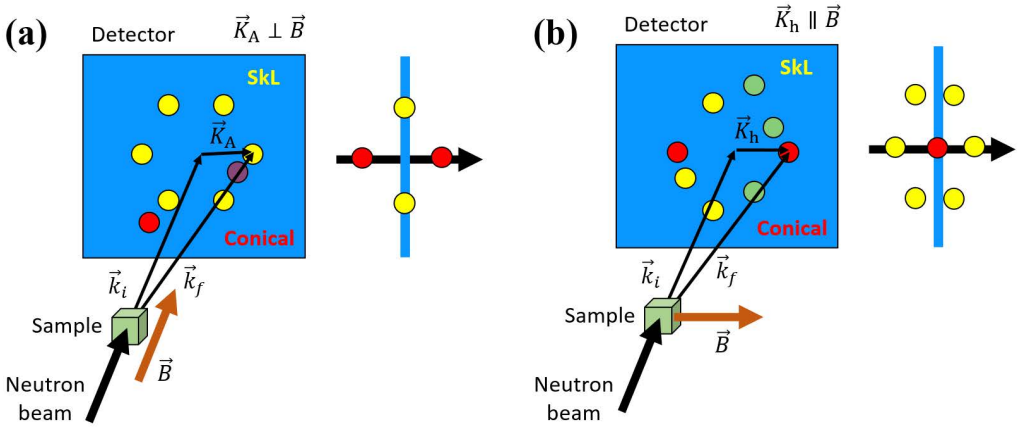

Figure 3.2: Scheme showing the typical SANS configurations to observe the skyrmion lattice (a) and the conical phase (b) in cubic chiral helimagnets. Yellow (a) and red (b) spots are observed at the neutron detector related, respectively, with the hexagonal packing of the SkL and the conical phase.

Experimental SANS studies in the configuration shown in Fig. 3.2(a), with the external magnetic field applied parallel to the neutron beam ($\vec{B} \parallel \vec{k}_i$), showed that six diffraction peaks arise in the *A-phase* region in the plane perpendicular to the magnetic field. The arising hexagonal structure is independent of the magnetic-field direction with respect to the principal crystallographic axes of the sample. This fact made it possible to interpret the *A-phase* as a two-dimensional hexagonal SkL [33]. Since then, the SkL was subsequently observed in other B20 type alloys [33, 54–56], multiferroic materials, such as $CuOSe_2O_3$ [57], and Co-Zn-Mn compounds with β-Mn structure [58].

Despite the large number of studies devoted to the MnSi-similar systems, the question about the nature and microscopic mechanisms responsible for the *A-phase* occurrence in these compounds is still to be answered. Grigoriev *et al.* [59] observed that the modulus of the propagation vector of the two-dimensional hexagonal structure K_A is equal to K_h. Based on this observation, they proposed that the observed structure represents a complex 2D modulation of spins rather than a close-packed skyrmion lattice. Regarding the formation of the *A-phase*, it has been proposed to be stabilized by thermal fluctuations [33, 60], or by a combined effect of induced uniaxial anisotropies and applied magnetic fields [61–63].

A few years ago, Laliena and Campo theoretically investigated the instability of the skyrmion textures and the important role of the thermal fluctuations in cubic helimagnets [36]. In fact, it was demonstrated that at zero temperature the only stable phases were the conical helix (CH) and the FFM. Moreover, it was found that a skyrmionic *A-phase* might exist at low temperatures. They also predicted that a new *unknown-state*, surrounded by the FFM, the CH, and the possible new low-T *A-phase*, might emerge in the low temperature region of the phase diagram, as depicted in Fig. 3.3.

Nakajima *et al.* explored the phase diagram of MnSi by performing SANS mea-

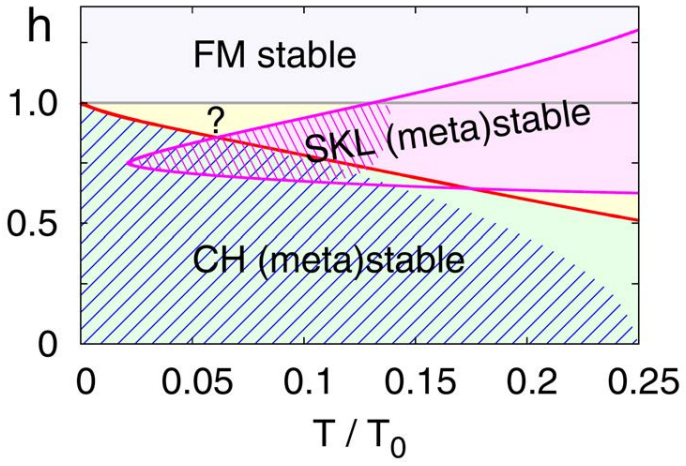

Figure 3.3: Theoretical phase diagram taken from [36]. The SkL is stable in the magenta region. The computations for the CH and the SkL are reliable in the regions filled with blue and magenta stripes, respectively. None of the known stationary points are stable in the yellow regions.

surements in equilibrium and also by doing fast quenching from the paramagnetic state to the low T region, cooling down through the well known *A-phase* with $\vec{B} \parallel \langle 001 \rangle$ [64, 65]. The results from those experiments showed metastable *A-phase* states captured at low T, in reasonable agreement with [36].

New magnetic states, located between the CH and the FFM states at low temperatures, were also reported in the insulator multiferroic Cu_2OSeO_3 for magnetic fields applied parallel to the $\langle 001 \rangle$ axis. One of them was recognized to be a skyrmionic state unrelated to the conventional SkL state, and the other was recognized to be a tilted CH state with a propagation vector not aligned with the magnetic field [66–69]. In $Co_7Zn_7Mn_6$, in addition to a conventional SkL phase just below T_c, a three-dimensionally disordered skyrmion state, stabilized by spin frustration, was also observed [67, 70]. In a recent report on the archetypical cubic helimagnet MnSi for $\vec{B} \parallel \langle 110 \rangle$, no new phase has been found [71]. However, the existence of the *unknown-state* in MnSi or $Fe_{1-x}Co_xSi$ predicted in Ref. [36] but never observed in these materials is still an open question.

In order to detect this *unknown state*, we carried out specific heat, d.c and a.c. magnetization experiments as a function of field and temperature to carefully explore the low T region of the phase diagram for each main crystallographic direction.

3.2 Experimental details

Several single crystals of MnSi were provided by a close collaboration with Prof. Yusuke Kousaka. The crystals were synthesized by Bridgman and floating zone methods [72]. For the macroscopic characterization measurements, three crystals were oriented, with X-ray Laue methods, along the three main cubic axis, $\langle 100 \rangle$, $\langle 110 \rangle$, $\langle 111 \rangle$, with sizes 3.1 × 1.1 × 0.6 mm^3, 2.8 × 1.1 × 1.1 mm^3 and

$2.1 \times 0.5 \times 0.6$ mm^3 for, respectively, samples labeled as A, B, and C. Small Angle Neutron Scattering (SANS) and muon spin rotation (μSR) experiments were also performed in single crystals oriented along the $\langle 111 \rangle$ direction. The structural chirality was evaluated by performing an absolute structure analysis. X-ray oscillation photographs were taken using a Bruker APEX area detector with Mo Kα radiation at room temperature. Based on the Flack parameter, the MnSi crystals were determined to have the left-handed crystal structure.

The specific heat of sample C ($m = 4.73$ mg) was measured using the relaxation method in a physical property measurement system (PPMS-9T), manufactured by Quantum Design. The crystal was oriented so that the magnetic field was applied along the $\langle 111 \rangle$ direction (see Fig. 3.4), for values ranging from 0 to 0.8 T using a zero field cooling (ZFC) procedure. The data were collected mainly in the low temperature region $2 < T < 10$ K, although for some selected fields the whole range $2 < T < 35$ K was measured in order to check the consistency compared with previous studies.

Magnetization measurements were carried out using the VSM option of a PPMS-14T manufactured by Quantum Design. Continuous $M(T)$ measurements were obtained under the zero field cooling (ZFC) and field cooling (FC) procedures for applied magnetic fields in the range $0.05 < B < 0.65$ T. Isothermal magnetization $M(B)$ data were collected in a field range from 0 to 0.8 T. All data was taken in a temperature range from 2 to 35 K.

In-phase (m') and out-of-phase (m'') components of the a.c. magnetization were measured using a SQUID magnetometer, manufactured by Quantum Design. The main frequency f and the a.c. amplitude $H_{\text{a.c.}}$ were 10 Hz and 3.9 Oe, respectively. In some experiments, f was varied between 0.3 and 1000 Hz. To ensure thermal equilibrium conditions any time, the cooling rate to the target temperature was slow as 1.5 K/min. Both a.c. magnetization and VSM isothermal magnetization experiments were conducted with increasing and decreasing B at fixed temperature below T_c, after ZFC procedure from the paramagnetic phase ($T > T_c = 29.5$ K).

The unpolarized SANS measurements were performed at the small-angle diffrac-

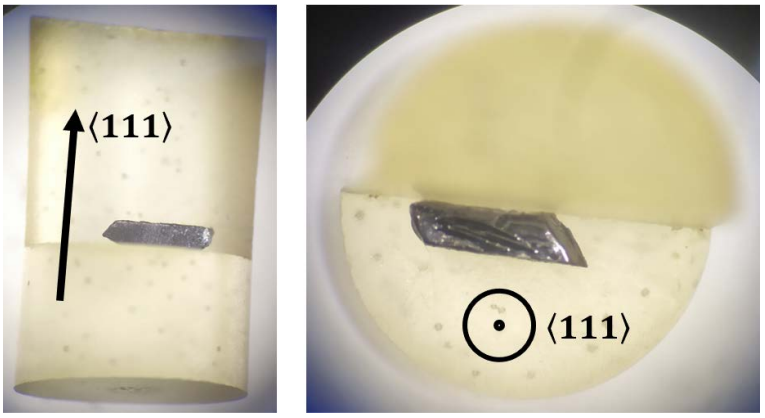

Figure 3.4: Sample C of MnSi used for the specific heat, d.c and a.c. magnetization experiments. The cubic axis $\langle 111 \rangle$ is signalled by a black arrow.

tometer D33 of the Institut Laue Langevin (ILL) in Grenoble, France [73]. The incident neutron beam with $\lambda = 6$ Å was collimated using a diaphragm of 10 mm diameter. The detector was placed at 5.3 m from the sample, which consisted of a crystal of size $7 \times 5 \times 2.5$ mm^3, labeled crystal 1, glued inside an Al container with Bostik diluted with acetone. Two stripes of Cd were also glued above and below the sample in order to reduce the background noise. The Al container was then placed inside an Oxford Instruments 7-T horizontal-field cryomagnet, which was demagnetized at the beginning of each temperature scan so that the remanent field was less than 0.1 mT. The cryomagnet was equipped with sapphire windows which allowed for applying the magnetic field either perpendicular or parallel to the incident neutron beam. Thus, the SANS patterns were collected in four different configurations, shown in Fig. 3.5. In order to integrate the scattered intensity, rocking scans were performed by rotating both sample and field around the vertical axis in steps of 0.5°, covering an angular range of ± 3.5°. At each temperature and magnetic field the SANS patterns were obtained by summing the intensities of all rocking scans. All data was analyzed with the help of GRASP software [74].

Additional SANS measurements were taken at the time-of-flight instrument TAIKAN in the materials and life science facility (MLF) in J-PARC, Japan [75]. An incident neutron beam of size 10×10 mm^2 with wavelengths from 0.7 to 7.6 Å was exposed on the sample. Two different single crystals were used, crystal 1, which was used at D33, and another crystal of cylindrical shape with 9 mm height and 7 mm diameter, labeled crystal 2.

Crystal 1 was glued with Araldite inside an Al container and loaded in a 10-T vertical field superconducting magnet of MLF. In this cryomagnet only the configuration with the magnetic field perpendicular to the incident neutron beam was allowed. Therefore, SANS patterns were collected with $\vec{B} \parallel \langle 111 \rangle \perp \vec{k}_i$, where the

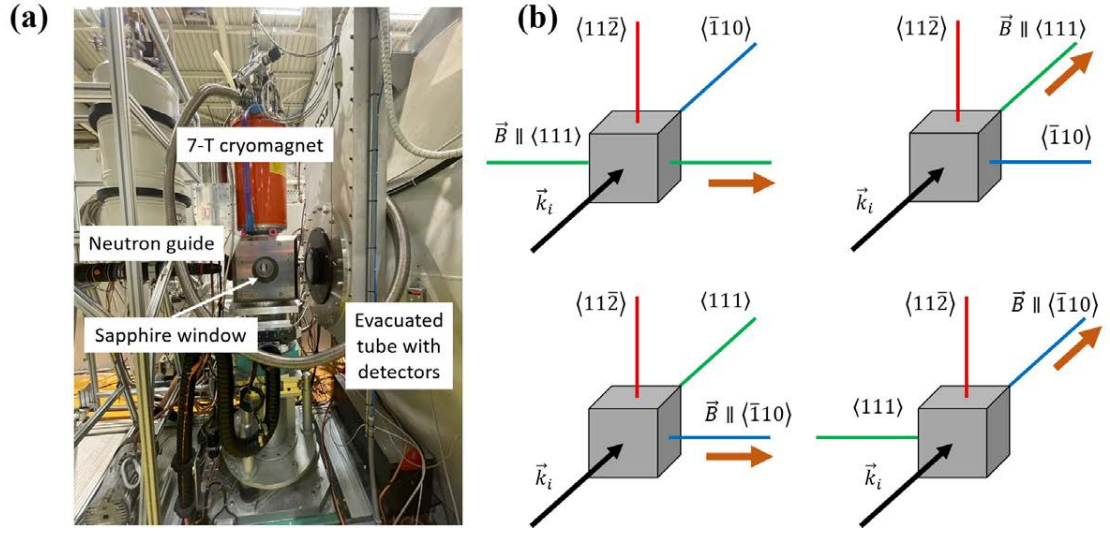

Figure 3.5: (a) Actual setup of the D33 instrument used in the SANS experiments. (b) The four configurations measured in D33: $\vec{B} \parallel \langle 111 \rangle \perp \vec{k}_i \parallel \langle 1\bar{1}0 \rangle$, $\vec{B} \parallel \langle 111 \rangle \parallel \vec{k}_i$, $\vec{B} \parallel \langle 1\bar{1}0 \rangle \perp \vec{k}_i \parallel \langle 111 \rangle$, $\vec{B} \parallel \langle 1\bar{1}0 \rangle \parallel \vec{k}_i$.

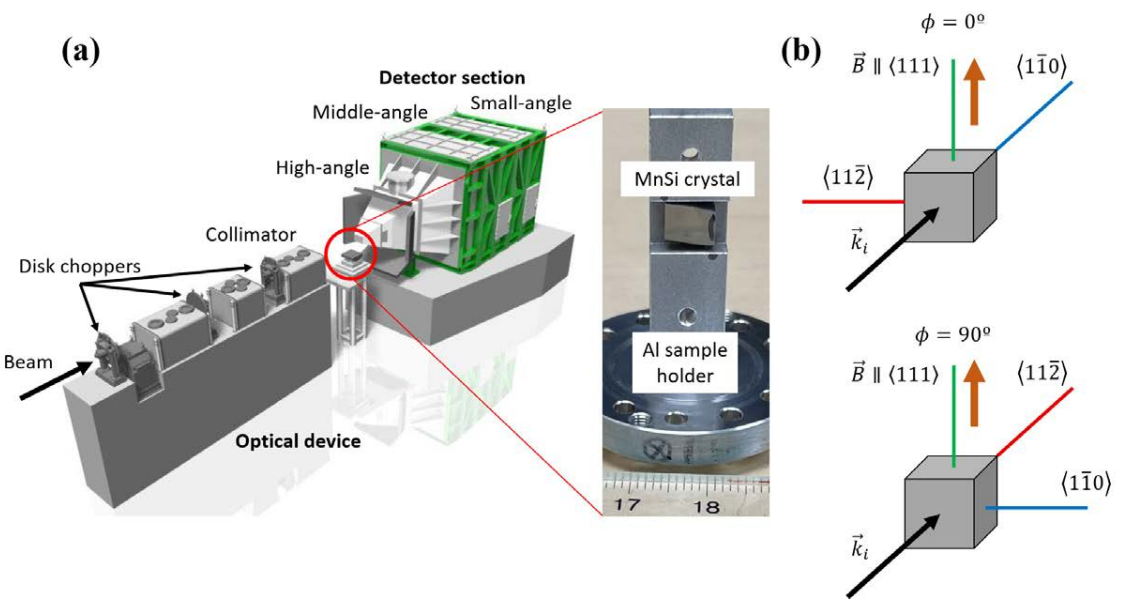

Figure 3.6: (a) Scheme of the TAIKAN instrument together with a picture of crystal 1 of MnSi used in the SANS experiments. (b) Initial and final configurations measured in TAIKAN for crystal 1 at each temperature and magnetic field: $\phi = 0°$: $\vec{B} \parallel \langle 111 \rangle \perp \vec{k}_i \parallel \langle 1\bar{1}0 \rangle$, $\phi = 90°$: $\vec{B} \parallel \langle 111 \rangle \perp \vec{k}_i \parallel \langle 11\bar{2} \rangle$.

crystal was rotated from $\phi = 0°$: $\vec{k}_i \parallel \langle 1\bar{1}0 \rangle$ to $\phi = 90°$: $\vec{k}_i \parallel \langle 11\bar{2} \rangle$ in steps of 15°, as shown in Fig. 3.6. For crystal 2 a horizontal field superconducting magnet (Cryogenic Limited) of MLF was used. The horizontal field 4T cryomagnet was applied such that the configuration $\vec{B} \parallel \langle 111 \rangle \perp \vec{k}_i \parallel \langle 1\bar{1}0 \rangle$ was measured. Detector efficiency, wavelength dependence and transmittance corrections were applied using the Utsusemi software [76].

The measurements in both instruments were performed in thermal equilibrium conditions at temperatures between 2 K and 35 K, and with applied magnetic fields below 0.8 T, always following a ZFC procedure from the paramagnetic phase, unless otherwise specified. For all data, a reference measurement in the paramagnetic region at 40 K was subtracted as a background contribution.

Zero-field (ZF) μSR experiments were performed on the LAMPF spectrometer installed on the M20 beamline at the TRI University Meson Facility (TRIUMF) in Vancouver, Canada. The produced beam of longitudinal spin polarized positive muons had a mean momentum 28.5 MeV/c. Two crystals with the same size: 4.86 $\times$ 3.65 $\times$ 1.65 mm^3 were mounted in the center of a Cu fork sample holder with thin Mylar tape and then attached to a gas-flow ^{4}He cryostat from Quantum Technology (Miss Piggy), as depicted in Fig. 3.7. Both the non-spin-rotated (NSR) configuration, in which the initial muon beam polarization $\vec{i}_\mu$ is parallel to the muon beam, and the spin-rotated (SR) configuration, where $\vec{i}_\mu$ is perpendicular to the muon beam, were measured at 2 K using ZFC and FC protocols, with previous calibration of instrument parameters at 40 K.

Transverse-field (TF) μSR experiments were carried out on the NuTime spec-

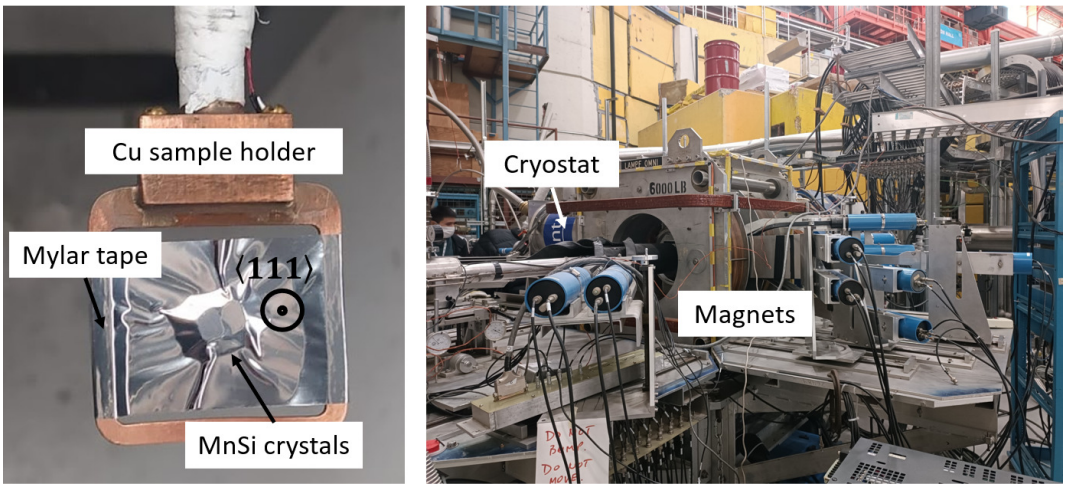

Figure 3.7: Setup of the ZF μSR experiments carried out on the M20 LAMPF spectrometer for the MnSi crystals.

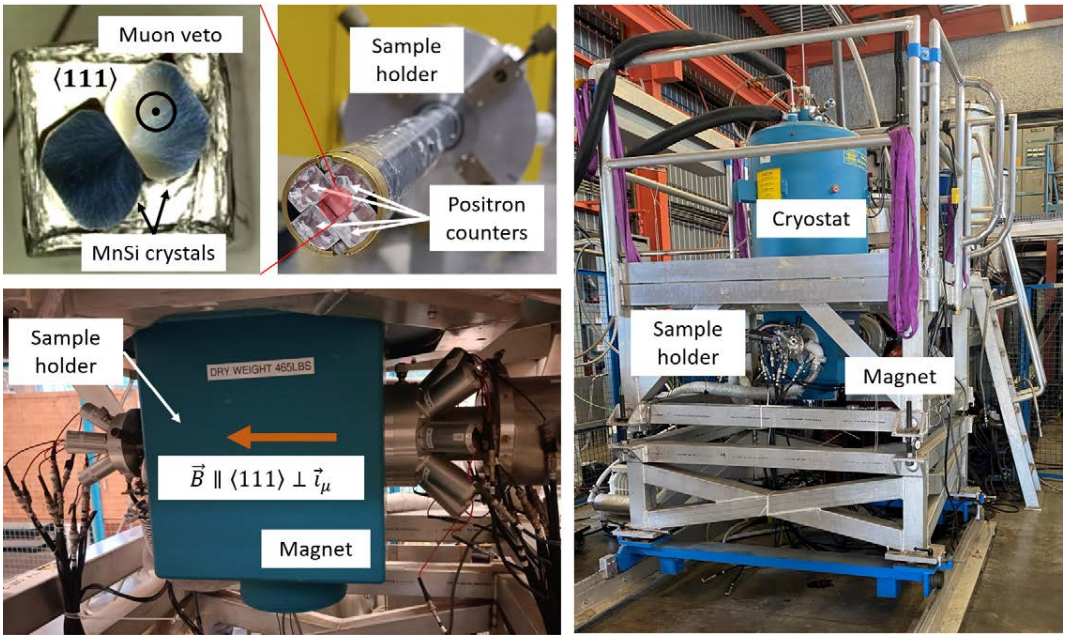

Figure 3.8: Setup of the TF μSR experiments carried out on the M15 NuTime spectrometer for the MnSi crystals.

trometer installed on the M15 beamline at TRIUMF. High voltage dual achromatic Wien filters rotate the μ^+ spin by 90° to create a fully (100 %) transverse spin polarization. The same crystals as in the ZF μSR experiments were placed on top of a "muon-veto" scintillator (made of $CaCO_3$), as illustrated in Fig. 3.8. The crystals were then covered with a Ag foil. The muon veto together with the four positron counters form a cryostat insert and sample holder. TF μSR spectra with approximately $3{\cdot}10^7$ muon decay events were taken under conditions of ZFC, where the external magnetic field was applied by a 7 T superconducting magnet in the config-

uration: $\vec{B} \parallel \langle 111 \rangle \perp \vec{i}_\mu$. The measurements were done in the temperature range 2 K to 50 K and field range 0 T to 0.75 T using an Oxford Instruments cryostat.

In both ZF and TF μSR experiments the crystals were oriented such that the muon beam was parallel to the $\langle 111 \rangle$ direction.

3.3 *B-phase* in the magnetic phase diagram of MnSi

Figure 3.9 shows the specific heat data of MnSi for a wide range of magnetic fields applied along the $\langle 111 \rangle$ direction. At zero magnetic field, a sharp peak can be observed on top of a broad shoulder, which indicates the onset of helimagnetic order $T_c = 29.0(2)$, in agreement with [77]. At higher magnetic fields, such as 0.2 and 0.25 T, a second peak corresponding to the SkL formation should emerge, however the resolution of our data is not enough to distinguish such contribution and only one broadened peak is observed, corresponding to the first-order transition between the helical/conical and the paramagnetic phase. For even higher fields, like 0.5 T, the peak is completely rounded, indicating a transition to the conical phase of second order. The inset of Fig. 3.9 shows the low temperature region in which the data were taken with more detail. However, only a constant decrease without any anomalous signal is observed for any magnetic field, suggesting no thermodynamic evidence of the *unknown state*.

Figure 3.10(a) shows the isothermal magnetization $M(B)$ curves for magnetic fields applied along the $\langle 111 \rangle$ direction at temperatures from 2 to 35 K. Starting from $B = 0$ the magnetization increases almost linearly. At low temperatures the initial quasilinear increase arises from an increasing anharmonicity of the helical modulation, a slight reorientation of the helical modulation, and changes of domain

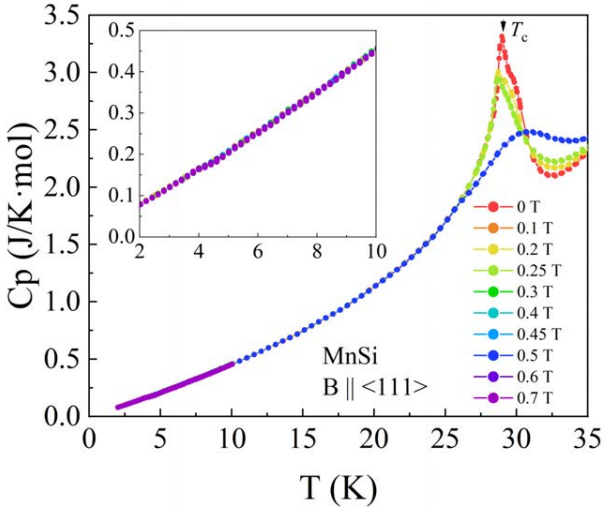

Figure 3.9: Specific heat data of MnSi for a wide range of magnetic fields applied along the $\langle 111 \rangle$ direction. The inset shows the low temperature region.

population [42, 78]. As can be observed from the inset in Fig. 3.10(a), there is a small hysteresis depending on the history of the magnetic field applied, which disappears at high temperatures. This is in agreement with the model in which for decreasing field, only one conical domain exists and therefore the behavior is linear. The crossover between the multidomain helimagnetic (HM) phase and the single domain CH phase, B_{c1}, can be determined as a maximum in the derivative of the magnetization dM/dB, as it is shown in Fig. 3.10(b). Above B_{c1} the linear increase is characteristic of a closing-in of the CH phase up to reaching the FFM state. This second critical field B_{c2} is determined as the inflection point in the magnetization as it reaches saturation (see Fig. 3.10(b)). On the field scale shown in Fig. 3.10 the magnetization appears almost saturated above B_{c2}, with a value of 0.4 μ_B per

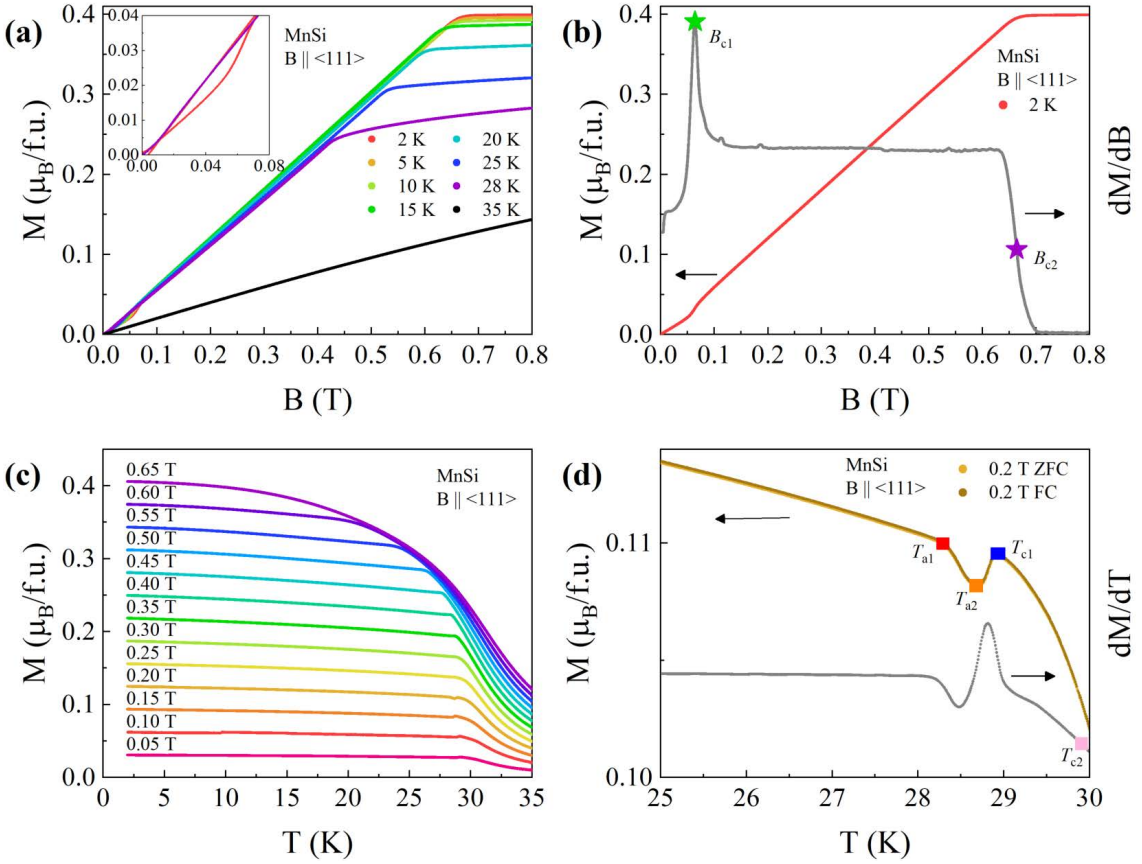

Figure 3.10: (a) Isothermal magnetization $M(B)$ curves of MnSi for magnetic fields applied along the $\langle 111 \rangle$ direction. The inset shows the low field data for increasing and decreasing field at 2 and 28 K. (b) Isothermal magnetization $M(B)$ at 2 K together with its field derivative dM/dB. The critical fields B_{c1} and B_{c2} are marked with a green and purple star, respectively. (c) Temperature dependence of the magnetization of MnSi for magnetic fields applied along the $\langle 111 \rangle$ direction. (d) ZFC and FC magnetization $M(T)$ at $B = 0.2$ T together with the ZFC temperature derivative dM/dT. The critical temperatures T_{a1}, T_{a2}, T_{c1} and T_{c2} are marked with a red, orange, blue and pink rectangle, respectively.

formula unit for the lowest temperatures. However, as reported in the literature up to ∼33 T [79], the highest fields studied, the magnetization is unsaturated and nonlinear characteristic of itinerant magnetism. No significant dependence of the magnetization with the sweep rate was observed.

Continuous ZFC $M(T)$ data are shown in Fig. 3.10(c) for fields in the range 0.05 to 0.65 T applied along the $\langle 111 \rangle$ direction. Fig. 3.10(d) shows the ZFC and FC magnetization curves measured at 0.2 T, together with the ZFC temperature derivative dM/dT and the critical temperatures which will be described next.

No appreciable difference is observed between the ZFC and FC protocols. At low temperatures the magnetization increases monotonically independently of the applied field. For temperatures near $T_{\rm c}$ and fields below 0.2 T, the magnetization presents a small maximum, labelled as $T_{\rm c1}$, followed by a drop characteristic of the transition to the paramagnetic (PM) state at high temperatures. At $B = 0.2$ T, the SkL in the *A-phase* is identified by sudden decrease of the magnetization at $T_{\rm a1}$, which reaches a minimum at $T_{\rm a2}$ followed by the maximum at $T_{\rm c1}$ (see Fig. 3.10(d)). For fields higher than 0.2 T, only the maximum at $T_{\rm c1}$ is observed and it decreases with increasing field until it disappears above 0.4 T. Finally, for $T > T_{\rm c}$ a point of inflection in the magnetization $T_{\rm c2}$ can be identified. The intermediate (IM) region between $T_{\rm c1}$ and $T_{\rm c2}$ corresponds with a fluctuation-disordered regime, characterized by strongly interacting chiral fluctuations that eventually induce a first-order Brazovskii transition to the magnetically ordered state [49, 80]. This interaction suppresses the correlation length and thus induces the point of inflection $T_{\rm c2}$.

A similar analysis was performed for the magnetization measurements with the magnetic fields applied along the $\langle 110 \rangle$ and $\langle 100 \rangle$ directions (see Appendix E). By combining all the critical fields and temperatures, the magnetic phase diagrams for the different crystallographic orientations measured are presented in Fig. 3.11.

While the field and temperature dependencies are similar, the perhaps most important difference concerns the field and temperature values of the anomalies. For field along $\langle 100 \rangle$ the value of $B_{\rm c1}$ is largest as expected of the magnetically hard axis, while $B_{\rm c1}$ is lowest for the magnetically soft $\langle 111 \rangle$ axis. This compares with the *A-phase*, where the signatures are weakest for the $\langle 111 \rangle$ axis. Both the anisotropy of the *A-phase* as well as $B_{\rm c1}$ are due to the same leading order magnetic anisotropy, which is fourth order in spin-orbit coupling [19, 20]. The same fourth-order anisotropy term causes the zero-field helical order to propagate along $\langle 111 \rangle$. The temperature dependence of the upper critical field $B_{\rm c2}$ is the same for all three directions, with a slightly higher value for the field along $\langle 100 \rangle$, probably due to the different shape of sample A compared with B and C.

Now we turn to the analysis of the a.c. magnetization. Figure 3.12(a) shows the d.c. field B dependence of m' at 2 K for $\vec{B} \parallel \langle 100 \rangle$, $\langle 110 \rangle$, and $\langle 111 \rangle$. For the three samples, the onsets of the CH and FFM phases are clearly observed at $B_{\rm c1}$ ∼0.1 T and $B_{\rm c2}$ ∼0.65 T, respectively. However, looking carefully at the curves (see inset of Fig. 3.12(a)), a small anomaly is clearly observed only for sample C, which is oriented with $\vec{B} \parallel \langle 111 \rangle$, between ∼ 0.35 and ∼ 0.62 T. Indeed, this anomaly was not detected in the analysis of the VSM magnetization data.

To discard any spurious sample effect, m' was measured at 2 K by increasing and decreasing the field from $0 \rightarrow 0.8 \rightarrow 0$ T in sample B but now oriented with

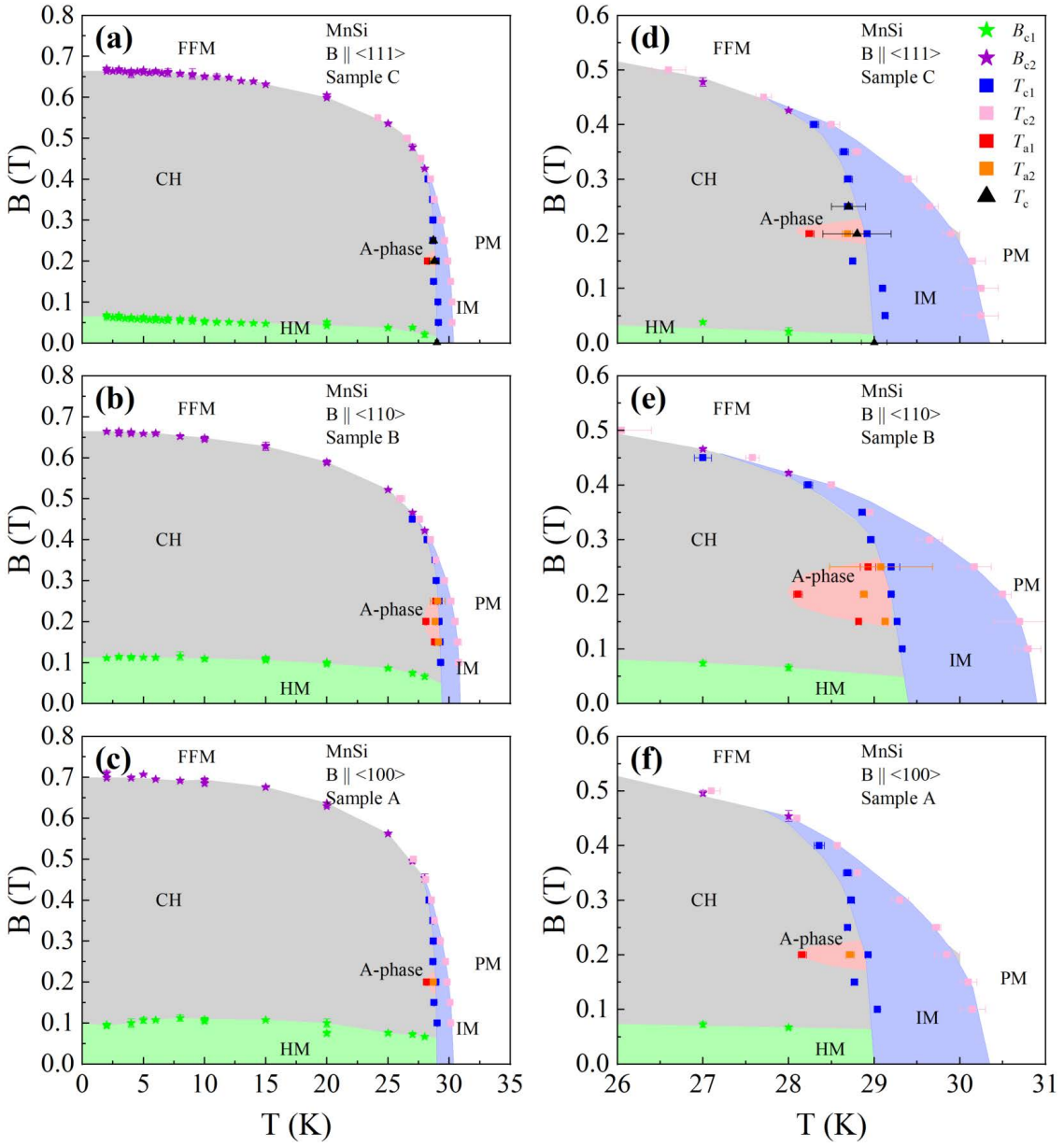

Figure 3.11: Magnetic phase diagrams for the different samples C [(a) and (d)], B [(b) and (e)], and A [(c) and (f)] of MnSi. A zoom of the high temperature region is shown in (d),(e) and (f). The critical fields and temperatures derived from the $M(B)$, $M(T)$ and $C_{\mathrm{p}}(T)$ data are marked with filled stars, squares and triangles, respectively. The labels indicate the helimagnetic (HM), conical helix (CH), forced ferromagnetic (FFM), skyrmion lattice (A-phase), intermediate (IM) and paramagnetic (PM) phases.

$\vec{B} \parallel \langle 111 \rangle$. The full magnetic field cycle is displayed in Fig. 3.12(b), which shows the hysterical behavior at the low field region due to the single domain formation. The detail of the new anomaly in sample B is shown in the inset of Fig. 3.12(b), where the difference between samples B and C can be due to the different demagnetization

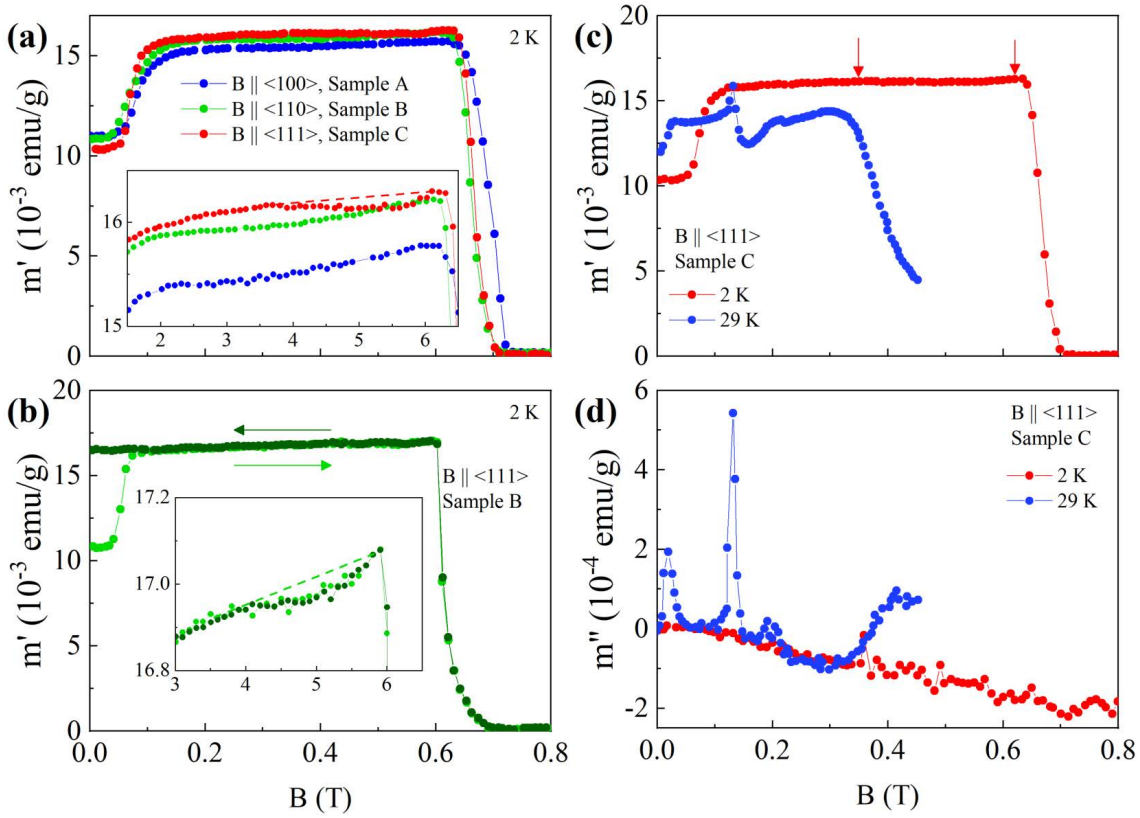

Figure 3.12: (a) B dependence of m' at 2 K for $\vec{B} \parallel \langle 100 \rangle$, $\langle 110 \rangle$ and $\langle 111 \rangle$ after zero-field cooling in MnSi. The inset shows a zoomed region where an anomaly is observed only for sample C. (b) For sample B at 2 K the full magnetic field cycle is displayed, recorded with increasing (light green) and decreasing (dark green) B from $0 \rightarrow 0.8 \rightarrow 0$ T. A hysterical behavior at the low field region can be observed due to the single domain formation. The inset shows the details of m' in the region of interest, where the dashed line is a guide for the eyes. The magnetic field dependence of both in-phase, m' (c) and out-of-phase m'' (d) susceptibilities at 2 K (red) and 29 K (blue) is also depicted for $\vec{B}$ applied along the $\langle 111 \rangle$ direction. The red down arrows in (c) represent the region where the novel state appears.

field effects in each sample. The absence of any detectable hysteresis in this region might suggest a continuous phase transition. The contrary happens in $CuOSe_2O_3$, where a remarkable hysteresis is present in its new low-T SkL phases [66, 67].

Moreover, the *A-phase* is clearly observed in our curves of m' and m'' measured at ∼29 K, as, respectively, a down pocket and a sharp peak, both arising at ∼0.17 T, for all the three orientations. It is depicted in Fig. 3.12(c) and (d) for sample C, oriented with $\vec{B} \parallel \langle 111 \rangle$. This is in agreement with the previously reported results for the *A-phase* in MnSi [81, 82]. However, the new low-T anomaly does not show any signal in the m'' taken at 2K, which seems to indicate that the nature of this new state is not skyrmionic (Fig. 3.12(d)).

Curves of m' vs H_{dc} were measured at several temperatures in the interval from 2 K to 8 K for the three orientations. The anomaly observed for the crystals oriented

along ⟨111⟩ at 2 K over ∼0.35 and ∼0.62 T is disappearing gradually as the temperature increases over $T \geq 6$ K. These curves are displayed in Fig. 3.13(a) for sample C. Both the depth and width in the m' valley decrease with increasing T, whereas the m' signal at the bottom (∼0.55 T) of the m' valley remains almost constant. For the other orientations (⟨110⟩ and ⟨100⟩), where no anomaly is observed at 2 K, a monotonous decreasing of the a.c. signal, as the temperature increases from 2 to 8 K, is observed.

The new anomaly observed in the curves m' was also studied at different frequencies (f) in the range spanning from 0.3–1000 Hz. In this frequency range, the curves do not show any remarkable difference. In the inset of Fig. 3.13(a), the magnetic field onsets, extracted from the curves measured at 2 K, are displayed for every frequency for the sample C, in the field range B covering the region from the CH to FFM states. The characteristic flat-valley defining the anomaly hardly changes against the change in f. It could suggest that the anomaly is nearly static, without accompanying any energy loss. In addition, a local and continuous rearrangement of the magnetic spin textures could explain these macroscopic frequency independent curves. Furthermore, the fact that no anomaly was observed in the heat capacity measurements for $\vec{B} \parallel \langle 111 \rangle$ could reveal that most of the magnetic entropy is consumed near T_c, and it hardly survives in the B region near FFM below 7 K.

Collecting all the interesting points from the a.c. susceptibility curves vs B and T, a new magnetic phase diagram for $\vec{B} \parallel \langle 111 \rangle$ is presented in Fig. 3.13(b). In this case, at low T, the CH and FFM phases are present together with a new region, termed *B-phase*, at relatively high magnetic fields. Whereas the typical *A-phase* is observed for the three orientations, ⟨100⟩, ⟨110⟩, and ⟨111⟩, the new *B-phase* is only visible for $\vec{B} \parallel \langle 111 \rangle$. This result indicates that the cubic magnetic anisotropy could play a role, together with the thermal fluctuations, in stabilizing such new state.

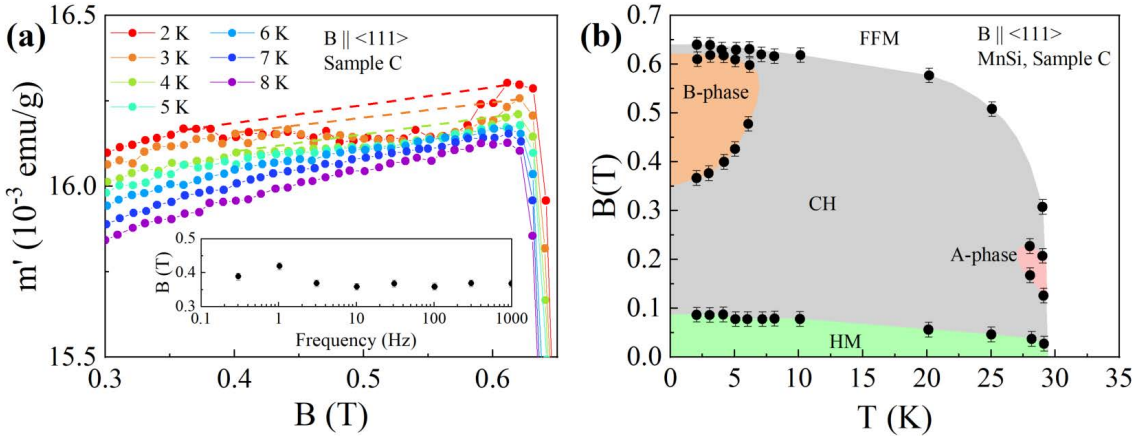

Figure 3.13: (a) B dependence of m' at different temperatures measured in sample C of MnSi. Inset shows magnetic field onset for the anomaly, extracted from the curves of m' at $T = 2$ K, as function of the frequency f. (c) Magnetic phase diagram for the MnSi single crystal for $\vec{B} \parallel \langle 111 \rangle$ deduced from characteristic points of m' measured versus temperature and magnetic field.

The MnSi phase diagrams for different orientations of the magnetic field have been the subject of huge interest [38, 42, 46, 61–63, 71, 77, 78, 81, 83]. However, the focus of those studies was put onto the conventional *A-phase* and onto the low field region ($B \leq 0.35$ T) for a few high symmetry directions, therefore skipping the vicinity of the FFM boundary at low T ($T \leq 10$ K). As it has been mentioned before, new low-T phases have been described in the phase diagram of Cu_2OSeO_3 oriented crystals along its easy axis $\langle 100 \rangle$. However, the *B-phase* described here shows very important differences. In MnSi, this *B-phase* does not show neither hysteretic behavior with the magnetic field nor any measurable signal in the out-of-phase component of the a.c. magnetization. In addition, in MnSi, the *B-phase* appears when the magnetic field is applied along the main cubic diagonal $\langle 111 \rangle$. All these facts together suggest a very different nature for the *B-phase* compared with any typical SkL or tilted CH phases. However, until this point, our macroscopic data could not provide further details about the microscopic nature of such a phase. Therefore, in order to clarify the nature of this *B-phase*, SANS and μSR experiments were also performed. The results from such experiments are explained in the next sections.

3.4 SANS studies of the *B-phase* and *A-phase*

The SANS pattern at zero field and 2 K with $\vec{B} \parallel \langle 111 \rangle \perp \vec{k}_i$ is shown in Fig. 3.14(a), where multiple peaks are observed in addition to those along the [111] direction.

Radial and angular integrations for each peak, depicted in Fig. 3.14(b) and (c), respectively, were carried out to trace the scattered intensity dependence on the scattering vector modulus (q) and azimuthal angle (θ). The peaks along the [111] direction appear at 90° and 270° on the detector, centered around $q_h = 0.03520(2)$ Å^{-1}. Another pair of peaks at 160° and 340° with a similar center $q'_h = 0.03507(2)$ Å^{-1} identifies that direction as $[11\bar{1}]$. Consequently, helices propagating along two of the four $\langle 111 \rangle$ axes can be observed in this configuration. Finally, the pair of peaks at 35° and 215° centered around $q_1 = 0.04055(2)$ Å^{-1} correspond to the [001] direction,

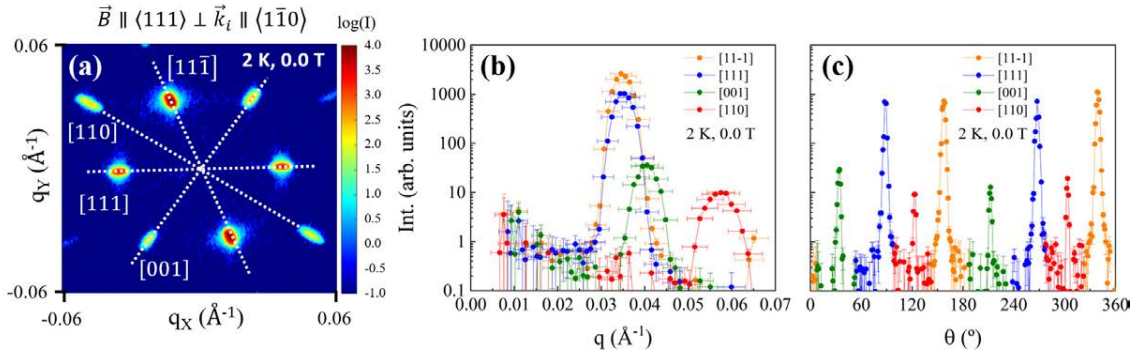

Figure 3.14: (a) SANS pattern of MnSi at zero field and 2 K with $\vec{B} \parallel \langle 111 \rangle \perp \vec{k}_i$. Scattering vector modulus q and azimuthal angle θ dependence are shown in (b) and (c), respectively. The scattered intensity is plotted in logarithmic scale.

while the pair of peaks at 125° and 305° with a center at $q_2 = 0.05738(5)$ Å^{-1} correspond to the [110] direction. Nevertheless, diffraction peaks in these directions result from multiple scattering, not additional domains, as they can be obtained as $\vec{q} = \vec{q}_{[111]} + \vec{q}_{[11\bar{1}]}$ and $\vec{q} = \vec{q}_{[111]} - \vec{q}_{[11\bar{1}]}$, in agreement with [42, 78].

Subsequently, our attention turns to the evolution of the SANS patterns with the magnetic field. Measurements were taken at 2, 3.5, 5, 15 and 28 K for the magnetic field applied along the $\langle 111 \rangle$ direction in the range $0 \leq B \leq 0.7$ T with $\Delta B = 0.02$ T. Fig. 3.15(a) and (c) depict typical SANS patterns at 2 K and 28 K, respectively, with $\vec{B} \parallel \langle 111 \rangle \parallel \vec{k}_i$, a configuration sensitive to magnetic modulations perpendicular to the field. In the HM or CH phases, no signal is expected at low fields due to the helix alignment with the magnetic field. However, even in the *B-phase* region no signal is detected, in contrast with the *A-phase*, where the corresponding hexagonal diffraction pattern is observed at 28 K, 0.2 T (see Fig. 3.15(c)).

The patterns in the complementary configuration with $\vec{B} \parallel \langle 111 \rangle \perp \vec{k}_i$, sensitive to magnetic modulations along the field, are displayed in Fig. 3.15(b) and (d). At zero field the multi-domain helical structure gives rise to diffraction peaks along the [111] and [11$\bar{1}$] directions, plus peaks due to multiple scattering. For fields $B \geq 0.1$ T, the helices propagating along the three unfavorable axes ([11$\bar{1}$], [1$\bar{1}$1], [$\bar{1}$11]) reorient toward the favorable axis [111], evidenced by the widening and weakening of peaks along [11$\bar{1}$]. For $B \geq 0.2$ T, when the single domain of conical helices propagating along the [111] direction emerges, the intensity of the reflections begins to decrease as more magnetic contribution shifts from the helical modulation to the ferromagnetic

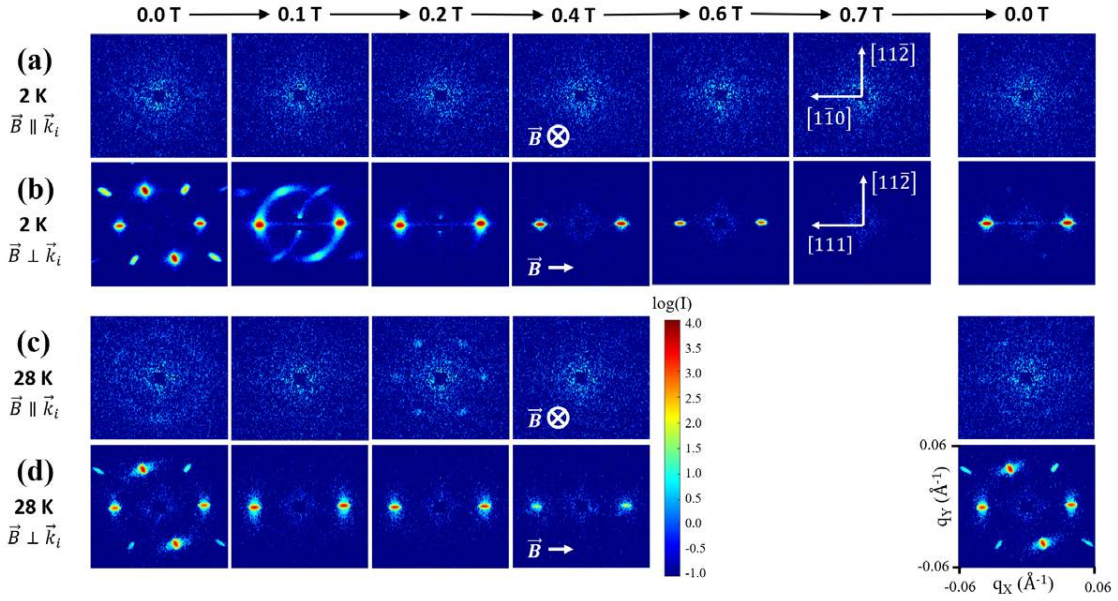

Figure 3.15: SANS patterns of MnSi obtained for different magnetic fields at 2 K [(a) and (b)], and 28 K [(c) and (d)], in the $\vec{B} \parallel \langle 111 \rangle \parallel \vec{k}_i$ and $\vec{B} \parallel \langle 111 \rangle \perp \vec{k}_i$ configurations. The scattered intensity is plotted in logarithmic scale. The crystallographic directions present in the detector plane for each configuration are shown in (a) and (b).

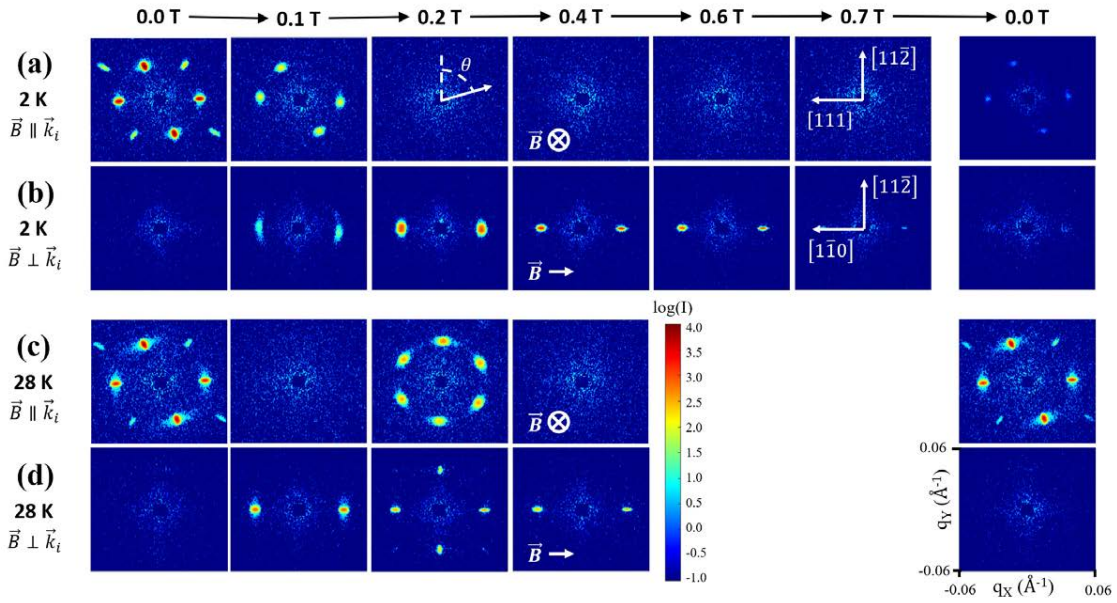

Figure 3.16: SANS patterns of MnSi obtained for different magnetic fields at 2 K [(a) and (b)], and 28 K [(c) and (d)], in the $\vec{B} \parallel \langle 1\bar{1}0 \rangle \parallel \vec{k}_i$ and $\vec{B} \parallel \langle 1\bar{1}0 \rangle \perp \vec{k}_i$ configurations. The scattered intensity is plotted in logarithmic scale. The azimuthal angle θ and the crystallographic directions present in the detector plane for each configuration are shown in (a) and (b).

contribution. Finally, for fields $B \geq 0.6$ T no magnetic scattering is observed, as the only propagation vector left $\vec{K}_{\mathrm{FM}} = (0, 0, 0)$ is hidden behind the direct neutron beam. In the process of decreasing the magnetic field from the ferromagnetic phase to zero field, the single domain of conical helices remains at 2 K, while at 28 K the multi-domain helical structure reappears.

Continuing to explore different configurations, SANS patterns were collected at 2, 15 and 28 K for the magnetic field applied along the $\langle 1\bar{1}0 \rangle$ direction in the range $0 \leq B \leq 0.7$ T with $\Delta B = 0.02$ T. Fig. 3.16 illustrates SANS patterns at 2 K and 28 K in the two configurations, $\vec{B} \parallel \langle 1\bar{1}0 \rangle \parallel \vec{k}_i$ and $\vec{B} \parallel \langle 1\bar{1}0 \rangle \perp \vec{k}_i$. In the former (see Fig. 3.16 (a) and (c)), the signal from the multi-domain helical structure diminishes as helices align with the magnetic field. Simultaneously, the complementary configuration reveals the formation of a single-domain conical helix along the magnetic field, evidenced by the appearance of two diffraction peaks along the $[1\bar{1}0]$ direction (Fig. 3.16(b) and (d)). Notably, the *A-phase* is clearly observed in both configurations at 28 K, 0.2 T, presenting as a hexagonal diffraction pattern for $\vec{B} \parallel \langle 1\bar{1}0 \rangle \parallel \vec{k}_i$ and two diffraction peaks along the vertical direction $[11\bar{2}]$ for $\vec{B} \parallel \langle 1\bar{1}0 \rangle \perp \vec{k}_i$ (see Fig. 3.16 (c) and (d)). As the magnetic field decreases, the zero-field multi-domain structure is recovered at 28 K. However, at 2 K, no signal is observed in either configuration, suggesting that the propagation vector lies neither parallel nor perpendicular to the $[1\bar{1}0]$ direction.

While these SANS results confirm that the *B-phase* differs from the conventional *A-phase*, discarding the possibility of a SkL structure, there is no clear distinction

with the CH phase. Therefore, a detailed analysis was undertaken, focusing on the intensity and propagation vector's temperature and magnetic field dependence.

To explore the evolution of scattered intensity concerning magnetic field and temperature, an integration over an arc of $0.0275 \leq q \leq 0.045$ Å^{-1} and an angular opening of $\Delta\theta = 20°$ around the diffraction peaks was performed. The results for the *A-phase* are depicted in Fig. 3.17. For $\vec{B} \parallel \langle 111 \rangle \parallel \vec{k}_i$ magnetic modulations

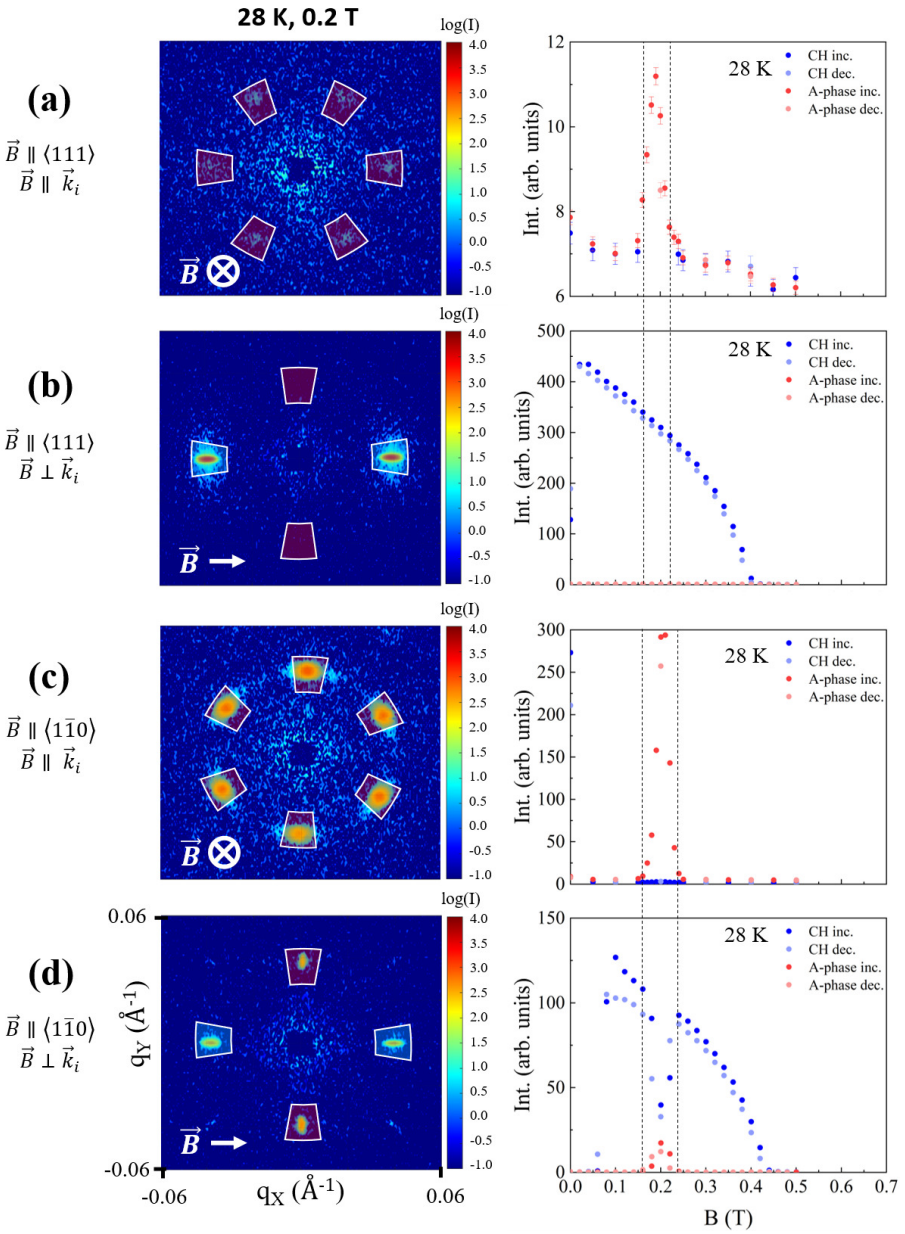

Figure 3.17: SANS patterns of MnSi at 28 K, 0.2 T and integrated intensity at 28 K with $\vec{B} \parallel \langle 111 \rangle \parallel \vec{k}_i$ (a), $\vec{B} \parallel \langle 111 \rangle \perp \vec{k}_i$ (b), $\vec{B} \parallel \langle 1\bar{1}0 \rangle \parallel \vec{k}_i$ (c) and $\vec{B} \parallel \langle 1\bar{1}0 \rangle \perp \vec{k}_i$ (d). The integration areas are shown in red for the peaks due to the *A-phase* and in blue for the conical helix (CH). The dotted lines in the integrated intensity indicate the boundaries of the *A-phase*.

give rise to peaks along three directions: $[1\bar{1}0]$, $[10\bar{1}]$ and $[01\bar{1}]$, with a modulus $K_{\mathrm{A}} = 0.0385(1)$ Å^{-1} (see Fig. 3.17(a)). These peaks are observed in the magnetic field range $0.16 \leq B \leq 0.22$ T. However, no evidence of the *A-phase* is observed in the configuration $\vec{B} \parallel \langle 111 \rangle \perp \vec{k}_i$, likely due to the faint signal of the SkL compared to the conical phase (see Fig. 3.17(b)). When the field is applied along the $\langle 1\bar{1}0 \rangle$ direction, the peaks arising from magnetic modulations can be observed in the $\vec{B} \parallel \vec{k}_i$ configuration along the $[11\bar{2}]$, [881] and [113] directions, with the same modulus as for $\vec{B} \parallel \langle 111 \rangle$ (see Fig. 3.17(c)). Since the vertical direction in the detector coincides with $[11\bar{2}]$, the *A-phase* is also clearly observed in the $\vec{B} \perp \vec{k}_i$ configuration in the range $0.16 \leq B \leq 0.24$ T (see Fig. 3.17(d)).

The integrated intensities for all temperatures measured in the configurations sensitive to magnetic modulations along the field ($\vec{B} \perp \vec{k}_i$) are displayed in Fig. 3.18. At 2 K with $\vec{B} \parallel \langle 111 \rangle$, a sudden increase in intensity is observed at the transition between the HM and CH phases (see Fig. 3.18(a)). The initial intensity at zero field accounts for roughly 1/4 of the maximum value at $B = 0.1$ T, consistent with the reorientation of the three other $\langle 111 \rangle$ domains. For higher fields, the intensity decreases due to the reduction of the magnetic structure's half-cone angle. Decreasing the field from saturation mirrors the behavior observed during field increase until $B = 0.4$ T. Beyond this point, a significant hysteresis emerges, where the intensity, far from fully recovering the maximum value reached during the increasing procedure, saturates at zero field at 3/4 of the maximum value. The results of the TAIKAN experiments, detailed in Appendix E, also show such hysteresis. Figure 3.19 shows a comparison between the integrated intensity measured at 2 K for crystal 1 and crystal 2 of MnSi in both TAIKAN and D33 instruments. In both crystals, the same decreasing field curve is obtained independently of the measured instrument or year by simply applying a multiplicative factor to the intensity. However, the increasing field curves do not overlap which each other, suggesting that the hysteresis depends on the instrument, sample shape and specific measurement sequence. Additional measurements show that the hysteresis disappears when performing a second cycle of increasing magnetic field (see Appendix E). Similar tendencies have been observed in MnSi [42] and $Mn_{0.96}Fe_{0.04}Si$ [84], showing discrepancies with the expected

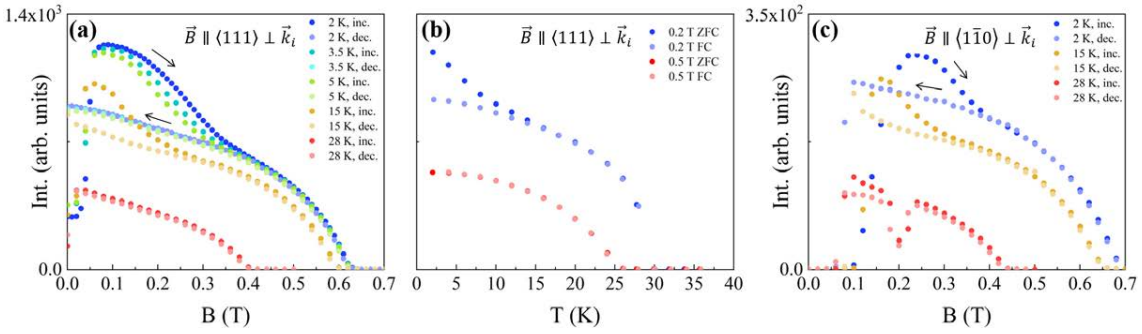

Figure 3.18: Evolution of the integrated intensity of MnSi with magnetic field and temperature for the $\vec{B} \parallel \langle 111 \rangle \perp \vec{k}_i$ [(a) and (b)] and $\vec{B} \parallel \langle 1\bar{1}0 \rangle \perp \vec{k}_i$ (c) configurations.

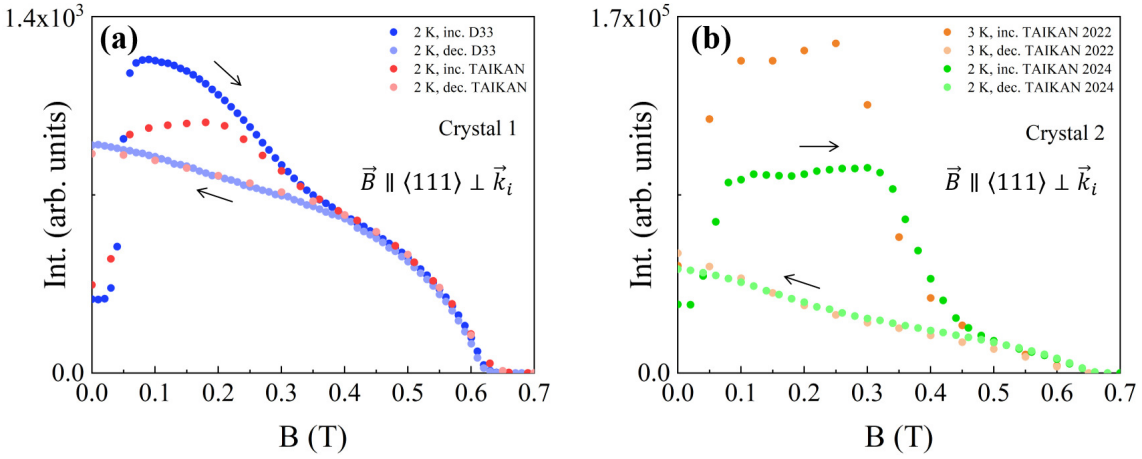

Figure 3.19: Evolution of the scaled integrated intensity for crystal 1 (a) and crystal 2 (b) of MnSi measured at 2 K in TAIKAN and D33 for the $\vec{B} \parallel \langle 111 \rangle \perp \vec{k}_i$ configuration.

theoretical curve and the results from [38, 69], although to our best knowledge no explanation has been given. As the temperature increases, qualitatively similar trends are observed, although the hysteresis diminishes, and at 28 K, nearly no hysteresis is present. Additional ZFC and FC patterns were collected at 0.2 T and 0.5 T for several temperatures. The integrated intensity is presented in Fig. 3.18(b). The ZFC and FC curves at 0.5 T exhibit no hysteresis, while the curves at 0.2 T display a small hysteresis below 15 K, in agreement with the field dependent curve. For both fields, the intensity decreases monotonically with increasing temperature, reflecting the diminishing contribution of ordered magnetic moments to the diffraction pattern. Similar results are observed when the field is applied along the $\langle 1\bar{1}0 \rangle$ direction for $B > 0.1$ T, although the hysteresis appears to be smaller (see Fig. 3.18(c)). For fields below 0.1 T, no intensity is observed as the helices are turned away from the magnetic field and towards the easy axis $\langle 111 \rangle$.

Subsequently, we examine the dependence of the propagation vector modulus K_h on magnetic field and temperature (see Fig. 3.20). A Gaussian fit to the $I(q)$ curves similar to the one shown in Fig. 3.14(b) was conducted to obtain K_h. Within the error bar, the obtained values are almost independent of both the magnitude and direction of the applied magnetic field, while they significantly increase with temperature, as observed in Fig. 3.20(a) and (c). The temperature dependence of K_h is more clearly appreciated in Fig. 3.20(b), where it is fitted to:

$$K_\mathrm{h} = K_\mathrm{h}(0) \left[1 + a \left(\frac{T}{T_\mathrm{c}} \right)^x \right] \tag{3.1}$$

The results yield $K_\mathrm{h}(0) = 0.03504(5)$ Å^{-1}, $a = 0.11(1)$, $x = 2.6(1)$ for $H = 0.2$ T, and $K_\mathrm{h}(0) = 0.03513(1)$ Å^{-1}, $a = 0.10(1)$, $x = 2.16(3)$ for $H = 0.5$ T, in good agreement with previous studies [42].

Although the intensity and propagation vector dependence on temperature and magnetic field allowed to discard a low temperature SkL or a tilted CH state as

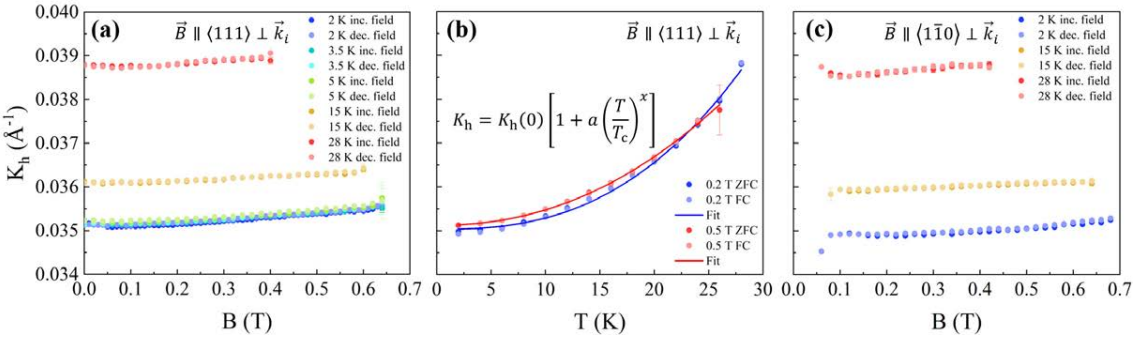

Figure 3.20: Evolution of the modulus of the helix propagation vector K_h of MnSi with magnetic field and temperature for the $\vec{B} \parallel \langle 111 \rangle \perp \vec{k}_i$ [(a) and (b)] and $\vec{B} \parallel \langle 1\bar{1}0 \rangle \perp \vec{k}_i$ (c) configurations.

the origin of the *B-phase*, the SANS results could not provide a decisive indication regarding the nature of such state. In order to obtain more information at the atomic level of its magnetic structure, μSR experiments were performed to detect the internal magnetic field.

3.5 Local field of MnSi investigated by μSR

Figure 3.21(a) reveals distinct differences between the Zero-Field (ZF) μSR spectra measured in the Spin-Rotated (SR) and Non-Spin-Rotated (NSR) configurations at 2 K obtained under ZFC and FC protocols. Notably, all oscillatory behavior nearly vanishes by 2 μs, yet the asymmetry at long times greatly differs.

Figure 3.21(b) displays the Fourier transform of the ZF μSR spectra measured in both configurations. These curves exhibit a consistent qualitative behavior, which reflects the symmetry of the muon implantation sites. In MnSi, muons occupy four crystallographically equivalent positions within the unit cell, corresponding to the $4a$ Wyckoff position (x, x, x), where $x_\mu = 0.532$ [85]. Due to the incommensurate nature of the magnetic structure, one should expect a continuous distribution of local fields at the $4a$ sites. However, muons located at sites with their local symmetry axis parallel to the $\langle 111 \rangle$ diagonals, referred to as h_1 sites, will all experience the same local field independently of the phase of the helix [85, 86]. This results in the prominent peak observed at $B_{h_1} = 0.091(1)$ T. In contrast, the remaining three muon sites, denoted as h_2 sites, are symmetrically located around the $\langle 111 \rangle$ diagonal, as it represents for them a threefold symmetry axis. This symmetry results in these muons perceiving an identical field distribution, ranging between $0.095 \leq B_{h_2} \leq 0.209$ T.

To discern the differences observed in the ZF μSR spectra, an extensive analysis was conducted across the entire time scale measured. Figure 3.22(a) presents the ZF μSR spectra collected in the SR configuration, where the positron detectors are placed such that $\vec{d}_p \parallel X$ and $\vec{i}_\mu \parallel X \perp \langle 111 \rangle$. Hence, recalling Eq.(2.72), the measured asymmetry signal can be expressed as:

$$A(t) = a_0 P_X(t) + A_\mathrm{off} \tag{3.2}$$

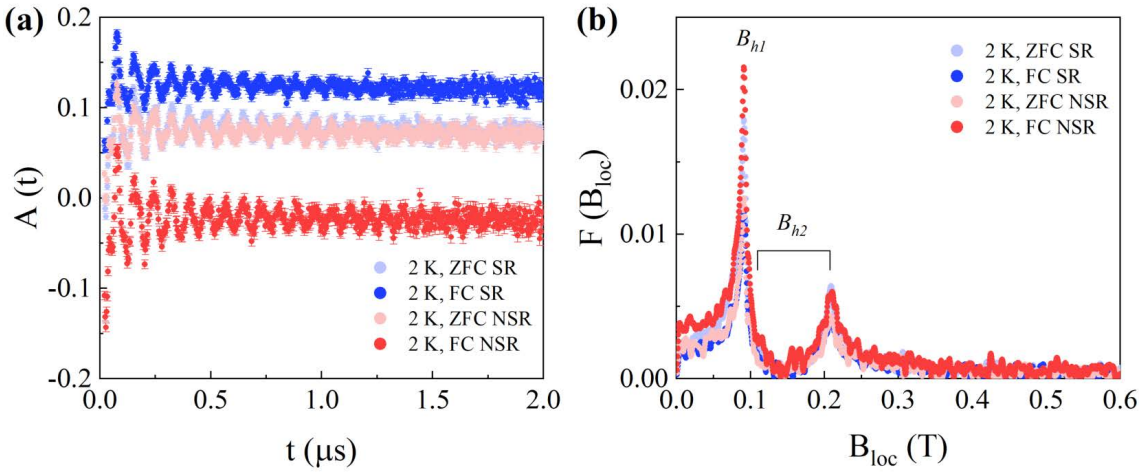

Figure 3.21: (a) Time dependence of the ZF μSR spectra of MnSi at 2 K. (b) Field dependence of the Fourier transform of ZF μSR spectra. The local field due to h_1 sites and the field distribution due to h_2 sites are also displayed. Data measured in the SR (blue) and NSR (red) configurations after ZFC and FC protocols are shown in light and dark filled circles, respectively.

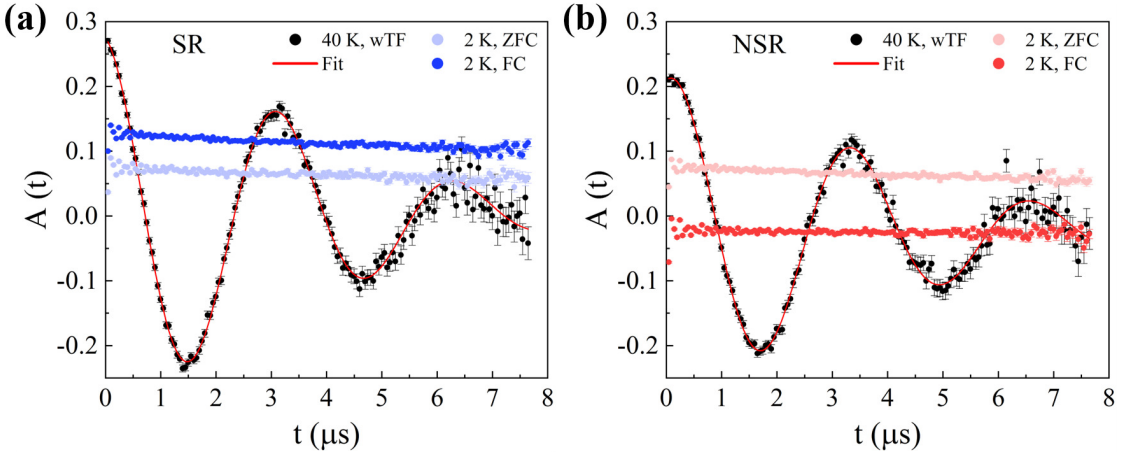

Figure 3.22: μSR spectra of MnSi in the SR (a) and NSR (b) configurations. The data measured at 40 K with a wTF is shown in black circles, while the red line corresponds to the fit according to Eq. (3.4). Data measured at 2 K after ZFC and FC protocols are shown in light and dark filled circles, respectively.

where A_{off} denotes a time-independent background and:

$$P_X(t) = \left\langle \left(\frac{B^X_{\text{loc}}}{B_{\text{loc}}}\right)^2 e^{-\lambda_Z t} + \left(1 - \left(\frac{B^X_{\text{loc}}}{B_{\text{loc}}}\right)^2\right) e^{-\left(\frac{\Delta^2 t^2}{2} + \lambda_X t\right)} \cos(\omega_\mu t) \right\rangle \tag{3.3}$$

The approach followed here is in line with methodologies from previous studies [87, 88], wherein the relaxation of the oscillatory component is attributed to a

combination of magnetic fluctuations and imperfections in the magnetic structure ($e^{-\lambda_X t}$), alongside a static distribution of ^{55}Mn nuclear moments ($e^{-\frac{\Delta^2 t^2}{2}}$). Due to the strong local field from itinerant electrons, the effect of nuclear spins is negligible in the component in which $\vec{B}_{\rm loc}$ is initially parallel to $\vec{i}_\mu$. Consequently, in this non-oscillatory component, the dynamical relaxation λ_Z solely depends on the muon spin-lattice interaction.

The initial asymmetry parameter a_0 was calibrated using data from the paramagnetic region at $T = 40$ K under a weak transverse field (wTF), as illustrated in Fig. 3.22(a). In this specific scenario, $B^X_{\rm loc}/B_{\rm loc} \ll 1$, so that Eq.(3.2) can be simplified as:

$$A(t) = a_0\, e^{-\left(\frac{\Delta^2 t^2}{2} + \lambda_X t\right)} \cos(\omega_\mu t) + A_{\rm off} \tag{3.4}$$

The fit to Eq.(3.4) is depicted as a red line in Fig. 3.22(a). Subsequently, the spectra measured at 2 K and zero field under both ZFC and FC conditions (represented by light and dark blue filled circles, respectively) were analyzed with a larger binning compared to Fig. 3.21. This approach effectively suppresses any minor oscillations due to spontaneous fields at muon sites. Consequently, at longer timescales, only the first term in Eq.(3.3) is relevant and Eq.(3.2) can be re-articulated as:

$$A(t \to \infty) = a_0 \left\langle \left(\frac{B^X_{\rm loc}}{B_{\rm loc}}\right)^2 \right\rangle e^{-\lambda_Z t} + A_{\rm off} \tag{3.5}$$

The fit to Eq.(3.5) was performed using the pre-calibrated values of a_0 and $A_{\rm off}$. In the NSR configuration, where $\vec{i}_\mu \parallel \vec{d}_p \parallel Z \parallel \langle 111 \rangle$, the same expressions from Eq.(3.2), Eq.(3.4) and Eq.(3.5) can be used by replacing X by Z. A similar procedure was employed for the data collected in the NSR configuration, as shown in Fig. 3.22(b). All parameters derived from the fits to Eq.(3.4) and Eq.(3.5) are shown in Table 3.1. Both the field $B = \omega_\mu/\gamma_\mu$ and the initial asymmetry a_0 are in agreement with the expected values from the experimental setup, while parameters Δ, λ_X and λ_Z are comparable with prior results [87, 89–92], ensuring the consistency of the fits.

Table 3.1: Parameters derived from the fits of the μSR spectra of MnSi to Eq.(3.4) and Eq.(3.5).

Parameter	40 K, wTF	2 K, ZFC	2 K, FC	40 K, wTF	2 K, ZFC	2 K, FC
		SR			NSR	
$B = \omega_\mu/\gamma_\mu$ (G)	23.90(7)	–	–	21.30(7)	–	–
Δ/γ_μ (G)	2.9(3)	–	–	3.0(3)	–	–
λ_X (μs^{-1})	0.07(2)	–	–	0.08(3)	–	–
a_0	0.262(4)	0.262	0.262	0.242(4)	0.242	0.242
$A_{\rm off}$	-0.007(1)	-0.007	-0.007	-0.013(2)	-0.013	-0.013
λ_Z (μs^{-1})	–	0.040(3)	0.033(1)	–	0.038(2)	0.038
$\langle (B^X_{\rm loc}/B_{\rm loc})^2 \rangle$	–	0.314(2)	0.515(2)	–	–	–
$\langle (B^Z_{\rm loc}/B_{\rm loc})^2 \rangle$	–	–	–	–	0.369(2)	0.045(2)

In particular, the fitting of the 2 K ZFC curve in both SR and NSR configurations yields $\left\langle \left(B^X_{\rm loc}/B_{\rm loc}\right)^2 \right\rangle = 0.314$ and $\left\langle \left(B^Z_{\rm loc}/B_{\rm loc}\right)^2 \right\rangle = 0.369$. These values are close to the theoretical estimate of 1/3 for a powder sample averaged over all orientations,

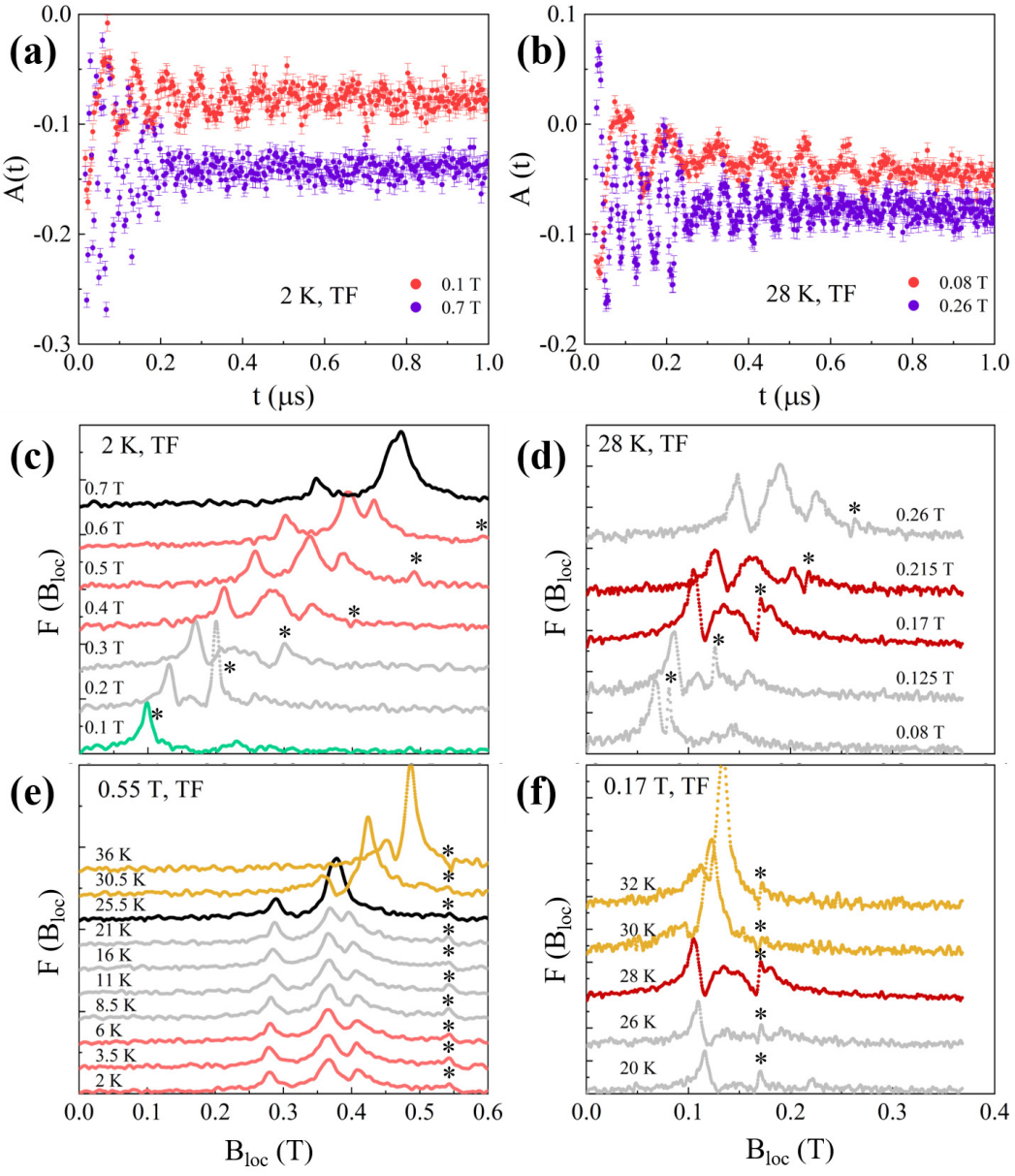

Figure 3.23: TF μSR spectra of MnSi for some selected applied fields at 2 K (a) and 28 (b). The field dependence of the Fourier transform of μSR spectra is shown at 2 K (c) and 28 (d). The temperature dependence of the Fourier transform of μSR spectra is shown at 0.55 T (e) and 0.17 T (f). The colors used in panels (c), (d), (e) and (f) indicate the different magnetic phases as deduced from previous experiments: helimagnetic (green), conical helix (grey), *B-phase* (light red), ferromagnetic (black), *A-phase* (dark red) and paramagnetic (dark yellow). The signal at the applied field value due to background muons is marked with black asterisks.

supporting the multi-domain helical structure observed at zero field in the SANS experiments. Meanwhile, the values $\left\langle \left(B^X_{\rm loc}/B_{\rm loc}\right)^2 \right\rangle = 0.515$ and $\left\langle \left(B^Z_{\rm loc}/B_{\rm loc}\right)^2 \right\rangle = 0.045$ for the 2 K FC curve imply that nearly the entire local magnetic field is now perpendicular to Z, i.e, the $\langle 111 \rangle$ direction. This behavior is consistent with the emergence of a single-domain helix, corroborated by the two magnetic reflections observed in the SANS experiments when the magnetic field is reduced from the FFM phase.

Next, we show the evolution of the μSR spectra with magnetic field and temperature. Figure 3.23(a) and (b) present the TF μSR spectra at 2 K and 28 K, respectively, for both the minimum and maximum fields measured. Here, oscillations are almost entirely suppressed by 1 μs, indicating a significant increase of the magnetic fluctuations. A better understanding of the magnetic field dependence is obtained by plotting the Fourier transformed data, shown in panels (c) and (d) of Fig. 3.23. At 2 K, the distribution shifts to higher values as the applied field increases. While the peak shape due to the h_1 sites remains relatively unchanged, the distribution due to the h_2 sites becomes increasingly narrow, eventually merging into a single peak three times bigger than the h_1 peak in the ferromagnetic phase [86] (see Fig. 3.23(c)).

This pattern aligns with expectations, as Mn moments in the conical phase shift from the helical modulation, which produces the field distribution, to the ferromagnetic contribution, which produces a single value. An additional peak is always present at the same value as the applied field, signaled by a black asterisk in panels (c), (d), (e) and (f) of Fig. 3.23, which can be due to muons stopping in the cryostat walls and other parts of the sample holder [93–98].

A similar trend is observed at 28 K, as illustrated in Fig. 3.23(d). However, the difference between the field distribution of the *A-phase* and the conical phase is not clear. This is better appreciated when examining the temperature dependence at a constant applied field, as depicted Fig. 3.23(e) and (f). In such scenarios, the field distribution is expected to remain constant unless a change in the magnetic state occurs. At 0.55 T, the distribution shows minimal change, retaining three distinct peaks, until the system approaches the FFM border. For higher temperatures the magnetic moments are no longer ordered, causing the h_1 and h_2 peaks to converge towards each other and to the applied field value (see Fig. 3.23(e)). In contrast, at 0.17 T, the primary difference between the *A-phase* and the conical phase seems to be a slight elevation in the h_2 field distribution, as observed in Fig. 3.23(f).

3.6 Proposed local magnetic model

In order to gain a deeper understanding of the internal field distributions and the new *B-phase* in MnSi, we introduce in this section a theoretical model centered on the magnetic structure at the atomic level.

The model developed by Laliena and Campo [36] did not include either any change in the modulus of the magnetic moment or any extra magnetic anisotropy term in its Hamiltonian, necessary to explain the anisotropic behavior observed for the new *B-phase*. However, it is expected that the effect of a very weak magnetic anisotropy,

related with the real cubic symmetry, would split the intrinsic degeneracy of the model between the three main cubic directions. Other theoretical mechanisms, in micromagnetic models at $T = 0$, based on the competition of magneto-crystalline anisotropies, but without considering the crucial role of the thermal fluctuations effect in the free energy, are invoked to explain the existence of the new states (SkL and tilted CH phases) observed in Cu_2OSeO_3 at low T [66, 67, 99]. It is clear that anisotropies must be present because the new states in Cu_2OSeO_3 and the new *B-phase* in MnSi appear only for specific directions of the crystal, namely, the anisotropy axis, which are, respectively, $\langle 100 \rangle$ and the $\langle 111 \rangle$. However, it is not still clear which is its hierarchy of energy scales. Moreover, the present observations reveal that the *B-phase* exists even in a system with a weak magnetic anisotropy, such as MnSi, compared with the related compound Cu_2OSeO_3 [67].

All the mentioned micromagnetic theoretical models have in common the fact that they are not taking into account the local details of the magnetic structure because they consider the density energy in the continuum approximation with a constant modulus averaged magnetic moment.

In MnSi (space group $P2_13$ No. 198), the four Mn atoms occupy the $4a$ Wyckoff position (x, x, x) with $x = 0.138$, located in the vertices of a tetrahedron [38]. Each Mn atom forms a helix, sharing a common propagation vector $\vec{K}_{\rm h} = (\delta,\, \delta,\, \delta)$, with $K_{\rm h} \sim 0.035\,^{-1}$. The starting point of our magnetic model is the symmetry analysis of these four helices. The magnetic representation for the Mn atoms, located at the $4a$ Wyckoff position (x, x, x) with $x = 0.138$, can be decomposed as a direct sum of Irreducible Representations (*irreps*) of the parent group $P2_13$ for the Λ point, $(\delta,\, \delta,\, \delta)$ as follows:

$$\mathrm{m}\Gamma_{4\mathrm{a}} = 4\mathrm{m}\Lambda_1(1) \oplus 4\mathrm{m}\Lambda_2(1) \oplus 4\mathrm{m}\Lambda_3(1)$$

The basis vectors for each *irrep* are listed in Table 3.2. The positions of the Mn atoms are labeled as: Mn1 $(x,\, x,\, x)$, Mn2 $\left(\bar{x} + \frac{1}{2},\, \bar{x},\, x + \frac{1}{2}\right)$, Mn3 $\left(\bar{x},\, x + \frac{1}{2},\, \bar{x} + \frac{1}{2}\right)$, Mn4 $\left(x + \frac{1}{2},\, \bar{x} + \frac{1}{2},\, \bar{x}\right)$. Each of these *irreps* splits the $4a$ Wyckoff position in two orbits formed by Mn1 in one orbit and the three other symmetry equivalents in the other.

For the Mn1 orbit, $\mathrm{m}\Lambda_1$ describes a magnetic moment pointing in the $\langle 111 \rangle$ direction, whereas in $\mathrm{m}\Lambda_2$ and $\mathrm{m}\Lambda_3$ the magnetic moment lies down in the perpendicular direction and correspond to right-handed and left-handed helices, respectively:

$$\begin{aligned} \psi_1^2 &= \left(1\ \frac{-1+\sqrt{3}i}{2}\ \frac{-1-\sqrt{3}i}{2}\right) \propto (2\,\bar{1}\,\bar{1}) + i\,(0\,1\,\bar{1}) \\ \psi_1^3 &= \left(1\ \frac{-1-\sqrt{3}i}{2}\ \frac{-1+\sqrt{3}i}{2}\right) \propto (2\,\bar{1}\,\bar{1}) - i\,(0\,1\,\bar{1}) \end{aligned} \tag{3.6}$$

In the other orbit, symmetry dictates that the magnetic moments must relate by rotations of $2\pi/3$ or $4\pi/3$ for $\mathrm{m}\Lambda_1$, $\mathrm{m}\Lambda_2$, $\mathrm{m}\Lambda_3$. To simplify the evaluation of each *irrep*'s constraints, the basis vector coefficients at the Mn2 site can be set to describe a helix propagating along the $\langle 111 \rangle$ direction, with coefficients $u = -\frac{1}{\sqrt{2}} + \frac{i}{\sqrt{6}}$, $v = \frac{1}{\sqrt{2}} + \frac{i}{\sqrt{6}}$, and $w = -\frac{2i}{\sqrt{6}}$. In such case, $\mathrm{m}\Lambda_3$ imposes:

Table 3.2: Basis vectors (BV) of each *irrep* present in the magnetic representation of the Mn 4*a* site for the space group $P2_13$ with $\vec{K}_{\rm h} = (\delta, \delta, \delta)$. The basis vectors components are expressed in terms of the crystallographic axis a, b and c.

irrep	BV	Mn1	Mn2	Mn3	Mn4
$\mathrm{m}\Lambda_1$	ψ_1^1	$(1\,1\,1)$	–		
	ψ_2^1	–	$(1\,0\,0)$	$(0\,1\,0)$	$(0\,0\,1)$
	ψ_3^1	–	$(0\,1\,0)$	$(0\,0\,1)$	$(1\,0\,0)$
	ψ_4^1	–	$(0\,0\,1)$	$(1\,0\,0)$	$(0\,1\,0)$
$\mathrm{m}\Lambda_2$	ψ_1^2	$\left(1\ \frac{-1+\sqrt{3}i}{2}\ \frac{-1-\sqrt{3}i}{2}\right)$	–		
	ψ_2^2	–	$(1\,0\,0)$	$(0\,1\,0)\cdot e^{i\frac{2\pi}{3}}$	$(0\,0\,1)\cdot e^{i\frac{4\pi}{3}}$
	ψ_3^2	–	$(0\,1\,0)$	$(0\,0\,1)\cdot e^{i\frac{2\pi}{3}}$	$(1\,0\,0)\cdot e^{i\frac{4\pi}{3}}$
	ψ_4^2	–	$(0\,0\,1)$	$(1\,0\,0)\cdot e^{i\frac{2\pi}{3}}$	$(0\,1\,0)\cdot e^{i\frac{4\pi}{3}}$
$\mathrm{m}\Lambda_3$	ψ_1^3	$\left(1\ \frac{-1-\sqrt{3}i}{2}\ \frac{-1+\sqrt{3}i}{2}\right)$	–		
	ψ_2^3	–	$(1\,0\,0)$	$(0\,1\,0)\cdot e^{i\frac{4\pi}{3}}$	$(0\,0\,1)\cdot e^{i\frac{2\pi}{3}}$
	ψ_3^3	–	$(0\,1\,0)$	$(0\,0\,1)\cdot e^{i\frac{4\pi}{3}}$	$(1\,0\,0)\cdot e^{i\frac{2\pi}{3}}$
	ψ_4^3	–	$(0\,0\,1)$	$(1\,0\,0)\cdot e^{i\frac{4\pi}{3}}$	$(0\,1\,0)\cdot e^{i\frac{2\pi}{3}}$

$$
\begin{aligned}
\vec{S}_{\vec{K}}^{\mathrm{Mn2}} &= u\cdot\psi_2^3 + v\cdot\psi_3^3 + w\cdot\psi_4^3 = \frac{1}{\sqrt{2}}(\bar{1}\,1\,0) - \frac{i}{\sqrt{6}}(\bar{1}\,\bar{1}\,2)\\
\vec{S}_{\vec{K}}^{\mathrm{Mn3}} &= u\cdot\psi_2^3 + v\cdot\psi_3^3 + w\cdot\psi_4^3 = \left[\frac{1}{\sqrt{2}}(0\,\bar{1}\,1) - \frac{i}{\sqrt{6}}(2\,\bar{1}\,\bar{1})\right]\cdot e^{i\frac{4\pi}{3}} = \vec{S}_{\vec{K}}^{\mathrm{Mn2}}\\
\vec{S}_{\vec{K}}^{\mathrm{Mn4}} &= u\cdot\psi_2^3 + v\cdot\psi_3^3 + w\cdot\psi_4^3 = \left[\frac{1}{\sqrt{2}}(1\,0\,\bar{1}) - \frac{i}{\sqrt{6}}(\bar{1}\,2\,\bar{1})\right]\cdot e^{i\frac{2\pi}{3}} = \vec{S}_{\vec{K}}^{\mathrm{Mn2}}
\end{aligned}
\tag{3.7}
$$

Therefore, the $\mathrm{m}\Lambda_3$ *irrep* fixes the helices propagating at Mn3 and Mn4 sites to be in-phase with the one at the Mn2 site. It is straightforward to verify that the other two *irreps* generate helices dephased by $\pm 2\pi/3$ at each site of the second orbit. The resulting magnetic structures for each *irrep* are depicted in Fig. 3.24.

Experimental μSR studies [87, 88] and theoretical analyses [100] have identified the magnetic configuration given by $\mathrm{m}\Lambda_3$ to be the most consistent with MnSi's physical properties, where the magnetic moments are contained in planes perpendicular to the $\langle 111\rangle$ direction adopting a quasi in-phase coupling with a small phase-shift angle between both orbits $\phi \sim 2^\circ$ (see Fig. 3.24). Crucially for this discussion, this phase-shift angle between both orbits is not fixed by the symmetry.

In order to evaluate the phase-shift evolution, a computational model, thoroughly described in Appendix C, was developed to fit the μSR spectra of MnSi. To analyze μSR spectra, two principal open-source tools were already avaiable: *musrfit* [101] and MuESR [102]. While *musrfit* offers robust capabilities and an user-friendly interface, its data analysis mainly relies on the use of phenomenological models. In order to integrate a physical model, additional programming is needed. This is solved

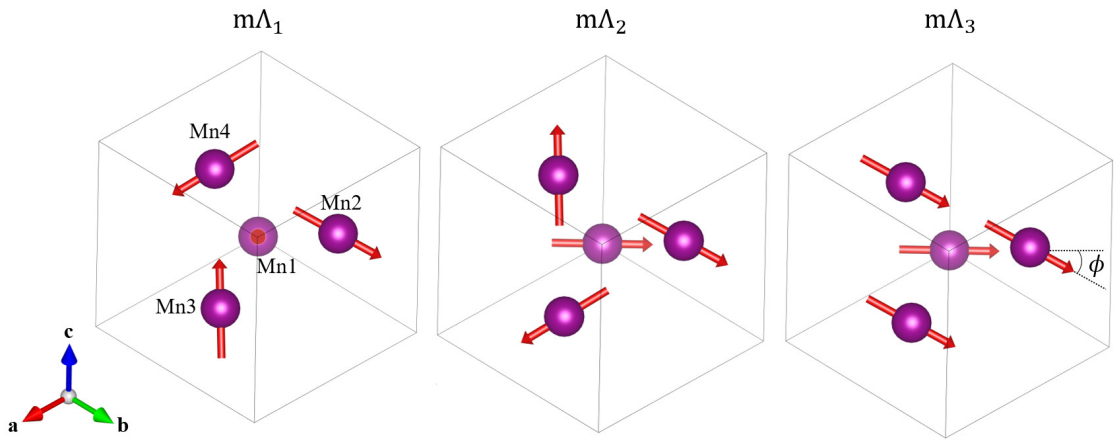

Figure 3.24: Magnetic structure described for each of the *irreps* present in the magnetic representation of the Mn $4a$ site for the space group $P2_13$ with $\vec{K}_\mathrm{h} = (\delta, \delta, \delta)$.

by MuESR, which evaluates the local field based on the magnetic structure and muon implantation sites provided by the user. Nonetheless, MuESR's functionality is confined to simulations, lacking an integrated data fitting feature. Hence, we opted for developing our own optimized code. In this computational model, the experimental setup, nuclear structure, magnetic structure and muon implantation site are needed as input variables. By combining these variables, the local field at the muon site is calculated, and the resulting asymmetry signal is fitted to the experimental data by varying the variables of the magnetic model and experimental setup.

Figure 3.25 presents several fitted curves at 2 K in the time domain and their Fourier transforms. For all applied fields, the data fits were satisfactory, achieving an agreement factor of $R_w < 12$ as defined in Appendix A.1. Comparable fitting outcomes for 15 K and 28 K are exhibited in Fig. 3.26. The adopted assumptions in the fits include:

- The crystal orientation was defined such that the initial muon spin direction $\vec{i}_\mu$ aligned parallel to $\langle 1\bar{1}0\rangle$ and perpendicular to the applied magnetic field $\vec{B}_\mathrm{ext}$, parallel to $\langle 111\rangle$.

- The cubic unit cell, with a lattice parameter $a = 4.558$ Å [37], hosted Mn atoms and muons at $4a$ sites. The positions were denoted as: $\vec{f}_{i,1} = (x_i, x_i, x_i)$, $\vec{f}_{i,2} = \left(\bar{x}_i + \frac{1}{2}, \bar{x}_i + 1, x_i + \frac{1}{2}\right)$, $\vec{f}_{i,3} = \left(\bar{x}_i + 1, x_i + \frac{1}{2}, \bar{x}_i + \frac{1}{2}\right)$, $\vec{f}_{i,4} = \left(x_i + \frac{1}{2}, \bar{x}_i + \frac{1}{2}, \bar{x}_i + 1\right)$, with specific coordinates for Mn ($x_\mathrm{Mn} = 0.138$) and muon ($x_\mu = 0.532$) sites [85].

- The magnetic structure was adapted from Eq.(C.5):

$$\vec{M}_{ld_\mathrm{m}} = m_\mathrm{h}\left[\vec{R}_{d_\mathrm{m}}\cos\left(\vec{K}_\mathrm{h}\cdot\vec{R}_l + \phi_{d_\mathrm{m}}\right) - \vec{I}_{d_\mathrm{m}}\sin\left(\vec{K}_\mathrm{h}\cdot\vec{R}_l + \phi_{d_\mathrm{m}}\right)\right] + m_\mathrm{u}\hat{n} \quad (3.8)$$

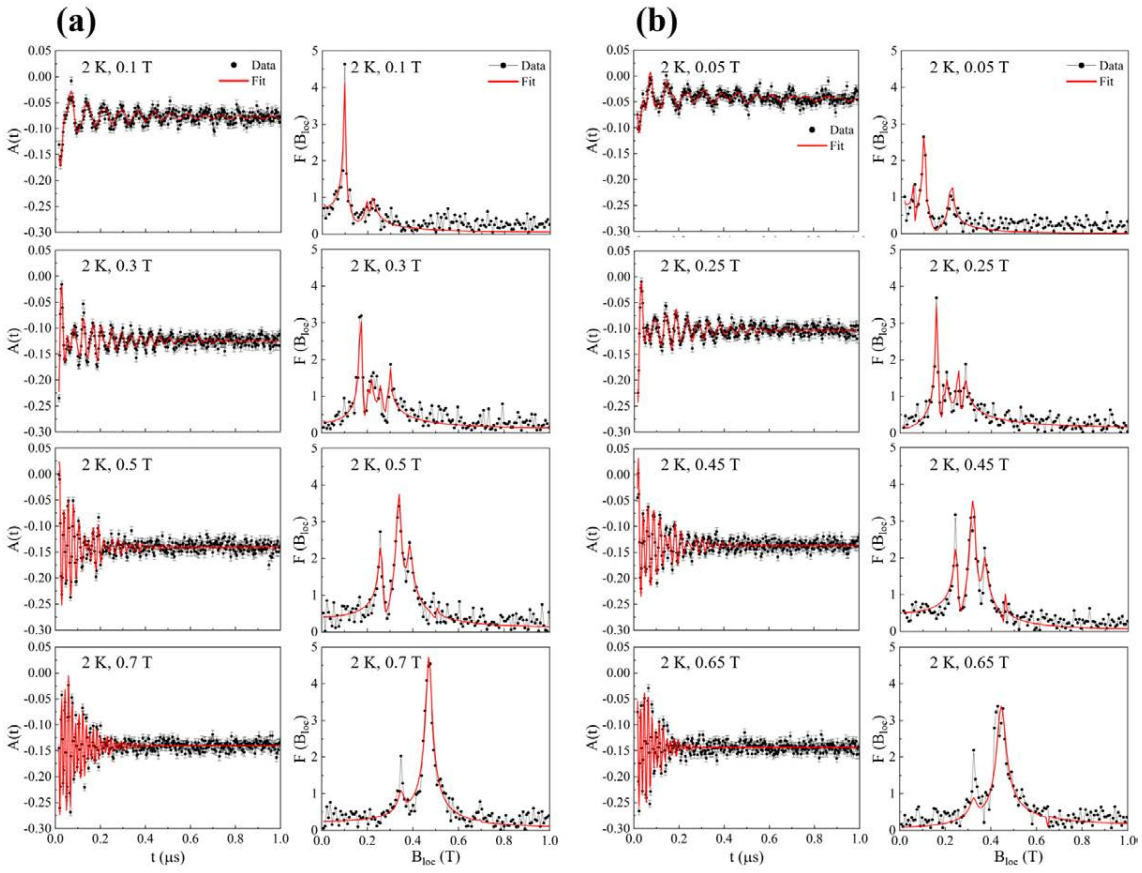

Figure 3.25: TF μSR spectra (left) and Fourier transformed signal (right) of MnSi for some selected applied fields at 2 K with increasing (a) and decreasing (b) field. The data are plotted as black circles, while the fitted curves are shown as red lines.

where m_{h} and m_{u} are the components of the Mn net magnetic moment m in the plane perpendicular and along the applied field, respectively. The values of m_{u} were taken directly from the experimental magnetization curves, then m_{h} was determined from $m^2 = m_{\mathrm{u}}^2 + m_{\mathrm{h}}^2$. The triad of vectors: $\vec{R}_{d_{\mathrm{m}}} = \frac{1}{\sqrt{2}}(\bar{1},\, 1,\, 0)$, $\vec{I}_{d_{\mathrm{m}}} = \frac{1}{\sqrt{6}}(\bar{1},\, \bar{1},\, 2)$, $\hat{n} = \vec{K}_{\mathrm{h}}/K_{\mathrm{h}} = \frac{1}{\sqrt{3}}(1,\, 1,\, 1)$ form an orthonormal basis. The value of K_{h} was determined from the SANS experiments. The phase-shift $\phi_{d_{\mathrm{m}}}$ is constrained to be ϕ for Mn1 and 0 for the other sites as per the mΛ_3 representation.

- The Lorentz radius was set to a value big enough to ensure the convergence of the dipolar and Lorentz fields, $R_{\mathrm{Lor}} = 90$ Å, covering approximately 120,000 magnetic moments inside the Lorentz sphere.

- The two MnSi crystals were modeled as cuboids (dimensions: $4.86 \times 3.65 \times 1.65$ mm^3). The field was applied along the shortest dimension, yielding a demagnetization factor of $N = 0.63$ [103].

- The local field variation across different unit cells was calculated using

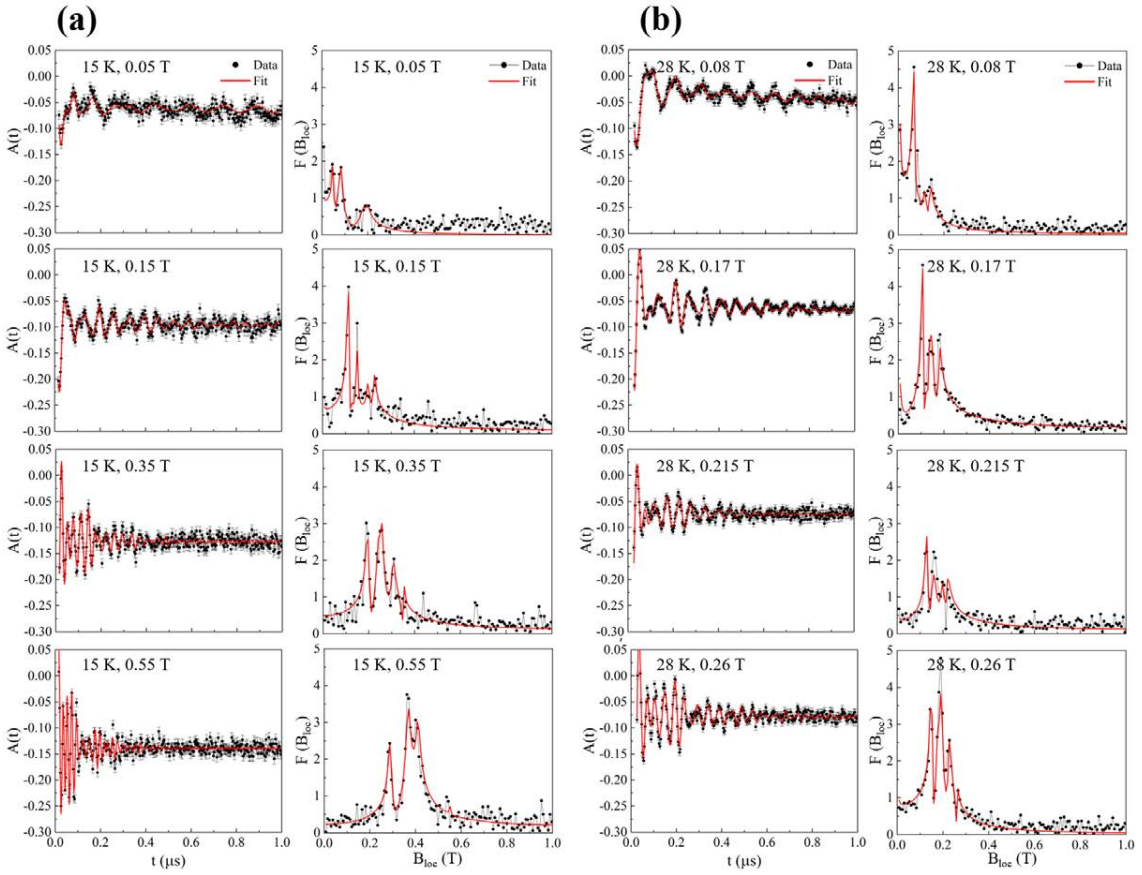

Figure 3.26: TF μSR spectra (left) and Fourier transformed signal (right) of MnSi for some selected applied fields at 28 K. The data are plotted as black circles, while the fitted curves are shown as red lines.

Eq.(C.22), with the argument of cosine and sine functions ranging from 0° to 360°.

- Both the distribution of nuclear moments and the initial asymmetry were fixed to the values determined from the ZF μSR spectra: $\Delta/\gamma_\mu = 3{\cdot}10^{-4}$ T, $a_0 = 0.26$, as they should not depend on the temperature or magnetic field.

For each temperature, the fitting of the μSR spectra measured at the lowest magnetic field applied yielded the value of the isotropic contact coupling and the spin-lattice relaxation rate, which were fixed as the magnetic field changed. The contact coupling A_{cont} showed a temperature-dependent decrease from -0.91(1) mol/emu at 2 K, to -0.88(2) mol/emu at 15 K, and -0.81(1) mol/emu at 28 K, which can be due to thermal fluctuations weakening the hyperfine interaction. The value at 2 K aligns with previous studies [85, 87, 88]. The relaxation rate was found to be almost negligible at 2 K and 15 K, $\lambda_Z < 0.03$, while at 28 K its value increased to 0.36(2).

A consistent time-independent background was maintained across the data set, while the fraction of muons stopping outside the sample s accounted for less than 1%. Therefore, only three parameters related to the magnetic model were fitted in

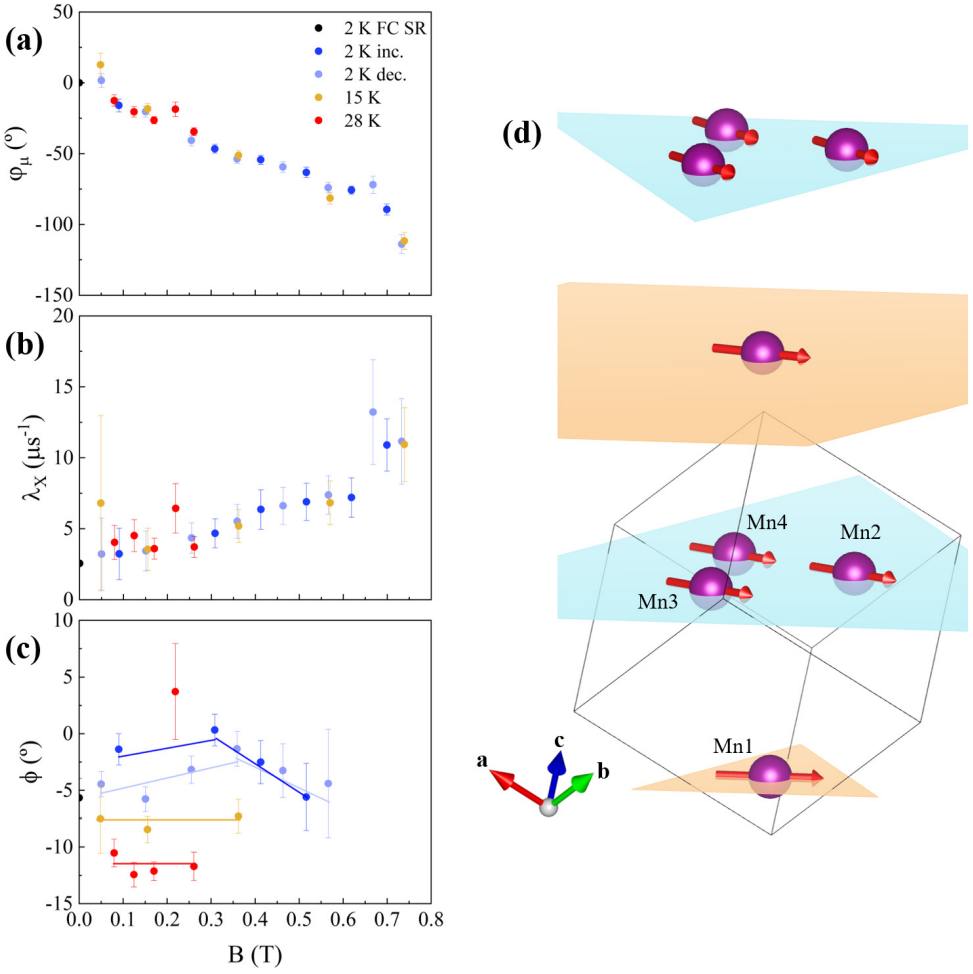

Figure 3.27: Temperature and field dependence of the three fitted parameters: the azimuthal angle φ_μ (a), the relaxation rate λ_X (b) and the angle between orbits ϕ_{d_m} (c). The solid lines in panel (c) serve as a guide to the eye. (d) Magnetic structure of MnSi as described by the mΛ_3 *irrep*. For simplicity only the magnetic atoms inside unit cells in the $\langle 111 \rangle$ direction are shown.

our model: the azimuthal angle φ_μ, the relaxation rate λ_X and the angle between orbits ϕ. Figure 3.27 depicts the fitted values for all data sets evaluated. The modulus of the azimuthal angle φ_μ increases linearly with the increasing external field, as expected from the instrument characteristics (see Appendix C.5.1). The relaxation rate λ_X also increases slowly at low fields, while it shows a marked rise at high fields, indicating a significant enhancement of the magnetic fluctuations at the FFM transition, as it has been observed in $GaV_4S_{8-y}Se_y$ [104]. Meanwhile, the phase-shift ϕ fluctuates around -5° at low fields for 2 K, and it increases linearly for $B > 0.3$ T. For higher temperatures, the value of ϕ becomes more negative with a linear dependence on the magnetic field, except for one value at 28 K, which clearly departs from the tendency. These values of ϕ are slightly larger than the ones reported in Ref. [88]. Such discrepancy could be originated on the small differences in the determination of A_{cont}, as it was shown that the effect of both parameters on

the local field distribution is similar [86].

Our results indicate two primary findings from the MnSi μSR spectra fits, which are discussed in the next subsections.

3.6.1 Origin of *B-phase*

The increase in ϕ is observed only in the phase diagram region where the *B-phase* was detected by a.c susceptibility. Thus, one qualitative picture about the nature of the *B-phase* could be that the temperature and/or the magnetic field produce a slight relative reorientation of these four conical helices, without any change in the wave-vector of the magnetic structure, but leading to a change in the modulus of the averaged magnetic moment. This slight reorientation should not affect the entropy or the wave-vector of the magnetic structure, and therefore, the effect in the heat capacity curves should be null. A possible new stationary point in which the averaged magnetic moment modulus should change due to a relative reorientation of the two orbits has not been considered in Ref. [36] and might correspond to the predicted *unknown state*, which should be consistent with the *B-phase* reported here.

Finally, we discuss the effect of this reorientation in the scattered intensity observed in SANS experiments. Such relationship is evaluated in Appendix D, which leads to the derivation of Eq.(D.20):

$$I_{\vec{K},-\vec{K}} \propto \left(m^2 - m_{\mathrm{u}}^2\right) \left[10 + 6\cos\left(\phi - 0.1334\right)\right] \tag{3.9}$$

Since Eq.(3.9) was obtained assuming a single-domain phase, it was compared with the SANS curves measured for decreasing fields in order to check its validity. The values of m_{u} were taken from the experimental magnetization curves, while the

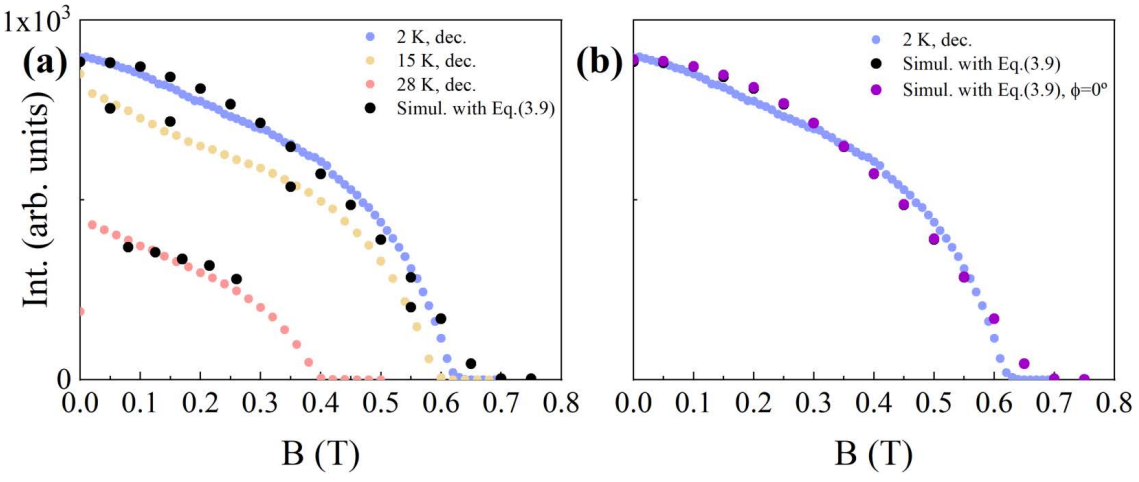

Figure 3.28: (a) Comparison between the experimental integrated intensity for $\vec{B} \parallel \langle 111 \rangle \perp \vec{k}_i$ and the simulated curves using Eq.(3.9) (black circles). (b) Comparison between experimental curve at 2 K and the simulated curves using Eq.(3.9) with ϕ determined from the μSR fits (black circles) and $\phi = 0°$ (purple circles).

fits to μSR data provided the angle ϕ. Consequently, the only free parameter was a scale, which included the Debye-Waller factor, so it was allowed to slightly decrease for higher temperatures.

Figure 3.28(a) shows the comparison between the experimental data and the calculated curve using Eq.(3.9). A good agreement is observed for all temperatures, validating the model.

However, it should be noted that the SANS intensity has a negligible dependence with ϕ, as mentioned in Ref. [87]. This effect is explicitly shown in Fig. 3.28(b), which depicts the comparison between the calculated curve with ϕ determined from the μSR fits and the calculated curve assuming $\phi = 0°$. Almost no difference is observed, demonstrating that the SANS technique exhibits limited sensitivity in resolving variations in the internal magnetic structure at the atomic scale. This limitation highlights the necessity for integrating SANS with complementary techniques, such as μSR, capable of capturing the fine details of magnetic ordering.

3.6.2 *A-phase* local field distribution

As can be observed in Fig. 3.26(b), the μSR spectra in the *A-phase* (28 K, 0.17 T and 0.215 T) were also well fitted with the same model used at 2 K and 15 K. However, the anomalous behavior of ϕ at 0.215 T (see Fig. 3.27(c)) indicates a discrepancy between the experimental *A-phase* and calculated CH field distributions, which could be a hint on the presence of the SkL. The increase in λ_X further supports this hypothesis, as it has been shown to provide a signature of the SkL phase in μSR measurements on other systems [104–106], where the magnetic fluctuations has been argued to reflect diffusive skyrmion state excitations [107].

We have carried out simulations of the CH and SkL magnetic structures in order to compare the expected signal for each phase. Two different models have been considered for the SkL. First, a simulation was performed assuming the SkL to be a hybridized triple-$\vec{Q}$ state with magnetization given by Eq.(I.5). The propagation and unit vectors were chosen such that they generate a SkL magnetization texture in the XY plane of the experimental frame: $\hat{e}_1 = (0, -1, 0)$, $\hat{e}_2 = (-\frac{\sqrt{3}}{2}, \frac{1}{2}, 0)$, $\hat{e}_3 = (\frac{\sqrt{3}}{2}, \frac{1}{2}, 0)$, $\vec{Q}_1 = K_{\mathrm{A}}(1, 0, 0)$, $\vec{Q}_2 = K_{\mathrm{A}}(-\frac{1}{2}, -\frac{\sqrt{3}}{2}, 0)$, $\vec{Q}_3 = K_{\mathrm{A}}(-\frac{1}{2}, \frac{\sqrt{3}}{2}, 0)$. The phase was set to: $\Delta_1 = \Delta_2 = \Delta_3 = \pi$, such that the magnetic moments point in the opposite direction of the applied magnetic field at the center of each skyrmion.

Next, a more sophisticated treatment was considered assuming a SkL with magnetization given by Eq.(I.2). The lattice of skyrmions was created in the XY plane of the experimental frame by adding to the center of the skyrmion ($\vec{r} = \vec{0}$) the hexagonal lattice vectors: $\vec{a}_1 = \frac{2\pi}{K_{\mathrm{A}}}\left(\frac{1}{2}\hat{y} + \frac{\sqrt{3}}{2}\hat{x}\right)$, $\vec{a}_2 = \frac{2\pi}{K_{\mathrm{A}}}\left(-\frac{1}{2}\hat{y} + \frac{\sqrt{3}}{2}\hat{x}\right)$. The helicity was set to define a Bloch skyrmion: $\Phi(\varphi) = \varphi + \pi/2$. Several trial functions for $\Theta(r)$ were tested. The one which yielded better results obeys:

$$\Theta(r) = \begin{cases} \pi\left(1 - \frac{r}{R}\right) & \text{if } r < R \\ 0 & \text{if } r > R \end{cases} \tag{3.10}$$

where $R = \pi/K_{\mathrm{A}}$ is the radius of each skyrmion.

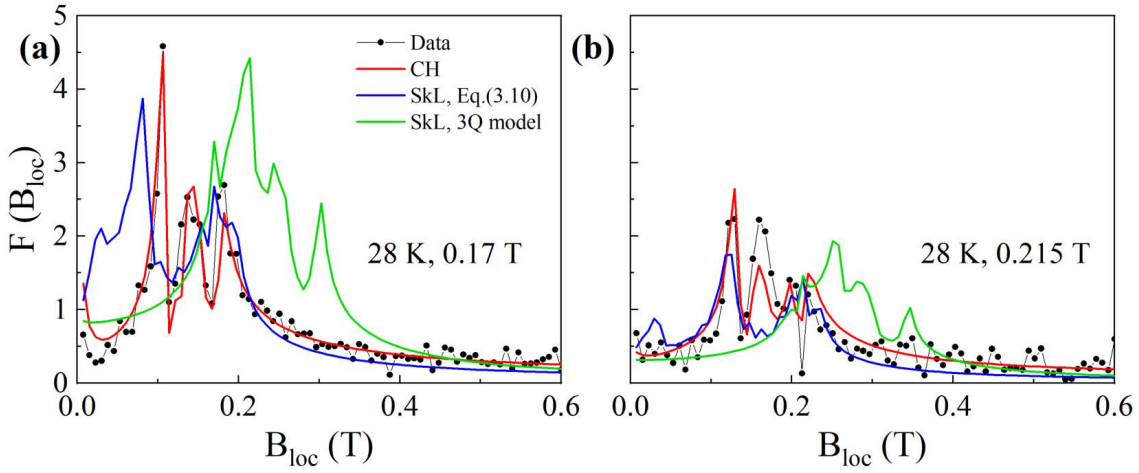

Figure 3.29: Internal field distributions at 28 K, 0.17 T (a) and 0.215 T (b) for the different magnetic structures: conical helix (red lines), SkL with magnetization field given by Eq.(I.2) and Eq.(3.10) (blue lines), and SkL assuming a triple-$\vec{Q}$ state (green lines). The Fourier transformed data are plotted as black circles.

For both models, the normalized spin texture was multiplied by the Mn net magnetic moment $m = 0.4\ \mu_B$. Next, the corresponding orientation matrix was applied such that $\vec{i}_\mu \parallel \langle 1\bar{1}0\rangle$ and $\vec{B}_{ext} \parallel \langle 111\rangle$. Finally, the rest of the parameters needed to generate the μSR spectra were set to be the same as the ones used in the CH model.

Figure 3.29 shows the comparison between the data and the simulated field distributions in the *A-phase* region (28 K, 0.17 T and 0.215 T).

As mentioned before, the h_1 and h_2 sites give rise to a sharp peak and a distribution of fields in the CH phase, respectively. Meanwhile, the signal derived from the SkL magnetic structure widens but retains an asymmetrical profile, with a higher weight at low fields in both SkL models. Nevertheless, the SkL characterized by the magnetization field as defined in Eq.(I.2) and Eq.(3.10) shows a higher similarity to the CH phase distribution compared to the SkL modeled on a triple-$\vec{Q}$ state. This observation underscores the critical need for meticulous modeling of the SkL state, as both models are not equivalent. Furthermore, this analysis suggests a plausible explanation for the good fit of the CH model to the field distribution of the *A-phase*: the local field encountered by muons is quite similar in the CH and SkL scenarios. It is also crucial to acknowledge the flexibility in determining $\Theta(r)$, which allows for an infinite number of solutions, leaving open the possibility of finding a function that yields an even more congruent distribution. Consequently, conducting a theoretical study to determine the specific shape of $\Theta(r)$ for the SkL in MnSi would be desirable.

An additional factor which should be considered arises from the SANS results. Specifically, the relatively weak signal of the SkL in comparison to the CH phase when $\vec{B} \parallel \langle 111\rangle \perp \vec{k}_i$, as illustrated in Fig. 3.17(b), may suggest a low skyrmion density within the crystal. Therefore, the proportion of muons sensitive to SkL may be too small, leading to a predominance of the CH phase signal. This hypothesis has

already been proposed in previous μSR studies conducted on Cu_2OSeO_3 [107, 108]. Furthermore, Lancaster *et al.* also performed TF μSR experiments on a thin film of MnSi [109]. Despite their experiments not conclusively detecting the SkL phase, they proposed that the observed phenomena could not be solely attributed to a single cone phase.

3.7 Conclusions

We have carried out specific heat, d.c and a.c. magnetization experiments in three oriented MnSi enantiopure crystals as a function of field and temperature to carefully explore the low T region of the phase diagram and detect the *unknown state*. For $\vec{B} \parallel \langle 111 \rangle$, we clearly see that a.c. magnetization presents a small flat-valley close to the FFM boundary at low T, well below T_C, suggesting the existence of a new *B-phase* that might correspond to the predicted *unknown state*.

In order to clarify the nature of this *B-phase* at low temperature near B_{c2}, SANS and μSR experiments were also performed. The SkL phase and the phenomena near T_c in MnSi have also been investigated in detail in order to understand the possible differences between this new phase (*B-phase*) and the SkL phase (*A-phase*). The results show that the *B-phase* could be compatible with the theoretical predictions if the new magnetic state is related with a relative reorientation of the four helices in the unit cell of MnSi. Additionally, the μSR experiments in the *A-phase* show a SkL field distribution quite similar to the CH one. The simulations performed allow to discard the triple-$\vec{Q}$ state as the responsible for the observed field distribution, although the determination of the exact profile of the SkL requires further theoretical study.

Part of the results presented in this chapter have been published in Ref. [110, 111].

Chapter 4

Presence of the *B-phase* in the disordered cubic chiral magnet $Fe_{0.75}Co_{0.25}Si$

The goal of this chapter is to study the presence and stability of both the new *B-phase* and the *A-phase* in the cubic magnet $Fe_{0.75}Co_{0.25}Si$. This system, with a different magnetic anisotropy than MnSi and where the disorder plays a pivotal role, serves as an ideal candidate to further explore the mechanisms that drive the emergence of new non-collinear magnetic states in chiral magnets.

The chapter starts with an examination of the magnetic properties of the $Fe_{1-x}Co_xSi$ family. Following this, we outline the d.c and a.c. magnetization, Small Angle Neutron Scattering (SANS) and muon spin rotation experiments we have performed. The magnetic phase diagrams are built from the macroscopic characterization measurements, and the a.c. magnetization results reveal the presence of an anomaly similar to that observed in MnSi. Next, we investigate the magnetic structure of both the *B-phase* and *A-phase* via SANS and muon spin rotation techniques, where the disorder clearly plays a role in the stability of both phases. The discussion extends to the influence of disorder on the local magnetic fields within the *A-phase* and *B-phase*. The chapter finishes by summarizing the principal findings from our study.

4.1 Magnetic properties of the $Fe_{1-x}Co_xSi$ family

The family of compounds $Fe_{1-x}Co_xSi$ have also the $B20$ structure with space group $P2_13$, where all transition-metal sites are crystallographically equivalent. The cell parameter decreases linearly with the increase in content of Co x, from $a \approx 4.485$ Å for FeSi to $a \approx 4.445$ Å for CoSi. [112, 113]. In contrast to MnSi, the system FeSi is a nonmagnetic insulator with strong electronic correlations [114] while its sibling CoSi is a diamagnetic semimetal [115]. Figure 4.1(a) shows the compositional phase diagram of $Fe_{1-x}Co_xSi$. For increasing Co content the series $Fe_{1-x}Co_xSi$ displays helimagnetic order in the range $0.05 \leq x \leq 0.8$, where the critical temperature T_c is maximum at $x = 0.35$ [51, 116–123].

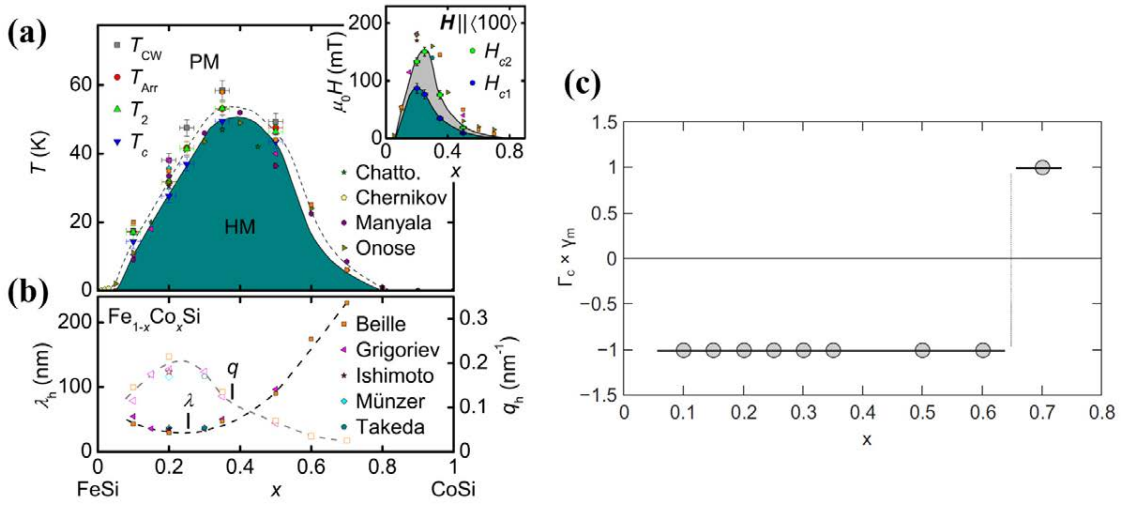

Figure 4.1: (a) Compositional phase diagram, where a helimagnetic (HM) and a paramagnetic (PM) regime are distinguished. Inset: Low-temperature critical fields as a function of the Co content x. (b) Helix wavelength λ_h, and its corresponding propagation vector, q_h, as a function of x. Values in (a) and (b) are summarized from [51, 54, 116–121, 124, 126, 129, 130]. Figure taken from [123]. (c) Dependence of the product of structural and magnetic chiralities $\Gamma_c \times \gamma_m$ on x. Figure taken from [122].

With increasing x the period of the helical modulation varies from about 200 to 2000 Å(see Fig. 4.1(b)), while the anisotropy of the system decreases [51, 116, 122, 124, 125]. Based on SANS experiments [51, 121, 126, 127] and Lorentz force microscopy [128] it was concluded that the propagation axis of the helix in $Fe_{1-x}Co_xSi$ is $\langle 100 \rangle$ for all x values, although the local disorder induced by the substitution of the Fe by Co results in an increasing random distribution of the helix propagation vectors K_h at large x [51, 125].

Furthermore, in the mixed $Fe_{1-x}Co_xSi$ compounds the sign of structural chirality Γ_c changes from right-handed to left-handed at $x = 0.2$. At the same time, the magnetic chirality γ_m depends on the concentration x as depicted in Fig. 4.1(c): for FeSi-based compounds ($x < x_C = 0.65$) the right-/left-handed structural chirality is accompanied by left-/right-handedness of the magnetic helix ($\Gamma_c \times \gamma_m = -1$), while the CoSi-based ($x > x_C$) compounds show left handed structural chirality along with left handedness of the magnetic spiral ($\Gamma_c \times \gamma_m = 1$) [122, 125, 126, 130]. Thus, the sign of magnetic chirality is dictated by the structural chirality and chemical elements (Fe, Co) as well.

The magnetic phase diagram of $Fe_{1-x}Co_xSi$ is very similar to the MnSi one, and, depending on the cobalt content, shows helimagnetic transition temperatures between a few kelvins and 50 K, while the critical fields vary between a few milliteslas and roughly 0.15 T [51, 54, 116, 121–125, 127, 129, 131].

The metastable skyrmion lattice (SkL) phase has also been observed in $Fe_{1-x}Co_xSi$ when performing a fast cooling through the *A-phase* [54, 123]. This feature is more prominent for $\vec{B} \parallel \langle 001 \rangle$ than $\vec{B} \parallel \langle 111 \rangle$. This thermodynamic

metastable SkL coexists with the conical phase and do not only appear at temperatures below the *A-phase* but also at fields smaller or higher than the fields required to stabilize the *A-phase*. Both the metastable SkL and the coexistence phase have been attributed to structural disorder due to the chemical substitution of Fe and Co [127]. The intensity of these skyrmion lattice correlations can be enhanced by increasing the cooling rate, which is much slower than that at which the low T metastable SkL appears in MnSi ($\sim$100 K/s) [64].

Thus, although $Fe_{1-x}Co_xSi$ and MnSi exhibit rather similar magnetic properties, there are strong differences of the underlying electronic structure, making $Fe_{1-x}Co_xSi$ an ideal system to test the general nature of skyrmion lattices. In particular, we focus on the compound $Fe_{0.75}Co_{0.25}Si$ ($x = 0.25$), which has the highest propagation vector of the $Fe_{1-x}Co_xSi$ family, making it suitable to study with the techniques employed throughout this thesis. Since we were also interested in the detection of the *B-phase*, d.c, a.c. magnetization, SANS and μSR experiments were performed on two oriented $Fe_{0.75}Co_{0.25}Si$ crystals as a function of field and temperature.

4.2 Experimental details

In the same way as for MnSi, several single crystals of $Fe_{0.75}Co_{0.25}Si$ were provided by Prof. Yusuke Kousaka. The synthesis was carried out by the floating zone method [72]. The structural chirality of all crystals was found to be left-handed, as expected for concentrations of x greater than 0.2 [130].

Magnetization measurements were carried out using the VSM option of a PPMS-14T manufactured by Quantum Design. Continuous $M(T)$ measurements were obtained under the ZFC procedure for applied magnetic fields in the range $0 < B < 0.2$ T. Isothermal magnetization $M(B)$ data were collected in a field range from 0 to 0.25 T. All data were taken in a temperature range from 2 to 45 K. In-phase (m') and out-of-phase (m'') components of the a.c. magnetization were measured using a SQUID magnetometer, manufactured by Quantum Design. The main frequency, a.c. amplitude and cooling rate values were the same as for MnSi samples. Same procedures as in MnSi were used to measure both a.c. magnetization and VSM isothermal magnetization experiments. For these measurements a single crystal with size $5 \times 2 \times 1.4$ mm^3 was oriented with the magnetic field along the $\langle 001 \rangle$ and $\langle 110 \rangle$ directions,

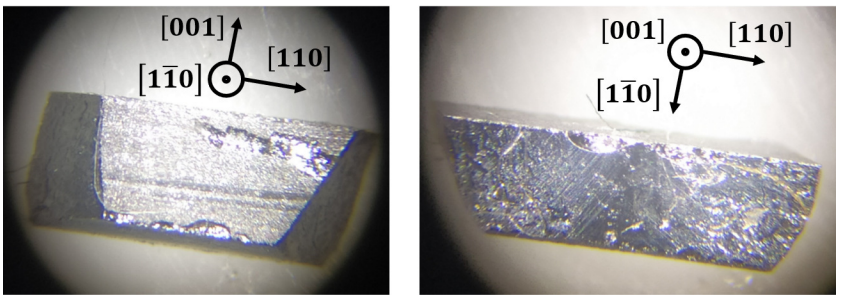

Figure 4.2: $Fe_{0.75}Co_{0.25}Si$ single crystal used for the d.c magnetization experiments. The main directions are signaled by black arrows.

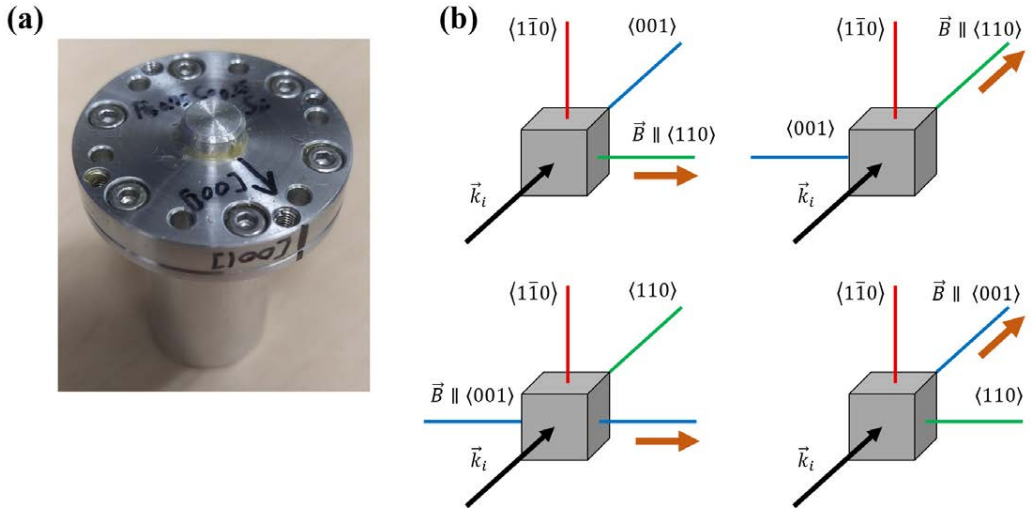

Figure 4.3: Left: sample holder of $Fe_{0.75}Co_{0.25}Si$. Right: the four configurations used in SANS experiments: $\vec{B} \parallel \langle 110 \rangle \parallel \vec{k}_i$ (a), $\vec{B} \parallel \langle 110 \rangle \perp \vec{k}_i$ (b), $\vec{B} \parallel \langle 001 \rangle \parallel \vec{k}_i$ (c) and $\vec{B} \parallel \langle 001 \rangle \perp \vec{k}_i$ (d).

as shown in Fig. 4.2.

The unpolarized SANS measurements were also performed at TAIKAN for a crystal of 7 mm diameter and 9 mm height. Same procedures as in MnSi were followed. Nevertheless, for this sample a 4-T horizontal field superconducting magnet (Cryogenic Limited) was used, which allowed to collect SANS patterns in four different configurations, shown in Fig. 4.3. The measurements were performed at temperatures between 2 K and 40 K, and with applied magnetic fields below 0.25 T, following a ZFC procedure from the paramagnetic phase. For all data, a reference measurement in the paramagnetic region at 50 K was subtracted as a background contribution.

ZF and TF μSR experiments were carried out on the M20 LAMPF and M15 NuTime spectrometers, respectively. Two pairs of crystals were used, each pair oriented

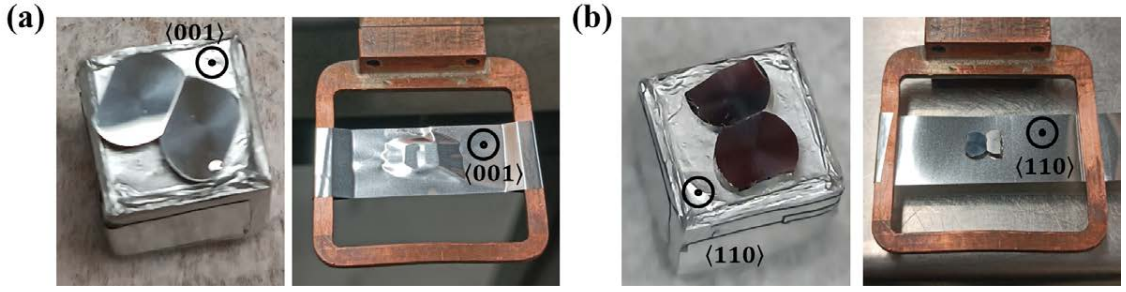

Figure 4.4: $Fe_{0.75}Co_{0.25}Si$ crystals oriented along the ⟨001⟩ (a) and ⟨110⟩ (b) directions. The sample setup for the M15 NuTime and M20 LAMPF spectrometers is shown on the left and right part, respectively.

along the $\langle 001 \rangle$ and $\langle 110 \rangle$ directions (see Fig. 4.4). ZF μSR data were collected at 2 K using ZFC and FC protocols for both NSR and SR configurations, with previous calibration in the paramagnetic region ($T = 50K$). TF μSR measurements were performed in the temperature range 2 K to 40 K and field range 0 T to 0.24 T for the configurations $\vec{B} \parallel \langle 110 \rangle \perp \vec{i}_\mu$ and $\vec{B} \parallel \langle 001 \rangle \perp \vec{i}_\mu$.

4.3 Magnetic phase diagram of $Fe_{0.75}Co_{0.25}Si$

Figure 4.5(a) shows the isothermal magnetization $M(B)$ curves for magnetic fields applied along the $\langle 001 \rangle$ direction at temperatures from 2 to 40 K. The magnetic field dependence resembles that of MnSi, with a initial quasilinear increase of the magnetization in the multidomain helimagnetic (HM) phase, a linear increase characteristic of the conical helix (CH) phase, and the saturation of the magnetization in the forced ferromagnetic (FFM) state. Similarly, a small hysteresis is observed at low fields (see inset of Fig. 4.5(a)) due to the formation of only one conical domain when the magnetic field is decreased from saturation. Such hysteresis decreases for higher temperatures but is not completely suppressed as opposed to MnSi, probably due to the higher anisotropy of Co atoms. The critical fields B_{c1} and B_{c2}, shown in Fig. 4.5(b), have been determined by applying the same criteria as in MnSi. The magnetization almost saturates above $B_{c2} = 0.218(5)$ T, with a value of 0.169 μ_B per formula unit for the highest field measured at 2 K. The lack of saturation of the FFM state is consistent with previous studies [51, 123, 132] and evidence the nature of $Fe_{0.75}Co_{0.25}Si$ as a itinerant magnet.

Continuous ZFC $M(T)$ data are shown in Fig. 4.5(c) for fields in the range 0.025 to 0.2 T applied along the $\langle 001 \rangle$ direction. Fig. 4.5(d) shows the ZFC curve measured at 0.06 T together with the temperature derivative dM/dT and the critical temperatures. At low fields, a sudden increase in the magnetization becomes evident with the rise in temperature, due to the development of the CH phase. This critical temperature is determined as a maximum in the derivative dM/dT, as it is shown in Fig. 4.5(d). Unlike MnSi, the emergence of this increase in $Fe_{0.75}Co_{0.25}Si$ is attributed to the significant temperature-dependent nature of the critical field for the helical-to-conical crossover [123]. As the temperature is increased, the magnetization reaches a plateau in the conical phase, followed by a small maximum labeled as T_{c2}. For higher temperatures, the magnetization drops as a result of the transition to the PM state. A point of inflection in the magnetization T_{c3} can be identified, which defines the IM region between T_{c2} and T_{c3}. In the range $0.04 \leq B \leq 0.075$ T, the SkL in the *A-phase* is identified by sudden decrease of the magnetization at T_{a1}, which reaches a minimum at T_{a2} followed by the maximum at T_{c2} (see Fig. 4.5(d)). For higher fields the maximum at T_{c2} slowly decreases until it disappears above 0.18 T.

A similar analysis was performed for the magnetization measurements with the magnetic field applied along the $\langle 1\bar{1}0 \rangle$ direction. By combining all the critical fields and temperatures, the magnetic phase diagrams for the different crystallographic orientations measured are presented in Fig. 4.6.

Both phase diagrams are in agreement with previous studies [54, 123]. The fourth-

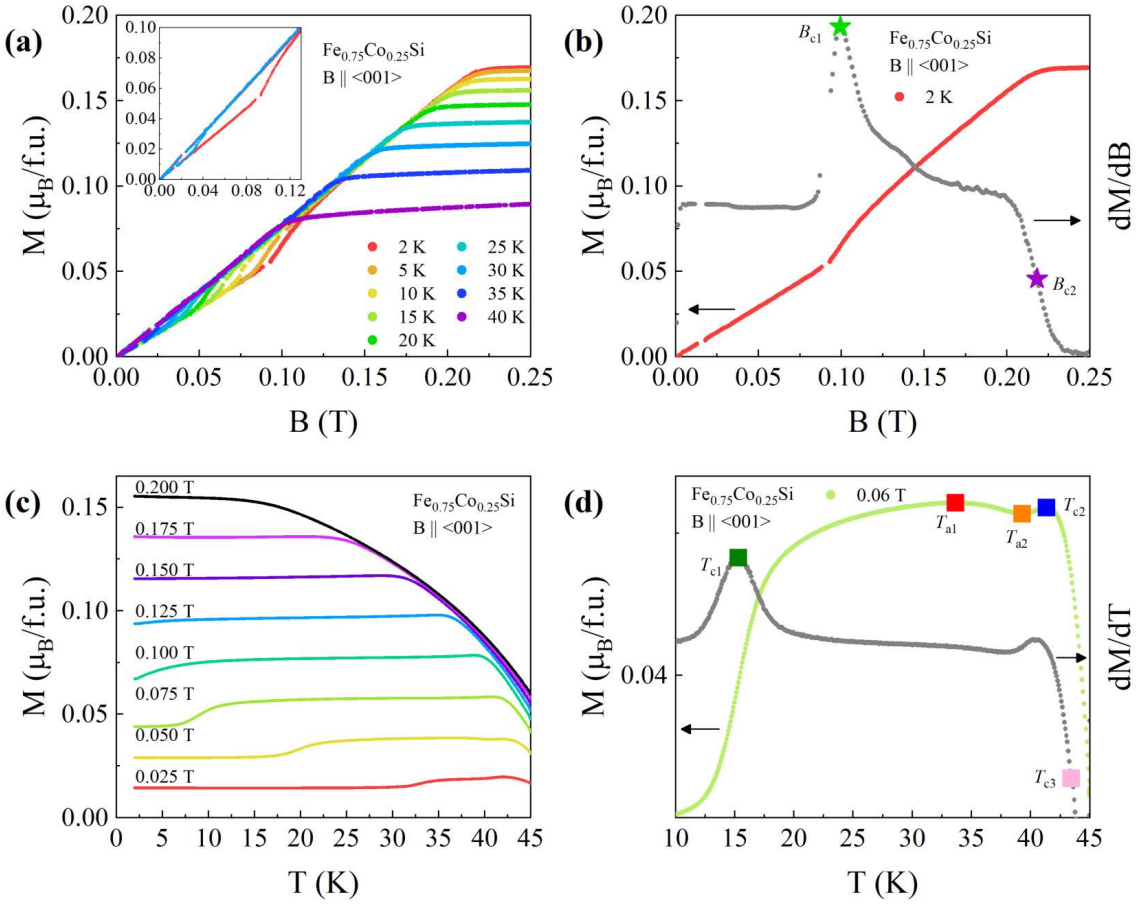

Figure 4.5: (a) Isothermal magnetization $M(B)$ curves of $Fe_{0.75}Co_{0.25}Si$ for magnetic fields applied along the $\langle 001 \rangle$ direction. The inset shows the low field data for increasing and decreasing field at 2 and 30 K. (b) Isothermal magnetization $M(B)$ at 2 K together with its field derivative dM/dB. The critical fields B_{c1} and B_{c2} are marked with a green and purple star, respectively. (c) Temperature dependence of the magnetization of $Fe_{0.75}Co_{0.25}Si$ for magnetic fields applied along the $\langle 001 \rangle$ direction. (d) ZFC magnetization $M(T)$ at $B = 0.06$ T together with the ZFC temperature derivative dM/dT. The critical temperatures T_{a1}, T_{a2}, T_{c1} and T_{c2} are marked with a red, orange, blue and pink rectangle, respectively.

order anisotropy term causes the zero-field helical order to propagate along $\langle 001 \rangle$ for $Fe_{0.75}Co_{0.25}Si$. Therefore, the value of B_{c1} is slightly lower for the magnetically soft $\langle 001 \rangle$ axis. Contrary to MnSi, the critical field B_{c1} decreases with increasing temperature for both orientations. The *A-phase* is present in a broader region for the $\langle 001 \rangle$ axis, implying this direction to be a hard axis for the helical pitch, as opposed to what is suggested by B_{c1}. Such discrepancy has been attributed to subleading crystalline anisotropies [123]. The temperature dependence of the upper critical field B_{c2} is almost the same for both directions, with small differences due to the demagnetization effects of the sample.

Figure 4.7(a) shows the B dependence of m' below 20 K with $\vec{B}$ along $\langle 001 \rangle$. The values of B_{c1} ~0.1 T and B_{c2} ~0.2 T were determined by the first derivative of m'.

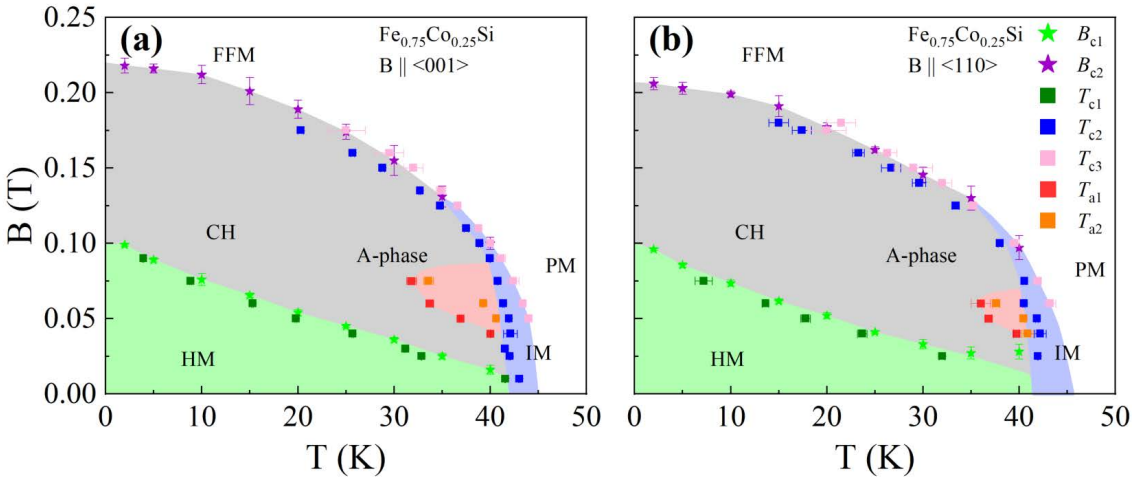

Figure 4.6: Magnetic phase diagrams of $Fe_{0.75}Co_{0.25}Si$ for fields applied along the $\langle 001 \rangle$ (a) and $\langle 1\bar{1}0 \rangle$ directions. The critical fields and temperatures derived from the $M(B)$ and $M(T)$ data are marked with filled stars and squares, respectively. The labels indicate the helimagnetic (HM), conical helix (CH), forced ferromagnetic (FFM), skyrmion lattice (A-phase), intermediate (IM) and paramagnetic (PM) phases.

A magnified view near B_{c2} is presented in the inset of Fig. 4.7(a), showcasing a slight decrease in m' initiated at the field denoted as B_d. The anomaly, located between $\sim$0.15 and $\sim$0.2 T for temperatures lower than 10 K, suggests the emergence of a new magnetic phase akin to the *B-phase* in MnSi. Additional measurements of m' were taken at 1.8 K by increasing the field from $-0.4 \rightarrow 0 \rightarrow 0.3$ T, as shown in Fig. 4.7(b). For clarity, the data at negative B are shown as a function of positive B values, with the full magnetic cycle shown in the inset of Fig. 4.7(b). The m' curves exhibit hysteresis at low fields due to single-domain formation, yet no detectable hysteresis is observed in the vicinity of the FFM state.

The panels (c) and (d) of Fig. 4.7 display the B dependence of m' and m'', respectively, between 20 and 44 K with $\vec{B}$ along $\langle 001 \rangle$. At $T = 38$ K, the down pocket on m' and the peak on m'' characteristic of the *A-phase* are evident, as shown in Fig. 4.7(d). Although the anomalies on m' and m'' diminish at $T = 44$ K, they persist even when the temperature is cooled down to 20 K in the increasing field procedure.

Collecting all the interesting points from the a.c. susceptibility curves, the magnetic phase diagrams for $\vec{B} \parallel \langle 001 \rangle$ with field-increasing and field-decreasing procedures are presented in Fig. 4.8(a) and (b), respectively. The *A-phase* is present in a large region of the phase diagram for the B-increasing process, but vanishes below 35 K for the B-decreasing process, suggesting a meta-stable *A-phase* below 35 K. Interestingly, under FC the *A-phase* in $Fe_{1-x}Co_xSi$ has been observed as a metastable state down to 2 K, particularly pronounced when the field aligns with the $\langle 001 \rangle$ direction [54, 123, 127]. Meanwhile, the *B-phase* is observed for both processes, indicating the B history at fixed temperature does not influence it.

By performing similar measurements, the magnetic phase diagram for $\vec{B} \parallel \langle 110 \rangle$

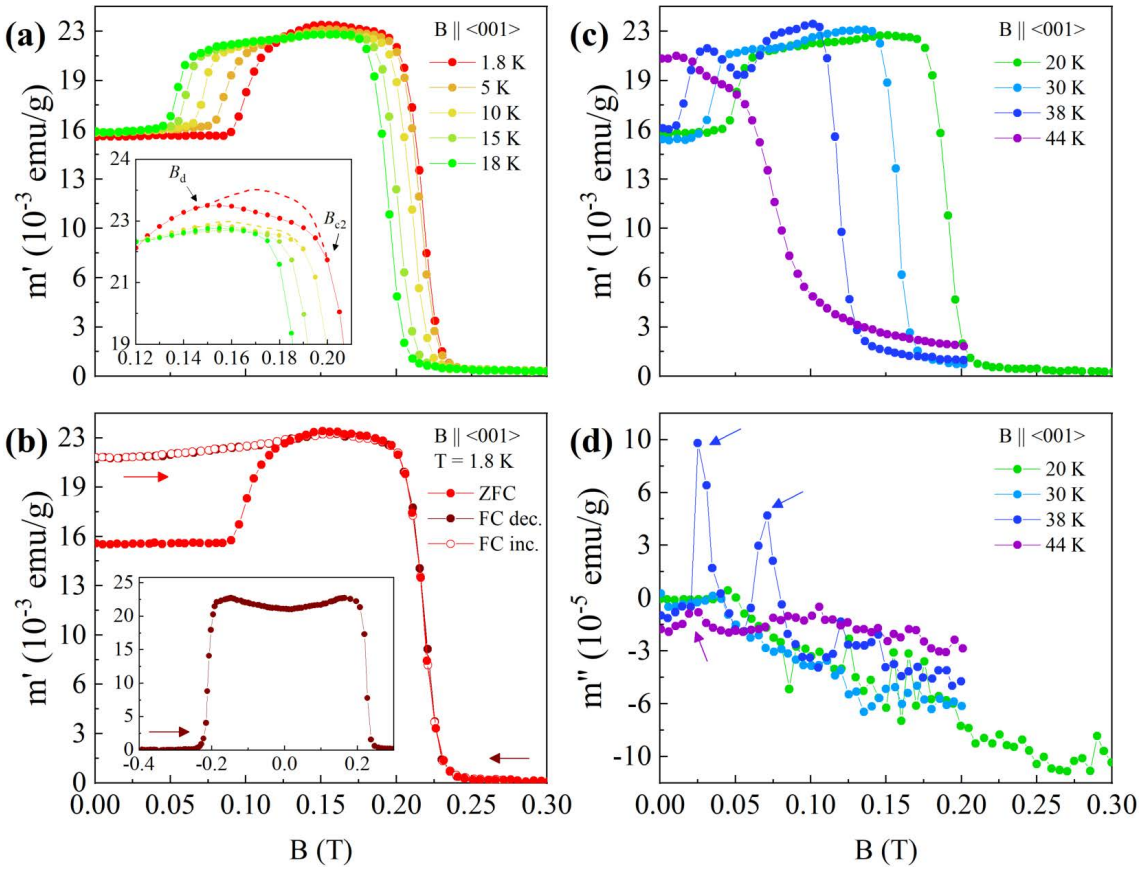

Figure 4.7: (a) B dependence of m' below 20 K for $\vec{B} \parallel \langle 001 \rangle$ on $Fe_{0.75}Co_{0.25}Si$. The inset shows the zoomed region where the anomaly is observed. The fields B_{c2} and B_d are indicated by arrows. (b) Comparison between the m' curve measured by increasing field with a ZFC procedure (filled red circles) and the m' curves recorded with decreasing (filled dark red circles) and increasing (empty red circles) B_{dc} from $-0.4 \rightarrow 0 \rightarrow 0.3$ T. The inset shows the full magnetic field cycle. B dependence of both in-phase, m' (c) and out-of-phase m'' (d) susceptibilities between 20 and 44 K for $\vec{B} \parallel \langle 001 \rangle$. The colored arrows signal the peaks characteristic of the *A-phase*.

with field-increasing and field-decreasing procedures are presented in Fig. 4.8(c) and (d), respectively. Two notable features can be observed: first, the presence of the *B-phase* even when B is not applied along the magnetic easy axis, and second, the considerable expansion of the *B-phase* region for the B-decreasing process. Such behavior was not observed neither in MnSi nor in $Fe_{0.75}Co_{0.25}Si$ with $\vec{B} \parallel \langle 001 \rangle$. Since $Fe_{0.75}Co_{0.25}Si$ has disorder due to the solid solution of Fe and Co, these results suggests that the *B-phase* is formed not only due to cubic magnetic anisotropy terms and thermal fluctuations, but also when disorder plays a role. Regarding the *A-phase* region, the discrepancy between increasing and decreasing processes is less pronounced compared to $\vec{B} \parallel \langle 001 \rangle$.

Given the distinct behavior of the *B-phase* in $Fe_{0.75}Co_{0.25}Si$ compared to MnSi, SANS and μSR experiments were conducted to provide deeper insights into the

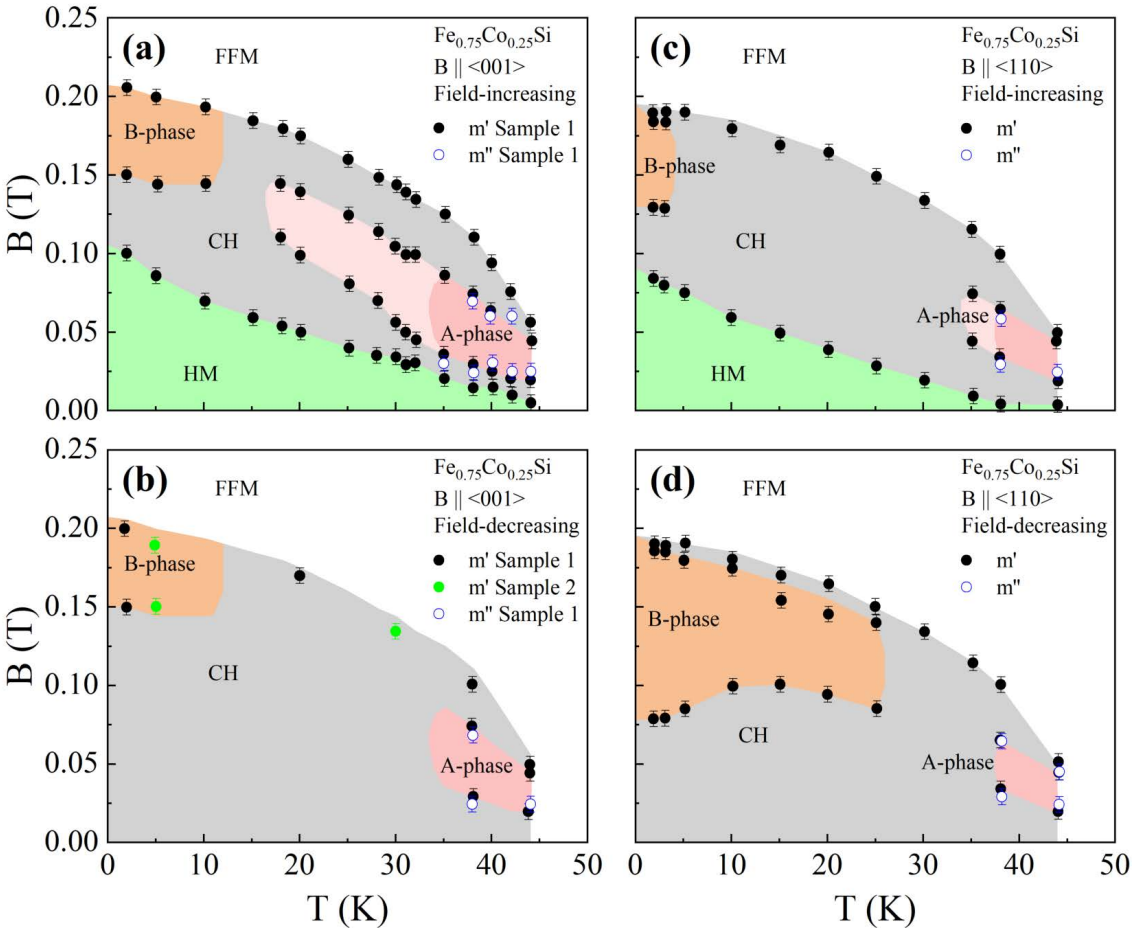

Figure 4.8: Magnetic phase diagram of $Fe_{0.75}Co_{0.25}Si$ for $\vec{B} \parallel \langle 001 \rangle$ deduced from characteristic points of m' and m'' measured versus temperature and magnetic field for field-increasing (a) and field-decreasing (b) procedures. Similar magnetic phase diagrams for $\vec{B} \parallel \langle 110 \rangle$ with field-increasing and field-decreasing procedures are shown in panels (c) and (d), respectively.

nature of this *B-phase*.

4.4 SANS inspection of $Fe_{0.75}Co_{0.25}Si$

Figure 4.9(a), (c), (e) and (f) depict typical SANS patterns at 3 K, 25 K and 40 K, respectively, with $\vec{B} \parallel \langle 001 \rangle \parallel \vec{k}_i$. For temperatures below 25 K, no signal is observed, consistent with a conical order propagating along the applied magnetic field. Nevertheless, at 30 K, weak intensity patterns emerge as the magnetic field is decreased below $B = 0.08$ T (see Fig. 4.9(e)). These patterns become more pronounced at 40 K, as shown in Fig. 4.9(f). At $B = 0.06$ T a six-fold pattern superimposed with an intensity ring is observed, visible in the azimuthal plot in panel (h). Similar results have been observed in $Fe_{0.7}Co_{0.3}Si$ for a slow FC procedure [127]. Therefore, the patterns observed both at 30 K and 40 K correspond to the *A-*

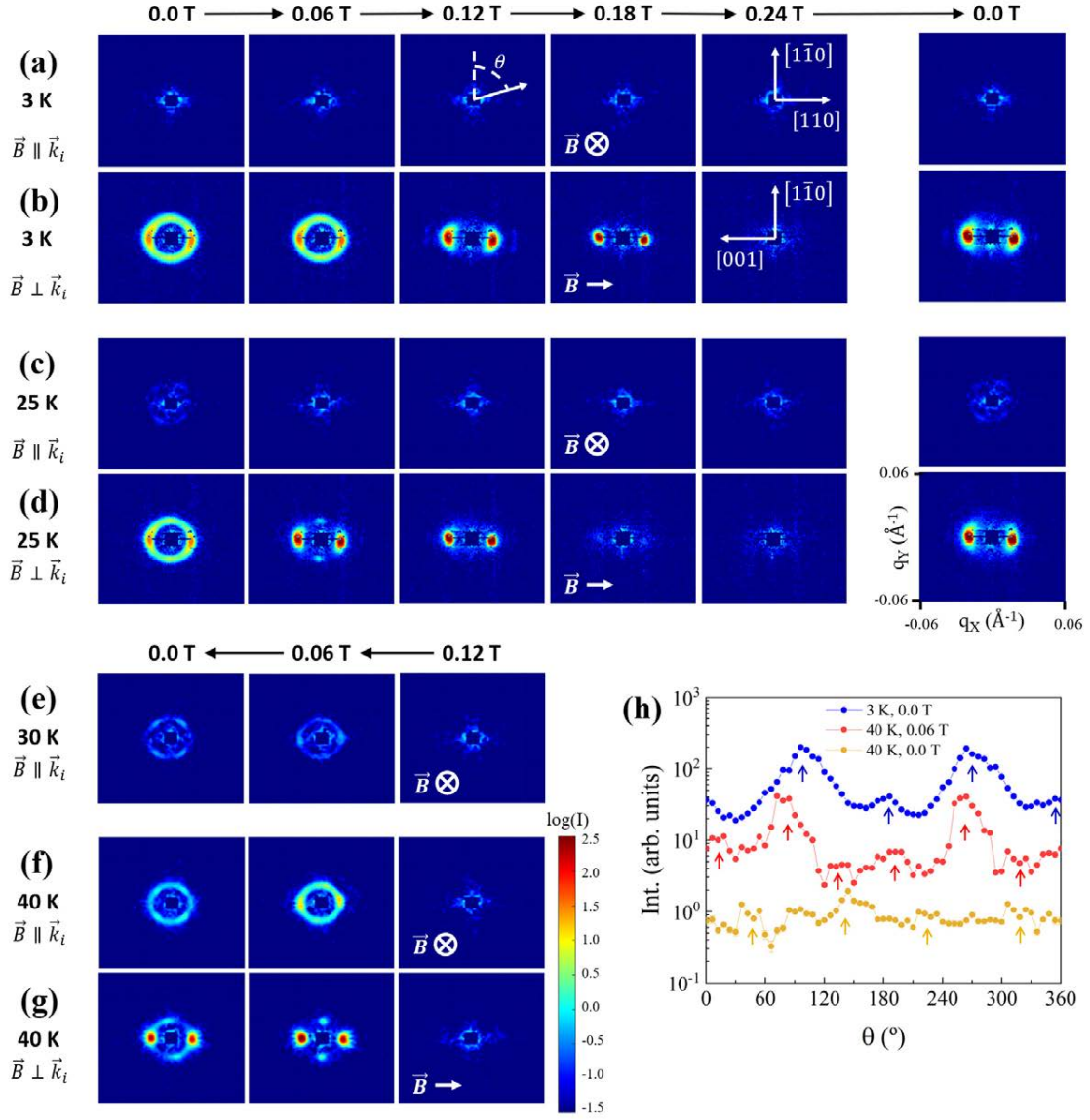

Figure 4.9: SANS patterns obtained for different magnetic fields at 3 K [(a) and (b)], 25 K [(c) and (d)], 30 K (e) and 40 K [(f) and (g)] in the $\vec{B} \parallel \langle 001 \rangle \parallel \vec{k}_i$ and $\vec{B} \parallel \langle 001 \rangle \perp \vec{k}_i$ configurations. The scattered intensity is plotted in logarithmic scale. The azimuthal angle θ and the crystallographic directions present in the detector plane for each configuration are shown in (a) and (b). (h) Azimuthal angle θ dependence of the scattered intensity for 3 K, 0.0 T with $\vec{B} \perp \vec{k}_i$ and 40 K, 0.06 T and 40 K, 0.0 T with $\vec{B} \parallel \vec{k}_i$. The colored arrows signal the observed peaks.

phase, where substitution disorder caused by Co atoms and weak anisotropy prevent the spin structure from locking to the crystalline structure, transforming the regular six-fold pattern into a ring of intensity [54, 127]. As the field decreases to zero, the scattering ring persists, but now two pairs of weak peaks appear at 45° from the vertical axis, indicative of a multidomain phase with helices mainly along the three $\langle 001 \rangle$ directions.

Patterns in the complementary configuration ($\vec{B} \parallel \langle 001 \rangle \perp \vec{k}_i$) are displayed in Fig. 4.9(b), (d) and (g). At zero field, two strong peaks along the [001] direction and a scattering ring suggest helical order with a domain oriented along the magnetic easy axis, plus multiple randomly oriented domains. As the magnetic field increases, the helices reorient towards the applied field, until a single domain along the [001] direction is formed. For $B > 0.18$ T no magnetic scattering is observed as the system reaches the ferromagnetic order, in agreement with our magnetization measurements and Ref. [133]. Upon decreasing the magnetic field, the two peaks along the [001] persist, indicating that the single domain of conical helices remains at zero field. Meanwhile, at 40 K and 0.06 T an additional pair of very weak peaks appear along the vertical direction $[1\bar{1}0]$, in agreement with the presence of the *A-phase*.

SANS patterns with the field along $\langle 110 \rangle$ are shown in Fig. 4.10. At 2 K with $\vec{B} \parallel \langle 110 \rangle \parallel \vec{k}_i$, the signal from the randomly oriented multi-domain helical or-

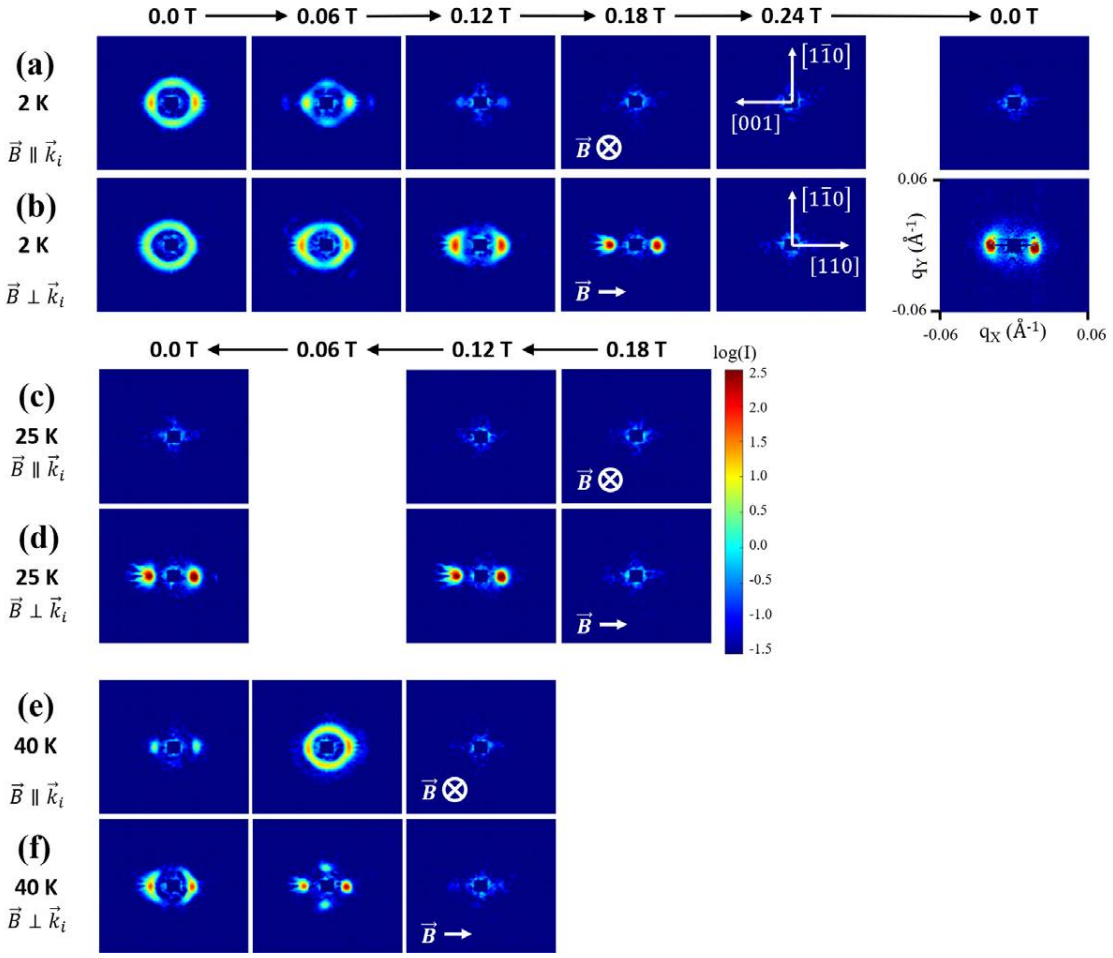

Figure 4.10: SANS patterns obtained for different magnetic fields at 2 K [(a) and (b)], 25 K [(c) and (d)], and 40 K [(e) and (f)] in the $\vec{B} \parallel \langle 110 \rangle \parallel \vec{k}_i$ and $\vec{B} \parallel \langle 110 \rangle \perp \vec{k}_i$ configurations. The scattered intensity is plotted in logarithmic scale. The crystallographic directions present in the detector plane for each configuration are shown in (a) and (b).

der disappears at $B > 0.06$ T as the helices align with the magnetic field (see Fig. 4.10(a)). Simultaneously, the scattering ring observed with $\vec{B} \parallel \langle 110 \rangle \perp \vec{k}_i$ transforms into the two diffraction peaks characteristic of the single-domain conical helix (see Fig. 4.10(b)). For $B > 0.18$ T the system reaches the ferromagnetic order and no signal is observed.

When the magnetic field is decreased towards zero the single domain of conical helices remains, evidenced by the presence of two peaks along the [110]. Figure 4.10(c) and (d) show similar results for 25 K. At 40 K, similar diffraction patterns

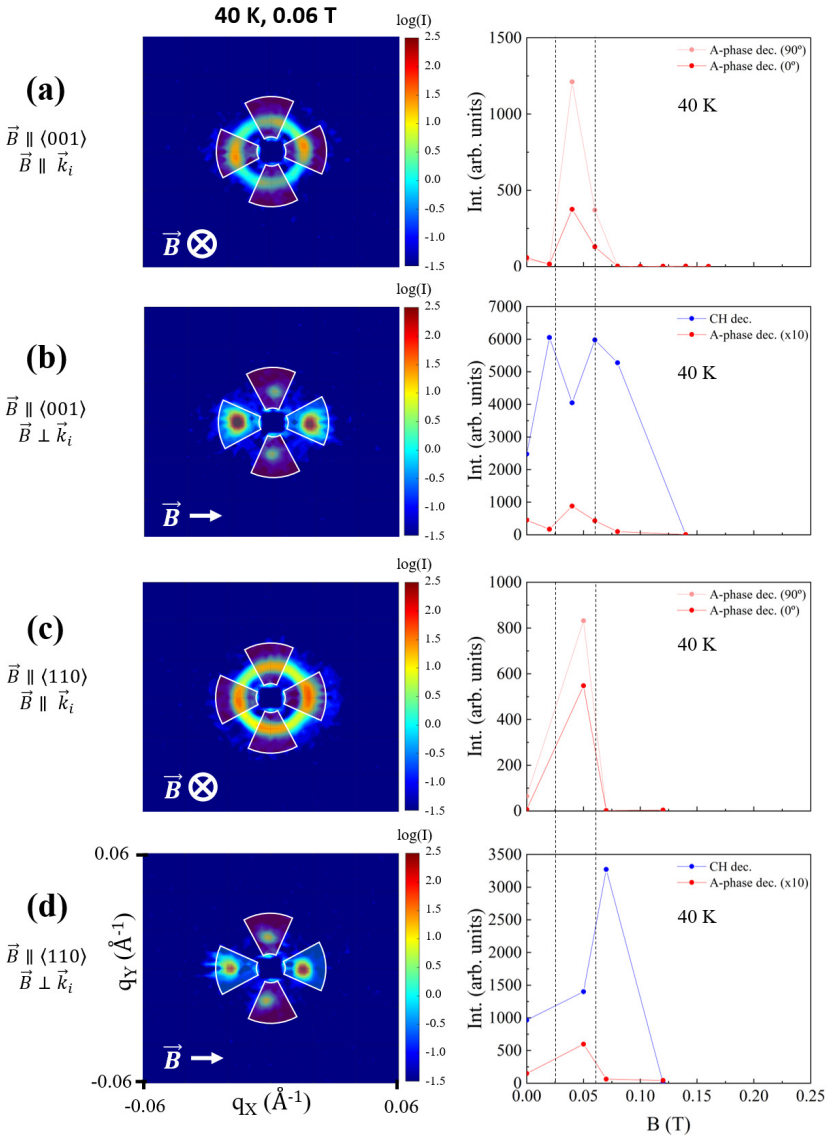

Figure 4.11: SANS patterns at 40 K, 0.06 T and integrated intensity at 40 K with $\vec{B} \parallel \langle 001 \rangle \parallel \vec{k}_i$ (a), $\vec{B} \parallel \langle 001 \rangle \perp \vec{k}_i$ (b), $\vec{B} \parallel \langle 110 \rangle \parallel \vec{k}_i$ (c) and $\vec{B} \parallel \langle 110 \rangle \perp \vec{k}_i$ (d). The integration areas are shown in red for the peaks due to the *A-phase* and in blue for the conical helix (CH). The dotted lines in the integrated intensity indicate the boundaries of the *A-phase*.

as observed for $\vec{B} \parallel \langle 001 \rangle$ indicate the formation of the *A-phase* at 0.06 T (see Fig. 4.10(e) and (f)). The presence of two diffraction peaks along [001] for $\vec{B} \parallel \vec{k}_i$ (see Fig. 4.10 (e)) supports the idea of a multidomain phase in which helices propagate mainly along the three $\langle 001 \rangle$ directions.

Further insight into the *A-phase* was obtained by integrating the scattered intensity using an arc of $0.006 \leq q \leq 0.026$ Å^{-1} and angular opening $\Delta\theta = 60°$ around the diffraction peaks. The results are plotted in Fig. 4.11. For all configurations the magnetic modulations give rise to peaks with modulus $K_A = 0.016(1)$ Å^{-1}. For $\vec{B} \parallel \vec{k}_i$, the six-fold pattern plus ring has appreciable intensity in a narrow region, the same where for $\vec{B} \perp \vec{k}_i$, the intensity of the vertical peaks increases, and the peaks due to the conical phase lose some intensity. These latter peaks do not vanish completely, indicating a possible coexistence of the *A-phase* and the CH phase. Due to the limited data points,the region where the *A-phase* exists cannot be determined accurately, and a range $0.025 \leq B \leq 0.06$ T is estimated.

The same integration procedure was carried out for all temperatures measured in the configurations with $\vec{B} \perp \vec{k}_i$. The results are displayed in Fig. 4.12(a) and (b). A similar behavior of the intensity curves has been observed in $Fe_{0.8}Co_{0.2}Si$ [54]. At 3 K with $\vec{B} \parallel \langle 001 \rangle$, the intensity increases for $B \geq 0.06$ T, reaching a maximum I_{max} at 0.15 T, while for higher fields the intensity drops. As the field is decreased from

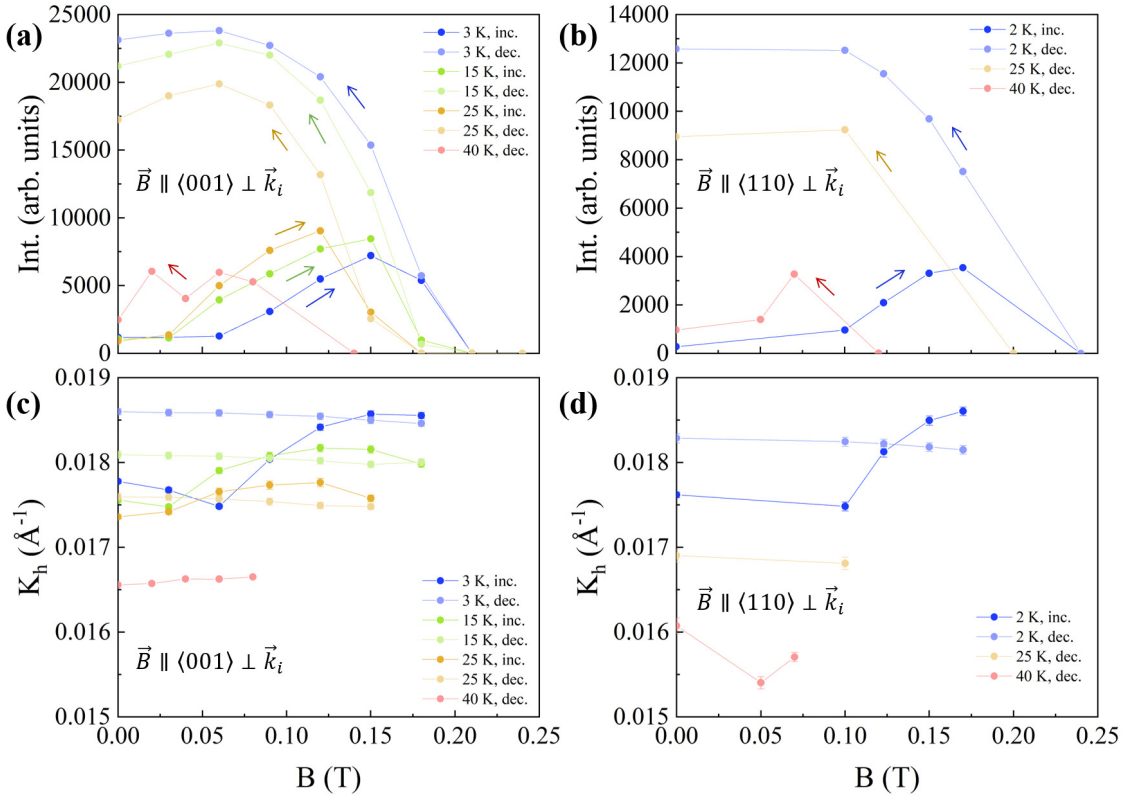

Figure 4.12: Evolution with magnetic field of the integrated intensity [(a) and (b)] and modulus of helix propagation vector K_h [(c) and (d)] for several temperatures in the $\vec{B} \parallel \langle 001 \rangle \perp \vec{k}_i$ and $\vec{B} \parallel \langle 110 \rangle \perp \vec{k}_i$ configurations, respectively.

the saturation, the intensity exhibits a pronounced hysteresis, reaching a saturation value at low fields around three times I_{max}. Contrary to MnSi, where the intensity did not recover the maximum value I_{max} achieved with increasing field (see Sec. 3.4), the intensity of the decreasing field curve in $Fe_{0.75}Co_{0.25}Si$ remains above I_{max} for the entirety of the fields measured, as expected from the formation of a single domain CH phase. As the temperature increases, qualitatively similar results are observed. The saturation value for decreasing fields decreases, indicating that fewer ordered magnetic moments contribute to the diffraction pattern. Meanwhile, the intensity increments at higher temperatures during the increasing field process. This feature suggests that anisotropy at low fields prevents the complete formation of a single domain. At higher temperatures, the thermal fluctuations weaken the anisotropy, in agreement with the decrease of B_{c1}, and the single domain is formed. Similar results are observed when the field is applied along the $\langle 110 \rangle$ for $B > 0.1$ T, although the maximum I_{max} is reached at 0.17 T.

In a procedure analogous to MnSi, a Gaussian fit to the $I(q)$ curves was performed to obtain the dependence of the propagation vector modulus K_h with magnetic field and temperature (see Fig. 4.12(c) and (d)). A significant dependence on the magnetic field is observed for the increasing field measurements, while the values remain practically constant in the decreasing process. In contrast to MnSi, the propagation vector modulus decreases for higher temperatures, i.e. the period of the helix gets bigger. Such dependence has been also observed in $Fe_{0.7}Co_{0.3}Si$, where an explanation based on the weakening of the DM interaction relative to the ferromagnetic exchange was suggested [127].

Considering all SANS results, the origin of the *B-phase* in $Fe_{0.75}Co_{0.25}Si$ seems to be different than the tilted conical phase or low temperature SkL phase proposed in Cu_2OSeO_3 [66, 67, 69], as no deviation of the propagation vector nor a ring of scattering was observed in the *B-phase* region. The new magnetic states observed in Cu_2OSeO_3 were proposed to arise for strong enough magnetocrystalline anisotropies. Given the weaker anisotropy of the compound under study, it is plausible to consider that these states are not energetically favorable in $Fe_{0.75}Co_{0.25}Si$.

In order to obtain more information at the atomic level of its magnetic structure, μSR experiments were performed to detect the internal magnetic field.

4.5 μSR exploration of the local field in $Fe_{0.75}Co_{0.25}Si$

To the best of our knowledge, this is the first instance of μSR spectra measurements in $Fe_{0.75}Co_{0.25}Si$. Figure 4.13(a) and (b) shows the ZF μSR spectra measured in the SR and NSR configurations at 2 K for $Fe_{0.75}Co_{0.25}Si$ crystals oriented along the $\langle 001 \rangle$ and $\langle 110 \rangle$ directions, respectively. A subtle difference is observed between spectra for different configurations. The relaxation in $Fe_{0.75}Co_{0.25}Si$ is faster than in MnSi, with no discernible oscillation after 0.3 μs.

Panels (c) and (d) of Fig. 4.13) show the Fourier transform of the ZF μSR spectra for the $\langle 001 \rangle$ and $\langle 110 \rangle$ directions, respectively. The field distributions are noisier than in MnSi, with a broad peak centered around $B_h = 0.05$ T, which can be attributed to different origins. First, since the substitution disorder can alter the

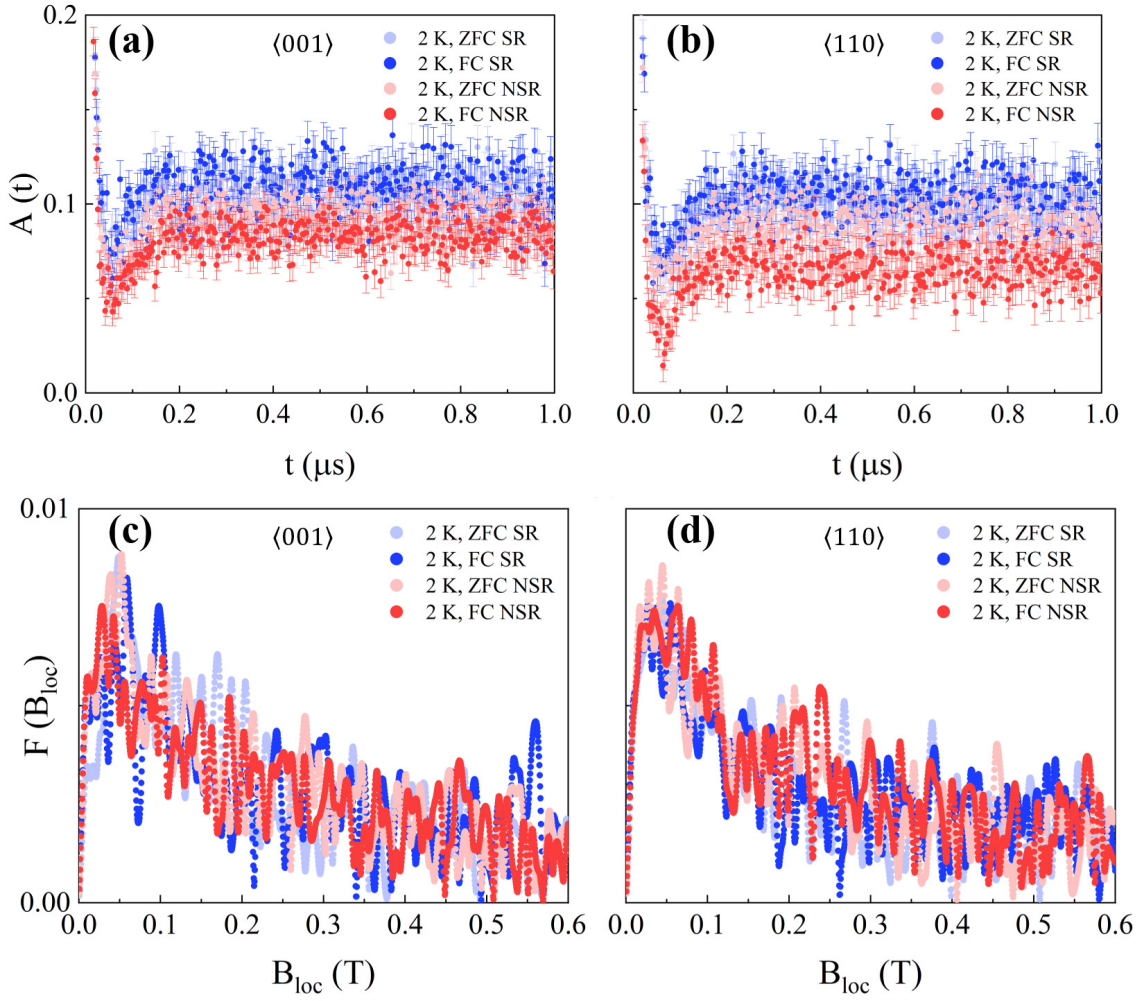

Figure 4.13: Time dependence of the ZF μSR spectra in the SR (blue) and NSR (red) configurations for $Fe_{0.75}Co_{0.25}Si$ crystals oriented along the ⟨001⟩ (a) and ⟨110⟩ directions (b). Field dependence of the Fourier transform of μSR spectra for the ⟨001⟩ (c) and ⟨110⟩ directions (d). Data measured at 2 K after ZFC and FC protocols are shown in light and dark filled circles, respectively.

electrostatic potential of the unit cell, it is plausible to consider muons stopping in a distribution of sites depending on the random occupancy of Fe and Co, and not only on 4*a* sites. Second, the disorder leads to imperfections in the magnetic structure. These fluctuations can contribute to a broadening of the field distribution, as they introduce a distribution of local magnetic fields experienced by the muons.

An analysis akin to that conducted for MnSi was applied to the ZF μSR spectra of $Fe_{0.75}Co_{0.25}Si$ over the entire measured time scale. Figure 4.14 presents the μSR spectra for all configurations. The data at 50 K and under weak transverse field (wTF) conditions were fitted to Eq.(3.4) (shown as red lines in Fig. 4.14), while the 2 K, zero-field data under ZFC and FC protocols were fitted to Eq.(3.5). The parameters derived from these fits are detailed in Table 4.1.

Notably, the relaxation rate λ_X in $Fe_{0.75}Co_{0.25}Si$ is significantly higher than in

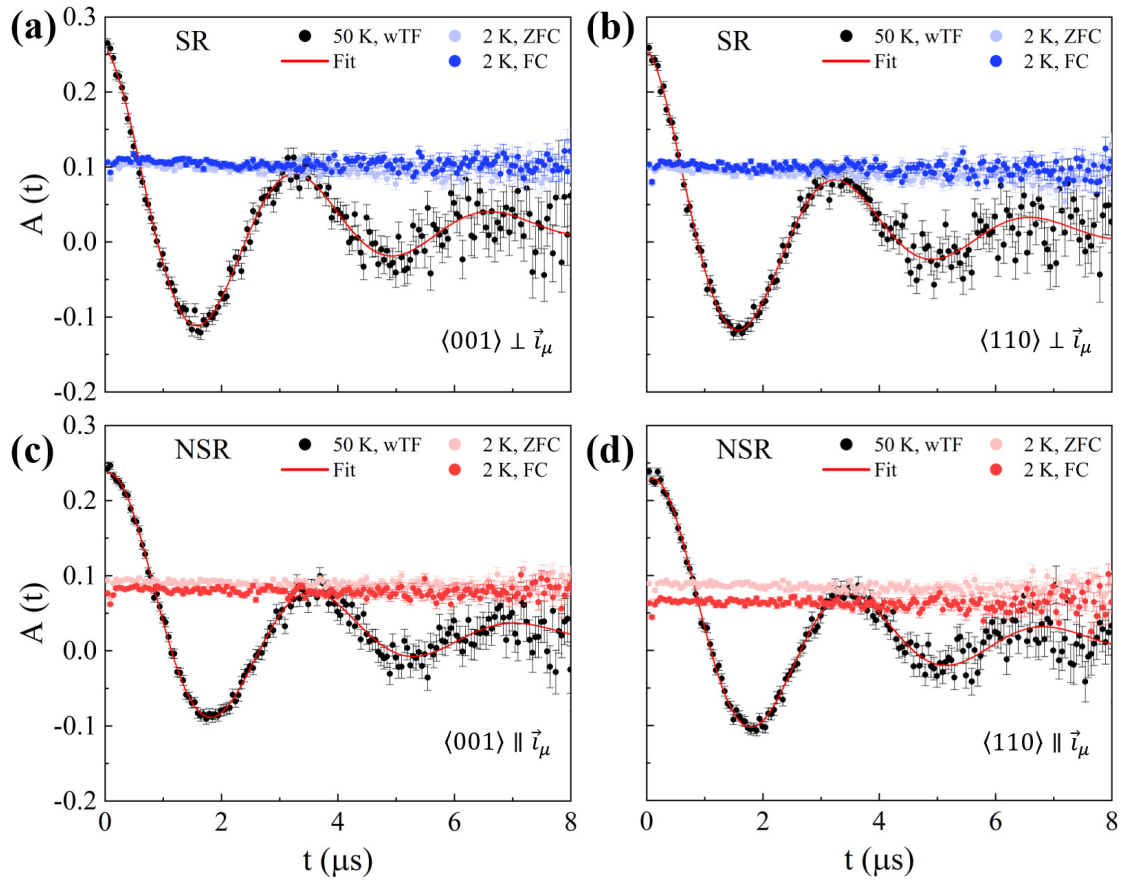

Figure 4.14: μSR spectra in the: SR configuration with $\langle 001\rangle \perp \vec{i}_\mu$ (a) and $\langle 110\rangle \perp \vec{i}_\mu$ (b), NSR configuration with $\langle 001\rangle \parallel \vec{i}_\mu$ (c) and $\langle 110\rangle \parallel \vec{i}_\mu$ (d). The data measured at 40 K with a wTF is shown in black circles, while the red line corresponds to the fit according to Eq. (3.4). Data measured at 2 K after ZFC and FC protocols are shown in light and dark filled circles, respectively.

MnSi, likely due to the magnetic structure's imperfections and magnetic fluctuations induced by substitutional disorder. This elevated rate prevented the simultaneous determination of the Gaussian contribution Δ, which was set to zero. The values of λ_Z, approximately three times lower than in MnSi, oscillate around 0.013 μs^{-1}, suggesting a weaker muon spin-lattice interaction, potentially attributable to the distinct magnetic environment in $Fe_{0.75}Co_{0.25}Si$. The long-time asymmetry values at 2 K, ZFC agree well with the averaged powder value of 1/3. Meanwhile, the decrease, but non-zero average, of $\left\langle \left(B^Z_{\rm loc}/B_{\rm loc}\right)^2 \right\rangle$ in the 2 K, FC curves, indicates the persistence of a multi-domain helical phase when decreasing the magnetic field from the FFM phase.

Next, we show the evolution of the μSR spectra with magnetic field and temperature. Figure 4.15(a) and (b) present the TF μSR spectra at 2 K for the lowest and highest fields measured with $\vec{B} \parallel \langle 001\rangle \perp \vec{i}_\mu$ and $\vec{B} \parallel \langle 110\rangle \perp \vec{i}_\mu$, respectively. Similar to the ZF spectra, oscillations are almost completely damped out by 0.3 μs.

Table 4.1: Parameters derived from the fits of the μSR spectra to Eq.(3.4) and Eq.(3.5).

Parameter	50 K, wTF	2 K, ZFC	2 K, FC	50 K, wTF	2 K, ZFC	2 K, FC
		SR, $\langle 001 \rangle$			SR, $\langle 110 \rangle$	
$B = \omega_\mu/\gamma_\mu$ (G)	22.0(1)	–	–	22.10(8)	–	–
Δ/γ_μ (G)	–	–	–	–	–	–
λ_X (μs^{-1})	0.37(1)	–	–	0.38(1)	–	–
a_0	0.239(3)	0.239	0.239	0.244(3)	0.244	0.244
A_{off}	0.020(1)	0.020	0.020	0.014(1)	0.014	0.014
λ_Z (μs^{-1})	–	0.015(3)	0.011(2)	–	0.018(3)	0.012(3)
$\langle (B^X_{\text{loc}}/B_{\text{loc}})^2 \rangle$	–	0.347(2)	0.367(2)	–	0.341(2)	0.364(2)
		NSR, $\langle 001 \rangle$			NSR, $\langle 110 \rangle$	
$B = \omega_\mu/\gamma_\mu$ (G)	21.2(1)	–	–	22.0(1)	–	–
Δ/γ_μ (G)	–	–	–	–	–	–
λ_X (μs^{-1})	0.382(9)	–	–	0.370(9)	–	–
a_0	0.226(2)	0.226	0.226	0.229(2)	0.229	0.229
A_{off}	0.022(1)	0.022	0.022	0.014(1)	0.014	0.014
λ_Z (μs^{-1})	–	0.012(3)	0.011(3)	–	0.012(3)	0.013(4)
$\langle (B^Z_{\text{loc}}/B_{\text{loc}})^2 \rangle$	–	0.310(2)	0.263(2)	–	0.323(2)	0.224(2)

The Fourier transformed data at 2 K and 40 K for each configuration are shown in panels (c) through (f). Regardless of the sample's orientation, a consistent field distribution evolution is observed. As the applied field increases at 2 K, a broad peak shifts towards higher values. Such peak becomes narrower when the temperature is increased to 40 K, yet no discernible change in its shape is evident, even in the FFM region. An additional peak, attributable to muons stopping outside the sample, is consistently observed at the applied field, and signaled by a black asterisk in panels (c), (d), (e) and (f).

The computational model employed for studying MnSi presents significant limitations when applied to $Fe_{0.75}Co_{0.25}Si$, as two critical parameters of the model are unknown: the muon implantation site and the contact coupling. While *ab initio* calculations based on the density-functional theory (DFT) might theoretically estimate the muon implantation site, obtaining experimental validation akin to the approach used for MnSi in Ref. [85] appears less feasible. This challenge is mainly due to the broad distribution of fields, as shown in our study for the two configurations $\vec{B} \parallel \langle 001 \rangle$ and $\vec{B} \parallel \langle 110 \rangle$, which complicates the observation of the angular dependence of the four muon precession frequencies.

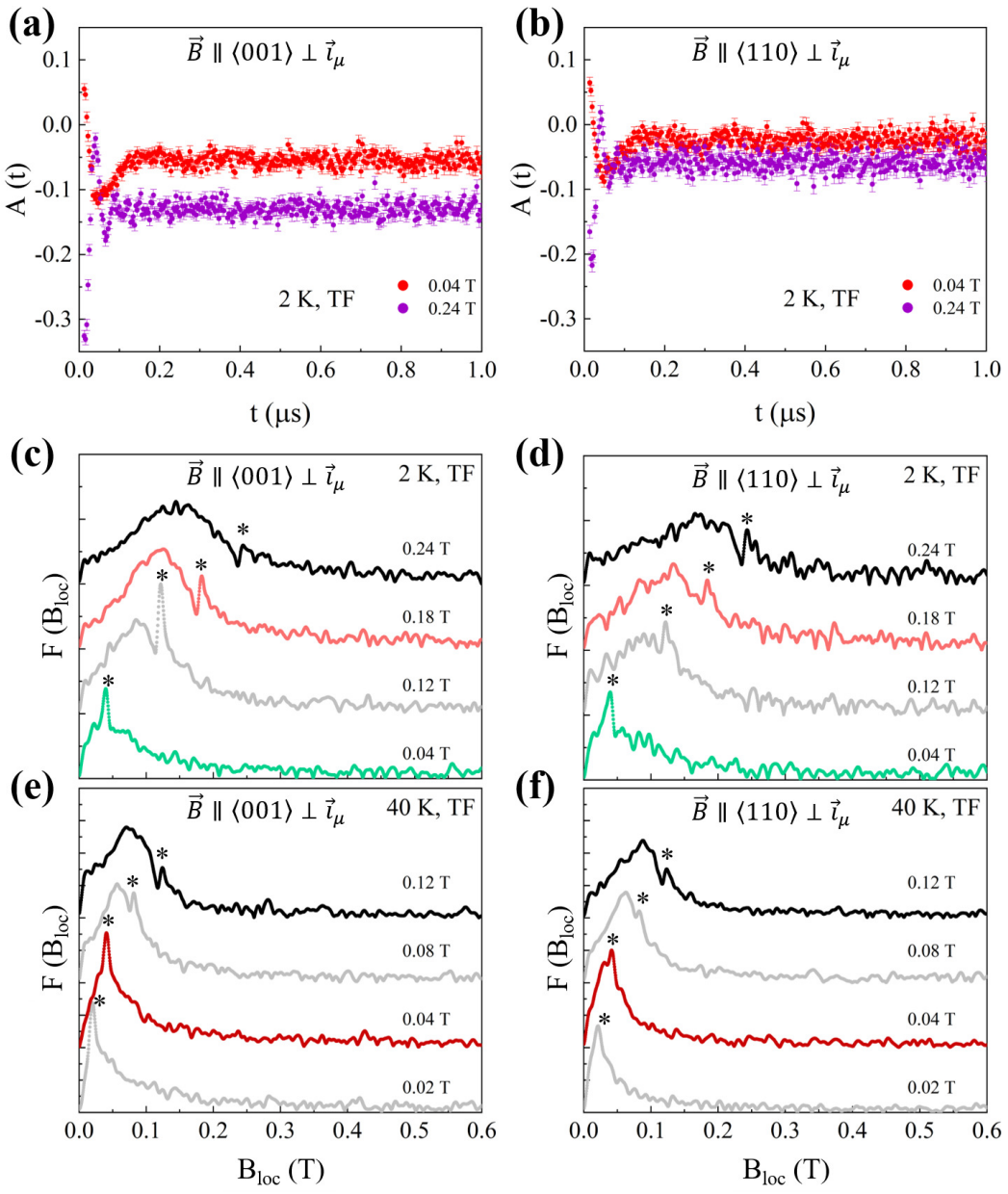

Figure 4.15: TF μSR spectra for some selected applied fields at 2 K with $\vec{B} \parallel \langle 001 \rangle \perp \vec{i}_\mu$ (a) and $\vec{B} \parallel \langle 110 \rangle \perp \vec{i}_\mu$ (b). The field dependence of the Fourier transform of μSR spectra is shown at 2 K [(c), (d)] and 40 K [(e), (f)]. The colors used in panels (c), (d), (e) and (f) indicate the different magnetic phases as deduced from previous experiments: helimagnetic (green), conical helix (grey), *B-phase* (light red), ferromagnetic (black) and *A-phase* (dark red). The signal at the applied field value due to background muons is marked with black asterisks.

4.6 Conclusions

The magnetic phase diagram of $Fe_{0.75}Co_{0.25}Si$ has been studied by d.c and a.c. magnetization, SANS and μSR experiments. An anomaly in the a.c. magnetization curves, similar to the one observed in MnSi, was observed even when the magnetic field is applied in a direction different than the easy axis. Furthermore, the stability of the *B-phase* depended on either the *B*-increasing or *B*-decreasing process and the direction of the applied field, which suggests that the effect of chemical disorder assists the appearance of the *B-phase*.

The presence of the *A-phase* was observed by SANS experiments, where the disorder transforms the six-fold pattern of the SkL into a ring of intensity. Additionally, a metastable *A-phase* below 35 K was confirmed, which can coexist with the CH phase. Although no additional information regarding the origin of the *B-phase* was provided by the SANS results, they allowed to discard the same origin as the new magnetic states reported in Cu_2OSeO_3.

The μSR results at ZF corroborated the multi-domain helical phase previously identified through SANS experiments. However, the analysis of the TF spectra showed a broad distribution of local fields, which prevents the extraction of more detailed information of the local field at the *A-phase* and *B-phase*. The origin of this distribution is suggested to be a combination of a range of possible muon implantation sites and an increase of the magnetic fluctuations induced by substitutional disorder.

Conclusions of Part I

The primary goal of Part I was to investigate the existence and properties of novel magnetic phases in helimagnetic materials, specifically focusing on $B20$ cubic chiral magnets MnSi and $Fe_{0.75}Co_{0.25}Si$. This exploration was driven by theoretical predictions suggesting an *unknown-state* within these materials. A combination of macroscopic characterization, SANS, and μSR techniques were employed to distinguish the properties and origin of the postulated state in relation to known magnetic phases like the conical helix (CH) or Skyrmion Lattice (SkL).

For MnSi, the detection of a distinct anomaly at low temperatures near the FFM boundary, particularly under a specific crystallographic orientation ($\vec{B} \parallel \langle 111 \rangle$), underscores a potential realization of the theorized *unknown state*, termed here *B-phase*. The analysis of this *B-phase* through SANS and μSR experiments indicates a magnetic state distinct from the conventional SkL, compatible with a relative reorientation of the four helices in the unit cell of MnSi. Meanwhile, the μSR experiments performed in the *A-phase* suggest a SkL profile more complex than the well-known triple-$\vec{Q}$ state.

$Fe_{0.75}Co_{0.25}Si$'s investigation revealed a similar anomaly in its magnetic phase diagram under varied magnetic field conditions, suggesting the influence of chemical disorder in the development of the *B-phase*. Such disorder also affects the structure and stability of the *A-phase*, as evidenced by the transformation of its characteristic six-fold pattern into a more disordered intensity ring in SANS experiments and the identification of a metastable *A-phase* coexisting with the CH phase. The *B-phase* in $Fe_{0.75}Co_{0.25}Si$, while exhibiting parallels with MnSi, also underscores the complex role of chemical disorder in the emergence and characteristics of these novel magnetic states, complicating the direct comparison of their origins.

In conclusion, the investigations into MnSi and $Fe_{0.75}Co_{0.25}Si$ not only corroborate the existence of an *unknown-state* – the *B-phase* – but also offer new perspectives on the intricate interplay between disorder, anisotropy and temperature in dictating the stability and characteristics of novel magnetic phases in cubic chiral magnets.

Looking ahead, future experimental efforts should prioritize advancing the understanding of the novel *B-phase* and further characterizing the *A-phase* in helimagnetic materials. Specifically, we plan to perform a.c. magnetization experiments in MnSi with the oscillating field perpendicular to $\langle 111 \rangle$, in order to sense the dynamic response in the same component as measured in SANS. Additional μSR experiments in MnSi and $Fe_{0.75}Co_{0.25}Si$ should also be designed to probe the local magnetic environments with increased precision. This could increase our understanding of the internal magnetic structures and fluctuations of both the *A-* and *B-phases*, providing a deeper insight into the magnetic complexity of these phases.

Bibliography of Part I

[1] L. Barron and J. Vrbancich, "Magneto-chiral birefringence and dichroism," Molecular Physics, vol. 51, pp. 715–730, feb 1984.

[2] L. D. Barron, "Chirality and magnetism shake hands," Nature Materials, vol. 7, pp. 691–692, 2021.

[3] G. H. Wagniere, On Chirality and the Universal Asymmetry: Reflections on Image and Mirror Image. Zurich: Wiley-VCH, 2007.

[4] S.-W. Cheong and X. Xu, "Magnetic chirality," npj Quantum Materials, vol. 7, pp. 2397–4648, 2022.

[5] S.-H. Yang, R. Naaman, Y. Paltiel, and S. S. P. Parkin, "Chiral spintronics," Nature Reviews Physics, vol. 3, pp. 328–343, 2021.

[6] Z. Shang, T. Liu, Q. Yang, S. Cui, K. Xu, Y. Zhang, J. Deng, T. Zhai, and X. Wang, "Chiral-Molecule-Based Spintronic Devices," Small, vol. 18, no. 32, p. 2203015, 2022.

[7] T. Yu, Z. Luo, and G. E. Bauer, "Chirality as generalized spin–orbit interaction in spintronics," Physics Reports, vol. 1009, pp. 1–115, 2023.

[8] H. Yu, J. Xiao, and H. Schultheiss, "Magnetic texture based magnonics," Physics Reports, vol. 905, pp. 1–59, apr 2021.

[9] S. A. Wolf, D. D. Awschalom, R. A. Buhrman, J. M. Daughton, S. von Molnár, M. L. Roukes, A. Y. Chtchelkanova, and D. M. Treger, "Spintronics: A Spin-Based Electronics Vision for the Future," Science, vol. 294, pp. 1488–1495, nov 2001.

[10] I. Žutić, J. Fabian, and S. D. Sarma, "Spintronics: Fundamentals and applications," Reviews of Modern Physics, vol. 76, pp. 323–410, apr 2004.

[11] A. Fert, V. Cros, and J. Sampaio, "Skyrmions on the track," Nature Nanotechnology, vol. 8, pp. 152–156, mar 2013.

[12] N. Romming, C. Hanneken, M. Menzel, J. E. Bickel, B. Wolter, K. von Bergmann, A. Kubetzka, and R. Wiesendanger, "Writing and Deleting Single Magnetic Skyrmions," Science, vol. 341, pp. 636–639, aug 2013.

[13] E. V. Altynbaev, N. M. Chubova, and S. V. Grigoriev, "Exotic Spin Structures in Transition-Metal Monosilicides and Monogermanides," Crystallography Reports, vol. 67, pp. 118–136, feb 2022.

[14] H. D. Flack and G. Bernardinelli, "Absolute structure and absolute configuration," Acta Crystallographica Section A Foundations of Crystallography, vol. 55, pp. 908–915, sep 1999.

[15] L. Vočadlo, G. D. Price, and I. G. Wood, "Crystal structure, compressibility and possible phase transitions in ϵ-FeSi studied by first-principles pseudopotential calculations," Acta Crystallographica Section B Structural Science, vol. 55, pp. 484–493, aug 1999.

[16] D. van der Marel, A. Damascelli, K. Schulte, and A. Menovsky, "Spin, charge, and bonding in transition metal mono-silicides," Physica B: Condensed Matter, vol. 244, pp. 138–147, jan 1998.

[17] S. V. Grigoriev, D. Chernyshov, V. A. Dyadkin, V. Dmitriev, E. V. Moskvin, D. Lamago, T. Wolf, D. Menzel, J. Schoenes, S. V. Maleyev, and H. Eckerlebe, "Interplay between crystalline chirality and magnetic structure in $Mn_{1-x}Fe_xSi$," Physical Review B, vol. 81, jan 2010.

[18] I. Dzyaloshinskii, "A GENERAL RELATION IN THE THEORY OF FERROMAGNETIC FERMI FLUIDS," Zh. Eksperim. i Teor. Fiz., vol. 46, 1964.

[19] P. Bak and M. H. Jensen, "Theory of helical magnetic structures and phase transitions in MnSi and FeGe," Journal of Physics C: Solid State Physics, vol. 13, pp. L881–L885, nov 1980.

[20] O. Nakanishi, A. Yanase, A. Hasegawa, and M. Kataoka, "The origin of the helical spin density wave in MnSi," Solid State Communications, vol. 35, pp. 995–998, sep 1980.

[21] I. Dzyaloshinsky, "A thermodynamic theory of "weak" ferromagnetism of antiferromagnetics," Journal of Physics and Chemistry of Solids, vol. 4, pp. 241–255, jan 1958.

[22] T. Moriya, "Anisotropic Superexchange Interaction and Weak Ferromagnetism," Physical Review, vol. 120, pp. 91–98, oct 1960.

[23] T. Skyrme, "A unified field theory of mesons and baryons," Nuclear Physics, vol. 31, pp. 556–569, Mar. 1962.

[24] A. O. Leonov, I. E. Dragunov, U. K. Rößler, and A. N. Bogdanov, "Theory of skyrmion states in liquid crystals," Physical Review E, vol. 90, Oct. 2014.

[25] S. L. Sondhi, A. Karlhede, S. A. Kivelson, and E. H. Rezayi, "Skyrmions and the crossover from the integer to fractional quantum Hall effect at small Zeeman energies," Physical Review B, vol. 47, pp. 16419–16426, June 1993.

[26] U. Al Khawaja and H. Stoof, "Skyrmions in a ferromagnetic bose–einstein condensate," Nature, vol. 411, pp. 918–920, June 2001.

[27] N. Nagaosa and Y. Tokura, "Topological properties and dynamics of magnetic skyrmions," Nature Nanotechnology, vol. 8, no. 12, pp. 899–911, 2013.

[28] M. Mochizuki, Microwave-Driven Dynamics of Magnetic Skyrmions Under a Tilted Magnetic Field: Magnetic Resonances, Translational Motions, and Spin-Motive Forces, pp. 183–206. Springer International Publishing, 2021.

[29] A. Fert, N. Reyren, and V. Cros, "Magnetic skyrmions: advances in physics and potential applications," Nature Reviews Materials, vol. 2, June 2017.

[30] A. N. Bogdanov and D. A. Yablonskii, "Thermodynamically stable "vortices" in magnetically ordered crystals.The mixed state of magnets," Sov. Phys. JETP, vol. 68, no. 1, p. 101, 1989.

[31] A. Bogdanov and A. Hubert, "Thermodynamically stable magnetic vortex states in magnetic crystals," Journal of Magnetism and Magnetic Materials, vol. 138, pp. 255–269, dec 1994.

[32] A. Bogdanov and A. Hubert, "The stability of vortex-like structures in uniaxial ferromagnets," Journal of Magnetism and Magnetic Materials, vol. 195, pp. 182–192, apr 1999.

[33] S. Mühlbauer, B. Binz, F. Jonietz, C. Pfleiderer, A. Rosch, A. Neubauer, R. Georgii, and P. Böni, "Skyrmion Lattice in a Chiral Magnet," Science, vol. 323, pp. 915–919, feb 2009.

[34] Y. Hu and B. Wang, "Reversible "triple-Q" elastic field structures in a chiral magnet," Scientific Reports, vol. 6, July 2016.

[35] B. Göbel, I. Mertig, and O. A. Tretiakov, "Beyond skyrmions: Review and perspectives of alternative magnetic quasiparticles," Physics Reports, vol. 895, pp. 1–28, Feb. 2021.

[36] V. Laliena and J. Campo, "Stability of skyrmion textures and the role of thermal fluctuations in cubic helimagnets: A new intermediate phase at low temperature," Physical Review B, vol. 96, oct 2017.

[37] O. Nakanishi, A. Yanase, and A. Hasegawa, "Electronic energy band structure of MnSi," Journal of Magnetism and Magnetic Materials, vol. 15-18, pp. 879–880, jan 1980.

[38] Y. Ishikawa, K. Tajima, D. Bloch, and M. Roth, "Helical spin structure in manganese silicide MnSi," Solid State Communications, vol. 19, pp. 525–528, jul 1976.

[39] Y. Ishikawa, G. Shirane, J. A. Tarvin, and M. Kohgi, "Magnetic excitations in the weak itinerant ferromagnet MnSi," Physical Review B, vol. 16, pp. 4956–4970, dec 1977.

[40] M. Tanaka, H. Takayoshi, M. Ishida, and Y. Endoh, "Crystal Chirality and Helicity of the Helical Spin Density Wave in MnSi. I. Convergent-Beam Electron Diffraction," Journal of the Physical Society of Japan, vol. 54, pp. 2970–2974, aug 1985.

[41] M. Ishida, Y. Endoh, S. Mitsuda, Y. Ishikawa, and M. Tanaka, "Crystal Chirality and Helicity of the Helical Spin Density Wave in MnSi. II. Polarized Neutron Diffraction," Journal of the Physical Society of Japan, vol. 54, pp. 2975–2982, aug 1985.

[42] S. V. Grigoriev, S. V. Maleyev, A. I. Okorokov, Y. O. Chetverikov, P. Böni, R. Georgii, D. Lamago, H. Eckerlebe, and K. Pranzas, "Magnetic structure of MnSi under an applied field probed by polarized small-angle neutron scattering," Physical Review B, vol. 74, dec 2006.

[43] S. V. Maleyev, "Cubic magnets with Dzyaloshinskii-Moriya interaction at low temperature," Physical Review B, vol. 73, may 2006.

[44] S. Buhrandt and L. Fritz, "Skyrmion lattice phase in three-dimensional chiral magnets from Monte Carlo simulations," Physical Review B, vol. 88, nov 2013.

[45] K. Koyama, T. Goto, T. Kanomata, and R. Note, "Observation of an itinerant metamagnetic transition in MnSi under high pressure," Physical Review B, vol. 62, pp. 986–991, jul 2000.

[46] S. V. Grigoriev, S. V. Maleyev, A. I. Okorokov, Y. O. Chetverikov, R. Georgii, P. Böni, D. Lamago, H. Eckerlebe, and K. Pranzas, "Critical fluctuations in MnSi near T_C: A polarized neutron scattering study," Physical Review B, vol. 72, oct 2005.

[47] C. Pappas, E. Lelièvre-Berna, P. Falus, P. M. Bentley, E. Moskvin, S. Grigoriev, P. Fouquet, and B. Farago, "Chiral Paramagnetic Skyrmion-like Phase in MnSi," Physical Review Letters, vol. 102, may 2009.

[48] S. V. Grigoriev, S. V. Maleyev, E. V. Moskvin, V. A. Dyadkin, P. Fouquet, and H. Eckerlebe, "Crossover behavior of critical helix fluctuations in MnSi," Physical Review B, vol. 81, apr 2010.

[49] M. Janoschek, M. Garst, A. Bauer, P. Krautscheid, R. Georgii, P. Böni, and C. Pfleiderer, "Fluctuation-induced first-order phase transition in Dzyaloshinskii-Moriya helimagnets," Physical Review B, vol. 87, apr 2013.

[50] S. V. Grigoriev, E. V. Moskvin, V. A. Dyadkin, D. Lamago, T. Wolf, H. Eckerlebe, and S. V. Maleyev, "Chiral criticality in the doped helimagnets $Mn_{1-y}Fe_ySi$," Physical Review B, vol. 83, jun 2011.

[51] S. V. Grigoriev, V. A. Dyadkin, D. Menzel, J. Schoenes, Y. O. Chetverikov, A. I. Okorokov, H. Eckerlebe, and S. V. Maleyev, "Magnetic structure of $Fe_{1-x}Co_xSi$ in a magnetic field studied via small-angle polarized neutron diffraction," Physical Review B, vol. 76, dec 2007.

[52] S. V. Grigoriev, V. A. Dyadkin, E. V. Moskvin, D. Lamago, T. Wolf, H. Eckerlebe, and S. V. Maleyev, "Helical spin structure of $Mn_{1-y}Fe_ySi$ under a magnetic field: Small angle neutron diffraction study," Physical Review B, vol. 79, apr 2009.

[53] B. Lebech, P. Harris, J. S. Pedersen, K. Mortensen, C. Gregory, N. Bernhoeft, M. Jermy, and S. Brown, "Magnetic phase diagram of MnSi," Journal of Magnetism and Magnetic Materials, vol. 140-144, pp. 119–120, feb 1995.

[54] W. Münzer, A. Neubauer, T. Adams, S. Mühlbauer, C. Franz, F. Jonietz, R. Georgii, P. Böni, B. Pedersen, M. Schmidt, A. Rosch, and C. Pfleiderer, "Skyrmion lattice in the doped semiconductor $Fe_{1-x}Co_xSi$," Physical Review B, vol. 81, jan 2010.

[55] X. Z. Yu, Y. Onose, N. Kanazawa, J. H. Park, J. H. Han, Y. Matsui, N. Nagaosa, and Y. Tokura, "Real-space observation of a two-dimensional skyrmion crystal," Nature, vol. 465, pp. 901–904, jun 2010.

[56] X. Z. Yu, N. Kanazawa, Y. Onose, K. Kimoto, W. Z. Zhang, S. Ishiwata, Y. Matsui, and Y. Tokura, "Near room-temperature formation of a skyrmion crystal in thin-films of the helimagnet FeGe," Nature Materials, vol. 10, pp. 106–109, dec 2010.

[57] S. Seki, X. Z. Yu, S. Ishiwata, and Y. Tokura, "Observation of Skyrmions in a Multiferroic Material," Science, vol. 336, pp. 198–201, apr 2012.

[58] Y. Tokunaga, X. Z. Yu, J. S. White, H. M. Rønnow, D. Morikawa, Y. Taguchi, and Y. Tokura, "A new class of chiral materials hosting magnetic skyrmions beyond room temperature," Nature Communications, vol. 6, jul 2015.

[59] S. V. Grigoriev, N. M. Potapova, E. V. Moskvin, V. A. Dyadkin, C. Dewhurst, and S. V. Maleyev, "Hexagonal spin structure of A-phase in MnSi: Densely packed skyrmion quasiparticles or two-dimensionally modulated spin superlattice?," JETP Letters, vol. 100, pp. 216–221, oct 2014.

[60] V. Laliena, G. Albalate, and J. Campo, "Stability of the skyrmion lattice near the critical temperature in cubic helimagnets," Physical Review B, vol. 98, dec 2018.

[61] M. N. Wilson, A. B. Butenko, A. N. Bogdanov, and T. L. Monchesky, "Chiral skyrmions in cubic helimagnet films: The role of uniaxial anisotropy," Physical Review B, vol. 89, mar 2014.

[62] A. B. Butenko, A. A. Leonov, U. K. Rößler, and A. N. Bogdanov, "Stabilization of skyrmion textures by uniaxial distortions in noncentrosymmetric cubic helimagnets," Physical Review B, vol. 82, aug 2010.

[63] H. Wilhelm, M. Baenitz, M. Schmidt, U. K. Rößler, A. A. Leonov, and A. N. Bogdanov, "Precursor Phenomena at the Magnetic Ordering of the Cubic Helimagnet FeGe," Physical Review Letters, vol. 107, sep 2011.

[64] T. Nakajima, H. Oike, A. Kikkawa, E. P. Gilbert, N. Booth, K. Kakurai, Y. Taguchi, Y. Tokura, F. Kagawa, and T. hisa Arima, "Skyrmion lattice structural transition in MnSi," Science Advances, vol. 3, jun 2017.

[65] T. Nakajima and T. hisa Arima, "Observation of Magnetic Skyrmions by Neutron Scattering," Journal of the Physical Society of Japan, vol. 88, p. 081006, aug 2019.

[66] A. Chacon, L. Heinen, M. Halder, A. Bauer, W. Simeth, S. Mühlbauer, H. Berger, M. Garst, A. Rosch, and C. Pfleiderer, "Observation of two independent skyrmion phases in a chiral magnetic material," Nature Physics, vol. 14, pp. 936–941, jun 2018.

[67] M. Halder, A. Chacon, A. Bauer, W. Simeth, S. Mühlbauer, H. Berger, L. Heinen, M. Garst, A. Rosch, and C. Pfleiderer, "Thermodynamic evidence of a second skyrmion lattice phase and tilted conical phase in Cu_2OSeO_3," Physical Review B, vol. 98, oct 2018.

[68] F. Qian, L. J. Bannenberg, H. Wilhelm, G. Chaboussant, L. M. Debeer-Schmitt, M. P. Schmidt, A. Aqeel, T. T. M. Palstra, E. Brück, A. J. E. Lefering, C. Pappas, M. Mostovoy, and A. O. Leonov, "New magnetic phase of the chiral skyrmion material Cu_2OSeO_3," Science Advances, vol. 4, sep 2018.

[69] L. J. Bannenberg, H. Wilhelm, R. Cubitt, A. Labh, M. P. Schmidt, E. Lelièvre-Berna, C. Pappas, M. Mostovoy, and A. O. Leonov, "Multiple low-temperature skyrmionic states in a bulk chiral magnet," npj Quantum Materials, vol. 4, apr 2019.

[70] K. Karube, J. S. White, D. Morikawa, C. D. Dewhurst, R. Cubitt, A. Kikkawa, X. Yu, Y. Tokunaga, T. hisa Arima, H. M. Rønnow, Y. Tokura, and Y. Taguchi, "Disordered skyrmion phase stabilized by magnetic frustration in a chiral magnet," Science Advances, vol. 4, sep 2018.

[71] L. J. Bannenberg, F. Weber, A. J. E. Lefering, T. Wolf, and C. Pappas, "Magnetization and ac susceptibility study of the cubic chiral magnet $Mn_{1-x}Fe_xSi$," Physical Review B, vol. 98, nov 2018.

[72] Y. Kousaka, N. Ikeda, T. Ogura, T. Yoshii, J. Akimitsu, K. Ohishi, J. ichi Suzuki, H. Hiraka, M. Miyagawa, S. Nishihara, K. Inoue, and J. ichiro Kishine, "Chiral Magnetic Soliton Lattice in MnSi," in Proceedings of the International Symposium on Science Explored by Ultra Slow Muon (USM2013), Journal of the Physical Society of Japan, mar 2014.

[73] C. D. Dewhurst, "D33—a third small-angle neutron scattering instrument at the Institut Laue Langevin," Measurement Science and Technology, vol. 19, p. 034007, jan 2008.

[74] C. D. Dewhurst, "Graphical reduction and analysis small-angle neutron scattering program: *GRASP*," Journal of Applied Crystallography, vol. 56, pp. 1595–1609, sep 2023.

[75] S. ichi Takata, J. ichi Suzuki, T. Shinohara, T. Oku, T. Tominaga, K. Ohishi, H. Iwase, T. Nakatani, Y. Inamura, T. Ito, K. Suzuya, K. Aizawa, M. Arai, T. Otomo, and M. Sugiyama, "The Design and q Resolution of the Small and Wide Angle Neutron Scattering Instrument (TAIKAN) in J-PARC," in Proceedings of the 2nd International Symposium on Science at J-PARC — Unlocking the Mysteries of Life, Matter and the Universe —, Journal of the Physical Society of Japan, sep 2015.

[76] Y. Inamura, T. Nakatani, J. Suzuki, and T. Otomo, "Development Status of Software "Utsusemi" for Chopper Spectrometers at MLF, J-PARC," Journal of the Physical Society of Japan, vol. 82, p. SA031, jan 2013.

[77] A. Bauer, M. Garst, and C. Pfleiderer, "Specific Heat of the Skyrmion Lattice Phase and Field-Induced Tricritical Point in MnSi," Physical Review Letters, vol. 110, apr 2013.

[78] S. V. Grigoriev, S. V. Maleyev, A. I. Okorokov, Y. O. Chetverikov, and H. Eckerlebe, "Field-induced reorientation of the spin helix in MnSi near T_c," Physical Review B, vol. 73, jun 2006.

[79] T. Sakakibara, H. Mollymoto, and M. Date, "Magnetization and Magnetoresistance of MnSi. II," Journal of the Physical Society of Japan, vol. 51, pp. 2439–2445, aug 1982.

[80] S. A. Brazovskii, "Phase transition of an isotropic system to a nonuniform state," Sov. Phys. - JETP, vol. 41, pp. 85–89, 1975.

[81] A. Bauer and C. Pfleiderer, "Magnetic phase diagram of MnSi inferred from magnetization and ac susceptibility," Physical Review B, vol. 85, jun 2012.

[82] K. Tsuruta, M. Mito, H. Deguchi, J. Kishine, Y. Kousaka, J. Akimitsu, and K. Inoue, "Nonlinear magnetic responses at the phase boundaries around helimagnetic and skyrmion lattice phases in MnSi: Evaluation of robustness of noncollinear spin texture," Physical Review B, vol. 97, mar 2018.

[83] A. Bauer, A. Chacon, M. Wagner, M. Halder, R. Georgii, A. Rosch, C. Pfleiderer, and M. Garst, "Symmetry breaking, slow relaxation dynamics, and topological defects at the field-induced helix reorientation in MnSi," Physical Review B, vol. 95, jan 2017.

[84] J. Kindervater, T. Adams, A. Bauer, F. X. Haslbeck, A. Chacon, S. Mühlbauer, F. Jonietz, A. Neubauer, U. Gasser, G. Nagy, N. Martin, W. Häußler, R. Georgii, M. Garst, and C. Pfleiderer, "Evolution of magnetocrystalline anisotropies in $Mn_{1-x}Fe_xSi$ and $Mn_{1-x}Co_xSi$ as inferred from small-angle neutron scattering and bulk properties," Physical Review B, vol. 101, Mar. 2020.

[85] A. Amato, P. Dalmas de Réotier, D. Andreica, A. Yaouanc, A. Suter, G. Lapertot, I. M. Pop, E. Morenzoni, P. Bonfà, F. Bernardini, and R. De Renzi, "Understanding the μSR spectra of MnSi without magnetic polarons," Physical Review B, vol. 89, May 2014.

[86] P. Dalmas de Réotier, A. Yaouanc, A. Amato, A. Maisuradze, D. Andreica, B. Roessli, T. Goko, R. Scheuermann, and G. Lapertot, "On the Robustness of the MnSi Magnetic Structure Determined by Muon Spin Rotation," Quantum Beam Science, vol. 2, p. 19, Sept. 2018.

[87] P. Dalmas de Réotier, A. Maisuradze, A. Yaouanc, B. Roessli, A. Amato, D. Andreica, and G. Lapertot, "Determination of the zero-field magnetic structure of the helimagnet MnSi at low temperature," Physical Review B, vol. 93, Apr. 2016.

[88] P. D. de Réotier, A. Maisuradze, A. Yaouanc, B. Roessli, A. Amato, D. Andreica, and G. Lapertot, "Unconventional magnetic order in the conical state of MnSi," Physical Review B, vol. 95, may 2017.

[89] R. S. Hayano, Y. J. Uemura, J. Imazato, N. Nishida, K. Nagamine, T. Yamazaki, Y. Ishikawa, and H. Yasuoka, "Spin Fluctuations of Itinerant Electrons in MnSi Studied by Muon Spin Rotation and Relaxation," Journal of the Physical Society of Japan, vol. 49, pp. 1773–1783, Nov. 1980.

[90] R. Kadono, T. Matsuzaki, T. Yamazaki, S. R. Kreitzman, and J. H. Brewer, "Spin dynamics of the itinerant helimagnet MnSi studied by positive muon spin relaxation," Physical Review B, vol. 42, pp. 6515–6522, Oct. 1990.

[91] I. M. Gat-Malureanu, A. Fukaya, M. I. Larkin, A. J. Millis, P. L. Russo, A. T. Savici, Y. J. Uemura, P. P. Kyriakou, G. M. Luke, C. R. Wiebe, Y. V. Sushko, R. H. Heffner, D. E. MacLaughlin, D. Andreica, and G. M. Kalvius, "Field Dependence of the Muon Spin Relaxation Rate in MnSi," Physical Review Letters, vol. 90, Apr. 2003.

[92] A. Yaouanc, P. D. d. Réotier, P. C. M. Gubbens, S. Sakarya, G. Lapertot, A. D. Hillier, and P. J. C. King, "Testing the self-consistent renormalization theory for the description of the spin-fluctuation modes of MnSi at ambient pressure," Journal of Physics: Condensed Matter, vol. 17, p. L129–L135, Mar. 2005.

[93] B. J. Sternlieb, G. M. Luke, Y. J. Uemura, T. M. Riseman, J. H. Brewer, P. M. Gehring, K. Yamada, Y. Hidaka, T. Murakami, T. R. Thurston, and R. J. Birgeneau, "Muon-spin-relaxation and neutron-scattering studies of magnetism in single-crystal $La_{1.94}Sr_{0.06}CuO_4$," Physical Review B, vol. 41, pp. 8866–8871, May 1990.

[94] J. E. Sonier, R. F. Kiefl, J. H. Brewer, J. Chakhalian, S. R. Dunsiger, W. A. MacFarlane, R. I. Miller, A. Wong, G. M. Luke, and J. W. Brill, "Muon-Spin Rotation Measurements of the Magnetic Field Dependence of the Vortex-Core Radius and Magnetic Penetration Depth in $NbSe_2$," Physical Review Letters, vol. 79, pp. 1742–1745, Sept. 1997.

[95] D. E. MacLaughlin, J. E. Sonier, R. H. Heffner, O. O. Bernal, B.-L. Young, M. S. Rose, G. D. Morris, E. D. Bauer, T. D. Do, and M. B. Maple, "Muon Spin

Relaxation and Isotropic Pairing in Superconducting $PrOS_4Sb_{12}$," Physical Review Letters, vol. 89, Sept. 2002.

[96] S. R. Dunsiger, A. A. Aczel, C. Arguello, H. Dabkowska, A. Dabkowski, M.-H. Du, T. Goko, B. Javanparast, T. Lin, F. L. Ning, H. M. L. Noad, D. J. Singh, T. J. Williams, Y. J. Uemura, M. J. P. Gingras, and G. M. Luke, "Spin Ice: Magnetic Excitations without Monopole Signatures Using Muon Spin Rotation," Physical Review Letters, vol. 107, Nov. 2011.

[97] R. Karl, F. Burri, A. Amato, M. Donegà, S. Gvasaliya, H. Luetkens, E. Morenzoni, and R. Khasanov, "Muon spin rotation study of type-I superconductivity: Elemental β-Sn," Physical Review B, vol. 99, May 2019.

[98] P. K. Biswas, F. N. Rybakov, R. P. Singh, S. Mukherjee, N. Parzyk, G. Balakrishnan, M. R. Lees, C. D. Dewhurst, E. Babaev, A. D. Hillier, and D. M. K. Paul, "Coexistence of type-I and type-II superconductivity signatures in ZrB_{12} probed by muon spin rotation measurements," Physical Review B, vol. 102, Oct. 2020.

[99] A. O. Leonov, C. Pappas, and I. Kézsmárki, "Field and anisotropy driven transformations of spin spirals in cubic skyrmion hosts," Physical Review Research, vol. 2, dec 2020.

[100] K. P. W. Hall and S. H. Curnoe, "Generalized model of MnSi-like spiral magnets," Physical Review B, vol. 104, sep 2021.

[101] A. Suter and B. Wojek, "Musrfit: A Free Platform-Independent Framework for μSR Data Analysis," Physics Procedia, vol. 30, pp. 69–73, 2012.

[102] P. Bonfà, I. J. Onuorah, and R. De Renzi, "Introduction and a Quick Look at MUESR, the Magnetic Structure and mUon Embedding Site Refinement Suite," in Proceedings of the 14th International Conference on Muon Spin Rotation, Relaxation and Resonance (μSR2017), Journal of the Physical Society of Japan, Feb. 2018.

[103] R. Prozorov and V. G. Kogan, "Effective Demagnetizing Factors of Diamagnetic Samples of Various Shapes," Physical Review Applied, vol. 10, July 2018.

[104] K. J. A. Franke, B. M. Huddart, T. J. Hicken, F. Xiao, S. J. Blundell, F. L. Pratt, M. Crisanti, J. A. T. Barker, S. J. Clark, A. Štefančič, M. C. Hatnean, G. Balakrishnan, and T. Lancaster, "Magnetic phases of skyrmion-hosting $GaV_4S_{8-y}Se_y$ ($y = 0, 2, 4, 8$) probed with muon spectroscopy," Physical Review B, vol. 98, Aug. 2018.

[105] A. Štefančič, S. H. Moody, T. J. Hicken, M. T. Birch, G. Balakrishnan, S. A. Barnett, M. Crisanti, J. S. O. Evans, S. J. R. Holt, K. J. A. Franke, P. D. Hatton, B. M. Huddart, M. R. Lees, F. L. Pratt, C. C. Tang, M. N. Wilson, F. Xiao, and T. Lancaster, "Origin of skyrmion lattice phase splitting in Zn-substituted Cu_2OSeO_3," Physical Review Materials, vol. 2, Nov. 2018.

[106] T. J. Hicken, S. J. R. Holt, K. J. A. Franke, Z. Hawkhead, A. Štefančič, M. N. Wilson, M. Gomilšek, B. M. Huddart, S. J. Clark, M. R. Lees, F. L. Pratt, S. J. Blundell, G. Balakrishnan, and T. Lancaster, "Magnetism and Néel skyrmion dynamics in $GaV_4S_{8-y}Se_y$," Physical Review Research, vol. 2, July 2020.

[107] T. J. Hicken, M. N. Wilson, K. J. A. Franke, B. M. Huddart, Z. Hawkhead, M. Gomilšek, S. J. Clark, F. L. Pratt, A. Štefančič, A. E. Hall, M. Ciomaga Hatnean, G. Balakrishnan, and T. Lancaster, "Megahertz dynamics in skyrmion systems probed with muon-spin relaxation," Physical Review B, vol. 103, Jan. 2021.

[108] T. Lancaster, R. C. Williams, I. O. Thomas, F. Xiao, F. L. Pratt, S. J. Blundell, J. C. Loudon, T. Hesjedal, S. J. Clark, P. D. Hatton, M. Ciomaga Hatnean, D. S. Keeble, and G. Balakrishnan, "Transverse field muon-spin rotation signature of the skyrmion-lattice phase in Cu_2OSeO_3," Physical Review B, vol. 91, June 2015.

[109] T. Lancaster, F. Xiao, Z. Salman, I. O. Thomas, S. J. Blundell, F. L. Pratt, S. J. Clark, T. Prokscha, A. Suter, S. L. Zhang, A. A. Baker, and T. Hesjedal, "Transverse field muon-spin rotation measurement of the topological anomaly in a thin film of MnSi," Physical Review B, vol. 93, Apr. 2016.

[110] K. Ohishi, Y. Kousaka, S. Iwasaki, J. Akimitsu, M. Pardo-Sainz, V. Laliena, J. Campo, M. Ohkuma, and M. Mito, "Small Angle Neutron Scattering Study near the Critical Field at Low Temperature in MnSi," in Proceedings of the 3rd J-PARC Symposium (J-PARC2019), Journal of the Physical Society of Japan, mar 2021.

[111] M. Ohkuma, M. Mito, M. Pardo, Y. Kousaka, S. Iwasaki, K. Ohishi, J. Akimitsu, K. Inoue, V. Laliena, and J. Campo, "New magnetic intermediate state, "*B-phase*," in the cubic chiral magnet MnSi," APL Materials, vol. 10, p. 041104, apr 2022.

[112] H. Watanabe, M. Ido, and H. Nakajima, "Electric Field Gradient in $Co_{1-x}M_xSi$ (M=Fe, Ni)," Journal of the Physical Society of Japan, vol. 47, pp. 1816–1820, dec 1979.

[113] K. Shimizu, H. Maruyama, H. Yamazaki, and H. Watanabe, "Effect of Spin Fluctuations on Magnetic Properties and Thermal Expansion in Pseudobinary System $Fe_xCo_{1-x}Si$," Journal of the Physical Society of Japan, vol. 59, pp. 305–318, jan 1990.

[114] V. Jaccarino, G. K. Wertheim, J. H. Wernick, L. R. Walker, and S. Arajs, "Paramagnetic excited state of FeSi," Physical Review, vol. 160, pp. 476–482, aug 1967.

[115] J. Wernick, G. Wertheim, and R. Sherwood, "Magnetic behavior of the monosilicides of the 3*d*-transition elements," Materials Research Bulletin, vol. 7, pp. 1431–1441, dec 1972.

[116] J. Beille, J. Voiron, and M. Roth, "Long period helimagnetism in the cubic B20 $Fe_xCo_{1-x}Si$ and $Co_xMn_{1-x}Si$ alloys," Solid State Communications, vol. 47, pp. 399–402, aug 1983.

[117] M. A. Chernikov, L. Degiorgi, E. Felder, S. Paschen, A. D. Bianchi, H. R. Ott, J. L. Sarrao, Z. Fisk, and D. Mandrus, "Low-temperature transport, optical, magnetic and thermodynamic properties of $Fe_xCo_{1-x}Si$," Physical Review B, vol. 56, pp. 1366–1375, jul 1997.

[118] M. K. Chattopadhyay, S. B. Roy, S. Chaudhary, K. J. Singh, and A. K. Nigam, "Magnetic response of $Fe_xCo_{1-x}Si$ alloys: A detailed study of magnetization and magnetoresistance," Physical Review B, vol. 66, nov 2002.

[119] N. Manyala, Y. Sidis, J. F. DiTusa, G. Aeppli, D. P. Young, and Z. Fisk, "Large anomalous Hall effect in a silicon-based magnetic semiconductor," Nature Materials, vol. 3, pp. 255–262, mar 2004.

[120] Y. Onose, N. Takeshita, C. Terakura, H. Takagi, and Y. Tokura, "Doping dependence of transport properties in $Fe_xCo_{1-x}Si$," Physical Review B, vol. 72, dec 2005.

[121] S. V. Grigoriev, S. V. Maleyev, V. A. Dyadkin, D. Menzel, J. Schoenes, and H. Eckerlebe, "Principal interactions in the magnetic system $Fe_{1-x}Co_xSi$: Magnetic structure and critical temperature by neutron diffraction and SQUID measurements," Physical Review B, vol. 76, sep 2007.

[122] S.-A. Siegfried, E. V. Altynbaev, N. M. Chubova, V. Dyadkin, D. Chernyshov, E. V. Moskvin, D. Menzel, A. Heinemann, A. Schreyer, and S. V. Grigoriev, "Controlling the Dzyaloshinskii-Moriya interaction to alter the chiral link between structure and magnetism for $Fe_xCo_{1-x}Si$," Physical Review B, vol. 91, may 2015.

[123] A. Bauer, M. Garst, and C. Pfleiderer, "History dependence of the magnetic properties of single-crystal $Fe_xCo_{1-x}Si$," Physical Review B, vol. 93, jun 2016.

[124] J. Beille, J. Voiron, F. Towfiq, M. Roth, and Z. Y. Zhang, "Helimagnetic structure of the $Fe_xCo_{1-x}Si$ alloys," Journal of Physics F: Metal Physics, vol. 11, pp. 2153–2160, oct 1981.

[125] S. Grigoriev, N. Chubova, L. Azarova, and O. Utesov, "Transition from spiral to ferromagnetic structure in $Fe_xCo_{1-x}Si$ compounds: Small-angle neutron scattering study," Annals of Physics, vol. 447, p. 169132, dec 2022.

[126] M. Takeda, Y. Endoh, K. Kakurai, Y. Onose, J. Suzuki, and Y. Tokura, "Nematic-to-Smectic Transition of Magnetic Texture in Conical State," Journal of the Physical Society of Japan, vol. 78, p. 093704, sep 2009.

[127] L. J. Bannenberg, K. Kakurai, F. Qian, E. Lelièvre-Berna, C. D. Dewhurst, Y. Onose, Y. Endoh, Y. Tokura, and C. Pappas, "Extended skyrmion lattice scattering and long-time memory in the chiral magnet $Fe_xCo_{1-x}Si$," Physical Review B, vol. 94, sep 2016.

[128] M. Uchida, Y. Onose, Y. Matsui, and Y. Tokura, "Real-Space Observation of Helical Spin Order," Science, vol. 311, pp. 359–361, jan 2006.

[129] K. Ishimoto, Y. Yamaguchi, J. Suzuki, M. Arai, M. Furusaka, and Y. Endoh, "Small-angle neutron diffraction from the helical magnet $Fe_{0.8}Co_{0.2}Si$," Physica B: Condensed Matter, vol. 213-214, pp. 381–383, aug 1995.

[130] S. V. Grigoriev, D. Chernyshov, V. A. Dyadkin, V. Dmitriev, S. V. Maleyev, E. V. Moskvin, D. Menzel, J. Schoenes, and H. Eckerlebe, "Crystal Handedness and Spin Helix Chirality in $Fe_{1-x}Co_xSi$," Physical Review Letters, vol. 102, jan 2009.

[131] K. Ishimoto, H. Yamauchi, Y. Yamaguchi, J. Suzuki, M. Arai, M. Furusaka, and Y. Endoh, "Anomalous region in the magnetic phase diagram of (Fe, Co) Si," Journal of Magnetism and Magnetic Materials, vol. 90-91, pp. 163–165, dec 1990.

[132] H. Watanabe, ichi Tazuke, and H. Nakajima, "Helical Spin Resonance and Magntization Measurement in Itinerant Helimagnet $Fe_xCo_{1-x}Si(0.3 \leq x \leq 0.85)$," Journal of the Physical Society of Japan, vol. 54, pp. 3978–3986, oct 1985.

[133] S. V. Grigoriev, K. A. Pshenichnyi, E. V. Altynbaev, S.-A. Siegfried, A. Heinemann, D. Honnecker, and D. Menzel, "On the Measurement of the Stiffness of Spin Waves in the $Fe_{0.75}Co_{0.25}Si$ Helimagnet by the Small-Angle Neutron Scattering Method," JETP Letters, vol. 107, pp. 640–645, May 2018.

Part II

Role of frustration and disorder in magnetic spinels

Central to our exploration of non-collinear magnetism is the phenomenon of magnetic frustration. This condition emerges when competing magnetic interactions within a lattice cannot be simultaneously satisfied. The result is a highly degenerate ground state, often leading to the suppression of conventional long-range order (LRO), or in some cases, to the adoption of non-collinear spin arrangements that better accommodate the competing interactions. Additionally, magnetic materials often exhibit disorder due to inherent structural irregularities. This disorder disrupts the symmetry and uniformity of the magnetic interactions within the material, providing another pathway to non-collinear magnetic structures. By relaxing the symmetry constraints that normally favor collinear alignments, disorder enables spins to orient in more complex configurations as they interact with the irregularly arranged local environments.

Therefore, the effects of frustration and disorder can be combined to enrich the landscape of possible magnetic configurations, leading to non-collinear and non-trivial spin textures. Spinels, with their versatile crystal structures and the ability to accommodate a wide range of chemical compositions, serve as an ideal platform for these studies. Their inherent geometric frustration, due to the tetrahedral and octahedral coordination of magnetic ions, coupled with the ease of introducing disorder through chemical doping or structural modifications, makes spinels exemplary materials for exploring the rich landscape of non-collinear magnetic phases.

Brief introduction to spinels

Spinels are a large group of compounds having the general formula AB_2X_4 (X = O, S, Se, Te), and are one of the most frequently stabilized structures in complex transition-metal oxides and chalcogenides. With over 200 identified or synthesized spinel compounds listed in references [1, 2], they have long captured the attention of scientists due to their unique structural properties and diverse range of physical phenomena.

Spinel compounds consist of a face-centered cubic (fcc) lattice of the X^{2-} anions, which is stabilized by interstitial cations. Figure II.1(a) displays the spinel structure, highlighting the two types of interstices in such an anion lattice: tetrahedral interstices with four nearest neighbors, forming the AX_4 units, and octahedral interstices with six nearest neighbors, forming the BX_6 units [3]. The A sublattice of the spinel structure forms a diamond lattice (see Fig. II.1(c)), while the B sublattice forms a 3D network of corner-sharing tetrahedra known as the pyrochlore lattice (see Fig. II.1(b)).

The most prevalent type of spinel is known as the "2-3 spinel", represented by the formula $A^{2+}B_2^{3+}X_4^{2-}$, where the quantity of trivalent B^{3+} cations is double that of divalent A^{2+} cations. In the *normal* spinel, A^{2+} cations are located at the A sites, and B^{3+} cations are situated at the B sites. Conversely, in the *inverse* spinel, B^{3+} cations occupy the A sites and the B sites are occupied by both A^{2+} and B^{3+} cations with a 1:1 ratio, as in $B^{3+}(A^{2+}B^{3+})X_4^{2-}$. The choice between normal and inverse spinel structures is decided by the crystal field stabilization energy of the cations occupying the A and B sites. A clear octahedral site preference is observed for ions

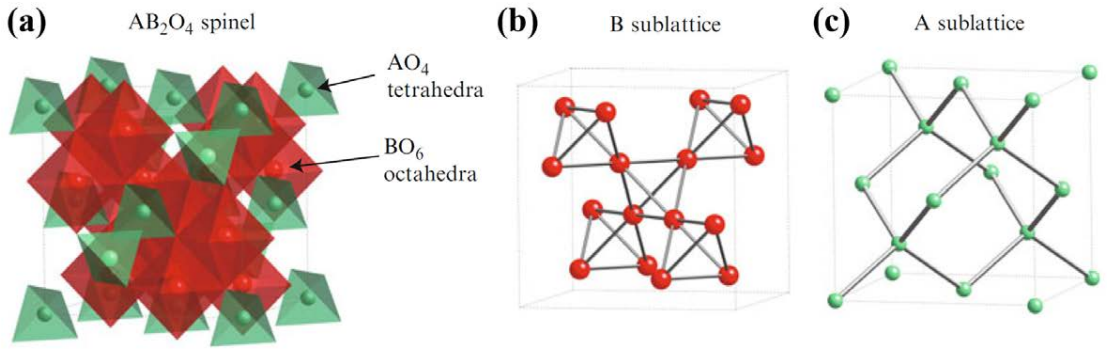

Figure II.1: (a) Spinel structure, emphasizing the two basic structural units of AX_4 tetrahedra and BX_6 octahedra. (b) B sublattice of spinel structure, which defines a pyrochlore lattice. (c) A sublattice (diamond lattice). Figure taken from [4].

with a d^3 configuration, whereas ions with d^0, d^1, d^2, d^4, and d^8 configurations show no site preference. Meanwhile, ions with d^5, d^6, d^7, d^9, and d^{10} configuration exhibit a preference for tetrahedral sites [5, 6]. However, in reality, even in seemingly normal spinel materials, a small level of mixing between the normal and inverse structures can occur, which provides a major source of disorder. Additionally, spinels with monovalent A^+ cations can also be formed, where the B ions are forced to have a mixed-valent situation with a 1:1 ratio of B^{3+} and B^{4+}.

Most of the spinels crystallize in the cubic structure with the space group (SG) $Fd\bar{3}m$, same as the mineral spinel $MgAl_2O_4$ [7, 8]. In the spinel structure, the cations occupy the Wyckoff positions (WP) $8a$ and $16d$, while the anions occupy the WP position $32e$ with atomic coordinates $(u\ u\ u)$. If the origin of the unit cell is taken at the center of symmetry, then for $u = 0.750$ the anions form an exactly cubic close-packed array and define a regular tetrahedron about the $8a$ sites and a regular octahedron about the $16d$ sites. $u > 0.750$ represents a compression of the coordination polyhedron, while $u < 0.750$ corresponds to elongation. It has also been proven that the lattice constants of binary and ternary spinels are a simple and approximately equal function of the effective radii of the octahedral and tetrahedral cations [1].

For further details, exhaustive reviews on spinel compounds can be found in Ref. [4, 9, 10].

Objectives of Part II

In Part II we focus on the rich variety of magnetism exhibited by spinels, which is a result of their complex structure and ability to accommodate both magnetic and non-magnetic cations in both the A and B sublattices. In particular, we explore the combined effect of frustration and disorder on the magnetic properties of two spinel families. Through a thorough investigation of these effects, we seek to reveal the mechanisms that govern non-collinear magnetism in these materials.

Initially, our attention is directed towards the spinel family $Mn_{1-x}Mg_xCr_2O_4$,

starting with the end member at $x = 0$. This well-studied system is notable for its frustration-driven incommensurate spiral states at low temperatures. In Chapter 5, we re-examine the magnetic phases present in $MnCr_2O_4$ with neutron diffraction, determining the symmetry of these magnetic structures through the use of the magnetic superspace group (MSSG) formalism and investigating the conditions under which multiferroicity may arise. This research enhances our comprehension on how frustration induces non-collinear magnetic phases in spinels.

We then address the impact of diamagnetic dilution in modulating magnetic properties. In Chapter 6, we explore how introducing disorder via chemical doping affects the stability and nature of magnetic phases through the $Mn_{1-x}Mg_xCr_2O_4$ series. Employing neutron powder diffraction (NPD), we study the transition from long-range order (LRO) to short-range order (SRO) as disorder increases and its impact on the material's magnetic ground state.

Lastly, in Chapter 7, the interplay of frustration and disorder is evaluated within the spinel family $CuCr_{2-x}Sn_xS_2Se_2$ as a case study. Through structural and magnetic characterization of $CuCr_{2-x}Sn_xSe_2S_2$ solid solutions, we aim to determine how this interaction influences the evolution of magnetic phases, from ferromagnetic (FM) to spin glass-like states. This objective seeks to elucidate the mechanisms behind the magnetic ground state transitions when varying the levels of frustration and chemical substitution.

Chapter 5

New $(\alpha\,\beta\,\gamma)$ incommensurate magnetic phase in the $MnCr_2O_4$ spinel

In this chapter, we revisit the magnetic phases present in the spinel $MnCr_2O_4$ to explore how frustration leads to the emergence of incommensurate magnetic states in this material.

We begin with a brief review of the previous theories and experimental investigations on ACr_2O_4 spinels. Following this, we provide the details on the sample preparation and experiments performed in this study. Subsequently, the results of the magnetization, specific heat and neutron diffraction experiments confirm the existence of three LRO magnetic phases; a ferrimagnetic phase with propagation vector $\vec{k}_{\mathrm{N}} = (0\,0\,0)$, an incommensurate spiral phase with $\vec{k}_{\mathrm{I1}} = (\delta\,\delta\,0)$, and a new one, never reported, with $\vec{k}_{\mathrm{I2}} = (\alpha\,\beta\,\gamma)$. The magnetic superspace group formalism [11–13] is used in this work to determine the global symmetry of the system (both of the magnetic and nuclear contributions) expressed with crystallographic rules. An explanation of the magnetic phase transitions based on experimental and theoretical results is also discussed, as well as the dependence of these transitions with the synthesis conditions. Finally, we explore the multiferroic potential of each magnetic phase and derive the direction of the electric polarization. The chapter concludes by summarizing the principal findings of this investigation.

5.1 Overview of ACr_2O_4 spinels

Chromium-based normal spinel oxides ACr_2O_4 are among the most studied ones in the condensed matter community due to the interplay between their magnetic, electric and structural properties as well as to their potential application to different key industry sectors, such as magnetic refrigerators, super-capacitors, solid oxide fuel cells, lithium-oxygen battery electrodes, catalytic materials and magnetic devices [14–21]. Several physical behaviors have been observed, which include magnetostriction, colossal magnetoresistance, multiferroicity, spin frustration and others [18, 22–37].

In these materials, the local crystal field produced by the oxygen anions O^{2-} splits the $3d$ orbitals of the Cr^{3+} cation into a low-lying t_{2g} triplet and a higher-energy e_g doublet, while the orbitals of the A^{2+} cations are split into a lower e_g doublet and a higher t_{2g} triplet [32, 38, 39]. An scheme of the crystal field effect is depicted in Fig. 5.1.

The main magnetic interaction is the strong J_{CrCr} antiferromagnetic direct exchange between the nearest neighbors cations [32, 38, 40, 41]. This interaction leads to a highly frustrated ground state on the pyrochlore sublattice. This frustration can only be released by the so-called spin-Jahn-Teller effect for compounds with non-magnetic A cations, where lattice distortions induce differences between the exchange coefficients originally uniform for each Cr^{3+}-Cr^{3+} pair. In contrast, if A cations are magnetic, the coupling of Cr^{3+} spins to the A cations spins on the bipartite diamond lattice removes the magnetic frustration, and the system apparently maintains the nearly cubic structure even in its low temperature magnetic state [25, 28, 32, 35, 36, 39, 42–45]. In this case, the Curie-Weiss temperatures (Θ_{CW}) in ACr_2O_4 were found to be significantly higher than the long-range magnetic ordering (LRO) temperature (T_N) for the non-Jahn-Teller magnetic cations (A=Mn, Co) [25, 32]. This ratio $|\Theta_{CW}|/T_N$ measures the degree of magnetic frustration.

For the cubic spinel systems (AB_2O_4), a theory of the ground state spin configuration was presented by Lyons, Kaplan, Dwight, and Menyuk (LKDM) almost 60 years ago [46] describing complex magnetic orders. In this theory, the degree of magnetic frustration is represented by the parameter $u = 4J_{BB}S_B/3J_{AB}S_A$, where J_{BB}, J_{AB} are the nearest-neighbor exchange interactions between spins S_B and S_A on the A and B sites. The possible values of u describe different magnetic structures, ranging from a Néel collinear configuration for $u \leq u_0 = 8/9$, to a LRO spiral structure, which is locally stable for $u_0 < u < u" \approx 1.298$, but unstable if $u > u"$. In particular, for $MnCr_2O_4$, where the A^{2+} ions are Mn^{2+} (S=5/2), the values reported for u are 1.6 [42] and 1.5 [25]. However, the importance of the J_{AA} exchange interaction in determining the spiral order has also been highlighted [32, 38, 40, 47, 48], since the LKDM theory does not take it into account.

Neutron diffraction studies reported that $MnCr_2O_4$ shows a ferrimagnetic (FIM) LRO, with an easy axis parallel to the $\langle 1\bar{1}0\rangle$ direction, below $T_N \sim 41$ K. When the

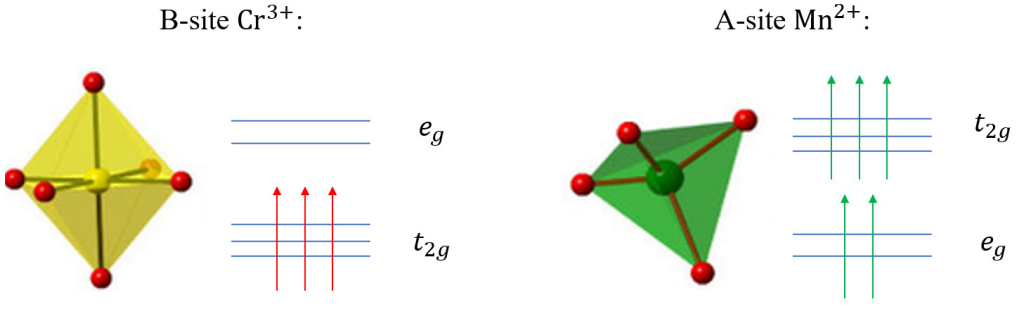

Figure 5.1: Effect of the crystal field on the $3d$ orbitals of: Cr^{3+} (yellow) in an octahedral B site (left), and Mn^{2+} (green) in a tetrahedral A site (right). The anions are marked by red spheres.

temperature decreases below $T_I \sim 18$ K, this ferrimagnetic phase coexists with a spiral short-range order (SRO) given by a propagation vector parallel to the $\langle 110 \rangle$ direction [25, 42, 47, 49]. Electron paramagnetic resonance (EPR) experiments were also compatible with the neutron scattering experiments [32, 50]. However dielectric measurements, in addition to the anomalies found at T_N and T_I in other reports, showed signatures of a lock-in temperature at $T_F \sim 14$ K [51].

Recently, Lin *et al.* [45] with magneto-electric, heat capacity and Raman spectroscopy studies on $MnCr_2O_4$ claimed for the existence of a first order magnetic phase transition from an incommensurate to commensurate state below $T_F \sim 17$ K anticipating that the oxygen content could be a key factor determining the magnetic ground state. These "unconventional" proposed magnetic orders at low temperatures also induce ferroelectricity, as has been reported in [36, 45].

However, there is not a definitive answer yet on the range of the measured incommensurate spiral phase appearing below T_N neither the existence of a new commensurate phase at the lowest temperatures as proposed [45]. Moreover, no systematic study has been reported on the role of the synthesis conditions on the magneto-structural properties in $MnCr_2O_4$. Therefore, in this chapter we reinvestigate the nuclear and magnetic structures of the $MnCr_2O_4$ spinel as a function of the temperature in samples synthesized under different conditions by using magnetization, specific heat and neutron diffraction experiments.

5.2 Sample preparation and experimental details

All samples were provided by a close collaboration with Prof. Yusuke Kousaka. Four different batches of micro-crystalline powder of $MnCr_2O_4$ were prepared under different synthetic conditions. All samples were obtained by the solid phase reaction method, in which powder of MnO and Cr_2O_3 with molar ratio 1:1 were mixed and heated up to 1200 °C for a time, t, under a reductive atmosphere, with Ar and H_2 with ratio 20:1, (samples S1R and S2R) or oxidizing, in atmospheric air conditions, (samples S1A and S2A). The annealing time t was 48 hours for samples S1R and S1A and 24 hours for samples S2R and S2A. Preliminary structural characterization at room temperature (RT) indicated that reductive samples (S1R and S2R) included only $MnCr_2O_4$, while for the oxidizing samples (S1A and S2A) also a minority impurity phase of Cr_2O_3 appeared.

Two additional single crystals of $MnCr_2O_4$ were prepared by a laser-diode-heated floating zone furnace (equipped with five 200 W lasers, Crystal Systems Corporation), shown in Fig. 5.2. To minimize the evaporation of MnO, the crystal growth was performed under 0.6 MPa of Ar atmosphere, and traveling speeds of feed and seed rods were set to be 20–22 mm/h. To compensate for the evaporation, the polycrystalline feed rod was composed of MnO and Cr_2O_3 in the molar ratio of 1.25:1. The first crystal, with a mass of 2.8 mg and labeled SC1R, was employed in the heat capacity and some magnetization measurements, while the second crystal, labeled SC2, was used for single-crystal neutron diffraction experiments.

The specific heat of SC1R at zero field and the magnetic properties of all the samples, were measured, respectively, in a physical properties measurement system

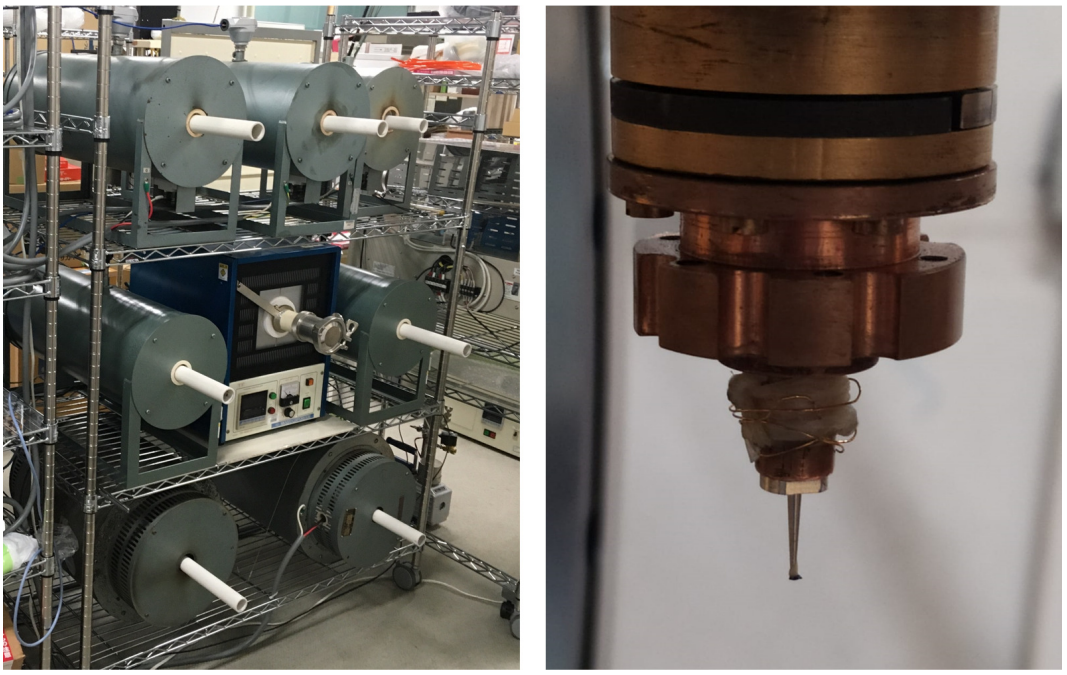

Figure 5.2: Left: laser-diode-heated floating zone furnace used in the synthesis of $MnCr_2O_4$ single crystals. Right: Sample SC2 mounted in the Eulerian cradle of the four-circle single-crystal diffractometer D9.

(PPMS-9T) and a magnetic properties measurement system (MPMS-XL5), both manufactured by Quantum Design.

NPD experiments in S1R were performed at different temperatures (1.6 K $\leq T \leq$ 300 K), on the two-axis spectrometer G.4.1, installed at the cold neutron guide G4 of the Laboratoire Léon Brillouin in Saclay, France. The wavelength of the incident neutrons was fixed at $\lambda = 2.419$ Å. A pyrolytic graphite filter efficiently eliminated higher-order contamination. The diffractograms were collected in an angular range from $5.0° \leq 2\theta \leq 85°$. For S1A, S2R and S2A samples the NPD experiments were performed at different temperatures (5 K $\leq T \leq$ 300 K) on the High Intensity Total Diffractometer NOVA, installed at the thermal guide BL21 of the Materials and Life Facility (MLF) in Tokai, Japan. We focus our analysis on the data set corresponding to the bank at $2\theta = 90°$, at which it is possible to observe the magnetic satellite peaks with the highest resolution possible. Additional measurements in S1R and S1A were also performed at S-HRPD (Super High Resolution Powder Diffractometer), installed at the thermal guide BL08 of MLF.

The measurements for SC2 were performed at the four-circle single-crystal diffractometer D9 in the Institut Laue Langevin (ILL) in Grenoble, France. The neutron beam wavelength was fixed to $\lambda = 0.8352$ Å by a Cu crystal in transmission geometry using the (220) planes. The incident neutron beam was collimated to a diameter of 3 mm. The crystal, a cylinder of 5 mm diameter and 5 mm height, was glued on top of an Al pin (see right side of Fig. 5.2). The pin was then mounted in the Eulerian cradle and cooled down to 10.5 K with a 4-circle He-flow cryostat. The evolution of 25 ω-scans of both nuclear and magnetic reflections was followed as the

temperature was decreased from 300 K to 10.5 K.

The Rietveld analysis of the diffraction data (explained in Appendix A) was performed with the help of the FullProf Suite [52]. Different tools, which include the ISODISTORT Suite [53, 54] and several utilities within the Bilbao Crystallographic Server [55–58], were also employed for the analysis of the magnetic symmetry (explained in Appendix B).

5.3 Results

5.3.1 Magnetization and heat capacity experiments

Magnetization versus temperature measurements have been done for all the four samples under the zero field cooling (ZFC) and field cooling (FC) modes with applied magnetic field $B = 0.02$ T , as it is depicted in Fig. 5.3. In all cases a sudden increase in the magnetization as the temperature decreases is observed at around $T_N = 41$ K,

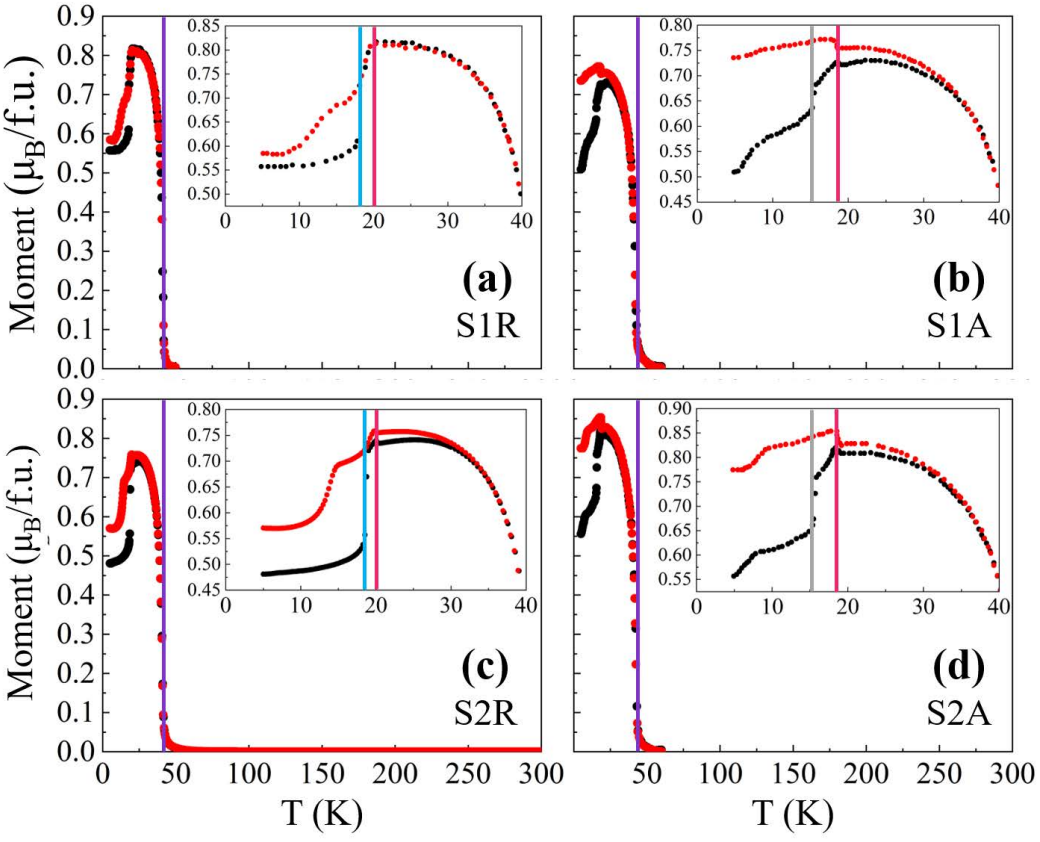

Figure 5.3: Temperature dependence of the magnetization with an applied magnetic field $B = 0.02$ T measured after zero field cooling (ZFC) (black dots) and field cooling (FC) (red dots) procedures for samples S1R (a), S1A (b), S2R (c) and S2A (d). T_N is showed with a purple line, while T_{I1}, T_{I2} and T_L are showed with blue, pink and grey lines in the inserts.

indicating a transition from the paramagnetic (PM) to a FIM state. The transition temperature T_N for each sample is shown in Fig. 5.3 with a purple vertical line.

In S1R and S2R two anomalies at $T_{I1} \approx 20$ K and $T_{I2} \approx 18$ K are observed (see the insert in Fig. 5.3 (a) and (c)). The magnetization curves for S1A and S2A show also two anomalies at lower temperatures at $T_{I1} \approx 19$ K and $T_L \approx 16$ K, this one more visible in the ZFC curves. T_{I1}, T_{I2} and T_L are showed in the insert of Fig. 5.3 with vertical blue, pink and grey lines.

The inverse susceptibility at high temperatures was fitted to a characteristic expression for ferrimagnetic ordering [32, 59, 60], given by:

$$\frac{1}{\chi} = \frac{T - \Theta_{CW}}{C} - \frac{\eta}{T - \theta_h}, \tag{5.1}$$

where C is the Curie constant, Θ_{CW} is the Curie-Weiss temperature. The first term is the high-T asymptote that has a Curie-Weiss form, and the second term is the hyperbolic low-T asymptote in which η and θ_h are functions of the molecular field coefficients defining the interactions between the A and B sub-lattices. The fitted $\chi^{-1}(T)$ for S2R by Eq.(5.1) gives the values $C = 7.79(3)$ emu·K/mol, $\Theta_{CW} = -427(3)$ K, $\eta = 1707(16)$ mol·K/emu, and $\theta_h = 26.8(2)$ K. The effective magnetic moment is determined to be $\mu_{eff} \sim 7.89(3)\,\mu_B$ ($\mu_{eff} = \mu_B\sqrt{3k_BC/N_A}$), which is close to the theoretical value ($\mu_{theo} = 8.04\,\mu_B$) expected for high-spin Cr^{3+} (S = 3/2) and Mn^{2+} (S = 5/2). The ratio of $|\Theta_{CW}|/T_N \sim 10$ indicates a significant magnetic frustration due to competing J_{CrCr}, J_{MnMn}, and J_{MnCr} exchange interactions at low temperatures.

Following the same analysis as was carried out by Winkler *et al.* [32], we can use

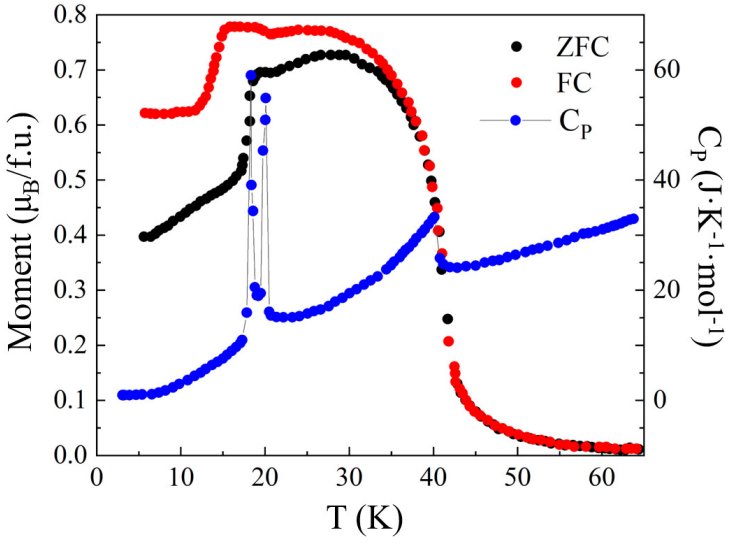

Figure 5.4: Temperature dependence of heat capacity C_P (blue dots) at zero field and ZFC (black dots) and FC (red dots) magnetization curves at $B = 0.02$ T for SC1R sample. The heat capacity curve shows clearly three transitions temperatures $T_N = 40$ K, $T_{I1} = 20$ K and $T_{I2} = 18$ K.

a Weiss mean-field (MF) model and relate the fitted parameters from Eq.(5.1) with the AFM exchange constants between sublattices, thus obtaining: J_{CrCr} = -38.0(5) K, J_{MnMn} = -8.4(2) K and J_{MnCr} = -13.9(2) K. From these values we can calculate the ratio $R \approx J_{\mathrm{CrCr}}/J_{\mathrm{MnCr}} \sim 2.74(4)$, which is slightly different to the reported values $R \approx 3$ [41] and 3.02 [32].

The temperature-dependent magnetization with an applied magnetic field B = 0.02 T under ZFC and FC protocols together with the heat capacity for the SC1R single crystal is depicted in Fig. 5.4. The ZFC and FC magnetization curves follow similar behavior as in its powder counterpart.

However the heat capacity curve $C_{\mathrm{P}}(T)$ shows at T_{N} = 41 K an anomaly, that corresponds well with the FIM transition temperature, followed by two sharp peaks at T_{I1} = 20 K and T_{I2} = 18 K, signaling that two phase transitions take place at these temperatures. Heat capacity curves for $MnCr_2O_4$ synthesized under air conditions reported by other authors [36, 48, 61] only developed a single anomaly at low temperatures. For temperatures below T_{N}, it is noticeable the different behavior of the magnetization and heat capacity curves depending on the atmosphere under which the sample was synthesized.

5.3.2 Neutron powder diffraction experiments

Some representative powder diffraction patterns collected between 1.6 K and 300 K are shown in Fig. 5.5 for all samples. In this section we will focus in a qualitative analysis of these patterns and for that reason only the low-Q part is plotted.

The first remarkable issue is the presence of an impurity phase for the oxidizing samples, S1A and S2A, which is clearly visible as a reflection at Q = 1.74 Å^{-1} detectable at all the temperatures with constant intensity. These reflections are showed in Fig. 5.5 (c) and (d) with an asterisk. In the next section we will see that this impurity correspond with Cr_2O_3 and amounts for around 3%.

In all four samples it is possible to observe an increase in the intensity of the reflection at Q = 2.1 Å^{-1} below $T_{\mathrm{N}} \sim 40$ K. This is related with the phase transition from the paramagnetic state to an ordered magnetic state with propagation vector $\vec{k}_{\mathrm{N}}$=(0 0 0) and it is associated to the ferrimagnetic state already reported. Also a bump in the background around Q = 1.46 Å^{-1} for temperatures in the vicinity of $T_{\mathrm{I1}} \gtrsim 20$ K is observed in all the samples. This bump is related with some magnetic SRO that anticipates the appearance of a set of new satellite reflections, indexed with an incommensurate propagation vector $\vec{k}_{\mathrm{I1}} = (\delta\, \delta\, 0)$, for $T \lesssim T_{\mathrm{I1}} = 20$ K. This propagation vector is in agreement with other NPD experiments done in $MnCr_2O_4$ [25, 42, 47, 49]. In Fig. 5.5 the satellite reflections associated to $\vec{k}_{\mathrm{I1}}$ are signaled with red symbols (asterisk and circles) for each sample.

For sample S1R (Fig. 5.5 (a)), a different set of satellite reflections develops for $T \lesssim T_{\mathrm{I2}}$ = 18 K, being the new incommensurate propagation vector $\vec{k}_{\mathrm{I2}} = (\alpha\, \beta\, \gamma)$. For this sample, at these temperatures, the simultaneous presence of $\vec{k}_{\mathrm{I1}}$ and $\vec{k}_{\mathrm{I2}}$ vectors is not detected. However, for sample S2R (Fig. 5.5 (b)) the same propagation vector $\vec{k}_{\mathrm{I2}}$ appears for $T \lesssim T_{\mathrm{I2}}$ = 18 K but some reminiscence of the reflections coming from $\vec{k}_{\mathrm{I1}}$ still survive until the lowest measured temperatures. Satellite reflections due to the $\vec{k}_{\mathrm{I2}}$ propagation vector are shown with blue symbols

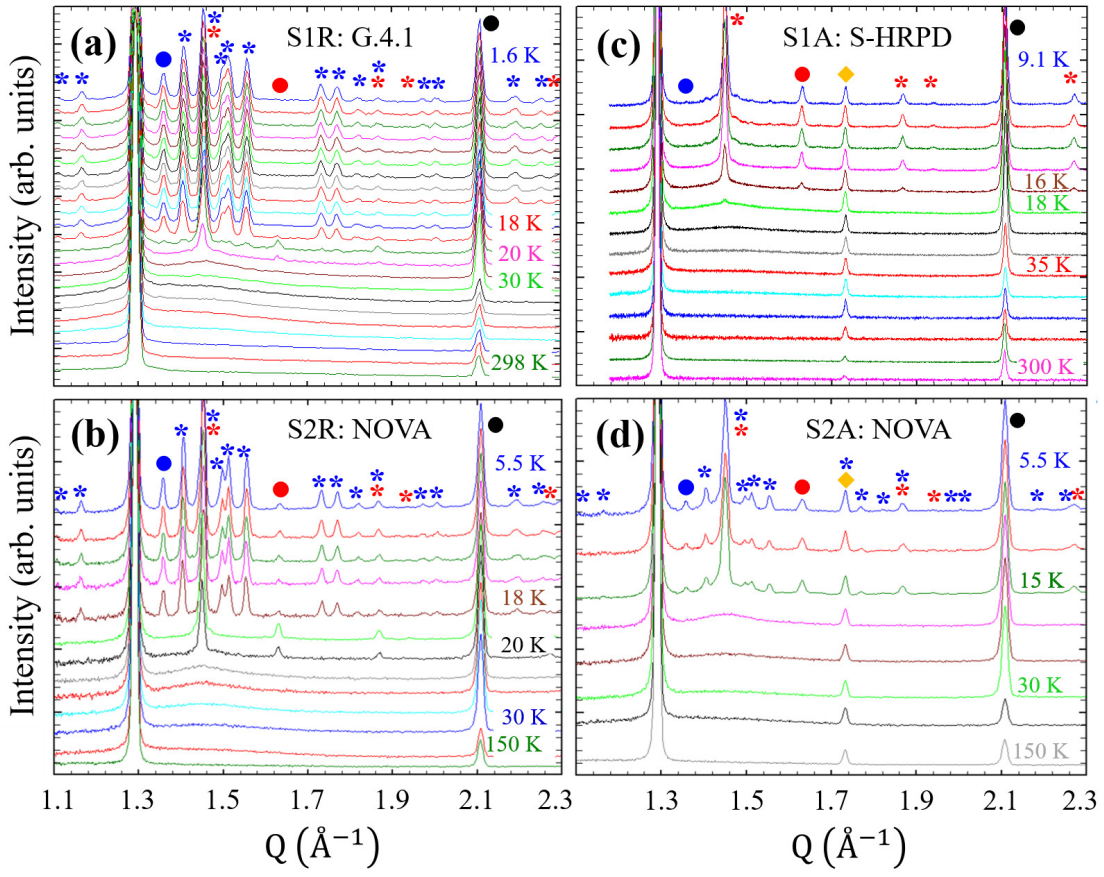

Figure 5.5: Low Q part of diffraction patterns obtained at different temperatures for S1R sample at G.4.1 (a), S2R sample measured at NOVA (b), S1A sample at S-HRPD (c), and S2A sample at NOVA (d). Reflections due to the Cr_2O_3 impurity in (c) and (d) are labeled with a yellow diamond. Satellite reflections due to $\vec{k}_{I1}$ and $\vec{k}_{I2}$ are respectively indicated with red and blue asterisks. The reflections mentioned in Fig. 5.6, $(2\,2\,0)+\vec{k}_N$, $(0\,0\,2)+\vec{k}_{I1}$ and $(1\,\bar{1}\,1)+\vec{k}_{I2}$ are respectively marked with black, red and blue circles.

(asterisks and circles) in Fig. 5.5.

The diffractograms for S1A (Fig. 5.5(c)) collected at $T \lesssim T_{I1} = 19$ K show reflections which can all be indexed with a unique $\vec{k}_{I1}$ till the lowest measured temperature. For the sample S2A (Fig. 5.5 (d)) at $T \lesssim T_{I1} = 19$ K, also both propagation vectors survive but in this sample the minority phase correspond to $\vec{k}_{I2}$.

The evolution with the temperature of the intensity for the $(2\,2\,0)$ nuclear reflection, which also has a magnetic contribution indexed with $\vec{k}_N$ (in black), the satellite $(0\,0\,2)+\vec{k}_{I1}$ (in red) and the satellite $(1\,\bar{1}\,1)+\vec{k}_{I2}$ (in blue) for the different samples is shown in Fig. 5.6. For samples S1R and S2R we clearly observe a sharp decrease in the intensity for the reflection $(2\,2\,0)$ at $T_{I2} = 18$ K, when the new $\vec{k}_{I2}$ propagation vector appears. However, in sample S1A or S2A no sharp decrease in the $(2\,2\,0)$ nuclear reflection intensity is observed because the new $\vec{k}_{I2}$ does not appear, like in

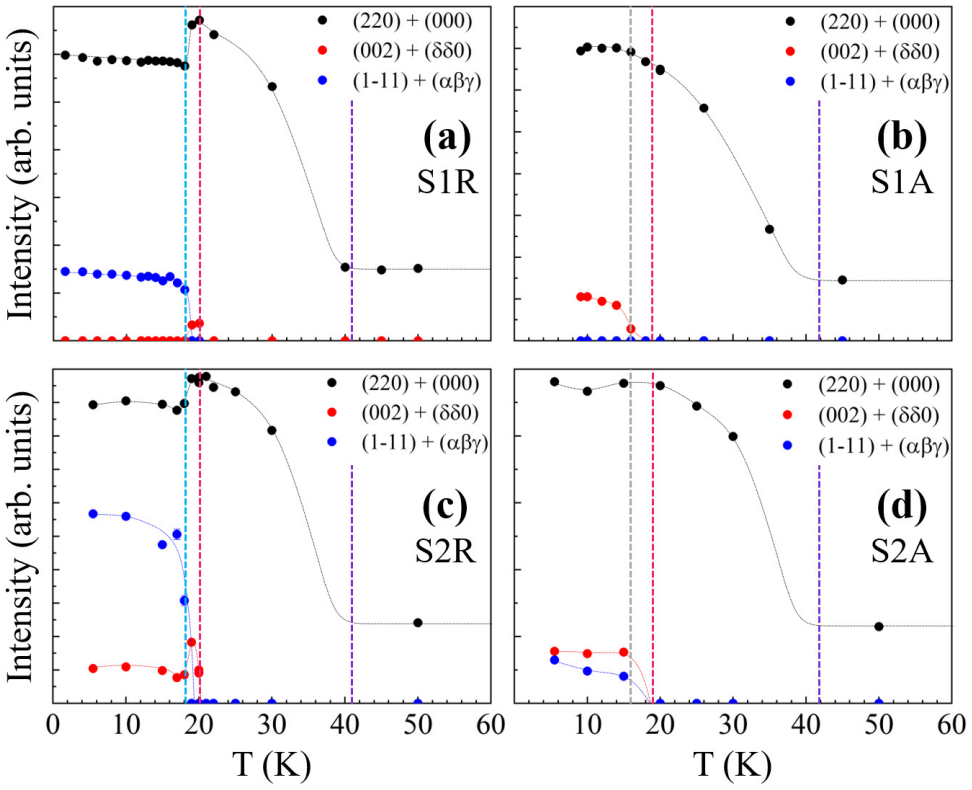

Figure 5.6: Evolution with temperature of the intensity of some magnetic reflections; $(2\,2\,0)+\vec{k}_{\mathrm{N}}$ in black, $(0\,0\,2)+\vec{k}_{\mathrm{I1}}$ in red and $(1\,\bar{1}\,1)+\vec{k}_{\mathrm{I2}}$ in blue for each sample. The transition temperatures determined from the magnetization measurements T_{N}, T_{I1}, T_{I2} and T_{L} are showed with purple, blue, pink and grey lines.

S1A, or its intensity is small, like in S2A, and therefore its relative effect in the high intensity $(2\,2\,0)$ line is imperceptible. The evolution of these intensities together with Fig. 5.5 allows to quantitatively distinguish between the different magnetic phases that are present, as will be discussed later in Sec. 5.5.2.

5.4 Analysis of the neutron powder diffraction experiments

In this section the Rietveld refinement and symmetry analysis of the diffractograms collected for all the samples at different temperatures will be presented in detail.

5.4.1 Paramagnetic Phase

The diffractograms at room temperature for all the samples were refined within the magnetic space group (MSG) $Fd\bar{3}m.1'$ in which the Mn, Cr and the O occupy, respectively, the Wyckoff positions (WP) $8a$, $16d$ and $32e$. Moreover for samples synthesized in oxidizing atmosphere (S1A and S2A) an impurity phase of Cr_2O_3,

with structural parameters given by Ref. [62], was refined to account for some extra peaks. For samples S1R and S2R, the impurity was not detected.

An improvement in the refinements for samples S1A and S2A was made by supposing that there is a relatively small defect, ϵ, of Mn^{2+} replacing the lack of Cr^{3+} on the B-sites. Since they were synthesized under air, we can suppose that a reaction like the following takes place in the synthesis process:

$$MnO + Cr_2O_3 + \frac{3}{2}\epsilon\, O_2 \rightarrow Mn_{1-2\epsilon}\left[Mn_\epsilon Cr_{1-\epsilon}\right]_2 O_4 + \epsilon\, Cr_2O_3$$

where the excess ϵ of O_2 (from the air) produces the impurity phase. No improvement was made by refining the occupancy of the O^{2-} ions, which suggests that no oxygen diffusion process takes place. At these temperatures, the main free structural parameters refined for $MnCr_2O_4$ were the lattice parameter a and the atomic position x of the O atom, which were in good agreement with Ref. [38]. The amount ϵ of Mn detected at the site 16*d* was 0.19(2) and 0.07(5) for, respectively, S1A and S2A. The weight percentage of impurity was 2.94(5)% for S1A and 3(1)% for S2A. All these parameters are listed in Table 5.1 for the sample S1A.

It was considered that the amount of the impurity phase determined in the paramagnetic phase is keep constant in the subsequent refinements done for each sample (S1A and S2A) at lower temperatures. Moreover, when the symmetry decreased, and therefore the WP split, as lowering the temperature, the occupancy ϵ of Mn at the site of the Cr 16*d* has been considered homogeneously shared among the new WP (e.g. 4*b* and 4*d* at $Imm'a'$ at $T = 35$ K).

5.4.2 (0 0 0) - Ferrimagnetic Phase

As the temperature decreases below 298 K, the diffraction patterns show no substantial changes. However, depending on each particular sample, below $\sim$ 41 K a magnetic intensity appear superimposed with some nuclear Bragg reflections indicating the presence of a $\vec{k}_N = (0\ 0\ 0)$ propagation vector. This behavior is common to all the four samples.

As mentioned before, the paramagnetic structure is described by the $Fd\bar{3}m.1'$ MSG, regardless of the impurity presence. Using Irreducible Representations concepts, we can decompose the magnetic representation for each of the WP 8*a* and 16*d* as direct sum of Irreducible Representations (*irreps*) of $Fd\bar{3}m.1'$, which is the little group of $\vec{k}_N = (0\ 0\ 0)$, as follows:

$$\begin{aligned} m\Gamma_{8a} &= 1\mathbf{m\Gamma_4^+(3)} \oplus 1m\Gamma_5^-(3) \\ m\Gamma_{16d} &= 1m\Gamma_2^+(1) \oplus 1m\Gamma_3^+(2) \oplus 2\mathbf{m\Gamma_4^+(3)} \oplus 1m\Gamma_5^+(3) \end{aligned}$$

which shows that the common *irrep* for both sites is $m\Gamma_4^+(3)$, according the notation of the Bilbao Crystallographic Server (BCS) [55–58]. This magnetic order could be described by 9 free parameters, 6 for the Cr site and 3 for the Mn one.

In order to obtain more information about the real symmetry of this magnetic phase we employed the k-SUBGROUPSMAG tool of the BCS which provides with the isotropy subgroups of the parent group $Fd\bar{3}m.1'$ that are compatible with the

Table 5.1: Structural refinement for sample S1A at $T = 298$, 30 and 9.1 K obtained from the patterns collected at S-HRPD. The fifth column (I_1^*) shows the results obtained considering the values that reproduce the parent WP as fixed parameters (i.e. $u = 0.73593(2)$).

	S1A: S-HRPD				
Phase	PM	FIM	I_1	I_1	I_1^*
T (K)	298	20	9.1	9.1	9.1
MSSG	$Fd\bar{3}m.1'$	$Imm'a'$	$Im'a'2(0\ 0\ \gamma)0ss$	$Bb'(\alpha\,\beta\,0)0$	$Bb'(\alpha\,\beta\,0)0$
#	227.129	74.559	46.1.12.4.m245.1	9.1.4.1.m39.1	9.1.4.1.m39.1
$\vec{k}$		(0 0 0)	(δ δ 0)	(δ δ 0)	(δ δ 0)
δ			0.62730(5)	0.62725(5)	0.62725(5)
irreps		$\mathrm{m}\Gamma_4^+(3)$	$\mathrm{m}\Gamma_4^+(3) \oplus \mathrm{m}\Sigma_2(1)$	$\mathrm{m}\Gamma_4^+(3) \oplus \mathrm{m}\Sigma_2(1)$	$\mathrm{m}\Gamma_4^+(3) \oplus \mathrm{m}\Sigma_2(1)$
a (Å)	8.43673(1)	5.96069(1)	5.96062(2)	8.4302(1)	8.4302(1)
b (Å)		5.96069(1)	8.42567(5)	5.9611(1)	5.9611(1)
c (Å)		8.42566(4)	5.96062(2)	8.42591(8)	8.42591(8)
γ (°)	90	90	90	135	135
Mn	$8a(\frac{1}{8}\ \frac{1}{8}\ \frac{1}{8})$	$4e(0\ \frac{1}{4}\ z)$	$4b(\frac{1}{4}\ y\ z)$	$4a(x\ y\ z)$	$4a(x\ y\ z)$
x				-0.02(2)	0.000
y			0.88(1)	0.28(3)	0.250
z		0.128(1)	0.0(1)	0.875(2)	0.875
Cr	$16d(\frac{1}{2}\ \frac{1}{2}\ \frac{1}{2})$	$4b(0\ 0\ \frac{1}{2})$	$4a(0\ 0\ z)$	$4a(x\ y\ z)$	$4a(x\ y\ z)$
x				0.47(2)	0.500
y				0.52(3)	0.500
z			0.5(1)	0.000(4)	0.000
		$4d(\frac{1}{4}\ \frac{3}{4}\ \frac{1}{4})$	$4b(\frac{1}{4}\ y\ z)$	$4a(x\ y\ z)$	$4a(x\ y\ z)$
x				0.23(2)	0.250
y			0.250(6)	0.54(3)	0.500
z			0.2(1)	0.25(1)	0.250
O	$32e(u\ u\ u)$	$8h(0\ y\ z)$	$8c(x\ y\ z)$	$4a(x\ y\ z)$	$4a(x\ y\ z)$
u , x	0.73593(2)		0.527(5)	-0.02(2)	0.000
y		0.476(2)	0.735(4)	0.52(5)	$0.472 = 2u$
z		0.736(1)	0.0(1)	0.268(2)	$0.264 = -u$
				$4a(x\ y\ z)$	$4a(x\ y\ z)$
x				-0.02(2)	0.000
y				0.06(3)	$0.028 = -2u - \frac{1}{2}$
z				0.267(3)	$0.264 = -u$
		$8i(x\ \frac{1}{4}\ z)$	$4b(\frac{1}{4}\ y\ z)$	$4a(x\ y\ z)$	$4a(x\ y\ z)$
x		0.222(2)		0.20(2)	$0.222 = 2u + \frac{3}{4}$
y			0.486(5)	0.51(4)	$0.472 = 2u$
z		0.515(1)	0.8(1)	0.485(4)	$0.486 = u - \frac{1}{4}$
			$4b(\frac{1}{4}\ y\ z)$	$4a(x\ y\ z)$	$4a(x\ y\ z)$
x				0.76(2)	$0.778 = -2u + \frac{1}{4}$
y			0.015(4)	0.1(1)	$0.028 = -2u - \frac{1}{2}$
z			0.7(1)	0.485(5)	$0.486 = u - \frac{1}{4}$
ϵ Mn($16d$)	0.19(2)	0.19	0.19	0.19	0.19
% wgt. Cr_2O_3	2.94(5)	2.94	2.94	2.94	2.94
R_{Bragg}	1.74	4.30	4.11	4.43	4.41

$\mathrm{m}\Gamma_4^+(3)$ as a primary *irrep*. Following this procedure 6 isotropy subgroups appeared ($R\bar{3}m'$, $I4_1/am'd'$, $Imm'a'$, $C2'/c'$, $C2'/m'$ and $P\bar{1}$) each of them with a different order parameter direction. For each one of them we split the parent WP for Mn($8a$),

Table 5.2: Structural and magnetic refinement for sample S1R at $T = 298$, 30, 20 and 1.6 K obtained from the patterns collected at G.4.1. The atomic coordinates, lattice parameters and magnetic moments are referred to the standard setting of the paramagnetic group.
*: the symmetry constraints of the MSSG impose $\vec{M}_s \parallel \langle 1\,1\,0\rangle$ for Mn atoms at $8b(\frac{1}{8}\ \frac{1}{8}\ \frac{1}{8})$ sites and Cr atoms at $8b(\frac{1}{2}\ \frac{1}{2}\ \frac{1}{2})$ sites, while $\vec{M}_s \parallel \langle 1\,\bar{1}\,0\rangle$ for Cr atoms at $8a(\frac{3}{4}\ 0\ \frac{1}{4})$ sites.

	S1R: G.4.1				
Phase	PM	FIM	I_1	I_1	I_2
T (K)	298	30	20	20	1.6
MSSG	$Fd\bar{3}m.1'$	$Imm'a'$	$Im'a'2(0\ 0\ \gamma)0ss$	$Bb'(\alpha\,\beta\,0)0$	$P1(\alpha\,\beta\,\gamma)0$
#	227.129	74.559	46.1.12.4.m245.1	9.1.4.1.m39.1	1.1.1.1.m1.1
$\vec{k}$		(0 0 0)	$(\delta\ \delta\ 0)$	$(\delta\ \delta\ 0)$	$(\alpha\ \beta\ \gamma)$
$\delta\ ,\ \alpha$			0.6233(4)	0.6216(5)	0.6597(1)
β					0.5999(1)
γ					0.1996(2)
irreps		$m\Gamma_4^+(3)$	$m\Gamma_4^+(3) \oplus m\Sigma_2(1)$	$m\Gamma_4^+(3) \oplus m\Sigma_2(1)$	$m\Gamma_4^+(3) \oplus m\mathcal{K}(1)$
a (Å)	8.4355(2)	8.4297(6)	8.4296(5)	8.4299(5)	8.4271(7)
b (Å)		8.4297(6)	8.4296(5)	8.4298(5)	8.4306(2)
c (Å)		8.426(1)	8.4255(9)	8.4253(9)	8.426(7)
$\vec{M}_0$		$\langle 1\ \bar{1}\ 0\rangle$	$\langle 1\ 1\ 0\rangle$	$\langle 1\ \bar{1}\ 0\rangle$	$\langle 1\ 0\ 0\rangle$
$\vec{M}_s$			$\langle 1\ 1\ 0\rangle^*$	$\langle 1\ 1\ 0\rangle$	$\langle 0\ 0\ 1\rangle$
$\vec{M}_c$			$\langle 0\ 0\ 1\rangle$	$\langle 0\ 0\ 1\rangle$	$\langle 0\ 1\ 0\rangle$
Mn	$8a(\frac{1}{8}\ \frac{1}{8}\ \frac{1}{8})$	$8e(\frac{1}{8}\ \frac{1}{8}\ \frac{1}{8})$	$8b(\frac{1}{8}\ \frac{1}{8}\ \frac{1}{8})$	$8a(\frac{1}{8}\ \frac{1}{8}\ \frac{1}{8})$	$4a(\frac{1}{8}\ \frac{1}{8}\ \frac{1}{8})$
$M_0(\mu_B)$		-2.92(3)	-3.37(3)	-3.37(3)	-3.11(4)
$M_s = M_c(\mu_B)$			0.80(8)	0.78(9)	2.8(2)
					$4a(\frac{7}{8}\ \frac{7}{8}\ \frac{7}{8})$
$M_0(\mu_B)$					-3.11(4)
$M_s = M_c(\mu_B)$					2.8(1)
Cr	$16d(\frac{1}{2}\ \frac{1}{2}\ \frac{1}{2})$	$8d(\frac{1}{2}\ \frac{1}{2}\ \frac{1}{2})$	$8b(\frac{1}{2}\ \frac{1}{2}\ \frac{1}{2})$	$8a(\frac{1}{2}\ \frac{1}{2}\ \frac{1}{2})$	$4a(\frac{1}{2}\ \frac{1}{2}\ \frac{1}{2})$
$M_0(\mu_B)$		1.20(8)	1.34(7)	1.40(7)	1.12(7)
$M_s = M_c(\mu_B)$			1.35(5)	1.29(5)	3.43(7)
					$4a(\frac{1}{4}\ \frac{3}{4}\ 0)$
$M_0(\mu_B)$					1.12(7)
$M_s = M_c(\mu_B)$					2.24(7)
		$8b(\frac{3}{4}\ 0\ \frac{1}{4})$	$8a(\frac{3}{4}\ 0\ \frac{1}{4})$	$8a(\frac{3}{4}\ 0\ \frac{1}{4})$	$4a(\frac{3}{4}\ 0\ \frac{1}{4})$
$M_0(\mu_B)$		1.00(4)	1.13(4)	1.09(4)	1.03(6)
$M_s = M_c(\mu_B)$			0.7(1)	0.4(1)	0.66(8)
					$4a(0\ \frac{3}{4}\ \frac{1}{4})$
$M_0(\mu_B)$					1.03(6)
$M_s = M_c(\mu_B)$					1.58(8)
R_{Bragg}	0.696	0.627	1.01	0.976	1.62
R_{Bragg} (Mag.)		1.80	3.87	4.06	3.22

Cr(16*d*) and O(32*e*) accordingly to the lower symmetry of each isotropy subgroup.

We were successful at fitting the data of this phase, in all the samples, with the centrosymmetric magnetic subgroup $Imm'a'$, which allows an order parameter direction along $\langle a\ \bar{a}\ 0\rangle$. In this case the parent Mn(8*a*), Cr(16*d*) and O(32*e*) became Mn(4*e*), Cr(4*b*), Cr(4*d*), O(8*h*) and O(8*i*) in the new MSG.

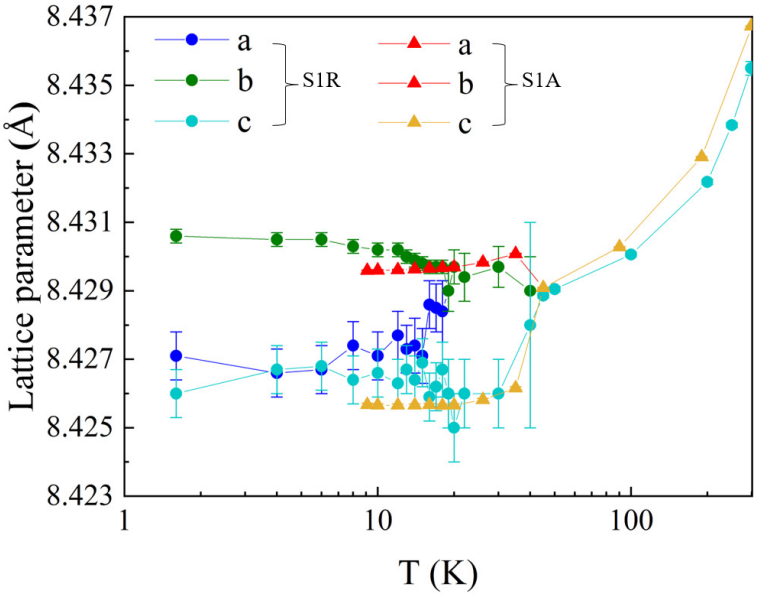

Figure 5.7: Temperature-dependent changes in the lattice parameters for samples S1R and S1A. To enable easy comparison at lower temperature values, the temperature axis is presented on a logarithmic scale. The lattice parameters are referred to the standard setting of the paramagnetic group.

The results of our Rietveld refinement of the S-HRPD diffractograms for S1A at 20 K are listed in the second column of Table 5.1 and show that the tetragonal structure is a quasi cubic one. Fig. 5.7 shows the evolution of the lattice parameters with temperature for samples S1R and S1A. The values are referred to the standard setting of the paramagnetic group. Table 5.1 shows the atomic coordinates in the standard setting of each MSG.

In this magnetic structure the magnetic moments of each Cr and Mn sub-lattices order ferromagnetically along the $\langle 1\ \bar{1}\ 0\rangle$ axis and are coupled antiferromagnetically, in accordance with the results from previous studies [25, 32, 42, 47, 49, 50, 63].

The observed and calculated diffractograms for selected temperatures of S1R, emphasizing the low Q part where magnetic signals are more visible, are depicted in Fig. 5.8 and the numerical values for the magnetic moments obtained from such refinements in sample S1R are also listed in the Table 5.2, where the atomic coordinates, lattice parameters and magnetic moments are referred to the standard setting of the paramagnetic group. For all the samples these values are similar. A schema of the (0 0 0) - FIM phase happening in all the samples can be found in Fig. 5.12(a).

5.4.3 $(\delta\ \delta\ 0)$ - Incommensurate Phase

As decreasing the temperature below T_{I1}=20 K, for the reduced samples, and T_{I1} = 19 K for the oxidized ones, new magnetic satellite reflections, indexed with a incommensurate propagation vector $\vec{k}_{\mathrm{I1}} = (0.6233(4)\, 0.6233(4)\, 0)$, the same for all the samples, appear. However the magnetic contribution at the nuclear Bragg reflections indexed with $\vec{k}_{\mathrm{N}} = (0\,0\,0)$ is still present and it even continues increasing. This can

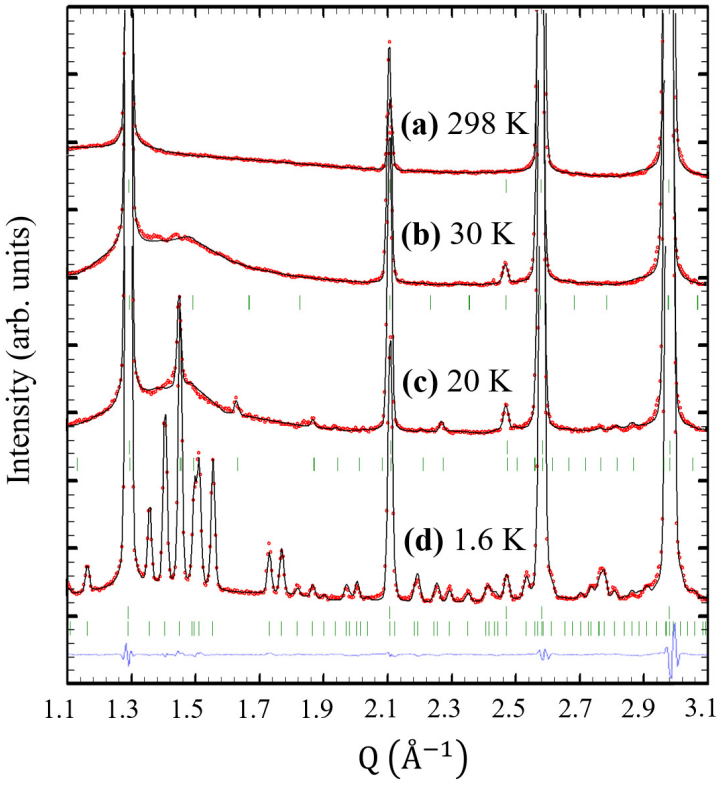

Figure 5.8: Representative Rietveld refinements at selected temperatures for sample S1R. In red are shown the observed points and in back continuous line the calculated pattern with the parameters shown in Table 5.2. The blue continuous line and the green ticks indicate the difference between the observed and calculated profile and the nuclear and satellite peaks generated by the magnetic superspace group, respectively.

be observed in Fig. 5.6.

Thus, the magnetic structure in this phase is described by two *irreps* at least, one for each propagation vector. In this case the decomposition of the magnetic representation of the space group $Fd\bar{3}m.1'$ and $\vec{k}_{I1} = (\delta\ \delta\ 0)$, with $\delta = 0.6233(4)$, for the WP $8a$ and $16d$ shows that the same four 1-d *irreps* are present at both sites according to:

$$\begin{aligned} \mathrm{m}\Gamma_{8a} &= 1\mathrm{m}\Sigma_1(1) \oplus 2\mathrm{m}\Sigma_2(1) \oplus 1\mathrm{m}\Sigma_3(1) \oplus 2\mathrm{m}\Sigma_4(1) \\ \mathrm{m}\Gamma_{16d} &= 2\mathrm{m}\Sigma_1(1) \oplus 4\mathrm{m}\Sigma_2(1) \oplus 3\mathrm{m}\Sigma_3(1) \oplus 3\mathrm{m}\Sigma_4(1) \end{aligned}$$

Therefore, the irreducible representations theory does not help to restrict the number of free parameters to unambiguously describe the magnetic structure.

In this magnetic phase it is not possible to use the Shubnikov magnetic groups, since the propagation vector implies an incommensurate structure, but we have to make use of the magnetic superspace group (MSSG) formalism [11–13]. Several MSSGs are compatible with the combination between $Fd\bar{3}m.1'$ and magnetic distortions for the Mn and Cr atoms, given by 2 superposed *irreps*: $\mathrm{m}\Gamma_4^+(3)$ for the

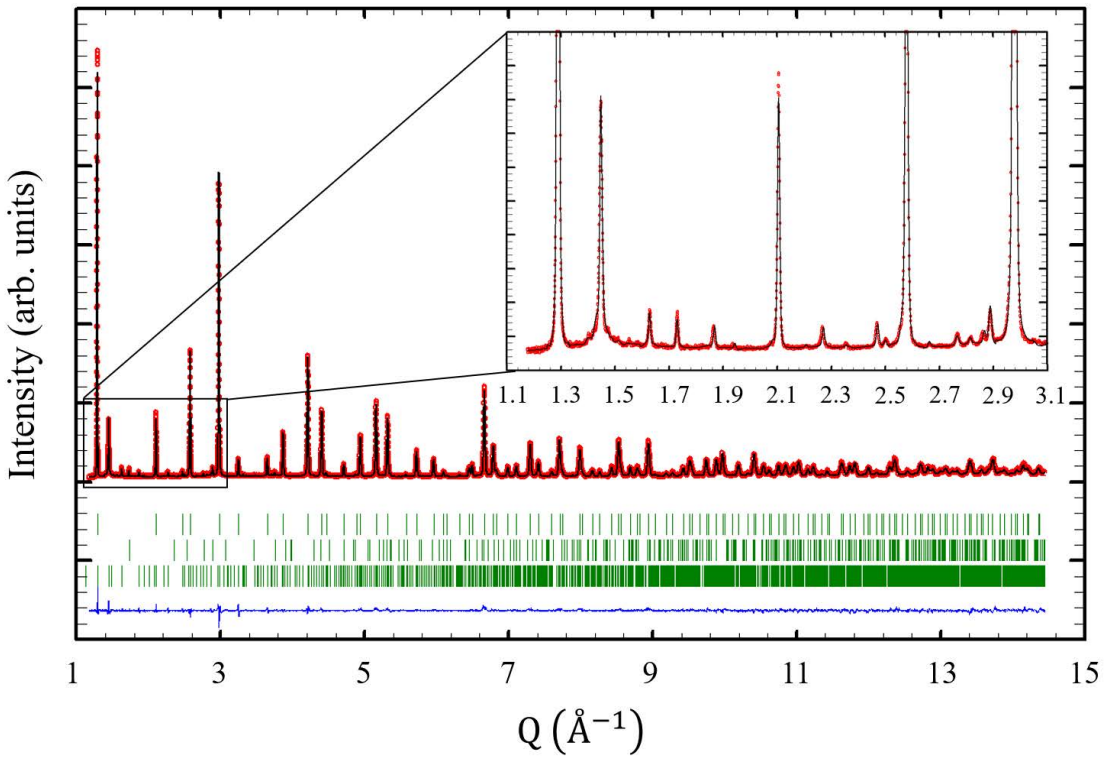

Figure 5.9: High resolution diffractogram collected at $T = 9.1$ K for sample S1A at the instrument S-HRPD. In red are shown the observed points and in back continuous line the calculated pattern with the parameters shown in Table 5.1. The blue continuous line and the green ticks indicate the difference between the observed and calculated profile and the nuclear and satellite peaks generated by the magnetic superspace group, respectively. The insert shows a zoom of the low-Q part, where the scale is the same as in Fig. 5.8.

propagation vector $\vec{k}_{\mathrm{N}} = (0\,0\,0)$ (Γ point) and depending on the irreducible magnetic representation chosen for $\vec{k}_{\mathrm{I1}} = (\delta\,\delta\,0)$, ($\Sigma$ point). From all the possible isotropy subgroups, we focused our analysis on the ones described by the *irrep* $\mathrm{m}\Gamma_4^+(3)$ with the order parameter direction along $\langle a\ \bar{a}\ 0\rangle$.

After a systematic analysis by trial and error, the best fit, depicted in Fig. 5.8(c), was obtained for two non-centrosymmetric MSSGs: $Im'a'2(0\,0\,\gamma)0ss$ and $Bb'(\alpha\,\beta\,0)0$ MSSGs, both described by a combination of the *irreps* $\mathrm{m}\Gamma_4^+(3)$ and $\mathrm{m}\Sigma_2(1)$. The quality of the refinement can be appreciated in Fig. 5.9, where the full diffractogram measured in S-HRPD for S1A at $T = 9.1$ K is shown together with the Rietveld fit and the difference between the calculated and observed profiles.

The $Im'a'2(0\,0\,\gamma)0ss$ MSSG is characterized by a tetragonal nuclear structure, whereas $Bb'(\alpha\,\beta\,0)0$ exhibits a monoclinic structure. The emergence of the I_1-phase is marked by a further splitting of the WP from Mn(4*e*), Cr(4*b*), Cr(4*d*), O(8*h*) and O(8*i*) in FIM-phase to Mn(4*b*), Cr(4*a*), Cr(4*b*), O(8*c*), O(4*b*) and O(4*b*) for the former MSSG; and to Mn(4*a*), Cr(4*a*), Cr(4*a*), O(4*a*), O(4*a*), O(4*a*) and O(4*a*) for the latter one. The results of the Rietveld refinement for S1A at 9.1 K can be found

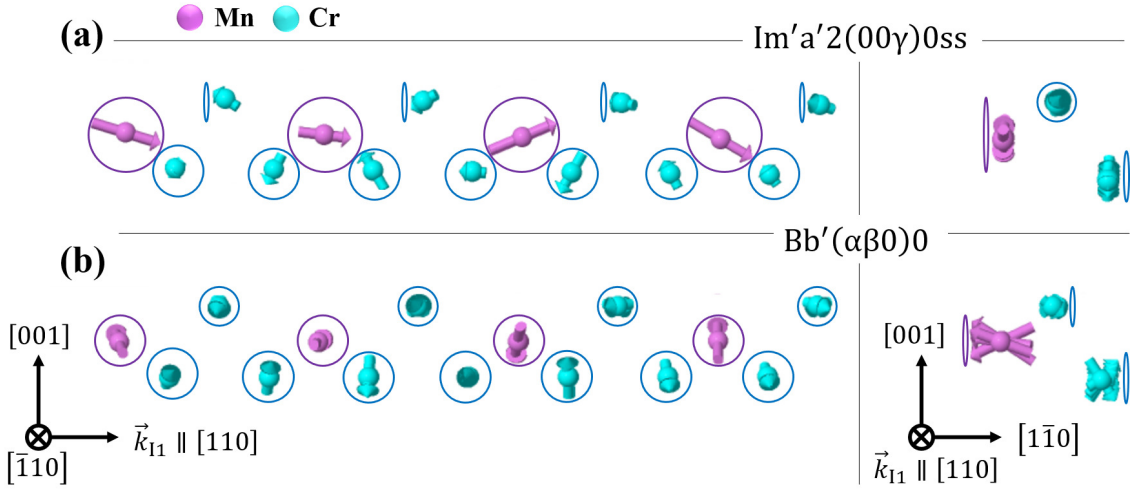

Figure 5.10: Magnetic structure in the $(\delta\ \delta\ 0)$ phase obtained from the refinements considering the symmetry constraints imposed by the MSSGs $Im'a'2(0\,0\,\gamma)0ss$ (a) and $Bb'(\alpha\,\beta\,0)0$ (b). Mn and Cr atoms are displayed in pink and blue colors, respectively.

in the third and fourth column of Table 5.1 for $Im'a'2(0\,0\,\gamma)0ss$ and $Bb'(\alpha\,\beta\,0)0$, respectively. A comparison with the fifth column of Table 5.1, in which the values that reproduce the parent WP were fixed (i.e. $u = 0.73593(2)$), shows that the monoclinic distortions are practically negligible.

However, the magnetic structure greatly differs for each MSSG, as it is shown in Fig. 5.10. For the $Im'a'2(0,0,\gamma)0ss$ MSSG, symmetry constraints impose that the net magnetic moment lies parallel to the propagation vector, i.e. $\vec{M}_{j,0} \parallel \langle 1\,1\,0\rangle$ (see Fig. 5.10(a)). Additionally, the propagation vector $\vec{k}_{I1}$ induces a cycloidal order for all Mn atoms and Cr atoms at $8b(\frac{1}{2}\ \frac{1}{2}\ \frac{1}{2})$ sites, with the modulated components $\vec{M}_{j,c}$ and $\vec{M}_{j,s}$ confined to the plane formed by the $\langle 1\,1\,0\rangle$ and $\langle 0\,0\,1\rangle$ directions. In contrast, Cr atoms at $8a(\frac{3}{4}\ 0\ \frac{1}{4})$ sites adopt a longitudinal conical magnetic structure due to modulations in the plane orthogonal to $\langle 1\,1\,0\rangle$.

Conversely, the $Bb'(\alpha\,\beta\,0)0$ MSSG does not impose any constraint on the magnetic configuration. Nevertheless, the best results from the fitting analysis were achieved for a transverse conical structure for all magnetic atoms (see Fig. 5.10(b)). In this configuration, the net magnetic moment aligns perpendicular to the propagation vector, i.e. $\vec{M}_{j,0} \parallel \langle 1\,\bar{1}\,0\rangle$. Furthermore, the magnetic modulations form cycloids within the plane defined by $\langle 1\,1\,0\rangle$ and $\langle 0\,0\,1\rangle$. For both examined MSSGs, the Cr and Mn sublattices remain coupled antiferromagnetically. The magnetic parameters derived from the refinements of sample S1R for these MSSGs are detailed in the third and fourth column of Table 5.2. The amplitude of the modulation waves $\vec{M}_{j,c}$, $\vec{M}_{j,s}$ was constrained to the same value, since no improvement in the refinement was observed if they acted as independent parameters.

Given the limitations of the refinement of powder diffractograms to correctly identify the magnetic symmetry of the $(\delta\ \delta\ 0)$ - phase, single-crystal neutron diffraction experiments were conducted on sample SC2. Figure 5.11(a) displays the elastic

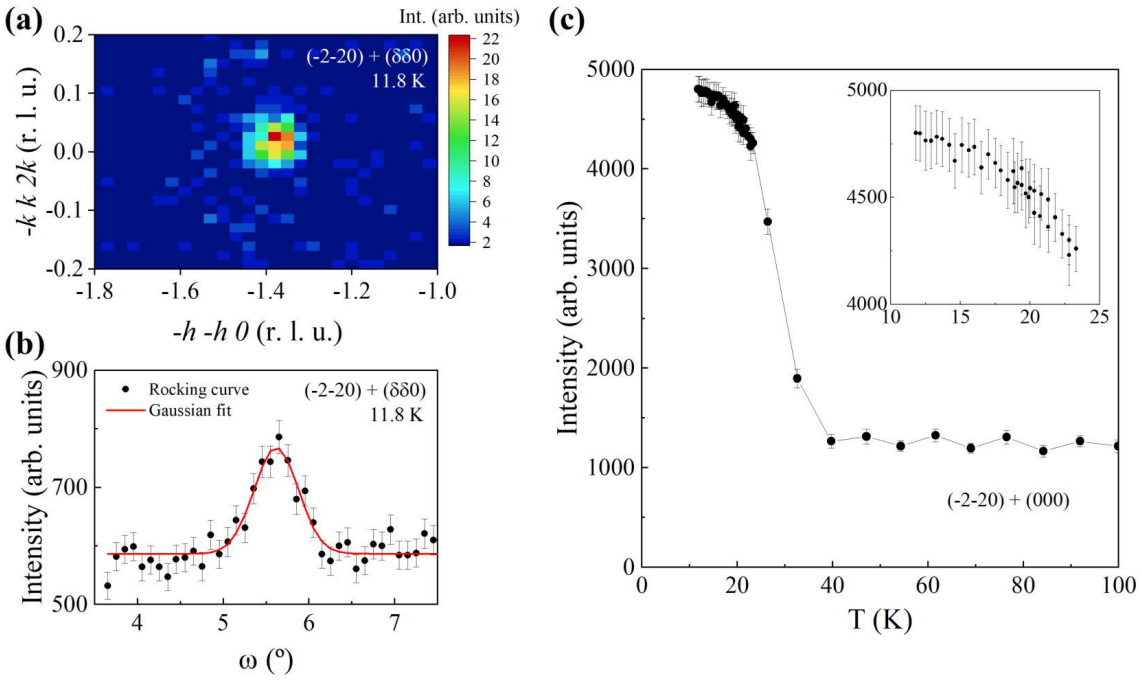

Figure 5.11: Single-crystal neutron scattering data measured on SC2. (a) Elastic scattering intensity in the reciprocal plane (a) and ω-scan (b) around the $(\bar{2}\,\bar{2}\,0)+\vec{k}_{\mathrm{I1}}$ satellite reflection at 11.8 K. The intensity in (a) is plotted in logarithmic scale. The red line in (b) denotes the fit of the rocking curve to a Gaussian curve. (c) Evolution with temperature of the integrated intensity of the $(\bar{2}\,\bar{2}\,0)+\vec{k}_{\mathrm{N}}$ reflection. The inset shows a zoom at low temperatures.

scattering intensity distribution around the $(\bar{2}\,\bar{2}\,0)+\vec{k}_{\mathrm{I1}}$ satellite reflection at 11.8 K. A pronounced peak is observed around $h=-1.4$, $k=0$, confirming the propagation vector $\vec{k}_{\mathrm{I1}}$ to lie along the [1 1 0] direction. Therefore, it is possible to discard equivalent domains with propagation vectors along other diagonals. Integration of the detector area across varying ω values produced the rocking curve depicted in Fig. 5.11(b). The data was well fitted by a Gaussian curve, where the area under the curve yielded the total intensity of the satellite reflection.

A similar procedure was followed for the $(\bar{2}\,\bar{2}\,0)+\vec{k}_{\mathrm{N}}\equiv(\bar{2}\,\bar{2}\,0)$ reflection. Figure 5.11(c) illustrates the temperature-dependent evolution of its integrated intensity. The abrupt jump in intensity below 40 K indicates that $\vec{M}_{j,0}\parallel\langle 1\,\bar{1}\,0\rangle$, as only the component of the magnetic moment perpendicular to the scattering vector contributes to the intensity of the magnetic Bragg peaks. The intensity increase is observed in both the (0 0 0) - FIM phase, in agreement with the magnetic structure described by $Imm'a'$, and the (δ δ 0) - Incommensurate phase (see inset in Fig. 5.11(c)). Thus, only the $Bb'(\alpha\,\beta\,0)0$ MSSG can satisfactorily account for the entirety of the experimental data measured. Such distinction could not be made from the powder data, as the intensity increment of the (2 2 0) reflection observed in Fig. 5.6 can be in fact due to four equivalent reflections: (2 2 0), $(\bar{2}\,\bar{2}\,0)$, $(2\,\bar{2}\,0)$, $(\bar{2}\,2\,0)$.

A schema of the (δ δ 0) - Incommensurate phase happening in all the samples can be found in Fig. 5.12(b).

5.4.4 (α β γ) - Incommensurate Phase

For the sample S1R, a different set of satellite reflections appear below T_{I2}=18 K which are indexed with the incommensurate propagation vector $\vec{k}_{I2}$ = (0.6597(1) 0.5999(1) 0.1996(2)). For this phase the magnetic contribution at the nuclear Bragg reflections ($\vec{k}_N$ = (0 0 0)) is also present, although its intensity slightly decreases, as can be observed in Fig. 5.6. As it was previously mentioned, for S1A no satellite reflections which could be indexed with $\vec{k}_{I2}$ were found down to the lowest temperature measured. Meanwhile, all $\vec{k}_N$, $\vec{k}_{I1}$ and $\vec{k}_{I2}$ vectors are detected below T_{I2}=18 K and T_{I2}=19 K, for, respectively, samples S2R and S2A (see Fig. 5.6). The simultaneous presence of $\vec{k}_{I1}$ and $\vec{k}_{I2}$ in these samples suggests the existence of micro-crystallites with different magnetic ordering.

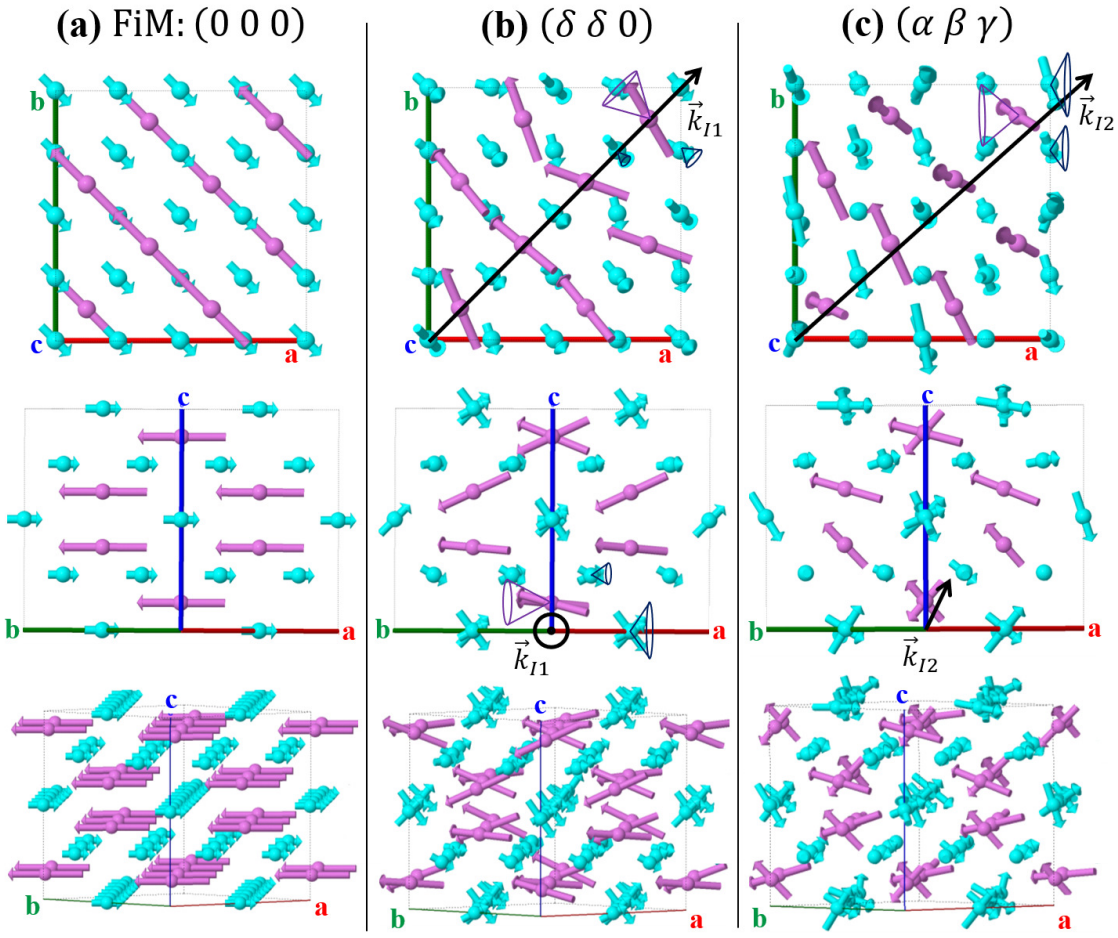

Figure 5.12: Views of the magnetic structures determined for each phase, (a) (0 0 0), (b) (δ δ 0) and (c) (α β γ). Mn and Cr atoms are displayed in pink and blue colors, respectively.

The magnetic structure in this phase is also described by two *irreps*. The decomposition of the magnetic representation of space group $Fd\bar{3}m.1'$ and $\vec{k}_{\mathrm{I2}}$ for the WP $8a$ and $16d$ gives $\mathrm{m}\Gamma_{8a} = 6\mathrm{m}\mathcal{K}(1)$ and $\mathrm{m}\Gamma_{16d} = 12\mathrm{m}\mathcal{K}(1)$, where the 1-d-*irrep* $\mathrm{m}\mathcal{K}(1)$ stands for a general point of the Brillouin Zone. Nevertheless, the *irrep* $\mathrm{m}\mathcal{K}(1)$ does not impose any constraint to the symmetry of the magnetic structure, which can be described by 18 free parameters, 12 for the Cr site and 6 for the Mn one.

Two MSSGs are compatible with the combination between the MSG $Fd\bar{3}m.1'$ and magnetic distortions for the Mn and Cr atoms, given by 2 superposed *irreps*: $m\Gamma_4^+(3)$ for the propagation vector $\vec{k}_{\mathrm{N}}$ (Γ point) and $\mathrm{m}\mathcal{K}(1)$ for $\vec{k}_{\mathrm{I2}} = (\alpha\,\beta\,\gamma)$ ($\mathcal{K}$-General Point). However, only in the case of the non-centrosymmetric $P1(\alpha\,\beta\,\gamma)0$ MSSG a good fit is obtained, as can be observed in Fig. 5.8(d).

At this point the only symmetry operations that remain for the nuclear structure are the centering of the faces, which implies that the WP are further split to $4a$ for all the atoms (see Table 5.2). Although the nuclear space group is triclinic, only the cell parameters were fitted independently, since no improvement in the refinement was observed if the cell angles were allowed to vary from 90°. In fact the deviation of the cell parameters respect the cubic case is quasi imperceptible, as can be read from Table 5.2.

The magnetic structure described by the $P1(\alpha\,\beta\,\gamma)0$ MSSG is also a transverse conical ferrimagnetic structure, but the net magnetic moment $\vec{M}_{j,0}$ is reoriented along $\langle 1\,0\,0\rangle$, while the modulated components $\vec{M}_{j,\mathrm{c}}$ and $\vec{M}_{j,\mathrm{s}}$ of the propagation vector $\vec{k}_{\mathrm{I2}}$ remain in the yz plane. In the same way as in the previous ($\delta\,\delta\,0$) phase, the amplitude of the modulation waves $\vec{M}_{j,\mathrm{c}}$, $\vec{M}_{j,\mathrm{s}}$ was constrained to the same value, since no improvement in the refinement was observed relaxing this constraint. Also the values of $\vec{M}_{j,0}$ were constrained to be the same for the split atoms that belonged to the same WP in the $Imm'a'$ MSG. The nuclear and magnetic parameters obtained from the refinements in sample S1R are listed in the fifth column of Table 5.2.

A schema of the (α β γ) - Incommensurate phase happening in S1R, S2R and S2A samples can be found in Fig. 5.12(c).

5.5 Discussion

5.5.1 Temperature evolution

Fig. 5.13(a), (b) and (c) show the evolution of the magnetic moment modulus M_j, the half-cone angle α and the net magnetic moment $M_{j,0}$, respectively, extracted from the Rietveld analysis of sample S1R. A visual representation of these parameters is depicted inside Fig. 5.13 (b). The number in the name of each j atom follows the order of appearance in Table 5.2.

Below $T_{\mathrm{N}} \sim 41$ K, where the $\vec{k}_{\mathrm{N}} = (0\,0\,0)$ ferrimagnetic phase is developed, M_j and $M_{j,0}$ are equivalent, and an increase in these values followed by a plateau is observed. The split in the WP of Cr is easily observed in Fig. 5.13(a) and (c), since one of the Cr sublattices (B1: Cr1 and Cr2) has a slightly higher value than the other one (B2: Cr3 and Cr4). Below $T_{\mathrm{I1}} = 20$ K, $\vec{M}_{j,0}$ remains at almost the same value as in the previous phase. However, a sudden increase for all the atoms in both the

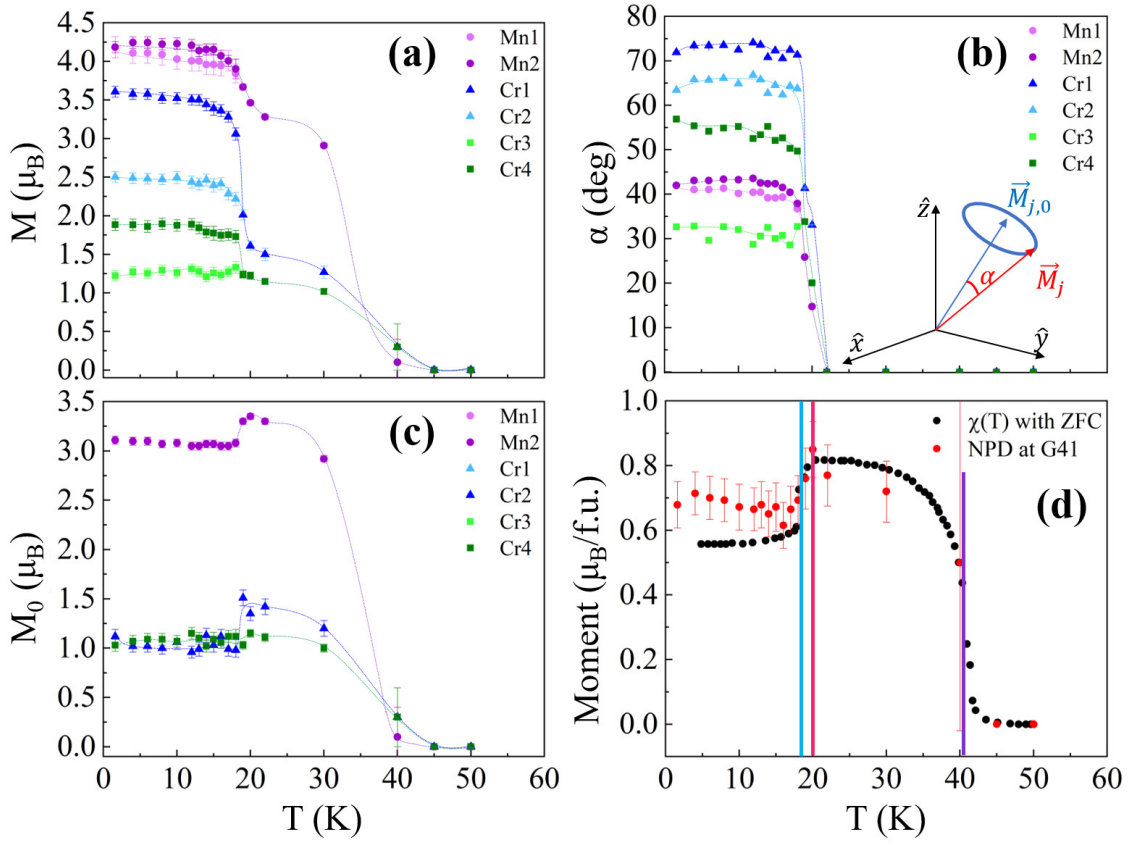

Figure 5.13: Temperature evolution of the parameters defining the magnetic structures: M_j (a), α (b), $M_{j,0}$ (c) extracted from the Rietveld analysis of sample S1R. A comparison between the magnetization obtained from the fits to the NPD data (red) and the susceptibility measured at ZFC (black) is shown in (d).

magnetic moment modulus M_j and the half-cone angle α signals the development of a conical magnetic structure in the $(\delta\,\delta\,0)$ phase (see Fig. 5.13(a) and (b)).

The half-cone angle values obtained at 20 K for the A, B1 and B2 sublattices are, respectively, 26°, 41° and 34°. Previous works reported for the same set of angles the values; 24°, 62°, 14° [42] and 28°, 85°, 11° [25]. However, in those studies the magnetic moment of both Mn^{2+} and Cr^{3+} were fixed to its spin-only value, while in this work they were consider as fitting parameters.

Below $T_{I2} = 18$ K the $(\alpha\,\beta\,\gamma)$ phase is developed, and the Mn are split into 2 different sublattices, which display a nearly identical behavior (see Fig. 5.13(a) and (b)). Meanwhile, the 2 Cr sublattices are further split into 4, and in both cases the split is divided into a sublattice with values for M_j and α that follow the previous tendency (Cr2 and Cr3), and another sublattice with a steep increase for these values (Cr1 and Cr4). As the temperature is decreased, all the sublattices values remain constant down to the lowest temperature measured. The saturation value for the Mn^{2+} is close to the calculated value of 4.3 μ_B [49], while in the B-sublattices none of the Cr^{3+} ions reach its theoretical saturation value of 3.87 μ_B. As it was mentioned before, the values of $\vec{M}_{j,0}$ in the $(\alpha\,\beta\,\gamma)$ phase were constrained to be the same for the

split atoms that belonged to the same WP in the $Imm'a'$ MSG. A small decrease in $\vec{M}_{j,0}$ can be observed in Fig. 5.13(c), in agreement with the evolution of the nuclear intensities observed in Fig. 5.6(a).

By plotting the component of the net magnetic moment $M_{j,0}$ which is parallel to the $\langle 1\,\bar{1}\,0\rangle$ direction, a good agreement is observed between the values obtained from the analysis of the NPD data and the net magnetization calculated from the ZFC susceptibility, which is shown in Fig. 5.13(d).

5.5.2 Synthesis conditions dependence

Taking into account both the results from the magnetization and heat capacity experiments and the analysis of the NPD experiments, a summary of the magnetic phases that are observed in each sample is presented in Fig. 5.14. The differences observed in the transition temperatures of these phases suggest a strong dependence between the magnetic ground state and the atmosphere in which the samples were synthesized. This idea was already pointed out in ref. [45, 64]. In particular, it seems that the synthesis of a sample under an oxidizing atmosphere prevents the full development of the $(\alpha\,\beta\,\gamma)$ phase at the lowest temperatures reached. The annealing time t also plays a role, since for samples S2R and S2A, where this time is smaller, we observe the simultaneous presence of the $(\delta\,\delta\,0)$ and $(\alpha\,\beta\,\gamma)$ phases. From the analysis of the NPD experiments, we can estimate the contribution of each magnetic phase in these samples to be: 22(5)% of $(\delta\,\delta\,0)$ and 78(5)% of $(\alpha\,\beta\,\gamma)$ for

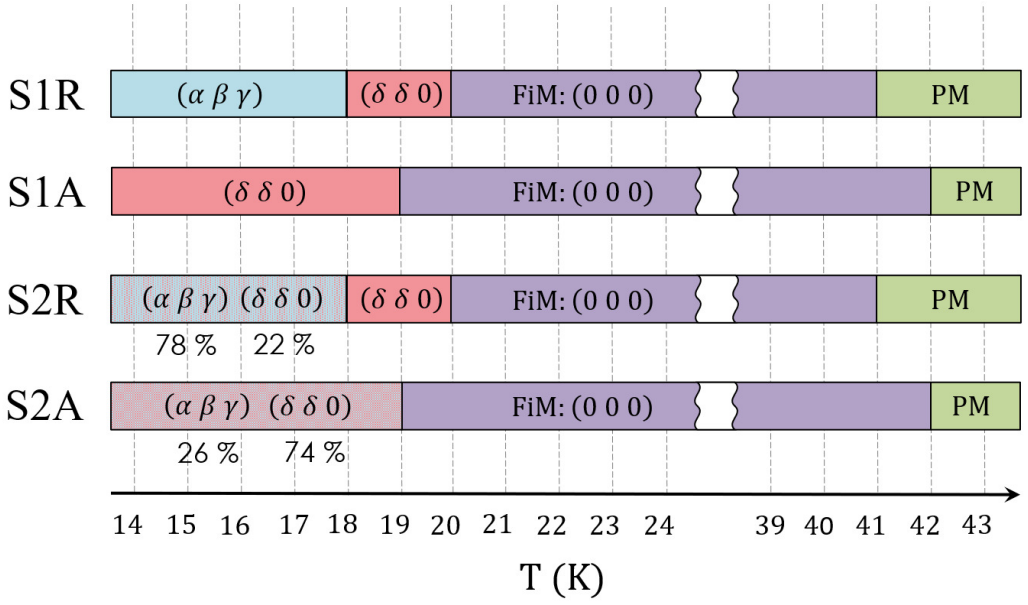

Figure 5.14: Magnetic phases observed for each sample together with their phase transition temperatures. Green: paramagnetic order, purple: (0 0 0) - FIM phase, pink: (δ δ 0) - Incommensurate phase, blue: (α β γ) - Incommensurate phase. For samples S2R and S2A, the percentages of each incommensurate phase present at the lowest temperature measured is given.

S2R, and 74(4)% of $(\delta\,\delta\,0)$ and 26(4)% of $(\alpha\,\beta\,\gamma)$ for S2A.

An explanation for the different magnetic ground states observed can be given in terms of the main exchange interactions competing in this system, which we have derived from the analysis of the magnetization data to follow $|J_{\mathrm{CrCr}}| > |J_{\mathrm{CrMn}}| > |J_{\mathrm{MnMn}}|$. Previous works [32, 40, 65] suggested that the interaction between nearest neighbors in B-sites, J_{CrCr}, results from the competition between a strong antiferromagnetic direct exchange between $d-d$ orbitals and an indirect 90° ferromagnetic interaction mediated by O^{2-}-p orbital. Meanwhile, the coupling between A and B-sites, J_{CrMn}, can be explained by a super-exchange Cr^{3+}-O-Mn^{2+} path. For Cr^{3+} ions, with empty e_g orbitals and half-filled t_{2g} orbitals, the 120° J_{CrMn} interaction is antiferromagnetic and weaker relative to the direct overlapping mechanism of the J_{CrCr} interaction. The interaction between A-sites, J_{MnMn}, can be associated with a super-exchange mechanism mediated also by oxygen anions, which gives rise to a weakly antiferromagnetic interaction.

If the J_{CrCr} interaction is dominated by the antiferromagnetic direct exchange term, then magnetic frustration on the B-sites is produced due to their spatial arrangement (pyrochlore sublattice). This frustration can be partially released through the J_{CrMn} interaction, which prevents the Jahn-Teller distortion [32, 35], in agreement with the almost negligible tetragonal and monoclinic distortions observed in our NPD experiments. The interplay between both interactions is expected to produce the transverse conical structure observed in the $(\delta\,\delta\,0)$ phase. As the temperature is decreased, the small J_{MnMn} interaction plays a role in destabilizing the $(\delta\,\delta\,0)$ magnetic ground state and a new distorted transverse conical structure is developed in the $(\alpha\,\beta\,\gamma)$ phase.

The impact of the synthesis conditions on the magnetic structure can be understood by considering the high dependence of J_{CrCr}, J_{CrMn} and J_{MnMn} on the distances between ions, specially for the Mn-O bonds [32, 36]. In the case of the samples S1A and S2A, a small defect ϵ, of Mn^{2+} is present on the A-sites and an excess ϵ of Mn^{2+} appears at the B-sites. In such case, the J_{MnMn} interaction would be weakened, therefore preserving the magnetic ground state developed in the $(\delta\,\delta\,0)$ phase.

By taking into account the calculated value of the exchange interactions, we can also deduce the parameter $u = 4J_{\mathrm{BB}}S_{\mathrm{B}}/3J_{\mathrm{AB}}S_{\mathrm{A}} \approx 2.2$. Previous neutron diffraction studies obtained $u = 1.6$ [42], 2.1 [49], 1.343 [47] and 1.5 [25]. The wide range of values for this parameter can be due to the different synthesis conditions. Nevertheless, all of them satisfy $u > u" \approx 1.298$, implying an unstable spiral LRO propagating along $\langle 110 \rangle$. Tomiyasu *et al.* [25] proposed that such instability is due to a weak magnetic geometrical frustration causing spiral short-range order. In our case, a value of $u = 2.2$, indicating that the $(\delta\,\delta\,0)$ phase is not the ground state, is in agreement with the appearance of the $(\alpha\,\beta\,\gamma)$ phase at lower temperatures.

Although there has been an extensive research on this material [18, 25, 32, 34, 36, 42, 45, 47–51, 61, 63], it has not been until recently that a new low-temperature phase transition has been proposed [45]. There, an incommensurate spiral spin order to a commensurate one (CSSO) transition is suggested, although no hint on the magnetic structure developed in this CSSO is given. As we have shown in this work, this transition is rather from one incommensurate conical to another, where the latest phase has also a incommensurate propagation vector $\vec{k}_{\mathrm{I2}}$. The aforementioned

sensitivity to the synthesis conditions can give an explanation on why this $(\alpha\,\beta\,\gamma)$ phase has not been reported before, as in previous studies no special precaution was taken regarding the synthesis of this compound under an oxidizing or reductive atmosphere.

It would be interesting to perform a similar systematic study for the $CoCr_2O_4$ spinel, where some studies have reported the existence of an incommensurate conical structure with propagation vector (0.63 0.63 0) below 26 K, and a transition into a commensurate propagation vector (2/3 2/3 0) plus two satellite peaks with propagation (0.035 0 0) and (0 0.035 0) at $\sim$ 14 K [22, 31, 66].

5.5.3 Model of multiferroicity in the incommensurate phases

Previous electric polarization experiments performed in $MnCr_2O_4$ [36, 45] showed that this compound is an improper multiferroic. Those results could be explained by two models, the inverse Dzyaloshinskii-Moriya (DM) [67–69] or the spin current coupling mechanism [70]. In the former model, the spiral magnetic order polarizes an oxygen through the magnetostriction, while in the later one the ferroelectric polarization of the electronic orbitals is induced without the involvement of a spin-lattice interaction. Recently, significant oxygen displacements observed by x-ray powder diffraction suggested that the inverse DM model could be more appropriate to interpret the ferroelectricity observed in ref. [36]. In our results however, the refined structural parameters do not have enough resolution to shed more light into this matter.

Nevertheless, for both models the spontaneous electric polarization is related to the canting of the spins ($\vec{S}_i$ and $\vec{S}_j$) on two neighboring sites (i and j), and can be mathematically expressed by the same expression:

$$\vec{P} \propto \vec{r}_{ij} \times \left(\vec{S}_i \times \vec{S}_j\right) \tag{5.2}$$

where $\vec{r}_{ij}$ represents the vector that connects the i and j sites. This polarization can also be expressed in terms of the propagation vector and the net magnetization $\vec{M}_{j,0}$ as in ref. [28, 31]: $\vec{P} \propto \vec{k} \times \vec{M}_{j,0}$. From this expression, it can be observed that a non-zero value of the electric polarization is present for transverse conical (cycloidal) modulations, where the spin rotation axis is not parallel to the propagation vector.

From the viewpoint of the magnetic symmetry, the non-centrosymmetric $Bb'(\alpha\,\beta\,0)0$ and $P1(\alpha\,\beta\,\gamma)0$ MSSGs have magnetic point groups (m' and 1, respectively) which allow the presence of such transverse conical structures, which implies the existence of multiferroicity in both $(\delta\,\delta\,0)$ and $(\alpha\,\beta\,\gamma)$ phases. Furthermore, from Table 5.2 we can quickly estimate the electric polarization to point along the $\langle 0\,0\,1\rangle$ direction in the $(\delta\,\delta\,0)$ phase, while for the $(\alpha\,\beta\,\gamma)$ phase the spontaneous polarization vector is expected to lie along the $\langle 0\,1\,\bar{3}\rangle$ direction. Such theoretical results are similar to the ones described in [36, 45] for the $(\delta\,\delta\,0)$ phase. However, for the new $(\alpha\,\beta\,\gamma)$ phase our results should be compared with experimental data in order to confirm that the mechanism responsible for the multiferroicity is the same before and after the transition at 18 K.

5.6 Conclusions

The nuclear and magnetic structures of the spinel $MnCr_2O_4$ are reinvestigated as function of the temperature in samples synthesized under different conditions by using magnetization, specific heat and neutron diffraction experiments.

Through these experiments we confirm the existence of three LRO magnetic phases; a FIM with propagation vector $\vec{k}_{\rm N} = (0\,0\,0)$, an incommensurate spiral phase with $\vec{k}_{\rm I1} = (\delta\,\delta\,0)$, and a new one, never reported, with $\vec{k}_{\rm I2} = (\alpha\,\beta\,\gamma)$. The global symmetry of each magnetic phase was determined using the MSSG formalism.

A possible explanation of the different magnetic ground states observed is given based on the competition among the main exchange interactions present in this system. The transition temperatures of the three LRO magnetic phases depend on the oxidizing or reductive atmosphere in which the samples were synthesized, and a possible explanation of these transitions based on experimental and theoretical results is also discussed. Finally, the presence of transverse conical magnetic structures in both $(\delta\,\delta\,0)$ and $(\alpha\,\beta\,\gamma)$ phases allow the existence of multiferroicity. Using the spin current model, we have derived the direction along which the spontaneous electric polarization should lie for each magnetic phase.

Part of the results presented in this chapter have been published in Ref. [71].

Chapter 6

Magnetic dilution effects on the frustration of the spinel family $Mn_{1-x}Mg_xCr_2O_4$

This chapter addresses the impact of diamagnetic dilution in modulating the properties of non-collinear magnetic states in spinels. Specifically, we examine the influence of disorder on the stability and nature of the magnetic phases present in solid solutions of the spinel family $Mn_{1-x}Mg_xCr_2O_4$.

Initially, we recapitulate prior findings within this spinel family. Next, details regarding sample preparation and the neutron powder diffraction experiments conducted in this study are provided. The results reveal a transition from long-range order to short-range order with increased disorder, and an explanation based on how disorder impacts exchange interactions and frustration is given. The key discoveries from our study are encapsulated in the chapter's conclusion.

6.1 Previous results in $Mn_{1-x}Mg_xCr_2O_4$

The end members of the spinel family $Mn_{1-x}Mg_xCr_2O_4$ are systems with a well-known geometrical frustration. As we have shown in the previous chapter, for $x = 0$ the ground state is a complex non-collinear magnetic structure which strongly depends on the synthesis conditions. Meanwhile, for $x = 1$, the onset of long-range magnetic ordering at $T_N \approx 13$ K [72–77] is accompanied by a structural distortion to tetragonal or lower symmetry [76–79] due to spin-lattice coupling [74, 76, 80, 81]. Magnetic Bragg peaks observed below T_N are indexed by several nonequivalent propagation vectors, including $\vec{k}_{L,1} = (\frac{1}{2}\,\frac{1}{2}\,0)$, $\vec{k}_{L,2} = (1\,0\,\frac{1}{2})$ and $\vec{k}_H = (0\,0\,1)$, which appear to vary between different samples, and the associated magnetic structure has not been fully solved [73, 76, 79, 82, 83].

However, less attention has been paid to the intermediate compounds of the family $Mn_{1-x}Mg_xCr_2O_4$, where to the best of our knowledge only Yokobori *et al.* [84] have studied their magnetic properties through susceptibility and single crystal neutron diffraction (SCND) experiments. A magnetic phase diagram $x-T$ was obtained from the magnetic susceptibility data, where it was found that the ferrimagnetic order

temperature T_N rapidly decreases and disappears at $x \sim 0.35$, while the spiral order temperature T_I slowly decreases towards 9 K at $x = 0.90$ and increases again above $x = 0.90$. Additionally, the spiral short-range correlations in $Mn_{0.07}Mg_{0.93}Cr_2O_4$ were studied by SCND. The real-space correlation lengths were estimated to be 12.7 Å and 4.4 Å along parallel and perpendicular to the propagation vector $\vec{k}_I = (\delta\, \delta\, 0)$, respectively, with $\delta = 0.68$. This was corroborated by neutron powder diffraction, in which a broad hump was developed as the temperature was lowered at $k_I = 1.5$ $Å^{-1} \sim \frac{2\pi}{a}|(2-\delta,\, 2-\delta,\, 0)|$. The spatial spin correlation was suggested to be the proper-screw type rather than the cycloid one, which implies the disappearance of the ferroelectricity observed in $MnCr_2O_4$.

Therefore, building on the observations by Yokobori *et al.* and the identified gaps in the study of intermediate compounds, this chapter aims to study the effect of magnetic dilution when substituting Mn^{2+} magnetic cations by Mg^{2+} diamagnetic cations using neutron powder diffraction (NPD).

6.2 Experimental details

Four powder samples of $Mn_{1-x}Mg_xCr_2O_4$ with $x = 0.15$, 0.30, 0.45 and 0.90 were prepared by Prof. Yusuke Kousaka by the solid phase reaction method, in which powder of MnO, MgO and Cr_2O_3 were combined in stoichiometric amounts and heated up to 1200 °C for 24 hours under a reductive atmosphere of Ar and H_2.

For samples with Mg content $x = 0.15$ and 0.90, NPD experiments were performed at different temperatures (1.6 K $\leq T \leq$ 298 K), on the two-axis spectrometer G.4.1, installed at the cold neutron guide G4 of the Laboratoire Léon Brillouin in Saclay, France. The wavelength of the incident neutrons was fixed at $\lambda = 2.423$ Å. A pyrolytic graphite filter efficiently eliminated higher-order contamination. The diffractograms were collected in an angular range from $5.0° \leq 2\theta \leq 85°$.

For samples with Mg content $x = 0.30$ and 0.45, NPD experiments were carried out on the high-flux 2-axis neutron diffractometer D1B of the Institut Laue-Langevin (ILL) in Grenoble, France. The neutron wavelength was fixed at $\lambda = 2.52$ Å, although some neutrons with $\lambda/2 = 1.26$ Å were also detected. This instrument has a detector covering an angular range of 128° with a resolution of 0.1°. A Radial Oscillating Collimator (ROC) was installed in order to eliminate the spurious signals produced by the sample environment.

The NPD data were analyzed using the FullProf Suite [52].

6.3 Neutron powder diffraction experiments

Figure 6.1 shows the powder diffraction patterns collected between 1.6 K and 298 K for all samples $x = 0.15$ (a), 0.30 (b), 0.45 (c) and 0.90 (d). Additional peaks observed for the samples measured at D1B at all temperatures are due to neutrons with $\lambda/2 = 1.26$ Å and marked with green diamonds (see Fig. 6.1(b) and (c)). The refinement through the Rietveld method allowed to confirm that the quantity of such neutrons represents a small percentage ($\sim 0.7\%$) of the total scattered neutrons.

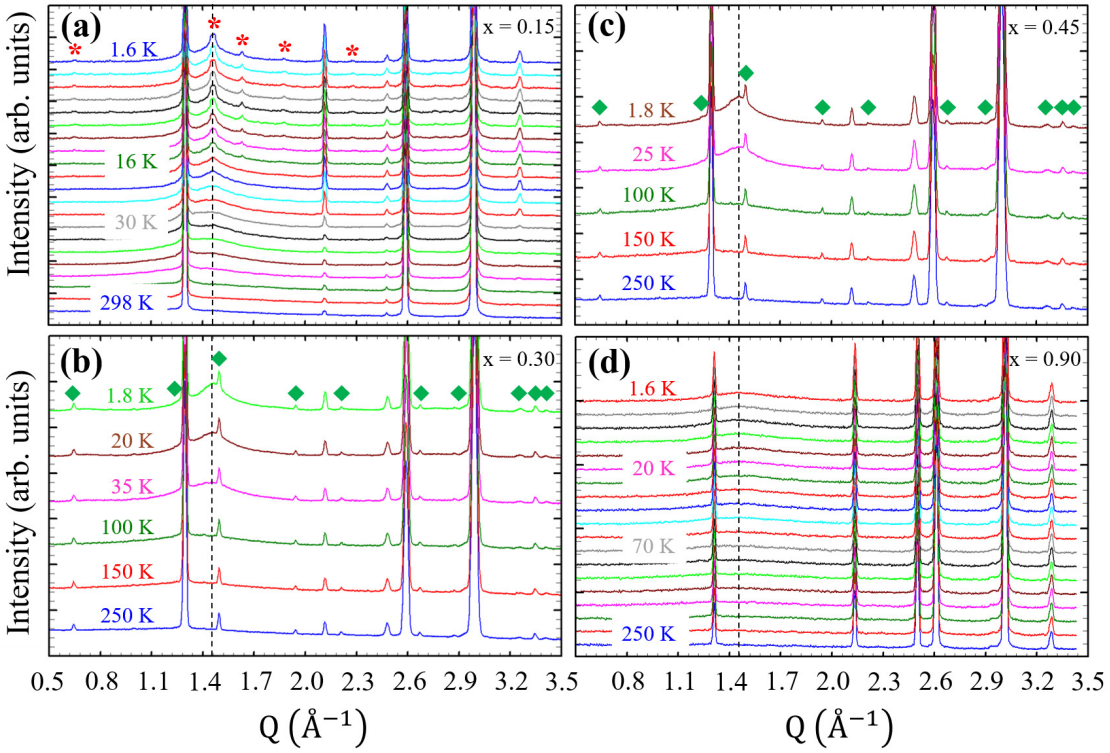

Figure 6.1: Diffraction patterns obtained at different temperatures for powder samples of $Mn_{1-x}Mg_xCr_2O_4$ with $x = 0.15$ at G.4.1 (a), $x = 0.30$ at D1B (b), $x = 0.45$ at D1B (c), and $x = 0.90$ at G.4.1 d). Satellite reflections due to $\vec{k}_{I1}$ are labeled with red asterisks. The bump related with SRO around $Q_b = 1.46$ Å^{-1} is indicated with a dotted line. For samples measured at D1B, reflections due to neutrons with $\lambda/2 = 1.26$ Å are marked with a green diamond.

For $x = 0.15$ (see Fig. 6.1(a)), similar to the $MnCr_2O_4$ case, an increase in the intensity of the reflection at $Q = 2.1$ Å^{-1} below $T_N \sim 30$ K is related with the onset of the long-range order (LRO) ferrimagnetic phase with propagation vector $\vec{k}_N$=(0 0 0). Additionally, a bump in the background around $Q_b = 1.46$ Å^{-1} is developed as the temperature decreases, related with some magnetic short-range order (SRO) that anticipates the appearance of the $(\delta\,\delta\,0)$ phase at $T_{I1} \sim 16$ K. This phase gives rise to satellite reflections (signaled by red asterisks in Fig. 6.1(a)) indexed with $\vec{k}_{I1} = (\delta\,\delta\,0)$, $\delta = 0.6133(8)$, similar to the values observed in $MnCr_2O_4$.

In the case of $x = 0.30$ (see Fig. 6.1(b)), a small increase in the nuclear peaks intensity below $T_N \sim 20$ K confirms the presence of the LRO ferrimagnetic phase. The bump at Q_b is also present, but no trace of new satellite peaks is observed even at the lowest temperature, suggesting that for this sample the SRO associated with the bump does not reach LRO.

Finally, in the samples $x = 0.45$ and 0.90 no change in the intensity of nuclear peaks is observed, suggesting that the disorder prevents even the ferrimagnetic phase from developing LRO. Meanwhile the bump at Q_b decreases its intensity as the content of Mg x increases, indicating a decrease in the correlation length which is

analyzed in more detailed in the next section.

6.4 Magnetic phase evolution with the Mg content

6.4.1 Nuclear structure

The Bragg peaks observed at room temperature for all the samples can be indexed by the same cubic crystal structure as for $MnCr_2O_4$, i.e. SG $Fd\bar{3}m$. No structural transition was observed for any value of x as the temperature was lowered.

To refine the nuclear structure we considered that the tetrahedral sites, WP $8a$, were occupied by Mn^{2+} and Mg^{2+} with a constrained occupancy according to $(1-x)$ Mn + x Mg. The refined values of x are in good agreement with the nominal ones. Same as in $MnCr_2O_4$, the Cr atoms occupy the octahedral sites (WP $16d$) and the O atoms the WP $32e$ with atomic coordinates (u u u). Equivalent and isotropic Debye-Waller factors were considered for all the atoms at each given WP. The parameters obtained from the Rietveld refinement for all the samples are listed in Table 6.1.

The obtained values of the cell parameter a had an intermediate value between those of $MnCr_2O_4$ (8.436 Å, see Sec. 5.3) and $MgCr_2O_4$ (8.33 Å [73–79]) and are shown in Fig. 6.2(a). As the content of Mg x is increased, the cell parameter a decreases due to the replacement of Mn^{2+} ions by the smaller Mg^{2+} cations (effective tetrahedral ionic radii of Mn^{2+} and Mg^{2+} are 0.66 Å and 0.57 Å, respectively [85]). As can be observed in Table 7.2, the cell parameter a slightly decreases with decreasing temperature for all $Mn_{1-x}Mg_xCr_2O_4$ samples.

Figure 6.2(b) shows the temperature evolution of the position parameter u of the oxygen atoms at the $32e$ WP for all samples. At RT the obtained value for $x = 0.15$ is 0.7360(6), which is very similar to the value obtained in $MnCr_2O_4$, $u = 0.73593(2)$ for sample S1A. For this sample, a small increase in u is observed below T_N, followed by a decrease below T_{I1}, indicating a small magneto-structural

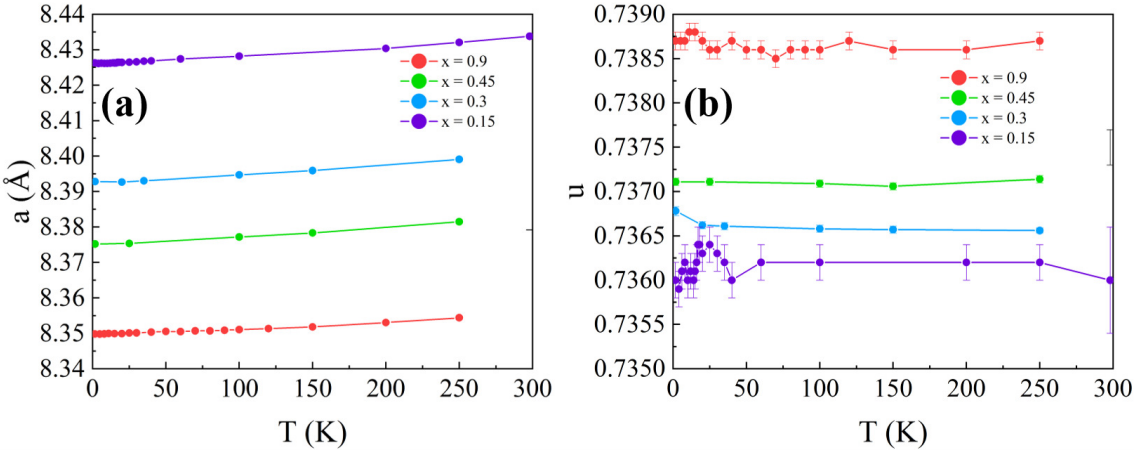

Figure 6.2: Temperature-dependent changes in the lattice parameter a (a) and the position parameter u of the oxygen atoms (b) for $x = 0.15$, 0.30, 0.45 and 0.90.

Table 6.1: Structural parameters obtained from Rietveld refinement of NDP patterns for the family $Mn_{1-x}Mg_xCr_2O_4$.

T (K)	a (Å)	u	x_{ref}	R_{Bragg}	M_0^{Mn} (μ_B)	M_0^{Cr1} (μ_B)	M_0^{Cr2} (μ_B)	R_{Mag}
			$Mn_{0.85}Mg_{0.15}Cr_2O_4$ ($x_{exp} = 0.15$)					
250	8.43209(7)	0.7362(2)	0.16(1)	0.703	–	–	–	–
100	8.42821(7)	0.7362(2)	0.16(1)	2.56	–	–	–	–
20	8.42643(5)	0.7363(2)	0.16(1)	0.755	2.56(4)	1.0(1)	0.78(7)	1.08
1.6	8.42631(5)	0.7360(2)	0.16(1)	0.69	2.93(3)	0.96(7)	0.82(4)	3.32
			$Mn_{0.70}Mg_{0.30}Cr_2O_4$ ($x_{exp} = 0.30$)					
250	8.39908(3)	0.73656(3)	0.286(5)	0.397	–	–	–	–
100	8.39471(3)	0.73658(4)	0.286(5)	0.882	–	–	–	–
20	8.39269(3)	0.73662(4)	0.286(5)	0.601	1.15(4)	0.16(7)	0.20(6)	10.5
1.8	8.39282(4)	0.73678(5)	0.286(5)	1.12	1.73(4)	0.17(8)	0.27(4)	5.25
			$Mn_{0.55}Mg_{0.45}Cr_2O_4$ ($x_{exp} = 0.45$)					
250	8.38149(3)	0.73714(4)	0.465(2)	0.975	–	–	–	–
100	8.37718(3)	0.73709(4)	0.465(2)	0.969	–	–	–	–
25	8.37538(3)	0.73711(4)	0.465(2)	1.06	–	–	–	–
1.8	8.37520(3)	0.73711(4)	0.465(2)	1.02	–	–	–	–
			$Mn_{0.10}Mg_{0.90}Cr_2O_4$ ($x_{exp} = 0.90$)					
250	8.35439(5)	0.7387(1)	0.90(1)	0.344	–	–	–	–
100	8.35105(6)	0.7386(1)	0.90(1)	0.590	–	–	–	–
20	8.34994(6)	0.7387(1)	0.90(1)	0.406	–	–	–	–
1.6	8.34983(6)	0.7387(1)	0.90(1)	0.275	–	–	–	–

coupling. As the content of Mg x is increased, u increases, suggesting a compression of the elongated coordination polyhedron, in line with the higher presence of Mg^{2+} cations.

All the refined parameters of the nuclear and magnetic structures are listed in Table 6.1 for several key temperatures.

6.4.2 Magnetic structure

In the case of $x = 0.15$ and 0.30, in which additional magnetic signals were observed, the satellite peaks were fitted by the same magnetic models as in $MnCr_2O_4$, i.e, the MSG $Imm'a'$ in the ferrimagnetic phase and the MSSG $Bb'(\alpha\,\beta\,0)0$ in the $(\delta\,\delta\,0)$ phase. However, since the Q-range covered in the experiments in $Mn_{1-x}Mg_xCr_2O_4$ was very reduced, the small tetragonal or monoclinic distortions were neglected in the refinement and a cubic structure was adopted.

The observed and calculated diffractograms at 1.6 K of $x = 0.15$, 0.30, 0.45 and 0.90 emphasizing the low Q part are depicted in Fig. 6.3. The numerical values for the magnetic moments obtained from such refinements are also listed in the Table 6.1, where the atomic coordinates, lattice parameters and magnetic moments are referred to the standard setting of the paramagnetic group.

The evolution of the magnetic moment modulus M_j and the half-cone angle α is shown in Fig. 6.3(e) and (f), respectively, for the sample with $x = 0.15$. The name of each j atom follows the same structure as in $MnCr_2O_4$. Similar to the analysis shown for S1R of $MnCr_2O_4$, the $\vec{k}_N = (0\,0\,0)$ ferrimagnetic phase is marked

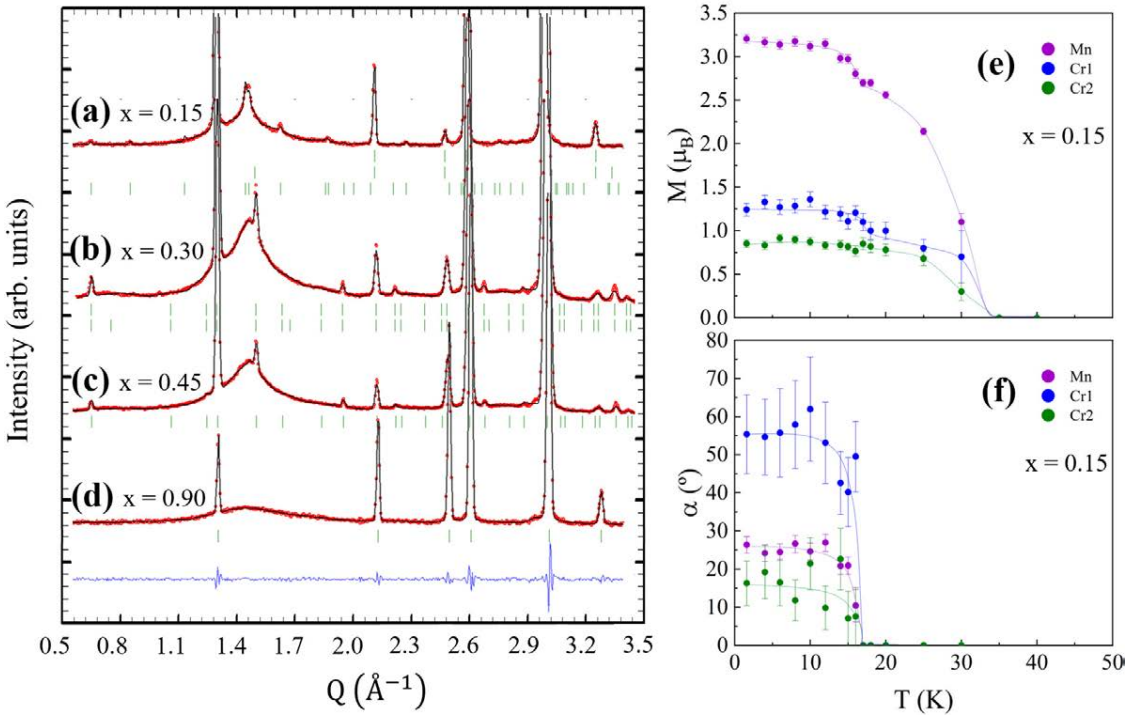

Figure 6.3: Representative Rietveld refinements at 1.6 K of $Mn_{1-x}Mg_xCr_2O_4$ with $x = 0.15$ (a), $x = 0.30$ (b), $x = 0.45$ (c) and $x = 0.90$ (d). In red are shown the observed points and in back continuous line the calculated pattern with the parameters shown in Table 6.1. The blue continuous line and the green ticks indicate the difference between the observed and calculated profile and the nuclear and satellite peaks generated by the magnetic superspace group, respectively. Panels (e) and (f) show the temperature evolution of the magnetic parameters M_j and α, respectively, extracted from the Rietveld analysis of $Mn_{0.85}Mg_{0.15}Cr_2O_4$.

by an increase in M_j and null values of α below $T_N \sim 30$ K. The small difference between the Cr sublattices is due to the split of the WP of Cr. Before the M_j values reach a plateau at smaller temperatures, a small increase is again observed, while the non-zero values of α below $T_{I1} \sim 16$ K signal the onset of the $(\delta\,\delta\,0)$ phase.

The half-cone angle values at 1.6 K for the A, B1 and B2 sublattices are, respectively, 26°, 55° and 16°. At the same time, the saturation value of M_j decreases for all atoms when compared with $MnCr_2O_4$ ($x = 0$), which suggests that the disorder induced by the Mg content prevents the magnetic moments from fully developing the LRO, increasing instead the SRO related with fluctuations and frustration, specially in the Cr sublattice.

The SRO was analyzed by fitting the bump observed in the background at $Q_b = 1.46$ Å$^{-1} = \frac{2\pi}{a}|(2\,2\,0) - \vec{k}_{I1}|$ to a Lorentzian curve, as can be observed in Fig. 6.4(a) and (b). In the case of $x = 0.15$, the bump slowly transforms into a wide peak as the temperature is lowered (see Fig. 6.1(a)), and therefore two simultaneous Lorentzian curves were used in the fitting procedure, one accounting for the broad bump and another for the better-defined peak, each one associated with SRO and

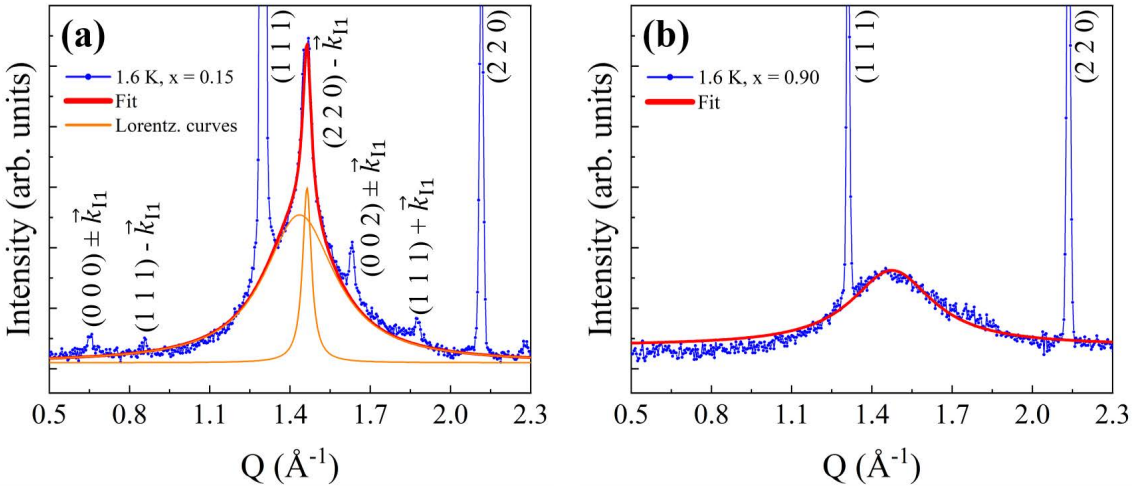

Figure 6.4: Fit of the bump observed at Q_b to a Lorentzian curve (red line) for $x = 0.15$ (a) and $x = 0.90$ (b). The contribution of each individual Lorentzian curve in (a) is indicated by orange lines. Some nuclear and magnetic peaks are indicated for clarity.

LRO, respectively.

At the lowest temperature the full width at half maximum (FWHM) of the Lorentzian curves was estimated to be between 0.37 Å^{-1} and 0.23 Å^{-1}, which is much larger than the the resolution limit 0.012(1) Å^{-1}, estimated from the nuclear Bragg reflection (1 1 1). For $x = 0.15$, the Lorentzian curve accounting for the LRO had a FWHM of 0.039(4) Å^{-1} at 1.6 K, which is around 4 times the resolution limit.

The real-space correlation lengths ξ associated with the FWHM are plotted in

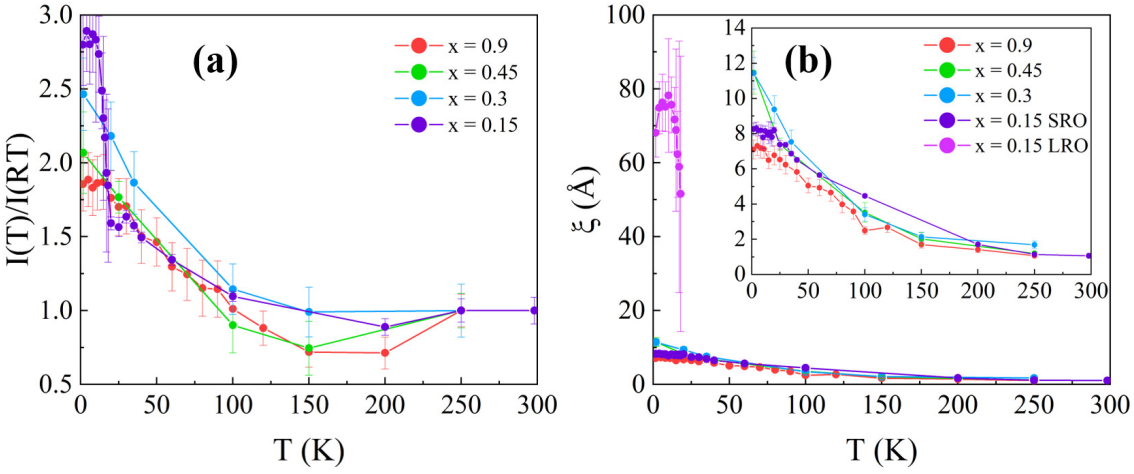

Figure 6.5: Parameters extracted from the Lorentzian curve fit: intensity normalized to the value observed at RT (a) and real-space correlation lengths ξ (b). The inset in (b) shows a zoom of the ξ values which correspond only to the SRO component of the fit.

Fig. 6.5, together with the intensity of the Lorentzian curves. As the temperature is lowered below 100 K, the magnetic scattering intensity gradually increases for all samples, while a sudden increase observed for $x = 0.15$ at $T_{I1} \sim 16$ K marks the onset of the $(\delta\,\delta\,0)$ phase (see Fig. 6.5(a)). The values of ξ reach a maximum value at 1.6 K between 7.1 Å and 11.5 Å for the SRO component, while the LRO component in $x = 0.15$ has a correlation length of 68(6) Å, corresponding to about 9 times the unit cell. Therefore, it appears that the $(\delta\,\delta\,0)$ phase does not fully reach LRO, but clusters of considerable size are formed.

6.5 Discussion

The magnetic phase diagram obtained by Yokobori *et al.* [84] for $Mn_{1-x}Mg_xCr_2O_4$ is corroborated and expanded by the results of our neutron diffraction studies, as can be seen in Fig. 6.6. As the temperature is decreased, the same ferrimagnetic LRO as observed in $MnCr_2O_4$ develops for concentrations of Mg $x < 0.45$. The ferrimagnetic order temperature T_N rapidly decreases with the Mg content and is

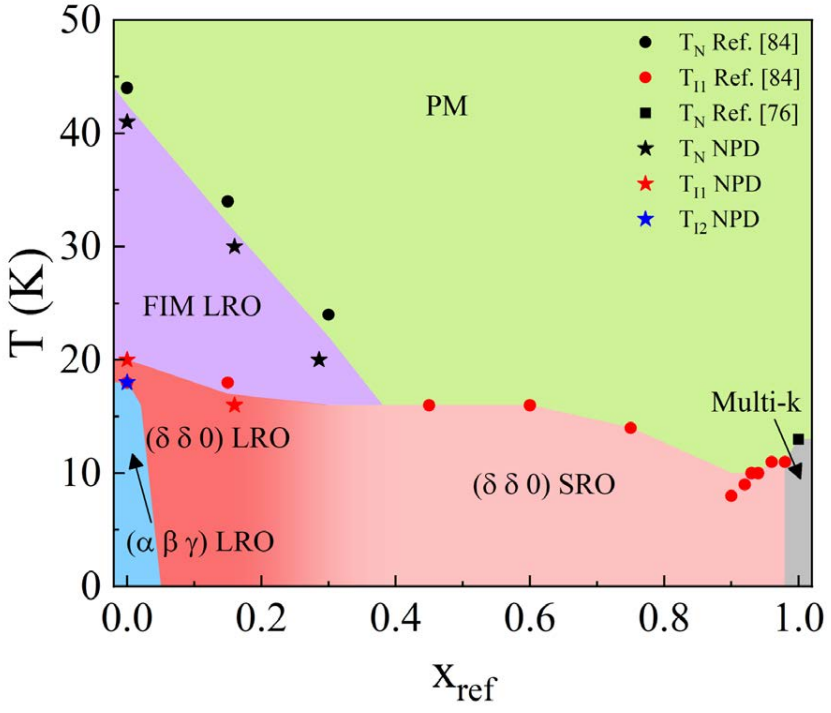

Figure 6.6: $x-T$ magnetic phase diagram for the family $Mn_{1-x}Mg_xCr_2O_4$ obtained by plotting T_N (black), T_{I1} (red), and T_{I2} (blue) determined from the analysis of NPD experiments (filled stars). The values of T_N and T_{I1} obtained by Yokobori *et al.* [84] (filled circles), as well as the value of T_N for $x = 1$ from Ref. [76] (black filled square) are also plotted. The different magnetic phases present are labeled as: paramagnetic (PM), ferrimagnetic long-range order (FIM LRO), $(\delta\,\delta\,0)$ incommensurate long-range order ($(\delta\,\delta\,0)$ LRO), $(\alpha\,\beta\,\gamma)$ incommensurate long-range order ($(\alpha\,\beta\,\gamma)$ LRO), $(\delta\,\delta\,0)$ incommensurate short-range order ($(\delta\,\delta\,0)$ SRO), and multiple $\vec{k}$ (multi-k).

no longer observed for $x > 0.3$. Meanwhile, the incommensurate spiral phase $(\delta\,\delta\,0)$ maintains the spiral LRO component observed in $MnCr_2O_4$ until $x = 0.15$. For higher values of x, the spiral component is only visible as a bump in the background at Q_b, indicating SRO. Such SRO is observed up to $x = 0.90$. Finally, the presence of the incommensurate spiral phase $(\alpha\,\beta\,\gamma)$ already disappears at $x = 0.15$.

As it was discussed in Sec. 5.5.2, in $MnCr_2O_4$ ($x = 0$) the J_{CrMn} interaction helps to partially release the magnetic frustration on the B-sites, while giving rise to the $(\delta\,\delta\,0)$ phase through its interplay with J_{CrCr}. Additionally, the small value of J_{MnMn} destabilizes the $(\delta\,\delta\,0)$ magnetic ground state and develops a new transverse conical structure in the $(\alpha\,\beta\,\gamma)$ phase. All these interactions are very sensitive to the distances between ions and even a small defect can prevent the development of the $(\alpha\,\beta\,\gamma)$ phase at low temperatures.

In the family of compounds $Mn_{1-x}Mg_xCr_2O_4$, two simultaneous effects determine the resulting magnetic ground state as the content of Mg, x, increases. First, the substitution of Mn^{2+} by diamagnetic Mg^{2+} cations results in a progressive weakening of J_{MnMn} and J_{CrMn}. Second, the compression of the Cr-O octahedrons indicated by the increase of the oxygen parameter suggests an strengthening of J_{CrCr}.

At $x = 0.15$ the amount of Mg is enough to make J_{MnMn} negligible and prevent the onset of the $(\alpha\,\beta\,\gamma)$ phase. Meanwhile, for $x > 0.15$, the J_{CrCr} interaction causes such magnetic frustration in the B sites that it cannot be released through the development of the LRO $(\delta\,\delta\,0)$ phase. Instead, the spiral components form small spin clusters, whereas the axial ferrimagnetic components form LRO. Finally, for $x > 0.3$, the J_{CrMn} interaction is weakened to the point that not even the axial components of the ferrimagnetic and $(\delta\,\delta\,0)$ phases can develop LRO.

6.6 Conclusions

Neutron diffraction experiments were performed to study the effect of magnetic disorder in $Mn_{1-x}Mg_xCr_2O_4$. No structural transition is observed for any of the samples. For low values of Mg content, i.e. $x = 0.15$, both the same LRO ferrimagnetic phase and $(\delta\,\delta\,0)$ incommensurate spiral phase as in $MnCr_2O_4$ are observed. As the Mg content is increased, the LRO ferrimagnetic phase is no longer observed above $x = 0.3$, while the spiral phase undergoes a transition from LRO to SRO and is only visible as a bump in the background up to $x = 0.90$. The correlation length of such SRO is determined by a fit to a Lorentzian curve, which indicates that small clusters of spiral order are formed. The magnetic order evolution with x is in agreement with Yokobori *et al.* [84]. An explanation is given based on the weakening of the exchange interactions and the compression of the Cr-O octahedrons as the content of diamagnetic Mg^{2+} cations increases.

Chapter 7

Reentrant spin glass behavior in the $CuCr_{2-x}Sn_xS_2Se_2$ spinels

This chapter focuses on the interplay of frustration and disorder within the spinel family $CuCr_{2-x}Sn_xS_2Se_2$, examining how this interaction influences the evolution of the magnetic ground states with different levels of frustration and chemical substitution.

We initiate the chapter with an overview of solid solutions in thiospinels and selenospinels. In the next section we detail the sample synthesis and experiments carried out in this study. The analysis of the d.c. and a.c. magnetization experiments suggest a gradual shift in the magnetic ground state from ferromagnetic to a spin glass-like configuration as disorder increases. A model based on the random competition of exchange interactions is proposed to understand the magnetism of these compounds. Subsequent sections describe the neutron powder diffraction results, from which the nuclear and magnetic structure of these compounds is determined. These investigations reveal ferromagnetic long-range order at lower Sn concentrations, which is suppressed at higher concentrations. Moreover, the high resolution transmission electron microscopy and neutron powder diffraction results identify an unexpected secondary monoclinic phase for high x, which is attributed to a chemical pressure mechanism. Finally, we construct a magnetic phase diagram by combining all the experimental results. The evolution of the magnetic phases is explained based on the combination of frustration and random Sn dilution. The chapter finishes with a synthesis of the study's key discoveries.

7.1 Solid solutions in thiospinels and selenospinels

The chalcogenide spinels with normal spinel-type structures AB_2X_4 have generated great interest because of their attractive physical properties, such as colossal magnetoresistance, multiferroicity, colossal magnetocapacitance, high thermoelectric performance, magnetic semiconducting properties and spin-glass behavior, among other properties [86–92].

The physical and structural properties of chalcogenide spinels are strongly influenced by the distribution of the metal ions in the structure [89, 93, 94]. Because the cationic and anionic distributions can change when substitution occurs, the physical

properties of these spinel materials may differ significantly from those of the end-members [95–101]. Additionally, thiospinels and selenospinels can undergo pressure-induced phase transitions toward a monoclinic Cr_3S_4-type phase, accompanied by significant alterations in the magnetic and electronic properties [102–105].

Both, the thiospinel $CuCr_2S_4$ and the selenospinel $CuCr_2Se_4$, have a normal spinel type structure with space group (SG) $Fd\bar{3}m$ and high ferromagnetic (FM) Curie temperatures T_C of 377 K and 430 K, respectively [106, 107]. Their magnetic properties can be explained by the double exchange model between Cr^{3+} and Cr^{4+} [108], in which the diamagnetic Cu^+ ions occupy the tetrahedral sites and the FM moment arises from a parallel alignment of the spins of Cr^{3+} and Cr^{4+} located at the octahedral sites [109–113]. This double-exchange interaction is also responsible for the metallic behavior of the electrical conductivity [114–116].

Chemical substitution of Cr sublattice with diamagnetic ions modifies the magnetic properties of $CuCr_2X_4$ (X = S, Se). In $CuCr_{2-x}M_xX_4$ spinels, where M=Sn^{4+} or Ti^{4+}, and Cu remains as a diamagnetic Cu^+ cation, an evolution from FM behavior to a spin-glass regime has been described in $CuCr_{2-x}Ti_xS_4$ [92], $CuCr_{2-x}Sn_xS_4$ [101], $CuCr_{2-x}Ti_xSe_4$ [117] and $CuCr_{2-x}Sn_xSe_4$ [99, 118]. Such evolution is explained in terms of magnetic frustration, which is triggered by the chemical substitutions of chromium by the M diamagnetic ions. Thus, in the previous magnetic dilutions the *randomness*, which is also, together with magnetic frustration, an important ingredient to explain the spin-glass like behavior, is originated only at the magnetic sublattice.

Analogous behavior has been observed when simultaneously substituting the Cr and S in $CuCr_{2-x}Sn_xS_{4-y}Se_y$, and therefore creating *randomness* in both, the magnetic sublattice and the exchange pathway networks. Thus, magnetometry measurements in $CuCr_{2-x}Sn_xS_2Se_2$ with $x = 0.2$ and 0.4 exhibited FM behavior, whereas antiferromagnetic (AF) one was observed for the samples with $x = 0.6$, 0.8, and 1.0 [119]. The comparison of μ_{theo} obtained from DFT calculations with the experimental data μ_{eff} on $CuCr_{2-x}Sn_xS_2Se_2$ demonstrated that Sn was a diamagnetic cation with a IV oxidation state and μ_{eff} was in agreement with the expected for $\left(Cu^{1+}\right)_{\text{tet}}\left[Cr^{3+}Cr^{4+}_{1-x}Sn^{4+}_x\right]_{\text{oct}}S_2Se_2$. DFT calculations suggested that the decrease in FM interactions, associated with the chemical substitution of Cr by Sn, stimulates the AF behaviour.

Thus, the scope of this chapter is to understand the magnetic structures of the family $CuCr_{2-x}Sn_xS_2Se_2$ with $x = 0.2$, 0.3, 0.4, 0.6, 0.8, and 1.0. In this family the amount of Sn controls the degree of dilution of the magnetic sublattice, for a given substitution of S by Se equal to 0.5. To reach our goal, as a first step, it will be necessary to determine and refine the crystalline structures of each member of the family and to quantify the degree of *random* substitution of Cr by Sn and, also, at the same time to verify if the anionic sublattice (S/Se) is fully *random* as function of the Sn content for the given Se content of 0.5, i.e. if the proposed model of $\left(Cu^{1+}\right)_{\text{tet}}\left[Cr^{3+}Cr^{4+}_{1-x}Sn^{4+}_x\right]_{\text{oct}}S_2Se_2$ is really satisfied or not. The employed experimental techniques will be a.c. and d.c. magnetization, variable temperature neutron powder diffraction experiments and high resolution electron microscopy.

7.2 Materials and methods

Powder samples of $CuCr_{2-x}Sn_xS_2Se_2$ were provided by a collaboration with Dr. Silvana Moris and Prof. Antonio Galdámez. The samples were prepared by directly combining high-purity elemental powders (99.99%, Aldrich) in stoichiometric amounts (∼0.5 g of compound). Powders were mixed manually in hexane with ∼5 wt% excess of S and Se in an agate mortar and pestle. Then, mixed powders were pressed into round-shaped pellets at ∼ 10 kPa, sealed in evacuated quartz ampoules and placed in a horizontal tubular programmable furnace. All processes were carried out under Ar atmosphere. The ampoules were slowly heated from RT to 500 °C at a rate of 150 °C/h and maintained at this temperature for 2 h, then were heated to 850 °C at a rate of 60 °C/h and kept for 10 days. Finally, the ampoules were slowly cooled to RT at a rate of 60 °C/h.

Magnetic measurements were performed on pelletized powder samples using a physical property measurement system (PPMS-9T), manufactured by Quantum Design, in a temperature range from 5 K to 300 K. Continuous susceptibility $\chi_{dc}(T) = M(T)/B$ measurements were obtained under the zero field cooling (ZFC) and field cooling (FC) protocols with applied magnetic field $B = 0.05$ T. Isothermal magnetization $M(B)$ data were collected at $T = 5$ K in a field range from 0 to 9 T. Hysteresis loops have been recorded at $T = 5$ K between 5 T and -5 T.

In-phase (χ') and out-of-phase (χ'') components of the a.c. susceptibility were measured using a superconducting quantum interference device (SQUID) magnetometer, manufactured by Quantum Design. The temperature dependence of the signal was measured between 5 and 300 K, with an a.c. amplitude $H_{a.c.}$ of 4 Oe and exciting frequencies f ranging between 1 and 10 kHz.

High resolution transmission electron microscopy (HRTEM) was performed in a JEOL 300FEG. The composition of the obtained materials was established by semi-quantitative chemical analysis using energy dispersive X-ray spectroscopy (EDXS). The samples were prepared by crushing the powders under n-butanol and dispersed over nickel grids covered with a porous carbon film.

Neutron powder diffraction (NPD) experiments were carried out on the high-flux 2-axis neutron diffractometer D1B of the Institut Laue-Langevin (ILL) in Grenoble, France. This instrument has a detector covering an angular range of 128° with a definition of 0.1°. A Radial Oscillating Collimator (ROC) was installed in order to eliminate the spurious signals produced by the sample environment. Data acquisitions were taken with two different neutron wavelengths, $\lambda = 1.28$ Å and 2.52 Å at several key temperatures in the range from 2 K to RT. For samples showing magnetic ordering, thermo-diffractograms were collected with 2.52 Å every 2 minutes as the samples were warmed from 2 K to RT.

For the analysis of the NPD data different tools were used, which include the FullProf Suite [52] and several utilities within the Bilbao Crystallographic Server [55–58].

7.3 Magnetic macroscopic characterization

7.3.1 d.c. susceptibility

Figure 7.1 shows the $\chi_{dc}(T)$ curves measured for all $CuCr_{2-x}Sn_xS_2Se_2$ samples under ZFC and FC protocols with $B = 0.05$ T. Although the shape of the ZFC $\chi_{dc}(T)$ curves change with the Sn concentration, they all present a common phenomenology: from 300 K, when lowering T, they display firstly an increase at T_1 followed by a drop at T_2 (more pronounced in the ZFC branch). T_1 was determined as the minimum of the derivative $d\chi_{dc}(T)/dT$, while T_2 was determined as the maximum of $\chi_{dc}(T)$ (see Fig. 7.1). Moreover, at T_{Irr}, which is very close to T_2 for low fields, an irreversibility between the ZFC/FC curves takes place, even for $x = 0.2$ (see inset of Fig. 7.1).

The inverse susceptibility dependence at high temperatures was fitted to the Curie-Weiss law, $\chi^{-1} = (T - \theta_{CW})/C$, where C is the Curie constant and θ_{CW} the Curie-Weiss temperature (see insets of Fig. 7.1). From the fitted value of C we can obtain the effective experimental magnetic moment for the Cr ions as: $\mu_{eff} = \mu_B\sqrt{3k_BC/N_A} \approx \sqrt{8C}$. The theoretical effective magnetic moment, μ_{theo}, has been calculated as:

$$\mu_{theo} = \sqrt{\mu^2_{Cr^{3+}} + (1-x)\mu^2_{Cr^{4+}}},$$

where $\mu^2_{Cr^{3+/4+}} = g^2_{Cr^{3+/4+}} S_{Cr^{3+/4+}}(S_{Cr^{3+/4+}} + 1)$ is the theoretical effective magnetic moment for $Cr^{3+/4+}$. The Landé factors and spin values are $g_{Cr^{3+}} = 2$, $g_{Cr^{4+}} = 1.86$, $S_{Cr^{3+}} = 3/2$ and $S_{Cr^{4+}} = 1$. The values of μ_{theo}, together with the experimental data T_1, T_2, T_{Irr}, and the parameters θ_{CW} and μ_{eff} obtained from the fits are summarized in Table 7.1.

Isothermal magnetization $M(B)$ data were collected for $CuCr_{2-x}Sn_xS_2Se_2$ samples at $T = 5$ K in a field range from 0 to 9 T. These curves are shown in Fig. 7.2(a). A clear evolution is observed as the content of Sn, x, replacing the octahedral Cr site is increased. A very small hysteresis is also observed at the full cycle at 5 K for the $x = 0.3$ compound, as can be seen in Fig. 7.2(b).

For the minimum studied Sn substitution, $x = 0.2$, we can observe that the d.c. susceptibility suddenly increases at $T_1 = 240$ K, while its magnetization isotherm saturates at high fields. Moreover, the high temperature fit of the inverse of the d.c. susceptibility gives a positive value for the Curie-Weiss temperature θ_{CW} close to the value of T_1. Hence, the sample $CuCr_{1.8}Sn_{0.2}S_2Se_2$ behaves mostly as a ferromagnet, and T_1 can be considered as a Curie temperature. However, looking more closely, we appreciate some discrepancies regarding the FM behavior: at low temperatures (≈ 7 K) there is an small irreversibility in the ZFC/FC curves and the magnetization at saturation condition, 3.8 μ_B, is relatively small compared with the calculated magnetization, 4.49 μ_B. As we will discuss later in detail, these small discrepancies with respect to a ferromagnet behavior could be explained by considering the existence of AF interactions between Cr^{3+} cations. The competition between ferromagnetic (Cr^{3+} - Cr^{4+}) and antiferromagnetic (Cr^{3+} - Cr^{3+}) interactions is one of the key ingredients for the appearance of a spin glass behavior, which will be the responsible for both the appearance of irreversibility in the ZFC/FC curves and the low values of the saturation magnetization [92, 120, 121].

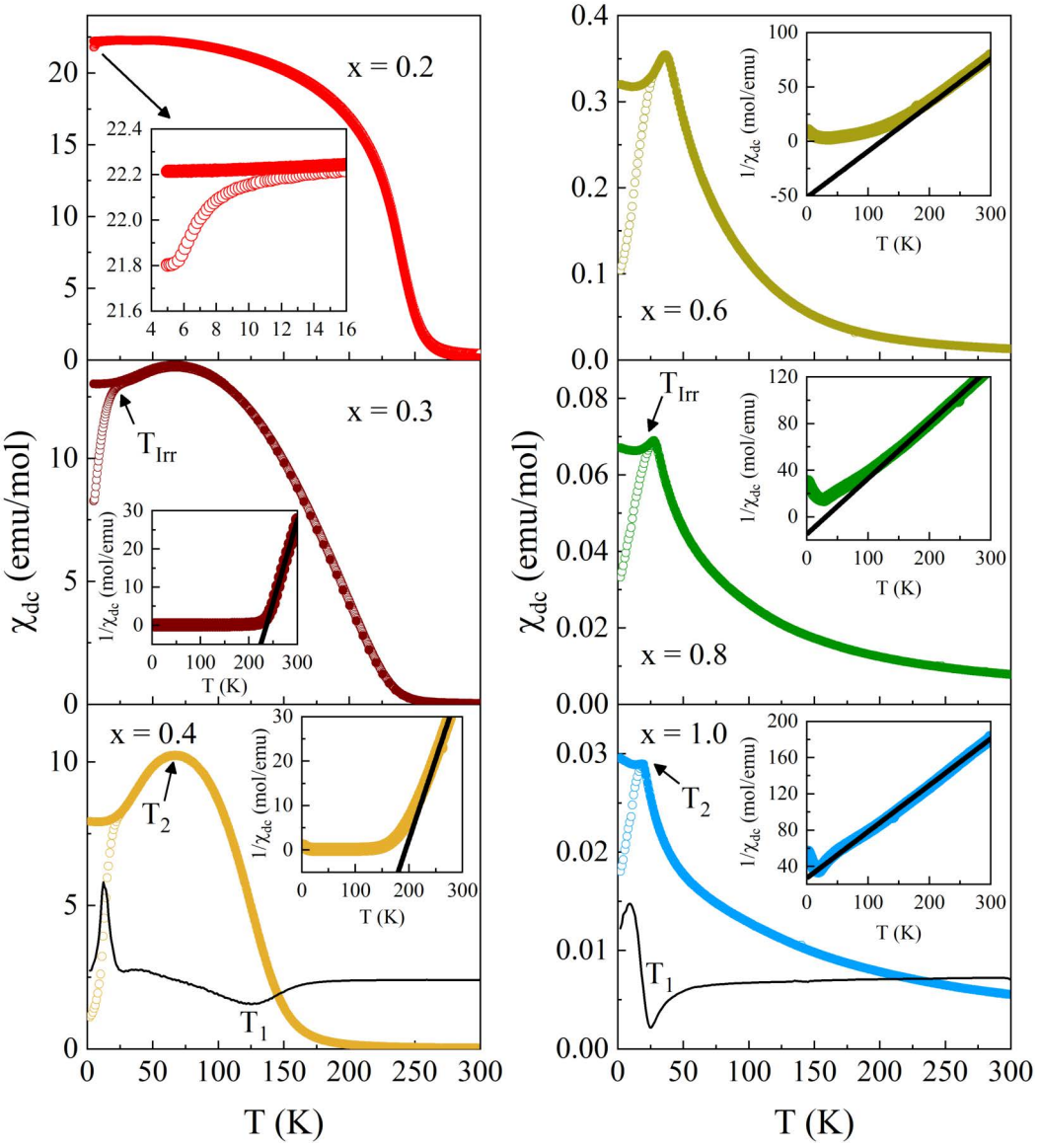

Figure 7.1: Zero Field Cool (ZFC) (open symbols) and Field Cool (closed symbols) d.c. susceptibility curves measured at 0.05 T for powder samples with $x = 0.2$, 0.3, 0.4, 0.6, 0.8 and 1.0. The inset of $x = 0.2$ is a detailed view of the low T region of the ZFC/FC curves. The insets of $x = 0.3$, 0.4, 0.6, 0.8 and 1.0 show the inverse d.c. susceptibility and the corresponding Curie-Weiss law fit. In the compounds $x = 0.4$ and 1.0 the derivative, $d\chi_{\rm dc}/dT$, has been included (black line) to show how T_1 is determined. The irreversibility in the ZFC/FC curves $T_{\rm Irr}$ is also signaled for the compounds $x = 0.3$ and 0.8.

The small irreversibility could also be assigned to the movement of magnetic domain walls in consonance with the weak hysteresis detected in the curve $M(B)$ at low temperatures and magnetic fields, for samples with $x = 0.2$, 0.3 and 0.4. The possibility of powder sample rotation is ruled out, as precautions were taken by using cotton to secure the powder within the magnetometer sample holder (capsule), and

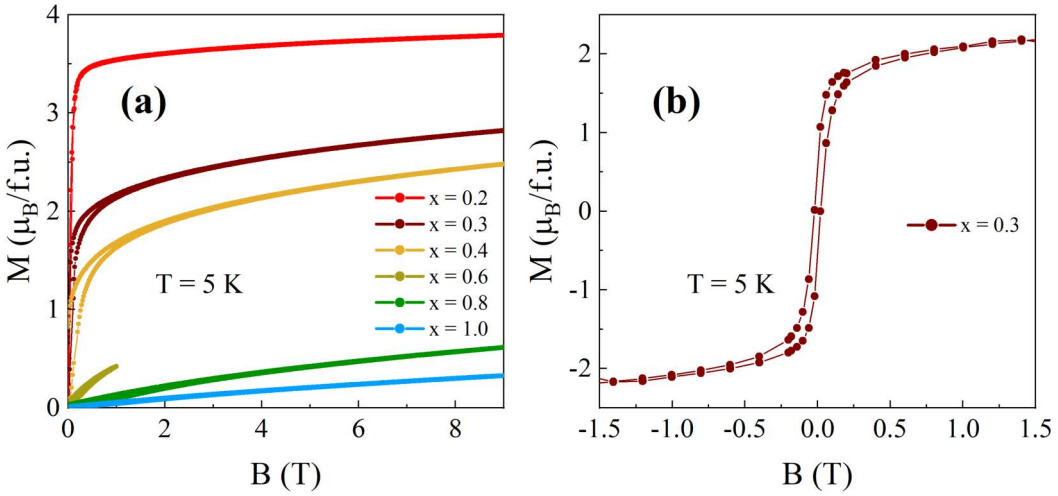

Figure 7.2: (a) Isothermal magnetization $M(B)$ data at 5 K for $x = 0.2$, 0.3, 0.4, 0.6, 0.8 and 1.0. (b) Hysteresis cycle for $x = 0.3$.

the magnetic field strength remains within acceptable limits.

The small value found in the magnetization saturation could also be justified by an itinerant electron ferromagnetism model due to double-exchange interactions. In this context, the magnetization saturation tends to be lower than expected in a localized spin model. However, the decrease of saturation value in $M(B)$ and the increase of the slope at high fields as we increase the value of x to 0.3 and 0.4 would indicate a stronger itinerant behavior, which is in direct contradiction with the Cr^{3+}-Cr^{4+} double exchange interactions becoming weaker.

For intermediate Sn concentration samples, $x = 0.3$ and 0.4, there is a significant change in the shape of the d.c. susceptibility curves, which begin to deviate appreciably from what is expected in an typical ferromagnet. Mainly, T_1 is significantly reduced (from 240 to 125 K), while the susceptibility decreases below T_2, the irreversibility at low T is enhanced, and the $M(B)$ curves no longer saturate. However, the compound still exhibits some of the hallmarks of a ferromagnet: namely, the shape of the $1/\chi_{dc}$ curve, the small hysteresis at $M(B)$, and the positive value of θ_{CW} (although in these cases it is significantly higher than T_1). Therefore, in these intermediate Sn concentration samples the exchange interactions have a dominant FM character but superposed with AF interactions, with the latter ones becoming more relevant as the concentration increases. In this context, T_2 would be the equivalent of a freezing temperature, $T_2 = T_f$.

For relatively high Sn concentration samples, $x = 0.6$ and 0.8, the shape of the magnetization curves clearly differ from those of a ferromagnet. The d.c. susceptibility curves display a sharper maximum at T_2, a strong ZFC/FC irreversibility and the ZFC branches abruptly decrease towards zero for $T < T_{Irr}$. In $1/\chi_{dc}$ a small turn up is observed at low T. Moreover, the magnetization isotherms display a linear increase with the applied field and the magnetization at $T = 5$ K and $B = 9$ T has drastically decreased (from 3.8 to 0.6 μ_B for respectively $x = 0.2$ and 0.8). Taking into account the increasingly small values of T_1 and θ_{CW}, and the linear in-

Table 7.1: Values of T_1, T_2, T_{Irr}, θ_{CW} and experimental (μ_{eff}) and theoretical (μ_{theo}) effective magnetic moments obtained from the fits for the different samples of $CuCr_{2-x}Sn_xS_2Se_2$. († Data from reference [119]).

x	T_1 (K)	T_2 (K)	T_{Irr} (K)	θ_{CW}(K)	θ_{CW}(K)†	μ_{eff} (μ_{B})	μ_{eff} (μ_{B})†	μ_{theo} (μ_{B})
0.2	240(2)	–	10(2)	+262(2)	+261.27	5.1(3)	4.97	4.53
0.3	200(10)	67(2)	24(2)	+234(2)	–	4.4(3)	–	4.45
0.4	125(5)	67(2)	26(2)	+197.7(3)	+189.44	4.6(1)	4.69	4.38
0.6	45(3)	36(1)	27(1)	+135.3(3)	+111.47	4.27(6)	4.49	4.22
0.8	32(2)	28(1)	25(1)	+44.4(1)	+29.46	4.21(9)	4.12	4.05
1	25(2)	19(1)	18(1)	-41.5(1)	-36.00	4.0(1)	3.99	3.87

crease of the magnetization curves with the applied field, this suggests that the AF interactions are playing a major role in these systems. In this case, T_1 cannot be seen as a true Curie temperature, whereas T_2 does seem to correspond to a freezing temperature as in the previous compounds.

Finally, for $x = 1$, although the shape of the $\chi_{\mathrm{dc}}(T)$ and $M(B)$ curves are very similar to those of 0.8, there is a fundamental difference, the θ_{CW} has become negative, which means that the interactions are predominantly AF in nature. This is also reflected in the form of the $1/\chi_{dc}$ curve, which is typical of an antiferromagnet.

As we can observe from Table 7.1, these results are in agreement to that of the previously published for $CuCr_{2-x}Sn_xS_2Se_2$ phases and confirm the reproducibility of the magnetic measurements [119]. Also a good agreement is obtained for the values of the effective magnetic moments when compared with the theoretical values expected for $Cu^{+}[Cr_1^{3+}Cr_{1-x}^{4+}Sn_x^{4+}]S_2Se_2$, confirming that Cu and Sn show diamagnetic behaviour with I and IV oxidation states, respectively.

7.3.2 a.c. susceptibility

Representative a.c. susceptibility curves for the compounds $CuCr_{1.7}Sn_{0.3}S_2Se_2$ ($x = 0.3$) and $CuCr_{1.6}Sn_{0.4}S_2Se_2$($x = 0.4$) are displayed in Fig. 7.3. The in-phase $\chi'(T)$ curves behave similar to the ZFC d.c. susceptibility, i.e. an increase at T_1 and a subsequent fall at T_2. An additional shoulder is also present at lower temperatures, which is better observed for $x = 0.3$. Regarding the out-of-phase component $\chi''(T)$, the $x = 0.3$ curve shows two broad peaks at the temperatures labeled $T_1^{\mathrm{ac}} = 185(10)$ K and $T_2^{\mathrm{ac}} = 83(2)$ K, and a well-defined peak at $T_3^{\mathrm{ac}} = 21(2)$ K for the lowest frequency measured $f = 0.9$ Hz (see Fig. 7.3(a)). The same qualitative behavior is observed for $x = 0.4$, where three well-defined peaks are located at $T_1^{\mathrm{ac}} = 145(5)$ K, $T_2^{\mathrm{ac}} = 69(2)$ K, and $T_3^{\mathrm{ac}} = 31(2)$ K for the lowest frequency measured $f = 10$ Hz (see Fig. 7.3(b)).

Comparing these temperatures with the ones determined from the d.c. susceptibility, a clear correspondence can be established. The Curie temperature T_1 corresponds with the first peak in $\chi''(T)$ at T_1^{ac}, which shows no frequency dependence. The broad peak at T_2^{ac} roughly coincides with the maximum of the in-phase com-

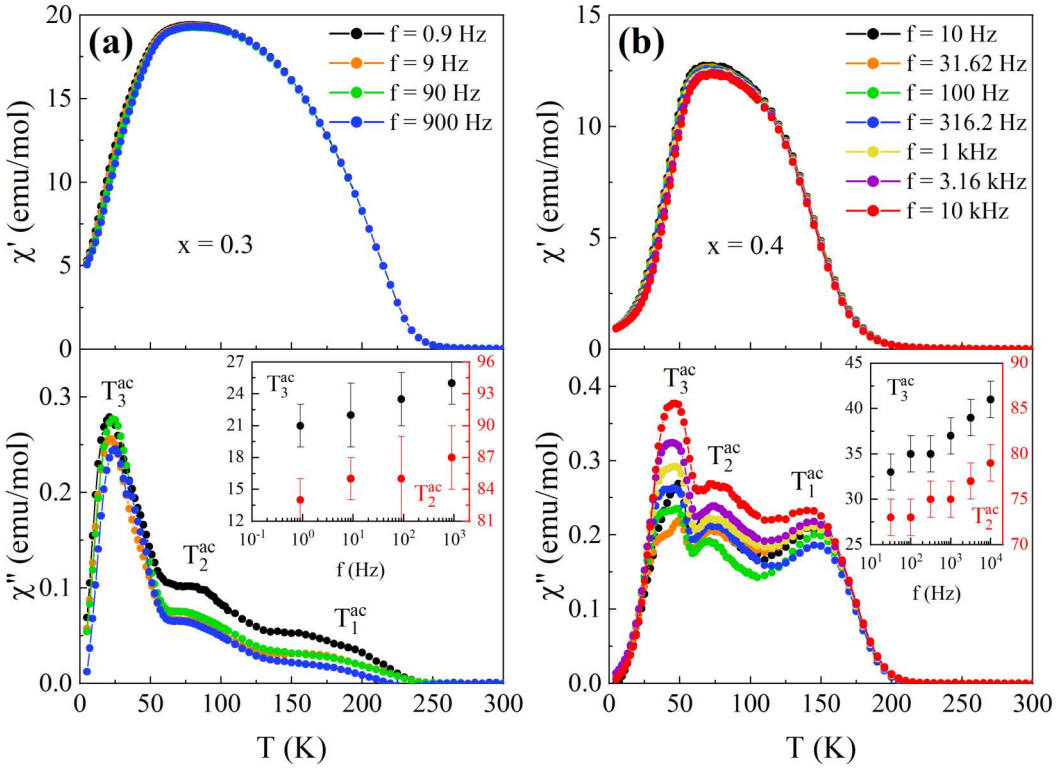

Figure 7.3: a.c. magnetic susceptibility ($\chi'(T)$ and $\chi''(T)$) curves for $CuCr_{2-x}Sn_xS_2Se_2$ samples with $x = 0.3$ (a) and 0.4 (b). The peaks of the out-of-phase component $\chi''(T)$ are labeled for clarity. The insets display the frequency dependence of T_2^{ac} and T_3^{ac} for $x = 0.3$ (a) and $x = 0.4$ (b).

ponent and d.c. susceptibility curves (T_2) and has a clear frequency dependence in both $\chi'(T)$ and $\chi''(T)$, displayed in the insets of Fig. 7.3. Finally, the sharp peak at T_3^{ac} correlates with the shoulder of the in-phase component and the splitting temperature between the ZFC and FC d.c. susceptibility curves (T_{Irr}), and also displays a clear frequency dependence. The linear relation between the logarithm of the applied frequency and the temperatures T_2^{ac} and T_3^{ac} further supports the freezing of the magnetic moments at low temperatures [117, 120, 122].

7.4 Neutron powder diffraction experiments

7.4.1 Nuclear structure

Neutron powder diffraction (NPD) data were collected with $\lambda = 1.28$ Å at different temperatures between 2 K and RT for powder samples of $CuCr_{2-x}Sn_xS_2Se_2$ with $x = 0.2$, 0.3, 0.4, 0.6, 0.8 and 1.0. Some representative patterns are shown in Fig. 7.4 for all samples.

The Bragg peaks observed in samples labeled with $x = 0.6$, 0.8 and 1.0 can all be indexed by the same cubic crystal structure with SG $Fd\bar{3}m$ (No. 227) and no evidence of magnetic long-range order (LRO) is found down to the lowest measured

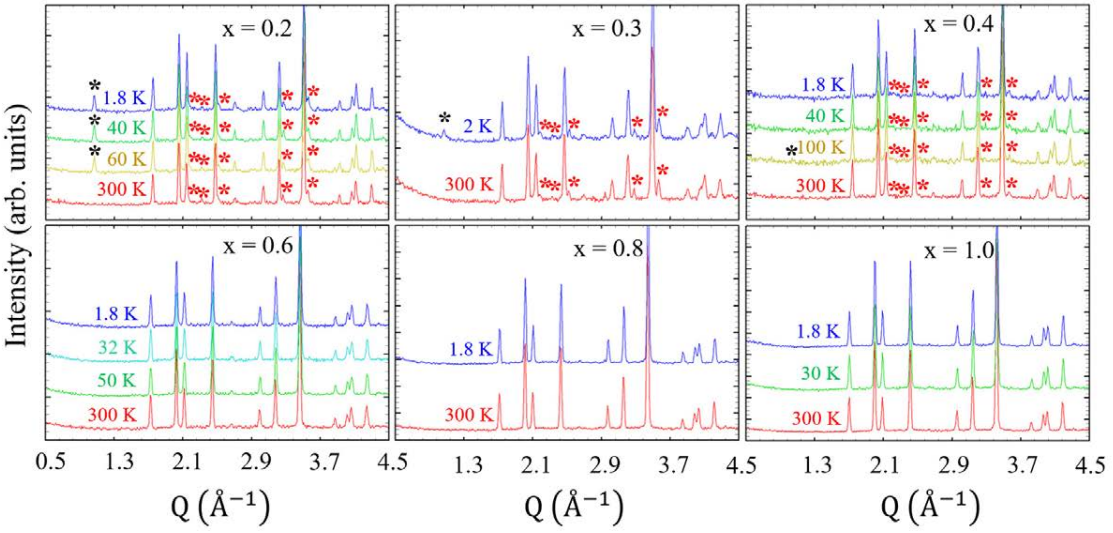

Figure 7.4: Low-Q region of some representative powder diffraction patterns collected with $\lambda = 1.28$ Å at different temperatures for powder samples of $CuCr_{2-x}Sn_xS_2Se_2$ with $x = 0.2$, 0.3, 0.4, 0.6, 0.8 and 1.0. The additional Bragg peaks, indexed by a monoclinic phase, are marked with red asterisks. The magnetic peak observed for $x = 0.2$, 0.3 and 0.4 is marked with a black asterisk.

temperature. Meanwhile, at RT the samples $x = 0.2$, 0.3 and 0.4 show the same Bragg peaks corresponding to a main cubic phase with SG $Fd\bar{3}m$ plus some additional peaks (marked by red asterisks in Fig. 7.4). Furthermore, as the temperature is decreased, an extra peak is observed for $x = 0.2$ and 0.3 at $Q \sim 1.08$ Å^{-1}, which suggests the development of some magnetic LRO. In the sample with $x = 0.4$, this peak shows a weak intensity at 100 K, and is not distinguishable at lower temperatures, implying that the magnetic LRO disappears as the temperature is decreased.

For all samples, the main phase with normal spinel-type structure was refined by means of the Rietveld method. We considered that the tetrahedral sites, Wyckoff position (WP) 8a, were occupied by Cu and the octahedral ones (WP 16d) by Sn^{4+}, Cr^{3+} and Cr^{4+}. Nevertheless, other models were also considered regarding the distribution of the Sn cation in the octahedral sites, however the best result was obtained when both the Cr and Sn cations were randomly distributed on WP 16d, as observed in $CuCr_{2-x}Sn_xS_4$ [101], $CuCr_{2-x}Sn_xSe_4$ [118], $CuCr_{2-x}Sn_xS_{4-y}Se_y$ [119] and similar Hf-doped $CuCr_2Se_4$ spinels [100]. The S and Se atoms occupied the WP 32e with atomic coordinates (u u u), where the best model also corresponded with a random distribution of both anions. This can be expected, since the effective ionic radii of S^{2-} and Se^{2-} are very similar (1.84 Å and 1.98 Å, respectively [85]). We constrained the occupancy of the WP 16d according to $(2-x)$ Cr + x Sn and the one for the chalcogenides to $(4-y)$ S + y Se. The refined values of x and y (x_{ref} and y_{ref}) did not differ greatly from the nominal ones (x_{nom}) and are shown in Table 7.2. Equivalent and isotropic Debey-Waller factors were considered for all the atoms at each given WP.

The model under consideration fits well the diffractograms, as can be observed in

Table 7.2: Structural parameters obtained from Rietveld refinement of NPD patterns for the family $CuCr_{2-x}Sn_xS_{4-y}Se_y$.

Cubic Phase									
T (K)	a (Å)	u	B_{ISO}(Cu)	B_{ISO}(Cr/Sn)	B_{ISO}(S/Se)	x_{ref}	y_{ref}	R_{Bragg}	μ_{Cr} (μ_B)
$CuCr_{1.8}Sn_{0.2}S_2Se_2$ ($x_{nom} = 0.2$, $y_{nom} = 2$)									
300	10.0906(1)	0.7440(2)	1.73(7)	1.0(1)	1.14(5)	0.18(5)	1.96(2)	3.42	–
60	10.0791(1)	0.7439(2)	1.42(5)	0.85(7)	0.94(3)	0.18	1.96	2.20	2.33(5)
40	10.0789(1)	0.7434(2)	1.31(6)	0.82(8)	1.02(4)	0.18	1.96	1.54	2.36(5)
1.8	10.0791(1)	0.7439(2)	1.47(6)	0.32(7)	0.82(3)	0.18	1.96	2.16	2.39(5)
$CuCr_{1.7}Sn_{0.3}S_2Se_2$ ($x_{nom} = 0.3$, $y_{nom} = 2$)									
300	10.1309(2)	0.7434(3)	3.9(1)	2.2(1)	2.47(8)	0.28(5)	1.93(2)	5.31	–
2	10.1189(2)	0.7446(4)	2.9(1)	1.8(1)	1.95(7)	0.28	1.93	3.91	1.1(1)
$CuCr_{1.6}Sn_{0.4}S_2Se_2$ ($x_{nom} = 0.4$, $y_{nom} = 2$)									
300	10.1595(1)	0.7435(2)	2.39(8)	1.7(1)	1.88(6)	0.37(5)	2.02(2)	1.75	–
100	10.1451(1)	0.7445(3)	1.93(9)	0.9(1)	1.58(5)	0.37	2.02	2.44	0.4(3)
40	10.1444(1)	0.7439(2)	1.95(8)	0.88(9)	1.44(5)	0.37	2.02	2.67	–
1.8	10.1443(1)	0.7440(2)	1.81(8)	1.01(9)	1.36(4)	0.37	2.02	2.91	–
$CuCr_{1.4}Sn_{0.6}S_2Se_2$ ($x_{nom} = 0.6$, $y_{nom} = 2$)									
300	10.2270(1)	0.7451(2)	2.18(7)	1.1(1)	1.39(5)	0.63(5)	1.98(2)	5.43	–
50	10.2112(1)	0.7447(2)	1.41(5)	0.65(6)	0.97(3)	0.63	1.98	4.91	–
32	10.2113(1)	0.7453(2)	1.44(6)	0.64(6)	1.04(3)	0.63	1.98	5.68	–
1.8	10.2115(1)	0.7446(2)	1.45(5)	0.69(6)	0.93(3)	0.63	1.98	5.20	–
$CuCr_{1.2}Sn_{0.8}S_2Se_2$ ($x_{nom} = 0.8$, $y_{nom} = 2$)									
300	10.29635(9)	0.7454(2)	2.41(5)	1.13(5)	1.32(4)	0.80(2)	1.94(2)	4.77	–
1.8	10.27778(9)	0.7453(1)	1.46(4)	0.55(4)	0.90(2)	0.80	1.94	4.92	–
$CuCrSnS_2Se_2$ ($x_{nom} = 1.0$, $y_{nom} = 2$)									
300	10.35932(7)	0.7457(1)	2.38(4)	0.96(5)	1.22(3)	1.05(2)	1.96(2)	3.67	–
30	10.34047(8)	0.7455(1)	1.52(4)	0.55(4)	0.83(2)	1.05	1.96	3.81	–
1.8	10.34075(8)	0.7457(1)	1.55(4)	0.57(4)	0.82(2)	1.05	1.96	3.41	–

Fig. 7.5(a), where the experimental and calculated NPD profile of $CuCr_{2-x}Sn_xS_2Se_2$ sample with $x = 1.0$ at 300 K is shown. The parameters obtained from the Rietveld refinement for all the samples are listed in Table 7.2. The obtained value of the cell parameter a for $x = 1.0$ had an intermediate value between those of $CuCrSnS_4$ [123] and $CuCrSnSe_4$ [124], similar to the values reported for $(Cu)_{tet}[Cr_{2-x}Sn_x]_{oct}S_{4-y}Se_y$ spinels [119]. This intermediate value supports the random distribution of S and Se anions. As the content x of Sn is decreased, the cell parameter a decreases linearly and obey the Vegard's law (see inset in top of Fig. 7.5). Such behavior can be understood by considering that the Cr^{4+} ions are replaced by the larger Sn^{4+} cations (effective octahedral ionic radii of Cr^{4+} and Sn^{4+} are 0.55 Å and 0.69 Å, respectively [85]). As can be observed in Table 7.2, the cell parameter a increases with increasing temperature for all $CuCr_{2-x}Sn_xS_2Se_2$ samples.

For the $x = 1.0$ sample, the u parameter of the atomic position (u u u) of the chalcogenide at the WP 32e is $u = 0.2543(1)$, which is in good agreement with the value obtained in $CuCr_{1.1}Sn_{0.9}S_{2.3}Se_{1.7}$, $u = 0.25484(4)$ [125].

For the $x = 0.2$, 0.3 and 0.4 samples the additional Bragg peaks (labeled with red asterisks in Fig. 7.4) are indexed by a monoclinic unit cell. An example is shown in Fig. 7.5(b), where the fit to the full diffraction pattern of $x = 0.2$ at 1.8 K is shown. Unfortunately, these peaks have considerable small intensity and appear next to Bragg peaks of the main cubic structure, which prevented the determination of the

Table 7.3: Lattice parameters obtained by LeBail fits of NPD patterns for the family $CuCr_{2-x}Sn_xS_2Se_2$.

Monoclinic Phase					
T (K)	a (Å)	b (Å)	c (Å)	β (°)	V (Å^3)
			$CuCr_{1.8}Sn_{0.2}S_2Se_2$		
300	11.190(4)	6.955(2)	13.545(4)	113.07(3)	969.9(5)
60	11.216(3)	6.939(1)	13.548(3)	113.16(3)	969.4(4)
40	11.194(3)	6.938(2)	13.539(2)	112.96(2)	968.3(4)
1.8	11.193(3)	6.952(2)	13.531(4)	113.14(3)	968.1(4)
			$CuCr_{1.7}Sn_{0.3}S_2Se_2$		
300	11.177(1)	6.957(1)	13.512(3)	113.22(1)	965.5(3)
2	11.166(1)	6.962(1)	13.549(2)	113.06(1)	969.1(2)
			$CuCr_{1.6}Sn_{0.4}S_2Se_2$		
300	11.200(1)	6.9690(9)	13.610(2)	113.453(8)	974.6(2)
100	11.197(4)	6.975(2)	13.587(4)	113.43(3)	973.7(6)
40	11.185(5)	6.982(2)	13.582(5)	113.35(3)	973.8(6)
1.8	11.185(4)	6.982(3)	13.568(5)	113.30(3)	973.2(6)

monoclinic space group unequivocally. Nevertheless, by performing LeBail fits, we determined the unit cell parameters, which are shown in Table 7.3.

7.4.2 Magnetic structure

The inset in Fig. 7.5(b) shows the 2D plots of the thermo-diffractograms collected at $\lambda = 2.52$ Å for $x = 0.2$ and 0.3. From them we can follow the evolution with temperature of the intensity of the magnetic peak marked with a black asterisk in Fig. 7.4 and estimate the onset of the magnetic ordering at $T_C \approx 220(10)$ and 200(5) for $x = 0.2$ and 0.3, respectively. These values agree well with the ones obtained from the magnetization measurements ($T_1 = 240$ K and 200 K for $x = 0.2$ and 0.3, respectively).

The presence of this magnetic peak, as well as the increase in intensity of some nuclear peaks for the samples $x = 0.2$, 0.3 and 0.4, can be indexed by a propagation vector $\vec{k} = (0\,0\,0)$. We can decompose the magnetic representation for the Cr atom, located at WP 16*d*, as a direct sum of Irreducible Representations (*irreps*) of the parent group $Fd\bar{3}m.1'$ for the Γ point, (0 0 0), of the Brillouin zone (BZ), as follows:

$$\mathrm{m}\Gamma_{16d} \;=\; 1\mathrm{m}\Gamma_2^+(1) \oplus 1\mathrm{m}\Gamma_3^+(2) \oplus 2\mathrm{m}\Gamma_4^+(3) \oplus 1\mathrm{m}\Gamma_5^+(3)$$

After a systematic trial and error procedure, the magnetic peak was correctly fitted by the 3d-*irrep* $\mathrm{m}\Gamma_4^+$ (see Fig. 7.5(b)), the only *irrep* which allows a FM order, in agreement with the magnetization measurements shown previously in Fig. 7.1 and Fig. 7.2.

In order to obtain more information about the real symmetry of this magnetic phase we employed the k-SUBGROUPSMAG tool of the BCS which provides with the isotropy subgroups of the parent group $Fd\bar{3}m.1'$ that are compatible with the $\mathrm{m}\Gamma_4^+$ as a primary *irrep*. Following this procedure six isotropy subgroups were found

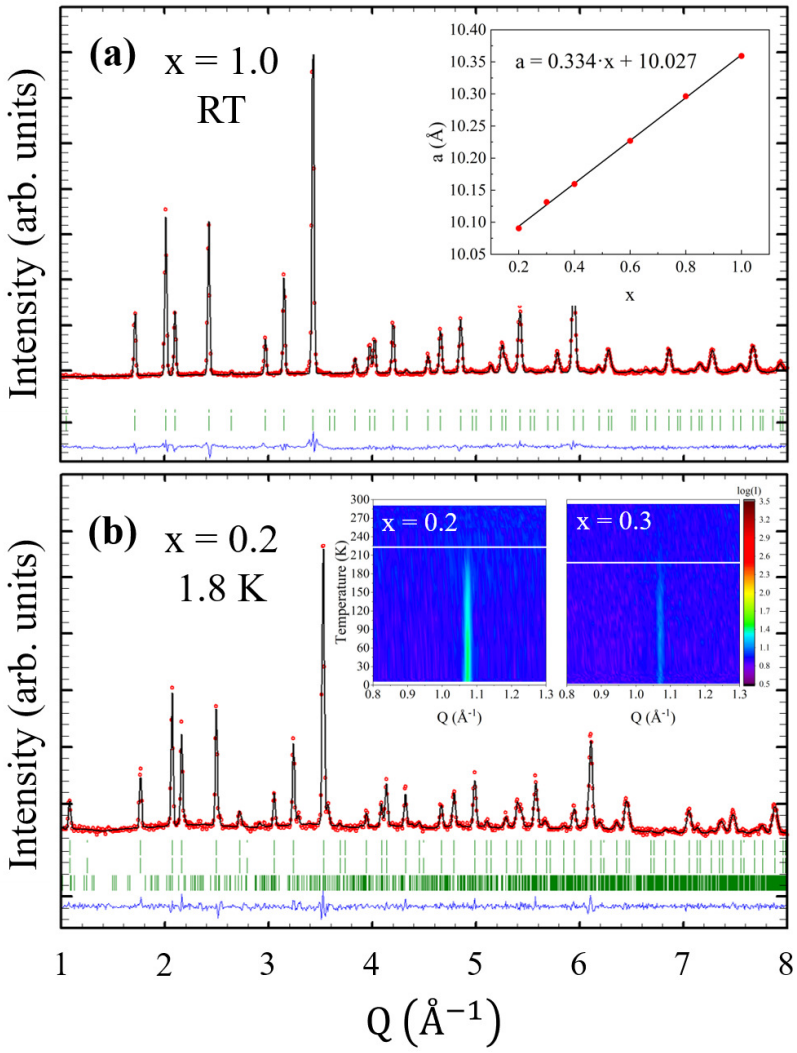

Figure 7.5: Representative NPD profile of $CuCr_{2-x}Sn_xS_2Se_2$, $x = 1.0$ at 300 K (a) and $x = 0.2$ at 1.8 K (b). In red are shown the observed points and in back continuous line the calculated pattern with the parameters shown in Table 7.2. The blue continuous line and the green ticks indicate the difference between the observed and calculated profile and the position of nuclear and magnetic Bragg reflections of the spinel-type structure, respectively. The inset in (a) shows the evolution of the cell parameter a versus x values for $CuCr_{2-x}Sn_xS_2Se_2$ at RT, where the black line denote the linear fit of the experimental data. The inset in (b) shows the 2D plots of the thermo-diffractograms collected at 2.52 Å for $x = 0.2$ and 0.3. The evolution of the intensity of the magnetic peak marked with a black asterisk in Fig. 7.4 allows to estimate the onset of the magnetic ordering.

($R\bar{3}m'$, $I4_1/am'd'$, $Imm'a'$, $C2'/c'$, $C2'/m'$ and $P\bar{1}$), each of them with a different order parameter direction. However, we could not determine which magnetic space group describes the symmetry of the system, since all the isotropy subgroups fitted successfully the data and we do not have additional information about the direction of the order parameter (magnetic measurements were performed on powder samples,

due to the difficulty to grow enough size single crystals).

Nevertheless, all the magnetic models converge to the same value for the modulus of the Cr magnetic moment, which is shown in Table 7.2 for each sample. For $x = 0.2$, the cation ordering model $Cu^{+}[Cr^{3+}_{1.0}Cr^{4+}_{0.8}Sn^{4+}_{0.2}]S_2Se_2$ predicts the determined value of 2.39(5) μ_B. For the $x = 0.3$ and 0.4 samples, the values of the magnetic moment obtained from the refinement are reduced to 1.1 μ_B and 0.4 μ_B respectively. It should be noted that the magnetic signal observed in the NPD data reflects only the average of the long-range ordered magnetic moments. Hence, these results agree well with our hypothesis of having a nearly or completely glassy system at low T, when the AF frustrated interactions developed for higher Sn content weaken the dominant FM interactions.

On the other hand, we do not observe any change in the intensity of the peaks indexed by the monoclinic phase (red asterisks in Fig. 7.4) with the temperature, which implies negligible magnetic ordering in this secondary phase.

7.5 High resolution transmission electron microscopy

In order to determine if the peaks indexed by the monoclinic phase correspond to a impurity phase or to a structural phase transition, the microstructural features of $CuCr_{2-x}Sn_xS_2Se_2$ ($x = 0.2$, 0.3 and 0.4) were studied by using HRTEM. Representative micro-crystals with undefined morphology formed by very narrow crystals which are pilled and caked are shown in Fig. 7.6.

Most crystals could be analyzed in terms of the cubic spinel-type structure ($Fd\bar{3}m$). In Fig. 7.6(a)-(d) observed distances of 2.1 and 3.8 Å between contrasts corresponding to (4 2 2) and (2 2 0) interplanar distances, respectively, can be appreciated. Typically, the observed most frequent orientation of the crystallites corresponds to the [1 1 1] zone axis. Besides, contrasts within small "wrinkle" regions are apparent (up to 8.4 Å), which could be an effect of disordered pilling of very thick crystals at the borders (high magnification image in the inset of Fig. 7.6(a)). The mean composition from several micro crystals, measured in different points, is roughly concordant with the nominal one.

In addition, in all cases some micro crystals with different symmetry, not compatible with a cubic spinel-type lattice, were detected. Figure 7.6(e)-(h) show representative images and electron diffraction (ED) patterns for such crystals. They could be indexed based on a monoclinic 4C Fe_7S_8-type structure [126], related to that of NiAs, with cell parameters $a \sim 2\sqrt{3}a_p$, $b \sim 2a_p$, $c \sim 4a_p$, being $a_p = 3.4$ Å. Thus, the observed distances of 5.1, 5.8 and 6.3 Å are assigned to the monoclinic $(2\,0\,0)_m$, $(1\,1\,0)_m$ and $(0\,0\,2)_m$, respectively. The cell parameter values are coherent with the ones obtained from the LeBail fits, confirming that the additional Bragg peaks correspond to a small secondary phase with different symmetry than the main cubic phase. Such phase probably also corresponds with the minor impurity phase observed in $CuCr_{1.6}Sn_{0.4}S_{2.3}Se_{1.7}$, which was suggested to affect the values of the electrical conductivity [125].

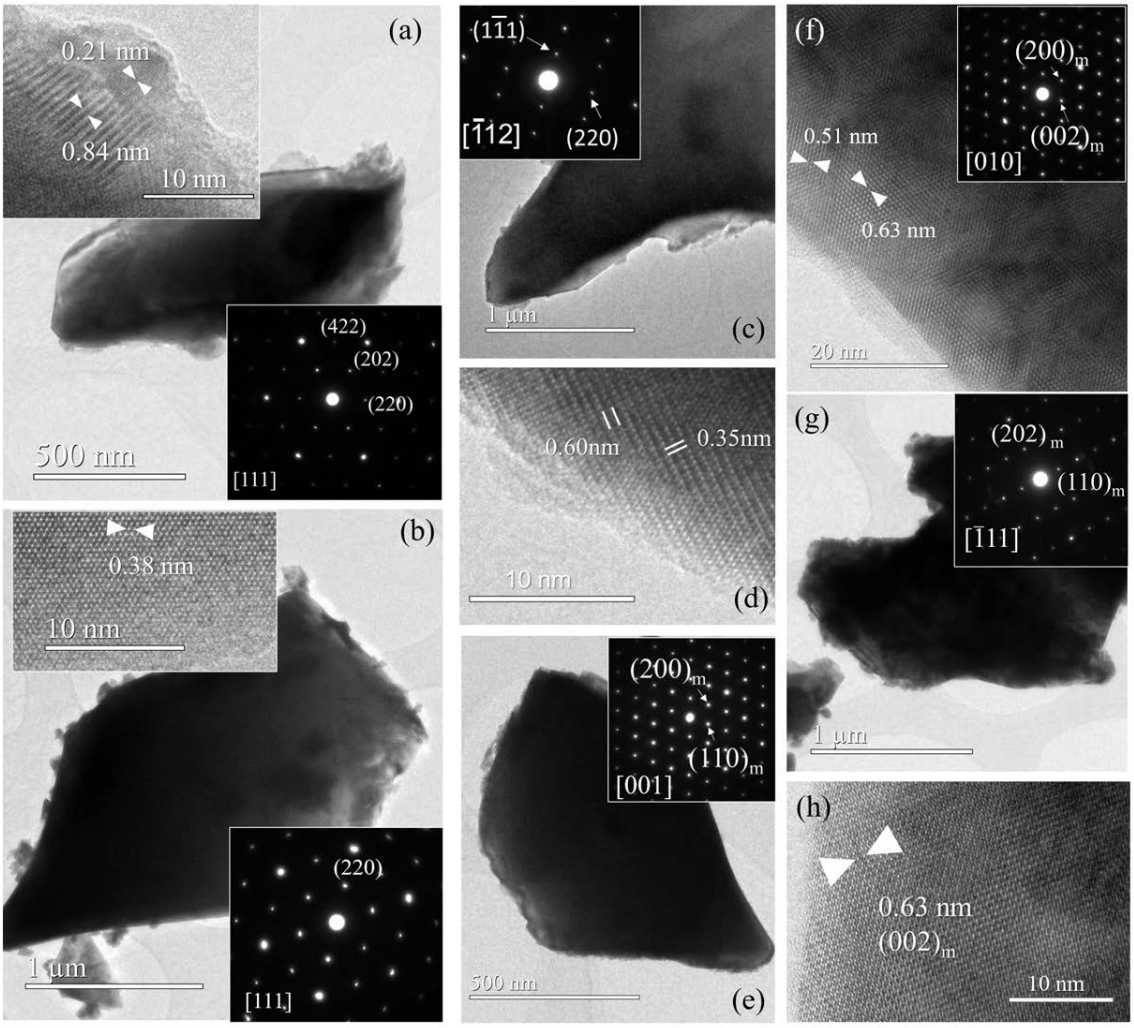

Figure 7.6: HRTEM images and ED patterns for spinel-type $CuCr_{2-x}Sn_xS_2Se_2$ with cubic symmetry for $x = 0.2$ (a), 0.3 (b), 0.4 (c) and (d). HRTEM images and ED patterns for crystals indexed considering the monoclinic Fe_7S_8-type phase for $x = 0.2$ (e) and (h), 0.3 (f), 0.4 (g).

7.6 Discussion

7.6.1 Monoclinic phase

The peaks indexed by the secondary monoclinic phase, confirmed by both NPD and HRTEM experiments, are similar to the ones reported for $CuCr_2Se_4$ measured under an applied pressure of 9.9 GPa [105]. In that study, they observed a cubic $Fd\bar{3}m$ to monoclinic structural transition which is completed at ~20 GPa. Although the space group was not determined due to significant overlap of adjacent Bragg peaks and high texture effects, the authors suggested that the system $CuCr_2Se_4$ transformed into a $CrMo_2S_4$-type structure with SG Cc, which in turn is a distorted variant of the Cr_3S_4-type phase (SG $C2/m$).

While all of the $A\mathrm{Cr_2S_4}$ sulfides (A = Mn - Zn, Cd, Hg) crystallize in the cubic $Fd\bar{3}m$ structure [127], the vast majority of $A\mathrm{Cr_2Se_4}$ selenides favors the $\mathrm{Cr_3S_4}$-type phase (A = Mn - Ni), and only a few selenide materials adopt the cubic structure (A = Cu, Zn, Cd, Hg) [102]. The comparison between both spinel families suggests that both the larger size and the more covalent character of $\mathrm{Se^{2-}}$ favor the adoption of this monoclinic structure for magnetic A cations. In addition, Efthimiopoulos *et. al* [105] argued that the $Fd\bar{3}m$ to monoclinic structural transition in $\mathrm{CuCr_2Se_4}$ could be facilitated by the size similarity between the $\mathrm{Cu^+}$ and $\mathrm{Cr^{3+}}$ cations ($r(\mathrm{Cu^+}) = 0.6$ Å and $r(\mathrm{Cr^{3+}}) = 0.615$ Å [85])

In our case, the system $\mathrm{CuCr_{2-x}Sn_xS_2Se_2}$ with the chalcogenide site equally and randomly occupied by $\mathrm{S^{2-}}$ and $\mathrm{Se^{2-}}$ anions develops an energetically favourable impurity monoclinic phase. Taking into account the evolution of the unit cell parameter a with x in Fig. 7.5(a), it can be deduced that the increase in content of Sn x induces an expansion of the unit cell volume. Such expansion can be seen as an internal negative pressure acting on the system, which lowers its density and makes the monoclinic phase not energetically favorable anymore for high concentrations of Sn.

Therefore, although the experiments performed in this study for $\mathrm{CuCr_{2-x}Sn_xS_2Se_2}$ were done at ambient pressure, a process involving chemical pressure due to the Sn incorporation could explain the Sn dependence of the monoclinic phase.

7.6.2 Sn content dependent magnetism

Taking into account the experimental results from both the magnetization and NPD measurements, a summary of the different magnetic phases observed as function of the Sn content is proposed in Fig. 7.7.

The results demonstrate a progressive change in the magnetic ground state of these compounds from a FM system, $\mathrm{CuCr_{1.8}Sn_{0.2}S_2Se_2}$, to a spin glass-like behavior in $\mathrm{CuCrSnS_2Se_2}$, in which AF interactions prevail, but without any observed LRO. To understand the magnetic behavior in the family $\mathrm{CuCr_{2-x}Sn_xS_2Se_2}$, we need to consider that $\mathrm{Cr^{3+}}$- $\mathrm{Cr^{4+}}$ interactions are FM (double exchange), while the $\mathrm{Cr^{3+}}$-$\mathrm{Cr^{3+}}$ ones are AF (super-exchange). Moreover, it is important to note that the system presents a random magnetic dilution, i.e. each cation ($\mathrm{Cr^{3+}}$, $\mathrm{Cr^{4+}}$ and $\mathrm{Sn^{4+}}$) is randomly connected with the others. Additionally, the Se and S anions are also randomly distributed, which will randomly modify the exchange pathways between the Cr cations.

When the amount of $\mathrm{Cr^{3+}}$ and $\mathrm{Cr^{4+}}$ cations in the system is the same, (i.e. $x = 0$, $\mathrm{CuCr_2S_2Se_2}$), the probability to find connected FM Cr pairs is maximal (over the percolation threshold, $p = 0.401$, for an octahedral sublattice in the spinel [128]), the degree of frustration is low, and, therefore, it leads to a FM LRO. For low Sn content ($x = 0.2$, 0.3 and 0.4), the dominant interaction is still FM, establishing a LRO at T_C confirmed by the onset of a magnetic peak in the NPD patterns. However, when Sn enters in the system, besides the magnetic dilution effect, the AF interaction between $\mathrm{Cr^{3+}}$ ions begins to grow at the expense of the FM one, which cause the increase of magnetic frustration and a blockage below T_2.

As the Sn content increases ($x = 0.6$, 0.8), although FM interactions are domi-

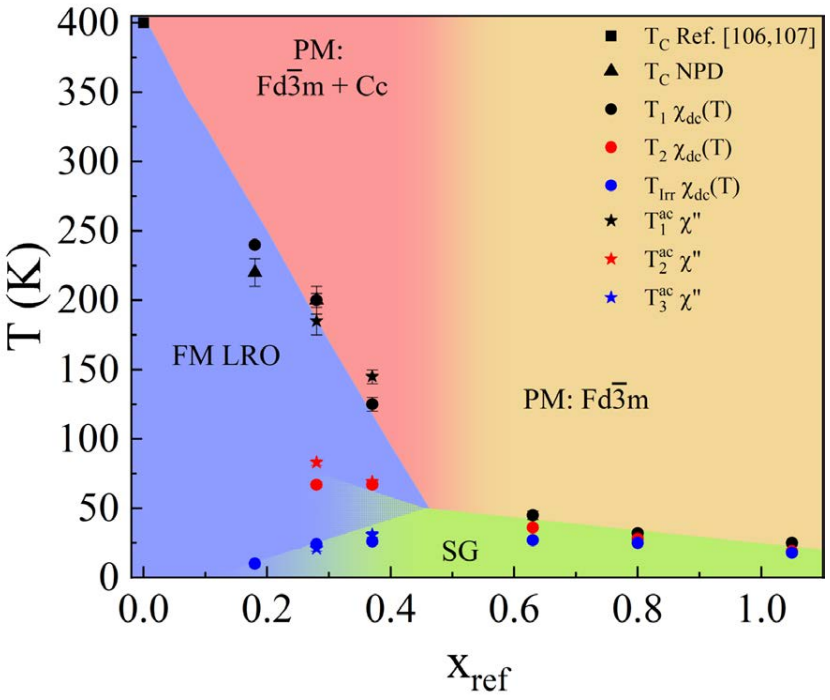

Figure 7.7: Magnetic ground state versus the refined x_{ref} value for the family $CuCr_{2-x}Sn_xS_2Se_2$ obtained by plotting the Curie temperature T_C (T_1, T_1^{ac}) (black), the freezing temperature T_f (T_2, T_2^{ac}) (red), and the irreversibility temperature T_{Irr} (T_3^{ac}) (blue) determined from the analysis of d.c. susceptibility (filled circles), a.c. susceptibility (filled stars) and NPD (filled triangles) experiments. The T_C for $x = 0$ is also plotted by averaging the values for $CuCr_2S_4$ and $CuCr_2Se_4$ from Ref.[106, 107] (black filled square). The different magnetic phases present are labeled as: paramagnetic (PM), ferromagnetic long-range order (FM LRO), spin glass-like (SG).

nant ($\theta_{CW} > 0$) they do not percolate all over the system. In this case, T_1 is not a true Curie temperature, provided that although the system tends to order itself, the process is not completed at any time. As in the previous case, at low enough temperatures, magnetic frustration becomes dominant throughout the crystal, leading to the freezing of most of the magnetic moments at T_2. In this case the FM pairs are grouped in isolated clusters (far from the percolation threshold) resulting in some short-range order (SRO) at T_1.

For $x = 1$, only AF interactions are present among the Cr^{3+} ions ($\theta_{CW} < 0$), however, the magnetic frustration and the dilution of the magnetic lattice with increasingly diamagnetic Sn^{4+} cations hamper the development of any magnetic LRO. In this scenario, T_1 and T_2 almost merge and cannot be considered critical temperatures but rather represent the onset of some reminiscent short-range order (SRO) over-imposed to a spin glass-like behavior, compatible with the absence of any magnetic signals in the NPD data. A similar behavior has been reported in the parent compounds $CuCr_{2-x}Sn_xSe_4$, in which no dilution exists in the chalcogenide site [118].

The landscape explained in the precedent paragraphs would predict the decreas-

ing of the electrical conductivity as the content of Sn^{4+} increases, from a metallic behavior, when the sample is ferromagnetic, to an insulator, for the AF or spin-glass like phase, due to the weakening of the Cr^{3+}- Cr^{4+} double exchange interactions. This is in agreement with the semiconducting behavior of the electrical conductivity measured for $CuCr_{2-x}Sn_xS_{2.3}Se_{1.7}$ and $CuCr_{2-x}Sn_xS_{1.7}Se_{2.3}$ (x = 0.4, 0.6 and 1.0) [125]. However, one should anticipate a metal-insulator transition occurring at intermediate compositions, which has not been measured yet.

Additionally, following the dependence of the Cr-Se/S bonds length with the Sn content, an increase is observed from 2.45994(7) Å (x = 0.2) to 2.5418(14) Å (x = 1.0). Such increase in the bond length results in a weakening of the Cr^{3+}-Cr^{4+} super-exchange interaction, and therefore it stimulates the AF interactions [118]. This is observed in $CuCr_{2-x}Sn_xS_4$, where the smaller S anions give as a result shorter bonds and Curie-Weiss temperatures θ_{CW} for x = 1, 0.8 indicating a stronger FM contribution [101]. Thus, it seems that the effect of the bond *randomness* is mainly due to the relative anion size and less important in determining the magnetic properties compared with the magnetic site *randomness*, as suggested by K.Belakroum *et.al* (2013) [122].

In particular, the complex behavior of the sample with x = 0.4 helps us to understand the magnetic behavior of the entire series. The existence of a tiny magnetic peak at 100 K in the NPD data implies the presence of FM LRO which is associated with the increase in the d.c. susceptibility curve at $T_1 = 125(5)$ K. Hence, for x = 0.4, T_1 is also a true Curie temperature, although only 0.4 μ_B are ordered due to the existence of frustration. At T = 40 K, the intensity of the magnetic peak is indistinguishable from the background contribution in the corresponding NPD diffractogram. Hence, the abrupt decrease in $\chi_{dc}(T)$ and the maximum in the out-of phase signal of the susceptibility ($\chi''(T)$) observed below 70 K, characteristic of the reentrant spin glass [92, 120], are associated with the loss of LRO. This might be explained assuming that for x = 0.4 Sn concentration, the probability to find a Cr^{4+} as first neighbor (in a frustrated magnetic lattice with 3+3 first neighbors) of a given Cr^{3+} site is smaller than the probability to find another Cr^{3+}. If it is the case, the number of Cr^{3+}- Cr^{3+} AF pairs with center in a given Cr^{3+} respect the number of Cr^{3+}- Cr^{4+} FM pairs will be larger, and therefore at low temperatures it might induce the creation of a spin glass-like magnetic ground state. This could be in agreement with the fact that $\chi''(T)$ has a visible frequency dependence for x = 0.4 at low temperatures (see Fig. 7.3(b)). Finally, at 2 K the spin glass state is already fully established in the whole system, causing the almost zero macroscopic magnetization as well as the absence of the NPD magnetic peak.

Special attention merits the region between $0.4 \leq x \leq 0.6$ in Fig. 7.7 in which, the potential presence of a critical point at around $x \sim 0.5$, where the PM, FM and SG phases could coexist, cannot be discarded. Regarding from previous section that the increase in x makes the monoclinic phase not energetically favorable anymore, our data appear to indicate some correlation between the absence of the monoclinic impurity and the appearance of SG state. However, at this stage more experimental work is needed to confirm this fact. For example, the evolution of the magnetic and nuclear structures as function of the pressure and the temperature.

A very similar magnetic phase diagram has been reported in $CuCr_{2-x}Ti_xS_4$ [92],

where the ground state below T_2 was assumed to be a coexistence of the ferromagnetic and spin glass states due to the freezing of the components of the magnetic moment perpendicular to the applied field, while the ground state below $T_{\rm Irr}$ was described by a freezing of all spin components. If we assume such hypothesis, the lines defined by T_2 and $T_{\rm Irr}$ could be explained by the G–T and A–T theories [129, 130]. These lines vanish with a crossover behavior when the system approaches the FM LRO phase. Furthermore, Kariya *et.al* speculated about the out-of phase signal of the susceptibility ($\chi''(T)$) exhibiting three characteristic temperatures [92], in perfect agreement with our results, which would corroborate the freezing of the transverse and longitudinal spin components at the G-T and A-T lines, respectively. However, a microscopic direct evidence of such freezing would be desirable. By following the intensity of the magnetic Bragg peaks and its surrounding background in NPD experiments with applied magnetic field, a confirmation of these ideas could be obtained.

7.7 Conclusions

New series of solid solutions spinels with formula $CuCr_{2-x}Sn_xS_2Se_2$ ($0.2 \leq x \leq 1.0$) have been synthesized and studied with d.c. and a.c. magnetization, high resolution transmission electron microscopy and neutron powder diffraction experiments to study its magnetic behavior.

The crystalline structure of these series of spinels has been refined and a new unexpected secondary monoclinic phase has been manifested.

Regarding the magnetic properties of these compounds, our combined magnetometry and NPD diffraction study allow us to conclude that a progressive change in the magnetic ground state takes place, with the compounds evolving from a FM system, $CuCr_{1.8}Sn_{0.2}S_2Se_2$, to a spin glass-like system $CuCrSnS_2Se_2$, in which AF frustrated interactions prevail, but without LRO. The magnetism of these compounds can be understood within the $Cu^{+}[Cr^{3+}_{1.0}Cr^{4+}_{1-x}Sn^{4+}_{x}]S_2Se_2$ model, in which a random competition between Cr^{3+} - Cr^{4+} FM interactions (double exchange) and Cr^{3+} - Cr^{3+} AF interactions (super-exchange) takes place.

Our results allow to propose a FM LRO for $x \leq 0.4$ samples which can be classified under the *irrep* $\mathrm{m}\Gamma_4^+$. In samples with relatively high Sn concentration ($x > 0.4$) the frustration and the random Sn diamagnetic dilution, become dominant. In these compounds FM LRO is suppressed and replaced by a magnetic state compatible with a spin glass-like behavior.

A paper summarizing the results presented in this chapter has been submitted to Physical Review B and is waiting for acceptance.

Conclusions of Part II

Part II focused on the exploration of the intricate magnetism inherent to spinel structures, particularly on the interplay of frustration and disorder within two spinel families: chromium-based normal spinel oxides ACr_2O_4 and chalcogenide spinels AB_2X_4. The multifaceted nature of these materials, capable of hosting magnetic and non-magnetic cations in both A and B sublattices, positions them at the forefront of condensed matter research, promising advancements in various technological applications.

In the case of $MnCr_2O_4$, our combination of magnetization, specific heat, and neutron powder diffraction (NPD) experiments have reaffirmed the presence of three long-range order (LRO) magnetic phases, introducing a previously unreported phase characterized by a novel incommensurate propagation vector. The application of magnetic superspace group formalism allowed for a precise determination of each phase's global symmetry, providing insights into the complex magnetic landscape driven by exchange interactions. Furthermore, the identification of transverse conical magnetic structures in these phases underpins the material's potential for multiferroicity.

Expanding our investigation to the $Mn_{1-x}Mg_xCr_2O_4$ series, neutron diffraction experiments elucidated the effects of magnetic disorder induced by Mg substitution. The gradual suppression of the LRO ferrimagnetic phase and the transition from LRO to short-range order (SRO) in the spiral phase as Mg content increases, underscore the delicate balance of exchange interactions and structural distortions in dictating magnetic order.

Finally, the study of $CuCr_{2-x}Sn_xSe_2S_2$ solid solutions revealed a fascinating evolution from ferromagnetic to spin glass-like systems with increasing Sn content, attributable to the competitive interplay between Cr^{3+}-Cr^{4+} ferromagnetic and Cr^{3+}-Cr^{3+} antiferromagnetic interactions. This transition, accompanied by the discovery of a secondary monoclinic phase, highlights the role of frustration and diamagnetic dilution in the emergence of complex magnetic states.

Collectively, these findings significantly contribute to our understanding of the mechanisms that rule non-collinear magnetism in spinel structures, demonstrating how frustration and disorder intricately influence the material's magnetic properties.

Looking ahead, it is imperative for future research to delve deeper into these compounds. For $MnCr_2O_4$, experimentally confirming the multiferroic nature of the novel incommensurate phase stands as a critical task. In the $Mn_{1-x}Mg_xCr_2O_4$ series, it is essential to not only corroborate and extend NPD findings but also to undertake a thorough macroscopic magnetic characterization. Additionally, further investigations into $CuCr_{2-x}Sn_xSe_2S_2$ solid solutions, focusing on the magnetic and

nuclear structure's evolution with pressure and temperature variations and probing the freezing of spin components in spin glass-like states, could unveil new dimensions of these complex materials.

Bibliography of Part II

[1] R. J. Hill, J. R. Craig, and G. V. Gibbs, "Systematics of the spinel structure type," Physics and Chemistry of Minerals, vol. 4, no. 4, pp. 317–339, 1979.

[2] Q. Zhao, Z. Yan, C. Chen, and J. Chen, "Spinels: Controlled Preparation, Oxygen Reduction/Evolution Reaction Application, and Beyond," Chemical Reviews, vol. 117, pp. 10121–10211, jul 2017.

[3] A. F. Wells, Structural Inorganic Chemistry. Oxford University Press, 5th ed., 1984.

[4] H. Takagi and S. Niitaka, "Highly Frustrated Magnetism in Spinels," in Introduction to Frustrated Magnetism, pp. 155–175, Springer Berlin Heidelberg, sep 2010.

[5] J. Dunitz and L. Orgel, "Electronic properties of transition-metal oxides-II," Journal of Physics and Chemistry of Solids, vol. 3, pp. 318–323, jan 1957.

[6] D. S. McClure, "The distribution of transition metal cations in spinels," Journal of Physics and Chemistry of Solids, vol. 3, pp. 311–317, jan 1957.

[7] W. Bragg, "XXX. The structure of the spinel group of crystals," The London, Edinburgh, and Dublin Philosophical Magazine and Journal of Science, vol. 30, pp. 305–315, aug 1915.

[8] S. Nishikawa, "Structure of Some Crystals of Spinel Group," Proceedings of the Tokyo Mathematico-Physical Society. 2nd Series, vol. 8, no. 7, pp. 199–209, 1915.

[9] V. Tsurkan, H.-A. K. von Nidda, J. Deisenhofer, P. Lunkenheimer, and A. Loidl, "On the complexity of spinels: Magnetic, electronic, and polar ground states," Physics Reports, vol. 926, pp. 1–86, sep 2021.

[10] A. Sundaresan and N. V. Ter-Oganessian, "Magnetoelectric and multiferroic properties of spinels," Journal of Applied Physics, vol. 129, feb 2021.

[11] A. Janner and T. Janssen, "Symmetry of incommensurate crystal phases. I. Commensurate basic structures," Acta Crystallographica Section A, vol. 36, pp. 399–408, may 1980.

[12] J. M. Perez-Mato, J. L. Ribeiro, V. Petricek, and M. I. Aroyo, "Magnetic superspace groups and symmetry constraints in incommensurate magnetic phases," Journal of Physics: Condensed Matter, vol. 24, p. 163201, mar 2012.

[13] J. Rodríguez-Carvajal and J. Villain, "Magnetic structures," Comptes Rendus Physique, vol. 20, pp. 770–802, nov 2019.

[14] Z. Lu, J. Zhu, E. A. Payzant, and M. P. Paranthaman, "Electrical Conductivity of the Manganese Chromite Spinel Solid Solution," Journal of the American Ceramic Society, vol. 88, pp. 1050–1053, apr 2005.

[15] H. Li and W. Chen, "Stability of $MnCr_2O_4$ spinel and Cr_2O_3 in high temperature carbonaceous environments with varied oxygen partial pressures," Corrosion Science, vol. 52, pp. 2481–2488, jul 2010.

[16] M. Hamad, "Simulated magnetocaloric properties of $MnCr_2O_4$ spinel," Processing and Application of Ceramics, vol. 10, no. 1, pp. 33–36, 2016.

[17] S. Chu, Y. Cui, and N. Liu, "The path towards sustainable energy," Nature Materials, vol. 16, pp. 16–22, dec 2016.

[18] K. Dey, A. Indra, S. Majumdar, and S. Giri, "Critical behavior and reversible magnetocaloric effect in multiferroic $MnCr_2O_4$," Journal of Magnetism and Magnetic Materials, vol. 435, pp. 15–20, aug 2017.

[19] W. Raza, F. Ali, N. Raza, Y. Luo, K.-H. Kim, J. Yang, S. Kumar, A. Mehmood, and E. E. Kwon, "Recent advancements in super-capacitor technology," Nano Energy, vol. 52, pp. 441–473, oct 2018.

[20] K. Manjunatha, V. J. Angadi, R. A. Ribeiro, E. Longo, M. C. Oliveira, M. R. Bomio, S. R. de Lázaro, S. Matteppanavar, S. Rayaprol, P. Babu, and M. Pasha, "Structural, electronic, vibrational and magnetic properties of Zn^{2+} substituted $MnCr_2O_4$ nanoparticles," Journal of Magnetism and Magnetic Materials, vol. 502, p. 166595, may 2020.

[21] M. Javed, A. A. Khan, J. Kazmi, M. A. Mohamed, M. S. Ahmed, and Y. Iqbal, "Impedance spectroscopic study of charge transport and relaxation mechanism in $MnCr_2O_4$ ceramic chromite," Journal of Alloys and Compounds, vol. 854, p. 156996, feb 2021.

[22] S. Funahashi, Y. Morii, and H. R. Child, "Two-dimensional neutron diffraction of YFe_2O_4 and $CoCr_2O_4$," Journal of Applied Physics, vol. 61, pp. 4114–4116, apr 1987.

[23] S. Lee, C. Broholm, W. Ratcliff, G. Gasparovic, Q. Huang, T. H. Kim, and S.-W. Cheong, "Emergent excitations in a geometrically frustrated magnet," Nature, vol. 418, pp. 856–858, Aug 2002.

[24] M. T. Rovers, P. P. Kyriakou, H. A. Dabkowska, G. M. Luke, M. I. Larkin, and A. T. Savici, "Muon-spin-relaxation investigation of the spin dynamics of geometrically frustrated chromium spinels," Physical Review B, vol. 66, p. 174434, nov 2002.

[25] K. Tomiyasu, J. Fukunaga, and H. Suzuki, "Magnetic short-range order and reentrant-spin-glass-like behavior in $CoCr_2O_4$ and $MnCr_2O_4$ by means of neutron scattering and magnetization measurements," Physical Review B, vol. 70, p. 214434, Dec 2004.

[26] H. Ueda, H. A. Katori, H. Mitamura, T. Goto, and H. Takagi, "Magnetic-Field Induced Transition to the 1/2 Magnetization Plateau State in the Geometrically Frustrated Magnet $CdCr_2O_4$," Physical Review Letters, vol. 94, p. 047202, feb 2005.

[27] J.-H. Chung, M. Matsuda, S.-H. Lee, K. Kakurai, H. Ueda, T. J. Sato, H. Takagi, K.-P. Hong, and S. Park, "Statics and Dynamics of Incommensurate Spin Order in a Geometrically Frustrated Antiferromagnet $CdCr_2O_4$," Physical Review Letters, vol. 95, p. 247204, dec 2005.

[28] Y. Yamasaki, S. Miyasaka, Y. Kaneko, J.-P. He, T. Arima, , and Y. Tokura, "Magnetic Reversal of the Ferroelectric Polarization in a Multiferroic Spinel Oxide," Physical Review Letters, vol. 96, p. 207204, 05 2006.

[29] M. Matsuda, M. Takeda, M. Nakamura, K. Kakurai, A. Oosawa, E. Lelièvre-Berna, J.-H. Chung, H. Ueda, H. Takagi, and S.-H. Lee, "Spiral spin structure in the heisenberg pyrochlore magnet $CdCr_2O_4$," Physical Review B, vol. 75, p. 104415, mar 2007.

[30] A. N. Yaresko, "Electronic band structure and exchange coupling constants in ACr_2X_4 spinels (A=Zn, Cd, Hg; X=O, S, Se)," Physical Review B, vol. 77, p. 115106, mar 2008.

[31] Y. J. Choi, J. Okamoto, D. J. Huang, K. S. Chao, H. J. Lin, C. T. Chen, M. van Veenendaal, T. A. Kaplan, and S.-W. Cheong, "Thermally or Magnetically Induced Polarization Reversal in the Multiferroic $CoCr_2O_4$," Physical Review Letters, vol. 102, p. 067601, 02 2009.

[32] E. Winkler, S. Blanco Canosa, F. Rivadulla, M. A. López-Quintela, J. Rivas, A. Caneiro, M. T. Causa, and M. Tovar, "Magnetocrystalline interactions in $MnCr_2O_4$ spinel," Physical Review B, vol. 80, p. 104418, Sep 2009.

[33] K. Tomiyasu, K. Horigane, T. Yokobori, Y. Kousaka, M. Takahashi, H. Hiraka, J. Akimitsu, and K. Yamada, "Unquenched Geometric Frustration Effect on Spiral Spin Correlation in Magnetically Ordered Phase," Journal of the Physical Society of Japan, vol. 78, p. 084704, aug 2009.

[34] N. Mufti, A. A. Nugroho, G. R. Blake, and T. T. M. Palstra, "Magnetodielectric coupling in frustrated spin systems: the spinels MCr_2O_4 (M = Mn, Co and Ni)," Journal of Physics: Condensed Matter, vol. 22, p. 075902, feb 2010.

[35] V. Kocsis, S. Bordács, D. Varjas, K. Penc, A. Abouelsayed, C. A. Kuntscher, K. Ohgushi, Y. Tokura, and I. Kézsmárki, "Magnetoelasticity in ACr$_2$O$_4$ spinel oxides (A=Mn, Fe, Co, Ni, and Cu)," Physical Review B, vol. 87, p. 064416, Feb 2013.

[36] K. Dey, S. Majumdar, and S. Giri, "Ferroelectricity in spiral short-range-ordered magnetic state of spinel MnCr$_2$O$_4$: Significance of topological frustration and magnetoelastic coupling," Physical Review B, vol. 90, p. 184424, nov 2014.

[37] Y. Li, S. Feng, Q. Lv, X. Kan, and X. Liu, "An investigation of reentrant spin-glass behavior, magnetocaloric effect and critical behavior of MnCr$_2$O$_4$," Journal of Alloys and Compounds, vol. 877, p. 160224, oct 2021.

[38] F. F. Fava, I. Baraille, A. Lichanot, C. Larrieu, and R. Dovesi, "On the structural, electronic and magnetic properties of MnCr$_2$O$_4$ spinel," Journal of Physics: Condensed Matter, vol. 9, no. 48, p. 10715, 1997.

[39] T. Suzuki, K. Adachi, and T. Katsufuji, "Correlation between magnetic, dielectric properties and crystal structure in MnT_2O$_4$ (T=V, Cr, Mn)," Journal of Magnetism and Magnetic Materials, vol. 310, pp. 780–781, mar 2007.

[40] C. Ederer and M. Komelj, "Magnetic coupling in CoCr$_2$O$_4$ and MnCr$_2$O$_4$: An LSDA + U study," Physical Review B, vol. 76, p. 064409, Aug 2007.

[41] S. Blanco-Canosa, F. Rivadulla, V. Pardo, D. Baldomir, J.-S. Zhou, M. García-Hernández, M. A. López-Quintela, J. Rivas, and J. B. Goodenough, "Enhanced Pressure Dependence of Magnetic Exchange in A^{2+}[V$_2$]O$_4$ Spinels Approaching the Itinerant Electron Limit," Physical Review Letters, vol. 99, p. 187201, Nov 2007.

[42] J. M. Hastings and L. M. Corliss, "Magnetic Structure of Manganese Chromite," Physical Review, vol. 126, pp. 556–565, Apr 1962.

[43] H. Gupta, M. Sinha, Balram, and B. Tripathi, "A study of the interatomic interaction in oxide spinel MnCr$_2$O$_4$," Physica B: Condensed Matter, vol. 192, pp. 343–344, dec 1993.

[44] S. Bordács, D. Varjas, I. Kézsmárki, G. Mihály, L. Baldassarre, A. Abouelsayed, C. A. Kuntscher, K. Ohgushi, and Y. Tokura, "Magnetic-Order-Induced Crystal Symmetry Lowering in ACr$_2$O$_4$ Ferrimagnetic Spinels," Physical Review Letters, vol. 103, p. 077205, aug 2009.

[45] G. T. Lin, Y. Q. Wang, X. Luo, J. Ma, H. L. Zhuang, D. Qian, L. H. Yin, F. C. Chen, J. Yan, R. R. Zhang, S. L. Zhang, W. Tong, W. H. Song, P. Tong, X. B. Zhu, and Y. P. Sun, "Magnetoelectric and Raman spectroscopic studies of monocrystalline MnCr$_2$O$_4$," Physical Review B, vol. 97, p. 064405, feb 2018.

[46] D. H. Lyons, T. A. Kaplan, K. Dwight, and N. Menyuk, "Classical Theory of the Ground Spin-State in Cubic Spinels," Physical Review, vol. 126, pp. 540–555, apr 1962.

[47] R. Plumier, "Reinvestigation of Magnetic Structures of $CoCr_2O_4$ and $MnCr_2O_4$ Obtained by Neutron Diffraction," Journal of Applied Physics, vol. 39, no. 2, pp. 635–636, 1968.

[48] Y. Zhou, Z. Yang, L. Li, Y. Xie, S. Lin, Y. Sun, and Y. Zhang, "Magnetic field and external pressure effects on the spiral order of polycrystalline $MnCr_2O_4$," Journal of Magnetism and Magnetic Materials, vol. 324, pp. 3799–3801, nov 2012.

[49] K. Dwight, N. Menyuk, J. Feinleib, and A. Wold, "Reduced Manganese Moment in Manganese Chromite," Journal of Applied Physics, vol. 37, no. 3, pp. 962–963, 1966.

[50] D. Tobia, J. Milano, M. T. Causa, and E. L. Winkler, "Temperature evolution of the effective magnetic anisotropy in the $MnCr_2O_4$ spinel," Journal of Physics: Condensed Matter, vol. 27, no. 1, p. 016003, 2015.

[51] N. Mufti, G. Blake, and T. Palstra, "Magnetodielectric coupling in $MnCr_2O_4$ spinel," Journal of Magnetism and Magnetic Materials, vol. 321, pp. 1767–1769, jun 2009.

[52] J. Rodríguez-Carvajal, "Recent advances in magnetic structure determination by neutron powder diffraction," Physica B: Condensed Matter, vol. 192, no. 1, pp. 55 – 69, 1993.

[53] H. T. Stokes, D. M. Hatch, and B. J. Campbell, "ISODISTORT, ISOTROPY Software Suite," iso.byu.edu, 2017.

[54] B. J. Campbell, H. T. Stokes, D. E. Tanner, and D. M. Hatch, "ISODISPLACE: a web-based tool for exploring structural distortions," Journal of Applied Crystallography, vol. 39, pp. 607–614, jul 2006.

[55] M. I. Aroyo, J. M. Perez-Mato, D. Orobengoa, E. Tasci, G. de la Flor, and A. Kirov, "Crystallography online: Bilbao Crystallographic Server," Bulgarian Chemical Communications, vol. 43, no. 2, pp. 183–197, 2011.

[56] M. I. Aroyo, J. M. Perez-Mato, C. Capillas, E. Kroumova, S. Ivantchev, G. Madariaga, A. Kirov, and H. Wondratschek, "Bilbao Crystallographic Server: I. Databases and crystallographic computing programs," Zeitschrift fur Kristallographie - Crystalline Materials, vol. 221, pp. 15–27, jan 2006.

[57] M. I. Aroyo, A. Kirov, C. Capillas, J. M. Perez-Mato, and H. Wondratschek, "Bilbao Crystallographic Server. II. Representations of crystallographic point groups and space groups," Acta Crystallographica Section A Foundations of Crystallography, vol. 62, pp. 115–128, mar 2006.

[58] J. Perez-Mato, S. Gallego, E. Tasci, L. Elcoro, G. de la Flor, and M. Aroyo, "Symmetry-Based Computational Tools for Magnetic Crystallography," Annual Review of Materials Research, vol. 45, pp. 217–248, jul 2015.

[59] L. Néel, "Antiferromagnetism and Ferrimagnetism," Proceedings of the Physical Society. Section A, vol. 65, pp. 869–885, nov 1952.

[60] F. Lotgering, "On the ferrimagnetism of some sulphides and oxides," Philips Research Reports, vol. 11, pp. 190–249, 1956.

[61] G. Lin, W. Tong, X. Luo, F. Chen, L. Yin, Y. Wang, L. Hu, Y. Zou, L. Yu, W. Song, and Y. Sun, "Magnetocrystalline interactions in spinel $MnCr_2O_4$ single crystal probed by electron spin resonance," Journal of Alloys and Compounds, vol. 711, pp. 250–257, jul 2017.

[62] R. E. Newnham and Y. M. de Haan, "Refinement of the α Al_2O_3 , Ti_2O_3 , V_2O_3 and Cr_2O_3 structures," Zeitschrift fur Kristallographie, vol. 117, pp. 235–237, 08 1962.

[63] N. Menyuk, K. Dwight, and A. Wold, "Ferrimagnetic spiral configurations in cobalt chromite," Journal de Physique, vol. 25, no. 5, pp. 528–536, 1964.

[64] E. Whipple and A. Wold, "Preparation of stoicheiometric chromites," Journal of Inorganic and Nuclear Chemistry, vol. 24, pp. 23–27, jan 1962.

[65] D. G. Wickham and J. B. Goodenough, "Suggestion Concerning Magnetic Interactions in Spinels," Physical Review, vol. 115, pp. 1156–1158, Sep 1959.

[66] L. J. Chang, D. J. Huang, W.-H. Li, S.-W. Cheong, W. Ratcliff, and J. W. Lynn, "Crossover from incommensurate to commensurate magnetic orderings in $CoCr_2O_4$," Journal of Physics: Condensed Matter, vol. 21, p. 456008, oct 2009.

[67] I. Dzyaloshinsky, "A thermodynamic theory of "weak" ferromagnetism of antiferromagnetics," Journal of Physics and Chemistry of Solids, vol. 4, no. 4, pp. 241–255, 1958.

[68] T. Moriya, "Anisotropic Superexchange Interaction and Weak Ferromagnetism," Physical Review, vol. 120, pp. 91–98, Oct 1960.

[69] I. A. Sergienko and E. Dagotto, "Role of the Dzyaloshinskii-Moriya interaction in multiferroic perovskites," Physical Review B, vol. 73, p. 094434, Mar 2006.

[70] H. Katsura, N. Nagaosa, and A. V. Balatsky, "Spin Current and Magnetoelectric Effect in Noncollinear Magnets," Physical Review Letters, vol. 95, p. 057205, 07 2005.

[71] M. Pardo-Sainz, A. Toshima, G. André, J. Basbus, G. J. Cuello, V. Laliena, T. Honda, T. Otomo, K. Inoue, Y. Hosokoshi, Y. Kousaka, and J. Campo, "New (α β γ)-incommensurate magnetic phase discovered in the $MnCr_2O_4$ spinel at low temperatures," Physical Review B, vol. 107, apr 2023.

[72] G. Blasse and J. Fast, "Néel temperatures of some antiferromagnetic oxides with spinel structure," Philips Res. Rep., vol. 18, no. 393, 1963.

[73] H. Shaked, J. M. Hastings, and L. M. Corliss, "Magnetic Structure of Magnesium Chromite," Physical Review B, vol. 1, pp. 3116–3124, apr 1970.

[74] S. E. Dutton, Q. Huang, O. Tchernyshyov, C. L. Broholm, and R. J. Cava, "Sensitivity of the magnetic properties of the $ZnCr_2O_4$ and $MgCr_2O_4$ spinels to nonstoichiometry," Physical Review B, vol. 83, feb 2011.

[75] S. Koohpayeh, J.-J. Wen, M. Mourigal, S. Dutton, R. Cava, C. Broholm, and T. McQueen, "Optical floating zone crystal growth and magnetic properties of $MgCr_2O_4$," Journal of Crystal Growth, vol. 384, pp. 39–43, dec 2013.

[76] L. Ortega-San-Martín, A. J. Williams, C. D. Gordon, S. Klemme, and J. P. Attfield, "Low temperature neutron diffraction study of $MgCr_2O_4$ spinel," Journal of Physics: Condensed Matter, vol. 20, p. 104238, feb 2008.

[77] M. C. Kemei, P. T. Barton, S. L. Moffitt, M. W. Gaultois, J. A. Kurzman, R. Seshadri, M. R. Suchomel, and Y.-I. Kim, "Crystal structures of spin-Jahn–Teller-ordered $MgCr_2O_4$ and $ZnCr_2O_4$," Journal of Physics: Condensed Matter, vol. 25, p. 326001, jul 2013.

[78] H. Ehrenberg, M. Knapp, C. Baehtz, and S. Klemme, "Tetragonal low-temperature phase of $MgCr_2O_4$," Powder Diffraction, vol. 17, pp. 230–233, sep 2002.

[79] S. Gao, K. Guratinder, U. Stuhr, J. S. White, M. Mansson, B. Roessli, T. Fennell, V. Tsurkan, A. Loidl, M. C. Hatnean, G. Balakrishnan, S. Raymond, L. Chapon, V. O. Garlea, A. T. Savici, A. Cervellino, A. Bombardi, D. Chernyshov, C. Rüegg, J. T. Haraldsen, and O. Zaharko, "Manifolds of magnetic ordered states and excitations in the almost Heisenberg pyrochlore antiferromagnet $MgCr_2O_4$," Physical Review B, vol. 97, apr 2018.

[80] O. Tchernyshyov, R. Moessner, and S. L. Sondhi, "Order by Distortion and String Modes in Pyrochlore Antiferromagnets," Physical Review Letters, vol. 88, jan 2002.

[81] H. J. Xiang, E. J. Kan, S.-H. Wei, M.-H. Whangbo, and X. G. Gong, "Predicting the spin-lattice order of frustrated systems from first principles," Physical Review B, vol. 84, dec 2011.

[82] H. Suzuki and Y. Tsunoda, "Spinel-type frustrated system $MgCr_2O_4$ studied by neutron scattering and magnetization measurements," Journal of Physics and Chemistry of Solids, vol. 68, pp. 2060–2063, nov 2007.

[83] X. Bai, J. A. M. Paddison, E. Kapit, S. M. Koohpayeh, J.-J. Wen, S. E. Dutton, A. T. Savici, A. I. Kolesnikov, G. E. Granroth, C. L. Broholm, J. T. Chalker, and M. Mourigal, "Magnetic Excitations of the Classical Spin Liquid $MgCr_2O_4$," Physical Review Letters, vol. 122, mar 2019.

[84] T. Yokobori, K. Tomiyasu, Y. Kousaka, H. Matsui, H. Hiraka, K. Iwasa, K. Yamada, and J. Akimitsu, "Neutron scattering study of spiral-type spin correlations in the frustrated spinel $Mn_{0.07}Mg_{0.93}Cr_2O_4$," Journal of Physics: Conference Series, vol. 320, p. 012039, sep 2011.

[85] R. D. Shannon, "Revised effective ionic radii and systematic studies of interatomic distances in halides and chalcogenides," Acta Crystallographica Section A, vol. 32, pp. 751–767, Sep 1976.

[86] A. P. Ramirez, R. J. Cava, and J. Krajewski, "Colossal magnetoresistance in Cr-based chalcogenide spinels," Nature, vol. 386, pp. 156–159, mar 1997.

[87] J. Hemberger, P. Lunkenheimer, R. Fichtl, H.-A. K. von Nidda, V. Tsurkan, and A. Loidl, "Relaxor ferroelectricity and colossal magnetocapacitive coupling in ferromagnetic $CdCr_2S_4$," Nature, vol. 434, pp. 364–367, mar 2005.

[88] S. Krohns, F. Schrettle, P. Lunkenheimer, V. Tsurkan, and A. Loidl, "Colossal magnetocapacitive effect in differently synthesized and doped $CdCr_2S_4$," Physica B: Condensed Matter, vol. 403, pp. 4224–4227, dec 2008.

[89] C. Bourgès, B. Srinivasan, B. Fontaine, P. Sauerschnig, A. Minard, J.-F. Halet, Y. Miyazaki, D. Berthebaud, and T. Mori, "Tailoring the thermoelectric and structural properties of Cu-Sn based thiospinel compounds [$CuM_{1+x}Sn_{1-x}S_4$ (M = Ti, V, Cr, Co)]," Journal of Materials Chemistry C, vol. 8, no. 46, pp. 16368–16383, 2020.

[90] V. A. Fedorov, Y. A. Kesler, and E. G. Zhukov, "Magnetic Semiconducting Chalcogenide Spinels: Preparation and Physical Chemistry," Inorganic Materials, vol. 39, pp. S68–S88, 2003.

[91] H. Sims, K. Ramasamy, W. H. Butler, and A. Gupta, "Electronic structure of magnetic semiconductor $CdCr_2Te_4$: A possible spin-dependent symmetry filter," Applied Physics Letters, vol. 103, p. 192402, nov 2013.

[92] F. Kariya, S. Ebisu, and S. Nagata, "Evolution from a ferromagnetic to a spin-glass regime in the spinel-type," Journal of Solid State Chemistry, vol. 182, pp. 608–616, mar 2009.

[93] J. Padiou, D. Bideau, and J. Troadec, "Propriétés magnétiques et électriques de thiospinelles quaternaires," Journal of Solid State Chemistry, vol. 31, pp. 401–405, mar 1980.

[94] F. Ozel, H. Kılıc, H. Coskun, I. Deveci, A. Sarılmaz, A. Balıkcıoglu, Y. Gundogdu, A. Aljabour, A. Ozen, S. Gezgin, A. Houimi, A. Yar, M. Kus, and M. Ersoz, "A general review on the thiospinels and their energy applications," Materials Today Energy, vol. 21, p. 100822, sep 2021.

[95] M. Gogoowicz, S. Juszczyk, J. Warczewski, and T. Mydlarz, "Ferrimagnetism of $Cu_{0.45}Co_{0.55}Cr_2S_{4-y}Se_y$," Physical Review B, vol. 35, pp. 7073–7080, may 1987.

[96] S. Tsuji, K. Kumagai, N. Matsumoto, and S. Nagata, "Metal-insulator transition in the spinel $CuIr_2(S_{1-x}Se_x)_4$ system studied by NMR," Physica C: Superconductivity, vol. 282-287, pp. 1107–1108, aug 1997.

[97] E. Maciążek, A. Molak, and T. Goryczka, "Influence of cobalt substitution on structure and electric conduction of $CuCr_2Se_4$," Journal of Alloys and Compounds, vol. 441, pp. 222–230, aug 2007.

[98] R. Li, Z. Qu, L. Zhang, L. Ling, W. Tong, and Y. Zhang, "Structure, magnetic and transport properties of Li-doped $CuCr_2Se_4$," Solid State Communications, vol. 150, pp. 2289–2293, dec 2010.

[99] I. Jendrzejewska, P. Zajdel, J. Mroziński, E. Maciążek, T. Goryczka, A. Hanc, and A. Kita, "X-Ray Investigations and Magnetic Properties of $CuCr_{2-x}Sn_xSe_4$ - Compounds," Solid State Phenomena, vol. 163, pp. 208–212, jun 2010.

[100] E. Maciążek, E. Malicka, A. Gągor, Z. Stokłosa, T. Groń, B. Sawicki, H. Duda, and A. Gudwański, "Semiconducting-metallic transition of singlecrystalline ferromagnetic Hf-doped $CuCr_2Se_4$ spinels," Physica B: Condensed Matter, vol. 520, pp. 116–122, sep 2017.

[101] P. Valencia-Gálvez, O. Peña, S. Moris, and P. Barahona, "Raman characterization of $CuCr_{2-x}Sn_xS_4$ spinels," Journal of the Chilean Chemical Society, vol. 64, pp. 4285–4289, mar 2019.

[102] R. Bouchard, "Spinel to defect NiAs structure transformation," Materials Research Bulletin, vol. 2, pp. 459–464, apr 1967.

[103] Y. Amiel, G. K. Rozenberg, N. Nissim, A. Milner, M. P. Pasternak, M. Hanfland, and R. D. Taylor, "Intricate relationship between pressure-induced electronic and structural transformations in $FeCr_2S_4$," Physical Review B, vol. 84, p. 224114, dec 2011.

[104] I. Efthimiopoulos, Z. T. Y. Liu, S. V. Khare, P. Sarin, V. Tsurkan, A. Loidl, D. Popov, and Y. Wang, "Structural transition in the magnetoelectric $ZnCr_2Se_4$ spinel under pressure," Physical Review B, vol. 93, p. 174103, may 2016.

[105] I. Efthimiopoulos, V. Tsurkan, A. Loidl, D. Zhang, and Y. Wang, "Comparing the Pressure-Induced Structural Behavior of $CuCr_2O_4$ and $CuCr_2Se_4$ Spinels," The Journal of Physical Chemistry C, vol. 121, pp. 16513–16520, jul 2017.

[106] T. Saha-Dasgupta, M. D. Raychaudhury, and D. D. Sarma, "Ferromagnetism in metallic chalcospinels $CuCr_2S_4$ and $CuCr_2Se_4$," Physical Review B, vol. 76, p. 054441, aug 2007.

[107] I. Nakatani, H. Nosé, and K. Masumoto, "Magnetic properties of $CuCr_2Se_4$ single crystals," Journal of Physics and Chemistry of Solids, vol. 39, pp. 743–749, jan 1978.

[108] F. Lotgering, "Ferromagnetism in spinels: $CuCr_2S_4$ and $CuCr_2Se_4$," Solid State Communications, vol. 2, pp. 55–56, feb 1964.

[109] C. Colominas, "Neutron-Diffraction Investigation of $CuCr_2Se_4$ and $CuCr_2Te_4$," Physical Review, vol. 153, pp. 558–560, jan 1967.

[110] M. Ballal and C. Mande, "X-ray spectroscopic study of the valency of copper in the spinels $CuCr_2X_4$ (X = O, S, Se, Te)," Solid State Communications, vol. 19, pp. 325–327, jun 1976.

[111] O. Yamashita, Y. Yamaguchi, I. Nakatani, H. Watanabe, and K. Masumoto, "Polarized Neutron Diffraction Study of a $CuCr_2Se_4$ Single Crystal," Journal of the Physical Society of Japan, vol. 46, pp. 1145–1152, apr 1979.

[112] D. Rodic, B. Antic, R. Tellgren, H. Rundlof, and J. Blanusa, "A change of magnetic moment of Cr ion with the magnetic phase transition in $CuCr_2Se_4$," Journal of Magnetism and Magnetic Materials, vol. 187, pp. 88–92, aug 1998.

[113] A. Kimura, J. Matsuno, J. Okabayashi, A. Fujimori, T. Shishidou, E. Kulatov, and T. Kanomata, "Soft x-ray magnetic circular dichroism study of the ferromagnetic spinel-type Cr chalcogenides," Physical Review B, vol. 63, p. 224420, may 2001.

[114] H. Hahn, C. De Lorent, and B. Harder, "Untersuchungen über ternäre Chalkogenide. VIII. Über die Struktur des CuV_2S_4, $CuCr_2S_4$, $CuCr_2Se_4$ und $CuCr_2Te_4$," Zeitschrift für anorganische und allgemeine Chemie, vol. 283, pp. 138–142, Jan. 1956.

[115] R. J. Bouchard, P. A. Russo, and A. Wold, "Preparation and Electrical Properties of Some Thiospinels," Inorganic Chemistry, vol. 4, pp. 685–688, May 1965.

[116] K. Oda, S. Yoshii, Y. Yasui, M. Ito, T. Ido, Y. Ohno, Y. Kobayashi, and M. Sato, "Unusual Anomalous Hall Resistivities of $CuCr_2S_4$, $Cu_{0.5}Zn_{0.5}Cr_2Se_4$ and Cr_3Te_4," Journal of the Physical Society of Japan, vol. 70, pp. 2999–3005, Oct. 2001.

[117] P. Barahona, A. Galdámez, F. López-Vergara, V. Manríquez, and O. Peña, "Crystal structure and magnetic properties of titanium-based $CuTi_{2-x}M_xS_4$ and $CuCr_{2-x}Ti_xSe_4$ chalcospinels," Journal of Solid State Chemistry, vol. 212, pp. 114–120, apr 2014.

[118] C. Pinto, A. Galdámez, P. Barahona, S. Moris, and O. Peña, "Crystal structure, Raman scattering and magnetic properties of $CuCr_{2-x}Zr_xSe_4$ and $CuCr_{2-x}Sn_xSe_4$ selenospinels," Journal of Magnetism and Magnetic Materials, vol. 456, pp. 160–166, jun 2018.

[119] S. Moris, P. Valencia-Gálvez, J. Mejía-López, O. Peña, P. Barahona, and A. Galdámez, "$(Cu)_{tet}(Cr_{2-x}Sn_x)_{oct}S_{4-y}Se_y$ Spinels: Crystal Structure, Density Functional Theory Calculations, and Magnetic Behavior," Inorganic Chemistry, vol. 58, pp. 13945–13952, oct 2019.

[120] A. I. Abramovich, L. I. Koroleva, and L. N. Lukina, "Spin-glass and reentrant spin-glass states in iron sulfospinels having dilute A and B sublattices," Physics of the Solid State, vol. 41, pp. 73–79, Jan. 1999.

[121] Y. Iijima, Y. Kamei, N. Kobayashi, J. Awaka, T. Iwasa, S. Ebisu, S. Chikazawa, and S. Nagata, "A new ferromagnetic thiospinel $CuCrZrS_4$ with re-entrant spin-glass behaviour," Philosophical Magazine, vol. 83, pp. 2521–2530, July 2003.

[122] K. Belakroum, Z. Ouili, A. Leblanc-Soreau, M. Hemmida, and H.-A. Krug von Nidda, "Magnetic properties of CuCrZrSe4," Journal of Magnetism and Magnetic Materials, vol. 334, pp. 130–135, May 2013.

[123] E. Riedel and W. Morlock, "Spinelle mit substituierten Nichtmetallteilgittern. VI. Röntgenographische und elektronische Eigenschaften, Mößbauer- und IR-Spektren des Spinellsystems $CuCrSn(S_{1-x}Se_x)_4$," Zeitschrift für anorganische und allgemeine Chemie, vol. 438, pp. 233–241, Feb. 1978.

[124] D. Mähl, J. Pickardt, and B. Reuter, "Züchtung und Untersuchung von Einkristallen der Verbindungen $CuCrZrSe_4$ und $CuCrSnSe_4$," Zeitschrift für anorganische und allgemeine Chemie, vol. 508, pp. 197–200, Jan. 1984.

[125] P. Valencia-Gálvez, D. Aravena, P. Barahona, S. Moris, and A. Galdámez, "Effects of Tin and Sulfur Chemical Substitution on the Structural and Electrical Properties of $CuCr_2Se_4$ Selenospinel," Applied Sciences, vol. 12, p. 1586, feb 2022.

[126] A. V. Powell, P. Vaqueiro, K. S. Knight, L. C. Chapon, and R. D. Sánchez, "Structure and magnetism in synthetic pyrrhotite Fe_7S_8: A powder neutron-diffraction study," Physical Review B, vol. 70, jul 2004.

[127] C. Rao and K. Pisharody, "Transition metal sulfides," Progress in Solid State Chemistry, vol. 10, pp. 207–270, jan 1976.

[128] D. Fiorani, L. Gastaldi, A. Lapiccirrella, S. Viticoli, and N. Tomassini, "Monte Carlo simulation of percolative phenomena in the cationic B-sublattice of spinels," Solid State Communications, vol. 32, pp. 831–832, Dec. 1979.

[129] J. R. L. d. Almeida and D. J. Thouless, "Stability of the Sherrington-Kirkpatrick solution of a spin glass model," Journal of Physics A: Mathematical and General, vol. 11, pp. 983–990, May 1978.

[130] M. Gabay and G. Toulouse, "Coexistence of Spin-Glass and Ferromagnetic Orderings," Physical Review Letters, vol. 47, pp. 201–204, July 1981.

Part III

Interplay of dimensionality, anisotropy and frustration in purely organic magnets

The properties of magnetic systems are intricately linked to their symmetry and dimensionality, D. A well-known example of this dependence are the systems with continuous SU(2) symmetry (Heisenberg model), which cannot achieve magnetic long-range order (LRO) at non-zero temperatures ($T \neq 0$) in dimensions $D \leq 2$, as stated by the Mermin-Wagner theorem [1].

Building on the fundamental insights provided by the Mermin-Wagner theorem, the study of low dimensional magnetism, particularly within quantum systems, has gained intense research interest. The reduced dimensionality of these materials leads to a strong interplay between different degrees of freedom, such as lattice, charge, orbital, and spin. In such scenario, quantum fluctuations and interactions become more dominant than in their higher-dimensional counterparts, giving rise to unique quantum states of matter. Consequently, low dimensional quantum magnets are viewed as promising materials due to their exotic properties and potential applications in various fields, including quantum information, condensed matter physics, and material science [2].

Moreover, the frustration in these quantum spin systems, which enhances quantum fluctuations, has allowed to explore exotic phenomena such as quantum Hall effects [3, 4], topological insulators [5], spin liquids [6], and superconductivity [7].

Within this broad landscape of low-dimensional quantum magnetism, organic magnets emerge as particularly interesting subjects of study. One of the most significant advantages of organic magnets is the highly isotropic nature of their electronic spin, closely aligning with the Heisenberg model, which arises from the presence of unpaired p electrons in their organic molecular structure [8]. Therefore, these materials, forming low-spin (either spin-1/2 or spin-1) systems, have attracted significant attention due to the emergence of novel quantum magnetic phenomena [9].

Purely organic magnets

Over the past two decades, there has been a significant effort to synthesize purely organic magnets [10, 11], inspired by the foundational theories of organic magnetism proposed by H. McConnell [12] and N. Mataga [13]. This pursuit was invigorated by the discovery of p-NPNN, the first organic radical demonstrating ferromagnetic long-range order at 0.65 K [14–17].

Organic radicals are particularly important because their spin arises from the p-electron shell, which has essentially negligible spin-orbit coupling, and therefore are archetypical systems to study low-dimensional Heisenberg magnetic models and the role of quantum fluctuations in them. Several organic radicals with one-dimensional (1D) network of linear chain [18–22], alternating chain [23–27], spin ladder [28–30], zig-zag chain (J1-J2 model) [31, 32], two-dimensional (2D) lattices [22, 33–38], and three-dimensional (3D) magnetic models [39–41] have been synthesized.

The magnetic moment in organic magnetic molecules (free radicals) resides in a highly reactive open shell occupied by a p-electron. A decrease in its reactivity is usually obtained by either steric shielding or electron delocalization, thus avoiding the production of diamagnetic species by dimerization. However, the intermolecular exchange interactions in organic crystals are governed by the overlap between the

molecular orbitals. Especially the antiferromagnetic exchange couplings are brought about by the overlap between single occupied molecular orbitals (SOMO's) [42]. Therefore, a balance between the stability and the magnetic interactions of the free radicals must be achieved in the design of purely organic systems. The molecular packing in the crystal, including the distances between open-shell orbitals, plays a crucial role, as too-close distances can lead to dimerization.

Properties of nitronyl nitroxide radicals

A significant amount of attempts in the design of purely organic magnets have involved nitroxide (-N-O·) radical derivatives, specially the nitronyl nitroxide (NN) family, as building blocks. They contain only the elements C, H, N, and O and are therefore fully organic. Nitronyl nitroxides are obtained following the route given in the literature [39, 43]. Starting from 2-nitrobutane, through 2,3-dimethyl-2,3-dinitrobutane,N,N'-(2,3-dimethyl–butane-2,3diyl)bis(hydroxylamine) (A) is synthesized. The dehydration condensation of (A) and corresponding aldehyde and successive oxidation gives a nitronyl nitroxide.

According to electron paramagnetic resonance (EPR) [44], nuclear magnetic resonance (NMR) [45] and polarized neutron diffraction (PND) [46–51] measurements, in these radicals the magnetism comes from the unpaired electron delocalized over the coordinating O atom and antibonding π^* orbitals in the O-N-C-N-O plane, i.e., the electron is distributed between 2 singly occupied molecular orbitals (SOMO) on two equivalent NO groups [22]. The intermolecular exchange interaction in organic crystals is governed by the overlap between the molecular orbitals, especially the NO radical has the advantage of making an antiferromagnetic (AFM) spin network by the overlap between SOMO's [14, 15, 42]. Therefore, intermolecular AFM interactions are expected for the contacts between the NO groups.

Nitronyl nitroxide molecular crystals show a variety of magnetic ground states, since small chemical changes to the rest of the molecule lead to significant changes in crystal structure, thereby altering the intermolecular overlaps and thus the magnetic interactions [52].

Objectives of Part III

By studying the magnetic properties of organic magnets ranging between 1D and 3D, in Part III we aim to understand how low anisotropy and frustration contribute to non-collinear magnetism in low-dimensional systems.

Therefore, we focus on organic magnets based on nitronyl nitroxide radicals, as they provide great flexibility to design lattices of different dimensionalities and have a highly isotropic nature. However, several challenges can be expected – such as the complexities of synthesizing high-quality single crystals, the weak magnetic signals, or the experimental limitations when characterizing these compounds under extreme conditions – which highlight the inherent difficulty in studying these materials. In particular, we focus on two purely organic magnets: 4-F-2-NN-BIP [= 4-fluoro-2-(1-oxyl-3-oxide-4,4,5,5-tetramethylimidazolin-2-yl) biphenyl] and TNN·CH_3CN

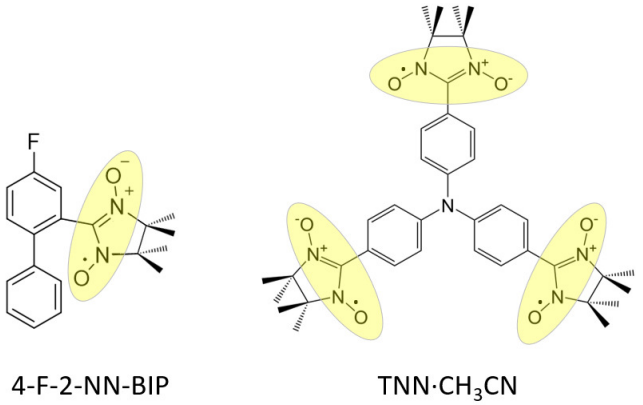

Figure III.1: Molecular structure of the organic magnets studied in this part, where the yellow ellipse denotes the delocalized spin 1/2.

[= Tris[4-(1-oxyl-3-oxide-4,4,5,5-tetramethyl-imidazolin-2-yl)phenyl]amine]. Figure III.1 illustrates the molecular structure of each compound.

In Chapter 8, the objective is to understand the magnetic properties of 4-F-2-NN-BIP, a system in between $D = 1$ and $D = 2$. Although there is no frustration in this system, its highly isotropic nature makes it an ideal candidate to verify theoretical Heisenberg model predictions. By combining numerical simulations with macroscopic characterization techniques at extremely low temperatures and under high magnetic fields, we try to determine the topology resulting from the magnetic exchange interactions. This approach helps in constructing the magnetic phase diagram and distinguishing the unique magnetic phases that emerge, thereby advancing our comprehension of the systems that exist in between one-dimensional (1D) and two-dimensional (2D) structures.

In Chapter 9, we focus on the exploration of the magnetic order in TNN·CH_3CN, a system which transitions from an effectively 2D triangular lattice to a three-dimensional (3D) structure as the temperature decreases. In this system, the interplay between frustration and low anisotropy leads to the emergence of novel quantum phases, as well as multiferroicity. We perform neutron diffraction and μSR experiments to elucidate its magnetic order at low temperatures and magnetic fields, and compare our findings with previous research and theoretical predictions of its multiferroic nature. This research adds a new dimension to our understanding of magnetic phenomena in highly isotropic frustrated systems in $D = 2$ and $D = 3$.

Chapter 8

Quantum phase transitions in the organic spin ladder 4-F-2-NN-BIP

In the following chapter we present 4-F-2-NN-BIP [= 4-fluoro-2-(1-oxyl-3-oxide-4,4,5,5-tetramethylimidazolin-2-yl) biphenyl], a novel purely organic magnetic compound. Our goal is to investigate the magnetic properties of this organic magnet, a system in between 1D and 2D structures with low-anisotropy and no frustration.

The chapter commences by exploring the theoretical properties and phase diagram of spin ladders. We then elaborate on the synthesis procedure and the experiments conducted to characterize this compound. Following this, the crystal structure is detailed, alongside an estimation of the main intermolecular exchange interactions. Together with the analysis of the EPR measurements, which show that the magnetic anisotropy is basically negligible, these results imply that this system can be well described by a $S = 1/2$ two-leg Heisenberg antiferromagnetic ladder. Next, the combination of the experimental magnetization data with exact diagonalization and quantum Monte Carlo calculations allow to obtain the relevant magnetic parameters of the system. The subsequent section delves into the specific heat measurements, and the results are compared with the theoretical model. A discussion for an anomaly observed in the isotherm magnetization curves is provided, together with several possible explanations. Finally, a magnetic phase diagram is constructed based on the analysis of specific heat, magnetization and susceptibility measurements at high magnetic fields and very low temperatures, which presents hints of a Tomonaga-Luttinger liquid phase. The concluding section encapsulates the chapter's key findings.

8.1 Introduction to spin ladders

The study of quantum spin systems has attracted much attention for several decades [30]. Recently spin-ladder systems, which are in the crossover region between one and two dimensions (see Fig. 8.1), have been at the focus of intensive research towards its understanding, since their magnetic properties critically depend on the topology, symmetry and spin, so that the evolution from 1D to 2D is not continuous. For example, Haldane's conjecture [53] predicted that the magnetic excitations in integer spin chains are gapped, while in half-integer spin chains they are gapless. In

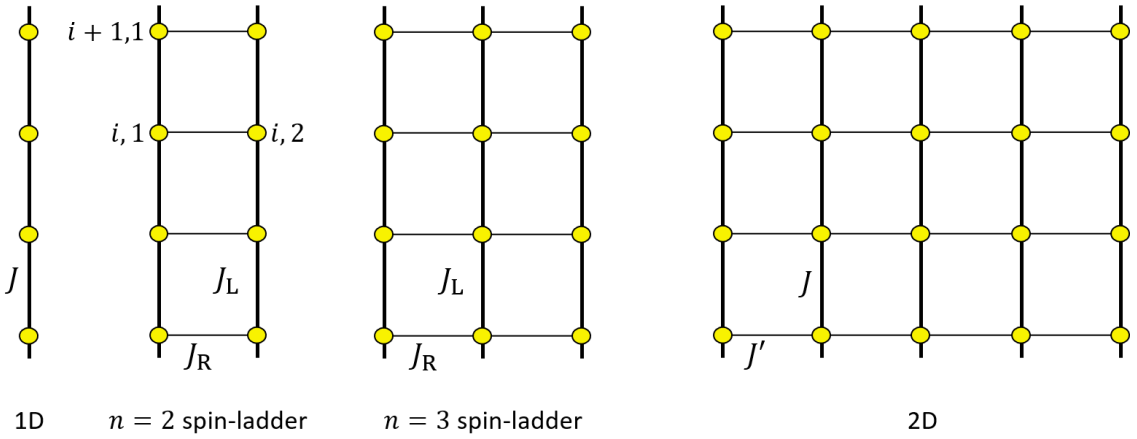

Figure 8.1: Schematic representation of the 1D chain ($n = 1$), two- ($n = 2$) and three-legged ($n = 3$) spin-ladder systems and 2D square lattice. Yellow circles represent $S = 1/2$ spins and thick and thin lines denote AFM interactions of different strength.

fact, a correspondence between a $S = 1/2$ n-leg spin-ladder and a chain ($n = 1$) with $S = n/2$ can be obtained through the nonlinear sigma model [54, 55], so that for $n = 2$, both the two-leg spin-ladder and the $S = 1$ chain have gapped excitations and a spin liquid ground state.

Besides the fundamental physics aspects related with these fascinating quantum and topological effects, the interest in spin-ladders has been also motivated by the theoretical prediction that superconductivity is expected to appear in a hole doped $S = 1/2$ two-leg spin ladder [56–60]. This possibility could open a new strategy for the development of novel superconducting materials.

In particular, if we consider isotropic AFM interactions and an external magnetic field B applied along the z-direction, then the $S = 1/2$ two-leg Heisenberg antiferromagnetic ladder (THAFL) is described by the Hamiltonian:

$$\mathcal{H} = J_{\mathrm{L}} \sum_{\alpha=1,2} \sum_{i} \vec{S}_{i,\alpha} \cdot \vec{S}_{i+1,\alpha} + J_{\mathrm{R}} \sum_{i} \vec{S}_{i,1} \cdot \vec{S}_{i,2} - g\mu_{\mathrm{B}} B \sum_{i} \left(S^z_{i,1} + S^z_{i,2} \right) \tag{8.1}$$

The physical properties of a spin-ladder are usually characterized by the ratio $\gamma = J_{\mathrm{R}}/J_{\mathrm{L}}$, which in the case of $\gamma \to \infty$ describes the limit of non-interacting dimers, while for $\gamma \approx 0$ the system describes the isolated 1D chain. Additionally, is important to consider that in real materials, an additional interladder coupling J' can be present.

For non-interacting dimers ($\gamma \to \infty$), the four eigenstates are: the singlet state $|s\rangle$ with energy $E_s = -3J_{\mathrm{R}}/4$, spin $S = 0$, and z-projection of the spin $S^z = 0$:

$$|s\rangle = \frac{|\uparrow\downarrow\rangle - |\downarrow\uparrow\rangle}{\sqrt{2}} \tag{8.2}$$

and three triplet states:

$$|t^+\rangle = |\uparrow\uparrow\rangle, \;\; |t^0\rangle = \frac{|\uparrow\downarrow\rangle + |\downarrow\uparrow\rangle}{\sqrt{2}}, \;\; |t^-\rangle = |\downarrow\downarrow\rangle \tag{8.3}$$

with $S = 1$, $S^z = 1, 0, -1$, and $E_{t^+} = J_\mathrm{R}/4 - g\mu_\mathrm{B}B$, $E_{t^0} = J_\mathrm{R}/4$, $E_{t^-} = J_\mathrm{R}/4 + g\mu_\mathrm{B}B$, respectively. The ground state is $|s\rangle$ below the critical value of the magnetic field, $B_\mathrm{c}^\mathrm{dimer} = J_\mathrm{R}$ and $|t^+\rangle$ above (see left side of Fig. 8.2).

Now, if we consider a ladder in the strong coupling regime ($\gamma \gg 1$), the finite leg coupling delocalizes triplets and creates bands of excitations with a bandwidth $\sim J_\mathrm{L}$ for each triplet branch. This leads to a magnetic phase diagram particularly interesting, represented on the right side of Fig. 8.2. At $T = 0$ with no external applied field, the ground state is a gapped, disordered quantum spin liquid [53]. As the applied magnetic field increases, the spin gap is reduced until a field B_c1, where there is a transition to a gapless state. The nature of the gapless phase depends crucially on the dimensionality of the spin system. For $T \lesssim J'/k_\mathrm{B}$, the weak interladder coupling induces a 3D long-range AFM order described as a Bose-Einstein condensate (BEC) of magnons [62–64], where the spin excitations are viewed as bosons. In the temperature range $J'/k_\mathrm{B} < T < J_\mathrm{L}/k_\mathrm{B}$, the interladder coupling is suppressed by the thermal fluctuations, effectively causing the ladders to behave as independent systems. This decoupling leads to the system being described by the Tomonaga-Luttinger liquid (TLL) model [65, 66], a theoretical framework for understanding

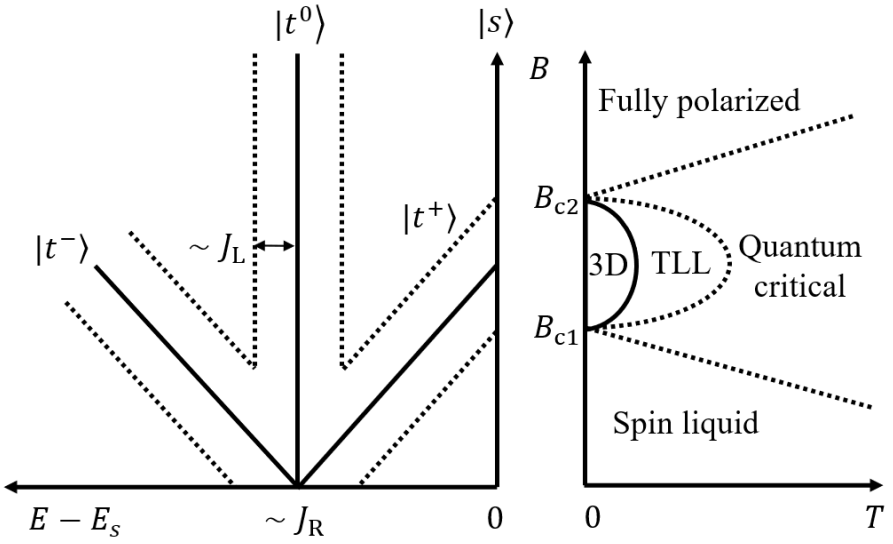

Figure 8.2: Left: energy of the triplets $|t^+\rangle$, $|t^0\rangle$, $|t^-\rangle$ and singlet $|s\rangle$ (solid lines) versus the applied magnetic field for an isolated dimer. The dotted lines represent the limits of the triplets excitation band when $J_\mathrm{L} \neq 0$. Right: phase diagram of weakly coupled spin ladders: crossovers (dotted lines) and phase transition (solid line) that only exists in the presence of an interladder coupling are sketched. Adapted from Ref. [61].

strongly correlated 1D systems with low-energy excitations exhibiting a linear spectrum [67, 68]. These excitations include phenomena such as spin-charge separation, where spin excitations (spinons) and charge excitations (holons) behave as independent quasiparticles, often with spinons carrying fractional spin. The strong effects of quantum fluctuations in 1D systems prevent the establishment of both long-ranged magnetic order and BEC, while inducing an algebraic decay of the correlation functions in a TLL [61]. For higher temperatures, $T > J_{\mathrm{L}}/k_{\mathrm{B}}$, the rungs decouple and the system behaves as a quantum critical paramagnet. Finally, at a higher field B_{c2} a second quantum critical transition is expected to occur to a fully polarized state.

Nevertheless, a major challenge in studying these systems is the difficulty in accessing the spin gap, which is often too large to allow for a detailed examination of the spectrum through the application of a magnetic field [30]. To the best of our knowledge, only one purely organic magnet (BIP-BNO) [28, 69] and a limited number of organometallic compounds – namely, CuHpCl, BPCB or $(\mathrm{Hpip})_2\mathrm{CuBr}_4$, DIMPY, $\mathrm{Cu(DEP)Br}_2$, $\mathrm{Cu(DEP)Cl}_2$ and $[\mathrm{Cu(pyz)}_{0.5}\mathrm{(gly)}]\mathrm{ClO}_4$) [61, 70–79] – have been synthesized which can be described by the $S = 1/2$ THAFL model and can be investigated with magnetic fields under 40 T.

8.2 Sample preparation and experimental details

Synthesis of 4-F-2-NN-BIP was carried out at Prof. Hosokoshi's laboratory at Osaka Prefecture University following the conventional procedure [39, 43] starting from 2-bromo-5-fluorobenzaldehyde through five steps. The obtained compounds were purified by column chromatography on silica gel with chloroform. Single crystals were grown by the recrystallization method. Slow evaporation from a concentrated solution of dry dichloromethane in heptane atmosphere at 50 °C yielded dark orange block single crystals of 4-F-2-NN-BIP.

X-ray diffraction data were collected on a Rigaku AFC-8R Mercury CCD RA-Micro7 diffractometer with a Japan Thermal Engineering XR-HR10K at the temperatures of 293 and 25 K employing graphite-monochromated Mo $K\alpha$ radiation. The crystal structure was determined from the data obtained by direct methods and refined by the full-matrix least-squares technique using SHELX-97 software [80]. The structural refinement was carried out using anisotropic and isotropic thermal parameters for the nonhydrogen atoms and the hydrogen atoms, respectively. The positions of all hydrogen atoms were placed at the calculated ideal positions.

The magnetization was measured in non-oriented crystals in the temperature range from 0.5 to 300 K and up to $B = 5$ T using a SQUID magnetometer (MPMS-XL, Quantum Design) equipped with a ^{3}He device (iHelium3, IQUANTUM). Magnetization curves up to 20 T at 0.5, 1.7, and 4.2 K were obtained by an inductive method in pulsed magnetic fields at the Institute for Materials Research (IMR), Tohoku University [81]. A pulsed magnetic field with nearly sinusoidal shape was generated with the rise time of 6 ms. Magnetization curves were normalized by the saturation value. The magnetization measurements at 0.1 K were performed using a force magnetometer [82] in static magnetic fields up to 14 T with a ^{3}He–^{4}He dilution refrigerator.

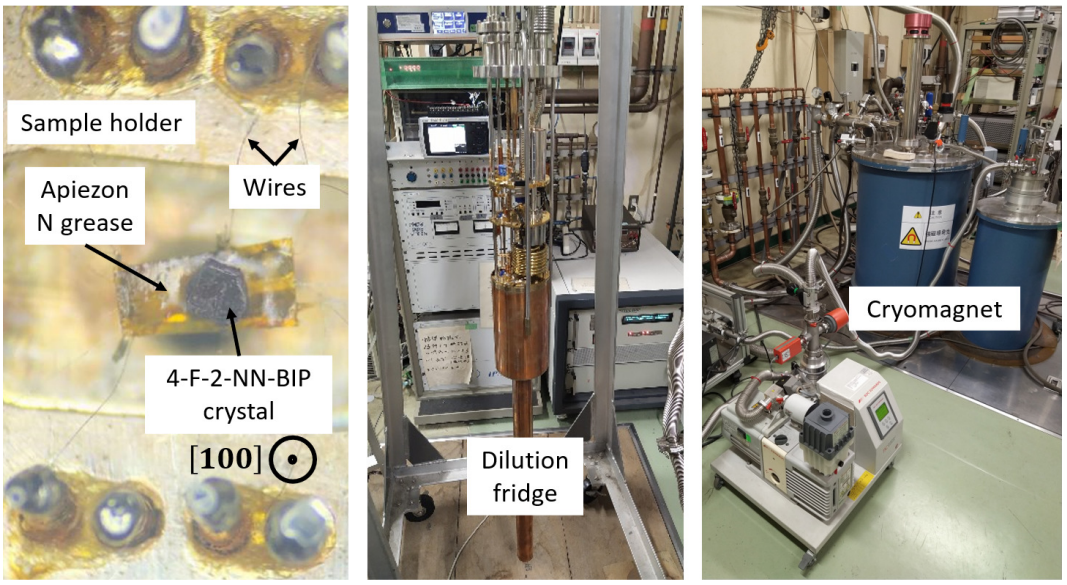

Figure 8.3: Setup of the specific heat experiment carried out in IMR for a 4-F-2-NN-BIP crystal of $m = 0.60$ mg and size $1 \times 1 \times 0.3$ mm^3.

The specific heat was measured at temperatures down to 0.35 K in magnetic fields up to 14 T using the relaxation method of a physical property measurement system (PPMS, Quantum Design). For measuring data at lower temperatures, a handmade apparatus with a dilution refrigerator was used at IMR, Tohoku University (see Fig. 8.3). Measurements from $T = 0.1$ to 0.6 K at $B = 0$, 4, 5, 8 and 9 T were performed using the relaxation method. First, the empty probe with Apiezon N grease inside was measured as calibration, so it could be subtracted from the measurements with sample. Additional measurements of the 4-F-2-NN-BIP sample at $B = 4$, 5 and 9 T were done using the dual-slope method [83]. All measurements were performed with the magnetic field applied parallel to the crystallographic a-axis of the crystals.

X-band Electron Paramagnetic Resonance (EPR) measurements were performed using a Bruker EMS and E500 spectrometer at a frequency of 9.5 GHz. The spectrometer is equipped with a continuous flow cryostat (Oxford Instruments) ESR900 for the measurements with the temperature range of 3.8–300 K and ESR910 for 1.5–4 K, respectively.

The *ab initio* molecular orbital (MO) calculations were performed using the software package Gaussian09 [84] using an hybrid UB3LYP exchange functional and the basis set 6-31G. The calculations were carried out on real molecules employing the crystallographic structures determined at 25 K. The convergence criterion was 10^{-7} Hartree. The magnetic exchange interactions J between neighboring radical units were estimated based on the Broken Symmetry (BS) approach proposed by Yamaguchi [85]:

$$\frac{J}{2} = \frac{^{\mathrm{LS}}E - {}^{\mathrm{HS}}E}{^{\mathrm{LS}}\langle S^2\rangle - {}^{\mathrm{HS}}\langle S^2\rangle} \tag{8.4}$$

where ${}^{\mathrm{LS}}E$ and ${}^{\mathrm{HS}}E$ denote the total energy of the low-spin and high-spin state and ${}^{\mathrm{LS}}\langle S^2\rangle$ and ${}^{\mathrm{HS}}\langle S^2\rangle$ are the total spin squared-average of the low-spin and high-spin state, respectively.

Exact diagonalization (ED) calculations were performed with both the PHI software [86] and the *fulldiag* package found in the Algorithms and Libraries for Physics Simulations (ALPS) project [87, 88] for a system size of 12 spins. Quantum Monte Carlo (QMC) simulations were performed with the *loop* [89] and *dirloop_sse* [90–92] packages provided with the ALPS libraries to obtain, respectively, the magnetic zero-field susceptibility versus temperature and the susceptibility under applied field versus temperature and magnetization versus magnetic field curves. The calculations were performed for system sizes $N = 256$, 1024 under periodic boundary condition for $S = 1/2$ spin.

8.3 Crystalline structure

Figure 8.4(a) shows the molecular structure of 4-F-2-NN-BIP, which has a delocalized $S = 1/2$ within a molecule. As it was previously mentioned, intermolecular AFM interactions should be expected from the contacts between different NN radicals.

The collected X-ray diffraction data showed no indication of a structural phase transition down to 25 K. The 4-F-2-NN-BIP compound crystallizes with the monoclinic space group $P2_1/c$, with cell parameters at 25 K of $a = 9.814(5)$ Å, $b = 8.513(4)$ Å, $c = 20.050(10)$ Å, $\beta = 97.106(7)^\circ$. All the parameters obtained from the refinement are listed in Table 8.1, except the atomic positions and anisotropic thermal factors, which are given in Tables G.1 and G.2 of Appendix G, respectively. The anisotropic thermal factors correspond to the following expression for the Debye-Waller factor of atom d:

$$T_d(hkl) = \\ = \exp\left(-\frac{1}{4}\left(\beta_{11}h^2a^{*2} + \beta_{22}k^2b^{*2} + \beta_{33}l^2c^{*2} + 2\beta_{12}ha^*kb^* + 2\beta_{13}ha^*lc^* + 2\beta_{23}kb^*lc^*\right)\right) \tag{8.5}$$

where h, k and l are the reflection indices and a^*, b^* and c^* are reciprocal cell parameters.

From the refined model we can see that the $S = 1/2$ magnetic moments are arranged in a ladder-like structure along the b-axis (see Fig. 8.4(c)). The rungs of this ladder are formed by a coupling J_{R} between the nitrogen N1 and oxygen O1 atoms related by a center of inversion symmetry with an interatomic distance of 4.244(3) Å, while the legs involve an interaction path J_{L} between oxygen O1 and O2 atoms related by a pure translation with a longer interatomic distance of 4.648(3) Å. As can be observed in Fig. 8.4(b), the ladder units are well separated by the biphenyl groups in the a-axis (the shortest inter-ladder distance is a O1-O1 bond of 5.843(4) Å) and by the methyl groups in the c-axis (the shortest distance between planes is a N2-O2 bond of 7.462(4) Å), and hence any magnetic exchange between ladders (J') is expected to be small.

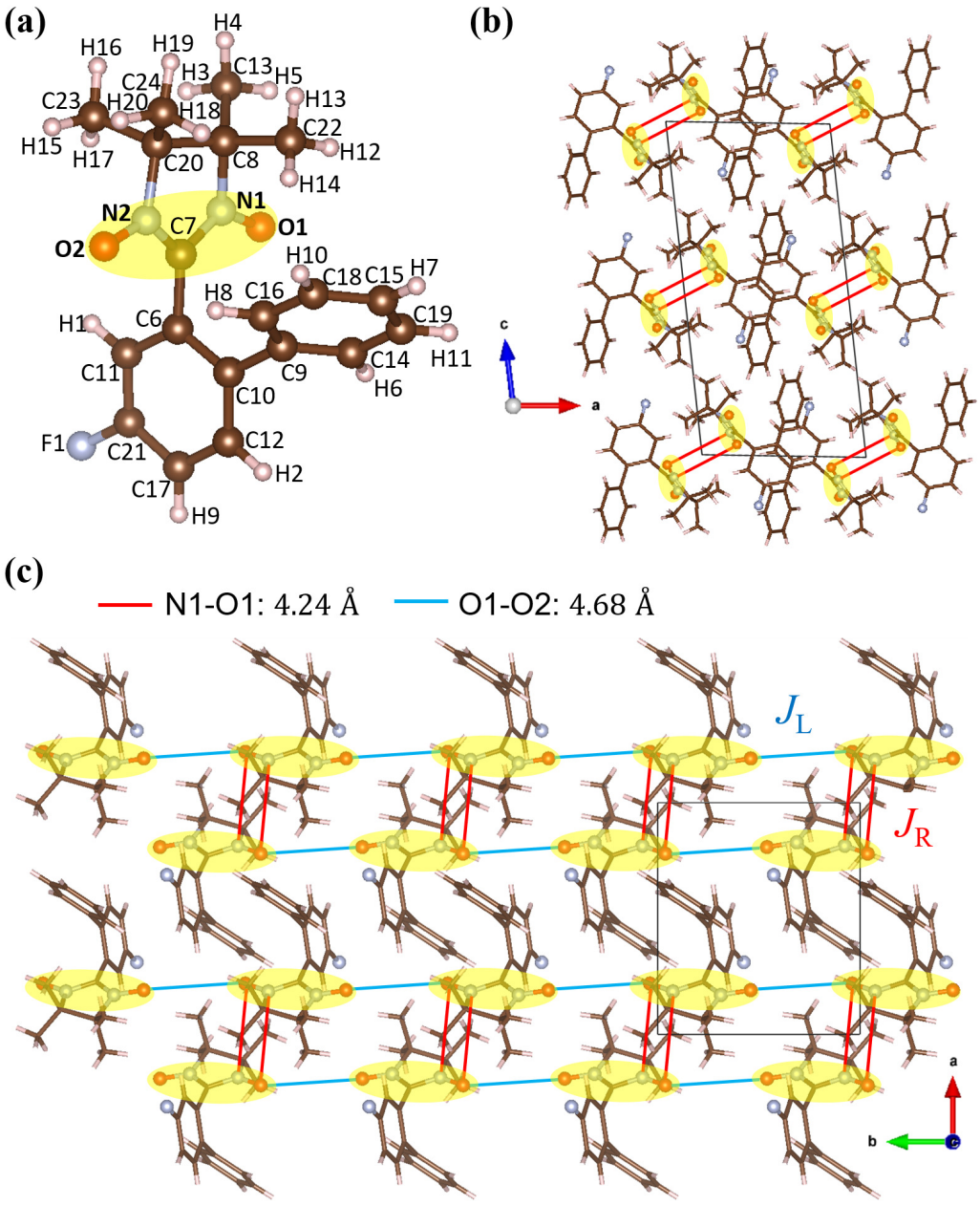

Figure 8.4: (a) Asymmetric unit of 4-F-2-NN-BIP, where the yellow ellipsoid denotes the delocalized spin 1/2. (b) Crystal structure of 4-F-2-NN-BIP forming the two-leg spin ladder in the *ac* plane. Hydrogen and carbon atoms are omitted for clarity. (c) View of the crystal structure in the *ab* plane.

The magnitude of the magnetic interaction is roughly estimated by applying Yamaguchi's formula [85] to the results of the MO calculation for the neighboring two asymmetric units connected by J_R or J_L. The estimated values are $J_R/k_B = 7.86$ K, $J_L/k_B = -0.04$ K for the crystal structure at 25 K, which suggests that the leg interaction is negligible and the system is close to independent AFM coupled dimers. Although MO calculations are useful to estimate the intermolecular packing

Table 8.1: Structural parameters for 4-F-2-NN-BIP at RT and 25 K obtained from the refinement of X-ray diffraction data.

Empirical formula	$C_{19}H_{20}FN_2O_2$	
Formula weight (g/mol)	327.37	
Space group	$P2_1/c$	
Z	4	
Temperature (K)	293(2)	25(2)
a (Å)	9.934(4)	9.814(5)
b (Å)	8.756(3)	8.513(4)
c (Å)	20.184(7)	20.050(10)
β (°)	97.690(6)	97.106(7)
Volume (Å^3)	1739.8(11)	1662.4(14)
Density (g/cm^3)	1.250	1.308
X-ray absorption coefficient (mm^{-1})	0.089	0.093
$F(000)$	692	692
Theta range (°)	2.70-24.99	3.26-27.50
Index ranges	$-11 \leq h \leq 11$	$-12 \leq h \leq 12$
	$-8 \leq k \leq 10$	$-10 \leq k \leq 9$
	$-23 \leq l \leq 22$	$-22 \leq l \leq 26$
Independent reflections	11287	12296
Parameters	221	221
R	0.0959	0.0802
R_w	0.1769	0.1721
Goodness of fit	1.078	1.096

responsible for magnetic interactions, in order to determine the exact values of the interactions, the analysis of the magnetic measurements is essential.

8.4 EPR spectroscopy

To estimate the magnitude of the magnetic anisotropy of 4-F-2-NN-BIP, the angular variation of the paramagnetic resonance peak appearing in the X band EPR spectrum was investigated using single-crystal samples. The measurements were performed by rotating the 4-F-2-NN-BIP crystals every 10° around the b and c-axis. The EPR measurements at 3.8 K are shown in Fig. 8.5(a). Following the position and width of the signal centered around 3400 G, the angular dependence of the g-factor was obtained for several temperatures. It can be observed that the g-factor follow a 180° periodic sine curve, and take extreme values when the magnetic field was applied parallel to each of the crystal axis, as can be seen in Fig. 8.5(b) for the values of 0° and 90° corresponding to the b and a-axis, respectively. Same measurements were performed for rotations of the crystals around the b-axis (not shown here), and similarly, extreme values of the g-factor were observed when the magnetic

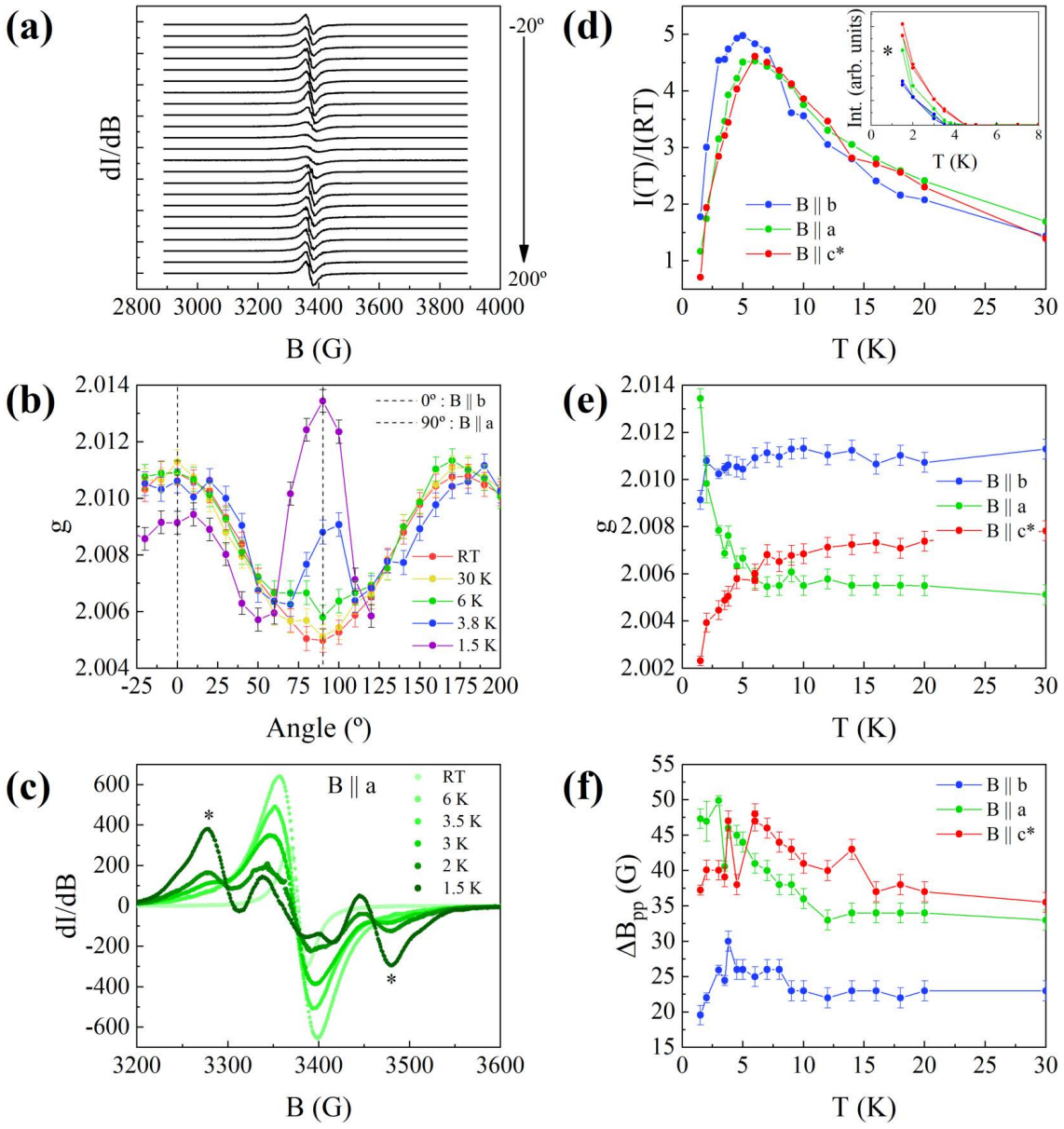

Figure 8.5: (a) Angular variation of the X band EPR spectrum at 3.8 K for 4-F-2-NN-BIP single-crystals. Measurements were performed by rotating the 4-F-2-NN-BIP crystals every 10° around the *c*-axis. (b) Dependence of the g-factor with the rotation angle around the *c*-axis for several temperatures. (c) Temperature evolution of the X band EPR spectrum when the applied magnetic field was parallel to the *a*-axis. Temperature dependence of the integrated intensity (d), g-factor (e) and linewidth (f) of the main signal for the directions in which the applied magnetic field was parallel to each of the crystal axis. The inset in (d) shows the intensity evolution of the PM impurity signals, marked with an asterisk in panel (c).

field was applied parallel to the *a* and *c*-axis.

A more detailed evolution of the signal with temperature was measured for the directions in which the applied magnetic field was parallel to each of the crystal

axis. Additional signals were observed in the EPR spectrum when the temperature was lowered below 4 K, as it is shown in Fig. 8.5(c) for the magnetic field applied parallel to the a-axis. Figure 8.5(d) shows the integrated intensity of the main signal corrected by the RT value. The results show the same behavior for the three axis, where the intensity increases as the temperature is lowered, until it reaches a maximum around 5 K and suddenly drops for lower temperatures. The temperature dependence of the integrated intensity is known to correspond to the magnetic susceptibility, due to the short-range correlations that are developed at low temperatures. As we will show later, a similar behavior is observed as in the magnetic susceptibility, with a broad peak around 5 K. The inset of Fig. 8.5(d) displays the temperature dependence of the additional signals intensity. The intensity of both signals, above and below 3400 G, has almost the same values, and their temperature evolution resembles the magnetic susceptibility of a paramagnet. These facts suggest that the additional signals likely originate from a small fraction of spins that remain unpaired below 5 K, which are subject to dipole-dipole interactions. Regarding the temperature dependence of the g-factor, shown in Fig. 8.5(e), the temperature region above 10 K show a constant g-value in all axial directions; while below 10 K, the g-value increases rapidly for $\vec{B} \parallel a$ and decreases for $\vec{B} \parallel b$ and $\vec{B} \parallel c$ as the temperature decreases. This behavior might indicate that the magnetic moment extends in the a-axis direction as the temperature is lowered. Finally, the linewidth follows the same dependency as the g-factor, increasing steadily for $\vec{B} \parallel a$, while showing a dome around 5 K for the other two directions (see Fig. 8.5(f)).

The g-factor values obtained from the analysis suggest that a very small magnetic anisotropy is present in 4-F-2-NN-BIP (largest deviations from ideal free electron g-value are around 0.6 %). Therefore, based on the intermolecular contacts within 5 Å and the high magnetic isotropy observed from EPR data, a $S = 1/2$ THAFL seems to be a plausible model to describe the magnetic topology of the system 4-F-2-NN-BIP.

8.5 Magnetic properties

Figure 8.6(a) shows the magnetic susceptibility curve at 0.1 T, where a small extrinsic Curie-like impurity contribution ($\sim 0.5\%$ of the total number of spins 1/2) was subtracted from the data. Magnetic susceptibility measurements under different applied magnetic fields are shown in Fig. 8.6(b). The general shape of the curves is typical of low-dimensional magnetic systems. In the present case, at low fields the curves possess a rounded maximum at around 5 K, due to the development of short-range AFM interactions, and an exponential temperature dependence below the peak, consistent with the gapped ground state of the THAFL model. As the magnetic field is increased, the position of the broad peak is shifted to lower temperatures while the exponential decay is replaced by a saturation value at intermediate fields, where the system becomes gapless, and by an exponential saturation at high fields, since the fully polarized ground state becomes gapped again.

The Curie-Weiss temperature θ, and the Curie constant C, were obtained from a fit of the 1 T data (see inset in Fig. 8.6(b)) to the Curie-Weiss law, $\chi(T) =$

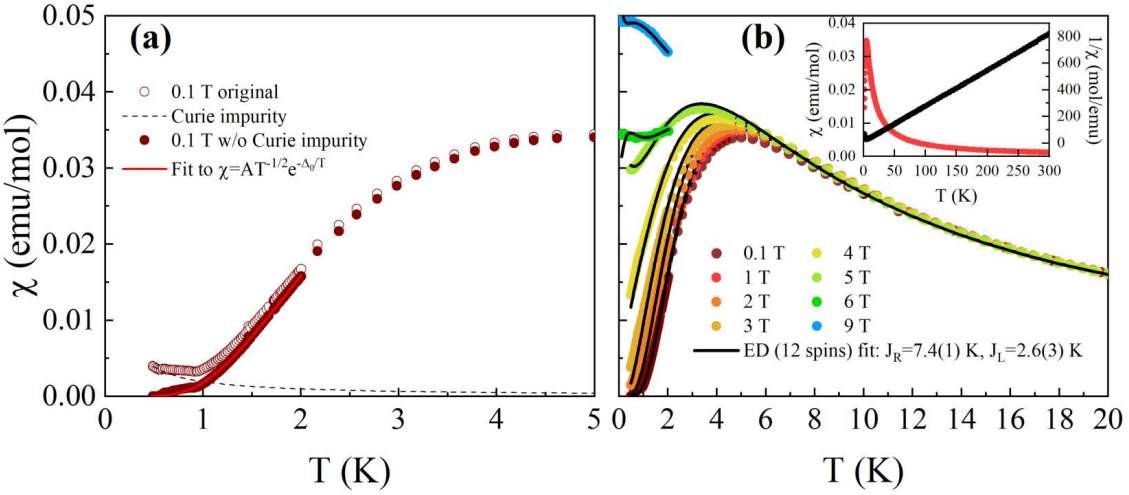

Figure 8.6: (a) Comparison of the magnetic susceptibility data of 4-F-2-NN-BIP at 0.1 T before (empty circles) and after (filled circles) subtracting a Curie-like impurity contribution (dashed line). The red line represents the fit to $\chi = Ae^{-\Delta_0/T}/\sqrt{T}$. (b) Magnetic susceptibility data for different applied magnetic fields (filled circles), together with the fitted curves obtained from ED calculations with 12 spins (black lines). The inset shows both the susceptibility (red circles) and inverse susceptibility (black circles) for the data measured at 1 T.

$C/(T-\theta)$, in the temperature range 25 K $< T <$ 300 K. The fitted parameters are $C = 0.3701(3)$ emu·K/mol, which is close to the theoretical value $C = 0.3751$ emu·K/mol for $S = 1/2$, $g = 2$; and $\theta = -2.6(1)$ K, in agreement with the AFM exchange interactions expected in 4-F-2-NN-BIP. The Curie-Weiss temperature θ already gives a hint on a non-negligible value for J_L, since from the MO calculations: $\theta \approx \frac{J_\mathrm{R}+2J_\mathrm{L}}{4k_\mathrm{B}} \approx 2$ K.

In order to estimate the value of the magnetic exchange interactions and corroborate the validity of the THAFL model, the data were fitted to a spin ladder model with 12 spins using ED calculations. The results yielded $J_\mathrm{R}/k_\mathrm{B} = 7.4(1)$ K, $J_\mathrm{L}/k_\mathrm{B} = 2.6(3)$ K for all data simultaneously (see Fig. 8.6(b)). In order to confirm these results, the data at 0.1 T and 5 T were compared with QMC simulations of 256 spins for a wide range of the (J_R, J_L)-parameter space. At each pair of values the quality of the agreement between theory and experiment was checked by calculating the residual sum of squares, $\chi^2 = \sum_i [\chi_\mathrm{QMC}(T_i) - \chi_\mathrm{exp}(T_i)]^2$ (see inset in Fig. 8.7(a), where the χ^2 values obtained for the 0.1 T data are shown). The best possible agreement (i.e the lowest χ^2 value) was obtained for a spin ladder model with $J_\mathrm{R}/k_\mathrm{B} = 7.5(2)$ K, $J_\mathrm{L}/k_\mathrm{B} = 2.5(1)$ K for 0.1 T and 5 T (see Fig. 8.7(a)). From the calculated values the spin gap is estimated to be $\Delta_0/k_\mathrm{B} = (J_\mathrm{R} - J_\mathrm{L})/k_\mathrm{B} = 5.0(3)$ K [93, 94]. This value is in close agreement with $\Delta_0 = 5.06(2)$ K, obtained from the fit of the 0.1 T susceptibility data in the low temperature range $0.5 \leq T \leq 2$ K to $\chi = Ae^{-\Delta_0/T}/\sqrt{T}$ [70, 72, 95, 96], as depicted in Fig. 8.6(a).

The isothermal magnetization curves at different temperatures for $B \leq 14$ T are shown in Fig. 8.7(b). At 0.1 K, no net magnetization is observed at low fields,

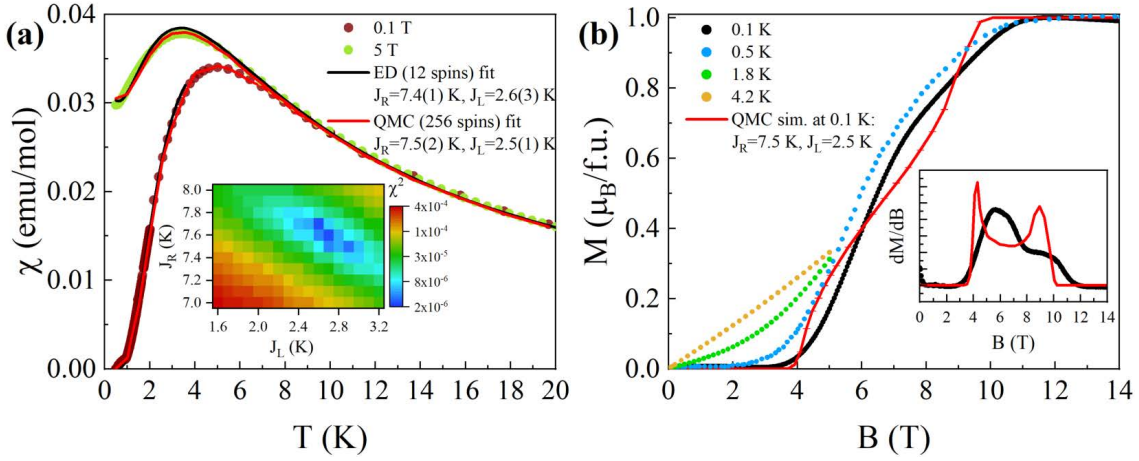

Figure 8.7: (a) Comparison between the susceptibility data at 0.1 T (brown circles) and 5 T (green circles) and the theoretical curves obtained from ED calculations with 12 spins (black lines) and QMC calculations with 256 spins (red lines). The best set of values for the exchange interactions were determined from the calculation of χ^2, which is shown in the inset for the 0.1 T data. (b) High-field magnetization curve of 4-F-2-NN-BIP at 0.1 K, 0.5 K, 1.8 K and 4.2 K, together with the theoretical curves obtained from QMC calculations with 1024 spins for J_R/k_B = 7.5(2) K, J_L/k_B = 2.5(1) K (red line). The dotted line follows the changed slope after B_{an} =7.2(2) T, which can be extrapolated to the origin. The inset shows the derivative dM/dB of both the magnetization data and theoretical curves at 0.1 K.

while above $B_{c1} = 4.3(3)$ T the magnetization increases linearly. In the field region of $B_{an} = 7.2(2)$ T, the magnetization curve changes the slope and reaches the saturation value at B_{c2} =10.6(5) T. Similar behavior is observed for the 0.5 K curve, while for higher temperatures (1.8 K, 4.2 K) the system enters the paramagnetic state and the magnetization increases linearly from zero field.

The saturation magnetization value is in agreement with the parallel alignment of 1 mol of $S = 1/2$ spins (1 μ_B/f.u.). For these spin-gapped systems, it is well known that at $T = 0$, the magnetization remains $M = 0$ for $B \leq B_{c1} = \Delta_0/(g\mu_B)$. Then, it reaches the saturation value $M = 1$ for $B \geq B_{c2} = J_R + 2J_L$ and increases from 0 to 1 for $B_{c1} \leq B \leq B_{c2}$ [70]. However, the change at B_{an} is not something expected in the magnetization spectrum of a spin-ladder. This anomaly is better seen in the derivative of the magnetization at 0.1 K (black circles in inset of Fig. 8.7(b)), since previous studies have shown that for a pure spin-ladder system, a symmetric double bump structure is observed [28, 72, 73]. In our case, although the bump positions are symmetric, the second bump is approximately half the value of the first one. At this point, a bond-alternating chain model could be considered, since the magnetic susceptibility dependence is undistinguishable between both models [73, 97] and the peaks in the dM/dB curve of a bond-alternating chain have different magnitudes. However, in such model the smaller peak is the first one, just the opposite to what we observe, and the inflection point between the two peaks is not at the center position [98].

The theoretical magnetization curves at 0.1 K were calculated from QMC simulations with 1024 spins for the set of values which fitted best the susceptibility data ($J_R/k_B = 7.5(2)$ K, $J_L/k_B = 2.5(1)$ K for 0.1 T and 5 T (red line in Fig. 8.7(b))). Although the critical field B_{c1} is correctly estimated, a bad agreement is observed for the critical field B_{c2}, while the curvature of the magnetization data is not well reproduced (bumps in the derivative curves are sharper and more symmetric).

8.6 Thermal measurements

Now we turn to the specific heat measurements. A field-independent lattice contribution: $C_{latt}(T) = \frac{12\pi^4}{5} N k_B \frac{1}{\theta_D^3} T^3$ with a Debye temperature of $\theta_D = 66$ K was

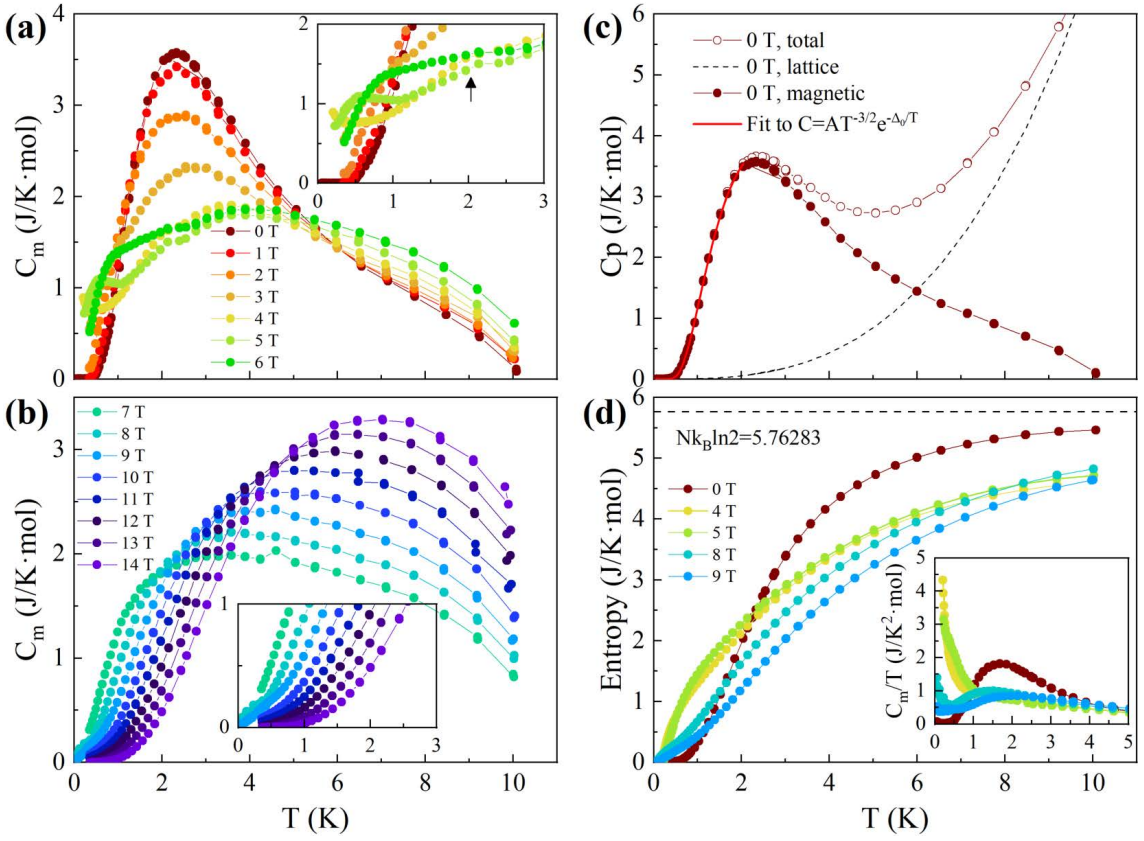

Figure 8.8: (a) Magnetic specific heat $C_m(T, B)$ of 4-F-2-NN-BIP for $B \leq 6$ T. (b) Magnetic specific heat $C_m(T, B)$ of 4-F-2-NN-BIP for $B \geq 6$ T. The insets in both (a) and (b) show a zoom of the low temperature data. The arrow in the inset of panel (a) indicates the shoulder peak mentioned in the main text. (c) Total (empty circles), lattice (dashed line) and magnetic (filled circles) contributions to the specific heat at 0 T. The red line represents the fit to $C_m = Ae^{-\Delta_0/T}/T^{3/2}$. (d) Magnetic entropy for 0, 4, 5, 8 and 9 T. The dashed line corresponds with the maximum theoretical magnetic entropy of N disordered spins $S = 1/2$. The inset displays C_m/T for the mentioned fields.

subtracted for all data, determined by a fit at higher temperatures for the $B = 0$ T data. The temperature dependence of each contribution to the specific heat at 0 T is shown in Fig. 8.8(c). The evolution of the magnetic specific heat with the field is displayed in Fig. 8.8(a) and Fig. 8.8(b), with a similar behavior to the ones observed in the $S = 1/2$ systems CuHpCl [72] and BPCB [74], as we will detail next.

As we can see in Fig. 8.8(a), a single broad peak in the magnetic specific heat C_{m} is observed for $B < B_{\mathrm{c1}} \approx 4$ T. This peak is attributable to the triplet excitations of the ladder, and is exponentially activated at lower temperatures due to the presence of the spin gap Δ_0. We can estimate the value of the gap from fitting the 0 T data in the low temperature range $0.05 \leq T \leq 2.5$ K to $C_{\mathrm{m}} = Ae^{-\Delta_0/T}/T^{3/2}$ [61, 71], as displayed in Fig. 8.8(c). The obtained value $\Delta_0/k_{\mathrm{B}} = 4.18(2)$ K is slightly smaller compared with the spin gap obtained from the susceptibility analysis. As the field increases, the gap is reduced by the Zeeman effect. In the field range $B_{\mathrm{c1}} < B \leq B_{\mathrm{an}} \approx 7$ T (see Fig. 8.8(a) and (b)), a second peak emerges at low T and the temperature dependence below it becomes linear, consistent with the presence of gapless spinon excitations and suggesting the formation of the TLL phase [68]. Additionally, a shoulder peak is observed around 2 K (see inset of Fig. 8.8(a)). For $B_{\mathrm{an}} < B \leq B_{\mathrm{c2}} \approx 11$ T (see Fig. 8.8(b)), the shoulder peak disappears and the low temperature behaviour departs from a linear dependence, indicating a more intricate ground state than the TLL regime. Finally, at $B > B_{\mathrm{c2}}$ (see Fig. 8.8(b)), the specific heat becomes exponentially activated again due to the opening of a field-dependent spin gap in the fully saturated phase.

Fig. 8.8(d) shows the entropy obtained via the integration of C_{m}/T for selected magnetic fields. At high temperatures, the magnetic entropy of the zero field data almost reaches the maximum value of N disordered spins $S = 1/2$, while higher field data have a reduced maximum entropy value, in agreement with a partial order induced by the applied magnetic field. Meanwhile, at low temperatures the entropy of the 4 and 5 T data reaches a maximum below 2 K, related with the unsaturated increase observed in the C_{m}/T data (see inset of Fig. 8.8(d)).

8.7 Discussion

8.7.1 Magnetization shape at B_{an}

Several theoretical models have been explored to explain the anomaly observed in the magnetization curves.

A similar anomaly was observed near the saturation field in the the weakly coupled $S = 1/2$ AFM dimer system $[\mathrm{Cu(pyz)_{0.5}(gly)}]\mathrm{ClO_4}$ [79]. In this compound, a spin canting due to Dzyaloshinskii-Moriya (DM) interactions was assumed to explain the kink, where the magnetization step accounted for around 2 % of the saturated moment. Contrarily, in 4-F-2-NN-BIP, the magnetization step of the anomaly represents about 30 % of the saturated moment, so an explanation based on DM interactions does not seem plausible.

We have also contemplated the role of extrinsic impurities in this anomaly, since they have been observed both in the EPR and susceptibility data. However, the magnetization curve at 0.5 K showing the anomaly at B_{an} has been reproduced in

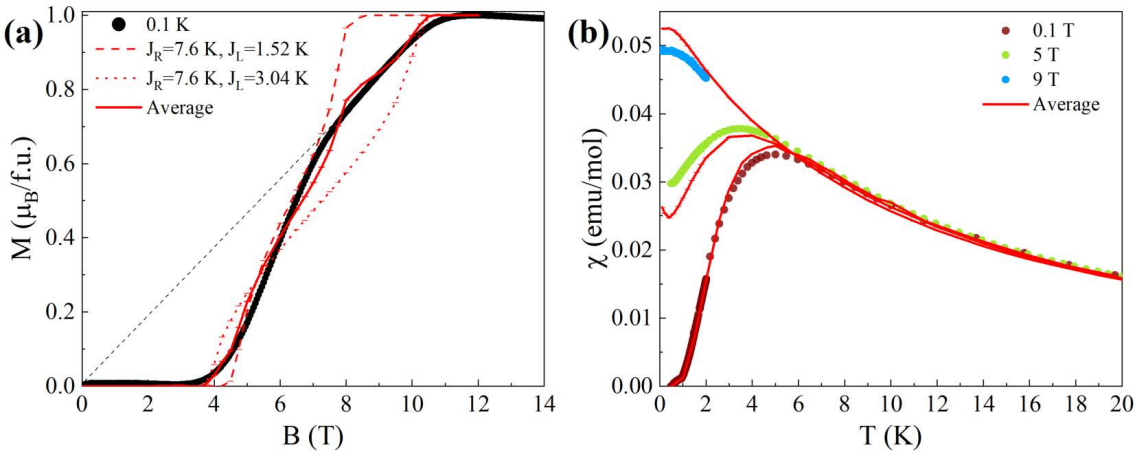

Figure 8.9: (a) Comparison of the 0.1 K magnetization curve (black circles) and the theoretical curves obtained from QMC calculations with 1024 spins for $J_R/k_B = 7.6$ K, $J_L/k_B = 1.52$ K (dashed red line), $J_R/k_B = 7.6$ K, $J_L/k_B = 3.04$ K (dotted red line), and the average of both curves (continuous red line). The dashed black line follows the changed slope after $B_{an} = 7.2(2)$ T, which can be extrapolated to the origin. (b) Comparison of the magnetic susceptibility data with the average of the aforementioned curves for QMC calculations with 256 spins (red lines) at selected fields .

different samples, confirming its intrinsic nature. Additionally, no Brillouin function dependence is observed in the low-field region of the magnetization curves, indicating a negligible contribution from paramagnetic impurities, so this hypothesis was ruled out.

The presence of additional exchange interactions has also been considered. According to [93], in the case that an additional diagonal exchange interaction J_D is present in a THAFL in the strong coupling regime, the system transitions to an Ising phase for $J_D = 2J_L/3$. In this phase, the system exhibits a magnetization plateau at half the saturation value, indicative of an ordered state with alternating singlets and triplets on neighboring rungs. This plateau exists due to a jump in the chemical potential as a function of band filling, translating to a gap in the spectrum of spinless fermions. Since no plateau at half the saturated value is observed in our magnetization curve data, we can estimate the upper bound for this exchange interaction to be: $J_D/k_B < (2J_L/3)/k_B = 1.73(7)$ K. Furthermore, the analysis of the intermolecular distances indicates that this interaction should occur between molecules separated by more than 5 Å, which makes this model unlikely.

Another proposed model to explain the data introduces two distinct ladder structures within the system, motivated by QMC simulations. Specifically, simulations with $J_R/k_B = 7.6$ K, $J_L/k_B = 1.52$ K accurately predict both B_{c1} and the magnetization curve's slope up to B_{an}, while the simulations using $J_L/k_B = 3.04$ K with the same J_R reproduce B_{c2}. Therefore, a weighted combination of these ladder structures was considered, where a 50% contribution (average) of each of them yielded the closest match to the experimental magnetization curve. Figure 8.9 shows how

the average of these two spin ladder models not only accounts for the magnetization curve's distinctive kink and critical field values, but also aligns with the observed susceptibility data. The different values of J_L might reflect a subtle variation in the O1-O2 bond length of around 0.06 Å. The unchanged value of J_R implies that the N1-O1 bond remains stable, so the variation occurs in the O2 atom, in agreement with the O2 atom having higher anisotropic thermal parameters than O1 (see Table G.2 of Appendix G). This variation proposes a lower symmetry structure than previously identified. However, no signal of a phase transition has been observed in the specific heat data below 10 K. Therefore, additional measurements to complete the whole temperature range from 10 K to RT would be desirable to prove or discard this hypothesis.

Finally, the observation that the altered slope after B_{an} can be extrapolated to the origin, as indicated by the dashed line in Fig. 8.9(a), suggests that the anomaly could be associated with a modification in the system's topology. Models in which the magnetic field alters the anisotropy or the strength of the exchange couplings merit consideration. However, further investigation is needed to develop a coherent microscopic model capable of explaining such magnetic field-induced changes.

8.7.2 Proposed magnetic phase diagram

Based on the results from the magnetization, susceptibility and specific heat data, we propose the magnetic phase diagram plotted in Fig. 8.10.

The critical temperatures derived from $d\chi/dT$ (orange squares) and the critical fields derived from the magnetization data (green triangles) are in good agreement with the C_m data, and allow to determine the phase boundaries between 3 distinct magnetic phases: a quantum disordered (QD) or spin liquid phase, a gapless phase and a fully spin polarized (SP) phase. Technically, quantum phase transitions occur only at $B_{c1,c2}$ for zero temperature ($T = 0$), while for temperatures above zero, the "phase boundaries" are simply crossover regions.

At $T = 0$ and $B < B_{c1}$, the ground state is a disordered spin liquid where thermodynamic quantities decay exponentially at low T and there is an effective spin gap $\Delta_{eff}^1 = g\mu_B(B_{c1} - B)$. As $B_{c1} \leq B \leq B_{an}$, the gap vanishes and we find a range of linear in T dependence for the specific heat and finite values for the susceptibility, which is characteristic for the Tomonaga-Luttinger liquid (TLL). The absence of any sharp peak in the specific heat at the lowest temperatures measured suggests that no long-range order takes place in the gapless regime, and therefore the interaction between ladders is small enough to maintain the TLL. The region $B_{an} \leq B \leq B_{c2}$ corresponds with the anomaly observed in the isotherm magnetization curves, where several models have been discussed. For the model of two ladder structures, the ground state would be described by a combination of one ladder reaching the saturation state, while the other remaining as a TLL. For $B > B_{c2}$ the ground state becomes fully polarized, and the thermodynamic quantities again decay exponentially with $\Delta_{eff}^2 = g\mu_B(B - B_{c2})$ at low T. For finite temperature, the spin liquid and TLL phases shrink gradually and disappears, and the gapless regime becomes a quantum critical (QC) paramagnet. As the temperature is increased even more one finds a classical regime for $T > 4$ K.

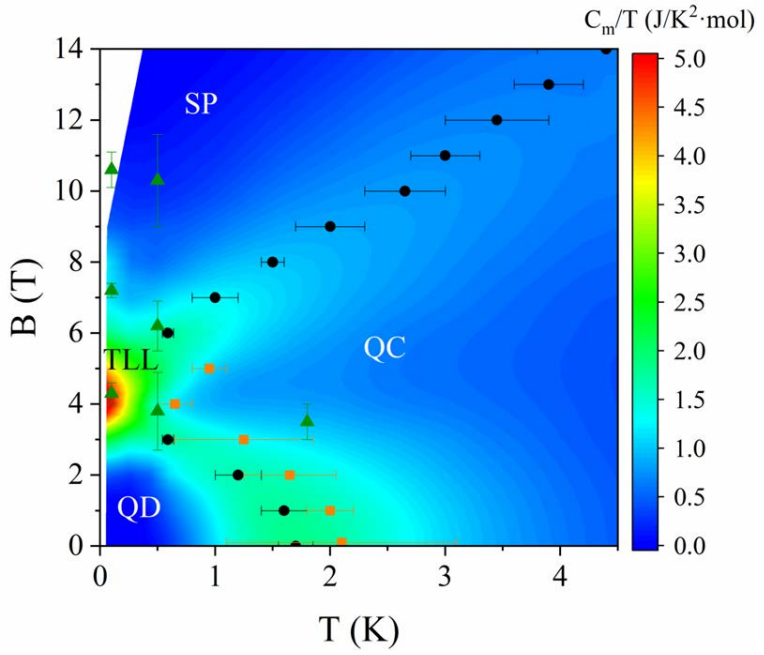

Figure 8.10: Field-temperature phase diagram of the spin–ladder compound 4-F-2-NN-BIP, showing quantum disordered (QD) or spin liquid, quantum critical (QC), spin Tomonaga-Luttinger liquid (TLL) and spin polarized (SP) phases. The contour plot shows the magnetic specific heat as C_{m}/T. Local maxima are indicated by black circles. Orange squares denote the maximum of $d\chi/dT$, while green triangles mark the critical fields obtained from the isotherm magnetization data.

8.8 Conclusions

We have presented the compound 4-F-2-NN-BIP, which is one of the few purely organic compounds described with a spin ladder model. This compound has been characterized by means of X-ray diffraction, electron paramagnetic resonance (EPR), specific heat, magnetization and susceptibility measurements at high magnetic fields and very low temperatures. Numerical calculations have also been performed in order to obtain the relevant magnetic parameters of the system.

The main exchange interactions are determined from the diffraction data and molecular orbital (MO) calculations. Together with the analysis of the EPR measurements, which showed that the magnetic anisotropy is basically negligible, these results imply that this system can be described by a $S = 1/2$ two-leg Heisenberg antiferromagnetic ladder. From the fit of the susceptibility data using quantum Monte Carlo (QMC) and exact diagonalization (ED) calculations, the magnetic exchange interactions for the spin ladder were estimated to be $J_{\mathrm{R}}/k_{\mathrm{B}} = 7.5(2)$ K and $J_{\mathrm{L}}/k_{\mathrm{B}} = 2.5(1)$ K. With the help of specific heat data we propose a magnetic phase diagram in which 3 distinct magnetic phases are present: a quantum disordered (QD) or spin liquid phase, a gapless phase (Tomonaga-Luttinger liquid (TLL) or quantum critical (QC) paramagnet); and a fully spin polarized (SP) phase. Additionally, a region in which the magnetization data deviates from the theory is observed, and

several models to account for this deviation are proposed.

Chapter 9

Magnetic long-range order in the organic triangular magnet TNN·CH_3CN

In this chapter we delve into the study of the purely organic compound TNN·CH_3CN, [= Tris[4-(1-oxyl-3-oxide-4,4,5,5-tetramethyl-imidazolin-2-yl)phenyl]amine], TNN for short. In particular, we aim to explore the magnetic long-range order in this highly isotropic frustrated system, which transitions from an effectively two-dimensional triangular lattice to a three-dimensional structure as the temperature decreases.

The chapter begins with a brief overview of the theoretical models dealing with triangular lattices, followed by a review of the previous results obtained in TNN. We then shift our focus to the magnetic order in the absence of an external magnetic field. This section presents the methodologies and results of single-crystal neutron diffraction and muon spin rotation experiments. Both density functional theory calculations and the computational model described in Appendix C are used to interpret the muon spin rotation results and elucidate the magnetic order taking place at zero field. Next, we explore the trimer formation at the 1/3 magnetization plateau. We detail the polarized neutron diffraction experiments, and apply the wavefunction and multipole expansion techniques to analyze the spin density distribution revealed by polarized neutron diffraction. The section also includes a comparison of the results with the theoretical ground state, as well as a discussion of muon spin rotation experiments conducted in this magnetization regime. We conclude the chapter by summarizing the results obtained in this research.

9.1 Theoretical models of spin triangles

Spin triangles have been the subject of intensive study both by theory and experimental point of view over the last few decades, due to effects such as spin-electric coupling [99–101], frustration [102, 103], and multiferroic ordering [104, 105].

Let's start by considering isolated triangles (referred to in the following as trimers) with equal antiferromagnetic (AFM) interactions J between spins of value 1/2. The Hamiltonian in a magnetic field applied along the z-axis is given by:

$$\mathcal{H} = J \sum_{\langle ij \rangle} \vec{S}_i \cdot \vec{S}_j - g\mu_B B \cdot \sum_{i=1}^{3} S_i^z \tag{9.1}$$

In zero magnetic field, each trimer has only two energy levels with spin quantum numbers $S = 3/2$ or $S = 1/2$, separated by $\frac{3}{2}J$. Both the $S = 1/2$ and the $S = 3/2$ states are fourfold degenerate (see top panel of Fig. 9.1(a)), where the ground states are two $S = 1/2$ doublets. Since the spin quantum number is not enough to characterize each ground state, the two doublets can be labeled as $|S^z, \tau^x\rangle$, where τ^x are the $(\pm 1/2)$ eigenvalues of:

$$\hat{\tau}^x = \frac{1}{3}\left[2\vec{S}_2 \cdot \vec{S}_3 - \vec{S}_1 \cdot \left(\vec{S}_2 + \vec{S}_3\right)\right] \tag{9.2}$$

The eigenstates chosen accordingly are listed in Table 9.1. Together with:

$$\hat{\tau}^y = \frac{1}{\sqrt{3}}\vec{S}_1 \cdot \left(\vec{S}_2 - \vec{S}_3\right) \tag{9.3}$$

$$\hat{\tau}^z = \frac{2}{\sqrt{3}}\text{‘} \left(\vec{S}_1 \times \vec{S}_2\right) \cdot \vec{S}_3 \tag{9.4}$$

$\vec{\tau} = (\hat{\tau}^x, \hat{\tau}^y, \hat{\tau}^z)$ can be seen as a pseudospin-1/2 operator which describes an effective orbital degree of freedom [104, 105]. The spin and orbital trimer operators commute with each other: $\left[\hat{\tau}^\alpha, \hat{S}^\beta\right] = 0$.

In a magnetic field, the ground states split into two twofold degenerate levels, of which the states with $S = 1/2$ and $S^z = 1/2$ remain the ground states. As a result, the magnetic moment jumps from zero to $g\mu_B/2$ immediately, as shown by the red line in the bottom panel of Fig. 9.1(a). A visual representation of both ground states is displayed in Fig. 9.1(b). Meanwhile, the $S = 3/2$ state completely splits into four in a magnetic field. As the field increases, the lowest-energy state with $S = 3/2$ takes over the $S = 1/2$ $S^z = 1/2$ doublet at $B = \frac{3J}{2g\mu_B}$. This leads to a second, final

Table 9.1: List of eigenstates and energies for the spin-1/2 triangle under a magnetic field.

S	S^z	τ^x	Eigenstate	Energy
3/2	-3/2	–	$\|\downarrow\downarrow\downarrow\rangle$	$3J/4 + 3g\mu_B B/2$
3/2	-1/2	–	$\frac{1}{\sqrt{3}}(\|\downarrow\downarrow\uparrow\rangle + \|\downarrow\uparrow\downarrow\rangle + \|\uparrow\downarrow\downarrow\rangle)$	$3J/4 + g\mu_B B/2$
3/2	+1/2	–	$\frac{1}{\sqrt{3}}(\|\uparrow\uparrow\downarrow\rangle + \|\uparrow\downarrow\uparrow\rangle + \|\downarrow\uparrow\uparrow\rangle)$	$3J/4 - g\mu_B B/2$
3/2	+3/2	–	$\|\uparrow\uparrow\uparrow\rangle$	$3J/4 - 3g\mu_B B/2$
1/2	-1/2	+1/2	$\frac{1}{\sqrt{6}}(\|\downarrow\downarrow\uparrow\rangle + \|\downarrow\uparrow\downarrow\rangle - 2\|\uparrow\downarrow\downarrow\rangle)$	$-3J/4 + g\mu_B B/2$
1/2	-1/2	-1/2	$\frac{1}{\sqrt{2}}(\|\downarrow\downarrow\uparrow\rangle - \|\downarrow\uparrow\downarrow\rangle)$	$-3J/4 + g\mu_B B/2$
1/2	+1/2	+1/2	$\frac{1}{\sqrt{6}}(\|\uparrow\uparrow\downarrow\rangle + \|\uparrow\downarrow\uparrow\rangle - 2\|\downarrow\uparrow\uparrow\rangle)$	$-3J/4 - g\mu_B B/2$
1/2	+1/2	-1/2	$\frac{1}{\sqrt{2}}(\|\uparrow\uparrow\downarrow\rangle - \|\uparrow\downarrow\uparrow\rangle)$	$-3J/4 - g\mu_B B/2$

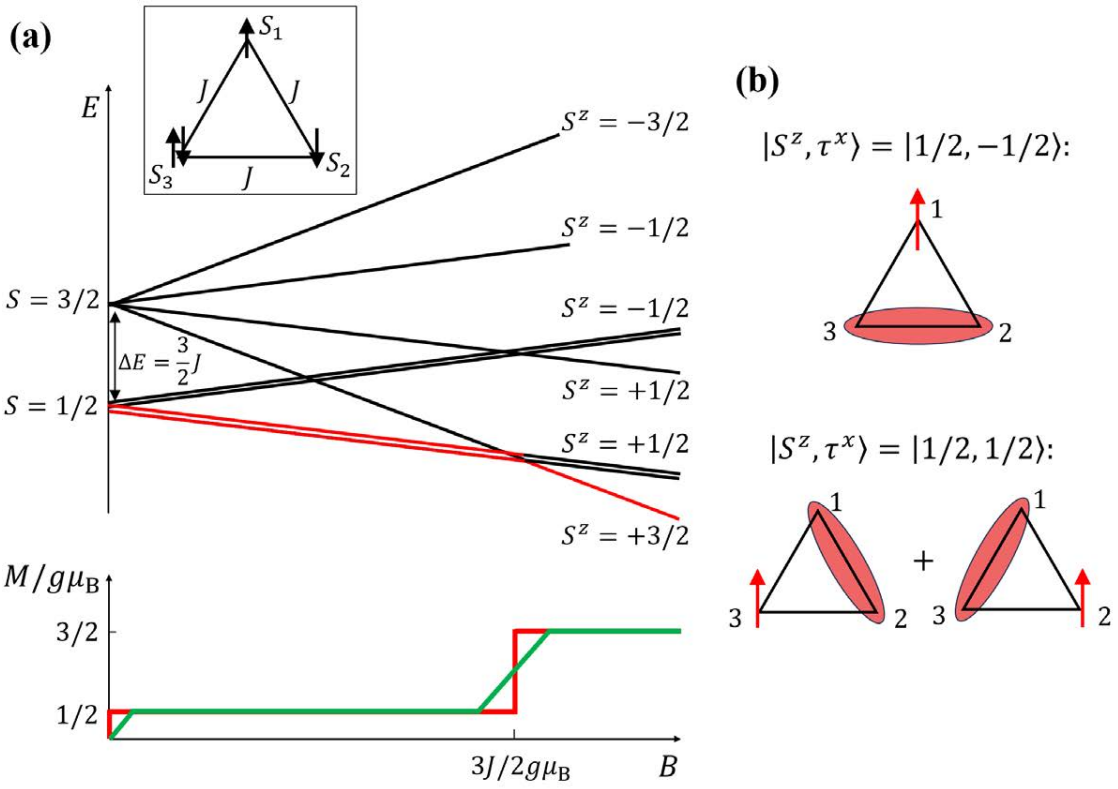

Figure 9.1: (a) Top: energy levels of the spin-1/2 triangle. The ground state for each value of the magnetic field is marked by a red line. The inset on the left depicts the spin triangle with equal interactions J between the spins located at the vertices. Bottom: magnetic moment of a single spin-1/2 triangle (red line) and interacting triangles (green line) as a function of field. (b) Visual representation of the ground states at low fields $|S^z = 1/2, \tau^x\rangle$.

jump of the magnetic moment, from $g\mu_B/2$ to $3g\mu_B/2$. Introducing an interaction between trimers, denoted as J', transforms the magnetization's two discrete jumps into gradual slopes (green line in the bottom panel of Fig. 9.1(a)), where the field range over which the magnetization changes, ΔB, is proportional to J'. From here on, the field region where the magnetic moment maintains a value of one third of its saturation level is referred to as the "1/3 plateau".

While this model allows to understand some of the basic magnetic properties of the triangular lattice, it falls short in capturing more intricate phenomena, such as the emergence of spontaneous electric dipoles, predicted in frustrated Mott insulators [104]. To address these complex aspects of the system, the minimal Hamiltonian required is the half-filled Hubbard model:

$$\mathcal{H} = -\sum_{ij\sigma} t_{ij} \left(c^\dagger_{i\sigma} c_{j\sigma} + \text{H.c.} \right) + \frac{U}{2} \sum_i (n_i - 1)^2 \tag{9.5}$$

where $c^\dagger_{i\sigma}$ and $c_{i\sigma}$ are the creation and annihilation operators of an electron with spin σ at a site i, U is the on-site repulsion, and n is the number operator. The

hopping constants are $t_{ij} = t$ for i and j in the same trimer, and $t_{ij} = t'(t'')$ when i and j are nearest-neighbor sites belonging to different trimers of the same layer (adjacent layers), as it is shown in Fig. 9.2(a).

In the strong coupling limit, $U \gg t$, the half-filled Hubbard model can be reduced to a trimerized Heisenberg Hamiltonian [105]:

$$\begin{aligned}\mathcal{H}_{\text{tri}} = J \sum_{\vec{r},\,\mu>\eta} \vec{S}_{\mu,\vec{r}} \cdot \vec{S}_{\eta,\vec{r}} + J' \sum_{\vec{r},\,\eta,\,\mu\neq\eta} \vec{S}_{\eta,\vec{r}} \cdot \vec{S}_{\mu,\vec{r}+\vec{e}_\eta} + \\ + J'' \sum_{\vec{r},\eta} \vec{S}_{\eta,\vec{r}} \cdot \vec{S}_{\eta,\vec{r}+\vec{u}_3} - g\mu_{\text{B}} B \cdot \sum_{\vec{r},\,\mu}^{3} S^z_{\mu,\vec{r}}\end{aligned} \tag{9.6}$$

Here we introduce the trimer coordinate, $\vec{r} = \sum_{i=1,2,3} n_i \vec{u}_i$, with $\vec{u}_i$ being primitive vectors for the trimer lattice and $\mu, \eta = 1, 2, 3$ denoting the three ions of each trimer. $\vec{e}_\eta$ are relative vectors between intralayer nearest-neighbor trimers (see Fig. 9.2(a)).

The exchange constants J, J' and J'' are proportional to t^2/U, t'^2/U and t''^2/U, respectively. Therefore, spin trimers are weakly coupled ($J \gg J'$, J''). If we consider virtual charge fluctuations, the system may lower its energy by varying the electron density from site to site, which leads to the appearance of a spontaneous electric dipole moment in each spin triangle [105]. The main contribution to the emergent in-plane polarization arises from intra-trimer loops:

$$P^x_{\vec{r}} = 4\sqrt{3}ea \left(\frac{t}{U}\right)^3 \left[\vec{S}_{1,\vec{r}} \cdot \left(\vec{S}_{2,\vec{r}} + \vec{S}_{3,\vec{r}}\right) - 2\vec{S}_{2,\vec{r}} \cdot \vec{S}_{3,\vec{r}}\right] \tag{9.7}$$

and

$$P^y_{\vec{r}} = 12ea \left(\frac{t}{U}\right)^3 \vec{S}_{1,\vec{r}} \cdot \left(\vec{S}_{2,\vec{r}} - \vec{S}_{3,\vec{r}}\right) \tag{9.8}$$

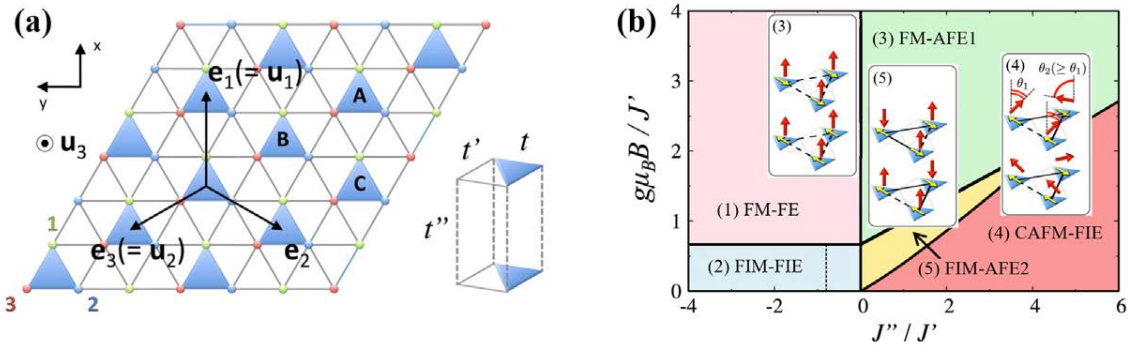

Figure 9.2: (a) Trimerized triangular lattice. Shaded triangles represent trimers with dominant hopping amplitude. The layers are stacked along the c direction. A, B, C are the indices for the three trimer sublattices. (b) Multiferroic phase diagram for the trimerized triangular lattice, as predicted by Kamiya and Batista. Adapted from Ref. [105].

where a is the distance between sites, and e is the electron charge. The microscopic mechanism for its appearance is the formation of a spin singlet in the trimer, which attracts an electron from the remaining vertex. By comparing Eq.(9.2), (9.3), (9.7) and (9.8), it is clear that $\hat{\tau}^{x,y}_{\vec{r}} \propto P^{x,y}_{\vec{r}}$.

Since the dipole moment depends on the spin configuration, Kamiya and Batista [105] predicted the mean-field (MF) multiferroic phase diagram shown in Fig. 9.2(b). As we will show in the next section, in TNN all interactions are AFM, so $J''/J' > 0$, which leads to three ordered phases. In the first phase, labeled (3), the magnetic moments (red arrows) are ordered in a canted antiferromagnetic (CAFM) configuration and the induced electric dipole moments (yellow arrows) are ordered ferrielectrically (FIE). As the magnetic field increases, a ferrimagnetic (FIM) and antiferroelectric (AFE) order appears in the second phase (4). For higher fields the third phase, labeled (5), is ferromagnetic (FM) with all spin triangles in the $S = 1/2$ $S_z = 1/2$ state, and AFE.

9.2 Previous results in TNN

The previous section highlighted the intriguing nature of $S = 1/2$ triangular-lattice systems, where the interplay of quantum fluctuations and geometric frustration can lead to the emergence of novel quantum phases. However, the quest for an ideal spin triangle model has been challenging. A notable example is the well known spin-triangle system $Na_9[Cu_3Na_3(H_2O)_9(\alpha\text{-}AsW_9O_{33})_2]\cdot 26H_2O$, commonly referred to as Cu_3 [106]. This system suffers from Jahn-Teller distortion, which makes the exchange interaction between one Cu-Cu pair stronger than those between the other pairs. To overcome such challenge, exploring new triangular spin networks using highly isotropic organic radical spins has emerged as a promising direction. Through careful design of organic tri-radicals, an equilateral triangle of $S = 1/2$ spins can be constructed, ensuring uniform exchange interactions. With this objective, Prof. Yuko Hosokoshi's group successfully synthesized the triangular compound TNN [107–110].

9.2.1 Crystalline structure

Fig. 9.3 presents the asymmetric unit of this molecular crystal, which includes both TNN and acetonitrile molecules. The TNN molecule contains three NN radicals, each bearing a delocalized spin S = 1/2, depicted as yellow ellipsoids. These radicals, connected to a nitrogen core via phenyl groups, create a spin triangle. The absence of the Jahn-Teller effect, due to spins being carried by organic radicals instead of transition-element ions, ensures uniform exchange interactions between spin pairs. Therefore, this unique structure makes TNN an ideal candidate for investigating the novel multiferroic phases predicted by Kamiya and Batista [105].

The crystal's nuclear structure is classified under the trigonal space group $R3c$, with lattice parameters at 100 K: $a = b = 15.062$ Å and $c = 29.927$ Å [107]. The structure features alternating layers of right-handed and left-handed isomers parallel to the ab-plane, as illustrated in Fig. 9.4. Each layer comprises a triangular lattice

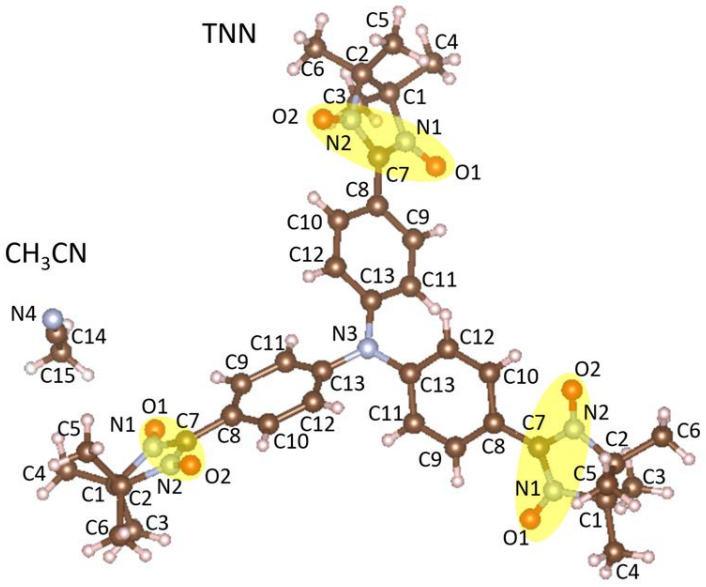

Figure 9.3: Asymmetric unit of TNN·CH_3CN, where the yellow ellipse denotes the delocalized spin 1/2. Hydrogen atoms are not labeled for clarity.

of TNN molecules with two sub-lattices: one formed by intramolecular exchange couplings J_1 between the oxygen atoms O1 and O2 separated 9.876 Å, and another by intermolecular ones between same oxygen atoms O1 (J_2) or O2 (J_2') with interatomic distances of 5.833 Å and 5.490 Å, respectively. Furthermore, intermolecular contacts along the c-axis facilitate inter-layer interactions J''.

9.2.2 Phase diagram

Previous specific-heat and magnetization measurements [108] were fitted by exact diagonalization (ED) calculations for a triangular lattice with intramolecular J_1 and intermolecular J_2 interactions, displayed in Fig. 9.5(c). The isotherm magnetization curve at 0.1 K was correctly described by $J_1 = 7.8$ K, $J_2 = 0.9$ K ($J_2/J_1 = 0.12$), as shown in Fig. 9.5(a).

Figure 9.5(b) shows a good agreement between such model and the specific heat data at 0 T and $T > 1$ K, where the bump around 5.5 K due to the coupling of spins 1/2 to a trimer was well reproduced. Below 1 K, the specific heat increased again, signaling the formation of the 2D triangular lattice. Moreover, an additional λ-shape peak was observed at $T_N = 0.25$ K. This suggested a LRO transition below T_N, which could not be reproduced by the calculations, as the LRO is due to the additional interlayer interactions J''.

The magnetic phase diagram (shown in Fig. 9.5(d)) was later determined in Ref. [111] by combining specific-heat, magnetization, dielectric capacitance, magnetic torque and magnetocaloric-effect measurements performed on single crystals. The magnetic field was applied perpendicular to the c-axis.

Five distinct ordered regions can be observed in the phase diagram of the system below 0.35 K, where the first one ($B = 0$ to 0.6 T) exhibits both AFM and AFE

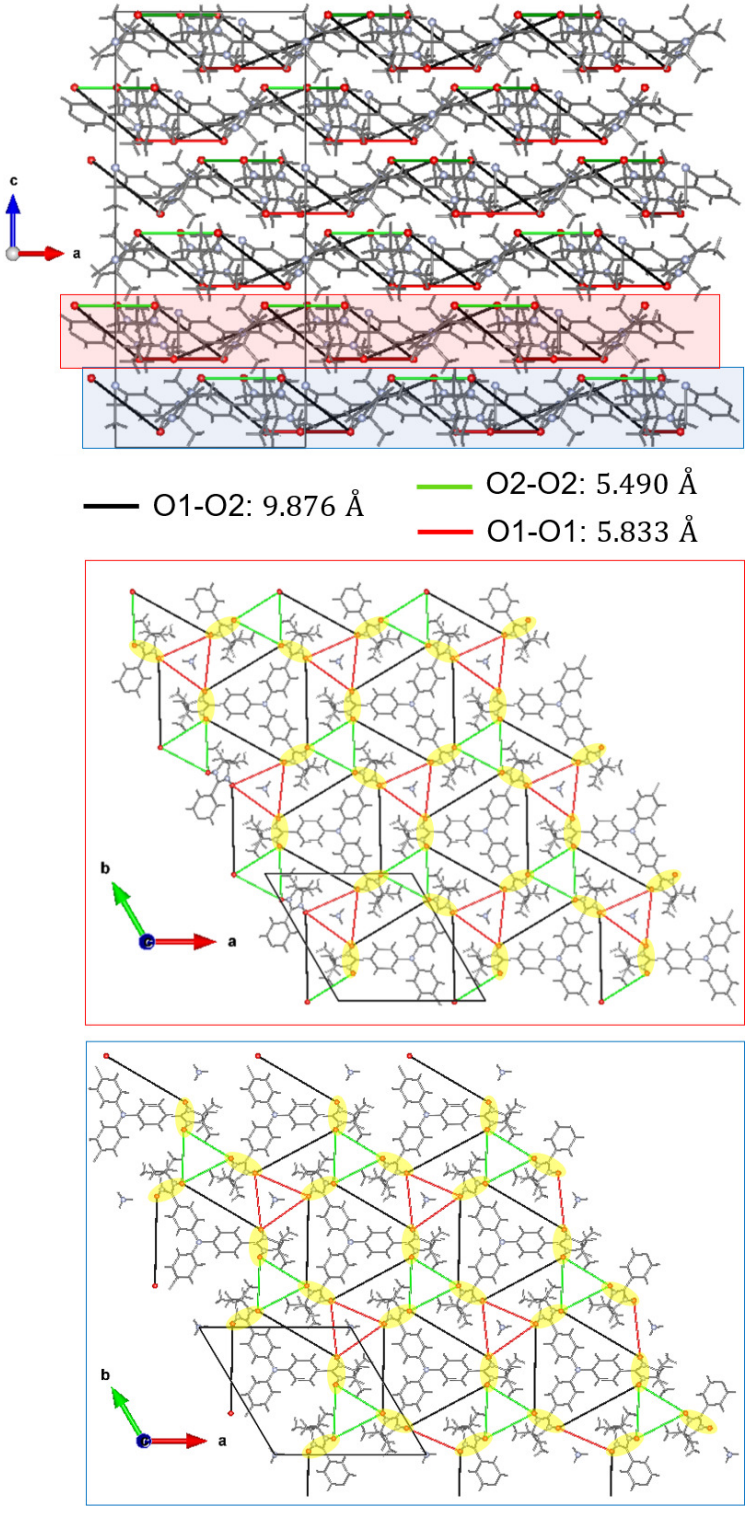

Figure 9.4: Crystal structure of TNN in the *ac* plane. The insets show the triangular lattice of left-handed (blue area) and right-handed (red area) isomers in the *ab* plane formed by intramolecular exchange couplings (black lines) and intermolecular ones (red and green lines). Hydrogen and carbon atoms are omitted for clarity.

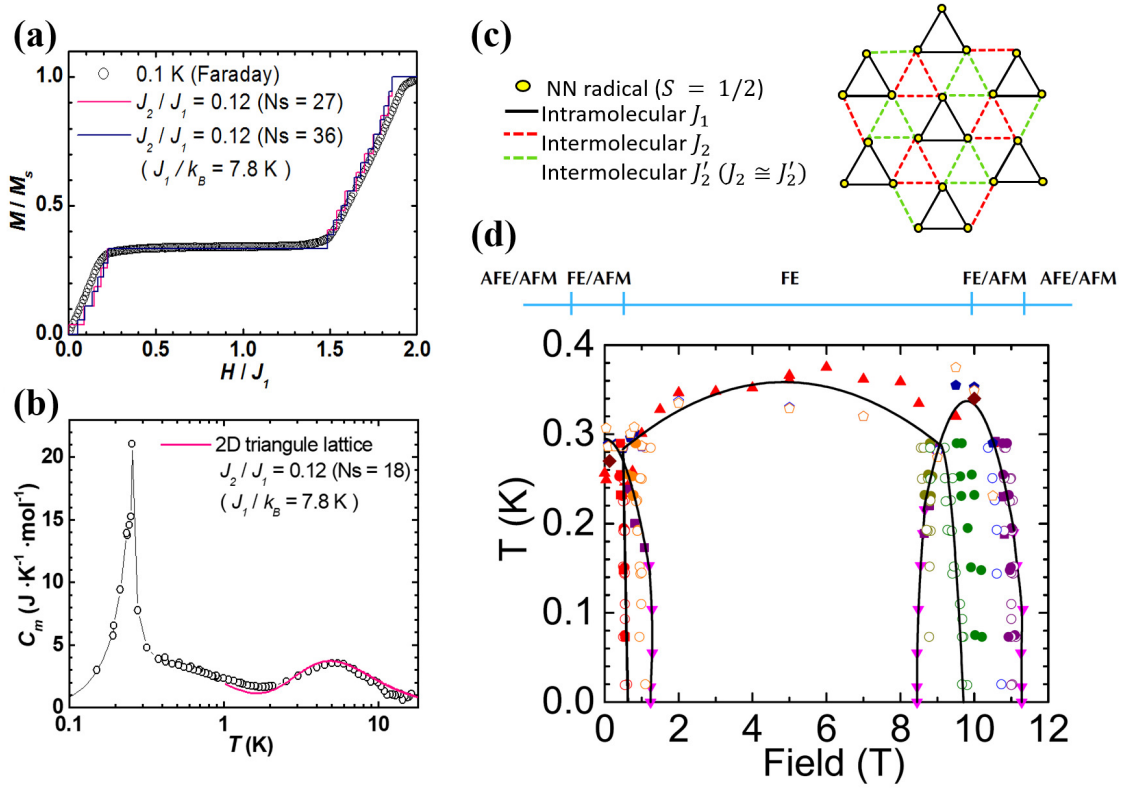

Figure 9.5: Isothermal magnetization curve at 0.1 K (a) and specific-heat measurement at 0 T (b) for a single crystal of TNN. The measured data is represented by empty circles, while the ED calculations are given by red and black solid lines. Taken from Ref. [108]. (c) Simplified model for the 2D triangular lattice develop in TNN. (d) Phase diagram of TNN from specific-heat peaks (triangles), dielectric capacitance peaks for field sweeps (circles) and temperature sweeps (pentagons), magnetocaloric-effect measurements (squares), magnetization measurements (diamonds), and torque (inverted triangles) measurements. A summary of the magnetic and electric phases is shown at the top. Taken from Ref. [111].

order. The second region (0.6 T to 1.25 T) displays AFM order but transitions to ferroelectric (FE) order. The third region (1.25 T to 8.49 T) is ferroelectrically ordered, but the transition to this region does not involve spin ordering and occurs at approximately 0.35 K. In this region, corresponding to the 1/3 plateau, it is expected that TNN molecules are in the twofold-degenerate state with $S = 1/2$ and $S_z = 1/2$. However, the nearly zero value of the spin entropy as the temperature decreases might indicate a lifting of the twofold degeneracy due to the formation of an induced electric dipole moment. The fourth region (8.49 T to 9.7 T) exhibits AFM and FE order, similar to the second region. Finally, the fifth region (approximately 9.7 T to the saturation field at 11.28 T) is characterized by AFM and AFE order, analogous to the first region. It is noteworthy that the dielectric response to an a.c. electric field applied parallel to the *ab*-plane was weak in all regions, confirming the theoretical prediction that the induced electric dipole moments align parallel to the

plane.

The results from Ref. [111] reveal multiferroic behavior in TNN, which is the first example for equilateral spin triangles. However, while macroscopic characterization measurements yield valuable insights, they fall short in providing intricate details about the magnetic structure which is developed at atomic or molecular scale within TNN.

To bridge this gap, we conducted single-crystal neutron diffraction (SCND) experiments at the diffractometers D19 and D10 in the Institut Laue Langevin (ILL) in Grenoble, France; aiming to determine the magnetic structure at zero field. Despite the potential of these experiments, we faced significant limitations regarding the quality of the crystals under study. These included their small size (less than 1 mm^3), not optimal crystallization evidenced by the presence of several twin peaks, and potential degradation due to atmosphere exposure. Therefore, no clear information regarding the presence or absence of long-range magnetic order could be extracted from those SCND experiments.

In a significant advancement, Prof. Hosokoshi's laboratory at Osaka Metropolitan University successfully synthesized new single crystals of non-deuterated TNN, approximately 1 mm^3 in size. The synthesis followed the procedure previously described in Ref. [110–112]. The size of these crystals was enough to facilitate the exploration of the phase diagram using muon spin rotation and neutron diffraction techniques. However, the exploration faced technical challenges due to the low ordering temperature of the material ($T_N = 0.25$ K), which imposed constraints when working with a dilution refrigerator and high magnetic fields, in particular for the muon spin rotation (μSR) experiments. Consequently, our goal was limited to the determination of the magnetic structures of TNN in the phases up to 2 T.

9.3 Zero-field magnetic structure

The starting point was the state at zero field, which according to the phase diagram should exhibit both AFM and AFE order. To determine the magnetic structure at the atomic scale, SCND emerged as the primary technique of choice. However, due to the limitations of this technique when dealing with organic magnets, it was necessary to complement these measurements with μSR experiments, providing information about the local field produced by the magnetic order.

9.3.1 Single crystal neutron diffraction

SCND measurements were carried out at the WOMBAT diffractometer, located within the OPAL reactor of the Australian Nuclear Science and Technology Organization (ANSTO) in Sydney, Australia [113]. A crystal of around 1.2 mm^3 was glued to a copper pin ($\phi = 2$ mm) with GE-Varnish (see Fig. 9.6). The orientation of the crystal was such that the vertical direction (along the pin) was parallel to the a-axis. The sample was then installed in the insert for the DL-1 He-3/He-4 dilution refrigerator with the help of Apiezon N grease. The neutron beam wavelength was fixed to $\lambda = 2.4105$ Å by vertically focusing Ge crystals using the (115) planes.

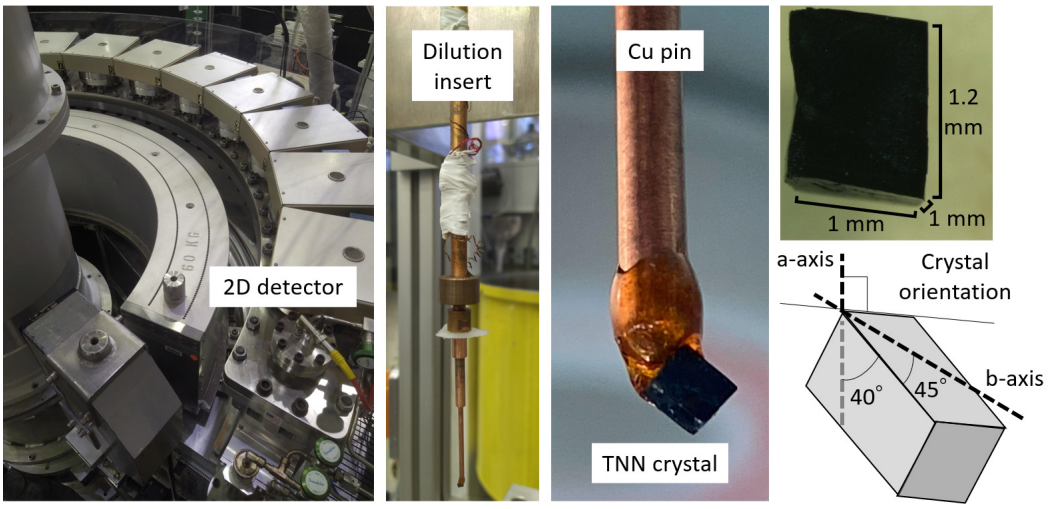

Figure 9.6: Setup of the single-crystal neutron diffraction experiment carried out on the WOMBAT diffractometer.

ω-scans were performed at 0.5 K (above $T_N = 0.25$ K) and 0.05 K (below T_N), with an acquisition time of 20 hours for each temperature. Reflections in the horizontal plane were measured using the 2D detector covering an angular range $15° < 2\theta < 136°$. For each temperature a total of 424 peaks, 106 of them unique, were integrated and corrected using the Int3D software [114].

The indexation of the Bragg reflections enabled the determination of the cell parameters: $a = 15.05(1)$ Å, $c = 29.64(7)$ Å at 0.5 K; and $a = 15.03(2)$ Å, $c = 29.70(7)$ Å at 0.05 K.

Figure 9.7 compares the integrated reflections at these two temperatures. Notably, there is no significant change in the intensity of the reflections, suggesting that magnetic order with a propagation vector $\vec{k} = (0, 0, 0)$ is absent. Furthermore, careful examination of the background at both temperatures did not reveal the appearance of new peaks at 0.05 K, effectively excluding the presence of magnetic order. However, it should be noted that the appearance of a lambda-shape peak in the specific heat measurements at T_N suggests the appearance of a magnetic LRO below 0.25 K.

To estimate the magnetic neutron signal's strength, simulations were conducted using the FullProf Suite [115]. These simulations assumed the saturated state above 11.28 T, which corresponds to a FM order with 1 μ_B per NN radical, expected to yield the most robust magnetic signal. However, the intensity of the strongest magnetic reflection, superposed on a nuclear reflection, only accounted for around 8% of the nuclear Bragg peak's intensity. Therefore, the lack of a detectable magnetic signal in our measurements at zero field, where the magnetic moments ordered in each radical are significantly less (one third) than those in the saturated state, might be attributed to its very low expected value, possibly falling below the threshold of experimental detection in a reasonable acquisition time.

This very low expected value of the magnetic signal is due to several factors: the small spin value ($S = 1/2$), the delocalization of the magnetic moment, a large

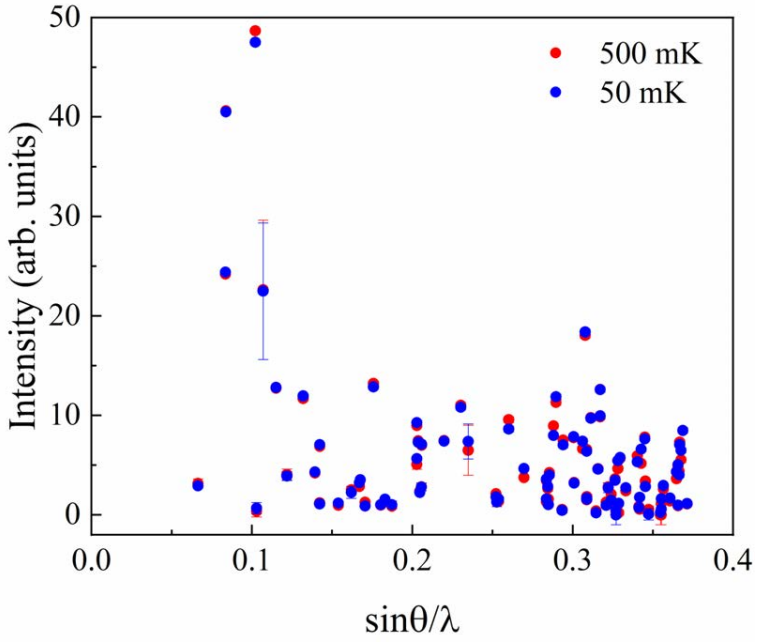

Figure 9.7: Comparison between the integrated intensities of reflections observed above (0.5 K, red) and below (0.05 K, blue) the transition temperature T_N. The acquisition time for each temperature was 20 hours.

unit cell volume (5866 Å), and the inherent challenges in synthesizing deuterated single crystals of adequate size and quality. Consequently, the SCND experiment conducted could not definitively confirm the nature of the magnetic order in TNN.

9.3.2 Zero- and longitudinal-field muon spin rotation

Due to the limitations of the SCND experiment to determine the magnetic structure of TNN, we considered next the use of μSR techniques, since they have proven effective in determining three-dimensional ordering in the organic magnets *p*-NPNN, 3-QNNN, DTDA, tanol suberate, TDAE-C_{60} and F4BImNN [52, 116–121]. In particular, zero-field (ZF) experiments allow to observe a spontaneous precession of the muon spin-polarization below the transition temperature if there is long-range order, whereas longitudinal-field (LF) experiments shed light into the dynamics of the magnetic ordering (for a detailed explanation see Chapter 2).

Therefore, ZF and LF μSR experiments were carried out on the DR 'Pandora' spectrometer installed on the M15 beamline at the TRI University Meson Facility (TRIUMF), Canada. The beam yielded a 95 % longitudinal spin polarization. Several crystals covering a volume of 10 mm × 10 mm × 2 mm ($\sim$ 200 mg) were glued in a random orientation to a silver holder with Apiezon N grease (see Fig. 9.8). The crystals were then covered with a Ag foil. Then the sample holder was introduced in the DR spectrometer, which has scintillation counters within its black box, and field adjustment coils and counters in its outside. μSR spectra with up to $4{\cdot}10^7$ muon decay events were taken in the temperature range 0.02 K to 10 K and field range 0

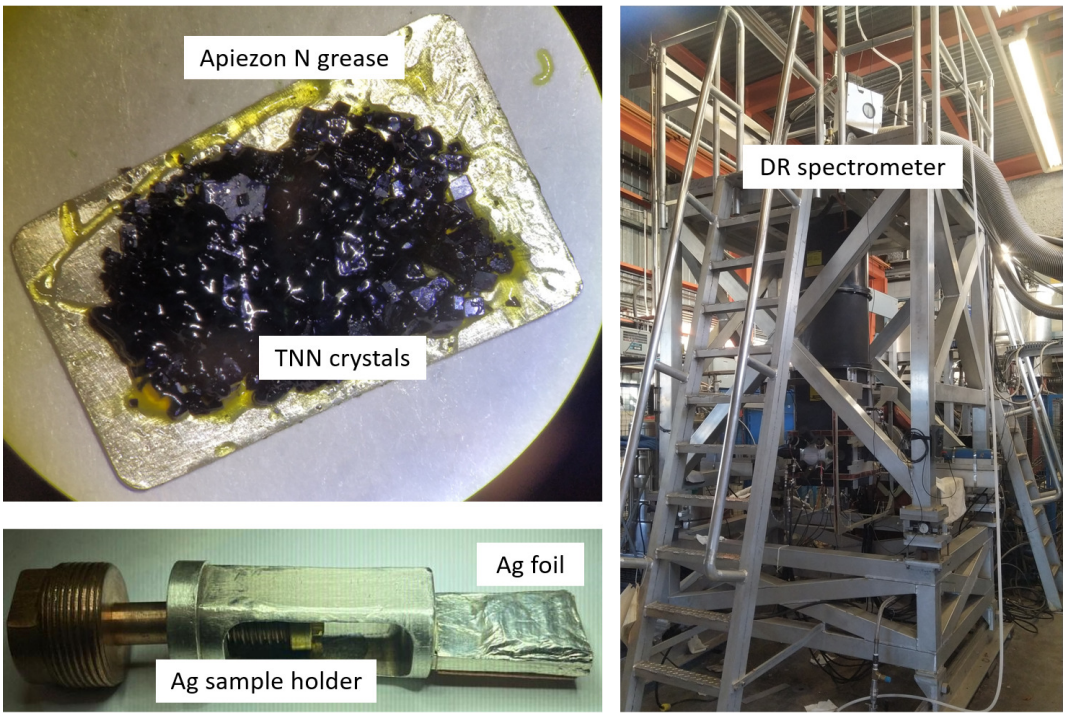

Figure 9.8: Setup of the ZF, LF and TF μSR experiments carried out on the M15 DR spectrometer for the TNN crystals.

T to 0.4 T using a superconducting Helmholtz magnet and an Oxford Instruments dilution refrigerator.

Figure 9.9(a) shows the μSR spectrum collected in the paramagnetic region ($T = 0.33$ K) when applying a weak transverse field (wTF). This field B_{wTF} induces an oscillation of the muon signal from which is possible to calibrate the initial asymmetry a_0. For this particular case, $B^Z_{\mathrm{loc}}/B_{\mathrm{loc}} \ll 1$, so combining Eq.(2.63), Eq.(2.65) and Eq.(2.66), we can express the asymmetry in the longitudinal geometry as:

$$A(t) = a_0 P_Z(t) = a_0\, e^{-\left(\frac{\Delta^2 t^2}{2} + \lambda t\right)} \cos(\omega_\mu t) \tag{9.9}$$

The fit of the μSR spectrum at $T = 0.33$ K to Eq.(9.9) yielded $a_0 = 0.223(2)$, $B_{\mathrm{wTF}} = \omega_\mu/\gamma_\mu = 23.40(3)$ G. For the small relaxation of the curve the best fit was obtained considering only a Lorentzian contribution $\lambda = 0.090(4)$ $\mu\mathrm{s}^{-1}$, in agreement with a more diluted environment for the magnetic moments (delocalized $S = 1/2$ in a huge unit cell).

The μSR spectra measured at zero field in the temperature interval of $0.017 < T < 0.330$ K are shown in Fig. 9.9(b). On a qualitative basis, every spectrum demonstrated an exponential-like relaxation without any observed oscillation as the temperature dropped below T_{N}. A more comprehensive analysis was conducted, focusing on the initial part of the μSR spectra (specifically, the average of the first 2 μs). This time-frame is known to be particularly sensitive to fast relaxation caused by magnetic order [121]. The results revealed no anomalies between the paramagnetic and ordered regimes, as can be seen in the inset of Fig. 9.9(b).

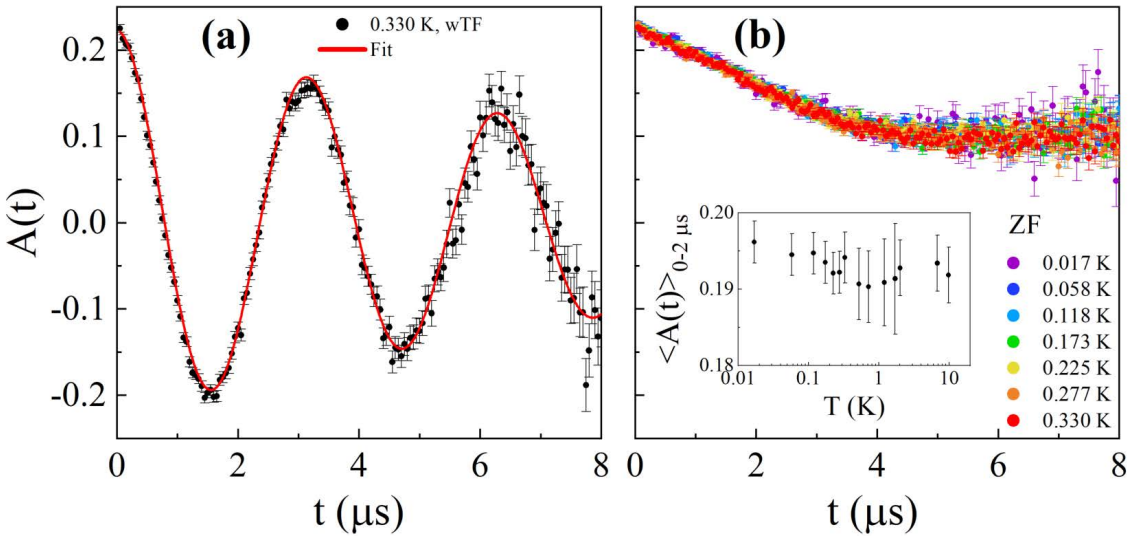

Figure 9.9: (a) μSR spectrum with a wTF applied at 0.33 K. The data is shown in black circles, while the red line corresponds to the fit according to Eq. (9.9). (b) μSR spectra at ZF for several temperatures. The inset shows the averaged asymmetry over the first 2 μs of each spectra.

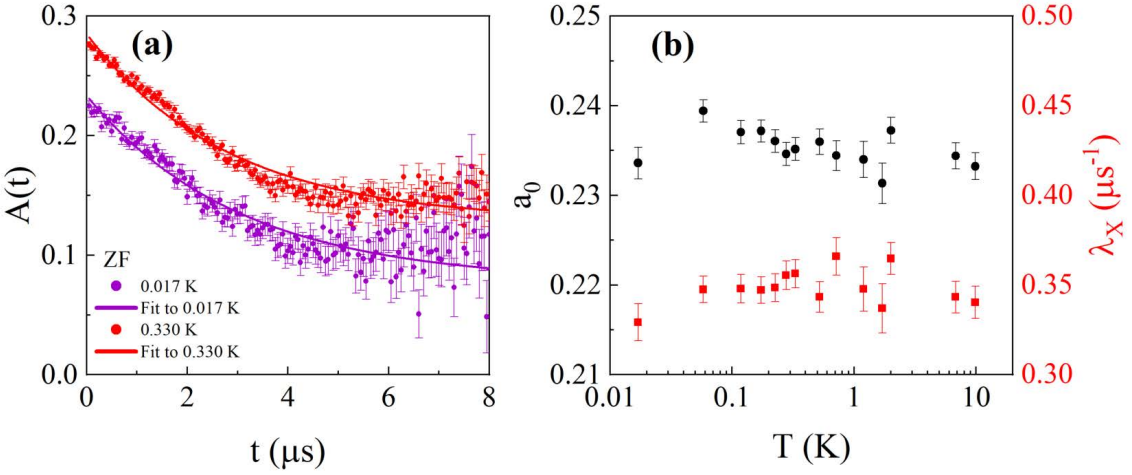

Figure 9.10: (a) ZF μSR spectra at 0.017 K (purple) and 0.330 K (red). The solid lines are the curves fitted according to Eq. (9.10). Both the data and theoretical curve at 0.330 K have been shifted by 0.05 for clarity. (b) Temperature evolution of the fitted parameters.

The asymmetry of all the ZF μSR spectra was best fitted by:

$$A(t) = a_0 \left[z e^{-\lambda_Z t} + (1 - z)\, e^{-\lambda_X t} \cos(\omega_\mu t) \right] \tag{9.10}$$

where a fast decaying oscillatory term (with frequency $\omega_\mu = \gamma_\mu \langle B_{\text{loc}} \rangle$ and relaxation rate λ_X) dominates the initial relaxation and a second slow exponential (λ_Z) dominates the long-time behavior. Phenomenologically, λ_X and λ_Z can be at-

tributed to the spin-spin and spin-lattice relaxation rates, respectively. The parameter $z \equiv \left\langle \left(\frac{B_{\rm loc}^Z}{B_{\rm loc}} \right)^2 \right\rangle$ was fixed to 1/3 for the ZF spectra since the random orientation of the glued crystals can be approximated to a powder.

Since all the measured spectra were exponential-like, no oscillatory behavior was included (i.e. $\langle B_{\rm loc} \rangle = 0$). The value of λ_Z was negligible in all the fits performed, so in the last refinement it was fixed to zero. An example of the fitted ZF curves is depicted in Fig. 9.10(a), while the temperature evolution of the parameters is shown in Fig. 9.10(b). The initial asymmetry a_0 is very close to the value obtained from the wTF spectra and doesn't indicate any asymmetry loss below $T_{\rm N}$. Similarly, the spin-spin relaxation rate λ_X doesn't show any transition as the temperature decreases.

In order to distinguish between static and dynamic local field contributions, longitudinal fields of up to 4000 G were applied at 0.02 K (see Fig. 9.11(a)). As the LF was increased, the asymmetry signal shifted to higher values, which can be better observed in the inset of Fig. 9.11(a), where the average of the first 2 μs of each spectra was calculated. Above LF = 500 G, the muon spin was fully polarized and the asymmetry remained constant in time. This suggests that the nature of the local fields is static, since a dynamic source would produce an observable relaxation even at very large fields. Figure 9.11(b) shows additional spectra taken at LF = 100 G for several temperatures. A similar analysis, as performed for the ZF data, indicates no anomalies across $T_{\rm N}$ (see inset of Fig. 9.11(b)), so the nature of the local fields keeps unchanged by the temperature or the LF applied.

LF spectra were also fitted to Eq. (9.10). For these data the parameter z was allowed to vary, since it is expected to increase towards 1 as more contribution of the local field corresponds to the applied LF ($B_{\rm loc}^Z/B_{\rm loc} \to 1$). As the LF was applied

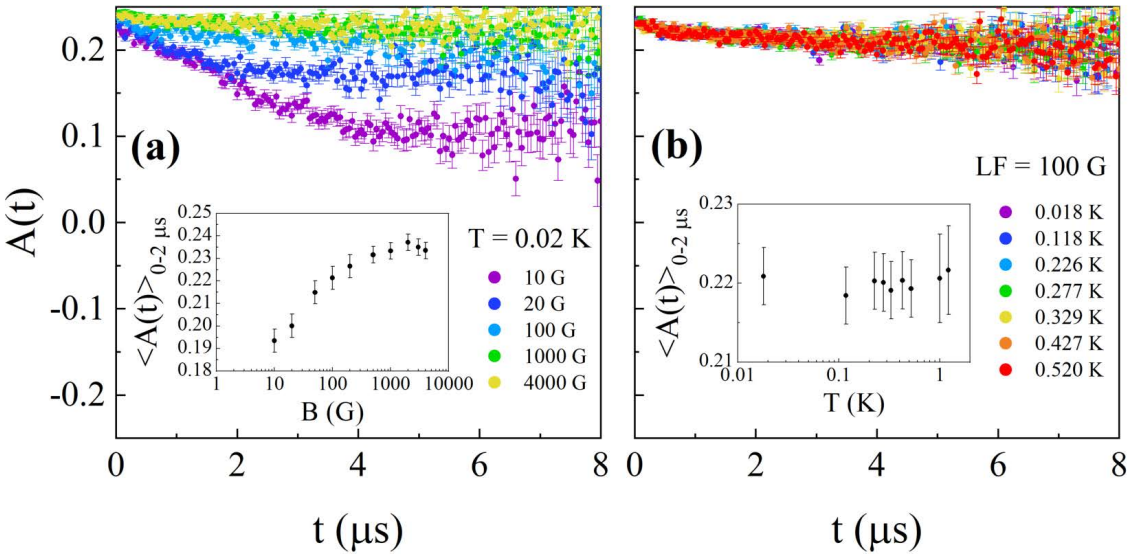

Figure 9.11: (a) μSR spectra at 0.02 K for several LF. (b) μSR spectra at LF = 100 G for several temperatures. The insets show the averaged asymmetry over the first 2 μs of each spectra.

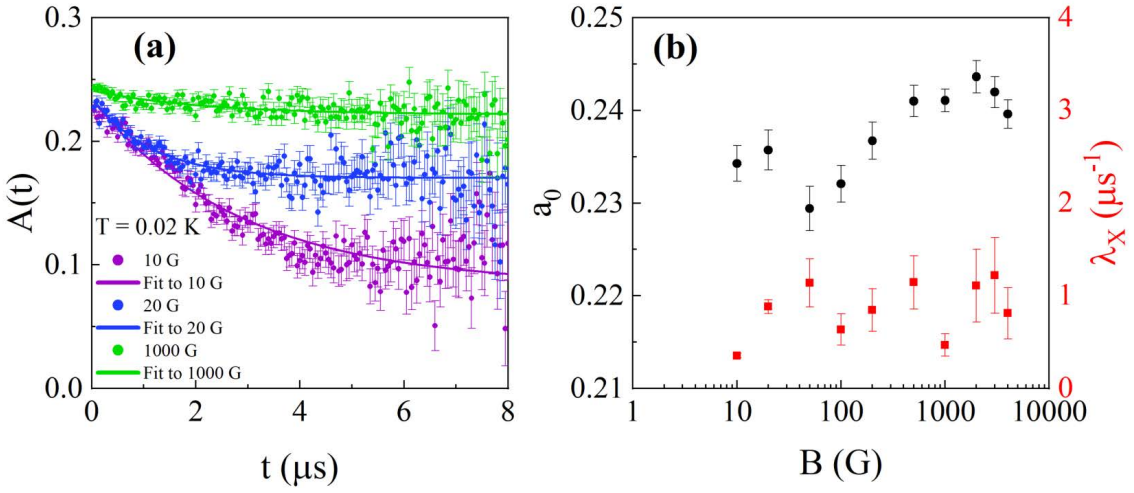

Figure 9.12: (a) LF μSR spectra at 0.02 K and 10 G (purple), 20 G (blue), 1000 G (green). The solid lines are the curves fitted according to Eq. (9.10). (b) Field evolution of the fitted parameters.

parallel to the muon spin polarization, the assumption $\langle B_{\rm loc}\rangle = 0$ was maintained for the oscillatory term. Figure 9.12 shows an example of the LF curves at 0.02 K fitted to Eq. (9.10). No clear LF dependence is observed for the fitted parameters, which further supports the static nature of the local fields.

9.3.3 Magnetic model

Now we shall provide a discussion for the absence of oscillations of the ZF μSR spectra in the magnetically ordered region ($T < T_{\rm N}$). Generally, two possible explanations can be given: the static local field vanishes because of the high symmetry of the magnetic structure at the muon site, or the local field fluctuates fast enough so that the dynamics fall outside of the μSR time window. However, as it has been shown previously that all LF spectra indicate a static nature of the local fiels, the second possibility is considered unlikely. Thus, we focus on the magnetic symmetry at the muon site.

First, the muon implantation site was determined by considering that the positively charged muon is attracted to regions of negative potential. The coordinates in the crystal in which the electronic potential is more negative (i.e. Hartree potential) were obtained by performing density functional theory (DFT) calculations based on the Vienna *ab initio* simulation package (VASP) [122–125]. The suggested μ^+ implantation site is: $(0,\, 0,\, 2/3 + z)$ with $z = 0.02$, which belongs to the 6*a* Wyckoff position of the space group $R3c$. Such muon site is located at $\simeq 1.326$ Å from the nitrogen of the acetonitrile CH_3CN^- ion. Given that the acetonitrile molecule holds the most significant negative charge within the unit cell, the proposed implantation site aligns well with the expected electrostatic interactions. Figure 9.13(a) shows the distribution of the muon sites in the unit cell of TNN. The zoomed region in Fig. 9.13(b) depicts the next-nearest neighbors of the muon site in the layers above

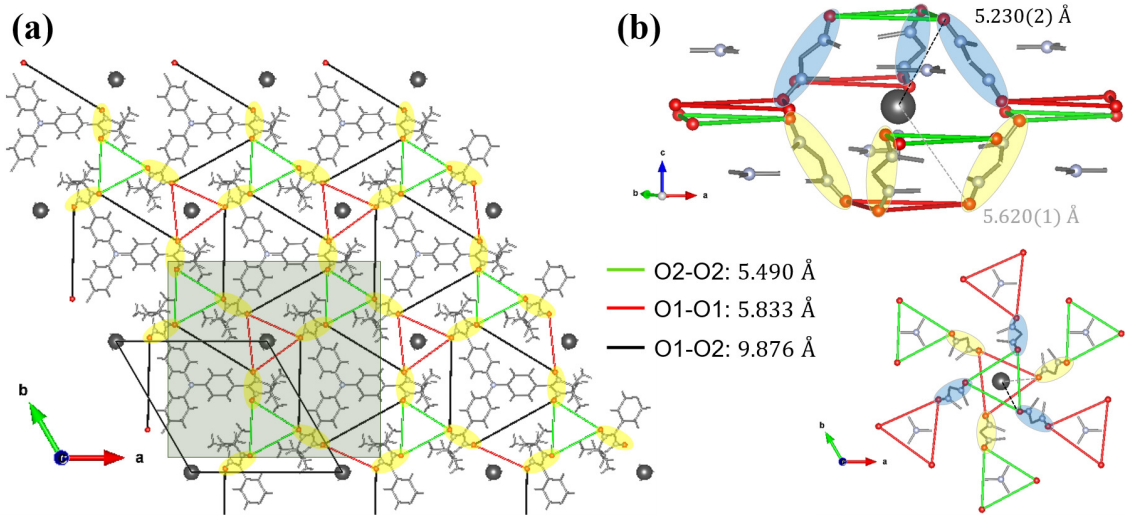

Figure 9.13: (a) Triangular lattice of left-handed isomers in the *ab* plane formed by intramolecular exchange couplings (black lines) and intermolecular ones (red and green lines). Hydrogen and carbon atoms are omitted for clarity, while muon sites are represented by dark grey balls. The shaded rectangle indicates the zoomed region shown in (b). (b) Next-nearest neighbors of muon site in the planes above and below it. The NN groups above and below the muon site are signaled by blue and yellow ellipses, respectively, while the distances from the muon site to O2 and O1 are marked by a dark grey and light grey dotted line, respectively.

and below it. As can be seen, it is in a high symmetric position relative to the NN groups, almost acting as an inversion symmetry center with equal distance to the closest oxygen atoms (μ^+-O1: 5.620(1) Å and μ^+-O2: 5.230(2) Å). Hence, it could be possible that some magnetic structure generates a dipolar field which almost cancels out at the muon site.

In order to find the magnetic structures compatible with the symmetry and a negligible local field at the muon site, the computational model described in Appendix C was used to simulate the μSR spectra of TNN. In this computational model, the experimental setup, nuclear structure, magnetic structure and muon implantation site are needed as input variables. By combining these variables, the local field at the muon site and the resulting asymmetry signal are calculated. For this approach, some simplifications were adopted, which include:

- The random oriented crystals were approximated to a powder.
- The magnetic moments were assumed to be localized on the center of the NN group, located at the 18*b* Wyckoff position of the space group $R3c$ $\vec{f}_{\mathrm{NN},1} = (0.5839, 0.5966, 0.4307)$. The muons were located at the 6*a* Wyckoff position $\vec{f}_{\mu,1} = (0, 0, 0.687)$. The positions were denoted as: $\vec{f}_{\mathrm{NN},i}$ and $\vec{f}_{\mu,j}$, where $i = 1 - 18$ and $j = 1 - 6$ reflect the positions generated by applying the symmetry operations of the space group.
- Since we are interested in the measurements performed at ZF, both the external

and demagnetization fields can be neglected. Additionally, the muon distance to the atoms in the NN group is big enough to neglect the contact hyperfine coupling. Therefore, the only contribution to the local field was considered to be the Lorentz and dipolar fields.

- The Lorentz radius was set to a value big enough to ensure the convergence of both Lorentz and dipolar fields, $R_{\mathrm{Lor}} = 70$ Å.
- Since at zero field the trimer is coupled to a total spin $S = 1/2$, the magnetic moment of the TNN molecule was assumed to be 1 μ_{B}, equally distributed in the 3 NN groups. This assumption is considered valid for the data measured at the lowest temperature, which is far from the order temperature ($T/T_{\mathrm{N}} = 0.017/0.250 < 0.1$), so that the thermal fluctuations can be neglected.
- The values for both the spin-spin relaxation and the initial asymmetry were taken from the ZF μSR spectra at 0.017 K: $\lambda_X = 0.33(1)$ $\mu\mathrm{s}^{-1}$, $a_0 = 0.234(2)$.

The next step involved identifying the magnetic structure's propagation vector. We first considered the presence of magnetic structures with propagation vector different from (0, 0, 0). However, in such configurations the propagation vector modulates the magnetic moments, leading to a non-uniform distribution across different positions within the material. As a consequence, muons implanted into such a structure will experience a dipolar field that is profoundly influenced by the magnetic moments' asymmetric distribution, challenging the possibility of these fields to neutralize each other due to symmetric arrangement. Thus, the only propagation vector compatible with an almost negligible local field at any given muon site should be given by $\vec{k}_{\mathrm{ZF}} = (0, 0, 0)$.

In order to restrict the possible combinations of the 18 magnetic moments in the unit cell, we carried out the irreducible representation analysis for the propagation vector $\vec{k}_{\mathrm{ZF}} = (0, 0, 0)$. The magnetic representation for the magnetic moments, located at the 18*b* Wyckoff position (x, y, z), can be decomposed as a direct sum of Irreducible Representations (*irreps*) of the parent group *R*3*c* for the Γ point, (0, 0, 0) as follows:

$$\mathrm{m}\Gamma_{18\mathrm{b}} = 3\mathrm{m}\Gamma_1(1) \oplus 3\mathrm{m}\Gamma_2(1) \oplus 6\mathrm{m}\Gamma_3(2)$$

The basis vectors for each *irrep* are listed in Table 9.2. The basis vectors components are expressed in terms of the crystallographic axes. The positions of the magnetic moments are labeled as: NN1 (x, y, z), NN2 ($-y$, $x-y$, z), NN3 ($-x+y$, $-x$, z), NN4 ($-y$, $-x$, $z+1/2$), NN5 ($-x+y$, y, $z+1/2$), NN6 (x, $x-y$, $z+1/2$).

After a trial and error analysis for each *irrep*, a solution was found which corresponds to the *irrep* $\mathrm{m}\Gamma_1$ and the combination of the basis vectors: $\psi_1^2 + \psi_1^3$.

The magnetic structure of this solution generates a Lorentz field which averages to zero and a dipolar field with modulus $B_{\mathrm{dip}} \sim 2.4$ G. In Figure 9.14(a), we present the simulated μSR spectrum that corresponds to this dipolar field value, together with our experimental data. The comparison reveals a notable agreement between the simulated and experimental results, which underscores the validity of our proposed

model. A scheme of the magnetic structure is shown in Fig. 9.14(b) and (c). Notably, the configuration is consistent with AFM intra-trimer, inter-trimer and inter-layer couplings. This arrangement leads to a macroscopic average of zero magnetization, as reported in previous studies [108, 111]. Moreover, by making use of Eq.(9.2), (9.3) and (9.4), it can be demonstrated that the magnetic structure exhibits AFE coupling between odd and even layers, in agreement with the theoretical predictions in Ref. [105].

The neutron signal produced by the magnetic structure was simulated using the FullProf Suite [115]. The strongest magnetic reflection which appears superimposed to a nuclear reflection is $(1\,1\,0) + \vec{k}_{\mathrm{ZF}} \equiv (1\,1\,0)$, where the intensity due to purely magnetic diffraction is around 4% of the nuclear Bragg peak. Meanwhile, $(0\,\bar{1}\,1)$ is the strongest magnetic reflection without a nuclear contribution, with a similar intensity as the $(1\,1\,0)$ reflection.

These values can be compared with the SCND results from Fig. 9.7. The first integrated reflection ($\sin\theta/\lambda = 0.066$) corresponds with $(1\,1\,0)$, and the intensity varies from 3.2(5) at 0.5 K to 2.9(2) at 0.05 K. Therefore, it is clear that in order to resolve the magnetic signal (4% of 3.2 = 0.128), much higher statistics are needed.

If we assume a normal distribution of the intensity N, the error σ can be expressed

Table 9.2: Basis vectors (BV) of each *irrep* present in the magnetic representation of the 18*b* site for the space group *R*3*c* with $\vec{k}_{\mathrm{ZF}} = (0, 0, 0)$. The basis vectors components are expressed in terms of the crystallographic axis *a*, *b* and *c*.

irrep	BV	NN1	NN2	NN3	NN4	NN5	NN6
$\mathrm{m}\Gamma_1$	ψ_1^1	$(1\,0\,0)$	$(0\,1\,0)$	$(\bar{1}\,\bar{1}\,0)$	$(0\,1\,0)$	$(1\,0\,0)$	$(\bar{1}\,\bar{1}\,0)$
	ψ_2^1	$(0\,1\,0)$	$(\bar{1}\,\bar{1}\,0)$	$(1\,0\,0)$	$(1\,0\,0)$	$(\bar{1}\,\bar{1}\,0)$	$(0\,1\,0)$
	ψ_3^1	$(0\,0\,1)$	$(0\,0\,1)$	$(0\,0\,1)$	$(0\,0\,\bar{1})$	$(0\,0\,\bar{1})$	$(0\,0\,\bar{1})$
$\mathrm{m}\Gamma_2$	ψ_1^2	$(1\,0\,0)$	$(0\,1\,0)$	$(\bar{1}\,\bar{1}\,0)$	$(0\,\bar{1}\,0)$	$(\bar{1}\,0\,0)$	$(1\,\bar{1}\,0)$
	ψ_2^2	$(0\,1\,0)$	$(\bar{1}\,\bar{1}\,0)$	$(1\,0\,0)$	$(\bar{1}\,0\,0)$	$(1\,1\,0)$	$(0\,\bar{1}\,0)$
	ψ_3^2	$(0\,0\,1)$	$(0\,0\,1)$	$(0\,0\,1)$	$(0\,0\,1)$	$(0\,0\,1)$	$(0\,0\,1)$
$\mathrm{m}\Gamma_3$	ψ_1^3	$(1\,0\,0)$	$\left(0\ \frac{-1-\sqrt{3}i}{2}\ 0\right)$	$\left(\frac{1-\sqrt{3}i}{2}\ \frac{1-\sqrt{3}i}{2}\ 0\right)$	$(0\,0\,0)$	$(0\,0\,0)$	$(0\,0\,0)$
	ψ_2^3	$(0\,1\,0)$	$\left(\frac{1+\sqrt{3}i}{2}\ \frac{1+\sqrt{3}i}{2}\ 0\right)$	$\left(\frac{-1+\sqrt{3}i}{2}\ 0\ 0\right)$	$(0\,0\,0)$	$(0\,0\,0)$	$(0\,0\,0)$
	ψ_3^3	$(0\,0\,1)$	$\left(0\ 0\ \frac{-1-\sqrt{3}i}{2}\right)$	$\left(0\ 0\ \frac{-1+\sqrt{3}i}{2}\right)$	$(0\,0\,0)$	$(0\,0\,0)$	$(0\,0\,0)$
	ψ_4^3	$(0\,0\,0)$	$(0\,0\,0)$	$(0\,0\,0)$	$(0\,1\,0)$	$\left(\frac{-1+\sqrt{3}i}{2}\ 0\ 0\right)$	$\left(\frac{1+\sqrt{3}i}{2}\ \frac{1+\sqrt{3}i}{2}\ 0\right)$
	ψ_5^3	$(0\,0\,0)$	$(0\,0\,0)$	$(0\,0\,0)$	$(1\,0\,0)$	$\left(\frac{1-\sqrt{3}i}{2}\ \frac{1-\sqrt{3}i}{2}\ 0\right)$	$\left(0\ \frac{-1-\sqrt{3}i}{2}\ 0\right)$
	ψ_6^3	$(0\,0\,0)$	$(0\,0\,0)$	$(0\,0\,0)$	$(0\,0\,\bar{1})$	$\left(0\ 0\ \frac{1-\sqrt{3}i}{2}\right)$	$\left(0\ 0\ \frac{1+\sqrt{3}i}{2}\right)$
	ψ_7^3	$(0\,0\,0)$	$(0\,0\,0)$	$(0\,0\,0)$	$(0\,1\,0)$	$\left(\frac{-1-\sqrt{3}i}{2}\ 0\ 0\right)$	$\left(\frac{1-\sqrt{3}i}{2}\ \frac{1-\sqrt{3}i}{2}\ 0\right)$
	ψ_8^3	$(0\,0\,0)$	$(0\,0\,0)$	$(0\,0\,0)$	$(1\,0\,0)$	$\left(\frac{1+\sqrt{3}i}{2}\ \frac{1+\sqrt{3}i}{2}\ 0\right)$	$\left(0\ \frac{-1+\sqrt{3}i}{2}\ 0\right)$
	ψ_9^3	$(0\,0\,0)$	$(0\,0\,0)$	$(0\,0\,0)$	$(0\,0\,\bar{1})$	$\left(0\ 0\ \frac{1+\sqrt{3}i}{2}\right)$	$\left(0\ 0\ \frac{1-\sqrt{3}i}{2}\right)$
	ψ_{10}^3	$(1\,0\,0)$	$\left(0\ \frac{-1+\sqrt{3}i}{2}\ 0\right)$	$\left(\frac{1+\sqrt{3}i}{2}\ \frac{1+\sqrt{3}i}{2}\ 0\right)$	$(0\,0\,0)$	$(0\,0\,0)$	$(0\,0\,0)$
	ψ_{11}^3	$(0\,1\,0)$	$\left(\frac{1-\sqrt{3}i}{2}\ \frac{1-\sqrt{3}i}{2}\ 0\right)$	$\left(\frac{-1-\sqrt{3}i}{2}\ 0\ 0\right)$	$(0\,0\,0)$	$(0\,0\,0)$	$(0\,0\,0)$
	ψ_{12}^3	$(0\,0\,1)$	$\left(0\ 0\ \frac{-1+\sqrt{3}i}{2}\right)$	$\left(0\ 0\ \frac{-1-\sqrt{3}i}{2}\right)$	$(0\,0\,0)$	$(0\,0\,0)$	$(0\,0\,0)$

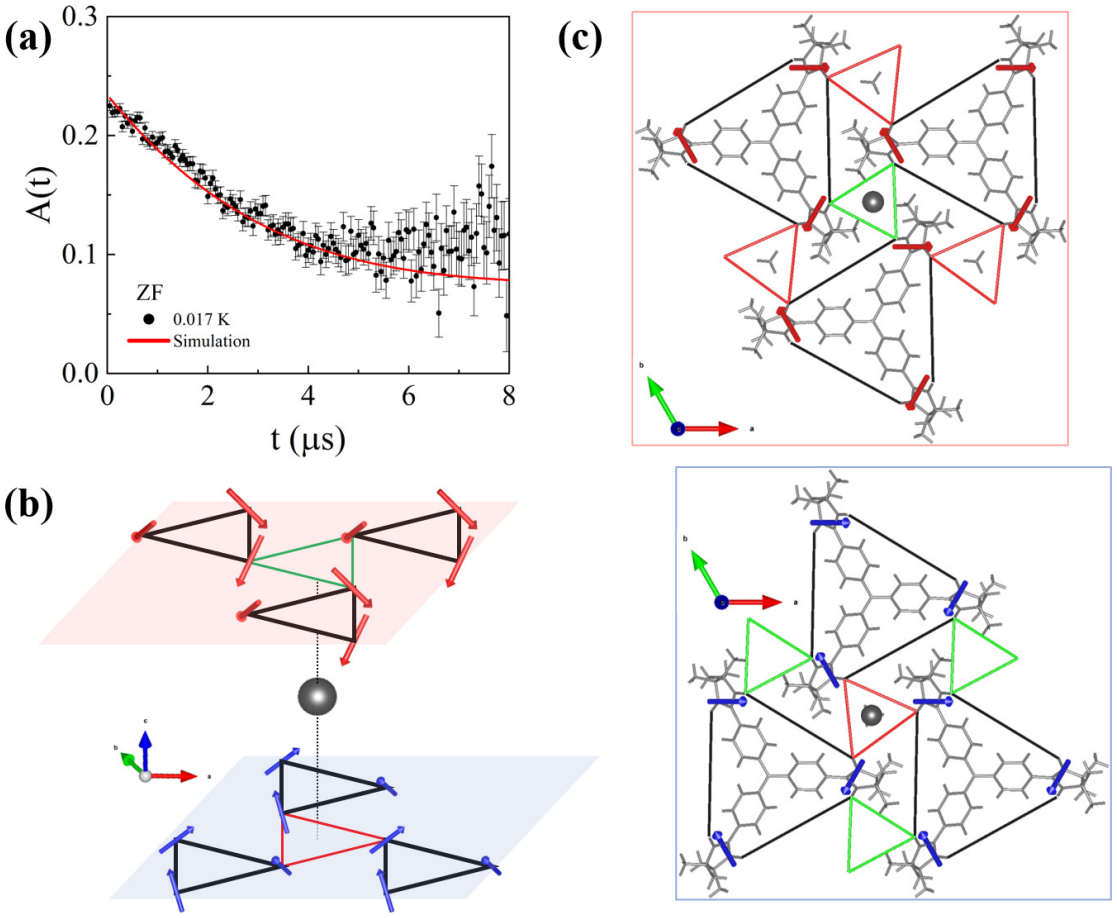

Figure 9.14: (a) ZF μSR spectrum at 0.017 K (black circles), together with the simulated spectrum (red line) for the magnetic configuration given by mΓ_1 and $\psi_1^2 + \psi_1^3$. (b) Scheme of the magnetic configuration in the planes above and below the muon site, represented by a dark grey ball. The nuclear and magnetic structures along the *ab* plane of the shaded areas are shown in (c), where all atoms are omitted for clarity.

as: $\sigma \propto 1/\sqrt{N}$. Since the intensity is proportional to the acquisition time, we can write: $\sigma \propto 1/\sqrt{t}$. At the same time, the magnetic signal N_M is proportional to the acquisition time: $N_M \propto t$. Therefore, with these considerations, an increase in the acquisition time of 4 times would imply a magnetic signal twice as large as the error bar. Considering that collecting the reflections took one day for each temperature, a minimum of 4 days for each temperature would guarantee enough statistics to resolve the magnetic signal. Similar considerations can be taken for the observation of the $(0\,\bar{1}\,1)$ reflection, since the background of the SCND experiment accounted for around 0.2.

9.4 Trimer formation at the 1/3 plateau

In this section, our investigation shifts focus towards the 1/3 plateau, which, according to the phase diagram, exhibits FE order below 0.35 K without involving a spin ordering transition [111]. As a result, previous approaches to elucidating the magnetic structure, such as SCND, were deemed not directly applicable or revealing for our purposes.

Consequently, we redirected our research objectives towards exploring the formation of trimers within this region, employing polarized neutron diffraction (PND) experiments. At high temperatures, the NN radicals in the TNN molecule are expected to act as independent paramagnetic $S = 1/2$ spins, coupling below 5.5 K to form the twofold-degenerate state with $S = 1/2$ and $S_z = 1/2$. However, the precise spatial arrangement of these coupled spins within the molecule remains undetermined. Therefore, our primary goal was to observe the change in spin density prompted by trimer formation under these temperature conditions. To enrich our analysis and provide information about the local field, these measurements were complemented with μSR experiments.

9.4.1 Polarized neutron diffraction

PND experiments were performed to measure the flipping ratio of several reflections and determine the spin density of the asymmetric unit of TNN. However, to effectively interpret the flipping ratios derived from PND experiments, accurate measurements of the magnetic moments at the specific temperatures and magnetic fields where the flipping ratios are recorded are desirable. In addition, a prior knowledge of the nuclear structure factors is crucial for interpreting the PND experiment results and reconstructing the spin density maps.

Magnetization curves

Previous magnetic measurements were performed on a powder sample using the VSM option of a PPMS-14T manufactured by Quantum Design. Isothermal magnetization $M(B)$ curves were collected at 2 K and 12 K in a field range $0 \leq B \leq 14$ T. A comparison between our measured data (empty circles) and the ones from Ref. [109] (filled triangles) is displayed in Figure 9.15, which shows totally reproducible results. From these curves, the sample magnetization at 9 T for 2 K and 12 K was deduced to be: 1.221(1) and 0.796(1) μ_B/f.u., respectively.

The isothermal magnetization data collected at 2 K and 12 K were also compared against the theoretical curves for ideal paramagnets possessing spin 1/2. At 12 K, the experimental results align well with a model that combines three Brillouin functions of spin 1/2, consistent with the behavior of the three NN radicals within the TNN molecule acting as independent paramagnetic entities with $S = 1/2$. At 2 K, a good agreement at low fields is observed for a single Brillouin function of spin 1/2, suggesting that by this temperature, the NN radicals have effectively coupled into a trimer with total spin 1/2.

Low temperature structure

In order to treat the flipping ratios from the PND experiment, a prior knowledge of the nuclear structure factors should be obtained to include them in Eq.(2.42). Therefore, previous unpolarized neutron diffraction measurements were performed at the four-circle single-crystal diffractometer D9 in the Institut Laue Langevin (ILL) in Grenoble, France.

A crystal of dimensions $1 \times 1 \times 1$ mm^3 was glued on top of an Al pin ($\phi = 2$ mm) with vacuum grease Bluestar (see Fig. 9.16). The pin was then mounted in the Eulerian cradle and cooled down to 12 K with a 4-circle He-flow cryostat. The wavelength of the incident neutron beam with size 4×4 mm^2 was fixed to $\lambda = 0.836$ Å by a Cu crystal in transmission geometry using the (220) planes. A total of 1486 ω-scans of Bragg peaks indexed by the space group $R3c$ and extending to $\sin\theta/\lambda = 0.7$ were collected with the D9 area detector. After merging, 1462 unique reflections were obtained. During the experiment the strong $(0\ 0\ \bar{6})$ reflection was re-measured every 100 reflections to check that the crystal, instrument and reactor were stable over the data collection. The centering of the measured reflections was used to determine the cell parameters at 12 K: $a = 15.139(3)$ Å, $c = 30.09(1)$ Å.

The peaks were integrated using the RACER program. The refinement was done using the FullProf Suite [115]. The scale factor, extinction correction, atom positions and anisotropic thermal factors were allowed to vary resulting in 292 variables. The fit converged with the agreement factors:

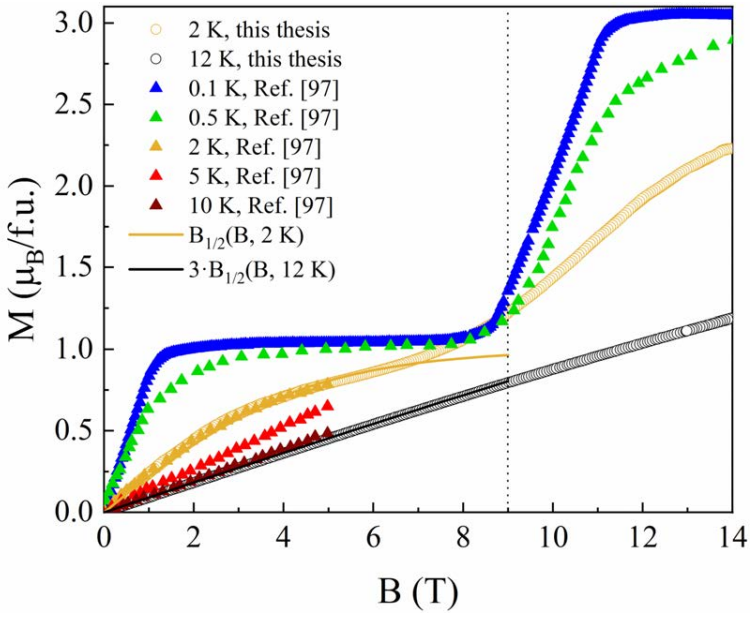

Figure 9.15: Comparison between the TNN magnetization curves measured in this thesis (empty circles), the magnetization curves taken from Ref. [109] (filled triangles) and the theoretical curves using the Brillouin function for spin 1/2. The dotted line indicates the magnetic field value at which the PND experiments were performed.

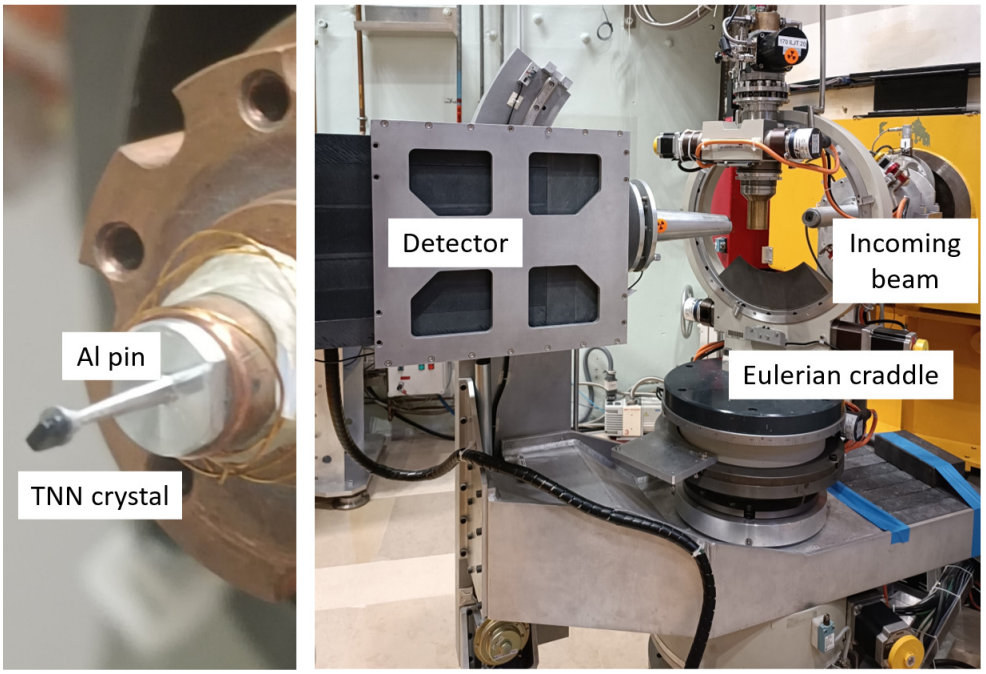

Figure 9.16: Setup of the single-crystal neutron diffraction experiments carried out on the D9 diffractometer for the TNN compound.

$$R = 0.124$$
$$R_w = 0.142$$
$$\chi^2 = 3.04$$

The value of the extinction correction was 0.007(1). The refined values of the atomic positions and anisotropic thermal factors are given in Tables H.1 and H.2 of Appendix H, respectively.

Spin density distribution

The same crystal used in the low-temperature structure determination was used for the PND experiment at the hot neutron diffractometer D3 in the Institut Laue Langevin (ILL) in Grenoble, France.

Flipping ratios at 12 K and 2 K for two orientations of the crystal relative to the vertical axis, given by the magnetic field, were measured (see Fig. 9.17). The Al pin with the crystal was then inserted into the 10 T cryomagnet and cooled down. A magnetic field of 9 T was applied in order to saturate the sample. The wavelength of the incident neutron beam was fixed to $\lambda = 0.8283$ Å by a Heusler crystal. The use of this monochromator also yielded a 92(1) % initial polarization of the neutron beam. The polarization was then changed between up and down states relative to the vertical magnetic field by a cryoflipper with 1.000(1) efficiency. The flipping ratios were measured at 12 K in a total of 173 reflections, 90 of them unique, up to

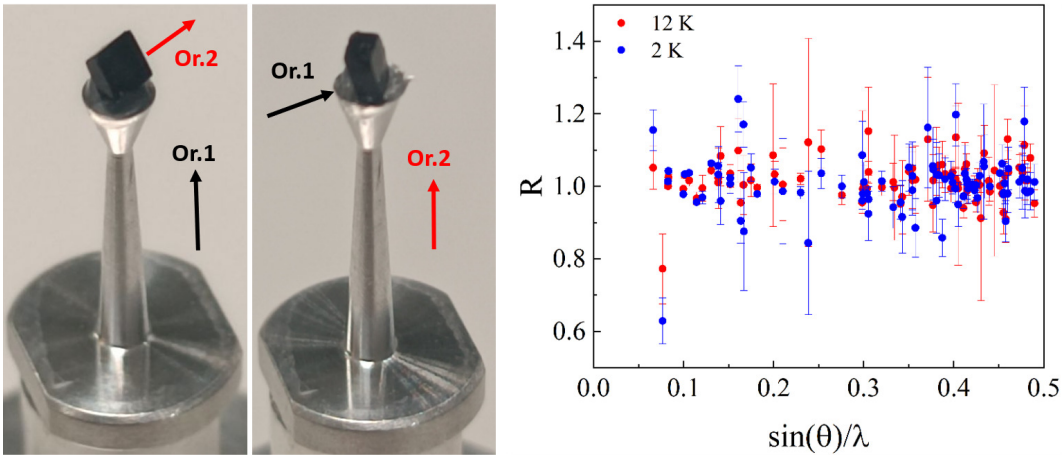

Figure 9.17: Left: TNN crystal glued to the Al pin in two different orientations, where the vertical axis is along the (-0.71 -0.69 0.12) crystallographic direction (Or.1) or along the (-0.39 0.34 -0.86) (Or.2). Right: Flipping ratios obtained at 12 K and 2 K.

$\sin\theta/\lambda = 0.5$. At 2 K the flipping ratios were measured in only 139 reflections, 86 of them unique. A comparison between both temperatures is shown in Fig. 9.17.

In order to effectively fit the experimental flipping ratios, two different approaches for modeling the spin density distribution have been used. These approaches, introduced in Chapter 2, are particularly useful for non-centrosymmetric crystal structures, where both the nuclear and magnetic structure factors can be complex numbers. The wavefunction expansion [126] offers a straightforward interpretation of the physical origin of the spin density distribution, while the multipole expansion [127] provides greater flexibility, revealing details that are challenging to handle using the wavefunction approach.

For both modeling approaches, we employed the FullProf Suite program [115]. Due to the limited amount of data available, we applied several constraints to prevent an over-parametrized model. Previous studies have demonstrated that spin density is negligible in atoms located at a significant distance from the nitronyl nitroxide radical. [46–51]. Consequently, our models only calculated the spin density in atoms within the NN group. Since the atoms of the NN radical are contained in the O-N-C-N-O plane, all of them shared the same reference coordinate system. This system was oriented such that the y axis aligned parallel to the bond connecting C7 to the phenyl group, the z axis was perpendicular to the O-N-C-N-O plane, and x completed the right-hand orthonormal system, as displayed in Fig. 9.18(a).

First, we analyzed the flipping ratios obtained at 12 K and 9 T using two distinct models. Initially, we employed the multipolar expansion method, considering only a spherical spin distribution on each atom (Model S). The ζ exponent and the n_l values of the Slater radial functions were fixed respectively to $\zeta = 2\alpha$, where α is atomic Slater exponent taken from the literature [128–130] and $n_l = 2(n-1)$, where n is the principal quantum number. Both parameters are listed in Table 9.3.

Next, the wavefunction approach was used considering p_z orbitals in the oxygen,

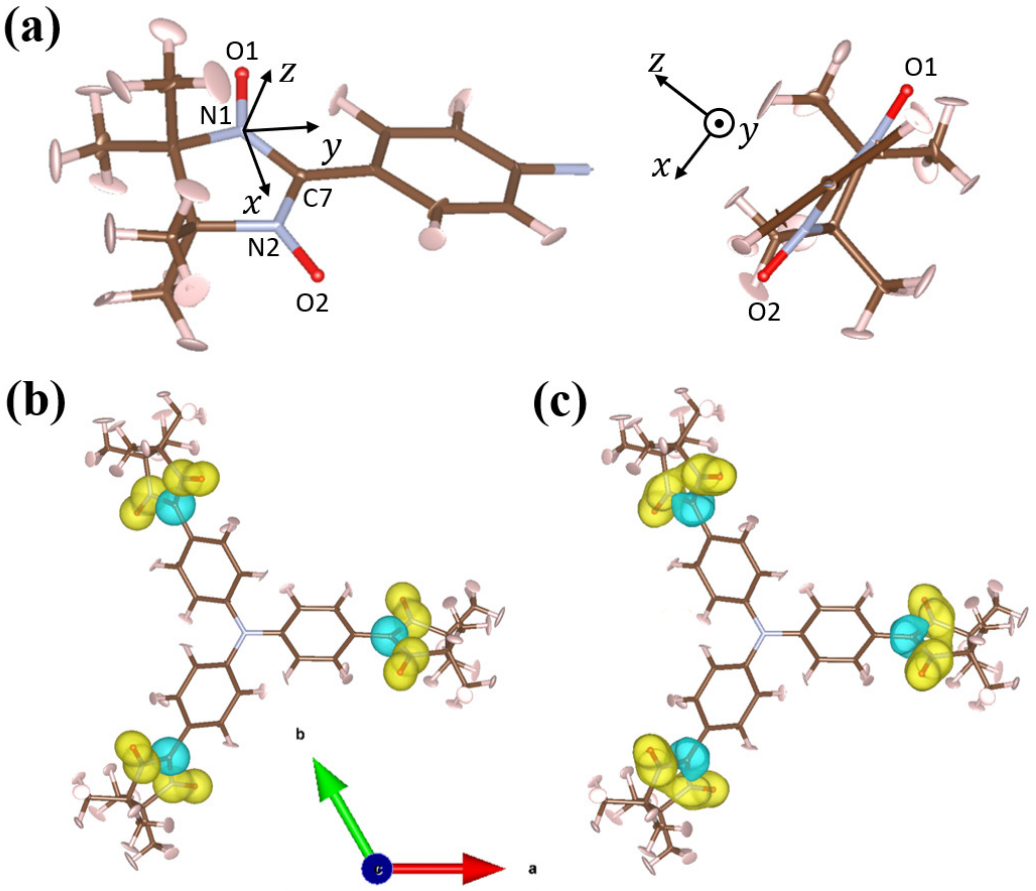

Figure 9.18: (a) Reference coordinate system used in the modeling of the spin density of the atoms in the nitronyl nitroxide group. *ab* plane view of the spin density distribution obtained at 12 K and 9 T from Model S (b) and P (c). The spin density is represented as an isosurface at 0.007 $\mu_B/Å^3$, where the yellow and blue colors denote positive and negative values, respectively.

nitrogen and carbon atoms (Model P). The parameters for the Slater radial functions n and α were fixed to the values previously mentioned, and are also listed in Table 9.3. In both models, the atoms belonging to the same species were constrained to

Table 9.3: Parameters for the radial component in the multipolar and wavefunction expansion approaches.

	Multipolar		Wavefunction	
Atom	ζ	n_l	α	n
O	4.50	2	2.25	2
N	3.90	2	1.95	2
C	3.44	2	1.72	2

Table 9.4: Main results of the models assumed for the flipping ratios at 12 K and 2 K, and 9 T.

T (K)	Model	Population (μ_B)					m (μ_B)	M (μ_B)	χ^2
	O1	N1	C7	N2	O2				
12	S	0.07(1)	0.09(2)	-0.09(3)	0.09(2)	0.07(1)	0.23(1)	0.69(4)	0.877
12	P	0.07(2)	0.17(4)	-0.22(5)	0.17(4)	0.07(2)	0.26(3)	0.78(8)	0.902
2	S	0.10(1)	0.13(2)	-0.11(2)	0.13(2)	0.10(1)	0.35(4)	1.1(1)	1.493
2	P	0.13(2)	0.20(3)	-0.22(4)	0.20(3)	0.13(2)	0.44(6)	1.3(2)	1.686

have the same population. Therefore, only three parameters were refined for each model.

The main results from these models are listed in Table 9.4, which includes the spin density population of the atoms in the nitronyl nitroxide group, the magnetization of each NN radical m, the magnetization per formula unit of the compound $M = 3m$, and the agreement factor of the fit χ^2. The spin density distributions obtained from each model are also shown in panels (b), (c), (d) and (e) of Fig. 9.18.

The total magnetization M obtained from the model refinements lies in the range between 0.69(4) to 0.78(8) μ_B/f.u., in good agreement with the magnetization results at 12 K (0.796(1) μ_B/f.u.). In Model S, a similar spin population is observed on the oxygen and nitrogen atoms, while the central C7 carbon has a negative spin population due to spin polarization effects, in good agreement with previous PND experiments on nitronyl nitroxide radicals [46–51]. Model P shares the same qualitative behavior, although there is a significant increase in the spin populations of N and C atoms. This results can be understood considering that the spin density from the SOMO orbital (π^* orbitals) is better described by p_z than s orbitals.

Next, the flipping ratios obtained at 2 K and 9 T were analyzed using the same models. The results are listed in Table 9.4. The total magnetization M agrees with the experimental magnetization at 2 K (1.221(1) μ_B/f.u.). Therefore, the PND results also confirm the trimer formation at 2 K. However, the agreement with the experimental data is worse than at 12 K, indicating that these models do not entirely capture the variation in the flipping ratios between both temperatures.

Next, the spin densities observed in the PND experiments are compared with the theoretical spin expectation values for the ground state of the 1/3 plateau.

9.4.2 Theoretical ground state

First, we introduce the lattice structure as shown in Fig. 9.19. The trimers on the even and odd layers are considered separately.

In the 1/3 plateau the magnetic field, applied along the z-axis, is large enough to polarize each trimer into the $S^z = 1/2$ state. The $S = 3/2$ excited states of the trimer can be projected out as long as the $3J/2$ gap is much larger than J' and J''. Therefore, the low-energy effective Hamiltonian can be obtained as $\mathcal{H}_{\text{eff}} = \mathcal{P}\,\mathcal{H}_{\text{tri}}\,\mathcal{P}$, where $\mathcal{P} = \sum_i |\psi_i\rangle\langle\psi_i|$ is the projector operator onto the $S = 1/2$ subspace, being

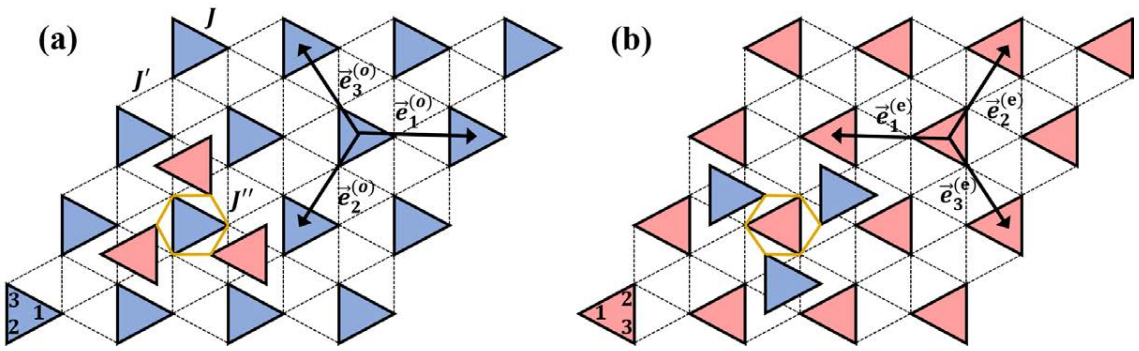

Figure 9.19: Lattice model of TNN·CH_3CN considering both the odd (a) and even (b) layers. The intra-trimer site indices 1-3 are labeled for each layer.

$|\psi_i\rangle$ the normalized states with total spin 1/2 [105]. Before calculating $\mathcal{H}_{\text{eff}}$ it is convenient to introduce the projected spin operators:

$$\vec{\tilde{S}}_{\mu,\vec{r}} \equiv \mathcal{P}\,\vec{S}_{\mu,\vec{r}}\,\mathcal{P} = \frac{1}{3}\vec{S}_{\vec{r}}\,(1 - 4\vec{\tau}_{\vec{r}}\cdot\vec{n}_\mu) \tag{9.11}$$

where $\vec{n}_\eta = (\cos\varphi_\mu,\, \sin\varphi_\mu,\, 0)$ with $\varphi_\mu = 4(\mu-1)\pi/3$ ($\mu = 1,\, 2,\, 3$) are parallel to the displacement vectors from the center of the trimer to each spin site. Replacing the spin operators of Eq.(9.6) with the projected operators of Eq.(9.11) gives:

$$\mathcal{H}_{\text{eff}} = -\frac{4J'}{9}\sum_{\vec{r},\,\eta}\vec{\tau}_{\mu,\vec{r}+\vec{e}_\eta}\cdot\vec{n}_\eta\,\vec{\tau}_{\vec{r}}\cdot\vec{n}_\eta + \frac{2J''}{3}\sum_{\vec{r}}\left(\tau^x_{\vec{r}}\tau^x_{\vec{r}+\vec{u}_3} + \tau^y_{\vec{r}}\tau^y_{\vec{r}+\vec{u}_3}\right) + \text{const.} \tag{9.12}$$

Upon examining Eq.(9.12), it becomes evident that energy minimization leads to AFM intralayer and interlayer couplings ($J', J'' > 0$) inducing a FE exchange between electric dipoles in the same layer, and an AFE coupling along the c direction.

In the fully-polarized spin-1/2 sector, only the orbital degrees of freedom remain. In order to determine the ground state, we can define the basis states:

$$|+\rangle \equiv |S^z = 1/2, \tau^x = 1/2\rangle = \frac{1}{\sqrt{6}}\left(|\uparrow\uparrow\downarrow\rangle + |\uparrow\downarrow\uparrow\rangle - 2|\downarrow\uparrow\uparrow\rangle\right) \tag{9.13}$$

$$|-\rangle \equiv |S^z = 1/2, \tau^x = -1/2\rangle = \frac{1}{\sqrt{2}}\left(|\uparrow\uparrow\downarrow\rangle - |\uparrow\downarrow\uparrow\rangle\right) \tag{9.14}$$

which verify: $\tau^x|\pm\rangle = \pm\frac{1}{2}|\pm\rangle$; $\tau^y|\pm\rangle = \frac{1}{2}|\mp\rangle$. The proposed ground state has a variational parameter $\phi \in [0,\, 2\pi)$, so that for any trimer:

$$|\phi\rangle_{\vec{r}} = \begin{cases} \cos\frac{\phi}{2}|+\rangle_{\vec{r}} + \sin\frac{\phi}{2}|-\rangle_{\vec{r}} & \vec{r} \in \text{even layer} \\ -\sin\frac{\phi}{2}|+\rangle_{\vec{r}} + \cos\frac{\phi}{2}|-\rangle_{\vec{r}} & \vec{r} \in \text{odd layer} \end{cases} \tag{9.15}$$

Therefore, $|\phi\rangle_{\text{odd}} = |\phi + \pi\rangle_{\text{even}}$. If we denote $\hat{u}(\phi) = (\cos\phi,\, \sin\phi,\, 0)$ we find:

$$\vec{\tau}\cdot\hat{u}(\phi)|\phi\rangle = \frac{1}{2}|\phi\rangle \tag{9.16}$$

That is, $|\phi\rangle$ is an eigenstate of the pseudospin in $\hat{u}(\phi)$ direction. Recalling the projected operators of Eq.(9.11), it is straightforward to obtain the expectation values for spins in even layers:

$$\langle \vec{S}_1 \rangle_{\text{even}} = \langle \phi | \vec{S}_1 | \phi \rangle = \frac{1}{3} \langle \phi | \vec{S} \, (1 - 4\tau^x) | \phi \rangle = \begin{pmatrix} 0 \\ 0 \\ \frac{1-2\cos\phi}{6} \end{pmatrix} \tag{9.17}$$

$$\langle \vec{S}_2 \rangle_{\text{even}} = \langle \phi | \vec{S}_2 | \phi \rangle = \frac{1}{3} \langle \phi | \vec{S} \, (1 - 4(-\tau^x - \sqrt{3}\tau^y)/2) | \phi \rangle = \begin{pmatrix} 0 \\ 0 \\ \frac{1+\cos\phi+\sqrt{3}\sin\phi}{6} \end{pmatrix} \tag{9.18}$$

$$\langle \vec{S}_3 \rangle_{\text{even}} = \langle \phi | \vec{S}_3 | \phi \rangle = \frac{1}{3} \langle \phi | \vec{S} \, (1 - 4(-\tau^x + \sqrt{3}\tau^y)/2) | \phi \rangle = \begin{pmatrix} 0 \\ 0 \\ \frac{1+\cos\phi-\sqrt{3}\sin\phi}{6} \end{pmatrix} \tag{9.19}$$

For spins in odd layers, we make $\phi \to \phi + \pi$, so that:

$$\langle \vec{S}_1 \rangle_{\text{odd}} = \begin{pmatrix} 0 \\ 0 \\ \frac{1+2\cos\phi}{6} \end{pmatrix} ; \; \langle \vec{S}_2 \rangle_{\text{odd}} = \begin{pmatrix} 0 \\ 0 \\ \frac{1-\cos\phi-\sqrt{3}\sin\phi}{6} \end{pmatrix} ; \; \langle \vec{S}_3 \rangle_{\text{odd}} = \begin{pmatrix} 0 \\ 0 \\ \frac{1-\cos\phi+\sqrt{3}\sin\phi}{6} \end{pmatrix} \tag{9.20}$$

From these expectations values, the dependence of the magnetization along the z-axis with ϕ can be calculated, assuming a g-factor equal to 2, as it is shown in Fig. 9.20.

Additionally, one should consider that the variational parameter ϕ is not fixed by the theory, and therefore can take any value. Therefore, in order to compare the spin expectation values with the spin densities observed in the PND experiments, an average over the whole ϕ range should be performed. This average yields an

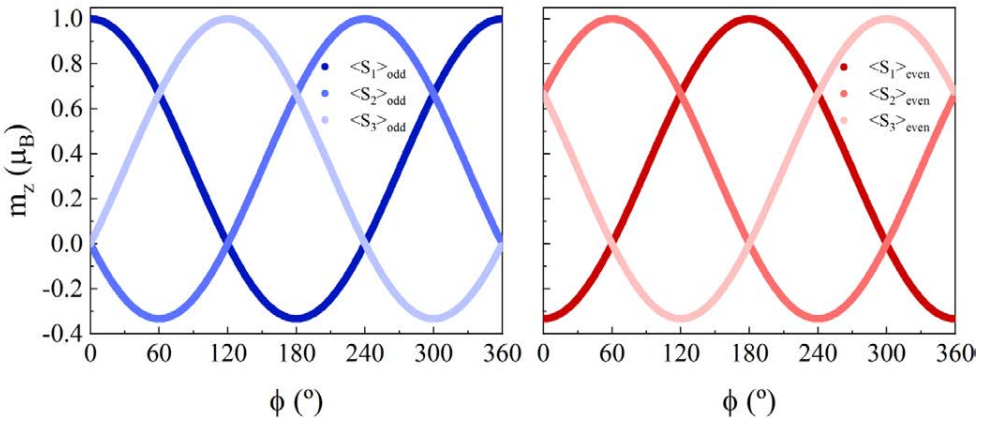

Figure 9.20: Dependence of the theoretical z-component of the magnetization with the variational parameter ϕ for odd and even layers.

expected value of 1/3 μ_B for all spins, in close agreement with the spin densities of each NN radical at 2 K (Model S yields 0.35(4) and Model P 0.44(6)), ensuring the consistency of our results.

9.4.3 Transverse-field muon spin rotation

In order to obtain additional information about the partial magnetic order and local field in the 1/3 plateau, transverse-field (TF) μSR experiments were also conducted at the DR 'Pandora' spectrometer, part of the M15 beamline at TRIUMF. High voltage dual achromatic Wien filters rotated the μ^+ spin by 90° to create a fully (100 %) transverse spin polarization. The same crystal samples as in the ZF and LF experiments were measured under analogous experimental conditions. TF-μSR spectra were collected in the temperature range 0.02 K to 10 K and field range 0.4 T to 2 T.

Figure 9.21(a) shows the μSR spectrum collected at 0.025 K when applying a TF of 1 T (black circles). For such high values of the applied field it is more useful to plot the Fourier transform of the data, which is shown in Fig. 9.21(b).

Since a double peak structure can be observed around 1.01 T, the asymmetry was fitted assuming the presence of two main frequencies:

$$A(t) = A_1\, e^{-\lambda_1 t}\, \cos(\gamma_\mu B_1 t + \varphi) + A_2\, e^{-\lambda_2 t}\, \cos(\gamma_\mu B_2 t + \varphi) + A_0 \qquad (9.21)$$

The evolution with field and temperature of the fitted parameters from Eq.(9.21) is shown in Fig. 9.22. Since for all fits we obtained constant values $A_0 = -0.015(5)$ and $\varphi = 63(8)°$, these parameters are not included in Fig. 9.22. At 0.4 T (see Fig. 9.22(a)), the behavior of the two contributions to the asymmetry is quite different. The component with a higher asymmetry shows almost no dependence of

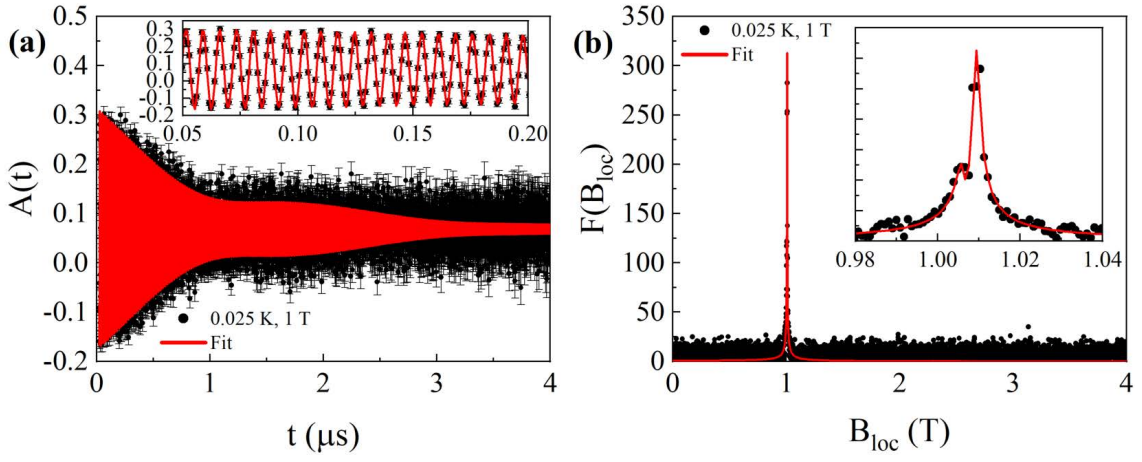

Figure 9.21: (a) μSR spectrum for a TF of 1 T at 0.025 K. The data is shown in black circles, while the red line corresponds to the fit according to Eq. (9.21). The inset shows a zoom of the initial part of the spectra. (b) Fourier transform of both the μSR spectra and the fitted curve. The inset shows a zoom around the signal.

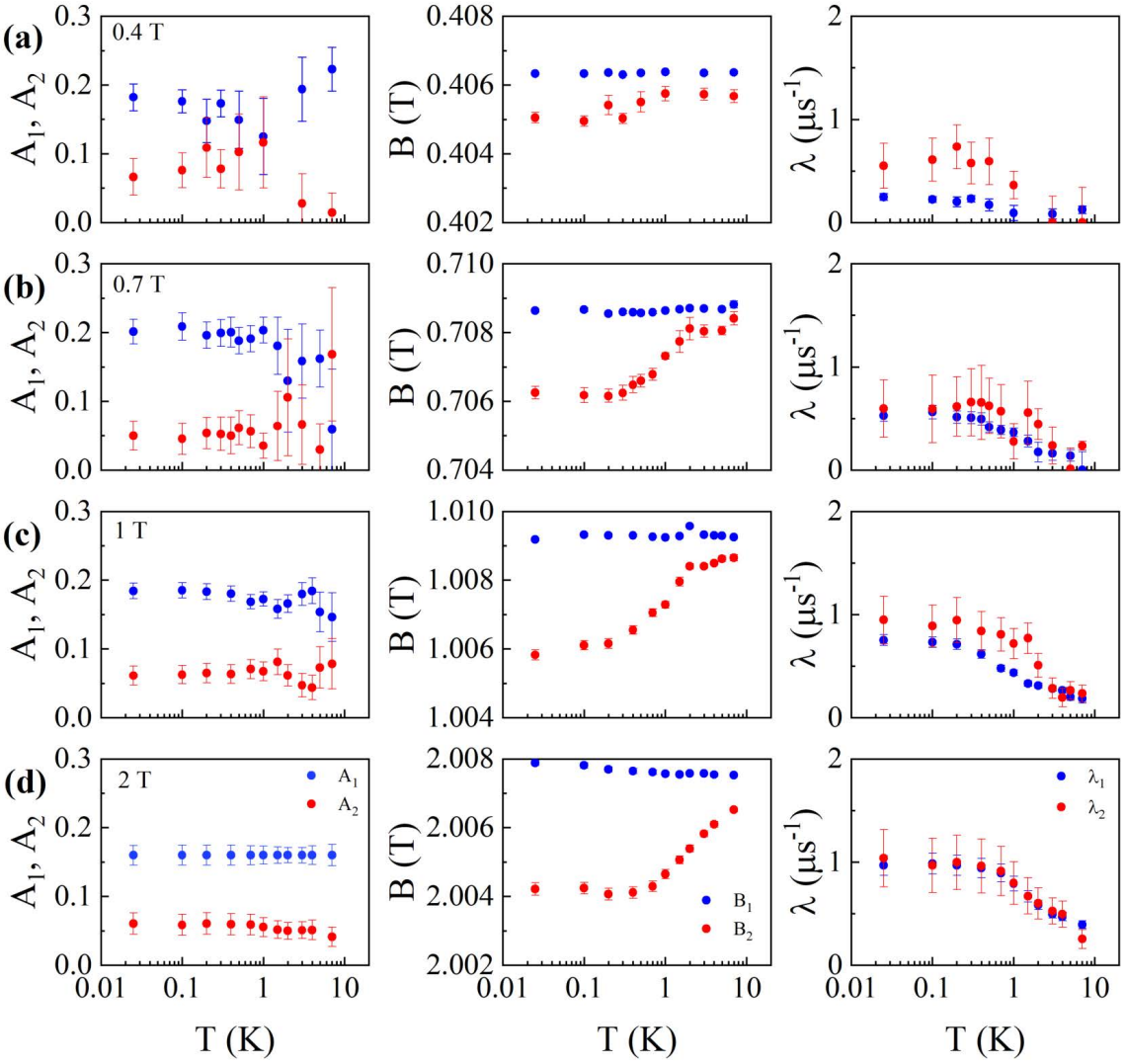

Figure 9.22: Temperature evolution of the fitted parameters from Eq.(9.21) at 0.4 T (a), 0.7 T (b), 1 T (c) and 2 T (d).

the local field with temperature and has a smaller relaxation rate, while for the other component the local field slightly decreases with the temperature and shows a maximum in the relaxation rate around T_N.

As the magnetic field is increased, the asymmetry of both contributions has the same ratio, while the difference in both local fields becomes larger. Additionally, the maximum around T_N in the relaxation rate of the low asymmetry component disappears above 1 T, as a general increase at all temperatures is observed. Such behavior is expected, as the absence of magnetic order in the plateau region (1.25 T to 8.49 T) can lead to an enhancement of the magnetic fluctuations. All these results together suggest that the component with lower asymmetry has a magnetic origin.

This conclusion is further supported by Fig. 9.23(a), where the temperature evolution of the difference in local fields, denoted as $\Delta B = |B_1 - B_2|$, is plotted.

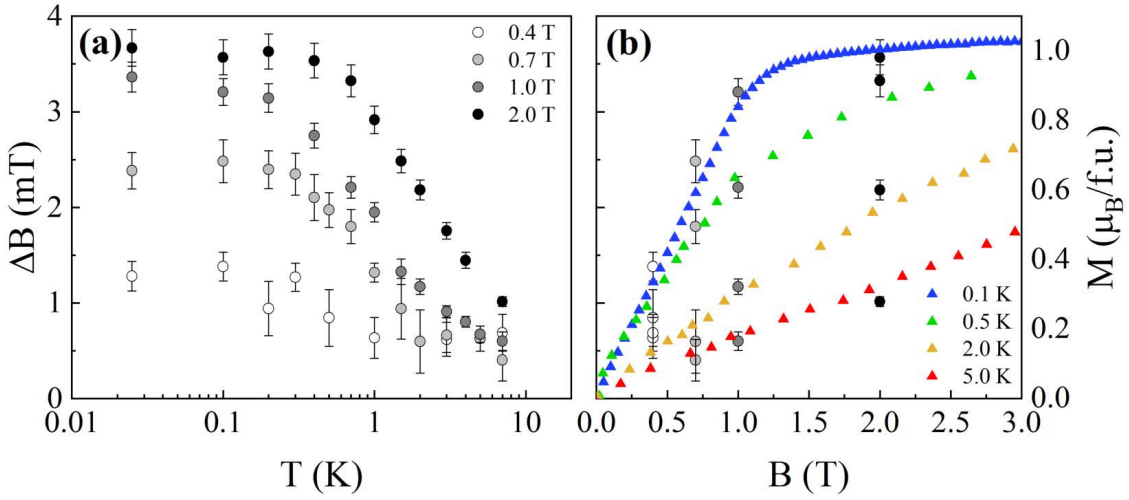

Figure 9.23: (a) Temperature evolution of the difference $\Delta B = |B_1 - B_2|$. (b) Comparison between the sample magnetization (adapted from Ref. [109]) and ΔB at some selected temperatures.

Additionally, Figure 9.23(b) offers a comparative analysis between the bulk magnetization (taken from Ref. [109]) and ΔB at different temperatures. Both the field and thermal dependence of the local fields difference matches very well the experimental data in the whole range, providing convincing evidence that the muons are probing the intrinsic magnetic properties of TNN.

In order to confirm the results from the theoretical model and PND experiments, we used again the computational model described in Appendix C to simulate the TF spectrum at 2 T and 0.025 K.

Similar simplifications as in Sec. 9.3 were taken, although the approximation of the random oriented crystals to a powder have two consequences here. First, the demagnetization factor for a powder of low densely packed spheres reduces to 1/3 [131], so that the Lorentz and demagnetization fields effectively cancel each other. Second, we can naively expect that the magnetic moments are aligned with the external field. However, the dipolar field depends on the relative orientation of the magnetic moments with the muon and atomic positions. In order to calculate the vectorial sum of the external and dipolar fields at different crystals, we create uniformly distributed rotation matrices, following the approach in Ref. [132], which are applied to the magnetic moments. The values for φ, λ and a_0 were taken from the previous analysis of the TF μSR spectrum at 2 T, 0.025 K.

In addition, both the PND experiments and the theoretical ground state suggest that the magnetic moment of the TNN molecule when the trimer is formed (1 μ_B) is equally distributed in the 3 NN group. Figure 9.24 compares the simulated spectrum with the experimental data.

Since all magnetic moments are the same, we can calculate the dipolar tensor $\hat{A}$:

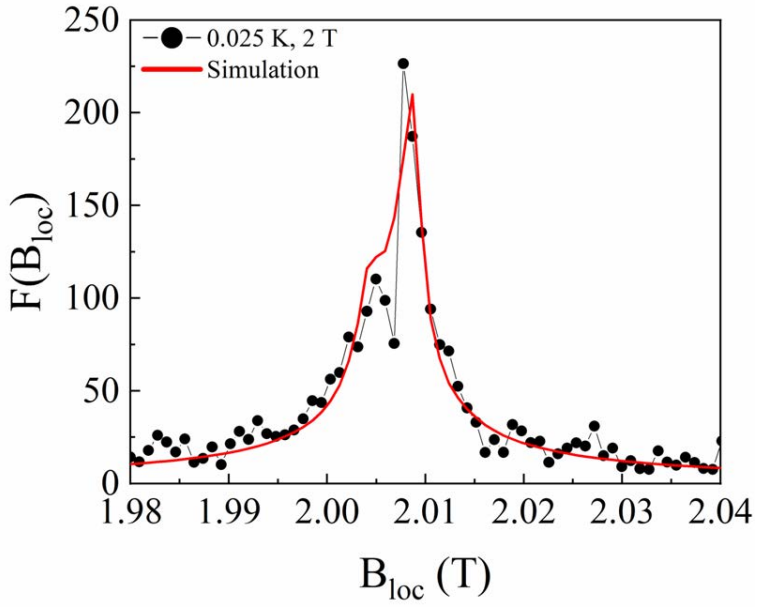

Figure 9.24: Fourier transform of the μSR spectra for a TF of 2 T at 0.025 K. The data is shown in black circles, while the theoretical distribution is depicted with a red line.

$$\begin{aligned}\vec{B}'_{\text{dip}} &= \frac{\mu_0}{4\pi}\sum_{i=1}^{N'}\left[-\frac{\vec{m}_i}{r_i^3}+\frac{3(\vec{m}_i\cdot\vec{r}_i)\vec{r}_i}{r_i^5}\right] = \frac{\mu_0}{4\pi}\sum_{i=1}^{N'}\hat{D}_{\vec{r}_i}\cdot\vec{m}_i = \frac{\mu_0}{4\pi}\left(\sum_{i=1}^{N'}\hat{D}_{\vec{r}_i}\right)\cdot\vec{m} \\ &= \frac{\mu_0}{4\pi}\hat{D}\cdot\vec{m} = \hat{A}\cdot\vec{m}\end{aligned} \tag{9.22}$$

For the nuclear structure of TNN, this results in:

$$\hat{A} = \begin{pmatrix} a_{\text{dip}} & d_{\text{dip}} & 0 \\ d_{\text{dip}} & b_{\text{dip}} & 0 \\ 0 & 0 & c_{\text{dip}} \end{pmatrix} = \begin{pmatrix} 0.0052 & -0.0007 & 0 \\ -0.0007 & 0.0044 & 0 \\ 0 & 0 & -0.0096 \end{pmatrix} \text{T}/\mu_{\text{B}} \tag{9.23}$$

Taking into account both the external magnetic field and the matrix elements of $\hat{A}$, muons will feel a smaller local field in crystals where the magnetic moments are aligned along the c-axis instead of lying in the ab plane. As can be deduced, the double peak structure observed in the field distribution is then solely due to the magnetic contribution of the sample.

Therefore, the TF μSR experiments corroborate the equal distribution of the magnetic moment of the TNN molecule in the 3 NN radicals.

9.5 Conclusions

We have studied the purely organic compound TNN·CH_3CN, focusing on the determination of its magnetic structure at low magnetic fields. With this purpose,

single-crystal neutron diffraction (SCND), polarized neutron diffraction (PND) and μSR experiments have been performed.

At zero field, the magnetic signal was too weak to be observed in the SCND experiments, highlighting the limitations of current neutron techniques. Nevertheless, by making use of a computational model and DFT calculations, the absence of oscillations in the ZF μSR spectra was shown to be compatible with a magnetic structure with high symmetry at the muon site. The proposed magnetic configuration was consistent with previous studies, as well as with theoretical predictions of its multiferroic nature.

The trimer formation was explored at the 1/3 plateau ($1.25 \leq B \leq 8.49$ T). After a magnetic and structural characterization at low temperature, the spin density distribution was obtained from PND experiments by using the wavefunction and multipole approach. The theoretical ground state was also determined as a combination of the $S = 1/2$ $S^z = 1/2$ doublet states. Meanwhile, the TF μSR results were shown to probe the intrinsic magnetic properties of TNN. The computational model used to interpret the μSR spectra agreed with the PND results and the theoretical model, where the magnetic moment in the TNN molecule is equally distributed among the 3 NN radicals.

Conclusions of Part III

Part III of this dissertation delved into the evolution of the magnetic properties with dimensionality in two purely organic magnets, 4-F-2-NN-BIP and TNN·CH_3CN. The unique structural and magnetic features of these compounds, coupled with their potential to test and verify Heisenberg models due to their highly isotropic nature, position them at the cutting edge of quantum magnetism research. The challenges encountered – ranging from synthesizing high-quality single crystals to detecting weak magnetic signals – underscore the intricate nature of these studies.

For 4-F-2-NN-BIP, a meticulous combination of experimental techniques including X-ray diffraction, electron paramagnetic resonance (EPR), specific heat, magnetization, and susceptibility measurements, alongside numerical simulations, has allowed to determine this system as a $S = 1/2$ two-leg Heisenberg antiferromagnetic ladder. The estimations of magnetic exchange interactions and the derived magnetic phase diagram highlight a complex quantum landscape, describing quantum disordered, gapless, and fully spin-polarized phases, alongside a deviation that suggests the presence of two distinct ladder structures. This model advances our understanding of quantum phases in low-dimensional structures, bridging the gap between theoretical predictions and experimental observations.

Turning the focus to TNN·CH_3CN, the investigation through single-crystal and polarized neutron diffraction, alongside μSR experiments, underscores the challenges in determining the magnetic order of purely organic materials. Despite these challenges, the integration of computational models and density functional theory (DFT) calculations with experimental data allows to propose a magnetic structure at zero-field, which aligns with its reported multiferroic nature. Meanwhile, the successful capture of the trimer formation within the TNN molecule at the 1/3 plateau enriches our comprehension of quantum ground states, as well as of the magnetic moment distribution in organic compounds.

Together, the studies on 4-F-2-NN-BIP and TNN·CH_3CN not only bridge theoretical predictions with experimental validation but also exemplify the sophisticated interplay of low anisotropy, magnetic frustration, and topology in the development of non-collinear magnetic phases in low-dimensional organic systems.

Future research in 4-F-2-NN-BIP should aim towards the clarification of the anomaly observed in the isothermal magnetization curves. The combination of additional specific heat measurements with EPR experiments at high magnetic field could provide the necessary details to construct a model capable of explaining such anomaly. Regarding TNN·CH_3CN, the study of the magnetic phases at higher fields ($B > 8.49$ T), in particular the determination of the magnetic order, would increase our understanding of the whole magnetic phase diagram.

Bibliography of Part III

[1] N. D. Mermin and H. Wagner, "Absence of Ferromagnetism or Antiferromagnetism in One- or Two-Dimensional Isotropic Heisenberg Models," Physical Review Letters, vol. 17, pp. 1133–1136, Nov. 1966.

[2] A. Vasiliev, O. Volkova, E. Zvereva, and M. Markina, "Milestones of low-D quantum magnetism," npj Quantum Materials, vol. 3, Mar. 2018.

[3] S. M. Girvin, The Quantum Hall Effect: Novel Excitations And Broken Symmetries, pp. 53–175. Springer Berlin Heidelberg, Jan. 2002.

[4] Z. F. Ezawa, Quantum Hall Effects: Field Theoretical Approach and Related Topics. WORLD SCIENTIFIC, Jan. 2008.

[5] X.-L. Qi and S.-C. Zhang, "Topological insulators and superconductors," Reviews of Modern Physics, vol. 83, pp. 1057–1110, Oct. 2011.

[6] Y. Zhou, K. Kanoda, and T.-K. Ng, "Quantum spin liquid states," Reviews of Modern Physics, vol. 89, Apr. 2017.

[7] M. Sato and Y. Ando, "Topological superconductors: a review," Reports on Progress in Physics, vol. 80, p. 076501, May 2017.

[8] X. Wang and Q. Zhang, "Organic quantum materials: A review," SmartMat, vol. 4, Mar. 2023.

[9] S. Tang and X. Wang, "Spin Frustration in Organic Radicals," Angewandte Chemie International Edition, vol. 63, Oct. 2023.

[10] J. Veciana and H. Iwamura, "Organic Magnets," MRS Bulletin, vol. 25, pp. 41–51, Nov. 2000.

[11] S. J. Blundell and F. L. Pratt, "Organic and molecular magnets," Journal of Physics: Condensed Matter, vol. 16, p. R771–R828, June 2004.

[12] H. M. McConnell, "Ferromagnetism in Solid Free Radicals," The Journal of Chemical Physics, vol. 39, pp. 1910–1910, Oct. 1963.

[13] N. Mataga, "Possible ferromagnetic states of some hypothetical hydrocarbons," Theoretica Chimica Acta, vol. 10, no. 4, pp. 372–376, 1968.

[14] M. Tamura, Y. Nakazawa, D. Shiomi, K. Nozawa, Y. Hosokoshi, M. Ishikawa, M. Takahashi, and M. Kinoshita, "Bulk ferromagnetism in the β-phase crystal of the *p*-nitrophenyl nitronyl nitroxide radical," Chemical Physics Letters, vol. 186, pp. 401–404, Nov. 1991.

[15] M. Takahashi, P. Turek, Y. Nakazawa, M. Tamura, K. Nozawa, D. Shiomi, M. Ishikawa, and M. Kinoshita, "Discovery of a quasi-1D organic ferromagnet, *p*-NPNN," Physical Review Letters, vol. 67, pp. 746–748, Aug. 1991.

[16] M. Kinoshita, P. Turek, M. Tamura, K. Nozawa, D. Shiomi, Y. Nakazawa, M. Ishikawa, M. Takahashi, K. Awaga, T. Inabe, and Y. Maruyama, "An Organic Radical Ferromagnet," Chemistry Letters, vol. 20, pp. 1225–1228, July 1991.

[17] Y. Nakazawa, M. Tamura, N. Shirakawa, D. Shiomi, M. Takahashi, M. Kinoshita, and M. Ishikawa, "Low-temperature magnetic properties of the ferromagnetic organic radical, *p*-nitrophenyl nitronyl nitroxide," Physical Review B, vol. 46, pp. 8906–8914, Oct. 1992.

[18] N. Tyutyulkov, G. Madjarova, and F. Dietz, "Nature of The Magnetic Interaction in Organic Radical Crystals. I. Alternant Systems," Molecular Crystals and Liquid Crystals Science and Technology. Section A. Molecular Crystals and Liquid Crystals, vol. 305, pp. 249–258, Oct. 1997.

[19] K. Takeda, K. Konishi, K. Nedachi, and K. Mukai, "Experimental Study of Quantum Statistics for the $S = \frac{1}{2}$ Quasi-One-Dimensional Organic Ferromagnet," Physical Review Letters, vol. 74, pp. 1673–1676, Feb. 1995.

[20] K. Mukai, M. Nuwa, K. Suzuki, S.-i. Nagaoka, N. Achiwa, and J. B. Jamali, "Magnetic Properties of 3-(4-R-Phenyl)-1,5-diphenyl-6-oxo- and -thioxoverdazyl Radical Crystals (R = OCH_3, CH_3, CN, and NO_2)," The Journal of Physical Chemistry B, vol. 102, pp. 782–787, Jan. 1998.

[21] K. Mukai, K. Konishi, K. Nedachi, and K. Takeda, "Bulk ferro- and antiferromagnetic behavior in 1,5-dimethyl verdazyl radical crystals with similar molecular structure," Journal of Magnetism and Magnetic Materials, vol. 140–144, pp. 1449–1450, Feb. 1995.

[22] Y. Hosokoshi, Y. Nakazawa, K. Inoue, K. Takizawa, H. Nakano, M. Takahashi, and T. Goto, "Magnetic properties of low-dimensional quantum spin systems made of stable organic biradicals PNNNO,F_2PNNNO, and PIMNO," Physical Review B, vol. 60, pp. 12924–12932, Nov. 1999.

[23] Y. Yoshida, N. Tateiwa, M. Mito, T. Kawae, K. Takeda, Y. Hosokoshi, and K. Inoue, "Specific Heat Study of an $S = \frac{1}{2}$ Alternating Heisenberg Chain System: F_5PNN in a Magnetic Field," Physical Review Letters, vol. 94, Jan. 2005.

[24] T. Sakai, "Field-induced spin liquids and orders in quasi-1D gapped systems," Journal of Magnetism and Magnetic Materials, vol. 272–276, pp. 865–866, May 2004.

[25] N. Maeshima, K. Okunishi, K. Okamoto, and T. Sakai, "Frustration-Induced η Inversion in the $S = \frac{1}{2}$ Bond-Alternating Spin Chain," Physical Review Letters, vol. 93, Sept. 2004.

[26] E. Canévet, B. Grenier, Y. Yoshida, N. Sakai, L.-P. Regnault, T. Goto, Y. Fujii, and T. Kawae, "Strong interplay between magnetic and structural properties in the spin-1/2 chain molecular compound D-F_5PNN," Physical Review B, vol. 82, Oct. 2010.

[27] H. Yamaguchi, Y. Shinpuku, T. Shimokawa, K. Iwase, T. Ono, Y. Kono, S. Kittaka, T. Sakakibara, and Y. Hosokoshi, "$S = \frac{1}{2}$ ferromagnetic-antiferromagnetic alternating Heisenberg chain in a zinc-verdazyl complex," Physical Review B, vol. 91, Feb. 2015.

[28] K. Nomura, Y. H. Matsuda, Y. Narumi, K. Kindo, S. Takeyama, Y. Hosokoshi, T. Ono, N. Hasegawa, H. Suwa, and S. Todo, "Magnetization Process of the $S = 1/2$ Two-Leg Organic Spin-Ladder Compound BIP-BNO," Journal of the Physical Society of Japan, vol. 86, p. 104713, oct 2017.

[29] K. Nomura, A. Ikeda, Y. Kohama, Y. H. Matsuda, S. Takeyama, N. Amaya, T. Ono, and Y. Hosokoshi, "Spin-lattice separation of the spin-ladder compound BIP-TENO by microsecond megagauss field," in 2018 16th International Conference on Megagauss Magnetic Field Generation and Related Topics (MEGAGAUSS), IEEE, Sept. 2018.

[30] R. A. L. Silva and M. Almeida, "Spin-ladder behaviour in molecular materials," Journal of Materials Chemistry C, vol. 9, no. 33, pp. 10573–10590, 2021.

[31] Y. Hosokoshi, K. Katoh, K. Inoue, and T. Goto, "Construction of a Quantum-Spin System of $S = 1/2$ Antiferromagnetic Chain with the Next-Nearest-Neighbor Interactions," Journal of the Physical Society of Japan, vol. 68, pp. 2910–2913, Sept. 1999.

[32] N. Maeshima and K. Okunishi, "Antiferromagnetic zigzag spin chain in magnetic fields at finite temperatures," Physical Review B, vol. 62, pp. 934–939, July 2000.

[33] Y. Miyazaki, T. Sakakibara, J. R. Ferrer, P. M. Lahti, G. Antorrena, F. Palacio, and M. Sorai, "Heat Capacity and Antiferromagnetic Phase Transition of the Organic Free Radical Magnet, 2-tert-Butylaminoxylbenzimidazole (BABI)," The Journal of Physical Chemistry B, vol. 106, pp. 8615–8620, July 2002.

[34] Y. Miyazaki, A. Inaba, M. Sorai, P. S. Taylor, and P. M. Lahti, "Magnetostructural Study of 2-(4-N-tert-Butylaminoxylphenyl)benzimidazole," The Journal of Physical Chemistry B, vol. 112, pp. 8144–8150, June 2008.

[35] A. S. Ovchinnikov, V. E. Sinitsyn, I. G. Bostrem, Y. Hosokoshi, and K. Inoue, "Magnetization and spin gap in two-dimensional organic ferrimagnet BIPNNBNO," Journal of Physics: Condensed Matter, vol. 24, p. 306003, July 2012.

[36] H. Yamaguchi, S. Nagata, M. Tada, K. Iwase, T. Ono, S. Nishihara, Y. Hosokoshi, T. Shimokawa, H. Nakano, H. Nojiri, A. Matsuo, K. Kindo, and T. Kawakami, "Crystal structure and magnetic properties of honeycomb-like lattice antiferromagnet p-BIP-V_2," Physical Review B, vol. 87, Mar. 2013.

[37] H. Yamaguchi, A. Toho, K. Iwase, T. Ono, T. Kawakami, T. Shimokawa, A. Matsuo, and Y. Hosokoshi, "Two-Dimensional Honeycomb Lattice Consisting of a New Organic Radical 2-Cl-6-F-V," Journal of the Physical Society of Japan, vol. 82, p. 043713, Apr. 2013.

[38] H. Yamaguchi, N. Uemoto, T. Okubo, Y. Kono, S. Kittaka, T. Sakakibara, T. Yajima, S. Shimono, Y. Iwasaki, and Y. Hosokoshi, "Gapped ground state in a spin-$\frac{1}{2}$ frustrated square lattice," Physical Review B, vol. 104, Aug. 2021.

[39] Y. Hosokoshi, M. Tamura, M. Kinoshita, H. Sawa, R. Kato, Y. Fujiwara, and Y. Ueda, "Magnetic properties and crystal structure of the p-fluorophenyl nitronyl nitroxide radical crystal: ferromagnetic intermolecular interactions leading to a three-dimensional network of ground triplet dimeric molecules," Journal of Materials Chemistry, vol. 4, no. 8, p. 1219, 1994.

[40] N. Amaya, T. Ono, Y. Oku, H. Yamaguchi, A. Matsuo, K. Kindo, H. Nojiri, F. Palacio, J. Campo, and Y. Hosokoshi, "Spin-1/2 Quantum Antiferromagnet on a Three-Dimensional Honeycomb Lattice Formed by a New Organic Biradical F_4BIPBNN," Journal of the Physical Society of Japan, vol. 86, p. 074706, July 2017.

[41] H. Yamaguchi, T. Okubo, S. Kittaka, T. Sakakibara, K. Araki, K. Iwase, N. Amaya, T. Ono, and Y. Hosokoshi, "Experimental Realization of a Quantum Pentagonal Lattice," Scientific Reports, vol. 5, Oct. 2015.

[42] Y. Hosokoshi, M. Tamura, D. Shiomi, N. Iwasawa, K. Nozawa, M. Kinoshita, H. A. Katori, and T. Goto, "Organic radical crystals, α-nitronyl nitroxide family: High-field magnetization study," Physica B: Condensed Matter, vol. 201, pp. 497–499, jul 1994.

[43] E. F. Ullman, J. H. Osiecki, D. G. B. Boocock, and R. Darcy, "Stable free radicals. X. Nitronyl nitroxide monoradicals and biradicals as possible small molecule spin labels," Journal of the American Chemical Society, vol. 94, pp. 7049–7059, oct 1972.

[44] J. A. D'Anna and J. H. Wharton, "Electron Spin Resonance Spectra of α-Nitronylnitroxide Radicals; Solvent Effects; Nitrogen Hyperfine Tensor; g Anisotropy," The Journal of Chemical Physics, vol. 53, pp. 4047–4052, Nov. 1970.

[45] J. W. Neely, G. F. Hatch, and R. W. Kreilick, "Electron-carbon couplings of aryl nitronyl nitroxide radicals," Journal of the American Chemical Society, vol. 96, pp. 652–656, Feb. 1974.

[46] A. Zheludev, M. Bonnet, E. Ressouche, J. Schweizer, M. Wan, and H. Wang, "Experimental spin density in the first purely organic ferromagnet: the β para-nitrophenyl nitronyl nitroxide," Journal of Magnetism and Magnetic Materials, vol. 135, pp. 147–160, July 1994.

[47] A. Zheludev, V. Barone, M. Bonnet, B. Delley, A. Grand, E. Ressouche, P. Rey, R. Subra, and J. Schweizer, "Spin density in a nitronyl nitroxide free radical. Polarized neutron diffraction investigation and ab initio calculations," Journal of the American Chemical Society, vol. 116, pp. 2019–2027, Mar. 1994.

[48] C. Adamo, A. di Matteo, P. Rey, and V. Barone, "Tuning of Structural and Magnetic Properties of Nitronyl Nitroxides by the Environment. A Combined Experimental and Computational Study," The Journal of Physical Chemistry A, vol. 103, pp. 3481–3488, Apr. 1999.

[49] Y. Pontillon, A. Caneschi, D. Gatteschi, E. Ressouche, J. Schweizer, and R. Sessoli, "Spin density in a ferromagnetic nitronyl nitroxide free radical," Physica B: Condensed Matter, vol. 267–268, pp. 51–55, June 1999.

[50] B. Gillon, M. A. Aebersold, O. Kahn, L. Pardi, and B. Delley, "Spin density in a triazole-nitronyl-nitroxide radical presenting linear ferromagnetic interactions: role of hydrogen bonding," Chemical Physics, vol. 250, pp. 23–34, Nov. 1999.

[51] M. Bonnet, D. Luneau, E. Ressouche, P. Rey, J. Schweizer, M. Wan, H. Wang, and A. Zheludev, "The Experimental Spin Density of Two Nitrophenyl Nitroxides: A Nitronyl Nitroxide and an Imino Nitroxide," Molecular Crystals and Liquid Crystals Science and Technology. Section A. Molecular Crystals and Liquid Crystals, vol. 271, pp. 35–53, Sept. 1995.

[52] S. Blundell, P. Pattenden, F. Pratt, K. Chow, W. Hayes, and T. Sugano, "Organic magnetism in nitronyl nitroxides studied by μSR," Hyperfine Interactions, vol. 104, no. 1/4, pp. 251–256, 1997.

[53] F. D. M. Haldane, "Nonlinear Field Theory of Large-Spin Heisenberg Antiferromagnets: Semiclassically Quantized Solitons of the One-Dimensional Easy-Axis Néel State," Physical Review Letters, vol. 50, pp. 1153–1156, apr 1983.

[54] G. Sierra, "The nonlinear sigma model and spin ladders," Journal of Physics A: Mathematical and General, vol. 29, pp. 3299–3310, June 1996.

[55] H.-J. Mikeska and A. K. Kolezhuk, One-dimensional magnetism, pp. 1–83. Springer Berlin Heidelberg, 2004.

[56] M. Sigrist, T. M. Rice, and F. C. Zhang, "Superconductivity in a quasi-one-dimensional spin liquid," Physical Review B, vol. 49, pp. 12058–12061, may 1994.

[57] E. Dagotto and T. M. Rice, "Surprises on the Way from One- to Two-Dimensional Quantum Magnets: The Ladder Materials," Science, vol. 271, pp. 618–623, feb 1996.

[58] M. Uehara, T. Nagata, J. Akimitsu, H. Takahashi, N. Môri, and K. Kinoshita, "Superconductivity in the Ladder Material $Sr_{0.4}Ca_{13.6}Cu_{24}O_{41.84}$," Journal of the Physical Society of Japan, vol. 65, pp. 2764–2767, sep 1996.

[59] E. Dagotto, "Experiments on ladders reveal a complex interplay between a spin-gapped normal state and superconductivity," Reports on Progress in Physics, vol. 62, pp. 1525–1571, nov 1999.

[60] S. Sachdev, Quantum Phase Transitions. Cambridge University Press, 2017.

[61] P. Bouillot, C. Kollath, A. M. Läuchli, M. Zvonarev, B. Thielemann, C. Rüegg, E. Orignac, R. Citro, M. Klanjšek, C. Berthier, M. Horvatić, and T. Giamarchi, "Statics and dynamics of weakly coupled antiferromagnetic spin-$\frac{1}{2}$ ladders in a magnetic field," Physical Review B, vol. 83, Feb. 2011.

[62] T. Giamarchi, C. Rüegg, and O. Tchernyshyov, "Bose–Einstein condensation in magnetic insulators," Nature Physics, vol. 4, pp. 198–204, mar 2008.

[63] T. Giamarchi and A. M. Tsvelik, "Coupled ladders in a magnetic field," Physical Review B, vol. 59, pp. 11398–11407, may 1999.

[64] T. Nikuni, M. Oshikawa, A. Oosawa, and H. Tanaka, "Bose-Einstein Condensation of Dilute Magnons in $TlCuCl_3$," Physical Review Letters, vol. 84, pp. 5868–5871, jun 2000.

[65] S. Tomonaga, "Remarks on Bloch's Method of Sound Waves applied to Many-Fermion Problems," Progress of Theoretical Physics, vol. 5, pp. 544–569, July 1950.

[66] J. M. Luttinger, "An Exactly Soluble Model of a Many-Fermion System," Journal of Mathematical Physics, vol. 4, pp. 1154–1162, Sept. 1963.

[67] F. D. M. Haldane, "General Relation of Correlation Exponents and Spectral Properties of One-Dimensional Fermi Systems: Application to the Anisotropic $S = 1/2$ Heisenberg Chain," Physical Review Letters, vol. 45, pp. 1358–1362, oct 1980.

[68] T. Giamarchi, Quantum Physics in One Dimension. Oxford University Press, dec 2003.

[69] K. Katoh, Y. Hosokoshi, K. Inoue, M. Bartashevich, H. Nakano, and T. Goto, "Magnetic properties of organic two-leg spin–ladder systems with $S = 1/2$ and $S = 1$," Journal of Physics and Chemistry of Solids, vol. 63, pp. 1277–1280, jun 2002.

[70] G. Chaboussant, P. A. Crowell, L. P. Lévy, O. Piovesana, A. Madouri, and D. Mailly, "Experimental phase diagram of $Cu_2(C_5H_{12}N_2)_2Cl_4$: A quasi-one-dimensional antiferromagnetic spin- Heisenberg ladder," Physical Review B, vol. 55, pp. 3046–3049, feb 1997.

[71] R. Calemczuk, J. Riera, D. Poilblanc, J.-P. Boucher, G. Chaboussant, L. Lévy, and O. Piovesana, "Thermodynamic properties of the spin-1/2 antiferromagnetic ladder under magnetic field," The European Physical Journal B, vol. 7, pp. 171–174, jan 1999.

[72] X. Wang and L. Yu, "Magnetic-Field Effects on Two-Leg Heisenberg Antiferromagnetic Ladders: Thermodynamic Properties," Physical Review Letters, vol. 84, pp. 5399–5402, jun 2000.

[73] B. C. Watson, V. N. Kotov, M. W. Meisel, D. W. Hall, G. E. Granroth, W. T. Montfrooij, S. E. Nagler, D. A. Jensen, R. Backov, M. A. Petruska, G. E. Fanucci, and D. R. Talham, "Magnetic Spin Ladder$(C_5H_{12}N)_2CuBr_4$: High-Field Magnetization and Scaling near Quantum Criticality," Physical Review Letters, vol. 86, pp. 5168–5171, may 2001.

[74] C. Rüegg, K. Kiefer, B. Thielemann, D. F. McMorrow, V. Zapf, B. Normand, M. B. Zvonarev, P. Bouillot, C. Kollath, T. Giamarchi, S. Capponi, D. Poilblanc, D. Biner, and K. W. Krämer, "Thermodynamics of the Spin Luttinger Liquid in a Model Ladder Material," Physical Review Letters, vol. 101, dec 2008.

[75] E. Čižmár, M. Ozerov, J. Wosnitza, B. Thielemann, K. W. Krämer, C. Rüegg, O. Piovesana, M. Klanjšek, M. Horvatić, C. Berthier, and S. A. Zvyagin, "Anisotropy of magnetic interactions in the spin-ladder compound$(C_5H_{12}N)_2CuBr_4$," Physical Review B, vol. 82, aug 2010.

[76] D. Schmidiger, P. Bouillot, S. Mühlbauer, S. Gvasaliya, C. Kollath, T. Giamarchi, and A. Zheludev, "Spectral and Thermodynamic Properties of a Strong-Leg Quantum Spin Ladder," Physical Review Letters, vol. 108, Apr. 2012.

[77] Z. Honda, H. Aruga Katori, M. Ikeda, M. Hagiwara, K. Okunishi, M. Sakai, T. Fukuda, and N. Kamata, "Magnetic Field-Induced Phase Transitions in the $S = 1/2$ Two-Leg Spin-Ladder Material $Cu(DEP)Br_2$," Journal of the Physical Society of Japan, vol. 81, p. 113710, Nov. 2012.

[78] T. Morimoto, T. Kida, Y. Narumi, Z. Honda, K. Kindo, and M. Hagiwara, "High-field Magnetism of the Spin-1/2 Two-leg Ladder $Cu(DEP)Cl_2$," in Proceedings of the 29th International Conference on Low Temperature Physics (LT29), Journal of the Physical Society of Japan, May 2023.

[79] M. J. Coak, S. P. M. Curley, Z. Hawkhead, J. P. Tidey, D. Graf, S. J. Clark, P. Sengupta, Z. E. Manson, T. Lancaster, P. A. Goddard, and J. L. Manson, "Asymmetric phase diagram and dimensional crossover in a system of spin-$\frac{1}{2}$

dimers under applied hydrostatic pressure," Physical Review B, vol. 108, Dec. 2023.

[80] G. Sheldrick, "Shelxl-97," Program for Crystal Structure Refinement, 1997.

[81] H. Nojiri, K.-Y. Choi, and N. Kitamura, "Manipulation of the quantum tunneling of nanomagnets by using time-dependent high magnetic fields," Journal of Magnetism and Magnetic Materials, vol. 310, pp. 1468–1472, mar 2007.

[82] T. Sakakibara, H. Mitamura, T. T. Takashi Tayama, and H. A. Hiroshi Amitsuka, "Faraday Force Magnetometer for High-Sensitivity Magnetization Measurements at Very Low Temperatures and High Fields," Japanese Journal of Applied Physics, vol. 33, p. 5067, Sept. 1994.

[83] S. Riegel and G. Weber, "A dual-slope method for specific heat measurements," Journal of Physics E: Scientific Instruments, vol. 19, pp. 790–791, oct 1986.

[84] M. J. Frisch, G. W. Trucks, H. B. Schlegel, G. E. Scuseria, M. A. Robb, J. R. Cheeseman, G. Scalmani, V. Barone, B. Mennucci, G. A. Petersson, H. Nakatsuji, M. Caricato, X. Li, H. P. Hratchian, A. F. Izmaylov, G. Z. J. Bloino, J. L. Sonnenberg, M. Hada, M. Ehara, K. Toyota, R. Fukuda, J. Hasegawa, M. Ishida, T. Nakajima, Y. Honda, O. Kitao, H. Nakai, T. Vreven, J. A. Montgomery, Jr., J. E. Peralta, F. Ogliaro, M. Bearpark, J. J. Heyd, E. Brothers, K. N. Kudin, V. N. Staroverov, R. Kobayashi, J. Normand, K. Raghavachari, A. Rendell, J. C. Burant, S. S. Iyengar, J. Tomasi, M. Cossi, N. Rega, J. M. Millam, M. Klene, J. E. Knox, J. B. Cross, V. Bakken, C. Adamo, J. Jaramillo, R. Gomperts, R. E. Stratmann, O. Yazyev, A. J. Austin, R. Cammi, C. Pomelli, J. W. Ochterski, R. L. Martin, K. Morokuma, V. G. Zakrzewski, G. A. Voth, P. Salvador, J. J. Dannenberg, S. Dapprich, A. D. Daniels, O. Farkas, J. B. Foresman, J. V. Ortiz, J. Cioslowski, and D. J. Fox, "Gaussian 09, Revision A.1," Gaussian, Inc., Wallingford CT, 2009.

[85] K. Yamaguchi, H. Fukui, and T. Fueno, "MOLECULAR ORBITAL (MO) THEORY FOR MAGNETICALLY INTERACTING ORGANIC COMPOUNDS. AB-INITIO MO CALCULATIONS OF THE EFFECTIVE EXCHANGE INTEGRALS FOR CYCLOPHANE-TYPE CARBENE DIMERS," Chemistry Letters, vol. 15, pp. 625–628, apr 1986.

[86] N. F. Chilton, R. P. Anderson, L. D. Turner, A. Soncini, and K. S. Murray, "PHI: A powerful new program for the analysis of anisotropic monomeric and exchange-coupled polynuclear d- and f-block complexes," Journal of Computational Chemistry, vol. 34, pp. 1164–1175, feb 2013.

[87] A. Albuquerque, F. Alet, P. Corboz, P. Dayal, A. Feiguin, S. Fuchs, L. Gamper, E. Gull, S. Gürtler, A. Honecker, R. Igarashi, M. Körner, A. Kozhevnikov, A. Läuchli, S. Manmana, M. Matsumoto, I. McCulloch, F. Michel, R. Noack, G. Pawłowski, L. Pollet, T. Pruschke, U. Schollwöck, S. Todo, S. Trebst, M. Troyer, P. Werner, and S. Wessel, "The ALPS project release 1.3: Open-source software for strongly correlated systems," Journal of Magnetism and Magnetic Materials, vol. 310, pp. 1187–1193, mar 2007.

[88] B. Bauer, L. D. Carr, H. G. Evertz, A. Feiguin, J. Freire, S. Fuchs, L. Gamper, J. Gukelberger, E. Gull, S. Guertler, A. Hehn, R. Igarashi, S. V. Isakov, D. Koop, P. N. Ma, P. Mates, H. Matsuo, O. Parcollet, G. Pawłowski, J. D. Picon, L. Pollet, E. Santos, V. W. Scarola, U. Schollwöck, C. Silva, B. Surer, S. Todo, S. Trebst, M. Troyer, M. L. Wall, P. Werner, and S. Wessel, "The ALPS project release 2.0: open source software for strongly correlated systems," Journal of Statistical Mechanics: Theory and Experiment, vol. 2011, p. P05001, may 2011.

[89] S. Todo and K. Kato, "Cluster Algorithms for General- S Quantum Spin Systems," Physical Review Letters, vol. 87, jul 2001.

[90] F. Alet, S. Wessel, and M. Troyer, "Generalized directed loop method for quantum Monte Carlo simulations," Physical Review E, vol. 71, mar 2005.

[91] A. W. Sandvik, "Stochastic series expansion method with operator-loop update," Physical Review B, vol. 59, pp. R14157–R14160, jun 1999.

[92] L. Pollet, S. M. A. Rombouts, K. V. Houcke, and K. Heyde, "Optimal Monte Carlo updating," Physical Review E, vol. 70, nov 2004.

[93] F. Mila, "Ladders in a magnetic field: a strong coupling approach," The European Physical Journal B, vol. 6, pp. 201–205, nov 1998.

[94] M. Reigrotzki, H. Tsunetsugu, and T. M. Rice, "Strong-coupling expansions for antiferromagnetic Heisenberg spin-one-half ladders," Journal of Physics: Condensed Matter, vol. 6, pp. 9235–9245, oct 1994.

[95] M. Troyer, H. Tsunetsugu, and D. Würtz, "Thermodynamics and spin gap of the Heisenberg ladder calculated by the look-ahead Lanczos algorithm," Physical Review B, vol. 50, pp. 13515–13527, nov 1994.

[96] D. C. Johnston, "Antiferromagnetic exchange in two-leg spin-1/2 ladders," Physical Review B, vol. 54, pp. 13009–13016, nov 1996.

[97] B. R. Patyal, B. L. Scott, and R. D. Willett, "Crystal-structure, magnetic-susceptibility, and EPR studies of bis(piperidinium)tetrabromocuprate(II): A novel monomer system showing spin diffusion," Physical Review B, vol. 41, pp. 1657–1663, jan 1990.

[98] J. C. Bonner, S. A. Friedberg, H. Kobayashi, D. L. Meier, and H. W. J. Blöte, "Alternating linear-chain antiferromagnetism in copper nitrate $Cu(NO_3)_2.2.5\ H_2O$," Physical Review B, vol. 27, pp. 248–260, jan 1983.

[99] M. Trif, F. Troiani, D. Stepanenko, and D. Loss, "Spin-Electric Coupling in Molecular Magnets," Physical Review Letters, vol. 101, Nov. 2008.

[100] M. F. Islam, J. F. Nossa, C. M. Canali, and M. Pederson, "First-principles study of spin-electric coupling in a $\{Cu_3\}$ single molecular magnet," Physical Review B, vol. 82, Oct. 2010.

[101] J. F. Nossa and C. M. Canali, "Cotunneling signatures of spin-electric coupling in frustrated triangular molecular magnets," Physical Review B, vol. 89, June 2014.

[102] S. Nakatsuji, Y. Nambu, H. Tonomura, O. Sakai, S. Jonas, C. Broholm, H. Tsunetsugu, Y. Qiu, and Y. Maeno, "Spin Disorder on a Triangular Lattice," Science, vol. 309, pp. 1697–1700, Sept. 2005.

[103] L. Seabra, T. Momoi, P. Sindzingre, and N. Shannon, "Phase diagram of the classical heisenberg antiferromagnet on a triangular lattice in an applied magnetic field," Physical Review B, vol. 84, Dec. 2011.

[104] L. N. Bulaevskii, C. D. Batista, M. V. Mostovoy, and D. I. Khomskii, "Electronic orbital currents and polarization in Mott insulators," Physical Review B, vol. 78, July 2008.

[105] Y. Kamiya and C. D. Batista, "Multiferroic Behavior in Trimerized Mott Insulators," Physical Review Letters, vol. 108, Feb. 2012.

[106] K.-Y. Choi, Y. H. Matsuda, H. Nojiri, U. Kortz, F. Hussain, A. C. Stowe, C. Ramsey, and N. S. Dalal, "Observation of a Half Step Magnetization in the $\{Cu_3\}$-Type Triangular Spin Ring," Physical Review Letters, vol. 96, Mar. 2006.

[107] M. Nakaji Master's thesis, Graduate School of Science, Osaka Prefecture University, 2009.

[108] K. Takada Master's thesis, Graduate School of Science, Osaka Prefecture University, 2012.

[109] A. Higashiguchi Master's thesis, Graduate School of Science, Osaka Prefecture University, 2013.

[110] K. Hyuga Master's thesis, Graduate School of Science, Osaka Metropolitan University, 2023.

[111] C. P. Aoyama, Experimental studies of low dimensional quantum antiferromagnets. PhD thesis, Graduate School, University of Florida, 2015.

[112] Y. Nakano, T. Yagyu, T. Hirayama, A. Ito, and K. Tanaka, "Synthesis and intramolecular magnetic interaction of triphenylamine derivatives with nitronyl nitroxide radicals," Polyhedron, vol. 24, pp. 2141–2147, Nov. 2005.

[113] A. J. Studer, M. E. Hagen, and T. J. Noakes, "Wombat: The high-intensity powder diffractometer at the OPAL reactor," Physica B: Condensed Matter, vol. 385–386, pp. 1013–1015, Nov. 2006.

[114] N. A. Katcho, L. Cañadillas-Delgado, O. Fabelo, M. T. Fernández-Díaz, and J. Rodríguez-Carvajal, "Int3D: A Data Reduction Software for Single Crystal Neutron Diffraction," Crystals, vol. 11, p. 897, July 2021.

[115] J. Rodríguez-Carvajal, "Recent advances in magnetic structure determination by neutron powder diffraction," Physica B: Condensed Matter, vol. 192, no. 1, pp. 55 – 69, 1993.

[116] L. Le, A. Keren, G. Luke, W. Wu, Y. Uemura, M. Tamura, M. Ishikawa, and M. Kinoshita, "Searching for spontaneous magnetic order in an organic ferromagnet. μSR studies of β-phase p-NPNN," Chemical Physics Letters, vol. 206, pp. 405–408, Apr. 1993.

[117] S. Blundell, P. Pattenden, R. Valladares, F. Pratt, T. Sugano, and W. Hayes, "Observation of a magnetic transition in para-pyridyl nitronyl nitroxide using zero-field μSR," Solid State Communications, vol. 92, pp. 569–572, Nov. 1994.

[118] P. Pattenden, R. Valladares, F. Pratt, S. Blundell, A. Fisher, W. Hayes, and T. Sugano, "μSR studies of magnetism in the organic systems p-NPNN and 3-QNNN," Synthetic Metals, vol. 71, pp. 1823–1824, Apr. 1995.

[119] F. Pratt, A. Goeta, F. Palacio, J. Rawson, and J. Smith, "ZF μSR of an organic weak ferromagnet with T_c=35 K," Physica B: Condensed Matter, vol. 289–290, pp. 119–122, Aug. 2000.

[120] S. J. Blundell, F. L. Pratt, T. Lancaster, I. M. Marshall, C. A. Steer, S. L. Heath, J.-F. Létard, T. Sugano, D. Mihailovic, and A. Omerzu, "μSR studies of organic and molecular magnets," Polyhedron, vol. 22, pp. 1973–1980, July 2003.

[121] S. J. Blundell, J. S. Möller, T. Lancaster, P. J. Baker, F. L. Pratt, G. Seber, and P. M. Lahti, "μSR study of magnetic order in the organic quasi-one-dimensional ferromagnet F4BImNN," Physical Review B, vol. 88, Aug. 2013.

[122] G. Kresse and J. Hafner, "*Ab initio* molecular dynamics for liquid metals," Physical Review B, vol. 47, pp. 558–561, Jan. 1993.

[123] G. Kresse and J. Hafner, "*Ab initio* molecular-dynamics simulation of the liquid-metal–amorphous-semiconductor transition in germanium," Physical Review B, vol. 49, pp. 14251–14269, May 1994.

[124] G. Kresse and J. Furthmüller, "Efficiency of ab-initio total energy calculations for metals and semiconductors using a plane-wave basis set," Computational Materials Science, vol. 6, pp. 15–50, July 1996.

[125] G. Kresse and J. Furthmüller, "Efficient iterative schemes for *ab initio* total-energy calculations using a plane-wave basis set," Physical Review B, vol. 54, pp. 11169–11186, Oct. 1996.

[126] E. Ressouche, J. X. Boucherle, B. Gillon, P. Rey, and J. Schweizer, "Spin density maps in nitroxide-copper(II) complexes. A polarized neutron diffraction determination," Journal of the American Chemical Society, vol. 115, pp. 3610–3617, may 1993.

[127] P. Brown, A. Capiomont, B. Gillon, and J. Schweizer, "Spin densities in free radicals," Journal of Magnetism and Magnetic Materials, vol. 14, pp. 289–294, dec 1979.

[128] W. J. Hehre, R. F. Stewart, and J. A. Pople, "Self-Consistent Molecular-Orbital Methods. I. Use of Gaussian Expansions of Slater-Type Atomic Orbitals," The Journal of Chemical Physics, vol. 51, pp. 2657–2664, Sept. 1969.

[129] W. J. Hehre, R. Ditchfield, R. F. Stewart, and J. A. Pople, "Self-Consistent Molecular Orbital Methods. IV. Use of Gaussian Expansions of Slater-Type Orbitals. Extension to Second-Row Molecules," The Journal of Chemical Physics, vol. 52, pp. 2769–2773, Mar. 1970.

[130] J. Luzón, Magnetic interaction mechanism in molecular materials. PhD thesis, University of Zaragoza, 2004.

[131] R. Bjørk and C. R. H. Bahl, "Demagnetization factor for a powder of randomly packed spherical particles," Applied Physics Letters, vol. 103, Sept. 2013.

[132] J. Arvo, FAST RANDOM ROTATION MATRICES, pp. 117–120. Elsevier, 1992.

General conclusions

This thesis has examined the phenomenon of non-collinear magnetism across three distinct material classes – chiral, spinel, and organic magnets – each under the influence of the Dzyaloshinskii-Moriya (DM) interaction, magnetic frustration from symmetric exchange interactions, or single-ion magnetic anisotropy.

Novel magnetic phases have been identified in chiral magnets, highlighting the critical role of DM interactions and the intricate interplay between disorder, anisotropy and temperature in dictating the stability and characteristics of such phases. The findings on magnetic spinels have revealed how magnetic frustration and disorder intertwine to influence the material's magnetic properties and manifest complex magnetic behaviors. The results on organic magnets have not only bridged theoretical predictions with experimental validation, but also exemplified the sophisticated interplay of structure, magnetism, and topology in low-dimensional organic systems.

These findings collectively underscore the multifaceted origins of non-collinear magnetism, propelled by intrinsic and extrinsic factors, and underscore the potential for topologically non-trivial magnetic textures across different material systems.

Conclusiones generales

Esta tesis ha examinado en profundidad el fenómeno del magnetismo no colineal en tres clases distintas de materiales – imanes quirales, espinelas magnéticas e imanes orgánicos – cada uno bajo la influencia de la interacción Dzyaloshinskii-Moriya (DM), la frustración magnética de las interacciones de canje simétricas, o la anisotropía magnética.

Se han identificado nuevas fases magnéticas en los imanes quirales, resaltando el papel crítico de las interacciones DM y la compleja interacción entre el desorden, la anisotropía y la temperatura al dictar la estabilidad y características de tales fases. Los hallazgos de las espinelas magnéticas han revelado cómo la frustración magnética y el desorden se entrelazan para influir en las propiedades magnéticas del material y manifestar comportamientos magnéticos complejos. Los resultados en los imanes orgánicos no solo han validado experimentalmente algunas predicciones teóricas, sino que también ejemplifican la sofisticada interacción de estructura, magnetismo y topología en sistemas orgánicos de baja dimensión.

Estos hallazgos en conjunto subrayan los orígenes multifacéticos del magnetismo no colineal, impulsados por factores intrínsecos y extrínsecos, y destacan el potencial de texturas magnéticas topológicamente no triviales en diversos sistemas de materiales.

Appendix A

The Rietveld method

A diffraction pattern can be viewed as a histogram of counts y_i measured at the detector for each value of the scattering variable x_i, which can be scattering angle ($2\theta_i$), time of flight (t_i) or energy (E_i). The Rietveld method [1] consists in minimizing the weighted squared difference between the observations y_i and the calculated $y_i^{\rm cal}$ against a set of different parameters ($\vec{\xi}$) related mainly with the atomic structure and microstructure of the sample and the optics of the instrument (monochromators, collimators, slits, pulse structure, ...):

$$\chi^2 = \sum_{i=1}^{n} w_i \{ y_i - y_i^{\rm cal}(\vec{\xi}) \}^2 \tag{A.1}$$

where w_i is the inverse of the variance (σ_i^2) of the observation y_i. In the case of powder diffraction, $y_i^{\rm cal}$ represent the calculated counts as follows:

$$y_i^{\rm cal} = \sum_{\phi} S_\phi \sum_{\vec{q}} I_{\phi,\vec{q}}\, \Omega(x_i - x_{\phi,\vec{q}}) + y_i^{\rm b} \tag{A.2}$$

The index ϕ runs over all the different phases, nuclear or magnetic, present at the powder with scale S_ϕ, the vector $\vec{q}$ labels a nuclear or magnetic Bragg reflection ($\vec{q} = \vec{H}$ or $\vec{q} = \vec{H} \pm \vec{K}$), $\Omega(x_i - x_{\phi,\vec{q}})$ is the peak-shape normalized function centered at the Bragg position $\vec{q}$ of phase ϕ, which includes the instrumental and sample microstructural effects, and $I_{\phi,\vec{q}}$ is the intensity of that Bragg reflection, which includes the modulus squared either of the nuclear structure factor $|N_{\vec{q}}|^2$ (Eq. 2.17) or the magnetic interaction vector $|\vec{M}_{\perp\vec{q}}|^2$ (Eq. 2.29), among other different corrections, such as asymmetry, transmission, preferred orientation, efficiencies, etc. The background is represented by $y_i^{\rm b}$.

The Rietveld method needs an initial, nuclear and/or magnetic, structural model as input. The model is used for the calculations of the nuclear structure factor (atomic coordinates, occupancies, Debye-Waller factors) or the magnetic interaction vector (magnetic atomic moments). The Bragg positions $x_{\phi,\vec{q}}$ are a function of the unit cell $(a, b, c, \alpha, \beta, \gamma)$.

In the case of single-crystal diffraction or polarized neutron diffraction experiments, the histogram counts y correspond to the square of the structure factor G^2 or to the flipping ratio R, respectively.

A.1 Agreement factors

The quality of the agreement between observed and calculated profiles can be measured by a set of conventional factors, such as:

Profile factor:

$$R = \frac{\sum_i |y_i - y_i^{\mathrm{cal}}|}{\sum_i y_i} \tag{A.3}$$

Weighted profile factor:

$$R_w = \left[\frac{\sum_i w_i |y_i - y_i^{\mathrm{cal}}|^2}{\sum_i w_i y_i^2}\right]^{1/2} \tag{A.4}$$

Chi-square:

$$\chi^2 = \sum_i w_i |y_i - y_i^{\mathrm{cal}}|^2 \tag{A.5}$$

The Bragg factor R_{Bragg} has the same expression as Eq. (A.3), but the sum is restricted to those points where there are Bragg contributions. The magnetic R-factor is defined as R_{Bragg} but is applied to magnetic intensities.

Appendix B

Magnetic crystallography

Recalling Eq. (2.28), Eq. (2.29) and Eq. (2.30), it is clear that the determination of the magnetic structure of a known crystalline solid is solely based on finding the quantities $\vec{K}$ and $\vec{S}_{\vec{K}d_{\mathrm{m}}}$, from which the magnetic moment of any atom within the crystal can be calculated through Eq. (2.27). The initial step involves experimentally identifying the propagation vector $\vec{K}$, typically achieved through powder neutron diffraction techniques. By precisely indexing the magnetic peaks, we are able to generate the magnetic lattice and subsequently determine the propagation vector. The measurement of intensities of magnetic peaks presents us with a series of non-linear equations, with the unknowns represented by the Fourier coefficients $\vec{S}_{\vec{K}d_{\mathrm{m}}}$, as outlined in Eq. (2.28) and Eq. (2.30).

In order to facilitate the analysis, the number of free independent parameters can be further reduced by taking into account the whole symmetry of the crystal structure. Consequently, the following sections will address the symmetry analysis concerning both commensurate and incommensurate magnetic structures.

B.1 Representation analysis

The principal method that has been used until recently for determining magnetic structures is the representation analysis (RA) [2–8]. The widespread adoption of RA can be attributed to two principal factors: firstly, its adaptability to both commensurate and incommensurate structures, as it offers a general method independent of the spin order complexity. Secondly, the early development of numerous software tools played a crucial role in facilitating the calculations involved in this method, thereby enhancing its accessibility and efficiency in practical applications.

B.1.1 Mathematical background

A representation of any group $\mathcal{G}$ is a mapping of the elements of $\mathcal{G}$ to a set of $n \times n$ matrices, $\Gamma = \{\Gamma(g)|g \in \mathcal{G}\}$, which have the same group structure under the abstract representation space in which the matrices are embedded, called the dimension of the representation. Two matrices are equivalent if there is a similar matrix multiplication. The number n is the dimension of the change of basis between

them, U, which is common to all matrices: $\Gamma'(g) = U\,\Gamma(g)\,U^{-1}$. A group can have an infinite number of representations of arbitrary dimension. Therefore, we can find an appropriate similarity transformation U to reduce the representation to block-diagonal form:

$$\Gamma = \sum_{\oplus\nu} n_\nu \Gamma^\nu = n_1\Gamma^1 \oplus n_2\Gamma^2 \oplus \cdots \oplus n_m\Gamma^m \tag{B.1}$$

If the dimensions of representations Γ^ν are the smallest possible, the sub-matrices for the different group elements are called irreducible representations (*irreps*). Since the *irreps* cannot be separated into smaller pieces, they offer the building blocks to construct almost any magnetic structure.

B.1.2 Landau theory

The efficacy of *RA* becomes more apparent when contextualized within the framework of Landau theory, which addresses symmetry-breaking structural phase transitions. Landau theory postulates that such transitions result from the condensation (the shift from a zero to a non-zero amplitude) of one or more collective degrees of freedom. These degrees of freedom transform in accordance with a single irreducible representation (*irrep*) of the space group of the high-symmetry phase, $\mathcal{G}_0$, referred to as the 'active *irrep*'. Therefore, applying *RA* enables the identification of the specific *irreps* that play a significant role in the phase transition, thus providing a deeper understanding of the symmetry changes and the emergent properties of the system in its low-symmetry phase.

B.1.3 Experimental steps

When performing real experiments, the usual steps followed for the determination of a magnetic structure using *RA* are:

1. Determine the propagation vector $\vec{K}$, crystallographic space group ($\mathcal{G}_0$) and positions of the magnetic atoms.

2. The *irreps* of $\mathcal{G}_0$ can be calculated (or obtained from tables) from the *irreps* of the "little group of $\vec{K}$", $\mathcal{G}_{\vec{K}}$, which is a subgroup of $\mathcal{G}_0$ constituted by the elements of $\mathcal{G}_0$ leaving the propagation vector $\vec{K}$ invariant. The *irreps* of $\mathcal{G}_{\vec{K}}$ are called "small representations".

3. The magnetic representation, Γ_{mag}, is a set of matrices given by the direct product:

$$\Gamma_{\text{mag}} = \tilde{V} \otimes \Gamma_{\text{perm}} \tag{B.2}$$

where $\tilde{V}$ is an axial representation describing the transformation of the magnetic moments and Γ_{perm} is a permutation representation describing the exchange of the atomic positions under the symmetry operations of $\mathcal{G}_{\vec{K}}$.

4. Decompose the magnetic representation into the sum of *irreps* of $\mathcal{G}_{\vec{K}}$.

5. The Fourier coefficients $\vec{S}_{\vec{K}d_{\mathrm{m}}}$ can be written as a linear combination of the *irreps* basis vectors:

$$\vec{S}_{\vec{K}d_{\mathrm{m}}} = \sum_{n\lambda} C_{n\lambda}^{\vec{K}\nu}\, \psi_{n\lambda}^{\vec{K}\nu}(d_{\mathrm{m}}) \tag{B.3}$$

   where ν labels the active *irrep* of $\mathcal{G}_{\vec{K}}$ and λ the component corresponding to the dimension of the *irrep*. The index n varies between one and the number of times Γ^{ν} is contained in the magnetic representation Γ_{mag} (see Eq. (B.1)). Therefore there will be $\lambda \cdot n$ basis vectors.

6. For each *irrep* Γ^{ν} appearing in the decomposition of Γ_{mag}, calculate its basis vectors $\psi_{n\lambda}^{\vec{K}\nu}(d_{\mathrm{m}})$ by hand (projector operator formula [9]) or using computing programs. The coefficients $C_{n\lambda}^{\vec{K}\nu}$, called "mixing coefficients", are the free parameters of the magnetic structure and have to be determined experimentally. Usually the number of such coefficients is much lower than the total number of Fourier components without considering symmetry.

B.2 Magnetic space groups (Shubnikov groups)

Another method for reducing the number of free parameters in commensurate magnetic structures is the theory of magnetic space groups [10, 11].

The basis of this approach is to include the symmetry invariance of the magnetic spins to the 230 space groups describing the position of atoms. For this purpose a new symmetry operator is introduced: the spin reversal operator $1'$, also called time reversal operator. It acts only on magnetic moments (axial vectors) as: $1'\vec{m} = -\vec{m}$, and can be combined with a symmetry operator $\hat{g}$ to form a new primed operator $\hat{g}'$. Since the $1'$ operator is sometimes associated with a color change (black to white or black to red), the magnetic symmetry theory is also termed black-white symmetry.

By combining the spin reversal group $\mathcal{R} = \{1, 1'\}$ with the 230 space groups $\mathcal{G}$, the 1651 magnetic space groups (or Shubnikov groups) are obtained. They can be classified into four types:

1. Type 1, or monochrome groups, corresponding to the original 230 space groups: $\mathcal{M} = \mathcal{G}$. No primed operators exist in these groups.

2. Type 2, or grey groups or paramagnetic groups, corresponding to the 230 space groups plus the product of spin reversal by all operators of the group: $\mathcal{M} = \mathcal{G} + \mathcal{G}1'$. These groups have twice the number of operators of the corresponding space group. They can only describe paramagnetic ordering because the operator $1'$ is always present and the only solution to the equation $1'\vec{m} = \vec{m}$ for an atom at whatever position is $\vec{m} = \vec{0}$.

3. Type 3, or black and white of first species (BW1); they are constructed from an equi-translational non-magnetic subgroup $\mathcal{H}$ containing half the elements

of the parent crystallographic group $\mathcal{G}$, so that $\mathcal{M} = \mathcal{H} + (\mathcal{G} - \mathcal{H})\,1'$. These groups have exactly half of their operators that are primed. Their corresponding point group (determining the macroscopic physical properties) is a colored group. There are 674 BW1 groups.

4. Type 4, or black and white of second species (BW2). As for type 3, $\mathcal{M} = \mathcal{H} + (\mathcal{G} - \mathcal{H})\,1'$, but now $\mathcal{H}$ contains anti-translations leading to primitive magnetic cells larger than primitive crystal cells: these groups have then a colored lattice. There are 517 BW2 groups.

Two different notations exist for describing the magnetic space groups: OG for Opechowski–Guccione [12] and BNS for Belov–Neronova–Smirnova [10]. They are identical, except for the black and white magnetic space groups of second species (type 4). However, the fact that only in 2010 a database with both notations OG and BNS was published, together with this method being only applicable to commensurate structures, made it less preferred than the *RA* approach.

B.3 Magnetic superspace group formalism

Recently, the magnetic space group approach has been fully generalized to include incommensurate structures beyond the 1651 Shubnikov groups [13–15].

In this general formalism, the magnetic structure is described by a basic structure, related to the nuclear paramagnetic cell, in addition to a series of d-magnetic modulation functions with propagation vector $\vec{k}_i$, and its n-harmonics, that describes the variation from the basic structure of the magnetic moments. These modulations are given by additional internal coordinates x_{3+i} $(i = 1, 2...d)$, one for each propagation vector, where $x_{3+i} = (\vec{k}_i \cdot \vec{r}_{lj})$ and $\vec{r}_{lj}$ represents the position of atom j in the l-th unit cell. The most general expression for the modulation functions can be written as a general real Fourier series:

$$\begin{aligned}\vec{M}_{lj}(x_4, x_5, ..., x_{3+d}) = \\ = \sum_{n_1=0}^{\infty} .. \sum_{n_d=0}^{\infty} \vec{M}_{j,\mathrm{s}}^{(n_1,...,n_d)} \sin(2\pi(n_1 x_4 + ... + n_d x_{3+d})) + \\ + \vec{M}_{j,\mathrm{c}}^{(n_1,...,n_d)} \cos(2\pi(n_1 x_4 + ... + n_d x_{3+d}))\end{aligned} \tag{B.4}$$

where implicitly the term $n = 0$ corresponds to a zero propagation vector and the other terms correspond to the incommensurate magnetic structure. If we consider only one propagation vector, then the magnetization $\vec{M}_{lj}$ can be expressed as:

$$\vec{M}_{lj}(x_4) = \vec{M}_{j,0} + \sum_{n=1}^{\infty} \left[\vec{M}_{j,\mathrm{s}}^{n} \sin(2\pi n x_4) + \vec{M}_{j,\mathrm{c}}^{n} \cos(2\pi n x_4) \right] \tag{B.5}$$

In most cases only one harmonic is considered, so that the sum is restricted to the first term $(n = 1)$:

$$\vec{M}_{lj} = \vec{M}_{j,0} + \vec{M}_{j,\mathrm{s}} \sin(2\pi x_4) + \vec{M}_{j,\mathrm{c}} \cos(2\pi x_4) \tag{B.6}$$

In order to take into account the invariance symmetry of a magnetic incommensurate structure, the operators belonging to a magnetic superspace group (MSSG) are formed by adding a translation of the internal coordinate x_4 to the operations of the magnetic space group of the basic structure. Adding this global phase translation of the modulation allows an additional type of structural transformation. This is possible because an arbitrary phase translation of the modulation in an incommensurate phase keeps the energy invariant, in the same way that arbitrary rotations, roto-inversions, translations and time reversal do.

If the *irrep* assigned to the magnetic order parameter is 1-D, there is a one-to-one correspondence between the MSSG associated to the magnetic phase and the *irrep*. Nevertheless, for multidimensional *irreps* several distinct MSSGs can be realized in the incommensurate phase depending on the direction taken by the order parameter within the representation space. Therefore, the superspace symmetry is, in general, more restrictive and more comprehensive, as the assignment of a given *irrep* is clearly insufficient to specify the symmetry of the incommensurate phase.

This formalism has been very recently implemented in the FullProf Suite [16], in combination with the ISODISTORT SUITE [17, 18] to allow for the refinement of neutron diffraction data.

Appendix C

Computational model

In order to provide a physical model which can explain the data obtained from experiments in large-scale facilities, a code has been developed in both Matlab (The Mathworks, Natick, MA, USA) and Python [19] programming languages. The reasons behind choosing those languages are: easy syntax, very efficient algorithms already developed, extensive and very flexible visualization capabilities, and availability for many different platforms.

The two main purposes of the code are: 1) simulating the magnetic diffraction pattern of exotic magnetic structures, such as incommensurate helices or skyrmions, and 2) simulating and fitting the internal field produced by these structures. By comparing the computed results with the experimental ones, we can check the validity of the proposed magnetic models.

Figure C.1 shows the working diagram of the code. First, a text file containing all the variables needed for the calculations is given to the program. Once this file is read, the experimental setup, nuclear structure and magnetic structure are defined. The last two objects allow the creation of a magnetic model. Depending on the goal of the code execution, additional variables can be read to obtain a SANS pattern, μSR spectrum, or both. If we are interested in the magnetic diffraction pattern, the incident neutron beam polarization should be given, while for the asymmetry signal calculation the muon implantation site is the variable needed. By combining these variables with the ones defined in the experimental setup and with the magnetic model, both the magnetic structure factor and the local field at the muon site are calculated. The next steps in the calculations allow to obtain the neutron scattered intensity and the asymmetry signal for a magnetic model. In the last block the experimental data is read and compared with the calculated one, so that a fitting of the data is possible by varying the variables of the magnetic model and experimental setup.

In the following sections, we describe the working of the several subroutines present.

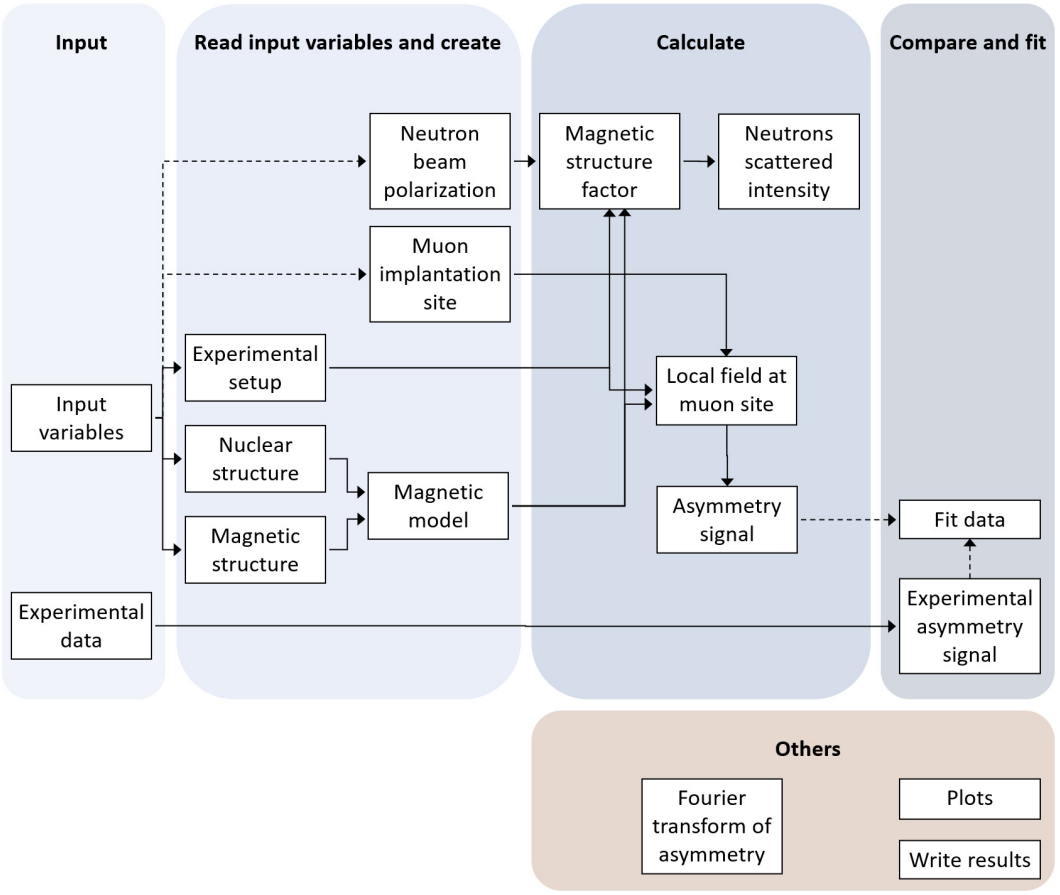

Figure C.1: Code working diagram. The broken lines indicate optional processes.

C.1 Experimental setup

The first step is to define the experiment geometry, which allow for the determination of the relative orientation of the applied magnetic field.

If we are simulating SANS experiments, the geometry assumed is the same as for $\vec{B} \perp \vec{k}_i$ in Section 2.3.5: neutron beam along X-axis, Y-axis corresponds with vertical direction, Z-axis is determined by applying the right-hand rule, detector in YZ-plane. The orientation of the external magnetic field is a variable which should be parallel to Z in the for $\vec{B} \perp \vec{k}_i$ configuration, while in the $\vec{B} \parallel \vec{k}_i$ geometry a rotation matrix can be applied to $\vec{B}$ and to the crystal system so that it lies along X. In the case of simulating μSR experiments, the geometry assumed is the same as in Section 2.5.2: the magnetic field is assumed to be applied along the Z-axis, while the initial muon polarization $\vec{i}_\mu$ is parallel to either the X or Z-axis depending on the setup: TF or LF/ZF, respectively. The muon beam is assumed to travel in the Z-direction. A summary of the different configurations is shown in Fig. C.2.

The orientation of the crystal relative to the experimental axes is given by specifying the variables $\vec{X}_{\text{exp}}$, $\vec{Z}_{\text{exp}}$ in terms of the crystallographic lattice basis. The Y-axis is calculated as $\vec{Y}_{\text{exp}} = \vec{Z}_{\text{exp}} \times \vec{X}_{\text{exp}}$, so that we can construct the transformation matrix $\hat{U}$ from the crystal frame to the experimental frame:

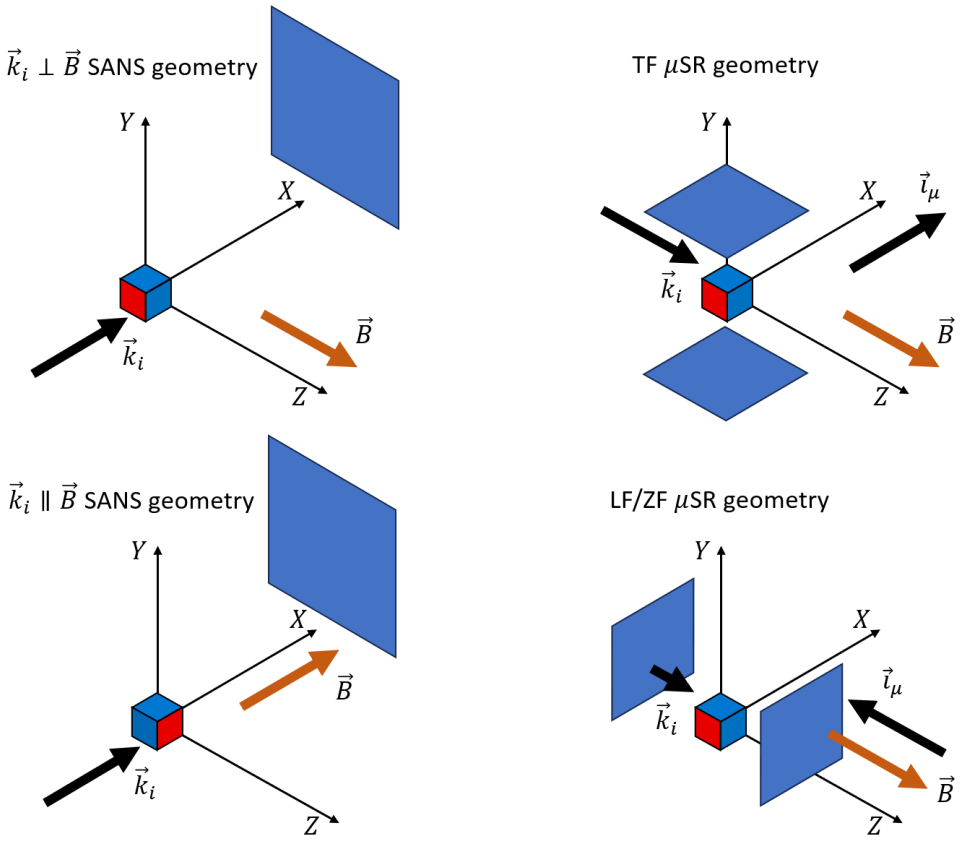

Figure C.2: Summary of the experimental geometries assumed for the simulations.

$$\hat{U} = \begin{pmatrix} X^1_{\text{exp}} & X^2_{\text{exp}} & X^3_{\text{exp}} \\ Y^1_{\text{exp}} & Y^2_{\text{exp}} & Y^3_{\text{exp}} \\ Z^1_{\text{exp}} & Z^2_{\text{exp}} & Z^3_{\text{exp}} \end{pmatrix} \Longrightarrow \hat{U}\vec{X}_{\text{exp}} = \begin{pmatrix} \vec{X}_{\text{exp}} \cdot \vec{X}_{\text{exp}} \\ \vec{Y}_{\text{exp}} \cdot \vec{X}_{\text{exp}} \\ \vec{Z}_{\text{exp}} \cdot \vec{X}_{\text{exp}} \end{pmatrix} = \begin{pmatrix} 1 \\ 0 \\ 0 \end{pmatrix} \tag{C.1}$$

C.2 Nuclear structure

This code is based on the assumption that the nuclear structure of the magnetic system under study is well-known. First, the lattice parameters ($a_\text{l}, b_\text{l}, c_\text{l}$ in Å and α, β, γ in degrees) are given as input variables. Next, for each species of atoms, only one position in fractional coordinates is needed. The whole content of the unit cell is created by applying the symmetry operations of the paramagnetic space group. Finally, the fractional coordinates $\vec{f}$ are converted to Cartesian coordinates $\vec{r}$ by the transformation matrix $\hat{M}$ [20, 21]:

$$\hat{M} = \begin{pmatrix} a_\text{l} & b_\text{l}\cos\gamma & c_\text{l}\cos\beta \\ 0 & b_\text{l}\sin\gamma & c_\text{l}\cot\gamma\cos\beta - c_\text{l}\csc\gamma\cos\alpha \\ 0 & 0 & c_\text{l}\sin(\beta)\sqrt{1-(\cot\gamma\cot\beta - \csc\gamma\csc\beta\cos\alpha)^2} \end{pmatrix} \tag{C.2}$$

C.3 Magnetic structure

The general expression of the Fourier coefficient for the atom d_{m} can be explicitly given by:

$$\vec{S}_{\vec{K}d_{\mathrm{m}}} = \frac{1}{2}\left(\vec{R}_{\vec{K}d_{\mathrm{m}}} + i\vec{I}_{\vec{K}d_{\mathrm{m}}}\right) e^{-i\phi_{\vec{K}d_{\mathrm{m}}}} \tag{C.3}$$

Hence, six real parameters define the $\vec{S}_{\vec{K}d_{\mathrm{m}}}$ vectors. The phase factor $\phi_{\vec{K}d_{\mathrm{m}}}$ is not generally needed, but it is convenient to use it when particular constraints between $\vec{R}_{\vec{K}d_{\mathrm{m}}}$ and $\vec{I}_{\vec{K}d_{\mathrm{m}}}$ are given.

Introducing this expression in Eq. (2.27), we obtain:

$$\begin{aligned}\vec{M}_{ld_{\mathrm{m}}} &= \\ &= \sum_{\langle\vec{K}\rangle}\left[\vec{R}_{\vec{K}d_{\mathrm{m}}}\cos\left(\vec{K}\cdot\vec{R}_l + \phi_{\vec{K}d_{\mathrm{m}}}\right) + \vec{I}_{\vec{K}d_{\mathrm{m}}}\sin\left(\vec{K}\cdot\vec{R}_l + \phi_{\vec{K}d_{\mathrm{m}}}\right)\right]\end{aligned} \tag{C.4}$$

where the sum is now over the total number of pairs $\vec{K}$, $-\vec{K}$ and their harmonics.

In the particular case of helical magnetic order, there is only a single pair $\vec{K}$, $-\vec{K}$, while the components of the Fourier coefficients are orthogonal: $\vec{R}_{\vec{K}d_{\mathrm{m}}}\cdot\vec{I}_{\vec{K}d_{\mathrm{m}}} = 0$. If $\vec{K}$ is perpendicular to the plane ($\vec{R}_{\vec{K}d_{\mathrm{m}}}$, $\vec{I}_{\vec{K}d_{\mathrm{m}}}$), the magnetic structure corresponds to a classical helix, while if $\vec{K}$ is within the ($\vec{R}_{\vec{K}d_{\mathrm{m}}}$, $\vec{I}_{\vec{K}d_{\mathrm{m}}}$) plane, the structure is called a cycloid. The helical magnetic structure can be generalized to the case of a conical magnetic order by including:

$$\begin{aligned}\vec{M}_{ld_{\mathrm{m}}} &= \\ &= \left[\vec{R}_{d_{\mathrm{m}}}\cos\left(\vec{K}\cdot\vec{R}_l + \phi_{d_{\mathrm{m}}}\right) \pm \vec{I}_{d_{\mathrm{m}}}\sin\left(\vec{K}\cdot\vec{R}_l + \phi_{d_{\mathrm{m}}}\right)\right]\cos\alpha + \vec{S}_{\vec{0}d_{\mathrm{m}}}\sin\alpha\end{aligned} \tag{C.5}$$

where α is the half-cone angle ($\alpha = 0$: helix, $\alpha < 1$: conical, $\alpha = 1$: ferromagnetic order, and $\vec{S}_{\vec{0}d_{\mathrm{m}}}$ is the Fourier coefficient which corresponds to a null propagation vector $\vec{K} = (0\,0\,0)$. The sign describes the structure helicity, + being for right-handed and − for left-handed ones.

Therefore, to create the magnetic structure it is enough to give the propagation vector $\vec{K}$ (in $\mathrm{\AA}^{-1}/2\pi$ units) and Fourier coefficients $\vec{S}_{\vec{K}d_{\mathrm{m}}}$ (in μ_{B} units) as input variables. The last variable needed is the number of unit cells N_{c} to be created along the Cartesian coordinates axes. The position of the magnetic atoms is then given by:

$$\vec{R}_{ld_{\mathrm{m}}} = \vec{R}_l + \vec{r}_{d_{\mathrm{m}}} = \hat{M}\begin{pmatrix} a_i - 1 \\ b_i - 1 \\ c_i - 1 \end{pmatrix} + \hat{M}\vec{f}_{d_{\mathrm{m}}} \tag{C.6}$$

where a_i, b_i, c_i are loop variables which take integer values from 1 to N_{c}. The positions of the atoms inside the unit cell $\vec{r}_{d_{\mathrm{m}}}$ are read from the nuclear structure.

C.4 Calculation of the SANS pattern

Once the magnetic structure has been created, we can proceed to calculate its SANS patter. The additional input variables needed in this subroutine are the initial neutron beam polarization $\vec{P}_i$ and the area of the detector we want to cover. Considering the typical SANS approximation, the scattering vector is given by Eq. (2.50), so the detector area is fully described by providing the range of q_Y and q_Z and the step Δq (in $\text{Å}^{-1}/2\pi$ units).

The next step is calculating the magnetic structure factor at the values of the scattering vector $\vec{q}$ corresponding to the detector area. By making Eq. (2.48) discrete we obtain:

$$\vec{M}_{\vec{q}} = \sum_{l,\, d_\text{m}} \vec{M}_{l d_\text{m}}\, e^{i\vec{q}\cdot\vec{R}_{l d_\text{m}}} \tag{C.7}$$

Here we have omitted the Debye-Waller factor $T_{d_\text{m}}(\vec{q})$ for simplicity, as it only contributes to the damping of the intensity. Next the magnetic interaction vector is calculated:

$$\vec{V}_{\vec{q}} = p\left[\hat{q}\times\vec{M}_{\vec{q}}\times\hat{q}\right] = p\left[\vec{M}_{\vec{q}} - \hat{q}\left(\hat{q}\cdot\vec{M}_{\vec{q}}\right)\right] \tag{C.8}$$

$p = 0.2695\cdot 10^{-14}$ m$/\mu_\text{B}$ is a conversion constant in which we have included the approximation for the atomic magnetic form factor $F_{d_\text{m}}(\vec{q}) \simeq 1$, which is true along the forward direction ($q_X = 0$).

In case is needed, the nuclear structure factor can also be computed as:

$$W_{\vec{q}} = \sum_{l,\, d} b_d\, e^{i\vec{q}\cdot\vec{R}_{ld}} \tag{C.9}$$

The scattering lengths of the atoms at sites d should be given as input variables.

Finally, the scattered intensity and final polarization of the scattered beam are calculated from Eq. (2.33) and Eq. (2.33). The scattered intensity in Eq. (2.33) can be further divided into the non-spin flip and spin flip components:

$$I_{\vec{q}} = I_{\vec{q}}^{\text{NSF}} + I_{\vec{q}}^{\text{SF}} \tag{C.10}$$

$$I_{\vec{q}}^{\text{NSF}} = W_{\vec{q}} W_{\vec{q}}^{*} + \vec{V}_{\vec{q}\parallel}\cdot\vec{V}_{\vec{q}\parallel}^{*} + \left(W_{\vec{q}}\vec{V}_{\vec{q}}^{*} + \vec{V}_{\vec{q}} W_{\vec{q}}^{*}\right)\cdot\vec{P}_i \tag{C.11}$$

$$I_{\vec{q}}^{\text{SF}} = \vec{V}_{\vec{q}\perp}\cdot\vec{V}_{\vec{q}\perp}^{*} - \text{i}\left(\vec{V}_{\vec{q}}\times\vec{V}_{\vec{q}}^{*}\right)\cdot\vec{P}_i \tag{C.12}$$

where $\vec{V}_{\vec{q}\parallel}$ and $\vec{V}_{\vec{q}\perp}$ are the components of the magnetic interaction vector parallel and perpendicular to the direction of the polarization vector: $\hat{P}_i = \vec{P}_i/|\vec{P}_i|$:

$$\vec{V}_{\vec{q}\parallel} = \left(\vec{V}_{\vec{q}}\cdot\hat{P}_i\right)\cdot\hat{P}_i \tag{C.13}$$

$$\vec{V}_{\vec{q}\perp} = \vec{V}_{\vec{q}} - \vec{V}_{\vec{q}\parallel} \tag{C.14}$$

C.5 Calculation of the μSR spectrum

The first input for this block is the muon implantation site. A similar procedure as for the atomic positions is followed, where only the fractional coordinates of one muon position are needed. The muon sites are then given by:

$$\vec{R}_{ld_\mu} = \vec{R}_l + \vec{r}_{d_\mu} = \hat{M} \begin{pmatrix} a_i - 1 \\ b_i - 1 \\ c_i - 1 \end{pmatrix} + \hat{M}\vec{f}_{d_\mu} \tag{C.15}$$

where a_i, b_i, c_i are the loop variables going through all unit cells and $\vec{f}_{d_\mu}$ are the fractional coordinates of a given muon site inside the unit cell.

Next the local magnetic field at a given muon site $\vec{B}_{\mathrm{loc},\, d_\mu}$ is computed according to Eq. (2.73) and Eq. (2.77), where each contribution is calculated as follows:

- The external field $\vec{B}_{\mathrm{ext}}$ is fully described by its modulus (in T) and orientation given as input variables.
- The hyperfine field $\vec{B}_{\mathrm{hyp}}$, from now on referred as contact field, is calculated following Eq.(2.76). To ensure that the sum is restricted to the nearest-neighbors to the muon site d_μ, the simulation considers only the magnetic atoms which fulfill the condition $|\vec{R}_{ld_\mu} - \vec{R}_{ld_\mathrm{m}}| \leq V_\mathrm{c}^{1/3}$, being V_c the unit cell volume. The contact field can be then expressed as:

$$\vec{B}_{\mathrm{hyp}} = \frac{\mu_0}{4\pi} \frac{n V_{\mathrm{mol}} A_{\mathrm{cont}}}{N' V_\mathrm{c}} \sum_{ld_\mathrm{m}}^{N'} \vec{M}_{ld_\mathrm{m}} = D \sum_{ld_\mathrm{m}}^{N'} \vec{M}_{ld_\mathrm{m}} \tag{C.16}$$

  where $\mu_0 = 4\pi \cdot 10^{-7}$ H/m $= 4\pi \cdot 9.274 \cdot 10^{-1}$ T·Å$^3/\mu_\mathrm{B}$. The Fermi contact field $\vec{B}_{\mathrm{Fermi}}$ is included into the isotropic contact coupling A_{cont}, which should be given as an input variable (in mol/emu units). V_{mol} refers to the volume of one mole of magnetic atoms, n is the number of magnetic atoms in a unit cell and N' is the number of magnetic atoms that satisfy $|\vec{R}_{ld_\mu} - \vec{R}_{ld_\mathrm{m}}| \leq V_\mathrm{c}^{1/3}$.
- The dipolar field $\vec{B}'_{\mathrm{dip}}$ and Lorentz field $\vec{B}_{\mathrm{Lor}}$ are adapted from Eq.(2.75) and Eq.(2.78):

$$\vec{B}'_{\mathrm{dip}} = \frac{\mu_0}{4\pi} \sum_{V_{\mathrm{Lor}}} \left[-\frac{\vec{M}_{ld_\mathrm{m}}}{r_i^3} + \frac{3(\vec{M}_{ld_\mathrm{m}} \cdot \vec{r}_i)\vec{r}_i}{r_i^5} \right] \tag{C.17}$$

$$\vec{B}_{\mathrm{Lor}} = \frac{\mu_0}{3} \sum_{V_{\mathrm{Lor}}} \frac{\vec{M}_{ld_\mathrm{m}}}{V_{\mathrm{Lor}}} \tag{C.18}$$

  where $\vec{r}_i = \vec{R}_{ld_\mu} - \vec{R}_{ld_\mathrm{m}}$. The sum is restricted to the magnetic moments inside the Lorentz sphere: $|\vec{R}_{ld_\mu} - \vec{R}_{ld_\mathrm{m}}| \leq V_{\mathrm{Lor}}^{1/3} = R_{\mathrm{Lor}}$. The Lorentz radius R_{Lor} should be given as an input variable (in Å).

- The demagnetization field $\vec{B}_{\rm dem}$ is calculated from Eq.(2.79):

$$\vec{B}_{\rm dem} = -\frac{\mu_0}{V_{\rm c}} \hat{N} \vec{M}_{\rm dem} \tag{C.19}$$

  $\vec{M}_{\rm dem}$ refers to the bulk magnetization (in $\mu_{\rm B}$/u.c. units), which can be given as an input variable or can be calculated from the magnetic structure as the magnetic moment contribution parallel to the external field. The demagnetization tensor should be given as an input variable.

Once the local field is calculated, the polarization function $P_\alpha(t)$ is obtained via Eq.(2.62).

C.5.1 Simplification

The brackets in Eq.(2.62) indicate that an average should be performed over $M(t)$, which in a brute force approach implies that the local field should be calculated at each muon site d_μ in every unit cell l. As an example, in a small cube of length $N = 20$ unit cells with 4 magnetic atoms per unit cell, the number of times that $\vec{B}'_{\rm dip}$ and $\vec{B}_{\rm Lor}$ are calculated is $4 \cdot 20^3 = 32000$. Furthermore, in a large enough Lorentz sphere (suppose $R_{\rm Lor} = 90\,$Å), the number of magnetic moments involved in calculating each field can be of the order of 120000. Nevertheless, the number of calculations can be greatly decreased by taking into account the symmetry of the magnetic structure, as it is shown next for the particular case of a conical structure.

Suppose we have already calculated the local field for a muon at $\vec{R}_{l,d_\mu}$. Eq.(C.17), Eq.(C.18) and Eq.(C.19) imply that $\vec{B}_{{\rm loc},\,d_\mu}$ depend on the magnetic moment at $\vec{R}_{l',d_{\rm m}}$, which can be expressed as:

$$\vec{M}_{l',d_{\rm m}} = \left[\vec{m}_{{\rm c},m} \cos\left(\vec{K}\cdot\vec{R}_{l'} + \phi_m\right) \pm \vec{m}_{{\rm s},m} \sin\left(\vec{K}\cdot\vec{R}_{l'} + \phi_m\right)\right] + \vec{m}_{{\rm u},m} \tag{C.20}$$

where: $\vec{m}_{{\rm c},m} = \vec{R}_{d_{\rm m}} \cos\alpha$; $\vec{m}_{{\rm s},m} = \vec{I}_{d_{\rm m}} \cos\alpha$; $\vec{m}_{{\rm u},m} = \vec{S}_{\vec{0}d_{\rm m}} \sin\alpha$ and for simplicity we have abbreviated d_m to m. Now we should calculate the local field in all the other unit cells.

Let's consider another unit cell, so that the muon is now at $\vec{R}_{l+h,d_\mu} = \vec{R}_{l,d_\mu} + \vec{x}_h$. For a magnetic moment to contribute to the local field the same as before, its new position should be $\vec{R}_{l'+h,d_{\rm m}} = \vec{R}_{l+h,d_\mu} - \left(\vec{R}_{l,d_\mu} - \vec{R}_{l',d_{\rm m}}\right) = \vec{R}_{l',d_{\rm m}} + \vec{x}_h$. Therefore the magnetic moment at the new position is given by:

$$
\begin{aligned}
&\vec{M}_{l'+h,d_{\mathrm{m}}} = \\
&\quad = \left[\vec{m}_{\mathrm{c},m}\cos\left(\vec{K}\cdot\vec{R}_{l'+h}+\phi_m\right) \pm \vec{m}_{\mathrm{s},m}\sin\left(\vec{K}\cdot\vec{R}_{l'+h}+\phi_m\right)\right] + \vec{m}_{\mathrm{u},m} = \\
&\quad = \left[\vec{m}_{\mathrm{c},m}\cos\left(\vec{K}\cdot\vec{R}_{l'}+\vec{K}\cdot\vec{x}_h+\phi_m\right) \pm \vec{m}_{\mathrm{s},m}\sin\left(\vec{K}\cdot\vec{R}_{l'}+\vec{K}\cdot\vec{x}_h+\phi_m\right)\right] + \\
&\quad + \vec{m}_{\mathrm{u},m} = ... = \\
&\quad = \left[\vec{m}_{\mathrm{c},m}\cos\left(\vec{K}\cdot\vec{R}_{l'}+\phi_m\right) \pm \vec{m}_{\mathrm{s},m}\sin\left(\vec{K}\cdot\vec{R}_{l'}+\phi_m\right)\right]\cos\left(\vec{K}\cdot\vec{x}_h\right) - \\
&\quad - \left[\vec{m}_{\mathrm{c},m}\sin\left(\vec{K}\cdot\vec{R}_{l'}+\phi_m\right) \mp \vec{m}_{\mathrm{s},m}\cos\left(\vec{K}\cdot\vec{R}_{l'}+\phi_m\right)\right]\sin\left(\vec{K}\cdot\vec{x}_h\right) + \\
&\quad + \vec{m}_{\mathrm{u},m} = \\
&\quad = \vec{M}_{\mathrm{C}}\cos\left(\vec{K}\cdot\vec{x}_h\right) + \vec{M}_{\mathrm{S}}\sin\left(\vec{K}\cdot\vec{x}_h\right) + \vec{m}_{\mathrm{u},m}
\end{aligned}
\tag{C.21}
$$

Introducing this expression in the position dependent magnetic fields:

$$
\begin{aligned}
&\vec{B}_{\mathrm{dep}} = \vec{B}_{\mathrm{hyp}} + \vec{B}'_{\mathrm{dip}} + \vec{B}_{\mathrm{Lor}} = \\
&\quad = D\sum_{ld_{\mathrm{m}}}^{N'}\vec{M}_{l'+hd_{\mathrm{m}}} + \frac{\mu_0}{4\pi}\sum_{V_{\mathrm{Lor}}}\left[-\frac{\vec{M}_{l'+h,d_{\mathrm{m}}}}{r_i^3} + \frac{3(\vec{M}_{l'+h,d_{\mathrm{m}}}\cdot\vec{r}_i)\vec{r}_i}{r_i^5}\right] + \frac{\mu_0}{3}\sum_{V_{\mathrm{Lor}}}\frac{\vec{M}_{l'+hd_{\mathrm{m}}}}{V_{\mathrm{Lor}}} = \\
&\quad = \left[D\sum_{ld_{\mathrm{m}}}^{N'}\vec{M}_{\mathrm{C}} + \frac{\mu_0}{4\pi}\sum_{V_{\mathrm{Lor}}}\left[-\frac{\vec{M}_{\mathrm{C}}}{r_i^3} + \frac{3(\vec{M}_{\mathrm{C}}\cdot\vec{r}_i)\vec{r}_i}{r_i^5}\right] + \frac{\mu_0}{3}\sum_{V_{\mathrm{Lor}}}\frac{\vec{M}_{\mathrm{C}}}{V_{\mathrm{Lor}}}\right]\cos\left(\vec{K}\cdot\vec{x}_h\right) + \\
&\quad + \left[D\sum_{ld_{\mathrm{m}}}^{N'}\vec{M}_{\mathrm{S}} + \frac{\mu_0}{4\pi}\sum_{V_{\mathrm{Lor}}}\left[-\frac{\vec{M}_{\mathrm{S}}}{r_i^3} + \frac{3(\vec{M}_{\mathrm{S}}\cdot\vec{r}_i)\vec{r}_i}{r_i^5}\right] + \frac{\mu_0}{3}\sum_{V_{\mathrm{Lor}}}\frac{\vec{M}_{\mathrm{S}}}{V_{\mathrm{Lor}}}\right]\sin\left(\vec{K}\cdot\vec{x}_h\right) + \\
&\quad + \left[D\sum_{ld_{\mathrm{m}}}^{N'}\vec{m}_{\mathrm{u},m} + \frac{\mu_0}{4\pi}\sum_{V_{\mathrm{Lor}}}\left[-\frac{\vec{m}_{\mathrm{u},m}}{r_i^3} + \frac{3(\vec{m}_{\mathrm{u},m}\cdot\vec{r}_i)\vec{r}_i}{r_i^5}\right] + \frac{\mu_0}{3}\sum_{V_{\mathrm{Lor}}}\frac{\vec{m}_{\mathrm{u},m}}{V_{\mathrm{Lor}}}\right] = \\
&\quad = \vec{B}_{\mathrm{dep,C}}\cos\left(\vec{K}\cdot\vec{x}_h\right) + \vec{B}_{\mathrm{dep,S}}\sin\left(\vec{K}\cdot\vec{x}_h\right) + \vec{B}_{\mathrm{dep,U}}
\end{aligned}
\tag{C.22}
$$

where $\vec{r}_i = \vec{R}_{l+h,d_\mu} - \vec{R}_{l'+h,d_{\mathrm{m}}} = \vec{R}_{ld_\mu} - \vec{R}_{l'd_{\mathrm{m}}}$. Eq.(C.22) implies that, once $\vec{B}_{\mathrm{dep,C}}$, $\vec{B}_{\mathrm{dep,S}}$ and $\vec{B}_{\mathrm{dep,U}}$ are calculated for a muon site in a given unit cell, the local field in all other unit cells can be obtained by simply multiplying by a cosine and sine factor. Furthermore, the argument of the cosine and sine functions $\vec{K}\cdot\vec{x}_h$ can be replaced by a continuous variable η, so that all the possible values of the local field in different unit cells are reproduced.

C.5.2 External field before sample

In the case of simulating TF spectra, there can be a small interval of time Δt before arriving to the sample in which the muon is only affected by the external field. In

such case, the muon polarization at the moment of implantation can be parametrized with the azimuthal angle φ_μ, given as an input variable (in π units):

$$\vec{i}_\mu = (\cos(\gamma_\mu B_{\text{ext}} \Delta t)\,,\ \sin(\gamma_\mu B_{\text{ext}} \Delta t)\,,\ 0) = (\cos\varphi_\mu,\ \sin\varphi_\mu,\ 0) \tag{C.23}$$

C.5.3 Background

In order to account for the muons stopping in the cryostat walls and other parts of the sample holder, a background signal can be added which is described as:

$$P_{\text{BG}}(t) = \cos(\gamma_\mu B_{\text{ext}} t + \varphi_\mu)\, e^{-\lambda_{\text{BG}} t} \tag{C.24}$$

So finally the experimental data can be compared with the computed signal:

$$A(t) = a_0 \left(P_\alpha(t) + s P_{\text{BG}}(t)\right) \tag{C.25}$$

where $a_0 = 0.26$ is the initial asymmetry and s accounts for the fraction of muons stopping outside the sample.

C.5.4 Fast Fourier transform

The Fourier transform of the asymmetry signal is done with the help of the FFT algorithm in Matlab [22]. By applying this algorithm, we can change from a signal dependent on discrete time $A(t_i)$ to one dependent on discrete magnetic fields $F(B_i)$. The change between the independent discrete variables is given by:

$$t_i = (i-1)\Delta_t \Rightarrow B_i = \frac{2\pi i}{\gamma_\mu L \Delta_t} \tag{C.26}$$

where $i = 1, 2, ..., L$, being $L \cdot \Delta_t$ the total length of time covered.

C.6 Fit to experimental data

Before fitting, the first step is to calculate the signal in Eq.(C.25) at the same values as the experimental time ones. Then the calculated signal is fitted to the experimental data using the *lsqnonlin* algorithm in Matlab [23], used to solve nonlinear least-squares problems. For our code the Levenberg-Marquardt method was applied.

Appendix D

SANS intensity in the *B-Phase*

The symmetry analysis of MnSi allows for a phase-shift ϕ_{d_m} between Mn orbits which is not fixed by symmetry. In order to determine its effect on the scattered intensity of a SANS experiment, we start from Eq.(2.27). If we consider either a helical, conical or FM phase, we can express the magnetic moment of the d-th atom inside the l-th unit cell as:

$$\vec{M}_{ld_\mathrm{m}} = \sum_{\{\vec{K}\}} \vec{S}_{\vec{K}d_\mathrm{m}} \mathrm{e}^{-\mathrm{i}\vec{K}\cdot\vec{R}_l} = \vec{S}_{\vec{K}d_\mathrm{m}} \mathrm{e}^{-\mathrm{i}\vec{K}\cdot\vec{R}_l} + \vec{S}_{-\vec{K}d_\mathrm{m}} \mathrm{e}^{\mathrm{i}\vec{K}\cdot\vec{R}_l} + \vec{S}_{\vec{0}d_\mathrm{m}} \tag{D.1}$$

The Fourier coefficients can be defined such that the magnetic moments propagate in the same direction as the external field: $\vec{K} \parallel \vec{B}_\mathrm{ext}$,

$$\vec{S}_{\vec{K}d_\mathrm{m}} = \frac{m_\mathrm{h}}{2}\, e^{-i\phi_{d_\mathrm{m}}} \left(\vec{R}_{d_\mathrm{m}} + i\vec{I}_{d_\mathrm{m}}\right) \tag{D.2}$$

$$\vec{S}_{-\vec{K}d_\mathrm{m}} \equiv \left(\vec{S}_{\vec{K}d_\mathrm{m}}\right)^* = \frac{m_\mathrm{h}}{2}\, e^{i\phi_{d_\mathrm{m}}} \left(\vec{R}_{d_\mathrm{m}} - i\vec{I}_{d_\mathrm{m}}\right) \tag{D.3}$$

$$\vec{S}_{\vec{0}d_\mathrm{m}} = m_\mathrm{u}\, \hat{n} \tag{D.4}$$

where the triad of vectors: $\vec{R}_{d_\mathrm{m}} = \frac{1}{\sqrt{2}}\,(\bar{1},\, 1,\, 0)$, $\vec{I}_{d_\mathrm{m}} = \frac{1}{\sqrt{6}}\,(\bar{1},\, \bar{1},\, 2)$, $\hat{n} = \vec{K}/K = \frac{1}{\sqrt{3}}\,(1,\, 1,\, 1)$ form an orthonormal basis. m_h and m_u are the components of the Mn net magnetic moment m in the plane perpendicular and along the applied field, respectively. Furthermore, we know from the experimental magnetization curves that:

$$m_\mathrm{u} = \begin{cases} A\, B_\mathrm{ext} & \text{if } B_\mathrm{ext} < B_\mathrm{c2} \\ m & \text{if } B_\mathrm{ext} > B_\mathrm{c2} \end{cases} \tag{D.5}$$

which implies:

$$m^2 = m_\mathrm{h}^2 + m_\mathrm{u}^2 \Longrightarrow m_\mathrm{h} = \sqrt{m^2 - m_\mathrm{u}^2} = \begin{cases} \sqrt{m^2 - A^2\, B_\mathrm{ext}^2} & \text{if } B_\mathrm{ext} < B_\mathrm{c2} \\ 0 & \text{if } B_\mathrm{ext} > B_\mathrm{c2} \end{cases} \tag{D.6}$$

Now we can calculate the magnetic structure factor:

$$\vec{M}_{\vec{q}} = \sum_{l,\, d_\mathrm{m}} \vec{M}_{l d_\mathrm{m}}\, e^{i\vec{q}\cdot\vec{R}_{l d_\mathrm{m}}} = \sum_{l,\, d_\mathrm{m}} \left(\vec{S}_{\vec{K} d_\mathrm{m}} \mathrm{e}^{-\mathrm{i}\vec{K}\cdot\vec{R}_l} + \vec{S}_{-\vec{K} d_\mathrm{m}} \mathrm{e}^{\mathrm{i}\vec{K}\cdot\vec{R}_l} + \vec{S}_{\vec{0} d_\mathrm{m}} \right) e^{i\vec{q}\cdot\vec{R}_{l d_\mathrm{m}}} =$$
$$= \frac{N_\mathrm{c}(2\pi)^3}{V_\mathrm{c}} \left[\sum_{d_\mathrm{m}} \vec{S}_{\vec{K} d_\mathrm{m}}\, e^{i\vec{q}\cdot\vec{r}_{d_\mathrm{m}}}\, \delta_{\vec{q},\vec{K}} + \sum_{d_\mathrm{m}} \left(\vec{S}_{\vec{K} d_\mathrm{m}} \right)^*\, e^{i\vec{q}\cdot\vec{r}_{d_\mathrm{m}}}\, \delta_{\vec{q},-\vec{K}} + \sum_{d_\mathrm{m}} \vec{S}_{\vec{0} d_\mathrm{m}}\, e^{i\vec{q}\cdot\vec{r}_{d_\mathrm{m}}}\, \delta_{\vec{q},\vec{0}} \right] \tag{D.7}$$

Here we have omitted the Debye-Waller factor $T_{d_\mathrm{m}}(\vec{q})$ for simplicity, as it only contributes to the damping of the intensity. Then:

$$\vec{M}_{\vec{K}} = \frac{N_\mathrm{c}(2\pi)^3}{V_\mathrm{c}} \sum_{d_\mathrm{m}=1}^{4} \vec{S}_{\vec{K} d_\mathrm{m}}\, e^{i\vec{K}\cdot\vec{r}_{d_\mathrm{m}}} = \frac{N_\mathrm{c}(2\pi)^3}{V_\mathrm{c}} \frac{m_\mathrm{h}}{2} \left(\vec{R}_{d_\mathrm{m}} + i\vec{I}_{d_\mathrm{m}} \right) \sum_{d_\mathrm{m}=1}^{4} e^{-i\phi_{d_\mathrm{m}}}\, e^{i\vec{K}\cdot\vec{r}_{d_\mathrm{m}}} \tag{D.8}$$

$$\vec{M}_{-\vec{K}} = \frac{N_\mathrm{c}(2\pi)^3}{V_\mathrm{c}} \sum_{d_\mathrm{m}=1}^{4} \left(\vec{S}_{\vec{K} d_\mathrm{m}} \right)^*\, e^{-i\vec{K}\cdot\vec{r}_{d_\mathrm{m}}} = \frac{N_\mathrm{c}(2\pi)^3}{V_\mathrm{c}} \frac{m_\mathrm{h}}{2} \left(\vec{R}_{d_\mathrm{m}} - i\vec{I}_{d_\mathrm{m}} \right) \sum_{d_\mathrm{m}=1}^{4} e^{i\phi_{d_\mathrm{m}}}\, e^{-i\vec{K}\cdot\vec{r}_{d_\mathrm{m}}} \tag{D.9}$$

$$\vec{M}_{\vec{0}} = \frac{N_\mathrm{c}(2\pi)^3}{V_\mathrm{c}} \sum_{d_\mathrm{m}=1}^{4} \vec{S}_{\vec{0} d_\mathrm{m}} = 4 \frac{N_\mathrm{c}(2\pi)^3}{V_\mathrm{c}} m_\mathrm{u}\, \hat{n} \tag{D.10}$$

Next the magnetic interaction vector is calculated:

$$\vec{V}_{\vec{q}} = p \left[\hat{q} \times \vec{M}_{\vec{q}} \times \hat{q} \right] = p \left[\vec{M}_{\vec{q}} - \hat{q} \left(\hat{q} \cdot \vec{M}_{\vec{q}} \right) \right] \tag{D.11}$$

$p = 0.2695 \cdot 10^{-14}\ \mathrm{m}/\mu_\mathrm{B}$ is a conversion constant in which we have included the approximation for the atomic magnetic form factor $F_{d_\mathrm{m}}(\vec{q}) \simeq 1$, which is true along the forward direction ($q_x = 0$). It yields:

$$\vec{V}_{\vec{K}} = p \left[\vec{M}_{\vec{K}} - \hat{K} \left(\hat{K} \cdot \vec{M}_{\vec{K}} \right) \right] = p \left[\vec{M}_{\vec{K}} - \hat{n} \left(\hat{n} \cdot \vec{M}_{\vec{K}} \right) \right] = p \vec{M}_{\vec{K}} \tag{D.12}$$

$$\vec{V}_{-\vec{K}} = p \vec{M}_{-\vec{K}} \tag{D.13}$$

$$\vec{V}_{\vec{0}} = p \vec{M}_{\vec{0}} \tag{D.14}$$

Finally, we obtain the neutron scattered intensity, where we only consider the magnetic scattering:

$$I_{\vec{q}} = \vec{V}_{\vec{q}} \cdot \vec{V}^*_{\vec{q}} - \mathrm{i} \left(\vec{V}_{\vec{q}} \times \vec{V}^*_{\vec{q}} \right) \cdot \vec{P}_i \tag{D.15}$$

Thus:

$$I_{\vec{K}} = 2p^2 \left(\frac{N_{\rm c}(2\pi)^3}{V_{\rm c}} \frac{m_{\rm h}}{2} \right)^2 \sum_{d_{\rm m}=1}^{4} e^{-i\phi_{d_{\rm m}}} e^{i\vec{K}\cdot\vec{r}_{d_{\rm m}}} \sum_{d_{\rm m}=1}^{4} e^{i\phi_{d_{\rm m}}} e^{-i\vec{K}\cdot\vec{r}_{d_{\rm m}}} \left(1 - \hat{n}\cdot\vec{P}_i\right) \quad \text{(D.16)}$$

$$I_{-\vec{K}} = 2p^2 \left(\frac{N_{\rm c}(2\pi)^3}{V_{\rm c}} \frac{m_{\rm h}}{2} \right)^2 \sum_{d_{\rm m}=1}^{4} e^{i\phi_{d_{\rm m}}} e^{-i\vec{K}\cdot\vec{r}_{d_{\rm m}}} \sum_{d_{\rm m}=1}^{4} e^{-i\phi_{d_{\rm m}}} e^{i\vec{K}\cdot\vec{r}_{d_{\rm m}}} \left(1 + \hat{n}\cdot\vec{P}_i\right) \quad \text{(D.17)}$$

$$I_{\vec{0}} = p^2 \left(4\frac{N_{\rm c}(2\pi)^3}{V_{\rm c}} m_{\rm u} \right)^2 \quad \text{(D.18)}$$

From Eq.(D.16) and (D.17) is easy to observe that for unpolarized neutrons ($\vec{P}_i = \vec{0}$) the intensity will be the same for the two positions, while if the beam is fully polarized along the propagation vector, the intensity at $\vec{q} = \vec{K}$ will be zero (same for $\vec{P}_i \parallel -\hat{n}$, $\vec{q} = -\vec{K}$).

Now we can express the explicit dependence of the scattered intensity of the satellite peaks ($\vec{q} = \pm\vec{K}$) with the phase-shift $\phi_{d_{\rm m}}$. For comparison purposes, it is useful to first determine the intensity $I_{\vec{K},-\vec{K}}$ for $\phi_{d_{\rm m}} = 0$. In such case:

$$\begin{aligned} I_{\vec{K},-\vec{K}} &= 2p^2 \left(\frac{N_{\rm c}(2\pi)^3}{2V_{\rm c}} \right)^2 m_{\rm h}^2 \sum_{d_{\rm m}=1}^{4} e^{-i\phi_{d_{\rm m}}} e^{i\vec{K}\cdot\vec{r}_{d_{\rm m}}} \sum_{d_{\rm m}=1}^{4} e^{i\phi_{d_{\rm m}}} e^{-i\vec{K}\cdot\vec{r}_{d_{\rm m}}} = \\ &= C\, m_{\rm h}^2 \left(e^{i\vec{K}\cdot\vec{r}_1} + 3e^{i\vec{K}\cdot\vec{r}_2} \right) \left(e^{-i\vec{K}\cdot\vec{r}_1} + 3e^{-i\vec{K}\cdot\vec{r}_2} \right) = \\ &= C\, m_{\rm h}^2 \left[10 + 6\cos\left(\vec{K}\cdot(\vec{r}_1 - \vec{r}_2) \right) \right] = \\ &= C\, \left(m^2 - m_{\rm u}^2 \right) \left[10 + 6\cos\left(\vec{K}\cdot(\vec{r}_1 - \vec{r}_2) \right) \right] \end{aligned} \quad \text{(D.19)}$$

Here we have simplified by using $\vec{K}\cdot\vec{r}_2 = \vec{K}\cdot\vec{r}_3 = \vec{K}\cdot\vec{r}_4$, since the positions of atoms Mn2, Mn3 and Mn4 are all at the same height regarding the (111) plane. The specific parameters of MnSi yield: $\vec{K}\cdot(\vec{r}_1 - \vec{r}_2) = -0.1334$.

Now, considering the constraint imposed by the mΛ_3 representation, where $\phi_{d_{\rm m}}$ takes the values ϕ for Mn1 and 0 for the other sites:

$$\begin{aligned} I_{\vec{K},-\vec{K}} &= C\, m_{\rm h}^2 \sum_{d_{\rm m}=1}^{4} e^{-i\phi_{d_{\rm m}}} e^{i\vec{K}\cdot\vec{r}_{d_{\rm m}}} \sum_{d_{\rm m}=1}^{4} e^{i\phi_{d_{\rm m}}} e^{-i\vec{K}\cdot\vec{r}_{d_{\rm m}}} = \\ &= C\, m_{\rm h}^2 \left(e^{i(\delta+\vec{K}\cdot\vec{r}_1)} + 3e^{i\vec{K}\cdot\vec{r}_2} \right) \left(e^{-i(\delta+\vec{K}\cdot\vec{r}_1)} + 3e^{-i\vec{K}\cdot\vec{r}_2} \right) = \\ &= C\, \left(m^2 - m_{\rm u}^2 \right) \left[10 + 6\cos\left(\delta + \vec{K}\cdot(\vec{r}_1 - \vec{r}_2) \right) \right] \end{aligned} \quad \text{(D.20)}$$

Appendix E

Additional magnetization and SANS data of MnSi

Figure E.1(a) shows the isothermal magnetization $M(B)$ curves for magnetic fields applied along the $\langle 110 \rangle$ direction at temperatures from 2 to 35 K. Continuous ZFC $M(T)$ data are shown in Fig. E.1(b) for fields in the range 0.05 to 0.65 T applied along the $\langle 110 \rangle$ direction. Similar $M(B)$ and $M(T)$ curves for magnetic fields applied along the $\langle 100 \rangle$ direction are shown in Fig. E.1(c) and (d), respectively.

For crystal 1 measured at TAIKAN, SANS patterns were collected at 2 and 28 K with $\vec{B} \parallel \langle 111 \rangle \perp \vec{k}_i$, where the crystal was rotated from $\phi = 0°$: $\vec{k}_i \parallel \langle 1\bar{1}0 \rangle$ to $\phi = 90°$: $\vec{k}_i \parallel \langle 11\bar{2} \rangle$ in steps of 15° in the magnetic field range $0 \leq B \leq 0.7$ T with $\Delta B = 0.1$ T (see Fig. E.2). Figure E.3(a) shows the SANS patterns at zero field and 2 K with $\phi = 0°$ and $\phi = 60°$, where helices propagating along two of the four $\langle 111 \rangle$ axes can be observed, plus additional diffraction peaks resulting from multiple scattering. The integrated intensities, obtained following the same integration procedure as detailed in the main text, for all ϕ values measured at 2 and 28 K are displayed in Fig. E.3(b).

Additional SANS patterns were collected at 2 K with $\vec{B} \parallel \langle 111 \rangle \perp \vec{k}_i \parallel \langle 1\bar{1}0 \rangle$ in the magnetic field range $0 \leq B \leq 0.75$ T with $\Delta B = 0.03$ T. The integrated intensities measured at 2 K in such configuration are displayed in Fig. E.4.

For crystal 2 measured at TAIKAN, SANS patterns were collected in 2022 at 3, 5, 15 and 28 K with $\vec{B} \parallel \langle 111 \rangle \perp \vec{k}_i$ in the magnetic field range $0 \leq B \leq 0.75$ T with $\Delta B = 0.05$ T (see Fig. E.5). Additional measurements were taken in 2024 at 2 K with $\vec{B} \parallel \langle 111 \rangle \perp \vec{k}_i$ in the magnetic field range $0 \leq B \leq 0.7$ T with $\Delta B = 0.02$ T. In this case, a second cycle was measured with increasing magnetic field after the conventional increasing – decreasing field cycle. A comparison between the SANS patterns collected at the first and second cycle with increasing field is displayed in Fig. E.6. The integrated intensities for all temperatures measured in 2022 and 2024 with $\vec{B} \parallel \langle 111 \rangle \perp \vec{k}_i$ are displayed in Fig. E.7(a) and (b), respectively.

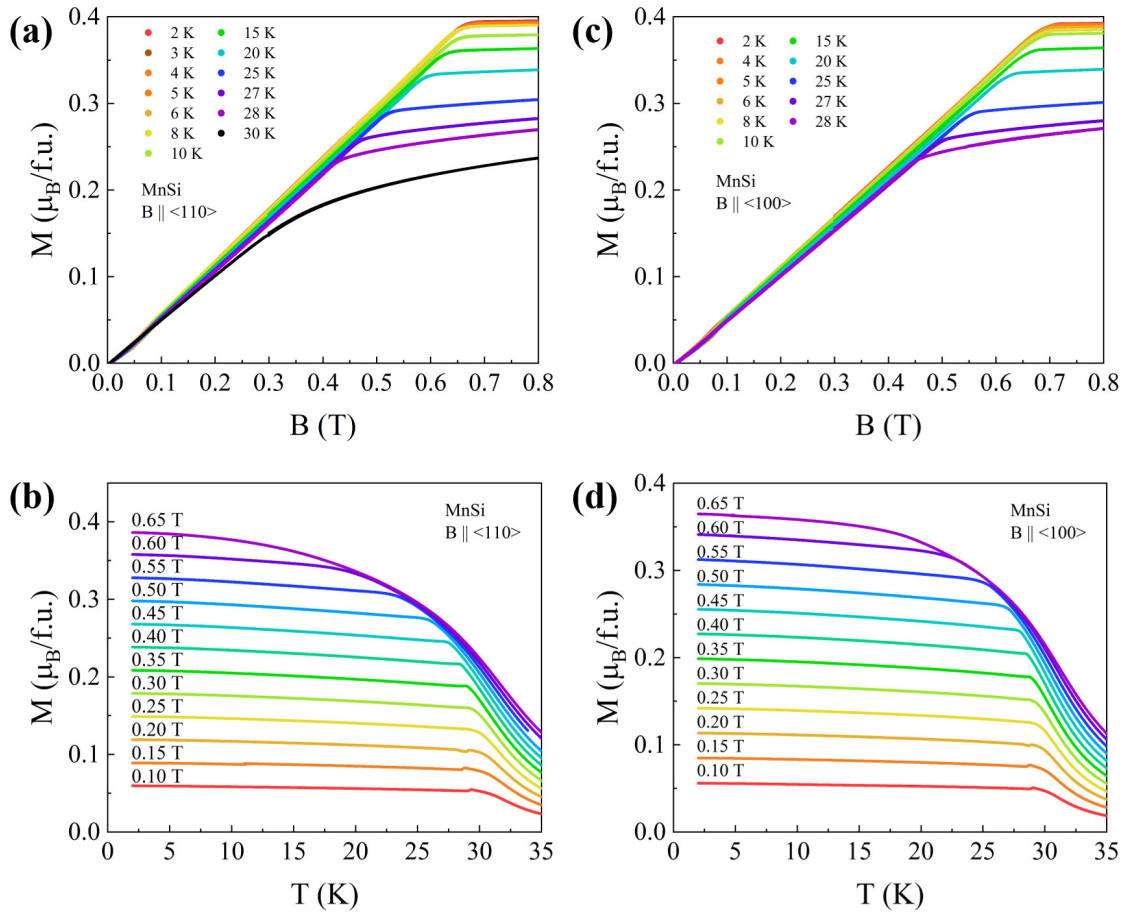

Figure E.1: Isothermal magnetization $M(B)$ curves (a) and temperature dependence of the magnetization $M(T)$ (b) of MnSi for magnetic fields applied along the $\langle 110 \rangle$ direction. $M(B)$ (c) and $M(T)$ (d) curves of MnSi for magnetic fields applied along the $\langle 100 \rangle$ direction.

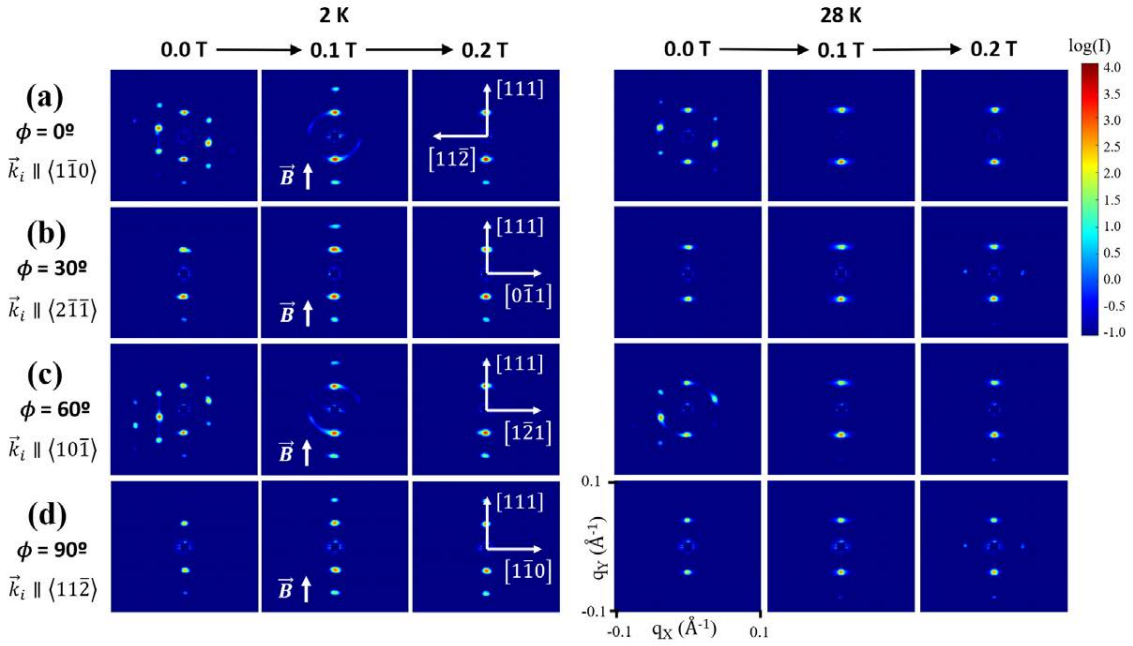

Figure E.2: SANS patterns of crystal 1 of MnSi obtained for different magnetic fields at 2 K and 28 K with $\phi = 0°$: $\vec{k}_i \parallel \langle 1\bar{1}0\rangle$ (a), $\phi = 30°$: $\vec{k}_i \parallel \langle 2\bar{1}\bar{1}\rangle$ (b), $\phi = 60°$: $\vec{k}_i \parallel \langle 10\bar{1}\rangle$ (c) and $\phi = 90°$: $\vec{k}_i \parallel \langle 11\bar{2}\rangle$ (d). The scattered intensity is plotted in logarithmic scale. The crystallographic directions present in the detector plane for each configuration are shown in (a) and (b).

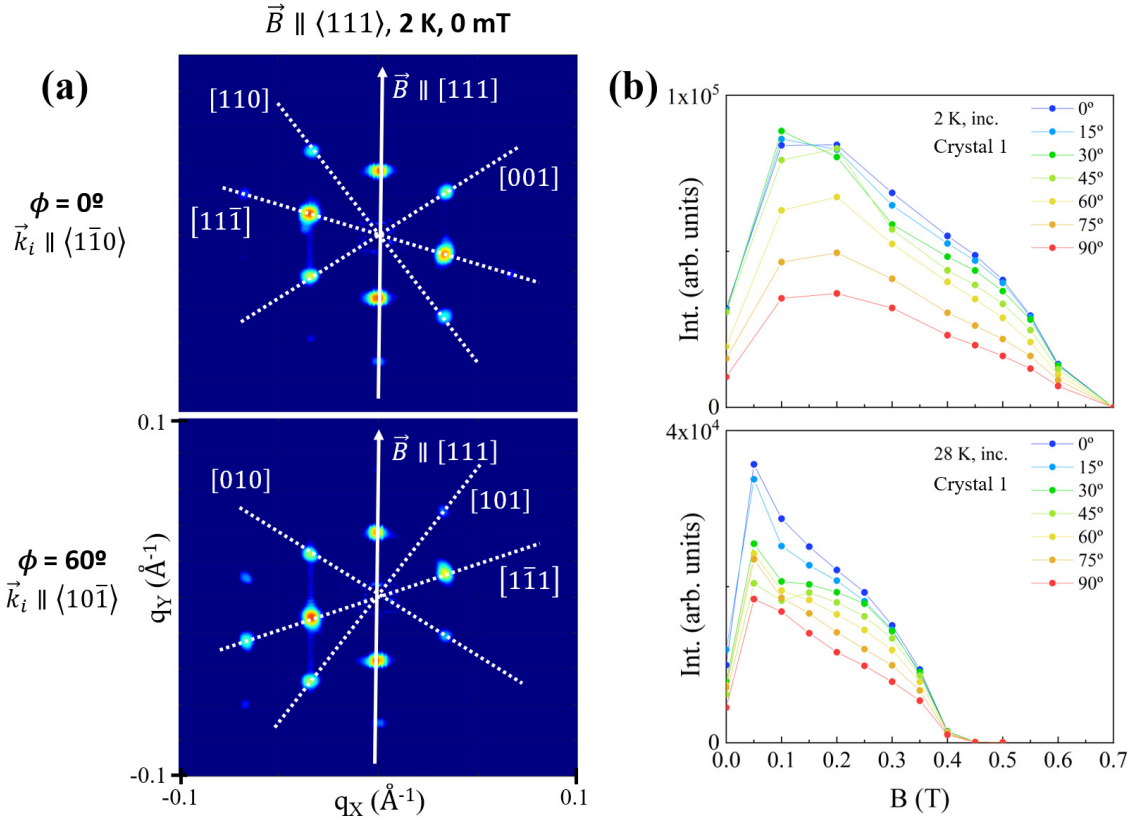

Figure E.3: (a) SANS patterns of crystal 1 of MnSi at 2 K, 0.0 T with $\phi = 0°$: $\vec{k}_i \parallel \langle 1\bar{1}0\rangle$ and $\phi = 60°$: $\vec{k}_i \parallel \langle 10\bar{1}\rangle$. (b) Integrated intensity at 2 K and 28 K as a function of the magnetic field and the angle ϕ.

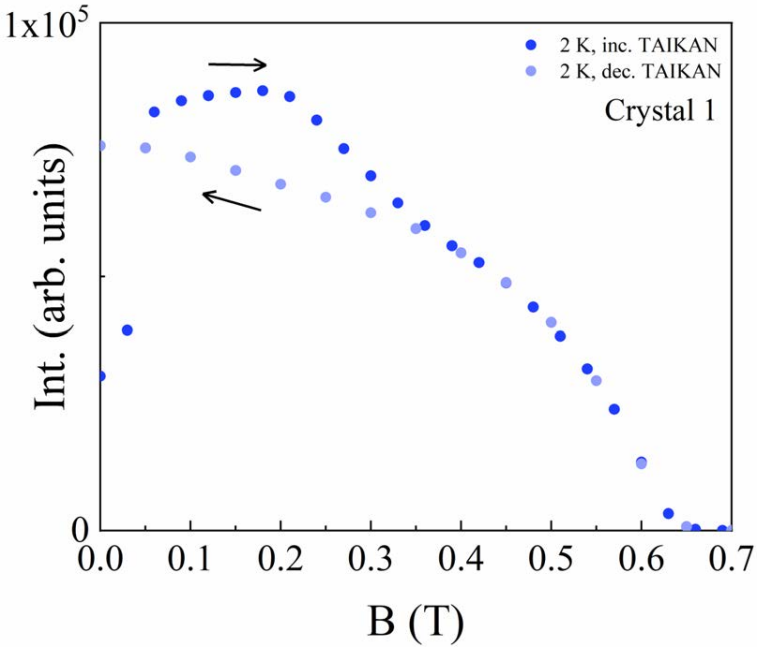

Figure E.4: Evolution of the integrated intensity of crystal 1 of MnSi at 2 K with magnetic field for $\vec{B} \parallel \langle 111 \rangle \perp \vec{k}_i \parallel \langle 1\bar{1}0 \rangle$.

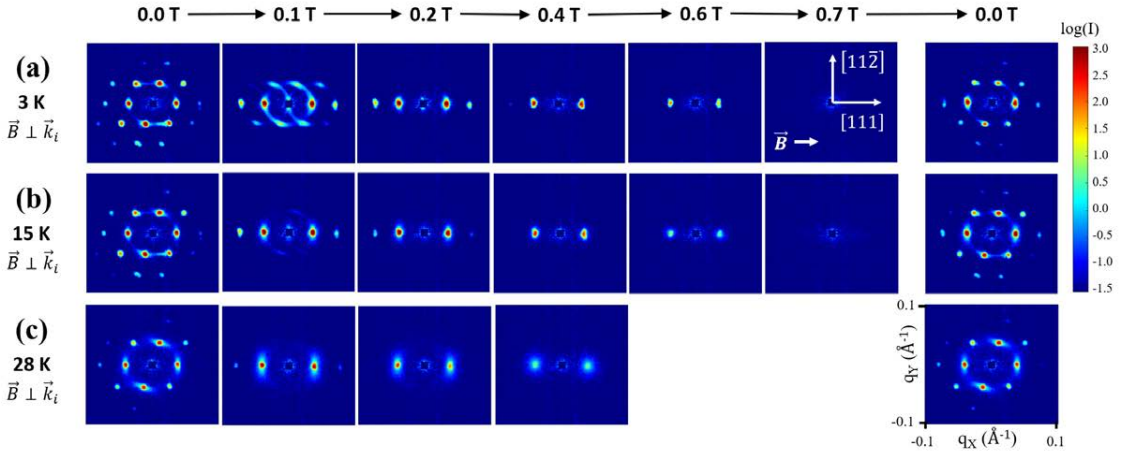

Figure E.5: SANS patterns of crystal 2 of MnSi obtained for different magnetic fields at 3 K (a), 15 K (b) and 28 K (c), in the $\vec{B} \parallel \langle 111 \rangle \perp \vec{k}_i$ configuration. The scattered intensity is plotted in logarithmic scale. The crystallographic directions present in the detector plane for each configuration are shown in (a).

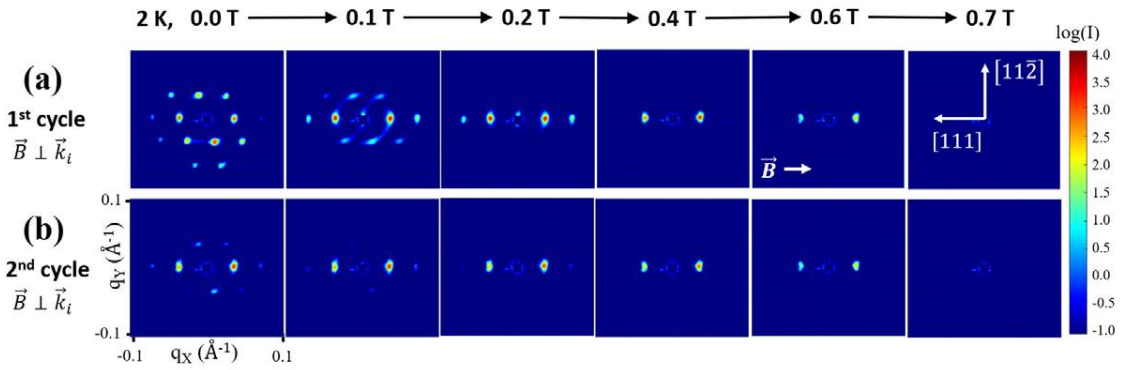

Figure E.6: SANS patterns of crystal 2 of MnSi obtained for different magnetic fields at 2 K following the first (a) and second cycle (b) with increasing magnetic field in the $\vec{B} \parallel \langle 111 \rangle \perp \vec{k}_i$ configuration. The scattered intensity is plotted in logarithmic scale. The crystallographic directions present in the detector plane for each configuration are shown in (a).

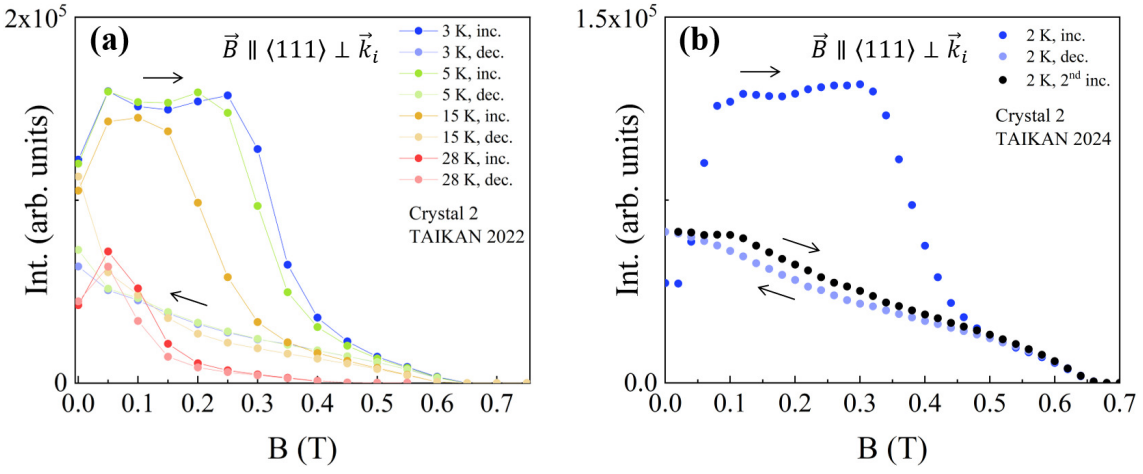

Figure E.7: Evolution of the integrated intensity of crystal 2 of MnSi with magnetic field and temperature for the $\vec{B} \parallel \langle 111 \rangle \perp \vec{k}_i$ configuration in 2022 (a) and 2024 (b).

Appendix F

Additional magnetization data of $Fe_{0.75}Co_{0.25}Si$

Figure F.1(a) shows the isothermal magnetization $M(B)$ curves for magnetic fields applied along the $\langle 110 \rangle$ direction at temperatures from 2 to 40 K. Continuous ZFC $M(T)$ data are shown in Fig. F.1(b) for fields in the range 0.025 to 0.2 T applied along the $\langle 110 \rangle$ direction.

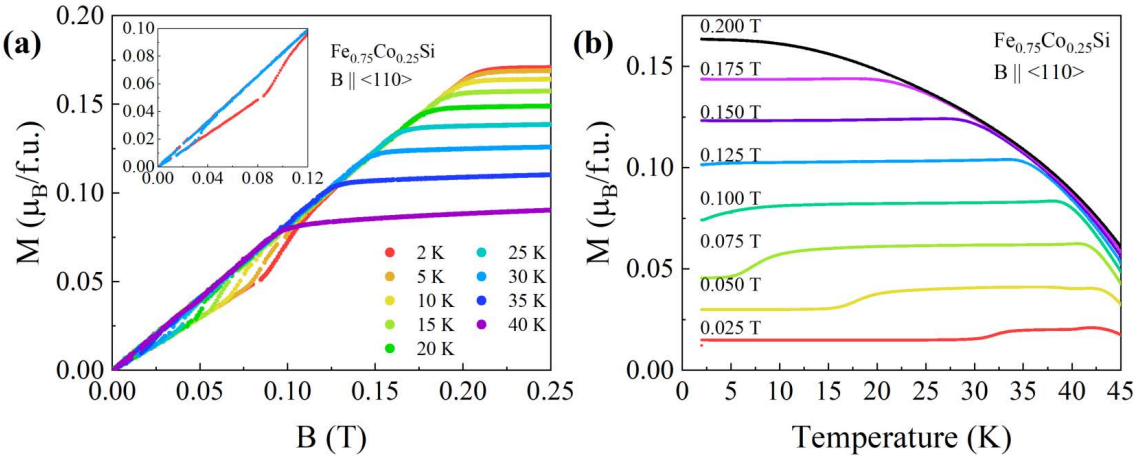

Figure F.1: (a) Isothermal magnetization $M(B)$ curves of $Fe_{0.75}Co_{0.25}Si$ for magnetic fields applied along the $\langle 110 \rangle$ direction. The inset shows the low field data for increasing and decreasing field at 2 and 30 K. (b) Temperature dependence of the magnetization of $Fe_{0.75}Co_{0.25}Si$ for magnetic fields applied along the $\langle 110 \rangle$ direction.

Figure F.2(a) shows the B dependence of m' at 1.8 K with $\vec{B}$ along $\langle 110 \rangle$ for the ZFC and FC procedures. The zoomed region where the anomaly is observed at 1.8 K and 5 K is shown in panel (b) of Fig. F.2. The panels (c) and (d) of Fig. F.2 display the B dependence of m' between 10 and 25 K and between 30 and 44 K, respectively, with $\vec{B}$ along $\langle 110 \rangle$.

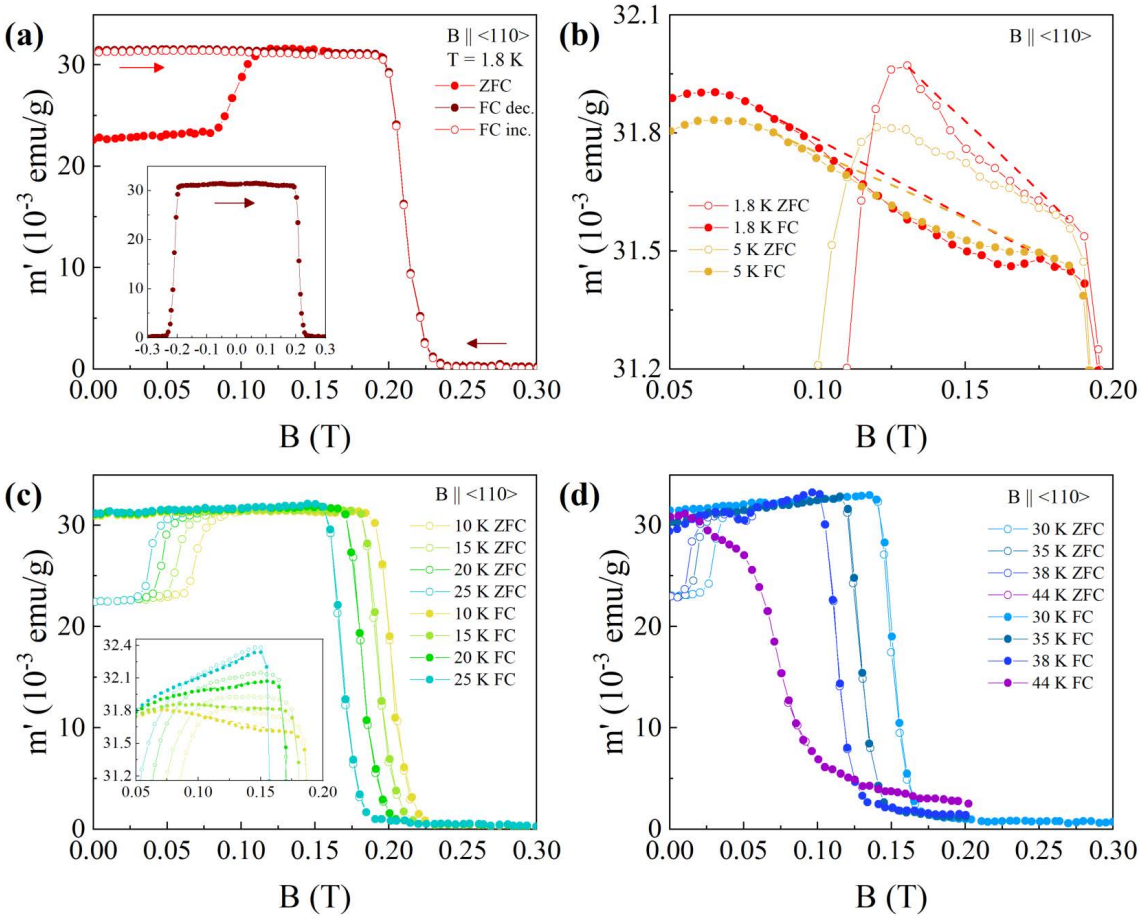

Figure F.2: (a) Comparison between the m' curve measured at 1.8 K on $Fe_{0.75}Co_{0.25}Si$ by increasing field with a ZFC procedure (filled red circles) and the m' curves recorded with decreasing (filled dark red circles) and increasing (empty red circles) B_{dc} from $-0.3 \rightarrow 0 \rightarrow 0.3$ T. The inset shows the full magnetic field cycle. (c) B dependence of m' between 10 and 25 K for $\vec{B} \parallel \langle 110 \rangle$ measured with ZFC and FC procedures. The inset shows the zoomed region where the anomaly is observed. (d) B dependence of m' between 30 and 44 K for $\vec{B} \parallel \langle 110 \rangle$ measured with ZFC and FC procedures.

Appendix G

Nuclear structure of 4-F-2-NN-BIP

Table G.1: Fractional coordinates and isotropic thermal parameters for the 4-F-2-NN-BIP asymmetric unit at 25 K.

Atom	x	y	z	B_{ISO}
F1	0.31143(12)	0.92623(13)	0.34962(5)	–
O1	0.21966(14)	0.46198(15)	0.53229(6)	–
O2	0.19129(15)	0.95972(15)	0.62037(7)	–
N1	0.18539(15)	0.57518(18)	0.56878(7)	–
N2	0.17064(16)	0.81250(19)	0.60969(7)	–
C6	0.32346(18)	0.7773(2)	0.51889(9)	–
C7	0.22745(18)	0.7243(2)	0.56512(8)	–
C8	0.10894(19)	0.5493(2)	0.62809(9)	–
C9	0.52052(18)	0.6900(2)	0.60261(8)	–
C10	0.46430(19)	0.7527(2)	0.53567(9)	–
C11	0.27075(19)	0.8381(2)	0.45647(9)	–
H1	0.1751	0.8561	0.4454	0.026
C12	0.55190(19)	0.7894(2)	0.48780(9)	–
H2	0.6479	0.7733	0.4984	0.025
C13	-0.0078(2)	0.4353(2)	0.60900(10)	–
H3	-0.0667	0.4754	0.5697	0.038
H4	-0.0618	0.4239	0.6467	0.038
H5	0.0296	0.3329	0.5983	0.038
C14	0.59847(19)	0.5530(2)	0.60743(9)	–
H6	0.6147	0.4978	0.5680	0.025
C15	0.63190(19)	0.5781(2)	0.72843(9)	–
H7	0.6714	0.5408	0.7711	0.026
C16	0.49714(19)	0.7687(2)	0.66096(9)	–
H8	0.4422	0.8609	0.6580	0.026
C17	0.50141(19)	0.8488(2)	0.42530(9)	–
H9	0.5614	0.8733	0.3930	0.027
C18	0.55369(19)	0.7132(2)	0.72360(9)	–
H10	0.5384	0.7685	0.7632	0.026
C19	0.65250(18)	0.4974(2)	0.67052(9)	–
H11	0.7042	0.4027	0.6739	0.026
C20	0.06568(19)	0.7208(2)	0.64204(9)	–
C21	0.3620(2)	0.8714(2)	0.41118(9)	–
C22	0.2133(2)	0.4780(3)	0.68223(10)	–
H12	0.2471	0.3785	0.6660	0.045
H13	0.1695	0.4588	0.7228	0.045
H14	0.2903	0.5507	0.6927	0.045
C23	-0.0733(2)	0.7677(2)	0.60466(12)	–
H15	-0.0866	0.8811	0.6092	0.047
H16	-0.1464	0.7114	0.6238	0.047
H17	-0.0761	0.7406	0.5570	0.047
C24	0.0746(3)	0.7644(3)	0.71557(10)	–
H18	0.1671	0.7414	0.7378	0.055
H19	0.0072	0.7033	0.7368	0.055
H20	0.0554	0.8767	0.7197	0.055

Table G.2: Anisotropic thermal factors for the 4-F-2-NN-BIP asymmetric unit at 25 K.

Atom	β_{11}	β_{22}	β_{33}	β_{12}	β_{13}	β_{23}
F1	0.0283(6)	0.0317(7)	0.0202(5)	0.0047(4)	-0.0009(5)	-0.0001(5)
O1	0.0234(7)	0.0240(7)	0.0269(7)	-0.0034(5)	0.0027(5)	0.0009(5)
O2	0.0251(7)	0.0228(7)	0.0332(7)	-0.0074(5)	0.0046(6)	-0.0028(6)
N1	0.0169(8)	0.0230(8)	0.0196(7)	-0.0003(6)	0.0009(6)	0.0010(6)
N2	0.0163(8)	0.0247(9)	0.0243(7)	-0.0027(6)	0.0022(6)	-0.0013(6)
C6	0.0163(9)	0.0206(9)	0.0211(8)	-0.0011(7)	0.0022(7)	0.0002(7)
C7	0.0150(8)	0.0225(9)	0.0191(8)	-0.0002(7)	-0.0011(6)	-0.0004(7)
C8	0.0185(9)	0.0292(10)	0.0187(8)	0.0014(7)	0.0021(7)	-0.0017(7)
C9	0.0135(8)	0.0229(9)	0.0210(8)	0.0006(7)	0.0009(6)	-0.0022(7)
C10	0.0180(9)	0.0194(9)	0.0202(8)	-0.0016(7)	0.0012(7)	-0.0002(7)
C11	0.0188(9)	0.0223(9)	0.0223(8)	-0.0010(7)	-0.0003(7)	0.0010(7)
C12	0.0175(9)	0.0205(9)	0.0246(9)	-0.0022(7)	0.0027(7)	-0.0013(7)
C13	0.0196(10)	0.0286(10)	0.0279(9)	0.0028(7)	0.0012(7)	-0.0046(7)
C14	0.0170(9)	0.0231(9)	0.0226(9)	-0.0005(7)	0.0030(7)	-0.0017(7)
C15	0.0176(9)	0.0265(10)	0.0209(8)	0.0042(7)	0.0000(7)	-0.0034(7)
C16	0.0158(9)	0.0244(10)	0.0237(9)	-0.0002(7)	0.0021(7)	0.0001(7)
C17	0.0222(9)	0.0215(9)	0.0251(9)	-0.0009(7)	0.0041(7)	-0.0012(7)
C18	0.0171(9)	0.0262(10)	0.0204(8)	0.0000(7)	0.0021(7)	-0.0031(7)
C19	0.0178(9)	0.0202(9)	0.0269(9)	0.0028(7)	0.0020(7)	0.0012(7)
C20	0.0173(9)	0.0299(11)	0.0268(9)	-0.0011(7)	0.0055(7)	-0.0024(7)
C21	0.0266(10)	0.0217(10)	0.0199(8)	0.0003(7)	-0.0020(7)	-0.0019(7)
C22	0.0205(10)	0.0409(12)	0.0265(9)	0.0066(8)	-0.0021(7)	-0.0031(8)
C23	0.0173(10)	0.0301(11)	0.0472(12)	-0.0013(9)	0.0047(9)	0.0010(8)
C24	0.0401(13)	0.0441(13)	0.0289(10)	-0.0067(9)	0.0145(9)	-0.0076(10)

Appendix H

Nuclear structure of $TNN{\cdot}CH_3CN$

Table H.1: Fractional coordinates for the TNN·CH_3CN asymmetric unit at 12 K.

Atom	x	y	z
O1	0.6401(07)	0.5407(07)	0.3709(07)
N1	0.5854(04)	0.5488(04)	0.4015(07)
N2	0.5377(04)	0.6057(04)	0.4594(07)
O2	0.5384(08)	0.6565(08)	0.4934(08)
C1	0.4719(06)	0.4776(06)	0.4029(07)
C2	0.4463(06)	0.5011(07)	0.4509(07)
C3	0.4272(07)	0.5085(07)	0.3647(08)
H1	0.4455(18)	0.5910(17)	0.3673(11)
H2	0.3458(16)	0.4591(17)	0.3620(09)
H3	0.4637(16)	0.5067(20)	0.3329(09)
C4	0.4455(06)	0.3668(06)	0.3961(07)
H4	0.3635(16)	0.3159(23)	0.3995(12)
H5	0.4792(16)	0.3389(14)	0.4228(09)
H6	0.4725(19)	0.3581(15)	0.3638(10)
C5	0.4482(08)	0.4312(07)	0.4877(07)
H7	0.5147(17)	0.4240(18)	0.4872(10)
H8	0.3808(16)	0.3576(16)	0.4865(10)
H9	0.4466(18)	0.4659(17)	0.5188(09)
C6	0.3473(07)	0.5067(07)	0.4532(07)
H10	0.3378(19)	0.5238(18)	0.4863(09)
H11	0.2849(14)	0.4314(17)	0.4449(11)
H12	0.3507(18)	0.5647(14)	0.4311(09)
C7	0.6169(06)	0.6271(05)	0.4312(07)
C8	0.7164(05)	0.7206(06)	0.4336(07)
C9	0.8024(08)	0.7299(07)	0.4090(07)
H13	0.7960(14)	0.6656(12)	0.3908(08)
C10	0.7293(06)	0.8074(06)	0.4560(07)
H14	0.6645(15)	0.8032(16)	0.4768(09)
C11	0.8948(06)	0.8205(06)	0.4088(07)
H15	0.9580(15)	0.8249(18)	0.3903(09)
C12	0.8226(06)	0.8991(06)	0.4553(07)
H16	0.8270(16)	0.9630(12)	0.4735(10)
C13	0.9058(05)	0.9054(06)	0.4322(08)
N3	0.0000(00)	0.0000(00)	0.4307(08)
N4	0.6667(00)	0.3333(00)	0.4769(08)
C14	0.6667(00)	0.3333(00)	0.4371(09)
C15	0.6667(00)	0.3333(00)	0.3897(08)
H17	0.6642(18)	0.4003(16)	0.3777(09)

Table H.2: Anisotropic thermal factors for the TNN·CH_3CN asymmetric unit at 12 K.

Atom	β_{11}	β_{22}	β_{33}	β_{12}	β_{13}	β_{23}
O1	0.00101(048)	0.00069(047)	0.00012(010)	0.00029(040)	0.00007(017)	-0.00005(017)
N1	0.00022(024)	0.00057(027)	0.00020(006)	0.00002(022)	0.00010(009)	0.00002(010)
N2	0.00030(027)	0.00030(027)	0.00024(006)	-0.00012(022)	-0.00016(010)	-0.00013(010)
O2	0.00118(050)	0.00077(051)	0.00012(010)	-0.00046(039)	0.00025(019)	-0.00013(018)
C1	0.00086(044)	0.00083(040)	0.00023(009)	0.00040(034)	0.00025(015)	0.00029(015)
C2	0.00054(040)	0.00089(042)	0.00030(008)	0.00010(035)	0.00035(015)	0.00003(015)
C3	0.00104(043)	0.00094(041)	0.00028(010)	0.00043(038)	-0.00005(015)	-0.00042(015)
H1	0.00446(134)	0.00304(118)	0.00108(028)	0.00254(112)	-0.00149(052)	-0.00014(048)
H2	0.00216(111)	0.00476(143)	0.00016(017)	-0.00103(093)	0.00036(032)	0.00046(040)
H3	0.00374(126)	0.00605(156)	0.00013(016)	0.00226(118)	-0.00033(035)	-0.00061(039)
C4	0.00099(043)	0.00099(043)	0.00013(008)	0.00036(036)	0.00007(015)	-0.00000(015)
H4	0.00058(102)	0.00673(195)	0.00126(037)	-0.00035(108)	-0.00001(047)	-0.00005(066)
H5	0.00485(124)	0.00274(104)	0.00045(022)	0.00234(103)	-0.00072(040)	0.00033(035)
H6	0.00544(156)	0.00085(094)	0.00077(026)	0.00099(102)	0.00063(049)	-0.00056(038)
C5	0.00237(055)	0.00116(044)	0.00025(010)	0.00047(040)	0.00050(019)	0.00028(016)
H7	0.00289(120)	0.00466(133)	0.00139(038)	0.00229(110)	-0.00080(052)	0.00109(055)
H8	0.00257(113)	0.00244(118)	0.00085(026)	-0.00150(085)	-0.00111(045)	0.00043(044)
H9	0.00540(139)	0.00359(126)	0.00057(023)	0.00361(120)	-0.00072(043)	-0.00020(041)
C6	0.00111(047)	0.00152(048)	0.00059(012)	0.00103(042)	0.00029(018)	0.00008(019)
H10	0.00574(155)	0.00459(140)	0.00008(019)	0.00242(129)	-0.00007(041)	-0.00033(039)
H11	0.00069(092)	0.00260(119)	0.00144(034)	0.00005(085)	0.00002(045)	-0.00038(047)
H12	0.00566(146)	0.00300(111)	0.00035(020)	0.00340(111)	-0.00074(040)	-0.00002(035)
C7	0.00111(039)	0.00078(033)	0.00017(007)	-0.00023(029)	0.00010(016)	0.00018(013)
C8	0.00044(037)	0.00109(041)	0.00014(006)	0.00049(030)	-0.00022(014)	-0.00020(014)
C9	0.00190(053)	0.00145(048)	0.00033(011)	0.00133(045)	0.00054(018)	0.00010(017)
H13	0.00309(100)	0.00075(073)	0.00041(016)	-0.00048(071)	-0.00002(029)	-0.00044(027)
C10	0.00023(035)	0.00057(037)	0.00014(078)	0.00009(031)	0.00012(012)	0.00012(013)
H14	0.00140(090)	0.00302(105)	0.00074(025)	0.00120(090)	0.00074(039)	-0.00011(040)
C11	0.00022(039)	0.00071(040)	0.00016(080)	0.00020(034)	-0.00016(015)	0.00000(014)
H15	0.00250(107)	0.00497(135)	0.00024(019)	0.00277(110)	0.00056(034)	0.00031(038)
C12	0.00008(036)	0.00019(038)	0.00026(009)	-0.00005(033)	0.00006(014)	-0.00013(015)
H16	0.00258(070)	0.00028(052)	0.00060(015)	-0.00061(052)	0.00077(026)	-0.00019(022)
C13	0.00019(038)	0.00112(046)	0.00021(006)	0.00005(027)	-0.00013(016)	-0.00021(016)
N3	0.00060(027)	0.00060(027)	0.00001(005)	0.00030(014)	0.00000(000)	0.00000(000)
N4	0.00244(045)	0.00244(045)	0.00047(011)	0.00122(023)	0.00000(000)	0.00000(000)
C14	0.00305(066)	0.00305(066)	0.00001(011)	0.00152(033)	0.00000(000)	0.00000(000)
C15	0.00390(083)	0.00390(083)	0.00005(012)	0.00195(042)	0.00000(000)	0.00000(000)
H17	0.00492(102)	0.00300(088)	0.00047(016)	0.00242(083)	0.00030(031)	-0.00007(030)

Bibliography

[1] H. M. Rietveld, "A profile refinement method for nuclear and magnetic structures," Journal of Applied Crystallography, vol. 2, pp. 65–71, jun 1969.

[2] E. F. Bertaut, "Representation analysis of magnetic structures," Acta Crystallographica Section A: Crystal Physics, Diffraction, Theoretical and General Crystallography, vol. 24, pp. 217–231, jan 1968.

[3] E. Bertaut, "Spin Configurations of Ionic Structures: Theory and Practice," in Spin Arrangements and Crystal Structure, Domains, and Micromagnetics, pp. 149–209, Elsevier, 1963.

[4] Y. Izyumov, V. Naish, and R. Ozerov, "Neutron Diffraction of Magnetic Materials," 1991.

[5] Y. Izyumov and V. Naish, "Symmetry analysis in neutron diffraction studies of magnetic structures: 1. A phase transition concept to describe magnetic structures in crystals," Journal of Magnetism and Magnetic Materials, vol. 12, pp. 239–248, aug 1979.

[6] Y. Izyumov, V. Naish, and V. Syromiatnikov, "Symmetry analysis in neutron diffraction studies of magnetic structures: 2. Changes in periodicity at magnetic phase transitions," Journal of Magnetism and Magnetic Materials, vol. 12, pp. 249–261, aug 1979.

[7] Y. Izyumov, V. Naish, and S. Petrov, "Symmetry analysis in neutron diffraction studies of magnetic structures: 3. An example: the magnetic structure of spinels," Journal of Magnetism and Magnetic Materials, vol. 13, pp. 267–274, nov 1979.

[8] Y. Izyumov, V. Naish, and S. Petrov, "Symmetry analysis in neutron diffraction studies of magnetic structures: 4. Theoretical group analysis of exchange Hamiltonian," Journal of Magnetism and Magnetic Materials, vol. 13, pp. 275–282, nov 1979.

[9] J. Rodríguez-Carvajal and F. Bourée, "Symmetry and magnetic structures," EPJ Web of Conferences, vol. 22, p. 00010, 2012.

[10] N. Belov, N. Neronova, and T. Smirnova Sov.Phys. Crystallogr., vol. 1, pp. 487–488, 1957.

[11] V. Koptsik, "Shubnikov groups," Handbook of Symmetry and Physical Properties of Crystal Structures, 1966.

[12] W. Opechowski, "Magnetic symmetry," Magnetism, 1965.

[13] A. Janner and T. Janssen, "Symmetry of incommensurate crystal phases. I. Commensurate basic structures," Acta Crystallographica Section A, vol. 36, pp. 399–408, may 1980.

[14] J. M. Perez-Mato, J. L. Ribeiro, V. Petricek, and M. I. Aroyo, "Magnetic superspace groups and symmetry constraints in incommensurate magnetic phases," Journal of Physics: Condensed Matter, vol. 24, p. 163201, mar 2012.

[15] J. Rodríguez-Carvajal and J. Villain, "Magnetic structures," Comptes Rendus Physique, vol. 20, pp. 770–802, nov 2019.

[16] J. Rodríguez-Carvajal, "Recent advances in magnetic structure determination by neutron powder diffraction," Physica B: Condensed Matter, vol. 192, no. 1, pp. 55 – 69, 1993.

[17] H. T. Stokes, D. M. Hatch, and B. J. Campbell, "ISODISTORT, ISOTROPY Software Suite," iso.byu.edu, 2017.

[18] B. J. Campbell, H. T. Stokes, D. E. Tanner, and D. M. Hatch, "ISODISPLACE: a web-based tool for exploring structural distortions," Journal of Applied Crystallography, vol. 39, pp. 607–614, jul 2006.

[19] M. S. Echeverría, "SANS and μSR studies of magnetic textures in chiral magnets," Master's thesis, Faculty of Science, University of Zaragoza, 2023.

[20] C. M. Duncan McKie, Essentials of crystallography. Oxford: Blackwell Scientific, 1986.

[21] C. Giacovazzo, Fundamentals of Crystallography. Oxford University Press, third ed., 2011.

[22] The MathWorks, Inc., "fft." `https://es.mathworks.com/help/matlab/ref/fft.html`.

[23] The MathWorks, Inc., "lsqnonlin." `https://es.mathworks.com/help/optim/ug/lsqnonlin.html`.